

Direct linking of host rock deformation structures to the emplacement, morphology and accommodation of high-level igneous intrusions: the Henry Mountains, Utah

by

Penelope Irene Rose WILSON

**This thesis is submitted in partial fulfilment of the degree of Doctor of Philosophy at
Kingston University, London.**

April 2015



Declaration

No part of this thesis has been previously submitted for a degree at this, or any other university. The work described in this thesis is entirely that of the author, except where reference is made to previously published work.

Penelope Wilson

School of Geography, Geology and the Environment,
Faculty of Science, Engineering and Computing,
Kingston University
April 2015

© Penelope Wilson

The copyright of this thesis rests with the author. No quotation or data from it should be published in any format, including electronic and the Internet, without the author's prior written consent. All information derived from this thesis must be acknowledged appropriately.

Abstract

Most studies of magmatic intrusions concentrate on geometry and internal architecture: only a few pay particular attention to emplacement-related deformation structures in the host rock that record how magma is accommodated within the crust. This research aims to develop a greater understanding of how igneous intrusive bodies are emplaced and accommodated within the shallow crust, using classic exposures found in the Henry Mountains, Utah. Two satellite intrusions to the Mt Hillers intrusive centre show highly contrasting geometries, host-rock deformation and accommodation structures and apparent emplacement mechanisms. Trachyte Mesa, the most distal satellite intrusion of Mt Hillers, has a relatively simple elongate (NW–SE) geometry, concordant with the Entrada Sandstone it intrudes. The intrusion is comprised of multiple, stacked intrusive sheets. Syn-emplacement deformation structures observed in the host rocks consist of a conjugate set of intrusion margin-parallel deformation bands and extensional brittle faults, the latter occurring at the tips of intrusive sheets. These structures, along with a post-emplacement set of intrusion margin parallel and perpendicular tensile joints, indicate extensional strain normal to the intrusion margin, consistent with a two-stage growth mechanism for individual sheets as well as the overall intrusion. In comparison, Maiden Creek shows a more complex intrusion geometry, including: lobate morphologies; steps and broken bridges; inclined sill sheets; and concave-upwards ‘laccolithic’ morphologies. A new model is proposed for the emplacement, evolution and final geometry of the intrusion, with a central elongate NE–SW lobe resulting from a principal north-easterly propagating magma flow. Lateral growth of the Maiden Creek intrusion resulted from radial spreading of magma from this main north-easterly flow trend towards the east and north-west. It is proposed that the southern Maiden Creek intrusion is comprised of two westerly-derived (saucer-shaped?) sills. Overlying these deeper-rooted sills is the newly identified Maiden Creek Shear Zone (MCSZ). This structure is an antithetic accommodation structure to magma flow. Substantial amounts of strain observed through microstructural analysis of shear zone samples suggest that the MCSZ played a critical role in accommodating magma emplacement. This study suggests that much can be learnt about intrusion geometries and emplacement mechanisms through detailed structural and kinematic analyses of the host rocks and intrusion–host rock contact.

*All the girls, all dance with the boys from the city
And they don't care to dance with me
Now it ain't my fault that the fields are muddy
And the red clay stains my feet*

*And it's under my nails and it's under my collar
And it shows on my Sunday clothes
Though I do my best with the soap and the water
But the damned old dirt won't go*

*But when I pass through the Pearly Gate
Will my gown be gold instead?
Or just a red clay robe with red clay wings
And a red clay halo for my head?*

*Now it's mud in the spring and it's dust in the summer
When it blows in a crimson tide
Until trees and leaves and the cows are the color
Of the dirt on the mountainside*

*But when I pass through the Pearly Gate
Will my gown be gold instead?
Or just a red clay robe with red clay wings
And a red clay halo for my head?*

*Now Jordan's banks, they're red and muddy
And the rolling water is wide
But I got no boat, so I'll be good and muddy
When I get to the other side*

*And when I pass through the Pearly Gate
Will my gown be gold instead?
Or just a red clay robe with red clay wings
And a red clay halo for my head?*

*I'll take the red clay robe with the red clay wings
And a red clay halo for my head*

Red Clay Halo - by Gillian Welch & David Rawlings

Acknowledgements

Where to start with the acknowledgments (there are too many people to mention)... A mahousive thank you goes to my various field assistants, without whom my field work would have been lonely and terrifying. I'd like to thank Leah for keeping me company during the early reconnaissance days, and for teaching me all there is to know about rattlesnakes (including that they can make a sound like a champagne bottle being opened). A huge thank you to my cuz, Mike (Ember) for breaking his back to get me some rock samples using Caine, for taking me slot canyon'ing and for teaching me to build and start a fire using only what nature has laid at our feet. An enormous, monster thank you goes to Sarah for being my field assistant and safety buddy during my extended second field season (and to Daniel for letting me 'steal her away' for so many weeks. There are too many amazing memories, too many funny stories and too many 'near-misses' to recount... Just as there should be attached to epic field trips. Enormous thanks also go to Ken, for starting me off with the fieldwork, and Woody for helping me finish off both field seasons. Thanks for them both for helping lug the heavy laser scan equipment to my outcrops every day for a week.

While thinking of the Henrys, I'd also like to thank Anne for providing fantastic conversation and great food at Luna Mesa, Nathan and the guys at Blondies for looking out for me and making "the best burger in the world" (and fry sauce!), and Randy for his amazing pesto that made camp meals something to look forward to, and for all the other folk of Hanksville who made me feel at home and part of the community. Thanks to all the rattlesnakes, black widow, brown recluse and scorpion arachnids for not biting me during my days in the desert. Posthumously, thanks Ed Abbey for all the advice on how to make it in the Utahn desert. Oh, and the Carolina boys for teaching me to "thug.... Carolina style". You guys rock! Here's to a reunion at Starr Springs soon!

A big thank you goes to Steve Nelson at BYU for generally being awesome, generous with his time, showing me around the northern Henry Mtns (and lots of other cool geology around Utah), and providing me with rock samples, thin sections, an original Hunt map (the list goes on!!), encouraging me, and for providing me with the best field assistant in Sarah.

I'd like to acknowledge Midland Valley for providing me with an Academic Licence for their Move™ software packages. I'd also like to thank the Geological Society of London for awarding me the Elspeth Matthews Award for field work (2012) which helped me greatly,

and VMSG, Kingston University and the Geological Society of America for the provision of travel grants to attend conferences.

I'd like to thank the Geological Society of America for granting me the opportunity to co-convene two thematic conference sessions at the 125th Anniversary Meeting in Denver, 2013. The sessions were a great success, and thanks to all who took part and attended.

Thanks go to all my supervisors, to Ian Jarvis, Jon Davidson and Bob Holdsworth; the latter of whom I'd like to thank for getting involved with the project part way through and providing guidance with the microstructural side of the work. I'd like to say an enormous thank you to my principal supervisor Ken McCaffrey for creating the project (thanks to Jon also for this! ☺), being a great supervisor and an even better friend. Thanks for all the support and encouragement along the way and over the years since my undergraduate days at Durham. Bob too!

There are too many friends who enrich my life to name them all here, but I thank y'all. Some have been there for me throughout all the highs and lows though, and I would like to say massive thank yous to Bex and Dami, Annabelle, Stu, Annie, Alex, Craigster, Leah, Sarah, Tom, John, Louise, Fabio, Madeleine (the best Made of Honour and house mate ever!) and Kat (my person)!

An enormous thank you goes to my family (Mum, Dad, Jimbo, Neus, and beautiful Little Lilly... photos of you and your gorgeous smile have made me smile through the write-up) for always being there for me and for supporting me in everything I do. Mum and Dad, I owe so much of my success to you! I am so grateful for all you have done for me, and continue to do for me. The past two years would have been even tougher without you helping me and Woody out. Thanks to my puss-tat Charlie for all the hugs and providing me with daily companionship. Lastly, and by no means least I want to say a huge thank you to my amazing husband and best friend Woody. Words can't express what you mean to me!! I am a stronger person and achieve more because I have you by my side. I love all my family dearly and this, I dedicate to y'all!

Contents

| | |
|---|-----------|
| TITLE | i |
| COPYRIGHT | ii |
| ABSTRACT | iii |
| ACKNOWLEDGEMENTS | v |
| CONTENTS | vii |
| LIST OF FIGURES | xiii |
| CHAPTER 1 | |
| 1. Introduction | 1 |
| 1.1. Shallow level intrusions | 2 |
| 1.1.1. <i>Definitions of sills and laccoliths</i> | 4 |
| 1.1.2. <i>Geometry and morphology of sills and laccoliths</i> | 5 |
| 1.2. Models for sill and laccolith emplacement | 11 |
| 1.2.1. <i>Gilbert's early work</i> | 11 |
| 1.2.2. <i>Mechanisms of emplacement</i> | 12 |
| 1.2.2.1. <i>Magma generation and ascent</i> | 12 |
| 1.2.2.2. <i>Initiation and level of sill emplacement</i> | 14 |
| 1.2.2.3. <i>Sill propagation and growth</i> | 15 |
| 1.3. Historic expeditions to the Henry Mountains | 19 |
| 1.3.1. <i>Gilbert and the Powell expeditions</i> | 19 |
| 1.3.2. <i>Hunt's 1930's USGS expeditions</i> | 27 |
| 1.3.3. <i>Recent field studies</i> | 30 |
| 1.4. This Study | 30 |
| 1.4.1. <i>Project aims</i> | 30 |
| 1.4.2. <i>Methods</i> | 32 |
| 1.4.2.1. <i>Field work</i> | 32 |
| 1.4.2.2. <i>Structural Data</i> | 34 |
| 1.4.2.3. <i>Rock Sampling</i> | 36 |
| 1.4.2.3.1. <i>Textural Studies & Crystal Size Distribution (CSD)</i> | 36 |
| 1.4.2.3.2. <i>Microstructures</i> | 37 |
| 1.4.2.4. <i>Laser scanning</i> | 38 |
| 1.4.2.4.1. <i>3D modelling</i> | 38 |
| 1.4.3. <i>Thesis Layout</i> | 45 |
| CHAPTER 2 | |
| 2. Geological setting | 46 |
| 2.1. Regional Geological Setting | 47 |

| | | |
|-------------------|---|------------|
| 2.2. | Tectonic and geological evolution of Utah, the Colorado Plateau and N. America | 47 |
| 2.2.1. | <i>Palaeoproterozoic to Mesoproterozoic (c. 2000 to 950 Ma)</i> | 53 |
| 2.2.2. | <i>Neoproterozoic to Early Palaeozoic (c. 950 to 541 Ma)</i> | 55 |
| 2.2.3. | <i>Cambrian to Permian (541 to 252 Ma)</i> | 57 |
| 2.2.4. | <i>Triassic to Jurassic (252 to 145 Ma)</i> | 58 |
| 2.2.5. | <i>Early Cretaceous (145 to 80 Ma)</i> | 61 |
| 2.2.6. | <i>Latest Cretaceous to Paleogene (80 to 35 Ma)</i> | 63 |
| 2.2.7. | <i>Latest-Paleogene to Present (~35 to 0 Ma)</i> | 64 |
| 2.3. | Uplift and Magmatism on the Colorado Plateau | 70 |
| 2.3.1. | <i>Dynamics (uplift) of the Plateau</i> | 70 |
| 2.3.2. | <i>Magmatism</i> | 71 |
| 2.4. | Geology of the Henry Mountains | 72 |
| 2.4.1. | <i>Stratigraphic Column</i> | 77 |
| 2.4.1.1. | <i>Cutler Formation (Roof Rocks to Mount Hillers)</i> | 79 |
| 2.4.1.2. | <i>Entrada Sandstone (Host Rocks to Trachyte Mesa and Maiden Creek)</i> | 80 |
| 2.4.1.3. | <i>Summerville Formation (Host rocks to Black Mesa).</i> | 82 |
| 2.4.1.4. | <i>Morrison Formation (Host Rocks to Sawtooth Ridge)</i> | 83 |
| 2.4.2. | <i>Henry Mountains Intrusions</i> | 84 |
| 2.4.2.1. | <i>The Five Igneous Centres</i> | 85 |
| 2.4.2.1.1. | <i>Mount Ellen</i> | 85 |
| 2.4.2.1.2. | <i>Mount Pennell</i> | 87 |
| 2.4.2.1.3. | <i>Mount Hillers</i> | 88 |
| 2.4.2.1.4. | <i>Mount Holmes</i> | 92 |
| 2.4.2.1.5. | <i>Mount Ellsworth</i> | 94 |
| 2.4.2.2. | <i>North-eastern satellite intrusion to Mount Hillers</i> | 94 |
| 2.4.2.2.1. | <i>Sawtooth Ridge</i> | 94 |
| 2.4.2.2.2. | <i>Black Mesa</i> | 96 |
| 2.4.2.2.3. | <i>Maiden Creek</i> | 99 |
| 2.4.2.2.4. | <i>Trachyte Mesa</i> | 100 |
| 2.5. | Deformation Structures in the Entrada Sandstone | 105 |
| 2.5.1. | <i>Deformation Bands and their classification</i> | 105 |
| 2.5.1.1. | <i>Kinematic-based classification</i> | 106 |
| 2.5.1.2. | <i>Deformation-mechanism classification</i> | 107 |

CHAPTER 3

| | | |
|---------------|---|------------|
| 3. | Deformation structures associated with the Trachyte Mesa intrusion, Henry Mountains, Utah: implications for sill and laccolith emplacement mechanisms. | 110 |
| 3.1. | Introduction | 112 |
| 3.2. | Geological Setting | 114 |
| 3.2.1. | <i>Henry Mountains</i> | 114 |
| 3.2.2. | <i>Trachyte Mesa Intrusion</i> | 115 |
| 3.3. | Field Observations | 117 |
| 3.3.1. | <i>Intrusion Geometry</i> | 118 |
| 3.3.2. | <i>Deformation Structures</i> | 120 |

| | | |
|---------------|--|------------|
| 3.3.2.1. | <i>Structural types and geometry</i> | 120 |
| 3.3.2.2. | <i>Structural Phases</i> | 123 |
| 3.4. | Spatial distribution of structures | 127 |
| 3.4.1. | <i>Structural transect profiles</i> | 127 |
| 3.4.2. | <i>Variations with intrusion margin trend</i> | 132 |
| 3.4.3. | <i>Deformation structures at the intrusion contact</i> | 132 |
| 3.5. | Kinematics | 134 |
| 3.6. | Discussion | 135 |
| 3.6.1. | <i>Deformation phases (pre-, syn-, and late-stage emplacement)</i> | 135 |
| 3.6.1.1. | <i>Phase 1 – Pre-emplacment deformation</i> | 137 |
| 3.6.1.2. | <i>Phase 2 – Syn-emplacment deformation</i> | 137 |
| 3.6.1.3. | <i>Phase 3 – Late-stage emplacement deformation</i> | 138 |
| 3.6.2. | <i>Modes of Emplacement</i> | 138 |
| 3.6.3. | <i>Emplacement and structural evolution</i> | 140 |
| 3.6.3.1. | <i>Stage 1 – Onset of sheet emplacement and radial growth of a thin “proto-sill” sheet</i> | 141 |
| 3.6.3.2. | <i>Stage 2 - Vertical inflation of sill sheet</i> | 143 |
| 3.6.3.3. | <i>Stage 3 - Emplacement of additional sill sheets</i> | 145 |
| 3.6.3.4. | <i>Stage 4 - Onset of sill-climbing</i> | 145 |
| 3.6.3.5. | <i>Stage 5 - Cooling and relaxation of intrusion</i> | 146 |
| 3.6.4. | <i>Sequence of stacking</i> | 147 |
| 3.6.5. | <i>Faulting at sill terminations</i> | 148 |
| 3.7. | Conclusions | 148 |

CHAPTER 4

| | | |
|---------------|---|------------|
| 4. | Fracture analysis of deformation structures associated with the Trachyte Mesa intrusion, Henry Mountains, Utah: implications for reservoir connectivity and fluid flow around sill intrusions. | 151 |
| 4.1. | Introduction | 153 |
| 4.2. | Geological Setting | 154 |
| 4.2.1. | <i>Trachyte Mesa Intrusion</i> | 154 |
| 4.2.2. | <i>The Entrada Sandstone Formation</i> | 155 |
| 4.3. | Study zone, sampling and analysis methods | 159 |
| 4.3.1. | <i>Outcrop traverse</i> | 159 |
| 4.3.2. | <i>Fracture analysis methods</i> | 160 |
| 4.3.2.1. | <i>Fracture network map</i> | 160 |
| 4.3.2.2. | <i>Measuring lengths and quantities</i> | 160 |
| 4.3.2.3. | <i>Node counting</i> | 162 |
| 4.3.3. | <i>Sample collection</i> | 162 |
| 4.4. | Results | 164 |
| 4.4.1. | <i>Outcrop fracture analysis</i> | 164 |
| 4.4.2. | <i>Hand specimens</i> | 172 |
| 4.4.3. | <i>Thin section analysis</i> | 173 |
| 4.4.3.1. | <i>Sample TMFS-1</i> | 173 |
| 4.4.3.2. | <i>Sample TMFS-2</i> | 173 |
| 4.4.3.3. | <i>Sample TMFS-3</i> | 176 |

| | | |
|---------------|---|------------|
| 4.4.3.4. | Sample TMFS-4 | 176 |
| 4.4.3.5. | Sample TMFS-5 | 176 |
| 4.4.3.6. | Sample TMFS-6 | 177 |
| 4.5. | Interpretations and Discussion | 178 |
| 4.5.1. | Fracture intensity and Topology variations across margin | 178 |
| 4.5.2. | Microstructural interpretations | 181 |
| 4.5.3. | Wider implications | 182 |
| 4.6. | Conclusions | 183 |

CHAPTER 5

| | | |
|---------------|---|------------|
| 5. | Intrusion – host rock deformation and contact geometries, Maiden Creek, Henry Mountains, Utah. | 185 |
| 5.1. | Introduction | 187 |
| 5.2. | Geological Setting | 189 |
| 5.2.1. | Maiden Creek intrusion | 192 |
| 5.3. | Intrusion geometries and deformation structures by domains | 194 |
| 5.3.1. | Zone 1: NE intrusion | 194 |
| 5.3.1.1. | Intrusion and host rock geometries | 194 |
| 5.3.1.2. | Syn-emplacement deformation structures | 194 |
| 5.3.2. | Zone 2: Eastern margin and ‘Whispering Wind Gully’ | 198 |
| 5.3.2.1. | Intrusion and host rock geometries | 198 |
| 5.3.2.2. | Syn-emplacement deformation structures | 204 |
| 5.3.2.2.1. | Zone 2a | 204 |
| 5.3.2.2.2. | Zone 2b | 205 |
| 5.3.3. | Zone 3: Southern intrusion and ‘Rattlesnake Gully’ | 209 |
| 5.3.3.1. | Intrusion and host rock geometries | 209 |
| 5.3.3.2. | Syn-emplacement deformation structures | 214 |
| 5.3.4. | Zone 4: NW margin | 217 |
| 5.3.4.1. | Intrusion and host rock geometries | 217 |
| 5.3.4.2. | Syn-emplacement deformation structures | 225 |
| 5.3.4.2.1. | Zone 4a | 225 |
| 5.3.4.2.2. | Zone 4b | 226 |
| 5.3.5. | Zone 5: SW Maiden Creek | 227 |
| 5.3.5.1. | Intrusion and host rock geometries | 227 |
| 5.3.5.2. | Syn-emplacement deformation structures | 227 |
| 5.4. | Discussion | 227 |
| 5.4.1. | Eastern margin (Zones 1, 2 and 3) | 232 |
| 5.4.1.1. | Lobes, Steps and Bridges | 236 |
| 5.4.1.2. | Kinematic partitioning | 237 |
| 5.4.2. | NW margin (Zone 4) | 237 |
| 5.4.3. | Unexposed SW margin (Zone 5) | 240 |
| 5.4.4. | A new model for development of the Maiden Creek intrusion | 241 |
| 5.5. | Conclusions | 246 |

CHAPTER 6

| | | |
|------------|--|-----|
| 6. | Syn-emplacement accommodation structures associated with the Maiden Creek intrusion, Henry Mountains, Utah. | 247 |
| 6.1. | Introduction | 249 |
| 6.2. | Geological Setting | 250 |
| 6.2.1. | <i>Henry Mountains</i> | 250 |
| 6.2.2. | <i>Maiden Creek Intrusion</i> | 252 |
| 6.2.3. | <i>Host rock–Entrada Sandstone</i> | 253 |
| 6.3. | Digital Mapping and 3D visualisation | 255 |
| 6.4. | Intrusion–host rock geometries in study area | 256 |
| 6.5. | Intrusion related deformation structures | 262 |
| 6.5.1. | <i>Deformation structures above the MCSZ</i> | 263 |
| 6.5.1.1. | <i>Deformation bands</i> | 263 |
| 6.5.1.2. | <i>Faults</i> | 263 |
| 6.5.1.3. | <i>Joints</i> | 263 |
| 6.5.2. | <i>Deformation structures below the MCSZ</i> | 265 |
| 6.5.2.1. | <i>Deformation bands</i> | 265 |
| 6.5.2.2. | <i>Pencil cleavage</i> | 265 |
| 6.5.2.3. | <i>Strike-slip faults</i> | 266 |
| 6.5.3. | <i>Deformation structures at the intrusion–sandstone contact</i> | 266 |
| 6.5.3.1. | <i>Lateral margin</i> | 266 |
| 6.5.3.2. | <i>Deformation on intrusion top surface</i> | 268 |
| 6.5.3.2.1. | <i>Stretched mineral lineations</i> | 268 |
| 6.5.3.2.2. | <i>Low-angle faults</i> | 268 |
| 6.5.3.2.3. | <i>Styolites</i> | 271 |
| 6.6. | Spatial distribution of deformation structures | 271 |
| 6.7. | Maiden Creek Shear Zone (MCSZ) | 273 |
| 6.7.1. | <i>Outcrop observations and spatial extent</i> | 273 |
| 6.7.2. | <i>Shear zone microstructures</i> | 274 |
| 6.7.3. | <i>Variations in character</i> | 277 |
| 6.8. | Discussion | 279 |
| 6.8.1. | <i>MCSZ: a syn-emplacement accommodation structure</i> | 279 |
| 6.8.2. | <i>Structural complexity and variations in strain within Rattlesnake Gully</i> | 281 |
| 6.8.3. | <i>Models for emplacement and geometry of the southern Maiden Creek intrusion: a pair of finger-like lobes or deep rooted sills?</i> | 281 |
| 6.9. | Conclusions | 286 |

CHAPTER 7

| | | |
|------|---|-----|
| 7. | Discussion & Conclusions | 288 |
| 7.1. | Summary of Project Aims | 289 |
| 7.2. | Geometries and kinematics of deformation structures as a tool for understanding intrusion emplacement mechanisms and morphologies | 289 |
| 7.3. | The importance of shear zones in accommodating the emplacement of intrusions in the shallow crust | 292 |

| | | |
|--------|---|-----|
| 7.4. | What controls intrusion emplacement: linking intrusion geometries, host rock deformation and accommodation structures, and space problems | 292 |
| 7.5. | Further Work | 295 |
| 7.5.1. | <i>Geophysical surveys</i> | 295 |
| 7.5.2. | <i>Microstructural analysis of intrusion-related deformation structures</i> | 296 |
| 7.5.3. | <i>Fracture spacing</i> | 297 |
| 7.5.4. | <i>Textural studies and crystal size distribution (CSD) of the intrusions</i> | 297 |

| | |
|-------------------|------------|
| REFERENCES | 299 |
|-------------------|------------|

| | |
|--|------------|
| APPENDIX – Digital Appendices on disk | 323 |
|--|------------|

Hardcopy:

- *Wilson, P.I.R. and McCaffrey, K.J.W., 2013. Intrusion space problem: digital mapping and analysis of the Maiden Creek satellite intrusion, Henry Mountains Utah. Geoscientist, 23 (6), 16–19.*

List of Digital Appendices:

Disk 1:

- *Glossary of Laccolith/ Sill terminology (after Corry, 1988)*
- *Regional Structural Data Table*
- *Trachyte Mesa Structural Data Table*
- *Maiden Creek Structural Data Table*
- *Sample Database*
- *Conference Presentations*

Disk 2:

- *Google Earth™ Project (kmz file)*
- *Terrestrial Laser Scan (TLS) Video Animations*
- *TLS methodology workflow*

LIST OF FIGURES

| Figure Number | Figure Caption | Page Number |
|------------------|---|-------------|
| Chapter 1 | | |
| 1.1 | Images of magmatic systems. | 3 |
| 1.2 | Images of idealised laccoliths. | 5 |
| 1.3 | Images of intrusive geometries. | 7 |
| 1.4 | Schematic graph showing the scaling relationship between the various forms of shallow crustal/ high-level intrusions (from Menand, 2008; based on Cruden & McCaffrey, 2002 and McCaffrey & Cruden, 2002). | 8 |
| 1.5 | Examples of seismic studies on sill geometries. | 10 |
| 1.6 | Growth models for laccolith intrusions (modified from Hunt, 1953, and Corry, 1988). | 16 |
| 1.7 | Models of sill emplacement and propagation (and ramp-flat morphologies). | 18 |
| 1.8 | Route of Powell's Expeditions and proximity to the Henry Mountains, Utah. | 20 |
| 1.9 | Photographs of highly-esteemed, American geologist and twice President of the Geological Society of America, Grove Karl Gilbert. | 22 |
| 1.10 | Map showing Gilbert's 1875 and 1876 expedition routes through the Henry Mountains (Hunt, 1988). | 23 |
| 1.11 | Examples of Gilbert's line-drawings from his 1876 Notebooks on the Geology of the Henry Mountains (from Hunt, 1988). | 24 |
| 1.12 | Examples of Gilbert's field sketches of Mount Hillers as viewed from the ESE. | 25 |
| 1.13 | A series of images of the Trachyte Mesa intrusion, Henry Mountains. | 26 |
| 1.14 | Examples of Gilbert's published illustrations (1877). | 27 |
| 1.15 | Field photographs from the 1936 USGS Field Party to the Henry Mountains (Hunt, 1997). | 28 |
| 1.16 | Digital scan of an original copy of Hunt's geological map of the Henry Mountains Region, Utah. | 29 |
| 1.17 | Model from a reconnaissance study of the Henry Mountains (LASI IV field trip, summer 2010) to be tested in the thesis. | 31 |
| 1.18 | Work flow of methodologies. | 33 |
| 1.19 | Example screen captures of the Maiden Creek digital mapping project in FieldMove™. | 34 |
| 1.20 | A series of images from the Maiden Creek Google Earth™ project. | 35 |
| 1.21 | Field photographs of laser scanning in the field. (a) Setting up the Leica ScanStation C10. | 39 |
| 1.22 | A series of images showing the laser scan data and interpretation. | 40 |
| 1.23 | Laser scan interpretation processes. | 42 |
| 1.24 | Example laser scan interpretations from the Trachyte Mesa intrusion study area. | 43 |
| 1.25 | Example laser scan interpretations from the Maiden Creek intrusion | 44 |

| | | |
|------------------|--|----|
| | study area. | |
| Chapter 2 | | |
| 2.1 | Location maps of the Colorado Plateau (CP). | 48 |
| 2.2 | Palaeogeographic and tectonic history of North America (Miall & Blakey, 2008). | 50 |
| 2.3 | Palaeogeographic and tectonic history of southwestern North America (Blakey & Ranney, 2008). | 51 |
| 2.4 | Nine key tectonostratigraphic phases of Utah's geologic history as outlined by Hintze & Kowallis (2009). | 52 |
| 2.5 | Simplified map showing the basement terranes and cratons of North America (adapted from Hoffman, 1988; and Bleeker and Hall, 2007). | 54 |
| 2.6 | Basement trends of North America. | 56 |
| 2.7 | Photographs of selected sedimentary rocks of the Henry Mountains region. | 60 |
| 2.8 | Palaeogeography and depositional environment map of North America during the late Cretaceous (80–100 Ma; from Hintze & Kowallis, 2009). | 61 |
| 2.9 | Predicted dynamic topography over western USA showing subsidence and uplift of the Colorado Plateau, based on a model of Farallon slab subduction (from Liu & Gurnis, 2010). | 62 |
| 2.10 | Laramide folding on the Colorado Plateau. | 64 |
| 2.11 | The geological evolution of the San Andreas Fault along the western coast of North America from ~30 Ma to present (modified after Irwin, 1990; re-drawn by USGS http://pubs.usgs.gov/gip/dynamic/Farallon.html). | 65 |
| 2.12 | A series of maps depicting magmatism and volcanism across western North America from 42 Ma to the present. | 66 |
| 2.13 | A series of map view reconstructions of volcanism across western North America from 36 Ma to the present (McQuarrie & Oskin, 2010). | 68 |
| 2.14 | Magmatism of the Colorado Plateau. | 69 |
| 2.15 | Location and geology of the Henry Mountains, Utah. | 74 |
| 2.16 | Contour maps for the Henry Mountains (excluding Mount Ellen) and Navajo Mountain, accompanied by a series of diagrams illustrating the space occupied by intrusive stocks and the theoretical space available for them (from Hunt, 1953). | 75 |
| 78 | Photographs showing significant geological structures of the Henry Mountains area in south-eastern Utah. | 76 |
| 2.18 | Simplified geological cross-section through Circle Cliffs Uplift, Capitol Reef National Park and the Henry Mountains (from the USGS; poster available in the Capitol Reef National Park Information Centre). | 78 |
| 2.19 | Stratigraphy of the Henry Mountains region. | 79 |
| 2.20 | Rock types of the Henry Mountains. | 81 |
| 2.21 | A series of figures relating to the northern three Henry Mountains: Mt Ellen; Mt Pennell; and Mt Hillers. | 86 |

| | | |
|------------------|---|-----|
| 2.22 | Mount Hillers and its satellite intrusions. | 89 |
| 2.23 | Photographs of Mount Hillers. | 90 |
| 2.24 | Southern margin of Mount Hillers. | 91 |
| 2.25 | A series of figures relating to the southern two Henry Mountains: Mt Holmes; and Mt Ellsworth. | 93 |
| 2.26 | Fence diagrams showing the subsurface geometries around Sawtooth Ridge, Black Mesa and Maiden Creek, as envisaged by Hunt (1953). | 95 |
| 2.27 | A series of figures relating to the Sawtooth Ridge intrusion. | 97 |
| 2.28 | A series of figures relating to the Black Mesa intrusion. | 98 |
| 2.29 | A series of figures relating to the Maiden Creek intrusion. | 100 |
| 2.30 | Fence diagrams showing the subsurface geometries at Trachyte Mesa, as envisaged by Hunt (1953). | 102 |
| 2.31 | A series of figures relating to the Trachyte Mesa intrusion. | 104 |
| 2.32 | Trachyte Mesa Feeder system. | 105 |
| 2.34 | Photographic examples of deformation bands (Fossen et al. 2007). | 107 |
| 3.35 | Classification of deformation bands. | 108 |
| Chapter 3 | | |
| 3.1 | Simplified geological maps of the study area. | 113 |
| 3.2 | Location of the study sections. | 116 |
| 3.3 | Photographs and interpretative sketches showing outcrop geometries of stacked sill sheets on the southern NW margin of Trachyte Mesa. | 119 |
| 3.4 | Summary stereoplots of field structural data. | 121 |
| 3.5 | Annotated field photographs showing examples of Phase 1 (a), Phase 2 (b–d), and Phase 3 (e–h) deformation structures. | 122 |
| 3.6 | Photomicrographs of Entrada sandstone (blue dye infilling pore space). | 123 |
| 3.7 | Cross cutting relationships between structural phases. | 125 |
| 3.8 | Annotated field photographs showing additional examples of Phase 2A (a–b) and 2B (c–e) structures and kinematics. | 127 |
| 3.9 | Field photographs and structural data demonstrating the arcuate trend of Phase 2B faults. | 129 |
| 3.10 | Structure along Trachyte Mesa transect TMTW. | 130 |
| 3.11 | Structure along Trachyte Mesa transect TMTE. | 131 |
| 3.12 | Photomicrographs of microstructures observed at the intrusion – sandstone contact. | 133 |
| 3.13 | Flow generated fabrics at the intrusion margin. | 136 |
| 3.14 | Schematic diagram outlining a two-stage growth model for sill emplacement at the Trachyte Mesa intrusion and associated deformation structures. | 142 |
| 3.15 | Faulting accompanying sill emplacement. | 146 |
| Table 3.1 | Summary table of deformation phases observed at in the host rocks to the Trachyte Mesa intrusion. | 124 |

| Chapter 4 | | |
|------------------|---|-----|
| 4.1 | Geological setting and study area. | 156 |
| 4.2 | Panoramic photograph of study area (sampling traverse across lateral margin of the Trachyte Mesa intrusion). | 157 |
| 4.3 | Photograph of a hand specimen (a) and photomicrographs of thin sections (b, c) of a deformation band. | 158 |
| 4.4 | Schematic image outlining principal method applied for fracture analysis (from Sanderson and Nixon, 2015). | 159 |
| 4.5 | Hand specimen photos and fracture analysis (circles). | 163 |
| 4.6 | Outcrop photographs and corresponding fracture interpretations for locality TMFS-1. | 166 |
| 4.7 | Outcrop photographs and corresponding fracture interpretations for locality TMFS-2. | 167 |
| 4.8 | Outcrop photographs and corresponding fracture interpretations for locality TMFS-3. | 169 |
| 4.9 | Outcrop photographs and corresponding fracture interpretations for locality TMFS-4. | 170 |
| 4.10 | Outcrop photographs and corresponding fracture interpretations for locality TMFS-5. | 171 |
| 4.11 | Outcrop photographs and corresponding fracture interpretations for locality TMFS-6. | 172 |
| 4.12 | Thin section photos and photomicrographs for each sample. | 174 |
| 4.13 | Fracture statistic triangular plots. | 179 |
| 4.14 | Fracture statistics and their variation with location for: (a) fracture line; and (b) branch line statistics. | 180 |
| 4.15 | Plot showing the difference between fracture and branch line dimensionless intensity values. Note the approximately 2:1 ratio. | 182 |
| Table 4.1 | Summary data table showing results of circular scan fracture analyses carried out in this study. | 165 |
| Chapter 4 | | |
| 5.1 | Schematic sketches illustrating geometries and evolution of: (a) magma fingers and lobes; and (b) steps and broken bridges. Images from Schofield (2009) and Schofield et al. (2012). | 189 |
| 5.2 | Location and geology maps of the Mount Hillers intrusive complex, Henry Mountains, Utah | 191 |
| 5.3 | Map of the Maiden Creek intrusion and study areas. | 192 |
| 5.4 | NE Maiden Creek Intrusion (Zone 1). | 195 |
| 5.5 | Structural stations MCSS-40 and -41 in Zone 1. | 196 |
| 5.6 | Eastern margin and 'Whispering Wind Gully' (Zone 2). | 199 |
| 5.7 | Series of field photographs showing various intrusion geometries in Zone 2. | 200 |
| 5.8 | Geometries and deformation structures in Zone 2a. | 202 |
| 5.9 | Overview field photographs and corresponding sketches of Whispering Wind Gully and Zone 2b, highlighting key geometries, structures and locations of structural stations. | 203 |

| | | |
|------------------|---|---------|
| 5.10 | Zone 2a deformation. | 206 |
| 5.11 | Deformation structures in Zone 2a. | 207 |
| 5.12 | Zone 3, Southern Intrusion and 'Rattlesnake Gully'. | 211 |
| 5.13 | Intrusion and host rock geometries in Zone 3. | 212 |
| 5.14 | Deformation structures within Rattlesnake Gully in Zone 3. | 215 |
| 5.15 | NW Maiden Creek (Zone 4). Aerial photograph of Zone 4. | 218 |
| 5.16 | Zone 4a and the north-western margin of the Maiden Creek intrusion. | 219 |
| 5.17 | Bleached sandstone ridge (Zone 4b). | 221 |
| 5.18 | Intrusion–host rock geometries and deformation structures in Zone 4b and on the top surface of the intrusion. | 222 |
| 5.19 | Further east on the northern margin, structural stations MCRD-17 and -18. | 223 |
| 5.20 | Schematic cross-sections across the intrusion margin in Zones 4a and 4b. See text for discussion. | 224 |
| 5.21 | SW Maiden Creek. | 228 |
| 5.22 | Spatial distribution of deformation structural trends over the Maiden Creek intrusion area. | 230/231 |
| 5.23 | The model of Horsman et al. (2009) for the geometry and magma flow directions for the Maiden Creek intrusion. | 232 |
| 5.24 | Schematic cross-sections across the intrusion in Zones 2a and 2b. | 235 |
| 5.25 | Table depicting observed relationships between depth of intrusion emplacement within a sedimentary basin, host rock properties, emplacement mechanisms and intrusion morphologies (from Schofield et al., 2012a). | 238 |
| 5.26 | Plot showing range over which wrench dominated transtension (WDTT) may vary when magma addition it included (after Teyssier and Tikoff, 1999). | 239 |
| 5.27 | Possible emplacement evolution for the Maiden Creek intrusion based on observations, kinematics and structural trends identified in this study and as discussed in text. | 243 |
| 5.28 | Same model as shown in Figure 5.27, annotated onto an oblique aerial view from Google Earth™. | 244 |
| 5.29 | Conceptual 3D model for the proposed sub-surface geometry of the Maiden Creek intrusion. | 245 |
| Chapter 6 | | |
| 6.1 | Maps of Henry Mountains and Mount Hillers intrusive complex. | 251 |
| 6.2 | Maps of study area. | 254 |
| 6.3 | Entrada Sandstone Formation (host-rock). | 255 |
| 6.4 | Panoramic photographs, annotated sketches and laser scan models showing outcrop geometries of the study area. | 257 |
| 6.5 | Examples of laser scan images and 3D modelling to map and visualise structural geometries in 3D. | 258 |
| 6.6 | Intrusion outcrop geometries and fabrics. | 260 |
| 6.7 | Summary stereoplots of field structural data. | 262 |

| | | |
|------------------|--|-----|
| 6.8 | Field photographs showing deformation structures in the host-rock sandstones above and below the MCSZ. | 264 |
| 6.9 | Field photographs showing deformation structures at the intrusion-sandstone contact. | 267 |
| 6.10 | Pussycat outcrop geometry and deformation kinematics. | 269 |
| 6.11 | Field photographs showing deformation structures on the top surface of intrusion. | 270 |
| 6.12 | Spatial distribution of deformation structures across the Southern Maiden Creek sill study area. | 272 |
| 6.13 | Outcrop photographs of the Maiden Creek Shear Zone (MCSZ). | 275 |
| 6.14 | A series of photomicrographs of MCSZ microstructures and fabrics, all indicating top-to-the-WNW movement. | 276 |
| 6.15 | Schematic cross section showing spatial distribution of deformation structures in the study area. | 278 |
| 6.16 | Three models for emplacement of the southern igneous bodies to the Maiden Creek intrusion | 285 |
| Chapter 7 | | |
| Table 7.1 | A comparison of geometries, deformation structures and emplacement models of the Trachyte Mesa and Maiden Creek intrusions. | 291 |
| 7.1 | Schematic block diagrams of idealised intrusions, based on the Maiden Creek (sill), Trachyte Mesa (laccolith) and Black Mesa (bysmalith) intrusions, from Horsman et al. (2009). | 294 |



Landform map of the Henry Mountains and surrounding area (Gilbert, 1877)



1. Chapter 1: Introduction

| | | | |
|----------------|-------------------|--|--------------|
| <i>Layout:</i> | 1.1. | Shallow level intrusions | p. 2 |
| | 1.1.1. | <i>Descriptive vs Genetic Definitions of sills and laccoliths</i> | p. 4 |
| | 1.1.2. | <i>Geometry and morphology of sills and laccoliths</i> | p. 5 |
| | 1.2. | Models for sill and laccolith emplacement | p. 11 |
| | 1.2.1. | <i>Gilbert's early work</i> | p. 11 |
| | 1.2.2. | <i>Mechanisms of emplacement</i> | p. 12 |
| | 1.2.2.1. | <i>Magma generation and ascent</i> | p. 12 |
| | 1.2.2.2. | <i>Initiation and level of sill emplacement</i> | p. 14 |
| | 1.2.2.3. | <i>Sill propagation and growth</i> | p. 15 |
| | 1.3. | Historic expeditions to the Henry Mountains | p. 19 |
| | 1.3.1. | <i>Gilbert and the Powell expeditions</i> | p. 19 |
| | 1.3.2. | <i>Hunt's 1930's USGS expeditions</i> | p. 27 |
| | 1.3.3. | <i>Recent field studies</i> | p. 30 |
| | 1.4. | This Study | p. 30 |
| | 1.4.1. | <i>Project aims</i> | p. 30 |
| | 1.4.2. | <i>Methods</i> | p. 32 |
| | 1.4.2.1. | <i>Field work</i> | p. 32 |
| | 1.4.2.2. | <i>Structural Data</i> | p. 34 |
| | 1.4.2.3. | <i>Rock Sampling</i> | p. 36 |
| | 1.4.2.3.1. | <i>Textural Studies & Crystal Size Distribution</i> | p. 36 |
| | 1.4.2.3.2. | <i>Microstructures</i> | p. 37 |
| | 1.4.2.4. | <i>Laser scanning</i> | p. 38 |
| | 1.4.2.4.1. | <i>3D modelling</i> | p. 38 |
| | 1.4.3. | <i>Thesis Layout</i> | p. 45 |

1.1. Shallow Level Intrusions

The evolution of magmatic systems (i.e. the 'magmatic cycle'; Marsh, 1989) can be divided into five distinct phases: (1) magma formation/ melting; (2) magmatic segregation; (3) ascent; (4) emplacement (intrusion); (5) and in some cases eruption (extrusion). The emplacement of magma into the upper few kilometres of the crust is an important process in magma storage and differentiation, which may ultimately feed surface volcanism (Fig. 1.1; Breikreuz & Petford, 2004; Thomson & Petford, 2008). Such shallow level intrusions can also play an important role in economic geology, through the formation of mineral deposits (e.g. Ramirez et al., 2006; Sparks et al., 2006), geothermal energy (e.g. Wohletz & Heiken, 1986), and source rock maturation and reservoir properties in hydrocarbon systems (Schutter, 2003a, b; Rodriguez Monreal et al., 2009; Jones et al., 2007).

Shallow level intrusion complexes (i.e. large volumes of igneous rock (magma) emplaced within the upper 2–10 km of the crust) comprise an important part of the sub-volcanic plumbing system (Fig. 1.1) in which magma is emplaced as a series of sub-horizontal, sheet-like intrusions (Hutton, 1996; Cruden & McCaffrey, 2001; Morgan et al., 2008). Shallow level intrusions include sills, laccoliths and lopoliths (Fig. 1.1c, d). Corry (1988) produced a geographical index of all the known laccoliths of the world (~900, 600 of which are situated in North America) and extrapolated the numbers to infer that there may be >5000 laccoliths globally, assuming that the proportion of laccoliths remains roughly equal from one continent to another. If true, this supports the idea that laccolith emplacement is an important intrusion process.

Fundamental to our understanding of the emplacement of magma into the subsurface is reconciling the intrusion 'space-problem' (Hutton, 1996). First recognised by Charles Lyell in the nineteenth century (Pitcher, 1993), the 'space-problem' (or 'room-problem') refers to the physical processes that allow the addition of substantial new volumes of magma into the crust. Shallow-level intrusions form in the upper crust, and therefore even with the additional thermal effects of the magmatic system, deformation processes are predominantly brittle. The role of faults and fractures in the emplacement of intrusive rocks is therefore an important process (Pollard & Johnson, 1973). Fracture-mediated intrusions generally fall into two categories (Ably et al., 2008): (1) exploitation of pre-existing structures, aided by tectonic and buoyancy forces (e.g. Hutton et al., 1990;

McCaffrey, 1992; Tikoff & Teyssier, 1992; Magee et al., 2013); and (2) the development of juvenile fractures due to hydraulic and buoyancy loads intrinsic to the magma itself (e.g. Pollard & Johnson, 1973; Clemens & Mawer, 1992; Ablay et al., 2008; Schofield, 2009).

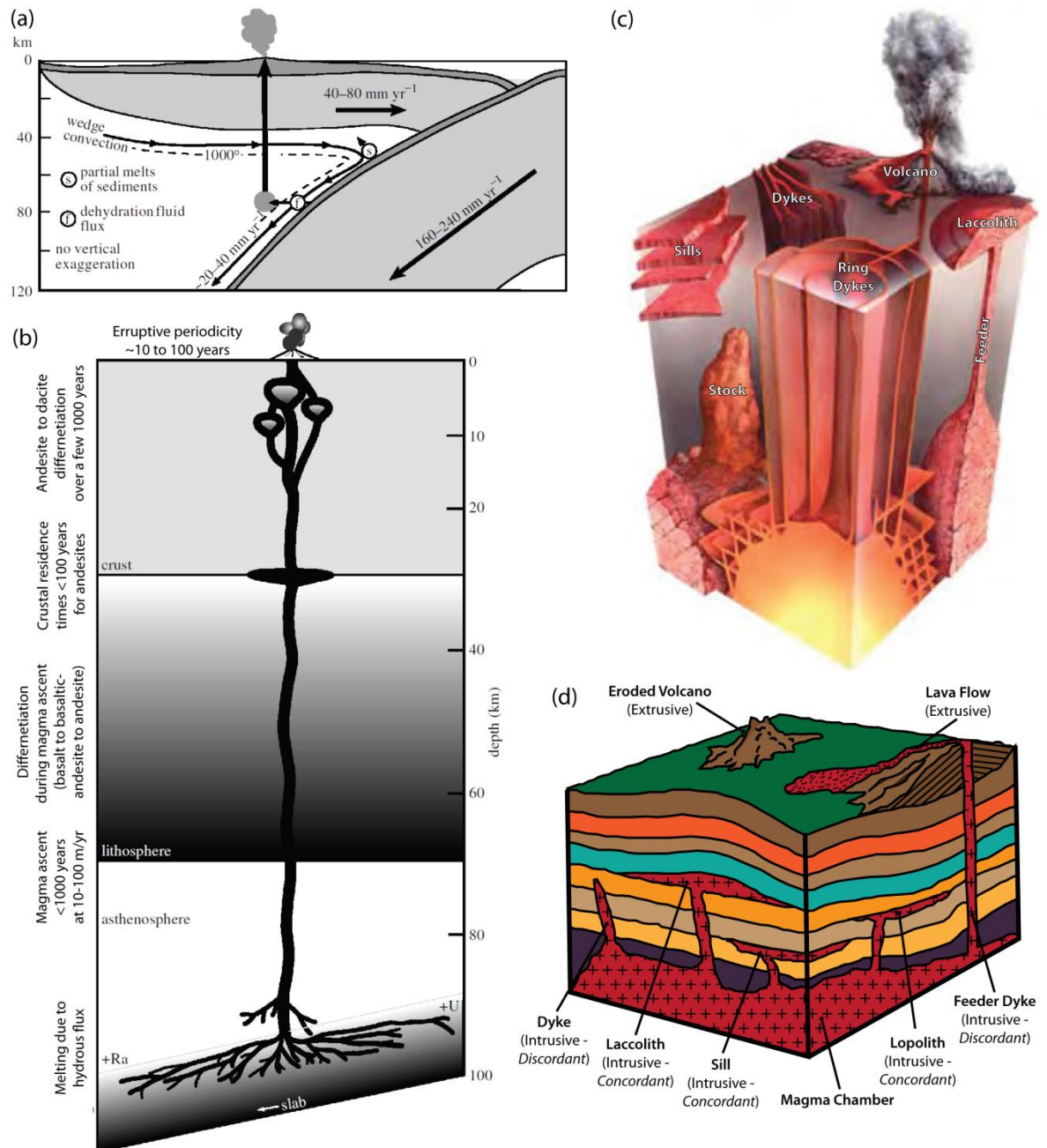


Figure 1.1. Images of magmatic systems. (a) Schematic cross-section across a subduction zone, illustrating the inferred mantle wedge dynamics and fluid fluxes (from Turner et al., 2000). (b) Schematic cross-section of the plumbing and reservoir system for an andesitic volcano with reference to magma transport and residence time-scales (from Turner et al., 2000, after Gill, 1981). (c) A central complex intrusive network (Hincks, 2004). (d) Schematic sketch showing the various types of minor intrusions and their possible relationships to a sub-volcanic magma chamber (modified from Thorpe and Brown, 1985). Sills, laccoliths and lopoliths are relatively concordant with sedimentary strata, whereas dykes are discordant. Note, the basal magma chamber depicted in the cartoon is generally accepted as being incorrect.

Many field-based studies of intrusions have focused on the geometry and internal architecture of sills, laccoliths and plutons, using a variety of methods including: field mapping of internal contacts and external margins (e.g. Morgan et al., 2008; Magee et al., 2012); geochronological studies (e.g. Coleman et al., 2004; Westerman et al., 2004); and magnetic and macroscopic fabric studies (e.g. de Saint Blanquat & Tikoff, 1997; Horsman et al., 2005; Stevenson et al., 2007b). In comparison, only a relatively small number of studies have paid significant attention to the structural processes that occur in the host rocks as these intrusions are emplaced (e.g. Anderson, 1951; Johnson & Pollard, 1973; Jackson & Pollard, 1990; Morgan et al., 2008; Thomson & Schofield, 2008). Furthermore, most papers that include observations on host-rock deformation structures do not consider the kinematic pathways and associated strains that can potentially preserve information concerning the emplacement mechanism and magma movement (flow) directions.

1.1.1. Descriptive vs Genetic Definitions of Sills and Laccoliths

Sills are defined as tabular igneous intrusions that are concordant with planar structures (bedding, cross-bedding, unconformities, and cleavage; Fig. 1.1) in the surrounding host rocks and display large length: thickness ratios (Corry, 1988). Laccoliths and lopoliths are also concordant intrusions with a concave-upwards upper contact and a concave-downwards lower contact respectively (Fig. 1.1). Corry (1988) distinguished laccoliths from sills by the non-linear, inelastic, large-scale deflection of roof host rocks that accompanied the emplacement of laccoliths (Fig. 1.2). Corry also made a distinction using an arbitrary thickness of 30 m: laccoliths are ≥ 30 m thick; sills are ≤ 30 m.

See the Glossary in Appendices for further definitions of the various types of intrusions.

Figure 1.2. (overleaf)

Images of idealised laccoliths. (a) Half-stereogram sketch of Mount Ellsworth, Henry Mountains, Utah from Gilbert (1877), illustrating uplifted roof rocks following igneous intrusion emplacement (background) prior to erosion leading to the current morphology of the landscape and exposure of the intrusion (foreground). (b) Gilbert's ideal laccolith (Gilbert, 1877; redrawn by Jackson & Pollard, 1988). (c) Revised schematic diagram of Gilbert's ideal laccolith following detailed mapping in the Henry Mountains (Jackson & Pollard, 1988).

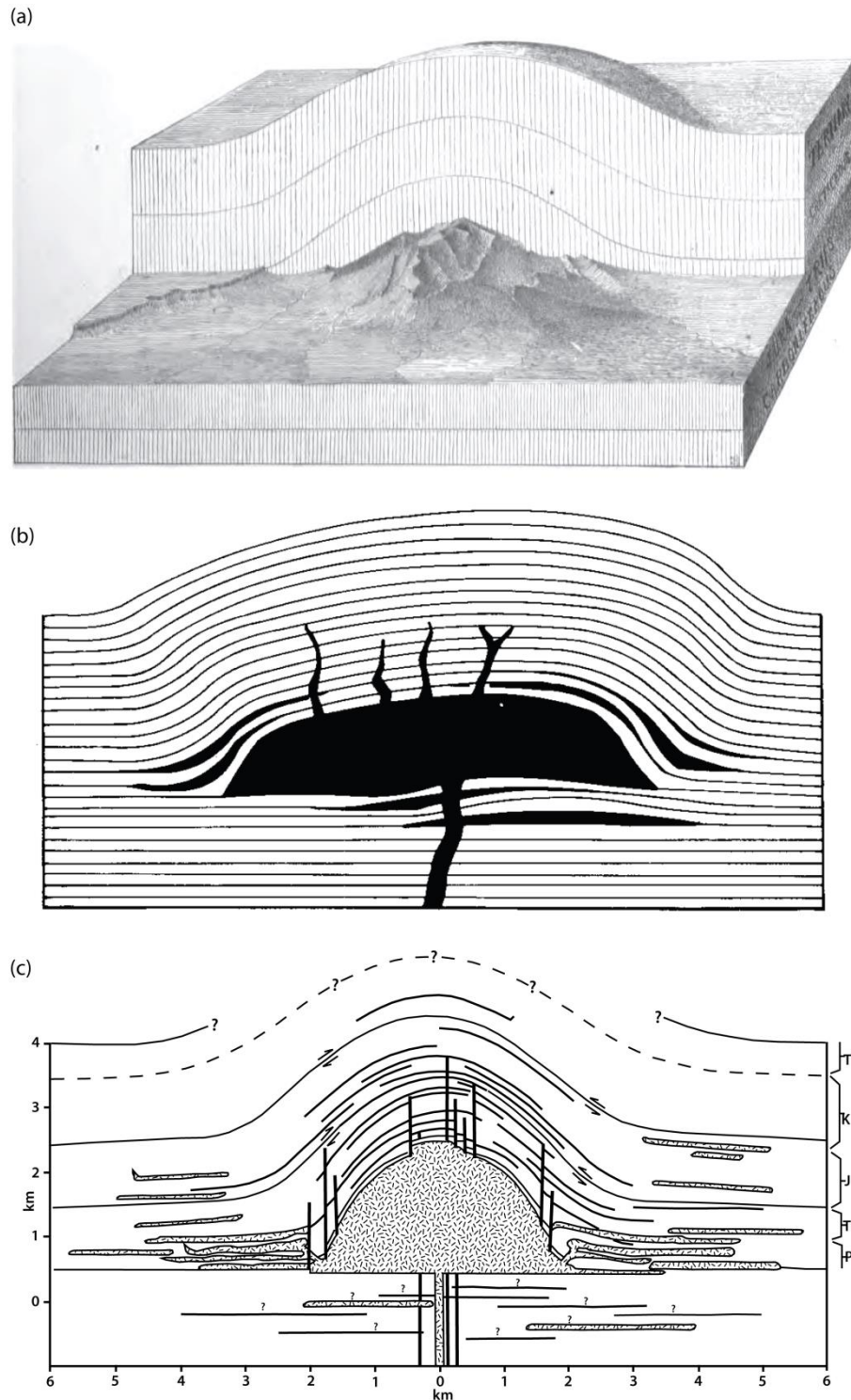


Fig. 1.2

1.1.2. Geometry and Morphology of Sills and Laccoliths

Gilbert (1877) described a single type of laccolith with a planar lower contact and concave-upwards upper contact, whilst also noting that laccolith intrusions may be stacked one above another. Figure 1.2 shows the 'ideal' form of a laccolith, as envisaged by Gilbert (1877), with the later revision of this sketch by Jackson and Pollard (1988), based on detailed mapping of the Henry Mountains, Utah, for comparison. Although visually similar, there are distinct and interesting differences between the models of

Gilbert (1877) and Jackson and Pollard (1988). Gilbert (1877) envisaged almost all of the intrusive system to be concordant with bedding, with the exception of a main feeder structure. In contrast, Jackson and Pollard (1988) showed an amalgamated dyke and sill model. Furthermore, in the model of Gilbert (1877), magma itself helps accommodate some of the doming and flexure of the overriding stratigraphy (i.e. magma/ sill sheets infilling space within fold hinge domains), enabling constant bed thicknesses to be maintained over the dome. Comparatively, in the model of Jackson and Pollard (1988), accommodation is entirely by flexural slip within the host rock.

Corry (1988) suggested that the various geometries of laccolith intrusions observed in the field form a continuous series between two distinct end members, these being punched (also known as bysmaliths) and Christmas-tree laccoliths (Fig. 1.3a). Punched laccoliths are described as roughly vertical cylindrical shaped intrusions, characterised by the development of shear fractures/ faults along the peripheral margin. The Black Mesa intrusion in the Henry Mountains, Utah is a classic example of a punched-laccolith, its southern margin defined by peripheral faults and a vertical cliff face, ~ 130 m high (de Saint Blanquat et al., 2006). In comparison, Christmas-tree laccoliths are the resulting structure formed from stacked sills, each tapering away from a central intrusive body. Corry (1988) characterised Christmas-tree laccoliths as domes, lacking any peripheral faults, and with continuous bedding overlying the intrusion. Westerman et al. (2004) presented the late Miocene granitic porphyry intrusive complexes on western Elba, Italy, as an example of a Christmas-tree laccolith.

Figure 1.3. *(overleaf)*

Images of intrusive geometries. (a) Models for two end-member laccolith geometries (punched and Christmas-tree laccoliths), after Corry (1988). (b) Schematic sketch of the morphology of saucer-shaped sills, based on intrusive complexes in the Karoo Basin, South Africa (from Malthe-Sørrensen et al., 2004; after Chevallier & Woodford, 1999). (c) Oblique-view and cross-section schematic diagrams for the evolution of magma fingers with time as fluidisation of host rock leads to the cessation of hydro-fracturing, this being replaced by a viscous-viscous magma to host rock relationship and the formation of an instability (from Schofield et al., 2012).

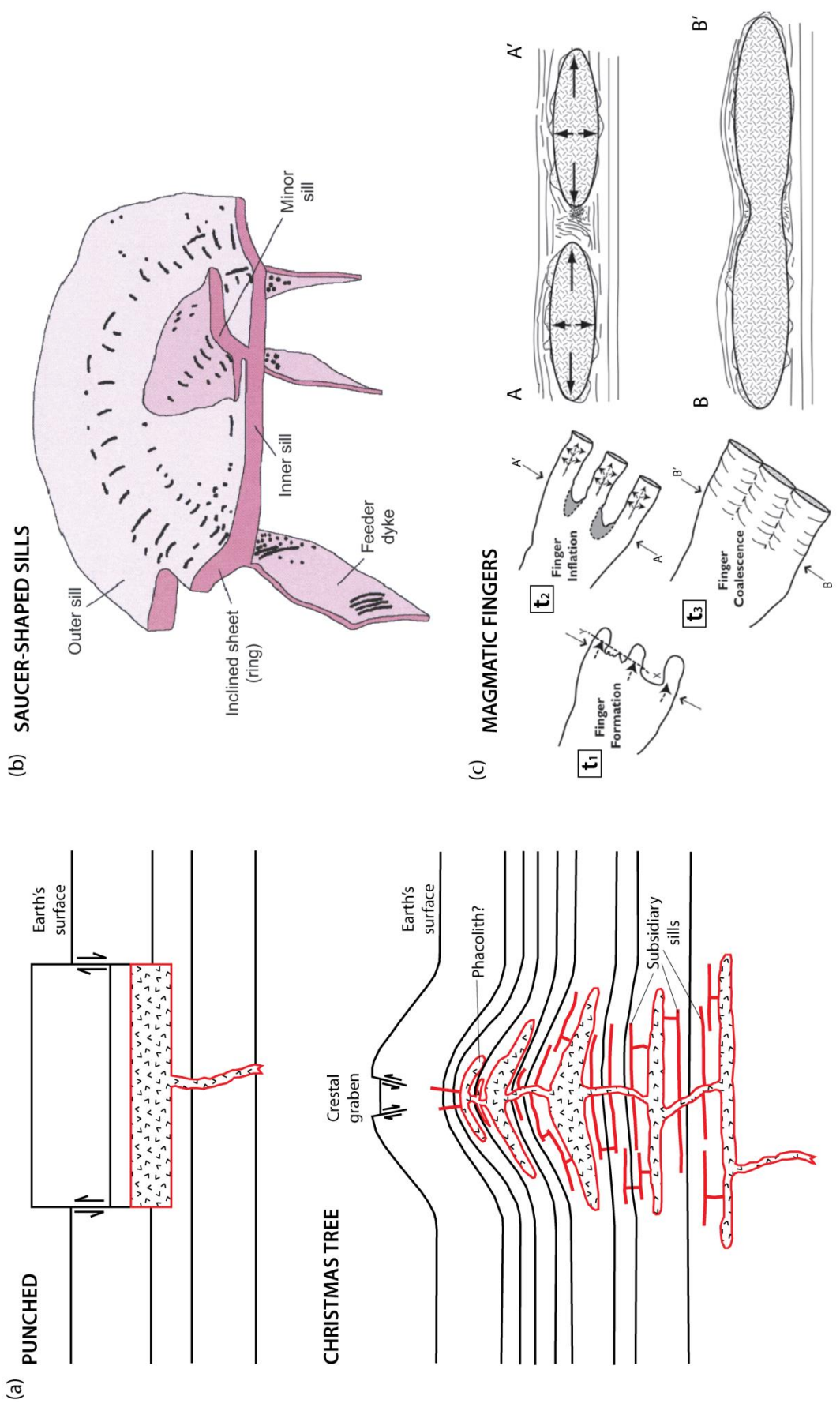


Fig. 1.3

In two studies of intrusion dimensions and geometries, McCaffrey and Petford (1997), and Cruden and McCaffrey (2001) suggested that there is a scale-dependent relationship between the (vertical) thickness and (horizontal) length of intrusions (Fig. 1.4). This relationship could be explained if the formation of sills and laccoliths play an important role in the formation of larger plutonic bodies. If sills grow mainly by lateral propagation, while laccoliths seem to grow by vertical thickening, it can be inferred that differing growth processes may be active across the scales of intrusion (e.g. Menand, 2008). A growing body of geochemical, geochronological and field textural evidence supports the idea that magma chambers and plutons develop and grow by amalgamation of numerous but distinct episodes of intrusion (Pitcher, 1970; Coleman et al., 2004; Glazner et al., 2004; Morgan et al., 2008).

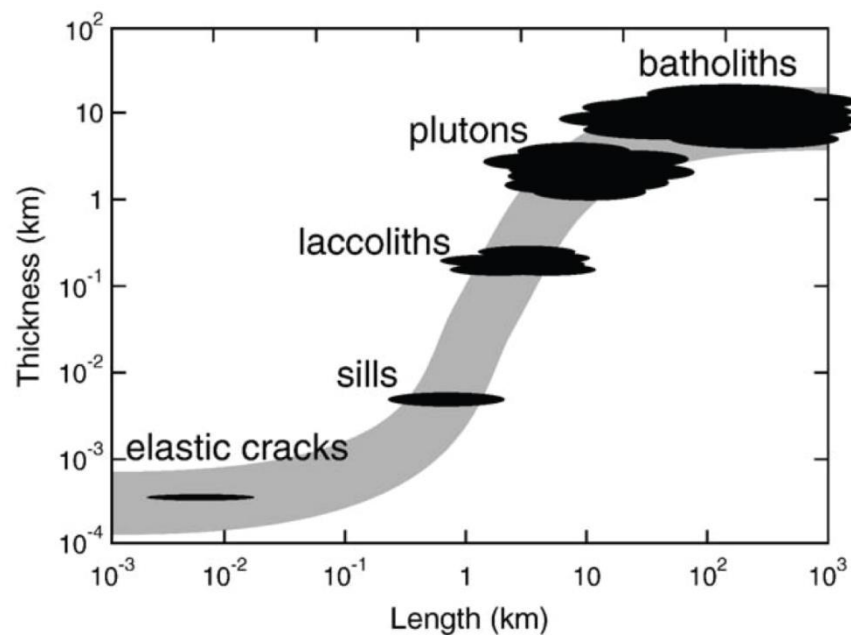


Figure 1.4. Schematic graph showing the scaling relationship between the various forms of shallow crustal/high-level intrusions (from Menand, 2008; based on Cruden & McCaffrey, 2002, and McCaffrey & Cruden, 2002). Intrusions are linked following an S-shaped growth law covering several orders of magnitude. Sills grow mainly by lateral propagation, while laccoliths seem to grow by vertical thickening.

Tabular and concave-upwards sill morphologies have been recorded in numerous studies (e.g. Du Toit, 1920; Leaman, 1975) and there is increasing evidence that saucer-shaped and stepped geometries are common for sills (Fig. 1.3b; e.g. Francis, 1982; Cartwright & Hanson, 2006; Thomson & Schofield, 2008; Schofield, 2009). Interpretation of 3D reflection seismic data has had a huge impact on our understanding and visualisation of

sub-surface intrusive geometries (Fig. 1.5; Thomson & Hutton, 2004; Cartwright & Hanson, 2006; Thomson, 2007; Thomson & Schofield, 2008; Schofield, 2009; Magee et al., 2013). Igneous bodies are typically characterised by very high amplitude seismic reflections (Thomson & Hutton, 2004) due to their high density and seismic velocity compared to the surrounding sediments (Fig. 1.5). These clear seismic signatures have provided geologists with the opportunity to visualise the 3D subsurface architecture of intrusive systems (Fig. 1.5b), with the most common geometry observed being saucer-shaped sill sheets (Cartwright & Hanson, 2006; Thomson & Schofield, 2008; Schofield, 2009). A limiting factor of the high density contrast between intrusions and the sedimentary host rocks is that, in most cases, only the geometry of the top surface is clearly imaged, and so the basal contact is less certain. It is possible that, for this reason, few laccolithic bodies have been described using seismic methods.

Recent studies have shown that tabular and saucer-shaped sill intrusions are often emplaced by the amalgamation of magma fingers, sheets and lobes (Pollard et al., 1975; Thomson & Hutton, 2004; Horsman et al., 2005; Stevenson et al., 2007a; Morgan et al., 2008; Schofield et al., 2010; Schofield et al., 2012a, b). Pollard et al. (1975) first reported finger-like geometries for a number of intrusions on the Colorado Plateau, having noted step-like geometries at intrusion contacts (initially referred to as 'straps' by Farmin, 1941; later termed 'Broken Bridges'; by Delaney & Pollard, 1981; Hutton, 2009; Schofield et al., 2012a, b). Magma fingers typically display short lengths, between 1 and 10 m (Pollard et al., 1975; Horsman et al., 2005), whereas lobate bodies range in size from hundreds of metres to kilometres in scale (Schofield et al., 2012a). For this reason, Schofield et al. (2012a) highlighted that magma fingers are a sub-seismic feature, whereas lobes can be resolved in seismic. Schofield (2009) proposed that fingers are an integral part of sill intrusions, with magma fingers growing to form lobes, and lobes coalescing to form sills (Fig. 1.3c). Schofield (2009) and Schofield et al. (2010) showed excellent field and seismic examples of magma fingers and lobate geometries forming saucer-shaped sills.

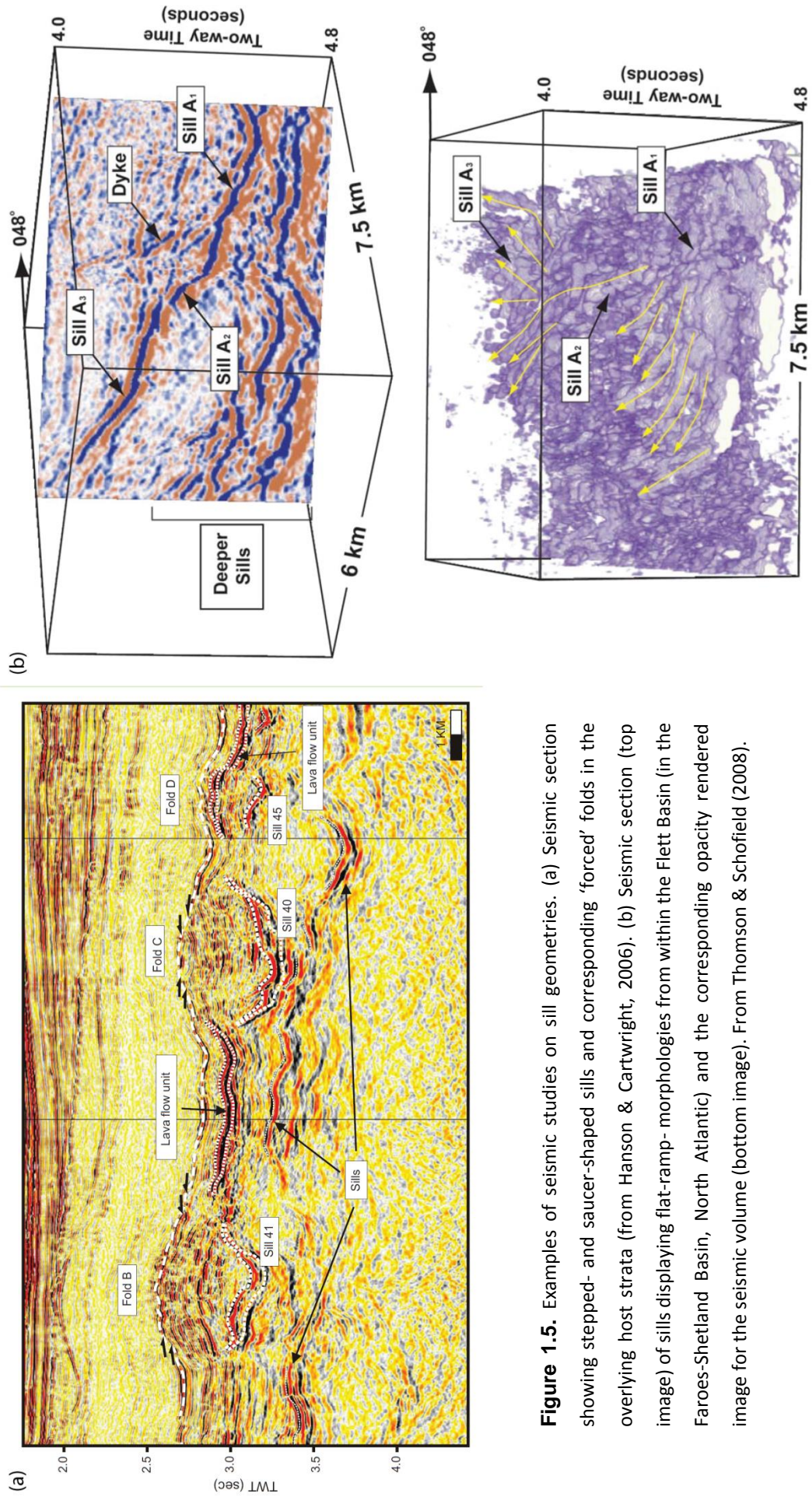


Figure 1.5. Examples of seismic studies on sill geometries. (a) Seismic section showing stepped- and saucer-shaped sills and corresponding 'forced' folds in the overlying host strata (from Hanson & Cartwright, 2006). (b) Seismic section (top image) of sills displaying flat-ramp- morphologies from within the Flett Basin (in the Faroes-Shetland Basin, North Atlantic) and the corresponding opacity rendered image for the seismic volume (bottom image). From Thomson & Schofield (2008).

1.2. Models for Sill and Laccolith Emplacement

1.2.1. *Gilbert's Early Work*

Gilbert's (1877) paper on the intrusions of the Henry Mountains, Utah is most likely the earliest detailed study of sill and laccolith intrusions and emplacement mechanisms. It was during his ground-breaking geological studies in the Henry Mountains that Gilbert (1877, 1896) first coined the term "laccolite", and the region is now regarded as one of the type localities for sill and laccolith intrusions. Gilbert (1877) described laccoliths as the result of magma that "...insinuated itself between two strata, and opened for itself a chamber by lifting all the superior beds", further suggesting that the creation of laccolith intrusions can be divided into two, mutually exclusive, phases: (1) emplacement of the intrusion as a tabular sill or sills; and (2) vertical growth through thickening of the sill sheets and a coincident cessation in radial spreading. More than a century later, much of the laccolith literature largely supports Gilbert's model for the genesis of laccoliths (e.g. Johnson & Pollard, 1973; Corry, 1988; Figs 1.2 & 1.4).

Gilbert (1877) proposed that the level at which sills and laccoliths are emplaced is controlled by the density contrast between the rising magma and the weight of the overburden, suggesting three alternative scenarios: (1) magma that is less dense than all the crust above it will migrate up through to the surface and build volcanoes; (2) if the upper portion of the crust is less dense than magma, but the lower portion is more dense, then the upwards migrating magma will stop at the level of the crustal density contrast, passing between the dense and less dense crust, or lifting upwards the lighter crust; and (3) if the crust is comprised of heterogeneous beds of alternating density, magma will be emplaced at a level where the beds above and below have a greater mean specific gravity than its own. Other authors (e.g. Bradley, 1965) have also proposed this model for sill and laccoliths occurring along isobaric surfaces (i.e. where magma pressure is the same as lithostatic pressure). However, this model for the 'level of neutral buoyancy' has, in more recent times, been proven fundamentally incorrect (e.g. Vigneresse & Clemens, 2000; Thomson & Hutton, 2004). If emplacement at a level of neutral buoyancy was the primary control, we would not see sills and laccoliths emplaced at multiple levels within a basin (Thomson & Hutton, 2004), nor would basaltic magmas have erupted at the Earth's surface as they are always more dense than the upper- and mid-crust. Magma pressure, rather than buoyancy, is likely the primary driving force for intrusion emplacement (Vigneresse & Clemens, 2000).

1.2.2. Mechanisms of Emplacement

Similar to Gilbert (1877), Corry (1988) divided the genesis of laccoliths into two cycles: (1) emplacement; and (2) growth. He further divided the emplacement phase into two stages: Stage 1 – the migration of magma vertically through the lithosphere; and Stage 2 – initiation of horizontal spreading following reorientation of the magma. The following sections (1.2.2.1 – 1.2.2.3) discuss the various stages and associated mechanisms of emplacement and growth in more detail.

1.2.2.1. Magma Generation and Ascent

The processes involved in magma generation and ascent are strongly coupled with the composition and rheology of the magma. Here we shall focus on intermediate (dacitic) magmas, akin to those observed in the Henry Mountains, Utah. Andesitic and dacitic magmas are most commonly associated with subduction zones (Fig. 1.1a), with dacitic volcanic rocks and granodiorite/ tonalite intrusions the dominant rock types. Andesites are rarely primary magmas. Instead they are usually derived from the differentiation of basaltic parental magmas (Grove & Kinzler, 1986; Ellam & Hawkesworth, 1988). Although basalt is the input, dacite and andesite are volumetrically the most dominant shallow level and extrusive rocks in subduction zones (Turner et al., 2000).

Annen et al. (2006) showed numerically that intermediate and acidic melts are generated from two distinct sources; partial crystallization of basalt sills to produce residual H₂O-rich melts; and partial melting of pre-existing crustal rocks. When basalt magmas are emplaced into continental crust, melting and generation of silicic magma can be expected. Melting occurs in the solid roof and the adjacent thermal boundary layer of the intrusive body, while at the same time there is crystallization in the convecting interior. Thus the magmas formed can be highly porphyritic (Huppert & Sparks, 1988). The time-scales for melting and crystallization in basalt-induced crustal melting are in the order of 100–1000 years (Huppert & Sparks, 1988), which is relatively short in the context of the lifetimes of large silicic magma systems (>1 m.y.) or to the time-scale for thermal relaxation of the continental crust (>10 m.y.). As crystallisation can occur deep in the crust, several of the features of silicic igneous systems can be explained without requiring large, shallow-level, long-lived magma chambers (a feature commonly drawn on images depicting magmatic systems, e.g. Fig. 1.1c, d). Every addition of basaltic melt to the

chamber will trigger rapid formation of silicic magma. This magma will freeze again in time-scales in the order of 100–1000 years, unless it ascends to higher levels (Huppert & Sparks, 1988). Therefore most dacitic volcanic rocks and granodiorite/ tonalite intrusions in the upper crust are likely fed by rapid ascent from deep feeder systems (Huppert & Sparks, 1988; Menand et al., 2015).

Silicic magmas commonly ascend tens of kilometres from their source to upper crustal emplacement levels (or in a few cases, extrusion at the Earth's surface; Fig. 1.1b). The magma ascent rate is a function of pressure in the magma storage region, rheological and physical properties of the magma (e.g. viscosity, density), and the size and resistance to flow within the feeder conduit (Rutherford & Gardiner, 1999).

The classical view of silicic eruptions fed by long-lived magma reservoirs that slowly differentiate between mafic recharges has generally been ruled out by recent studies (Clemens & Mawer, 1992; Vigneresse & Clemens, 2000; Petford et al., 1994; Menand et al., 2015). The currently accepted model is that granitic magmas ascended via propagating fractures, as dykes, over extremely short time periods. Clemens and Mawer (1992) discounted the concept of long-distance diapiric transport of granitoid magmas, on the basis of thermal and mechanical grounds, and noted that there is the distinct lack of field evidence to support diapiric rise of such magmas. Furthermore, studies such as Marsh (1984), Mahon et al. (1988) and Menand et al. (2015) suggested that magma ascent through fractures would be >100 times faster than diapiric ascent, and is therefore the more efficient method.

Various studies have also emphasised the role played by active faults and shear zones, and pre-existing country rock structures in controlling the emplacement and growth of magma bodies at depth (e.g. Hutton et al., 1990; McCaffrey, 1992; Neves et al., 1996; Holdsworth et al., 1999; Snoke et al., 1999; Passchier et al., 2005). Active tectonics leads to permeability anisotropies in the source rock, in addition to localised mineral reactions that form reaction channels (Daines, 2000; Burchardt, 2009).

1.2.2.2. *Initiation and Level (Depth) of Sill Emplacement*

To form horizontal sills and flat-floored laccoliths, magma transport must reorient from vertically climbing (i.e. ascent via dykes) to horizontally spreading. Sill emplacement preferentially occurs in the brittle upper-crust by a process of tensile fracture between stratigraphic units (Anderson, 1938), allowing magma to propagate in a horizontal orientation (Roberts, 1970). Assuming that dykes are the likely feeder systems, for a sill to form, a rotation of the maximum principal compressive stress is required. Factors influencing the development of this sub-horizontal maximum stress are likely to be both internal (e.g. magma-pressure/ buoyancy; Anderson, 1951; Francis, 1982) and external (e.g. lithological and mechanical contrasts; MacCarthy, 1925; Mudge, 1968; Kavanagh et al., 2006; Menand, 2008). Anderson (1951) proposed a mechanism for the reorientation of magma whereby repeated injection of dykes leads to rotation of the stress field at a given point, causing magma intruding vertically to rotate onto a horizontal plane. Anderson's mechanism for the initiation of horizontal sill emplacement has been corroborated by recent studies, such as Parsons and Thompson (1991), Valentine and Krogh (2006), and Burchardt (2009).

MacCarthy (1925) noted the regularity with which laccoliths intrude into shale beds or along planes of unconformity. Other studies have also suggested that crustal anisotropies controlled the level at which sills and laccoliths might form from an ascending dyke. Analysing data from 54 sill and laccolith intrusions, Mudge (1968) reported two important observations: first, the palaeo-depth of emplacement ranged from c. 900 to 2300 m; and second, that most intrusions had intruded along well-defined bedding planes and were covered by beds of impermeable mudstone and siltstones, concurring with the observations of MacCarthy (1925). Mudge (1968) suggested that the overlying mudstones and siltstones acted as an impermeable barrier to magma and steam, halting vertical migration, and forcing the magma to spread laterally along the base of the impermeable horizon. Mudge (1968) further argued that the palaeo-depth of emplacement is, to some extent, controlled by the palaeo-depth of the impermeable mudstone/ siltstone horizon, and changes in the mechanical strength of key minerals with varying depth. In his model, mudstone/ siltstones behave in a brittle manner above 900 m (ductile at depths >900 m) and fracture to allow channelised flow of magma through the impermeable horizon.

Kavanagh et al. (2006) used gelatine-based laboratory experiments to show that lithological discontinuities and rigidity contrasts can control the formation and dynamics of sills, and that magma is most likely to propagate at interfaces separating upper, rigid strata from lower, weaker strata. Menand (2008) subsequently built upon the work of Kavanagh et al. (2006), highlighting that formation of a sill itself provides a favourable rigidity anisotropy for the emplacement of subsequent sills, thus supporting the amalgamation of sills by accretion (e.g. as seen at Trachyte Mesa, Henry Mountain, Utah; Morgan et al., 2008).

1.2.2.3. *Sill Propagation and Growth*

Once a sub-horizontal sill has developed, it is thought to propagate laterally by tensile fracturing in the direction of least resistance (Gilbert, 1877; Anderson, 1938). Through their studies in the Henry Mountains, Johnson and Pollard (1973), and Pollard and Johnson (1973) concluded that sill thickness is a linear function of their length, and once a sill reaches a critical length/ diameter it will inflate vertically. This vertical inflation stage then leads to the formation of a laccolith. Koch et al. (1981), Jackson and Pollard (1988, 1990), Kerr and Pollard (1998) and others have suggested that the radial extent of the intrusion may be controlled by the effective thickness of the overburden and the elastic properties of the overlying sandstone. However, as discussed by Corry (1988), other factors such as magma viscosity, strain rate and sheet thickness should also be considered.

Hunt (1953) proposed three models for laccolith emplacement and growth (Fig. 1.6a–c): (1) radial growth only, with magma emplaced at a constant thickness, and country rocks displaced both vertically and laterally (i.e. a “bulldozing” mechanism; Model B of Hunt, 1953, fig. 70, p. 142); (2) simultaneous vertical and horizontal growth (Model C of Hunt, 1953); and (3) two-stage growth, comprising radial growth of a thin sheet, followed by dominantly vertical growth and associated vertical uplift of the overriding host rocks (i.e. a “two-stage growth” mechanism; Model A of Hunt, 1953). Hunt (1953) preferred simultaneous vertical and horizontal growth having identified flaws in both end member cases (models 1 and 3 in Fig. 1.6; see p.142 in Hunt, 1953).

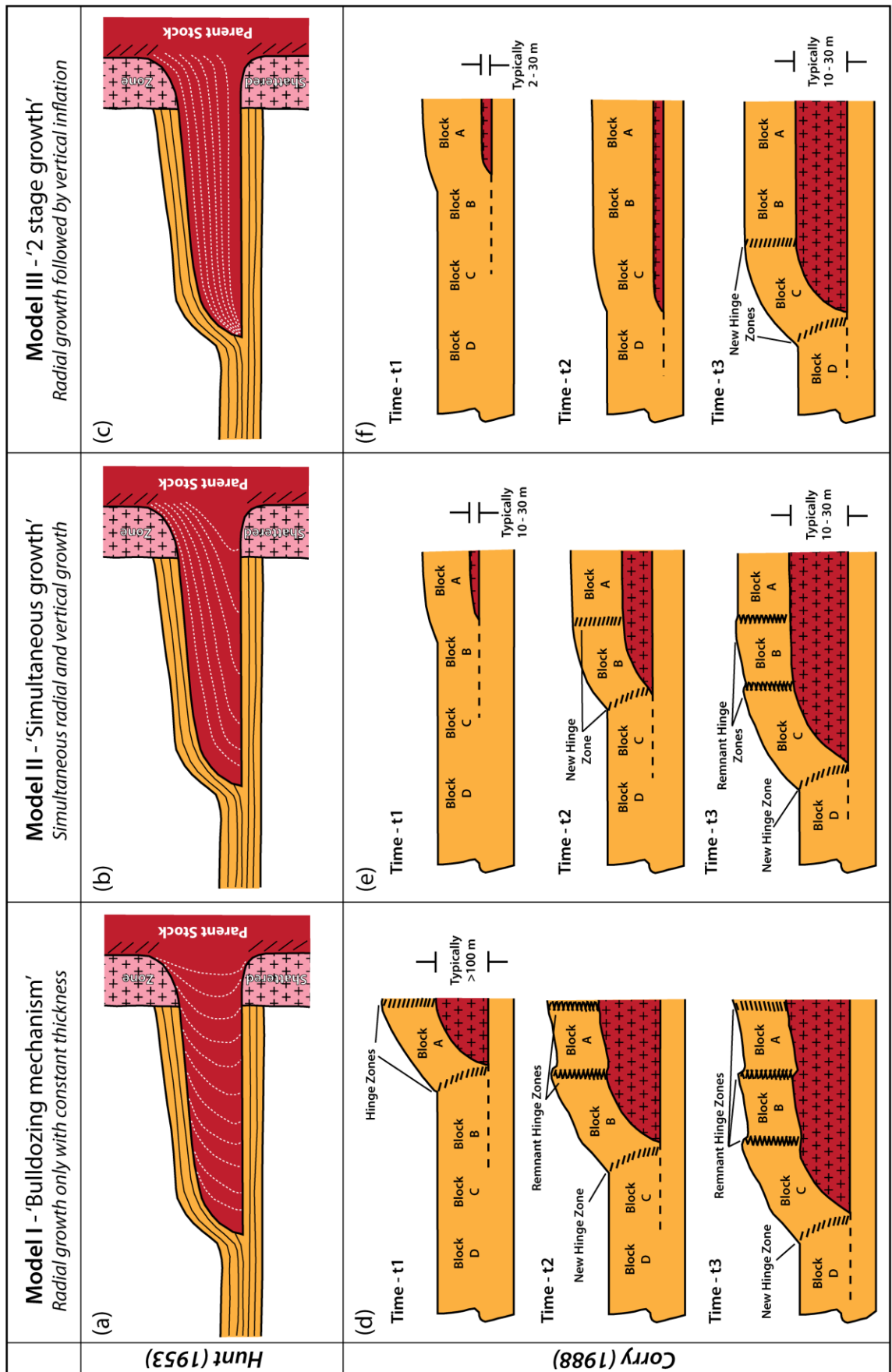


Figure 1.6. Growth models for laccolith intrusions (modified from Hunt, 1953, and Corry, 1988). (a), (b) and (c) correspond to Models B, C and A of Hunt (1953) respectively, and show three different mechanisms of laccolith growth: (a) bulldozing; (b) simultaneous growth; and (c) 'two-stage' growth. Based on the three models of Hunt (1953), (d), (e) and (f) correspond to Models 1, 2, and 3 of Corry (1988) for laccolith growth and expected deformation of the country rock.

Building on the work of Gilbert and Hunt, Corry (1988) offered three possible modes of laccolith growth and expected deformation in the overlying sediments (Fig. 1.6d – f). He advocated a ‘two-stage’ growth model (Model 3 – with radial growth only until t_2 , followed by vertical growth only) as being best supported by field observations. In this scenario new hinge zones are created at the top and front edge of the intrusion margin. Corry (1988) argued against the other two models (Model 1 – radial growth only while thickness remains constant; Model 2 – simultaneous radial and vertical growth) predicting that a wake of remnant hinge zones would be expected behind the laterally expanding intrusion and finding no evidence for these remnant hinge zones in the field. Corry (1988) noted that the plate bending models of Pollard and Johnson (1973) would result in a sequence of laccolith intrusion similar to Model 2 (simultaneous radial and vertical growth), highlighting that no evidence for remnant hinge zones has been observed in their studies.

Pollard and Johnson (1973) presented a theoretical model using continuum mechanics to explain the formation of peripheral dykes at the tips of laccolith intrusions (Fig. 1.7a) using field observations from the Henry Mountains. They suggested that dykes forming at the periphery of the intrusions result from flexural/ elastic bending of the overburden layers (contractional over the centre and extensional over the periphery). Thompson and Schofield (2008) suggested that the main control on the development of faults at sill sheet terminations is the depth of formation (Fig. 1.7b). In their model, at shallower depths, cohesive strength along bedding planes is less, and thus favours the development of flexural slip folding. In their model, as depth increases, higher shear stresses are required for flexural slip, thus favouring mechanical failure of the rock through fracture/ faulting (cf. Stearns, 1978).

Sill propagation rates and resultant geometries may be a consequence of viscous dissipation and viscosity-controlled dynamics (Menand, 2008). Modelling of Kavanagh et al. (2006) showed that for this reason sills propagate quickly, which may thus induce non-elastic deformations in the surrounding rocks that could allow them to deviate upwards from their horizontal interface, and assist in the formation of step structures and saucer-shaped sills (Fig. 1.7a; Malthe-Sørensen et al., 2004; Menand, 2008). Schofield (2009), in contrast, suggested that fluidisation of the host-rock plays an intrinsic part in the process of sill propagation and deviation (e.g. sill climbing).

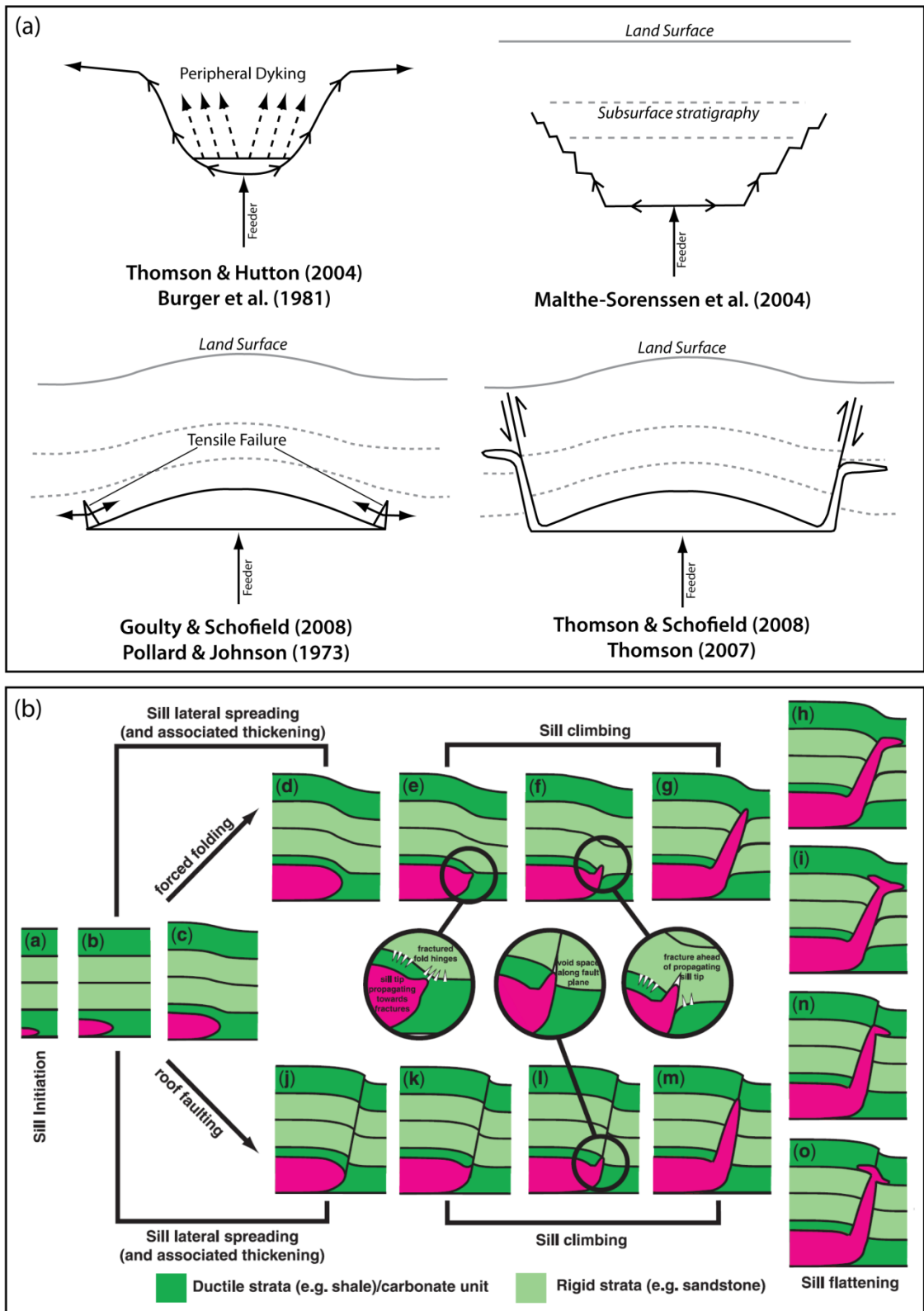


Figure 1.7. Models of sill emplacement and propagation (and ramp-flat morphologies). (a) Four models for the emplacement of saucer-shaped sills (after Schofield, 2009; derived from seismic data and models from a number of papers, noted in the figure). (b) Schematic model for sill propagation within sedimentary basins (from Thomson & Schofield, 2008). Localised sill-climbing occurs when magma makes contact with and propagates along open fractures associated with forced folds in the overlying sediments (stages e–g), or faults associated with faulting of roof rocks (stages j–m). At some point the magma will again reorient and propagate once more along a horizontal plane (sill-flattening).

1.3. Historic Expeditions to the Henry Mountains

1.3.1. *Gilbert and the Powell Expeditions*

In 1869 intrepid explorer, scientist and decorated Civil War hero John Wesley Powell, along with nine companions, embarked on a daringly adventurous, three month expedition of the American West: travelling almost 1000 miles down through uncharted canyons along the Green and Colorado Rivers in four small boats (Fig. 1.8a; Gilbert, 1877; Powell, 1961; Dolnick, 2001). Embarking on their journey along the Green River, the ten men tackled dangerously strong currents and roaring rapids, losing one of the boats and supplies less than 80 miles into the trip. Four crew members left the company during the expedition: one leaving after a month; three leaving at a place now known as Separation Canyon, never to be seen again (Hunt, 1953). Two days after Separation Canyon, Powell and his five remaining crew emerged from the Grand Canyon at the mouth of the Virgin River (now below Lake Mead), succeeding in their venture to become the first known group of non-indigenous men to travel down the Colorado River through the Grand Canyon (Dolnick, 2001).

After securing funding, Powell with nine companions (only his cousin returning from the original company of men from the 1869 expedition) embarked on a second expedition of the Green and Colorado Rivers in 1871: this time carrying out mapping and more detailed scientific studies that would later be published (Powell, 1895, 1961).

During both expeditions, Powell was afforded a good view of the Henry Mountains in south-eastern Utah (Fig. 1.8). The last of the mountain ranges to be added to the map of the contiguous lower 48 United States, the Henrys did not appear on any map until 1872, following their discovery by Powell in 1869. Initially referred to as the Unknown Mountains, Powell officially named the range after Joseph Henry, a physicist at the Smithsonian who helped Powell secure funding for the expeditions (Hunt, 1988). Observing the two southern Henry Mountains from distance, Powell commented that they were structural domes associated with “lavas”. With a long-standing debate on the nature of volcanoes as controversial “craters of elevation” (Lyell, 1830; von Buch, 1836) still unresolved, Powell organised for Gilbert to visit the Henrys to investigate the “lavas” further (Hunt, 1988).

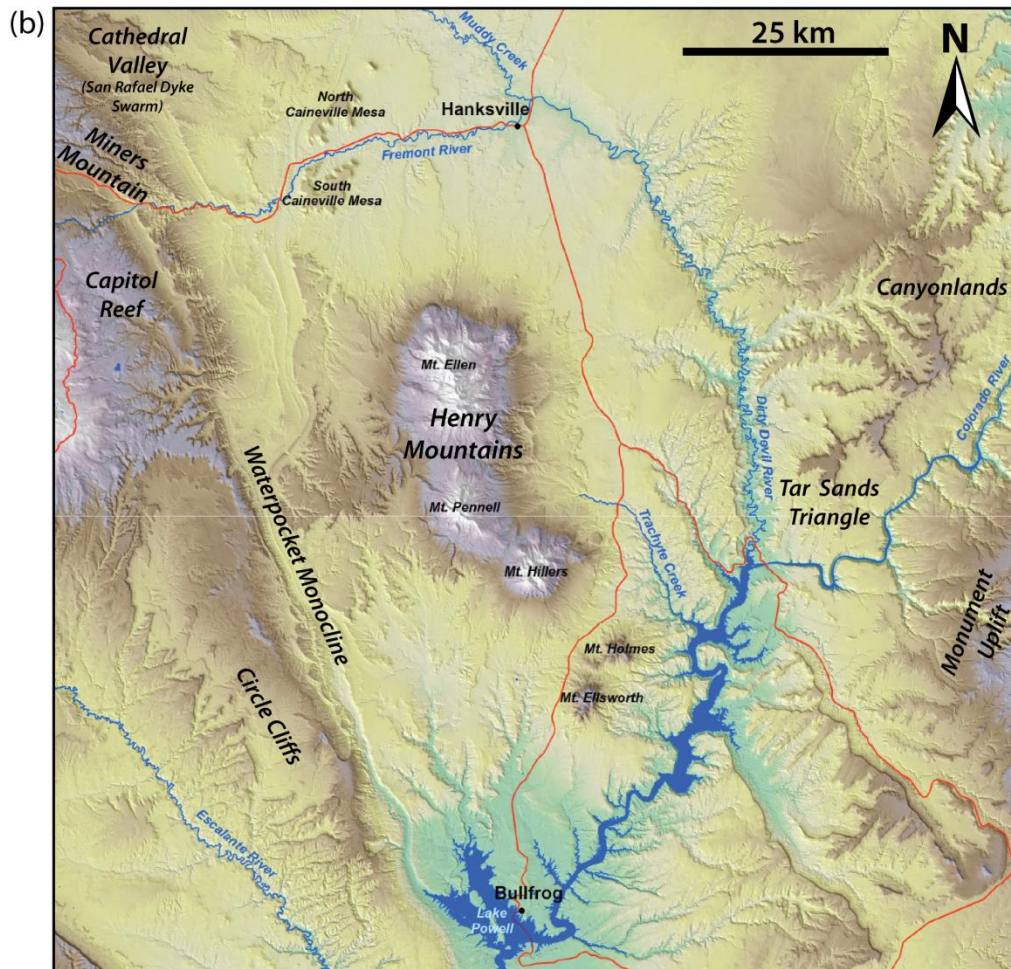
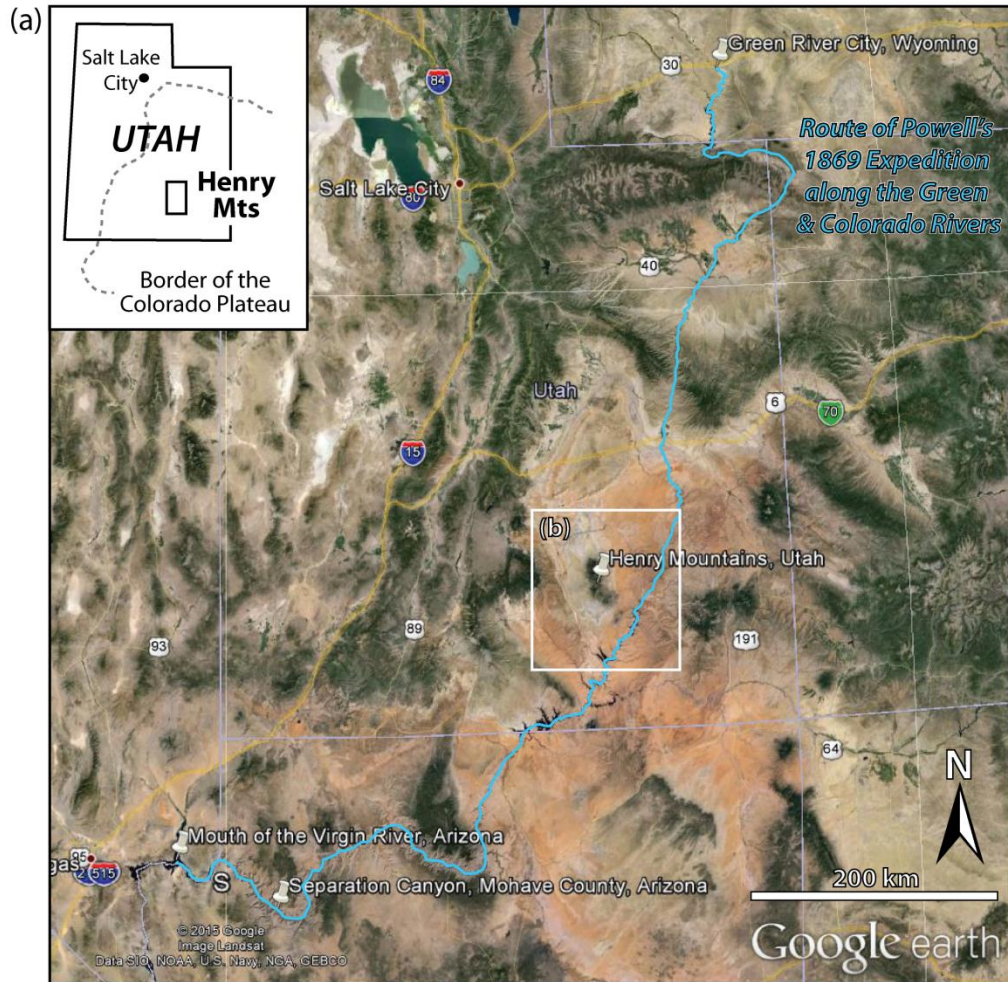


Fig. 1.8

Figure 1.8. (previous page)

Route of Powell's Expeditions and proximity to the Henry Mountains, Utah. (a) Map from Google Earth™ showing Powell's 1869 expedition route through the Wild West along the Green and Colorado rivers, starting from Green River City, Wyoming in the north, travelling south through Utah, then west through the Grand Canyon and finishing at the once mouth of the Virgin River in Arizona. Location pins highlight route start and end points, Separation Canyon and the Henry Mountains (also see Google Earth™ kmz project in Appendices for locations). State borders and grid lines are shown. Inset: (top left) simplified map showing the location of the Henry Mountains within Utah and on the Colorado Plateau (adapted from Morgan et al., 2008). (b) Topographic map of the Henry Mountains region in south-eastern Utah. Note the Colorado River (and modern day Lake Powell) to the south and east. Key geological structures and features are highlighted. Location of (b) shown on (a).

Between 1875 and 1876, Grove Karl Gilbert (Fig. 1.9) carried out field studies in the Henrys. Gilbert and his party travelled from Salt Lake City to the Henrys as a pack train (a team of mules and horses), from Salina Canyon, south via Fishlake and east via Rabbit Valley (Gilbert, 1877; Hunt, 1988). Gilbert spent only one week in the Henrys in 1875, and then two months when he returned in 1876 (Hunt, 1953). Figure 1.10 shows Gilbert's 1875 and 1876 expedition routes on a map of the Henrys (Hunt, 1988). In 1875, Gilbert approached the Henrys from the south-west, initially looking at the southern flank of Mount Hillers, and then onto Mount Ellsworth, before traversing northwards via the north-easterly satellite intrusions of Mount Hillers, through the Pennellen Pass and finally over the crest of Mount Ellen. Following the reconnaissance trip in 1875, the longer trip in 1876 followed a far more complex route, weaving around the five mountains and appearing to re-visit certain localities on a number of occasions.

Gilbert navigated his way about the ruggedly harsh Utahn desert by following often faint, prehistoric Indian trails and secondary trails made by various wildlife (including coyotes, foxes, mule deer and jack rabbits), the latter trails normally leading to sources of water (Hunt, 1988). Enduring the unrelenting heat of the arid climate, interspersed with thunder and lightning storms that can turn slot canyons and dried up river beds into torrents with flash flooding (even when miles away, but within the same catchment area), Gilbert explored the geology of the challenging and rugged landscape. Although access to the area is now far easier, many of these risks are still applicable today. In addition to the unforgiving nature of the natural environment, Gilbert and his party also had to endure the threat of hostile native western Indians: three explorers were murdered by Shivwits

Indians in the lower Grand Canyon after leaving the Powell expedition, 7 years prior to the Gilbert expeditions; and a further three explorers were killed by Mojave Apache Indians when the Wheeler expedition party were ambushed in Arizona 5 years earlier (Hunt, 1953).

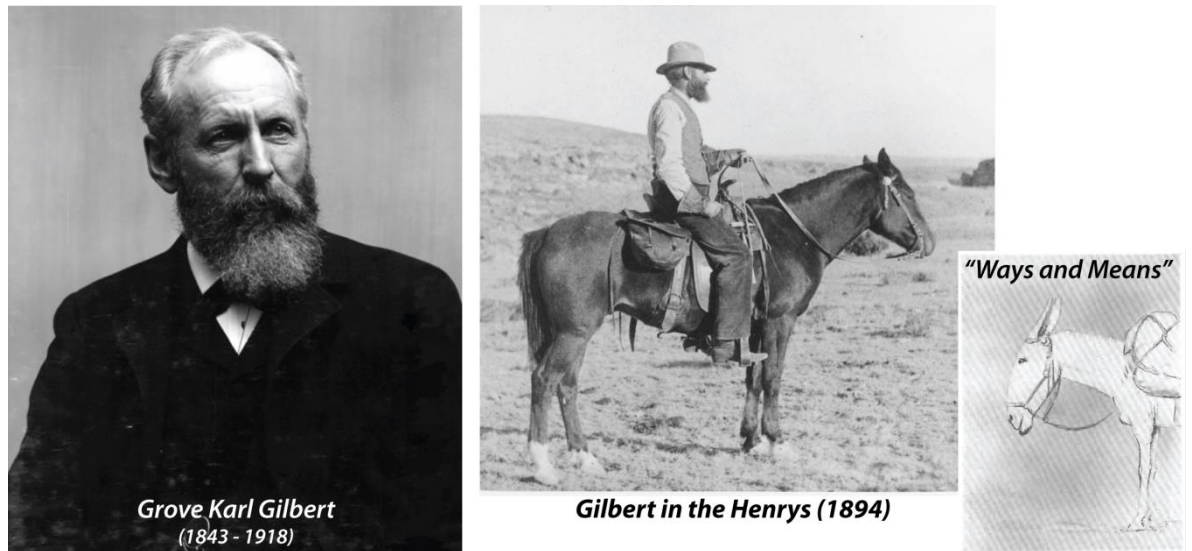


Figure 1.9. Photographs of highly-esteemed, American geologist and twice President of the Geological Society of America, Grove Karl Gilbert. Left, photograph from Hunt (1988). Right, photograph of Gilbert on a horse while visiting the Henry Mountains in 1894 (courtesy of US National Academy of Sciences Archives) with Gilbert’s drawing of one of the mules from his 1875–1876 pack-train expeditions to the Henrys, entitled “Lazarus, Duke of York” (Hunt, 1953, 1988; Gilbert’s Notebook 2).

Gilbert’s 10 notebooks from his two trips to the Henrys are equal in stature to his groundbreaking publications (1877; 1896) that transpired from them, with incredibly detailed note making, not only describing the geological features and interpretations, but also reporting the locations of camps, distances between them, incidents of note (e.g. recounting each time one of the mules took a tumble off a cliff), ration provisions, encounters with other people, and the weather. In addition to this is Gilbert’s excellent art work (mostly line drawings; Figs 1.11–1.13), accurately depicting the various landscapes and geological structures (compare field sketches with photos in Figs 1.11–1.13). Such is the quality of Gilbert’s notebooks, Charles Hunt dedicated time to typing them up and scanning the numerous field sketches, publishing the memoir on Gilbert’s Henry Mountains notebooks in the late 1980s (Hunt, 1988). Gilbert’s published sketches are both beautiful works of art, as well as excellent illustrative examples of geological architectures (Fig. 1.14).

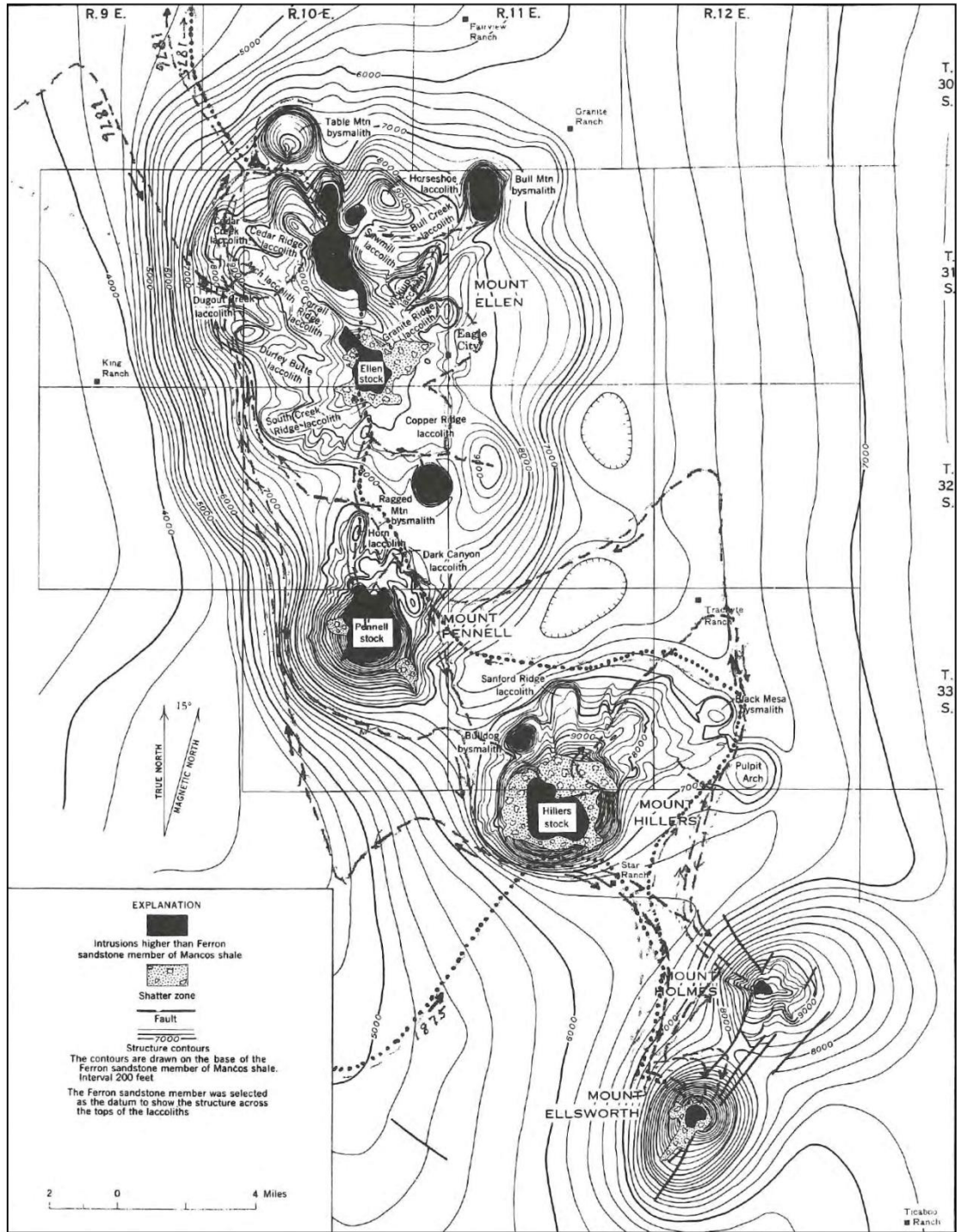


Figure 1.10. Map showing Gilbert's 1875 and 1876 expedition routes through the Henry Mountains (Hunt, 1988).

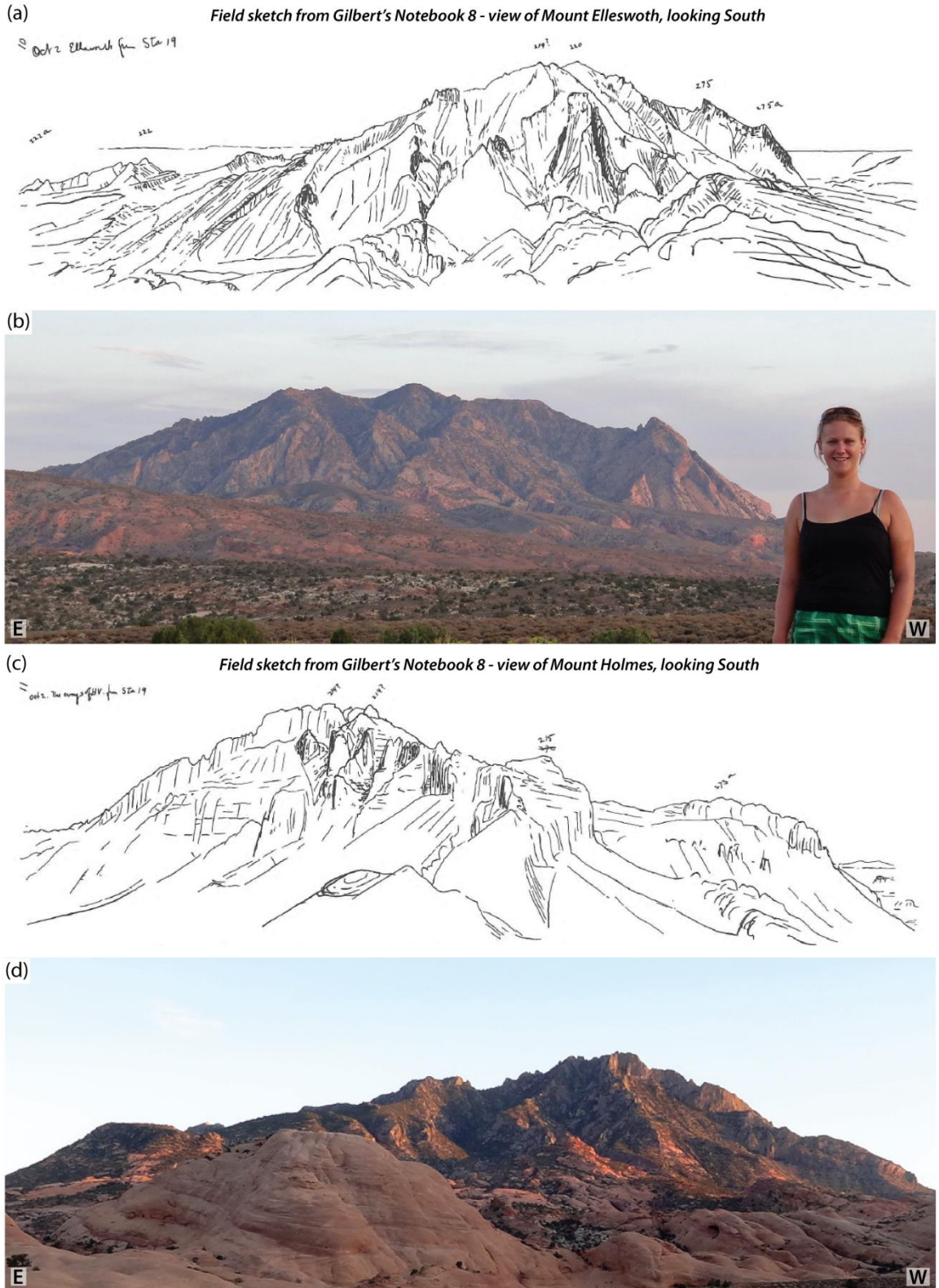


Figure 1.11. Examples of Gilbert's line-drawings from his 1876 Notebooks on the Geology of the Henry Mountains (from Hunt, 1988). (a) and (c) are line-drawings of Mounts Ellsworth and Holmes respectively, with (b) and (d) recent field photographs for comparison.

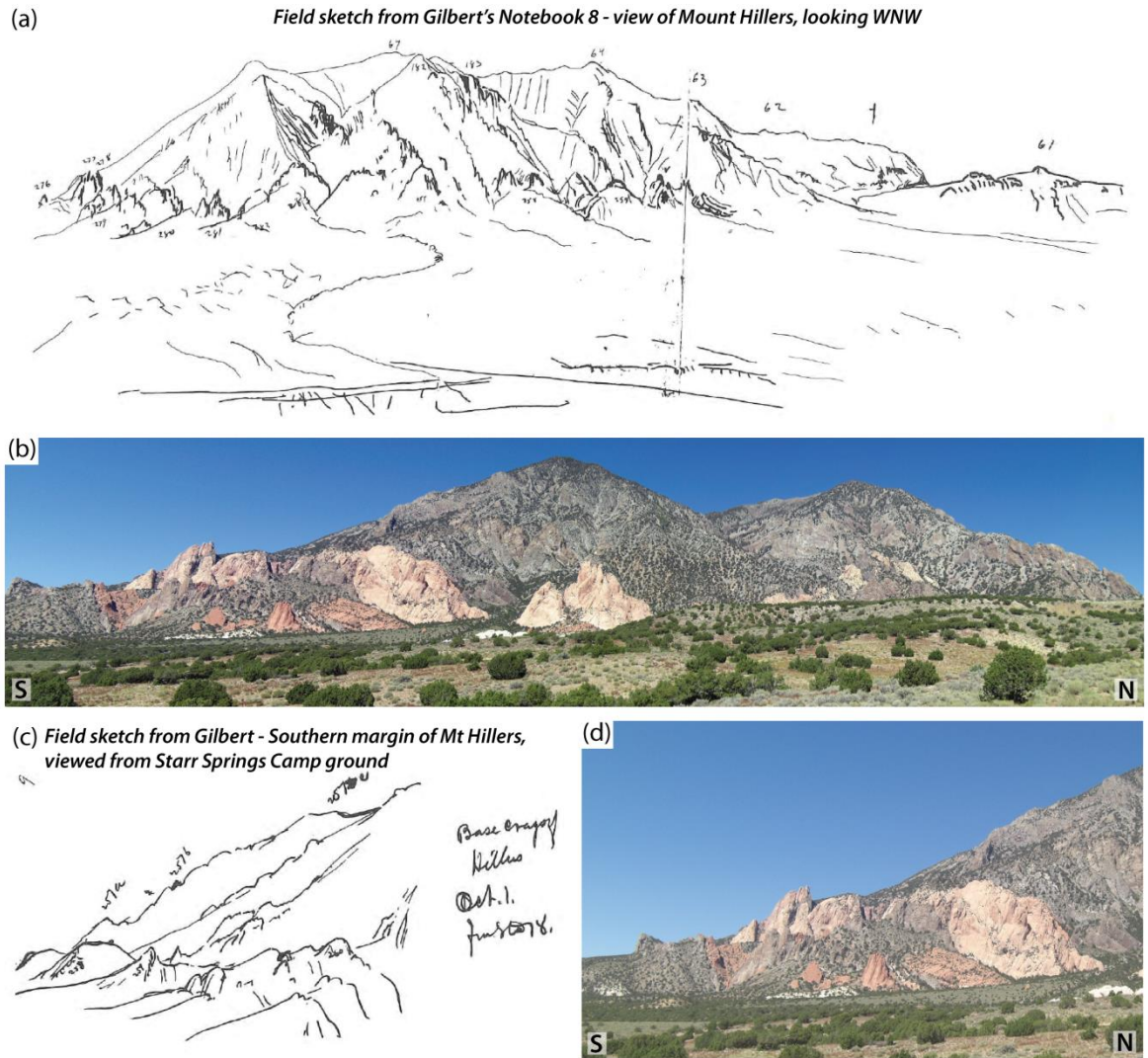
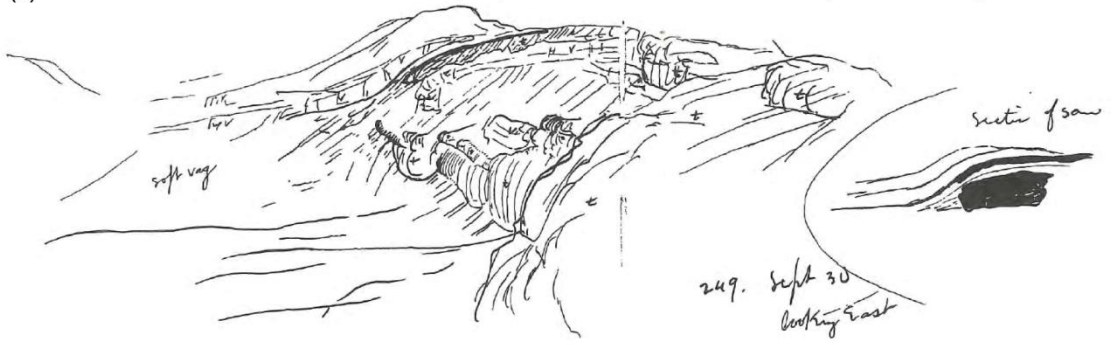


Figure 1.12. Examples of Gilbert’s field sketches of Mount Hillers as viewed from the ESE, both of the whole mountain (a) and zoomed in on the southern margin and the sandstone “teeth” (c). Recent photographs (b) and (d) are provided for comparison.

Figure 1.13. (overleaf)

A series of images of the Trachyte Mesa intrusion, Henry Mountains. (a) Field sketch of the south-western margin of Trachyte Mesa (originally referred to as Howell Laccolith) from Gilbert’s 1876 Henry Mountains Notebooks (from Hunt, 1988), with a schematic diagram showing the intrusion–host rock geometry. (b) Photograph for comparison. (c) Photograph from 1936 of the Hunt party and their pack train, surveying the south-western margin of Trachyte Mesa (Hunt, 1997). (d) Colour photograph for comparison.

(a) Field sketch from Gilbert's Notebook 8 (30 Sept 1876) - Howell Laccolith (aka Trachyte Mesa) looking East



(b)



(c)

Pack train of the 1936 USGS field party (Trachyte Mesa)



(d)



Fig. 1.13.

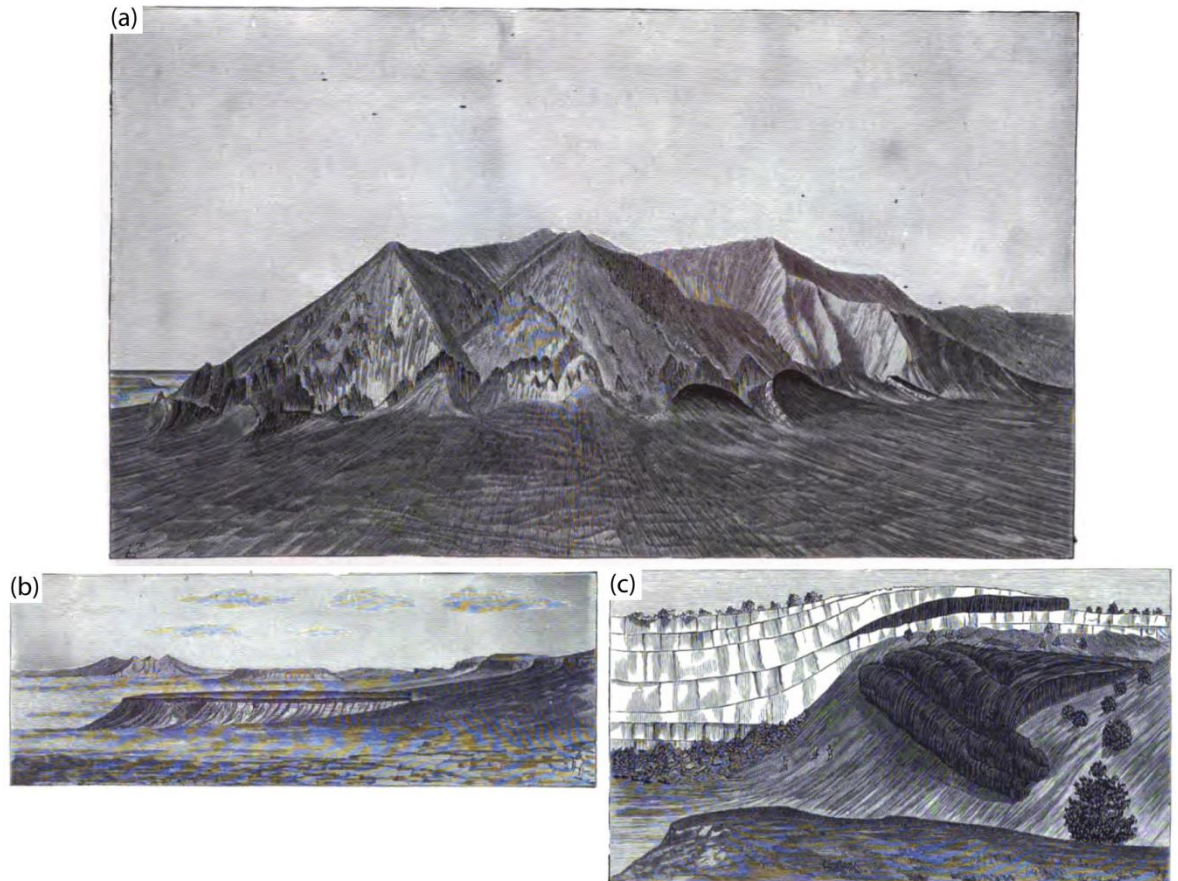


Figure 1.14. Examples of Gilbert's published illustrations (1877). (a) Mount Hillers, as viewed from the south. (b) The elongate Trachyte Mesa intrusion (Howell Laccolith) as viewed from the north. (c) The southwestern lateral margin of Trachyte Mesa, looking to the NE.

1.3.2. *Hunt's 1930's USGS Expeditions*

Charles Hunt (Fig. 1.15b) was the next geologist to carry out significant studies of the Henry Mountains, 60 years after the revolutionary work of Gilbert. The last of the big pack-train surveys, Hunt carried out field studies in the Henrys for a few months each year from 1935 to 1939 (Fig. 1.15a; Hunt, 1953, 1997). With the invention of the motorised vehicle, base camps were established in spots that were reachable by truck, these largely situated to the north of the Henrys (e.g. Hanksville). For mapping of more inaccessible parts of the northern mountains, and for all of the southern mountains, camps could only be reached and supplies carried by pack-train, using 12 to 15 pack mules (Fig. 1.15c; Hunt, 1953). Over the course of the survey, Hunt and his party stayed at over 200 camps. Research publications, including the first detailed geological map of the area, were delayed until 1953 due to the Second World War (Fig. 1.16; Hunt, 1953).

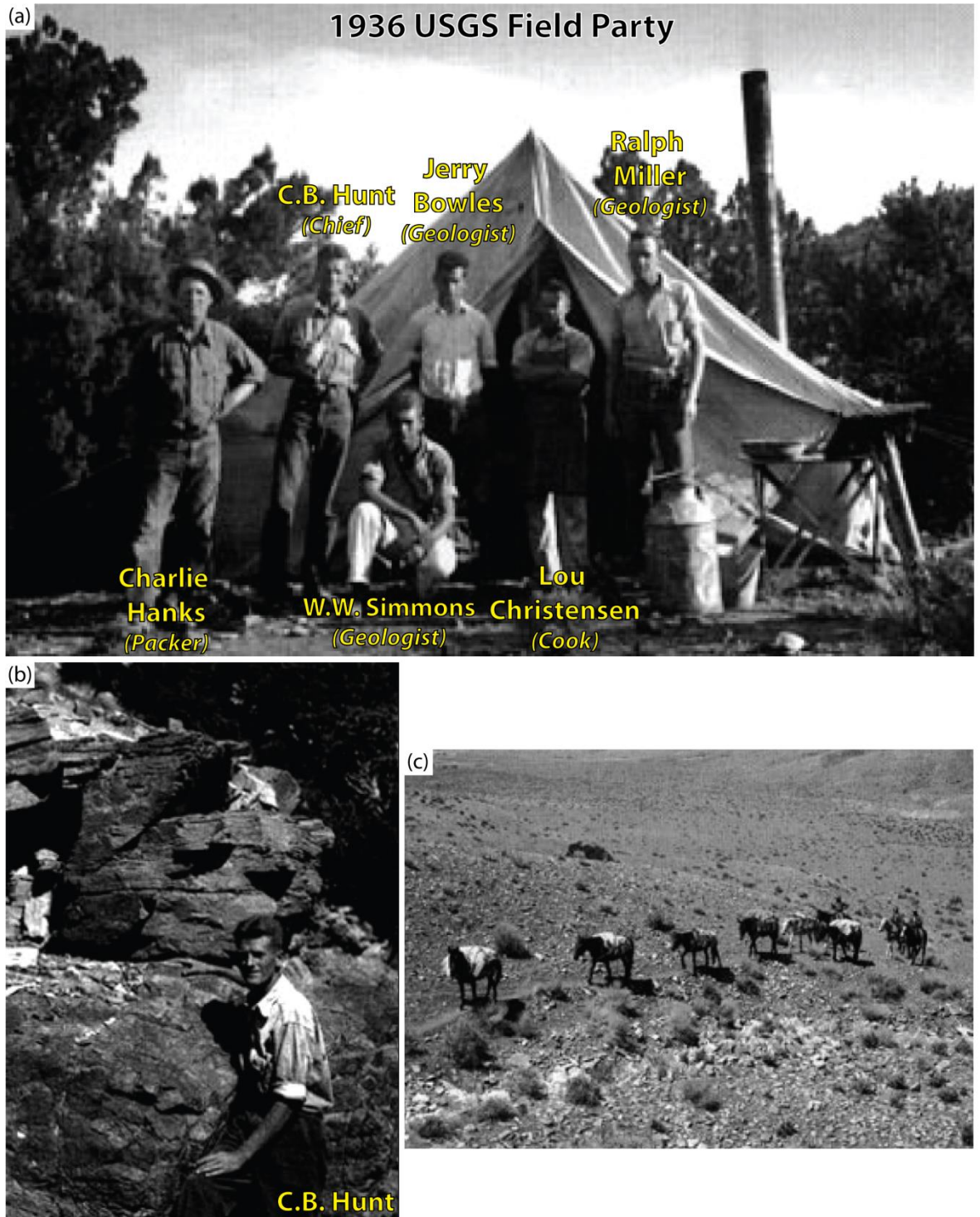


Figure 1.15. Field photographs from the 1936 USGS Field Party to the Henry Mountains (Hunt, 1997). (a) The field party at one of their 200 plus campgrounds. (b) Charles Hunt examining an intrusion–host rock contact near Mount Ellen, north Henry Mountains. (c) Pack train carrying supplies to a spike camp at Fourmile Spring.



Figure 1.16. Digital scan of an original copy of Hunt's geological map of the Henry Mountains region, Utah.

1.3.3. Recent Field Studies

Following the work of Hunt, the next group of geologists to carry out significant research in the Henry's were a group from Stanford University (Arvid Johnson, Dave Pollard and to a lesser extent, Attila Kilinc). Their field activities focused mainly on Mounts Hillers, Holmes and Ellsworth during the late 1960s and early 1970s, working on an NSF project 'Mechanical Analysis of Rock Deformation Associated with High-level Intrusions' (Johnson & Pollard, 1971).

Many geologists have worked more recently in the Henrys, with notable recent studies including: Nelson et al., 1992; Nelson and Davidson, 1993; Habert and de Saint Blanquat, 2004; Horsman et al., 2005; de Saint Blanquat et al., 2006; Morgan et al., 2008; and Wetmore et al., 2009. Other geologists have had the opportunity to visit the classic outcrops of the Henrys thanks to publically organised field excursions, such as the GSA 2005 and 2010 LASI (Laccolith and Sill Intrusions) IV field excursions (Morgan et al., 2005, Horsman et al., 2010).

1.4. This Study

1.4.1. Project Aims

This research aims to develop a greater understanding of how igneous intrusive bodies are emplaced and accommodated within the shallow crust. Key questions that will be addressed in this thesis include:

- What is the effect of emplacement of shallow-crustal intrusions on the surrounding country rock?
- How is the additional volume of magma accommodated within the crust, the so called "space problem"?
- Can we use style of deformation to infer sub-surface intrusion geometries?
- What can the style of deformation tell us about emplacement mechanism?
- What controls the emplacement mechanism?

Figure 1.17 shows an initial model for emplacement-related deformation envisaged following a reconnaissance study of the Henry Mountains (LASI IV field trip, summer 2010). This model will be tested in the thesis.

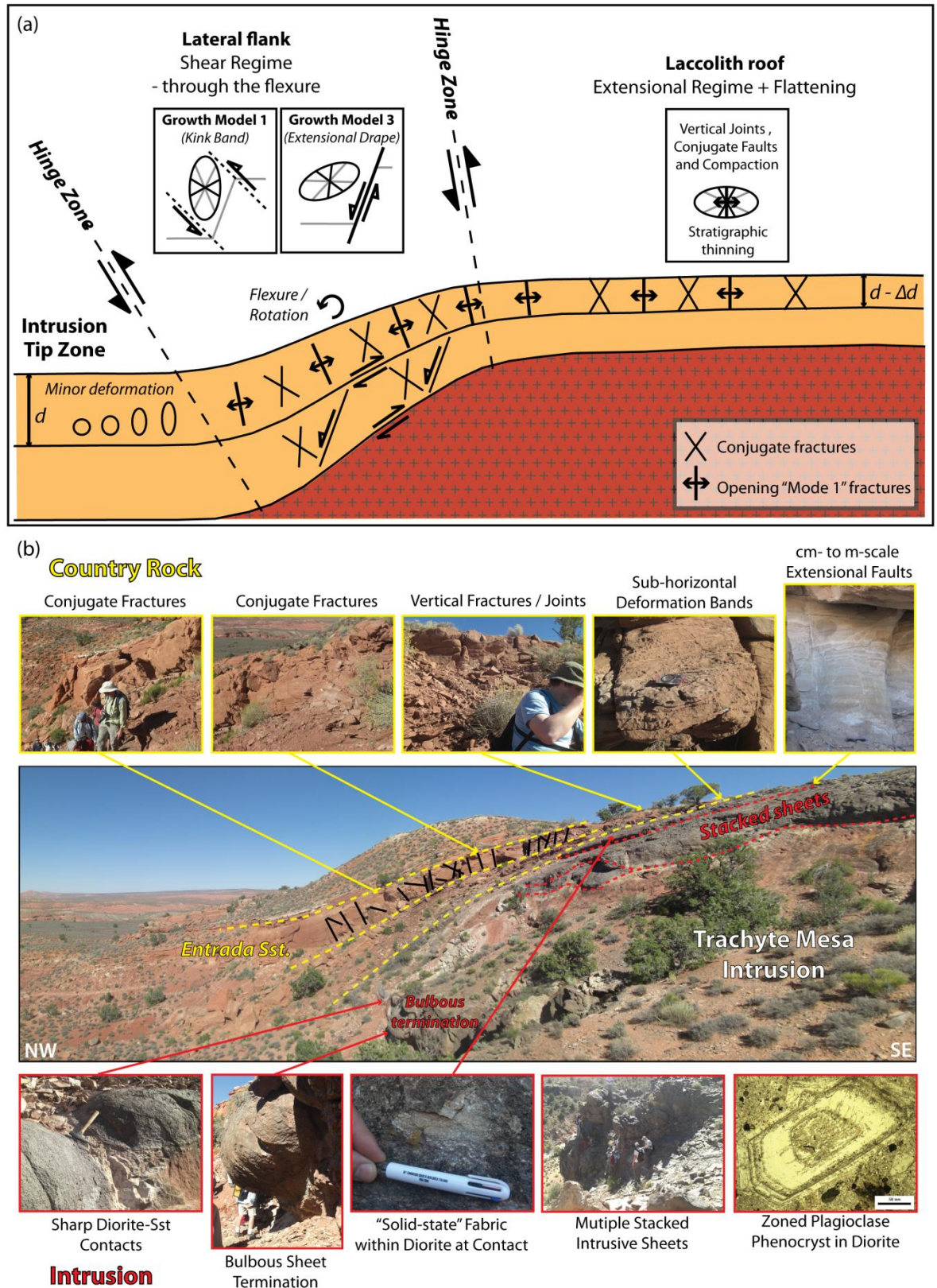


Figure 1.17. Model from a reconnaissance study of the Henry Mountains (LASI IV field trip, summer 2010) to be tested in the thesis. (a) Schematic cartoon summarising the styles of host-rock deformation structures expected in different zones surrounding a laccolith intrusion. (b) Photograph showing a lateral flank of the Trachyte Mesa intrusion (laccolith). Note correlation of deformation features with those predicted in (a). Inset photos highlight key features in the host-rocks (yellow) and within the intrusion (red).

1.4.2. Methods

Figure 1.18 provides a summary of the workflows applied during this research, from pre-fieldwork planning, to post-fieldwork analysis and integration.

1.4.2.1. Field Work

Field work for this study was carried out over two field seasons in the Henry Mountains, Utah (Fig. 1.8) during the summers of 2011 and 2012. Field work focused on two satellite intrusions to the Mount Hillers Intrusive Complex: the Maiden Creek and Trachyte Mesa intrusions. Alongside these detailed studies, a wider regional reconnaissance of the area was also carried out (see Appendices for locations). Field work comprised of observations and note taking, detailed structural data collection, rock sampling, and also the acquisition of terrestrial laser scans (TLS; Jones et al., 2005; Hodgetts et al., 2005; Jones et al., 2009).

A combination of conventional and digital mapping methods (McCaffrey et al., 2005) was applied during field work. Outcrop localities, bedding data and sample stations were recorded on a tablet PC using FieldMove™ (Clelland et al., 2011; Fig. 1.19). Some outcrop details were also recorded using the Field Note application within FieldMove™ (Fig. 1.19b). However, detailed structural data were recorded into a field notebook and transferred to an Excel spreadsheet each evening, and analysed using stereonet plotting software.

Google Earth™ has been used at various stages of the project as a quick reference tool for both visualisation and shared learning. Due to its increased usability, Google Earth™ proved very useful for pre-field work reconnaissance and planning. Published maps (Fig. 1.20a–c) and cross-sections can be easily georeferenced to overview the geological setting (though precision and accuracy are an issue for detailed studies). Post-field work, outcrop and sample locations may be quickly loaded as Google Earth™ pins with attached summary balloons populated with photos, images, and descriptive text (Fig. 1.20d, e). The project can then be shared with colleagues, regardless of location, via a kmz file (see Appendices).

Figure 1.18. *(overleaf)*

Work flow of methodologies.

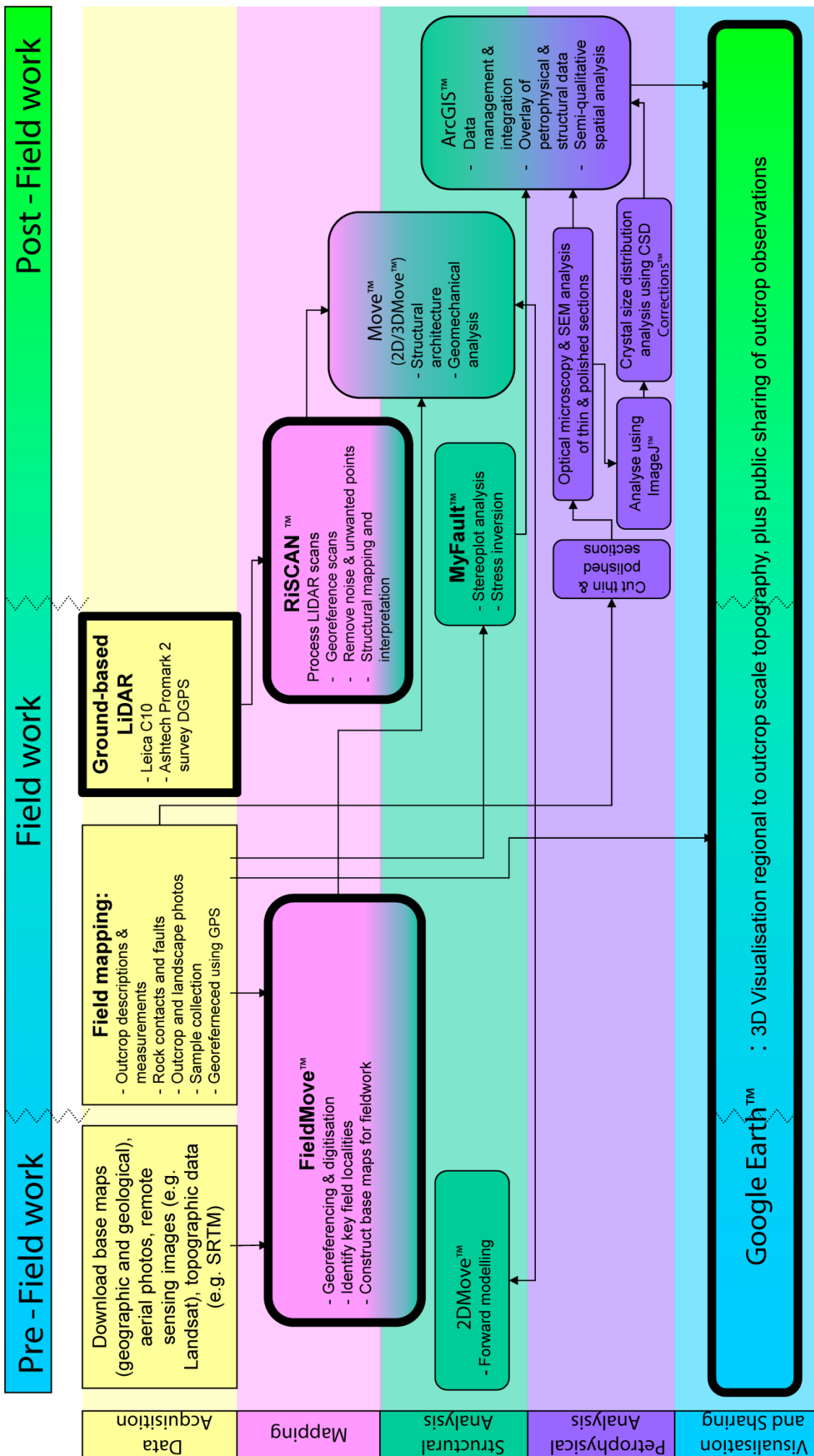


Fig. 1.18

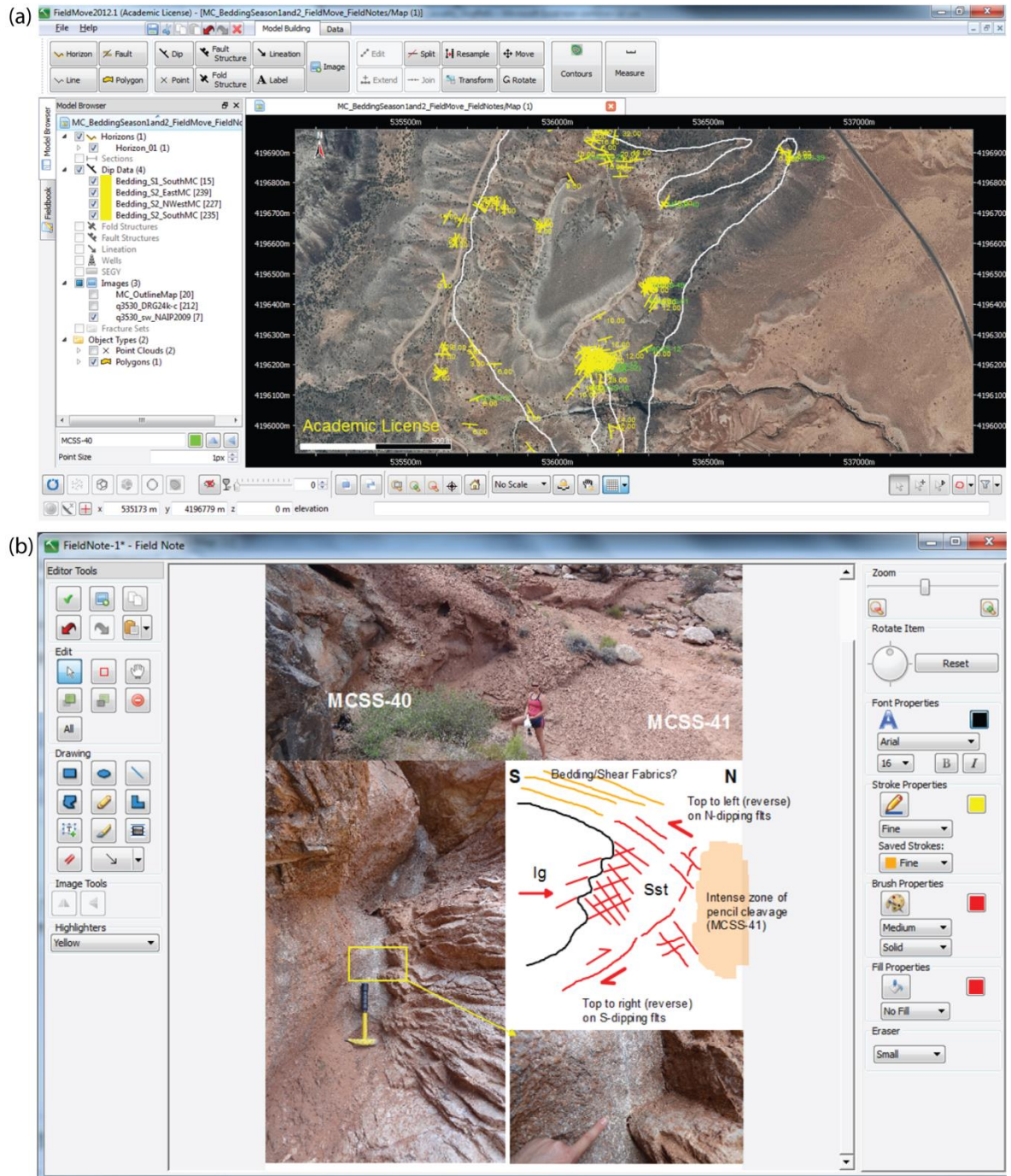


Figure 1.19. Example screen captures of the Maiden Creek digital mapping project in FieldMove™. (a) Georeferenced bedding measurements (in yellow) and intrusion outline (as suggested by Horsman et al., 2005) mapped onto an aerial image of the field area (in white). (b) An example of a Field Note outcrop record.

1.4.2.2. Structural Data

Detailed kinematic and geometrical analyses were carried out at outcrops across the study areas. Constraining the geometric, kinematic and spatial distribution of emplacement-related deformation structures is fundamental to answering the 5 questions outlined above (section 1.4.1).

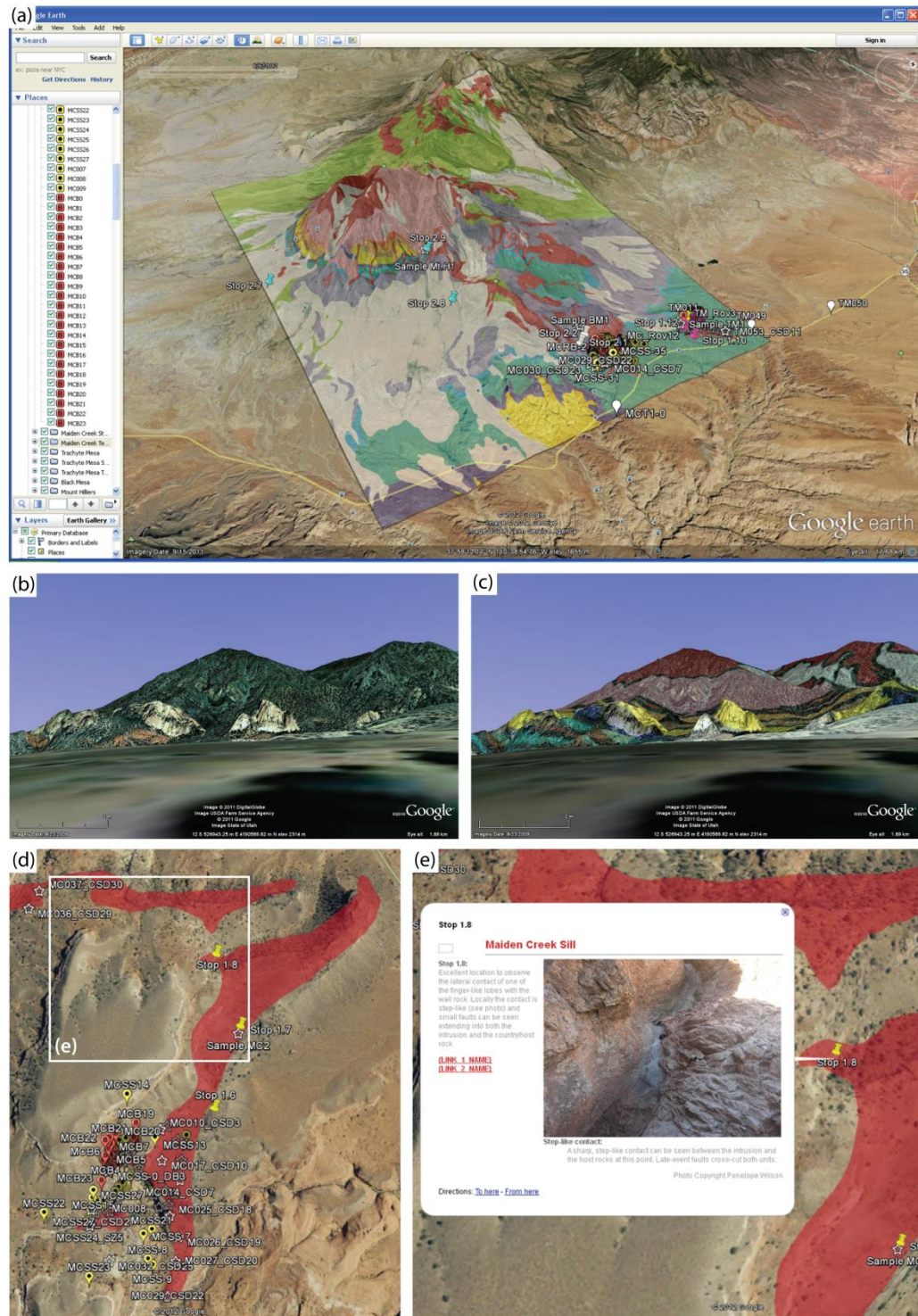


Figure 1.20. A series of images from the Maiden Creek Google Earth™ project (see Appendices for the kmz file). (a) Published geological map (Larson et al., 1985) draped over topography in Google Earth™. (b) and (c) The southern margin of Mount Hillers, Henry Mountains, as seen in Street View, with the geological map draped over the topography in (c). (d) Igneous outcrop draped over the topography (in red) with locations of labelled structural stations marked by yellow pins. (e) An example of a pop-out balloon with a photograph of an outcrop and field observations.

At each structural station, a representative structural dataset (including: deformation type; geometry; kinematics; phase/ timing; character) was collected (minimum of 30

measurements per station; >50 in areas of high intensity deformation). In total, 6045 structural measurements were recorded across 120 structural stations. Of these, 3986/80 (structure/ stations) were recorded at Maiden Creek, 1656/34 at Trachyte Mesa, and 403/6 across the wider region. These data were then analysed using MyFault™ stereoplot and kinematic inversion software. The structural database is available in the Appendices. Note, structural measurements were recorded using the following format: planar data (e.g. bedding, faults) as dip direction and dip (e.g. 151/83); and linear data (e.g. slickenlines, pencil cleavage intersection lines) as plunge and azimuth (e.g. 83-151). Any reference to structural data throughout the thesis will be presented in this format.

1.4.2.3. *Rock Sampling*

Systematic rock sampling was carried out during both field seasons. Sampling during Field Season 1 primarily focused on the collection of igneous intrusive samples for petrographic and textural studies (e.g. crystal size distribution and core-rim textures), following an initial pilot study (see Appendices) carried out on a small (5 in total) suite of intrusive samples collected during the LASI IV field trip to the Henry Mountains in the summer of 2010. A smaller suite of structural (rock deformation) samples was also collected for preliminary microstructural studies. An additional suite of structural samples, including deformation band samples for a fracture spacing study (see Chapter 4), was collected during Field Season 2. In total, 72 igneous rock samples and 49 structural samples were collected (see Appendices).

1.4.2.3.1. *Textural Studies & Crystal Size Distribution (CSD)*

Textural characteristics of igneous rocks are the outcome of a complex and dynamic interaction between crystal nucleation and growth (Cashman & Marsh, 1988) and can reveal much about a magma's history, storage, mode of transport and emplacement. Core-rim textures of zoned phenocrysts reflect changes in physical conditions and composition of the magma with time (e.g. Davidson et al., 2007). These textures can be used to document the history of ascent (mineral cores) and emplacement (mineral rims) within intrusions, i.e. magma pathways (Morgan et al., 2006). Crystal size is a measure of growth rate and age, and as such, the population of crystal sizes within an igneous rock provides important information regarding crystal size, nucleation and time residence

histories within a magma system (Marsh, 1988a). Quantitative three-dimensional, Crystal Size Distribution (CSD) data can provide considerably more information on petrological issues than mean, modal or maximum crystal size data (e.g. Cashman & Marsh, 1988; Marsh, 1988a, b; Cashman, 1990; Higgins, 2000).

Consistent CSD throughout an intrusive body would suggest that the textural characteristics of the magma had already been determined before being emplaced. Conversely, varying CSD would imply that the magma was still in a state of flux during emplacement, continuing to crystallise and cool during and/ or post emplacement. Therefore, CSD can provide important clues as to the viscosity and rheological properties of the magma being emplaced. In order to test the above hypothesis, 72 igneous samples were collected for both textural and CSD studies (36 of these from Trachyte Mesa, 30 from Maiden Creek). For both satellite intrusions, samples were collected systematically: across the entire length of the exposed intrusions and, where identifiable, from vertical sections through multiple sill sheets (see Appendices). In addition, a suite of samples have been provided by Prof. Steve Nelson (Brigham Young University, Utah). These include samples from all five intrusive centres, and satellite intrusions of the northern intrusive centres (Mounts Ellen and Pennell), including The Horn, which is composed of syenite (The Horn being the most evolved intrusion in the range).

Note, although a full suite of samples were collected for CSD studies, the decision was made to focus analytical studies towards host-rock deformation, and so only a small number of CSD samples were analysed. A summary of the CSD samples are available in the Appendices, which are planned to be analysed at a future date.

1.4.2.3.2. Microstructures

As a rock deforms, accumulating strain is accommodated by specific deformation processes occurring at the microscale. These processes facilitate changes in the rock's internal structure, shape and/ or volume (Fossen, 2010). Study of the resulting microstructures can reveal much information about the deformation mechanisms (i.e. brittle versus plastic) associated with the various emplacement events. A total of 49 oriented samples (20 from Trachyte Mesa, 29 from Maiden Creek) were collected for microstructural analysis. The aim of this analysis was to provide further insights into the

accommodation and deformation mechanisms (e.g. volume reduction through cataclasis) and by proxy, the emplacement mechanism. Microstructural studies included: (1) transmitted optical microscopy analysis of deformation structures and fault kinematics; (2) SEM studies to resolve sub-grain deformation textures and fabrics; (3) optical microscopy, reflected light microscopy, and both qualitative and quantitative scanning electron microscopy (SEM) studies to analyse alteration products associated with contact metamorphism and fluidisation. See Appendices for a summary of these samples.

1.4.2.4. Laser scanning

Terrestrial laser scanning (TLS) techniques are becoming more widely applied for geological field studies (e.g. McCaffrey et al., 2005; Buckley et al., 2008a; Jones et al., 2009; Seers & Hodgetts, 2013). TLS provides a means of acquiring high resolution spatial information data, which allows geological outcrops to be digitally captured and interpreted away from the field environment (e.g. virtual outcrops; Buckley et al., 2010b). These digital images allow 3D photorealistic models to be created for interpretation and visualisation. These 3D outcrop models are a valuable tool for integrating outcrop data with intrusion geometries and their extrapolation into the subsurface.

At selected localities, at both Trachyte Mesa and Maiden Creek, regional (360° panorama) and high resolution laser scans were acquired to capture the 3D complexity of the intrusion geometries (Fig. 1.21). TLS was carried out using a Leica ScanStation C10, in combination with an AshTech Pro2 DGPS (Fig. 1.21a, b). A more detailed account of the methodology and scan locations is presented in the Appendices.

1.4.2.4.1. 3D Modelling

Laser scan data provide unprecedented detail and allows spatial variation of fracture attributes to be quantified. The laser scan data (georeferenced and registered using Cyclone™) was interpreted using RiSCAN PRO™, Gocad™ and Move™ software to create a 3D geological framework model of emplacement-related deformation structures. As well as capturing the overall geometry of exposed intrusive bodies, TLS also helped to capture fracture and bedding geometries from inaccessible outcrops (Figs 1.22–1.25). Examples of this are shown in Chapter 6 and in Appendices.

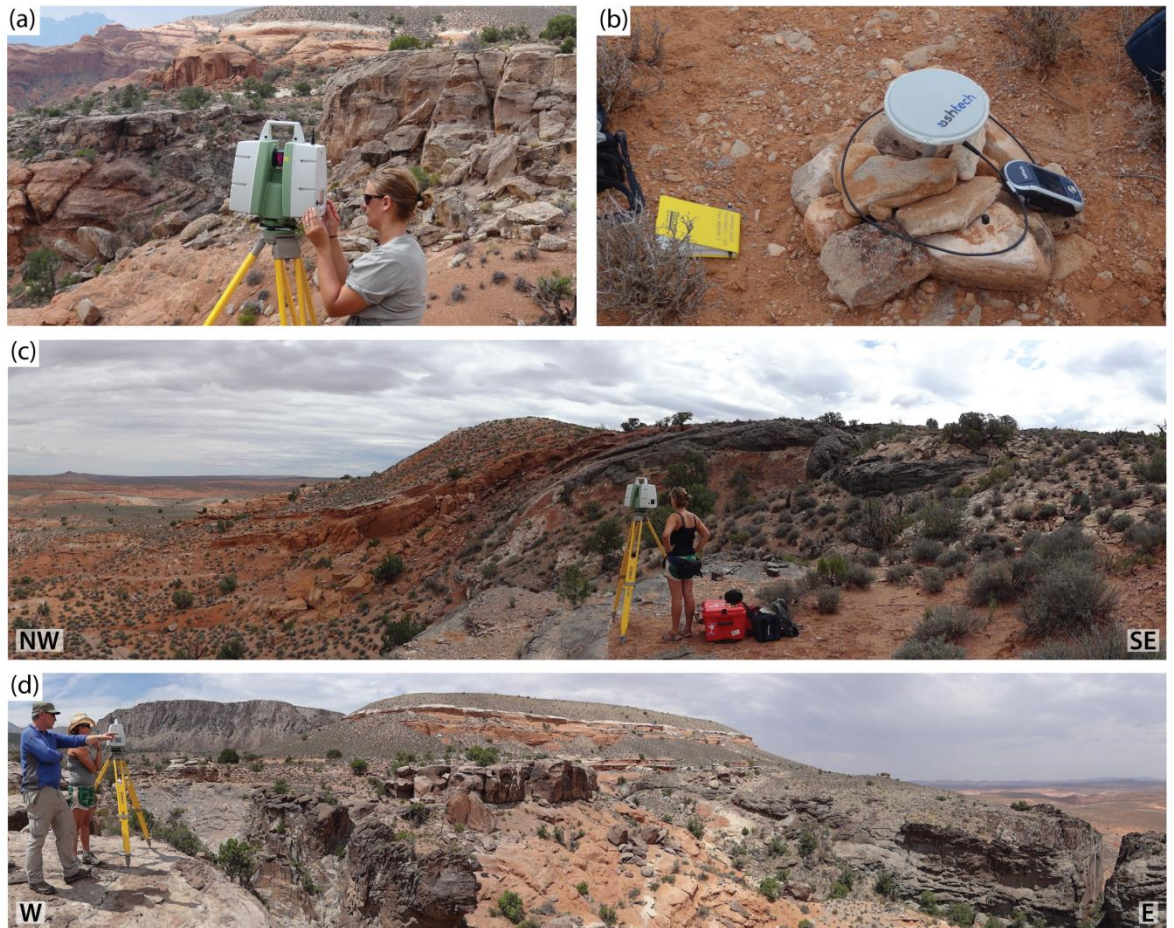


Figure 1.21. Field photographs of laser scanning in the field. (a) Setting up the Leica ScanStation C10. (b) The AshTech Pro2 DGPS base station. (c) and (d) Panorama views of the laser scan areas for the Trachyte Mesa (c) and Maiden Creek (d) intrusions.

Figure 1.21. (overleaf)

A series of images showing the laser scan data and interpretation. (a) Field photograph of the view from Scan Station 1 in the southern Maiden Creek intrusion study area (see kmz file in Appendices for Scan Station locations). Laser scanner height is ~1.6 m. (b) Interpreted point cloud data (intrusion outcrops highlighted in teal colour) in RiSCAN PRO™. View similar to (a). (c) Field photograph of deformed sandstones at the head of the gully, visible in (a). (d) Equivalent interpreted laser scan point cloud in RiSCAN PRO™ (intrusion in purple). (e) Same view as (d) with reduced point cloud density in order to highlight fault interpretation. (f) Equivalent view to (d) and (e), showing 3D fault planes and intrusion surface interpreted from point cloud data (in GoCAD™). (g) Field photograph of complex intrusion–host rock contact. (h) Interpreted point cloud data of outcrop shown in (g) in RiSCAN PRO™ (intrusion in teal; fractures picked in deformed sandstone in green). (i) Equivalent view to (h) showing 3D fault planes in deformed sandstone (in GoCAD™).

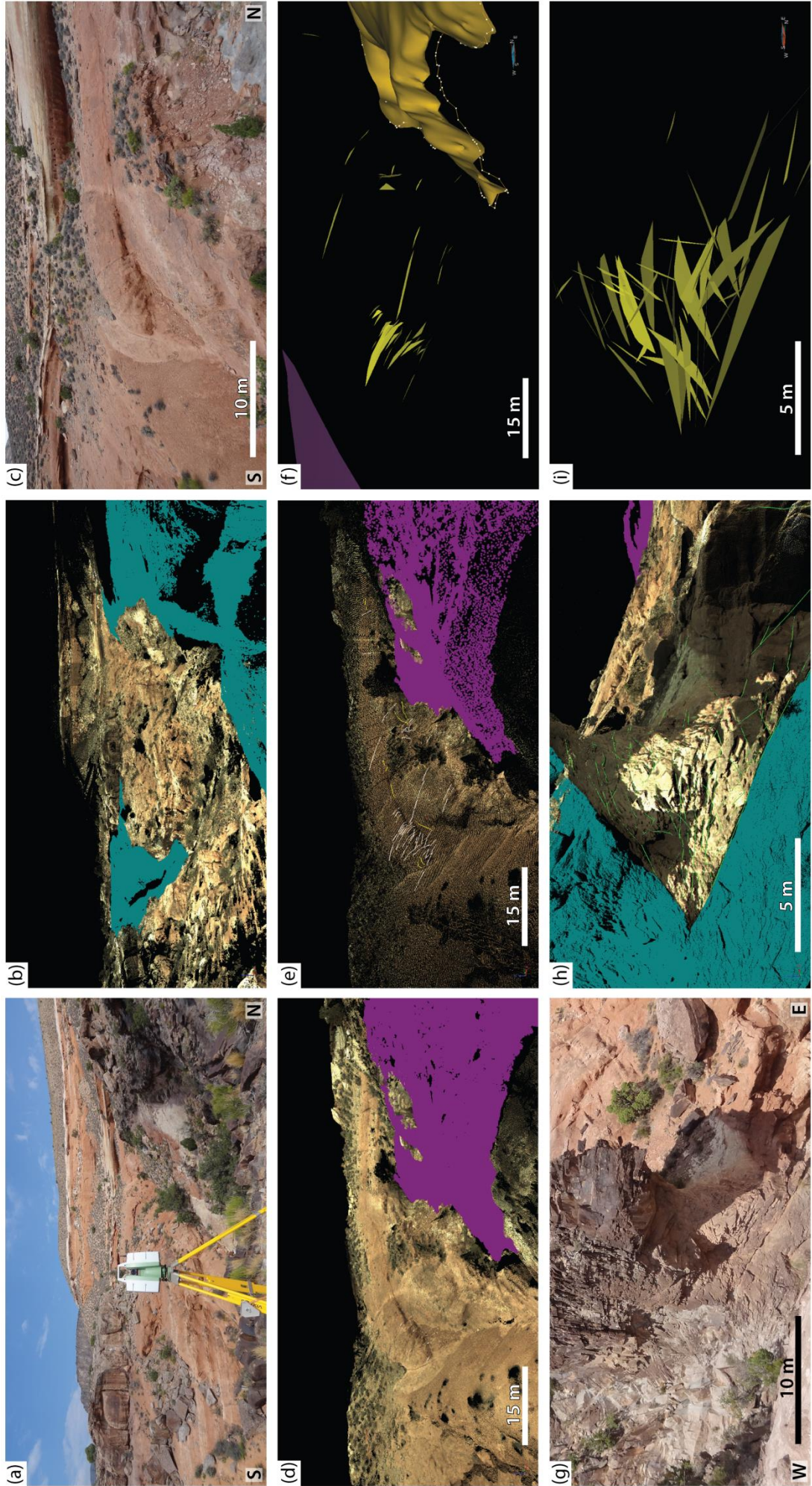


Fig. 1.21

Figure 1.23. *(overleaf)*

Laser scan interpretation processes. (a) Cleaning (removing vegetation and non in-situ rocks) the point cloud database in RiSCAN PRO™. (b) Structural interpretation (picking fault traces and contacts) in RiSCAN PRO™. (c) Fault surface creation: extrapolating 2D/ 2.5D interpretations into 3D surfaces in GoCAD™. (d) Creating pseudo-wells in GoCAD™ to extract azimuth and dip data from 3D planes.

Figure 1.24. *(overleaf)*

Example laser scan interpretations from the Trachyte Mesa intrusion study area. (a) Screen capture of RiSCAN PRO™ project of laser scan point cloud data. (b) Zoom in of structurally complex zone showing dip-slip faults associated with sill sheet terminations; area highlighted in (a). See inset photo for comparison. (c) Zoom in of a climbing sill, propagating along a syn-emplacment fault, area highlighted in (a). (d) Active interpretation of laser scan point cloud data (same view as (a)). Inset shows zoom-in to highlight fracture picking. QR code provides link to fly through movie of the TM laser scan project (see also Appendices for fly through movie). See Chapter 3 for more details.

Figure 1.25. *(overleaf)*

Example laser scan interpretations from the Maiden Creek intrusion study area. (a) Screen capture of RiSCAN PRO™ project of laser scan point cloud data. (b) Zoom in of structurally complex zone where a shear zone (MCSZ) separates low-/ moderately-deformed sandstones above from highly deformed sandstones below and between two igneous lobes, area highlighted in (a). See inset photo for comparison. (c) Zoom in of folded sandstone units around irregular lateral margin of igneous lobe, area highlighted in (a). (d) Active interpretation of laser scan point cloud data (same view as (a)). Inset shows zoom-in to highlight fracture picking. QR code provides link to fly through movie of the MC laser scan project (see also Appendices for fly through movie). See Chapter 6 for more details.

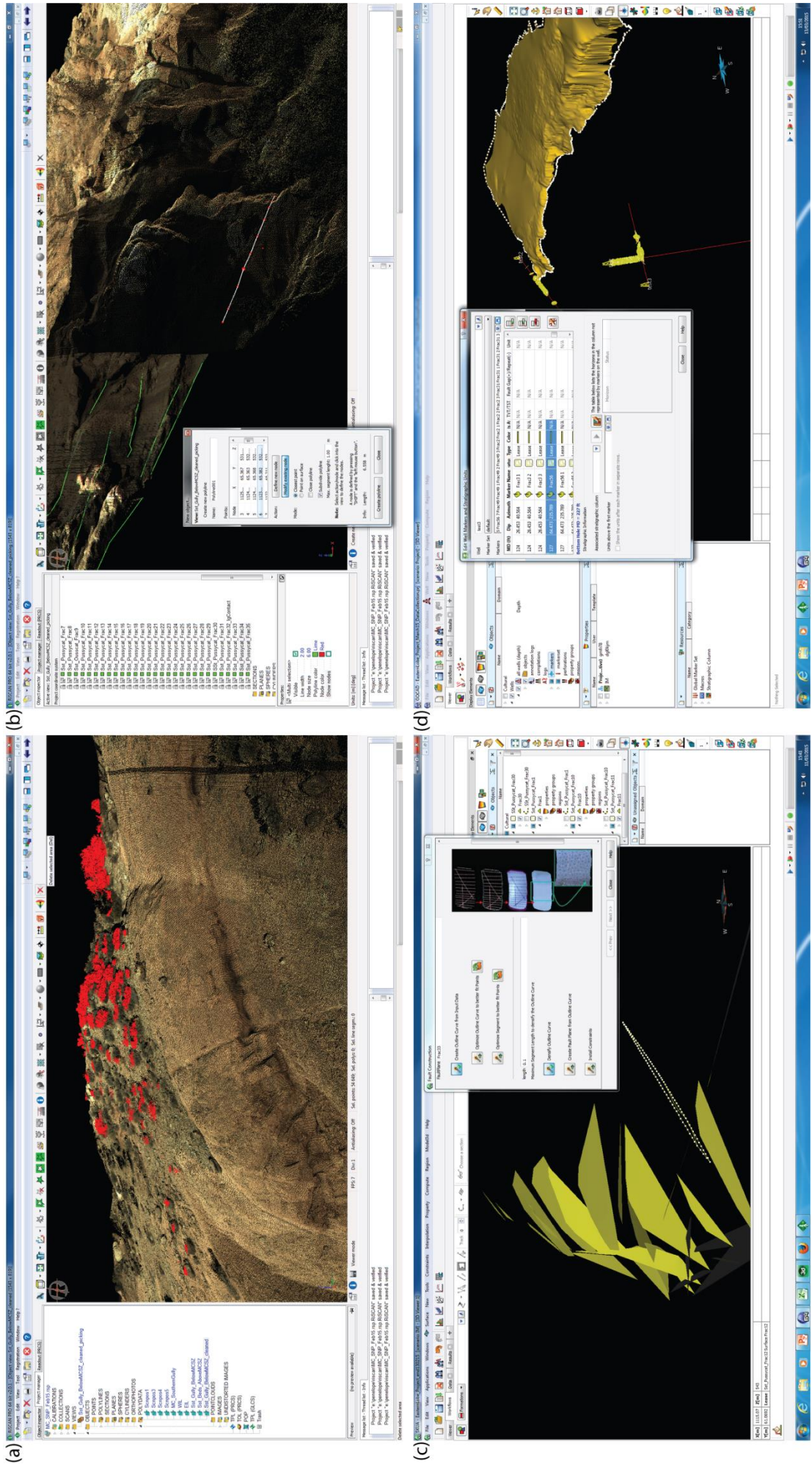


Fig. 1.22

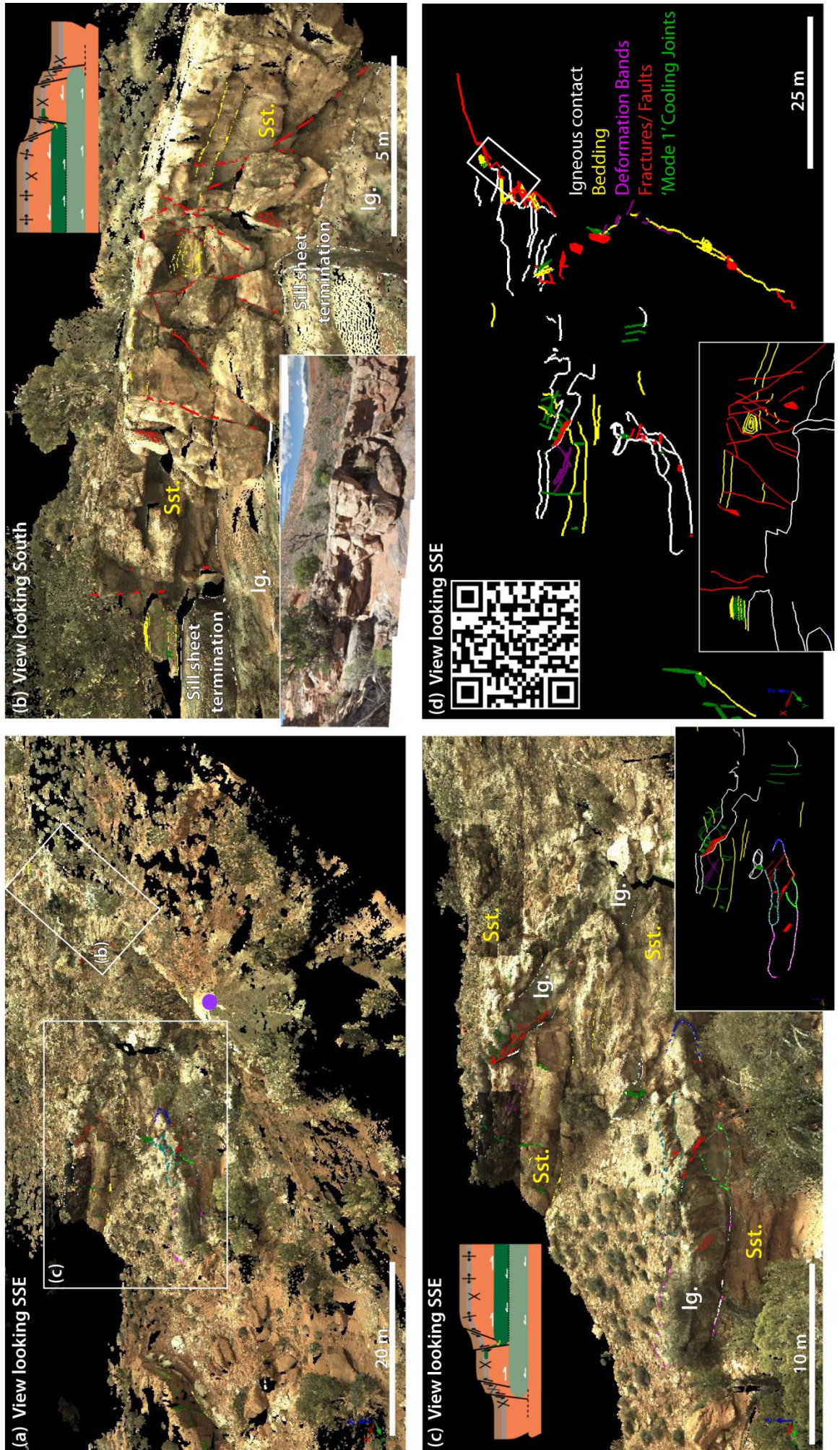


Fig. 1.24

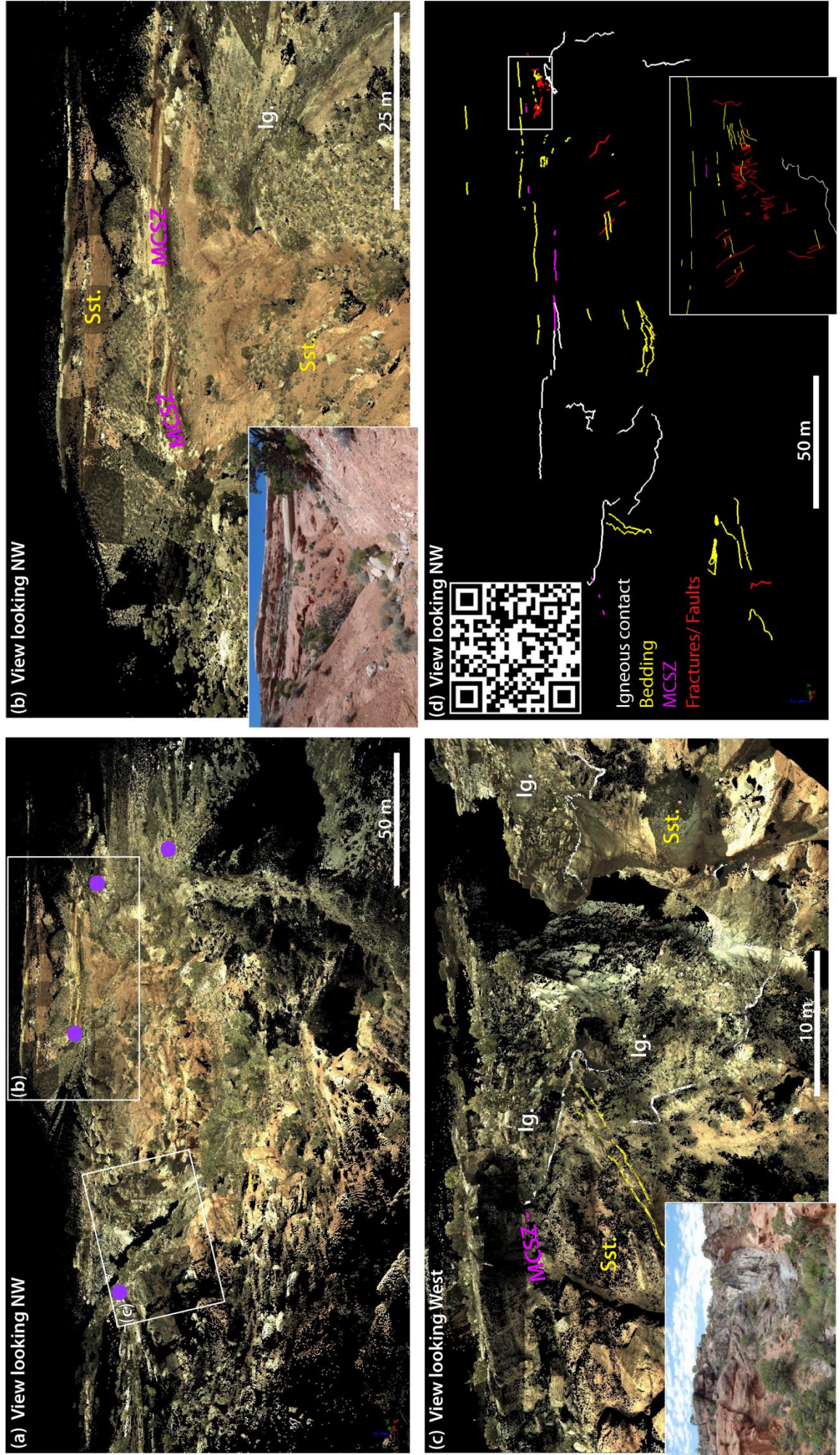


Fig. 1.25

1.4.3. *Thesis Layout*

Chapter Two provides a detailed geological setting for the Henry Mountains, Utah with a synopsis of their tectonic and geological evolution with respect to the Colorado Plateau and the North American continent.

Chapter Three presents field observations and structural data of the Trachyte Mesa intrusion (satellite intrusion to Mount Hillers, Henry Mountains) and tests the emplacement models of Hunt (1953) and Corry (1988) in relation to host rock deformation, in order to identify the mode of emplacement.

Chapter Four gives a detailed fracture spacing study in the host rocks to the Trachyte Mesa intrusion and discusses the importance of the results with respect to fluid flow modelling of host rocks to igneous intrusions.

Chapter Five uses field observations and structural data from the Maiden Creek intrusion (satellite intrusion to Mount Hillers) and discusses host rock deformation and fault kinematics in relation to intrusion geometries and emplacement mechanisms.

Chapter Six presents a further detailed study of the southern section of the Maiden Creek intrusion, in particular the Maiden Creek Shear Zone, and discusses accommodation structures that tackle the intrusion 'space problem'.

Chapter Seven summarises and discusses the main implications of the thesis as a series of short discussions, linking intrusion geometries and host rock deformation structures to emplacement mechanisms, while addressing the intrusion 'space problem' and how the addition of magma is accommodated at depth.



2. Chapter Two: Geological Setting

| | | | |
|--------|---------------|---|---------------|
| Layout | 2.1. | Regional Geological Setting | |
| | 2.2. | Tectonic and Geological Evolution of Utah, the Colorado Plateau and N. America | p. 47 |
| | 2.2.1. | <i>Palaeoproterozoic to Mesoproterozoic (c. 2000 to 950 Ma)</i> | p. 53 |
| | 2.2.2. | <i>Neoproterozoic to Early Palaeozoic (c. 950 to 541 Ma)</i> | p. 55 |
| | 2.2.3. | <i>Cambrian to Permian (541 to 252 Ma)</i> | p. 57 |
| | 2.2.4. | <i>Triassic to Jurassic (252 to 145 Ma)</i> | p. 58 |
| | 2.2.5. | <i>Early Cretaceous (145 to 80 Ma)</i> | p. 61 |
| | 2.2.6. | <i>Latest Cretaceous to Palaeogene (80 to 35 Ma)</i> | p. 63 |
| | 2.2.7. | <i>Latest-Paleogene to Present (~35 to 0 Ma)</i> | p. 64 |
| | 2.3. | Uplift and Magmatism on the Colorado Plateau | p. 70 |
| | 2.3.1. | <i>Dynamics (uplift) of the Plateau</i> | p. 70 |
| | 2.3.2. | <i>Magmatism</i> | p. 71 |
| | 2.4. | Geology of the Henry Mountains | p. 72 |
| | 2.4.1. | <i>Stratigraphic Column</i> | p. 77 |
| | 2.4.1.1. | <i>Cutler Formation (Roof Rocks to Mount Hillers)</i> | p. 79 |
| | 2.4.1.2. | <i>Entrada Sandstone (Host Rocks to Trachyte Mesa and Maiden Creek)</i> | p. 80 |
| | 2.4.1.3. | <i>Summerville Formation (Host rocks to Black Mesa).</i> | p. 82 |
| | 2.4.1.4. | <i>Morrison Formation (Host Rocks to Sawtooth Ridge)</i> | p. 83 |
| | 2.4.2. | <i>Henry Mountains Intrusions</i> | p. 84 |
| | 2.4.2.1. | <i>The Five Igneous Centres</i> | p. 85 |
| | 2.4.2.1.1. | <i>Mount Ellen</i> | p. 85 |
| | 2.4.2.1.2. | <i>Mount Pennell</i> | p. 87 |
| | 2.4.2.1.3. | <i>Mount Hillers</i> | p. 88 |
| | 2.4.2.1.4. | <i>Mount Holmes</i> | p. 92 |
| | 2.4.2.1.5. | <i>Mount Ellsworth</i> | p. 94 |
| | 2.4.2.2. | <i>North-eastern Satellite Intrusions to Mount Hillers</i> | p. 94 |
| | 2.4.2.2.1. | <i>Sawtooth Ridge</i> | p. 94 |
| | 2.4.2.2.2. | <i>Black Mesa</i> | p. 96 |
| | 2.4.2.2.3. | <i>Maiden Creek</i> | p. 99 |
| | 2.4.2.2.4. | <i>Trachyte Mesa</i> | p. 100 |
| | 2.5. | Deformation Structures in the Entrada Sandstone | p. 105 |
| | 2.5.1. | <i>Deformation Bands and their Classification</i> | p. 105 |
| | 2.5.1.1. | <i>Kinematic-based Classification</i> | p. 106 |
| | 2.5.1.2. | <i>Deformation-mechanism Classification</i> | p. 107 |

2.1. Regional Geological Setting

The Henry Mountains are situated in south-eastern Utah on the Colorado Plateau (Fig. 2.1). The Colorado Plateau Province is centred on the Four Corners region of the south-western USA and covers much of southern and eastern Utah, western Colorado, north-western New Mexico and northern Arizona states (Fig. 2.1), spanning an area of 337,000 km². The Plateau is one of the three physiographic provinces of the Intermontane Plateaus (comprising the Columbia Plateau, Colorado Plateau, and Basin and Range Provinces), with an average elevation of ~1525 m (~5000 ft) above sea level. The Plateau is bound on all sides by significant topographical/ structural features, making it a distinct terrain (Fig. 2.1). To the east, the Plateau is bounded by the Southern Rocky Mountains in Colorado, and to the north-east, by the Uinta and Wasatch Mountains of Utah (Fig. 2.1b). In southern Colorado and New Mexico, the eastern margin of the Colorado Plateau is defined by the Rio Grande rift: a ~N–S trending continental rift zone that separates the Plateau from the intercontinental American craton to the east (Fig. 2.1). The Mogollon Rim, an approximately 320 km (200 mile) long escarpment, marks the south-western edge of the Plateau (Fig. 2.1b). To the west, the Colorado Plateau is bounded by the Basin and Range Province in western Utah and Nevada (Fig. 2.1).

2.2. Tectonic and Geological Evolution of Utah, the Colorado Plateau and N. America

Although not exempt from deformation and magmatism, the Colorado Plateau has, relative to its surrounding regions, behaved as a separate terrane throughout much of the Phanerozoic era, experiencing a long period of relative tectonic quiescence (Allmendinger et al., 1987; Burchfiel et al., 1992; Nelson et al., 1992). This is supported by the sedimentary record, which indicates that Utah and the western edge of the Colorado Plateau, with a relatively flat landscape, remained near sea-level (slightly above, or slightly below), throughout most of the last 2 billion years (Figs 2.2 & 2.3; Hintze & Kowallis, 2009). Only during the last 80 million years has the Colorado Plateau risen to significantly above sea-level (Liu & Gurnis, 2010; Roberts et al., 2012). However, despite being a separate terrane, many of the tectonic events that shaped North America impacted (directly or indirectly) on the plateau. Hintze and Kowallis (2009) divided Utah's geological history into 9 key phases, all of which can be related to the broader tectonic history of North America. These phases are depicted in Figure 2.4, and are discussed in more detail in the following sections. Figures 2.2 and 2.3 show palaeogeographic maps

and tectonic reconstructions (from Cambrian to present) for North America (Miall & Blakey, 2008) and the Colorado Plateau (Blakey & Ranney, 2008).

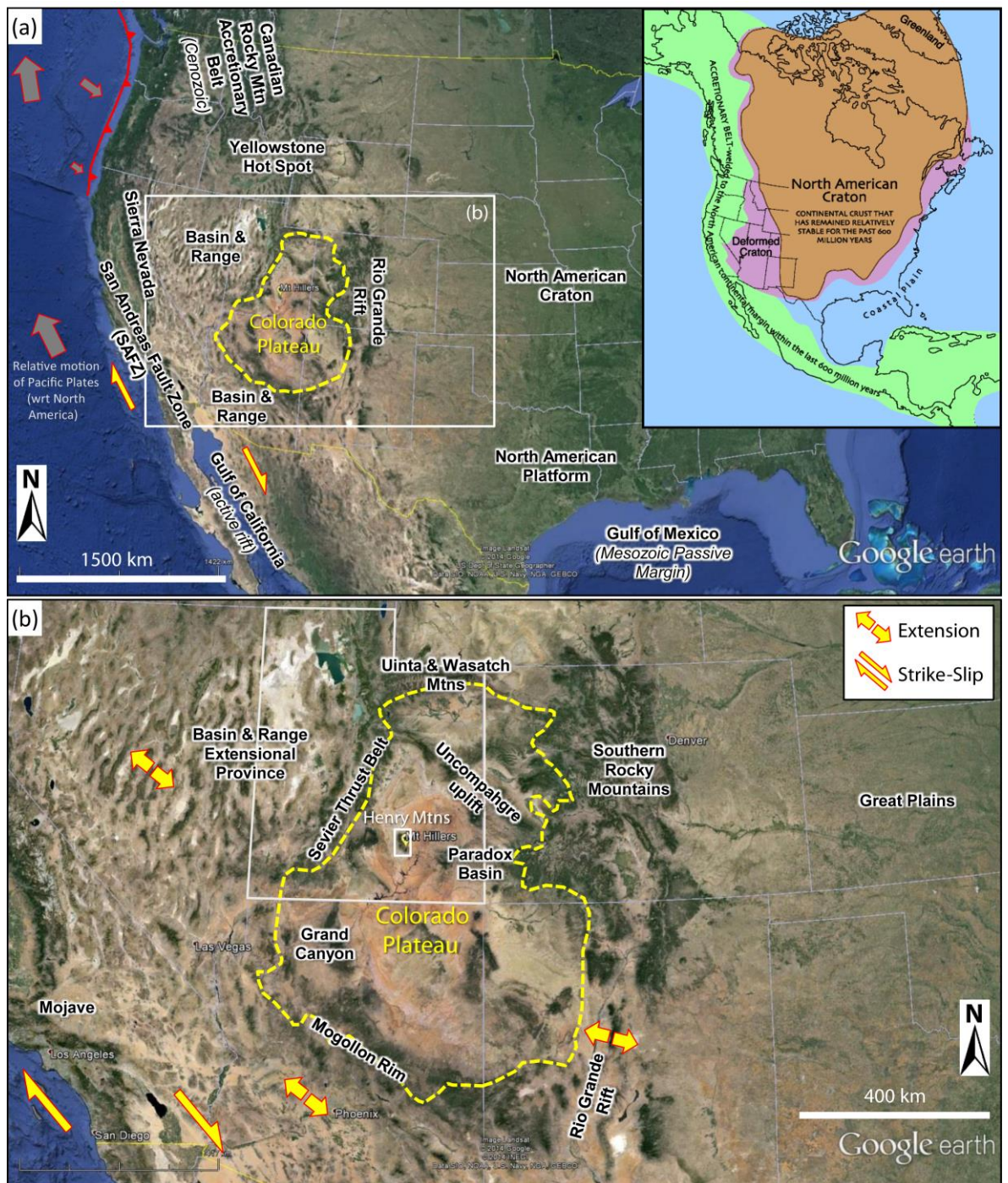


Figure 2.1. Location maps of the Colorado Plateau (CP). (a) Present day map of the CP in relation to the North American continent. The image is from Google Earth™ and shows current USA state borders. The outline of the CP is highlighted by the dashed yellow line. Key geological areas are highlighted. Kinematics are shown for the west coast. Inset: simplified cratonic map for North America (from the USGS). (b) Enlarged map of the CP. The location of map (b) is shown by the white box in (a). Kinematics for the SW region of North America are indicated by the arrows. The main topographical/ structural features that bound and denote the rim of the CP are shown. The location of the Henry Mountains on the CP is indicated by the small white box.

Figure 2.2. *(overleaf)*

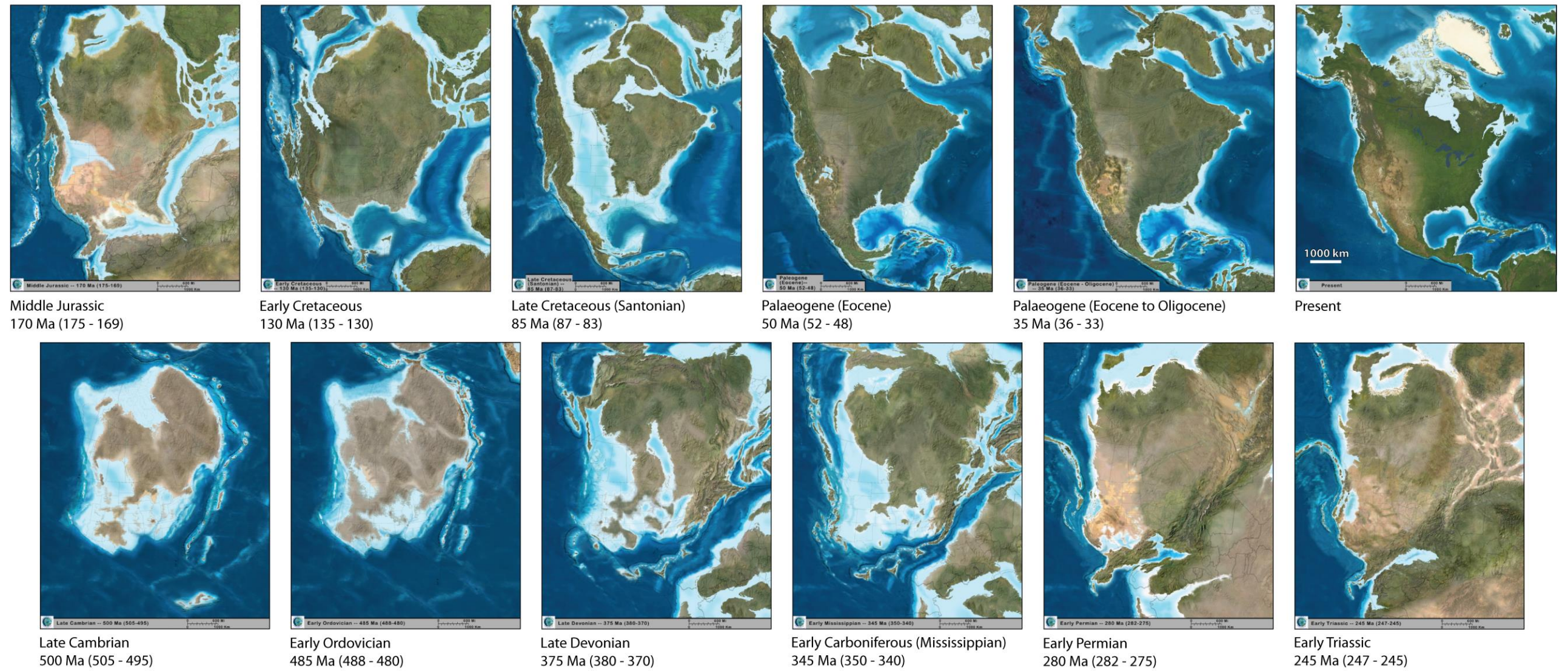
(a) Palaeogeographic and tectonic history of North America (Miall & Blakey, 2008), including: most of the Arctic; the Caribbean; the Pacific Margin; parts of Europe; South America; and Africa (© Ron Blakey, Colorado Plateau Geosystems; <http://cpgeosystems.com/namkeypaleogeography.html>). (b) Palaeolatitude history of North America from the later Neoproterozoic, through the Phanerozoic, to present day (after Hintze & Kowallis, 2009). Palaeolatitudes are shown every 40 million years. Utah's position is highlighted. Palaeolatitudes were produced using palaeomagnetic records. The present-day outline of North America is shown for reference. The tectonostratigraphic "Phases" shown below the geological timescale correspond to the 9 key phases of Hintze and Kowallis (2009), illustrated in Fig. 2.4.

Figure 2.3. *(overleaf)*

Palaeogeographic and tectonic history of southwestern North America (Blakey & Ranney, 2008), including: the Colorado Plateau; Southern and Central Rocky Mountains; Basin and Range; and Pacific Margin (© Ron Blakey, Colorado Plateau Geosystems; <http://cpgeosystems.com/namkeypaleogeography.html>).

(a)

Palaeogeographic and Tectonic History of North America:
 North America including most of the Arctic, the Caribbean, the Pacific Margin,
 and parts of Europe, South America, and Africa



© Ron Blakey, Geosystems (<http://cpgeosystems.com/namkeypaleogeography.html>)

(b)

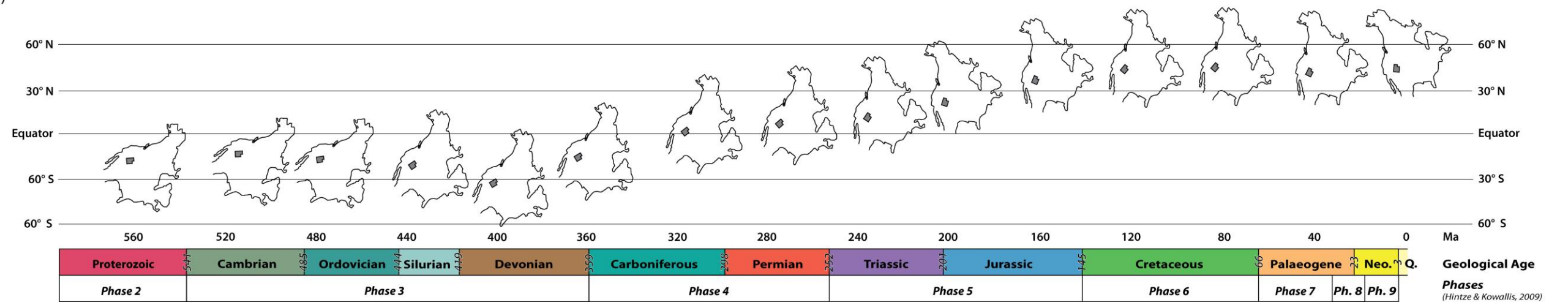
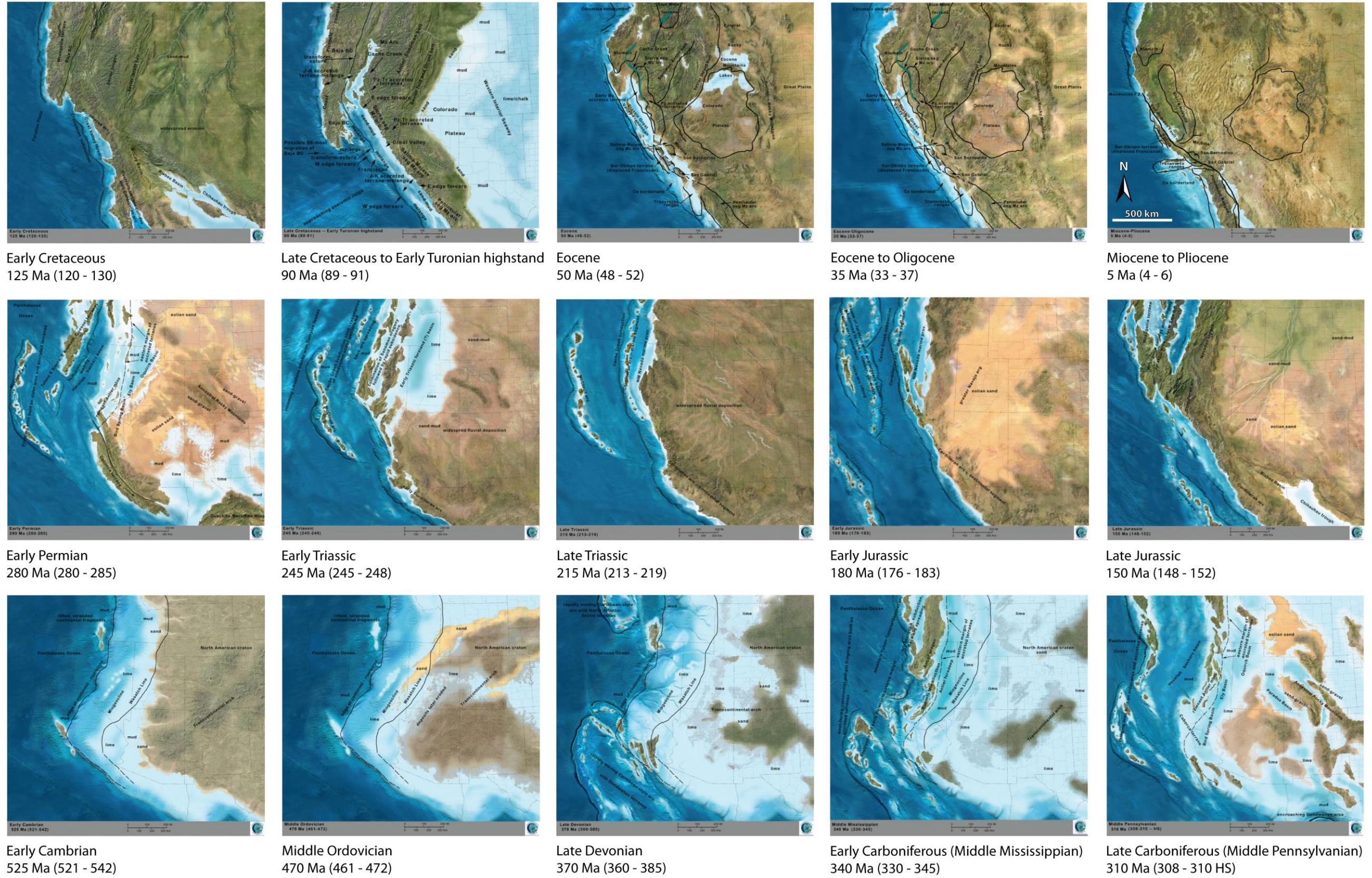


Fig. 2.2

**Palaeogeographic and Tectonic History of Southwestern North America:
Colorado Plateau, Southern and Central Rocky Mountains, Basin and Range, and Pacific Margin**



© Ron Blakey, Colorado Plateau Geosystems (<http://cpgeosystems.com/swnampaleogeography.html>)

Fig. 2.3

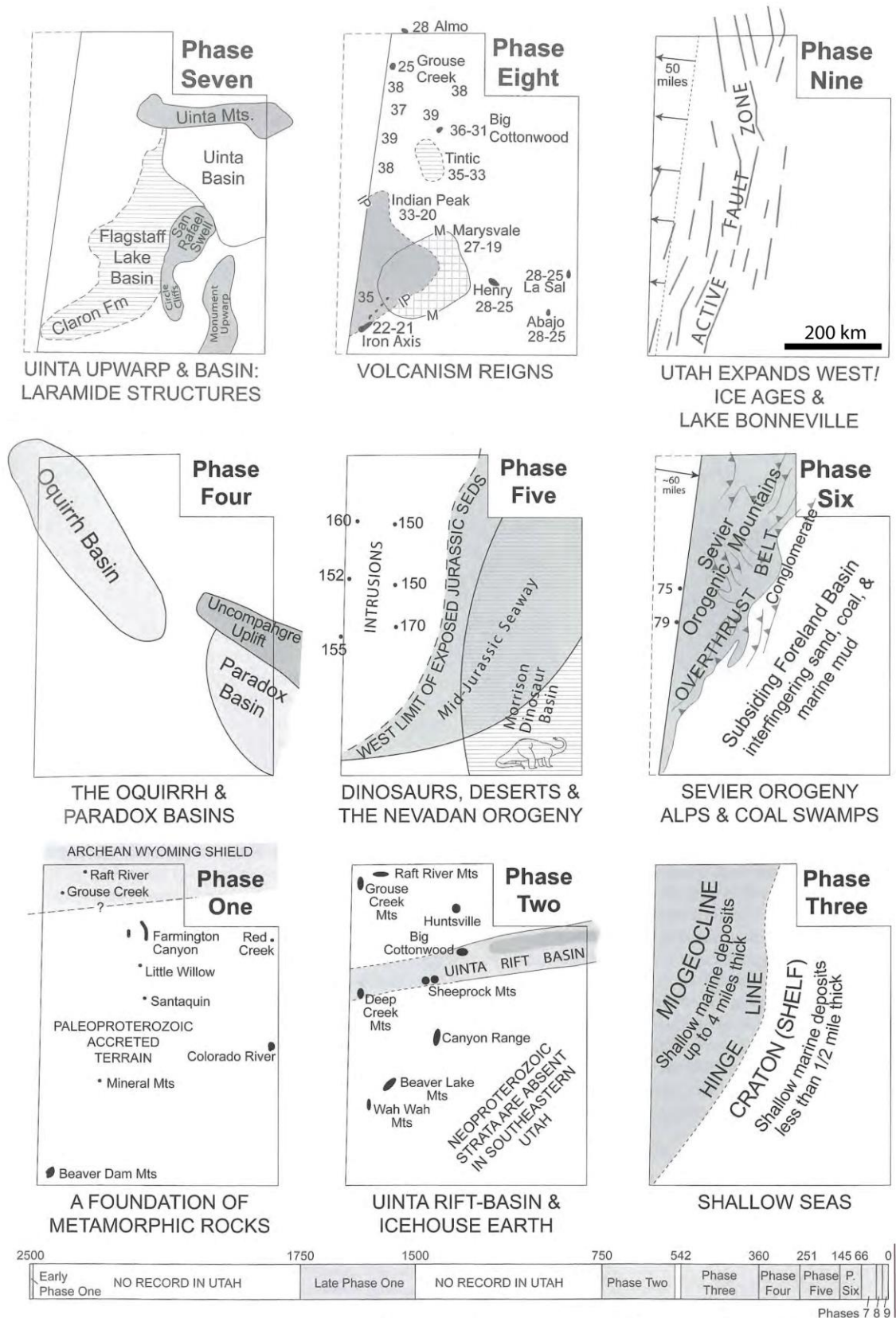


Figure 2.4. Nine key tectonostratigraphic phases of Utah’s geologic history as outlined by Hintze and Kowallis (2009). **Phase 1** (Early Proterozoic) – Foundation of metamorphic basement terranes; **Phase 2** (Neoproterozoic) – Uinta Rift basin and ice-house earth conditions; **Phase 3** (Cambrian–Devonian) – shallow carbonate seas; **Phase 4** (Carboniferous–Permian) – far field tectonics of the Alleghanian Orogeny and formation of the Oquirrh and Paradox basins; **Phase 5** (Triassic–Jurassic) – arid deserts and the intermittent shallow seaway to Canada; **Phase 6** (Cretaceous) – the Sevier Orogeny and the coal swamps on the flanks of

the Cretaceous Interior Seaway (foreland basin); **Phase 7** (Early Palaeogene) – plateau uplift, Laramide folding and formation of the Uinta mountains; **Phase 8** (Oligocene–Early Miocene) – Tertiary intrusions and volcanism; **Phase 9** (Neogene–present) – eastwards extension along the Wasatch Fault.

2.2.1. Palaeoproterozoic to Mesoproterozoic (c. 2000 to 950 Ma)

The early- to mid-Proterozoic era was dominated by orogenic accretionary events with the assembly and growth of the North American continent: part of the globally significant assembly of the Proterozoic supercontinent of Rodinia (Fig. 2.5; Li et al., 2008). This timeframe represents **Phase 1** of Hintze and Kowallis (2009) for their geological evolution of Utah (Fig. 2.4). During the early Palaeoproterozoic Orosirian period (c. 2050 to 1800 Ma), the Slave, Rae-Hearne and Superior major cratons, along with smaller fragments of Archean continental crust, were sutured together, marking the onset of the assembly of the N. American (Laurentian) Archean core (Fig. 2.5; Hoffman, 1988; Bleeker & Hall, 2007). This was the start of a long period (~1 billion years) of continental accretionary events, as a series of arcs and associated flanking sediments were subsequently added to the south-eastern edge of the growing N. American continent during three significant orogenic events. The first of these accretionary events was the Yavapai orogeny (1710 to 1680 Ma) during the Statherian period, adding the 1.8–1.7 Ga Yavapai terrane to the south-eastern edge of the continent (Fig. 2.5; Whitmeyer & Karlstrom, 2007). This was shortly followed after by the Mazatzal orogeny (1650 to 1600 Ma) during the Calymmian period, resulting in the accretion of the 1.7–1.65 Ga Mazatzal arc and flanking sediments along the south-eastern margin of the Yavapai terrane (Fig. 2.5). Voluminous, subduction-related granitic magmatism accompanied these accretionary events. The final orogenic event of the Proterozoic was the prolonged Ectasian to Stenian, Grenville orogeny (1300 to 950 Ma). During this orogeny, the 1.3–1.0 Ga Llano-Grenville province, along with an unidentified continent (long since rifted away; Whitmeyer & Karlstrom, 2007), was accreted onto the eastern and south-eastern edge of the N. American continent (Fig. 2.5).

The oldest known rocks of the Colorado Plateau are Palaeoproterozoic gneisses and schists, with metamorphic ages dating from ~1.7–1.5 Ga (Hintze & Kowallis, 2009; Fillmore, 2011). However, these rocks also preserve older Archean signatures within zircon crystals. These Palaeoproterozoic rocks are found in Utah, south of the Archean Wyoming shield (Fig. 2.4, Phase 1). As shown in Figure 2.2b, throughout much of the Proterozoic, the Laurentian continent lay within the southern hemisphere.

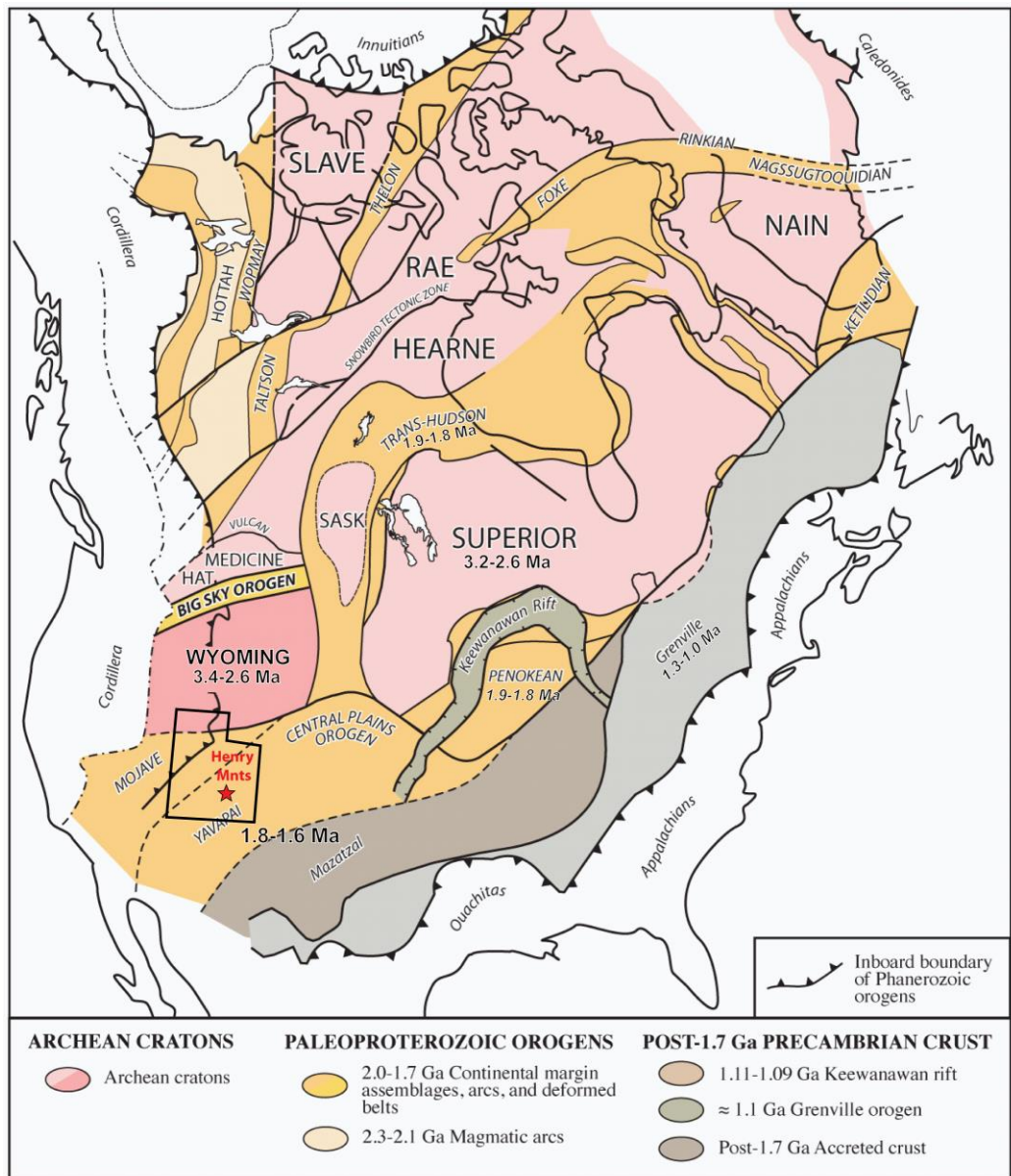


Figure 2.5. Simplified map showing the basement terranes and cratons of North America (adapted from Hoffman, 1988; and Bleeker & Hall, 2007). Outline of Utah State is highlighted in black, along with the location of the Henry Mountains (red star) for reference.

Kinematics during the Mesoproterozoic reflected ~NW directed thrusting (Fig. 2.6) associated with the various accretionary events on the eastern margin of the craton. NE–SW trending contractional structures developed along the eastern continental margin with coincidental NE–SW directed extension within the continental interior (Fig. 2.6b). Such NE–SW directed extension created a series of NW–SE striking normal faults (Fig. 2.6). Marshak and Paulsen (1996) proposed two phases of rift development during the Mesoproterozoic: NE–SW extension (1.5–1.3 Ga), as mentioned above; and NW–SE extension (1.1 Ga), coeval with the Grenvillian orogeny and opening of a NE–SW trending mid-continental rift system (MCR; Fig. 2.6a, b). Timmons et al. (2001) also described the

earlier of these two events, with NE–SW extension, although their timing for this event was younger (1.3–1.0 Ga) than the 1.5–1.3 Ga age assigned by Marshak and Paulsen (1996).

2.2.2. Neoproterozoic (c. 950 to 541 Ma)

Phase 2 of Hintze and Kowallis (2009) falls within the Neoproterozoic period (Fig. 2.4). Following the Grenville orogeny, N. America experienced a time of relative tectonic quiescence and stability from the Tonian through to the Cryogenian (c. 950–800 Ma), as the final assembly of the Rodinia supercontinent ensued elsewhere (Li et al., 2008). This stability, however, was relatively short-lived and by 800 Ma, extension and rifting had commenced, creating a series of N–S trending normal faults across the N. American continent (Fig. 2.6c; Marshak & Paulsen, 1996; Marshak et al., 2000). By 750 Ma, the break-up of the Rodinia supercontinent was underway (Timmons et al., 2003; Li et al., 2008). A continent (possibly Australia or China) rifted away from the western margin of N. America (Laurentia), initiating the opening of the proto-Pacific Ocean and establishing a passive margin on the western edge of N. America. The upper hinge of this passive margin forms the western edge of the present-day Colorado Plateau province (Figs 2.3 & 2.4; Hintze & Kowallis, 2009). By the Ediacaran (~635–541 Ma), rifting was occurring on the eastern edge of N. America, with the collapse of the Grenville orogeny at ~600 Ma, and the opening of the Iapetus Ocean (precursor to the Atlantic Ocean) by ~550 Ma (Li et al., 2008).

In summary, by the end of the Proterozoic, three dominant basement trends had been established: NW–SE, NE–SW and N–S (the earlier two trends common across the whole craton, whilst the latter system was more localised to the Colorado Plateau; Fig. 2.6). These basement fabrics played an important role during the Phanerozoic.

2.2.3. Cambrian to Permian (541 to 252 Ma)

Fragmentation of Rodinia continued during the Cambrian period, giving rise to the continents of Laurentia, Baltica, and the southern supercontinent of Gondwana (Fig. 2.2a). During the Cambrian, N. America (Laurentia) partly straddled the equator, and the Colorado Plateau was situated at latitude $\sim 30^\circ$ S (Fig. 2.2b). A period of slow marine advance of shallow seas across N. America culminated in the near complete submergence of the continent (Figs 2.2–2.4, **Phase 3**; Hintze & Kowallis, 2009). The continent was surrounded by ocean (Fig. 2.2a): the Panthalassic Ocean to the north and west; the Iapetus Ocean to the south; and the Khanty Ocean to the east (Miall & Blakey, 2008). The seas reached western Utah by the late Early Cambrian (Hintze & Kowallis, 2009).

By the Ordovician, the continents and smaller fragments were on the move again as the assembly of the Pangea supercontinent began (Fig. 2.2a; Miall & Blakey, 2008). The eastern-side of N. America was again subjected to most of the collisional activity (Fig. 2.2a), with four successive orogenic events (building the Ouchita-Appalachian mountain belt; Fig. 2.5; Hatcher, 2010) spanning much of the early Phanerozoic: the Taconic; the Acadian; the Ouachita-Marathon; and the Alleghanian orogenies (Fig. 2.5). The Ordovician Taconic Orogeny (~ 550 – 440 Ma; Hatcher, 2010) resulted in the Taconic (Bronson Hill) island arc being accreted/ thrust onto the eastern margin of Laurentia as the Iapetus Ocean began to close (east-dipping subduction zone). The effects of the Taconic orogeny were focused from Newfoundland to Georgia. The Devonian Acadian Orogeny (~ 425 – 375 Ma; Hatcher, 2010) involved the collision of a series of Avalonian continental fragments with Laurentia. The effects of the Acadian orogeny were focused in New England and Newfoundland, reaching as far south as Alabama. The Carboniferous to early-Permian Ouachita-Marathon Orogeny (~ 350 – 290 Ma; Poole et al., 2005) resulted from the South American continent colliding with Laurentia after the intervening ocean was subducted, forming the Ouachita Mountains. The effects of this orogeny were focused from Arkansas to Texas (Fig. 2.5). The mid-Carboniferous to Late Permian Alleghanian Orogeny (~ 325 – 260 Ma; N. American equivalent to the European Variscan/ Hercynian orogeny; Hatcher, 2010) resulted from the African continent colliding with the Euramerica supercontinent, forming the Appalachian Mountains (Fig. 2.5). The Alleghanian orogeny was focused on a region from Alabama to New Jersey, extending north and southwest.

During the Palaeozoic era, western N. America was relatively stable and tectonically quiescent. The palaeolatitude was sub-tropical (Fig. 2.2b), with deposition taking place in

dominantly shallow-marine environments (Fig. 2.3). During Devonian times, these environments led to the deposition of a number of economically important petroleum source rocks (including the Bakken Formation; Webster, 2011), which supply the recent shale gas/ oil boom in the USA.

At some point, likely during the Late Devonian, a subduction zone established along the western edge of the N. American continent as the oceanic Farallon Plate was forced beneath the continental N. American Plate (Fig. 2.3). This resulted in the Sierra Nevada Arc magmatism in eastern California and Oregon, and the Late Devonian to early Carboniferous (Mississippian) Antler Thrust Belt in Nevada and Idaho (Dickinson & Lawton, 2003).

During the Carboniferous period (Late Mississippian to Pennsylvanian; ~330 to 300 Ma), progressive orogenic activity along the eastern margin of N. America led to inversion of many Proterozoic rifts in the continental interior, raising a chain of basement-cored uplifts: the Ancestral Rockies, stretching from Texas to Oklahoma and northwest to Oregon (Fig. 2.4, **Phase 4**; Dickinson & Lawton, 2003; Hintze & Kowallis, 2009). These topographic highs were accompanied by significant, adjacent flexural basins. Two of these uplifts, the Uncompahgre and Piute Uplifts, were situated on the present-day Colorado Plateau; and the Paradox Basin associated with, and located on the southern margin of the Uncompahgre Uplift.

In Utah, two large (~5 km thick) NW-trending basins continued to develop (Fig. 2.4, Phase 4): the Paradox Basin (to the southeast); and the Oquirrh Basin (in the northwest). Deposition in the Paradox Basin was in a sabkha (supratidal/ arid; characterised by deposition of evaporites) coastal environment, while the Oquirrh Basin was entirely marine dominated (Hintze & Kowallis, 2009). The stratigraphy of both the late Carboniferous and the Permian displays a cyclic sequence, likely linked to global sea-level fluctuations in response to global icehouse cycles (Hintze & Kowallis, 2009). The final culmination of the Pangea supercontinent occurred during the Permian (Fig. 2.2a).

2.2.4. Triassic to Jurassic (252 to 145 Ma)

Phase 5 of Hintze and Kowallis (2009) covers the Early Mesozoic era. Pangea began to break apart in the Triassic (Fig. 2.2a), with rifting first occurring along the Appalachian-

Ouachita-Marathon orogeny in N. America (Fig. 2.5; Moulin et al., 2010). Consequently, significant syn-rift volcanoes grew in Texas, and rift shoulders rose along the entire rift. Once again, Utah and the Colorado Plateau were relatively unaffected by such rifting and the associated volcanism to the east. It was also largely unaffected by the short-lived localised compressional deformation of the Late Permian to Early Triassic Sonoma Orogeny along the west margin (~250 Ma; Gabrielse et al., 1983), which was focused in western Nevada and southern Oregon (Figs 2.2a & 2.3).

During the Triassic and Jurassic, N. America moved progressively northwards, with the continent crossing the equator sometime during the Permo-Triassic (Fig. 2.2b). The Triassic stratigraphy of Utah marks a transition from dominantly marine to non-marine deposition (Fig. 3; Hintze & Kowallis, 2009). The Triassic rock record on the Colorado Plateau opens with shallow marine deposits of the Moenkopi Formation, and closes with petrified forests, river flood plain and swampy lake deposits of the Chinle Formation (a phase of erosion separates these two vastly different environments; Fig. 2.7a; Hintze & Kowallis, 2009; Fillmore, 2011).

The Jurassic stratigraphy of the Colorado Plateau reflects varying depositional environments. The early Jurassic was dominated by significant aeolian (desert) sand dune deposits of the Glen Canyon Group, covering the entire region. These deposits include The Wingate, Kayenta, and Navajo sandstones (known as the Greater Navajo Erg; Figs 2.3 & 2.7b, c). By the middle Jurassic, a shallow finger-like seaway began to extend southwards from Canada, covering much of Utah (Fig. 2.2a; Hintze & Kowallis, 2009; Fillmore, 2011). This shallow marine incursion led to the deposition of the San Rafael Group. Marine sediments (e.g. Carmel Formation) were deposited on the floor of this narrow seaway, while arid environments still dominated its margins, leading to the deposition of evaporites and further aeolian sandstones (e.g. Entrada Sandstone; Fig. 2.7d). The Late Jurassic saw the deposition of the world-renowned (dinosaur-rich) Morrison Formation. The Jurassic Morrison River marked a distinct change in drainage patterns in N. America (from westward-dominated to eastward-dominated; Fig. 2.3), marking the onset of the early development of a magmatic arc (in California) and the Nevadan Orogenic Belt (Fig. 2.4, **Phase 5**; Hintze & Kowallis, 2009; Fillmore, 2011). Muddy deposits dominate the stratigraphy of the Morrison Formation (e.g. Fig. 2.7e).

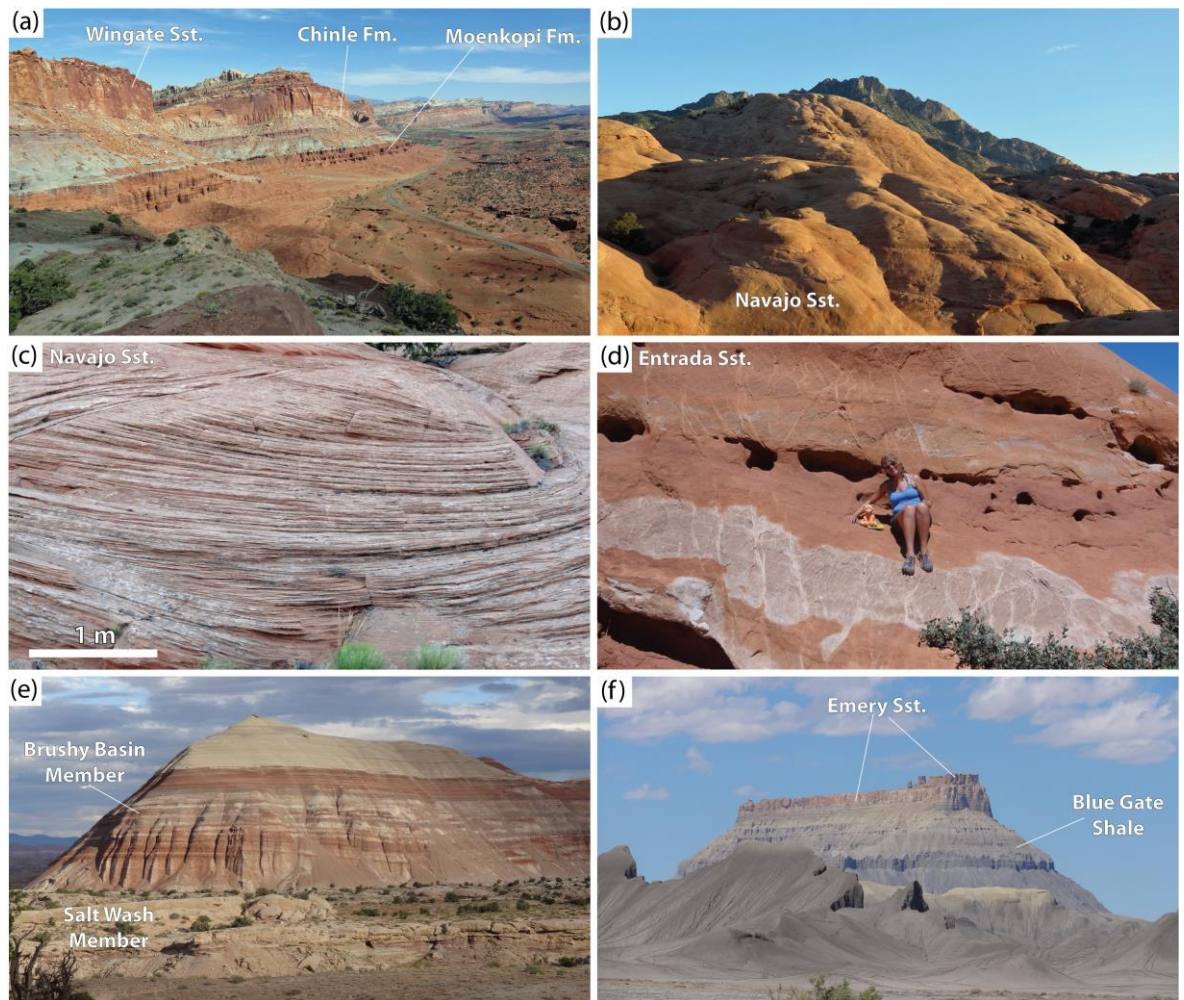


Figure 2.7. Photographs of selected sedimentary rocks of the Henry Mountains region. (a) Triassic sediments: Capitol Reef National Park. View looking SE from Chimney Rock. From the base of the cliff upwards the stratigraphy units are: the Moenkopi Formation; the Chinle Formation (the slope forming unit); and the Wingate Sandstone (the steep cliff unit) of the Glen Canyon Group. A sharp discontinuity exists between the Chinle and the Wingate. Height of cliff face is ~250 m. (b) Lower Jurassic sediments: Navajo Sandstone of the Glen Canyon Group, view looking south from Rt. 276 towards Mount Holmes (peak in background). The photo shows the distinctive rounded dome geomorphology characteristic of the Navajo Sandstone. (c) Cross-bedding in the Navajo sandstone. (d) Mid-Jurassic sediments: Entrada Sandstone of the San Rafael Group (a road-side outcrop along Rt. 276, east of the Henry Mountains). (e) Late Jurassic sediments: the multi-coloured (“tie-dyed”) Brushy Basin Member of the Morrison Formation along the San Rafael Swell, to the north of Rt. 24, near Caineville. Height of mound is ~100 m. (f) Cretaceous sediments: Factory Butte. View from Rt. 24, looking north. The most photographed geological feature in Utah, Factory Butte is one of many buttes and mesas found on the bluish badlands of the Upper Blue Hills (just to the north of the Henry Mountains). The buttes and mesas are comprised of the Blue Gate Shale Member topped by the resistant Emery Sandstone (or Muley Canyon Sandstone Member) of the Mancos Shale (Fig. 2.18). Factory Butte is ~350 m high.

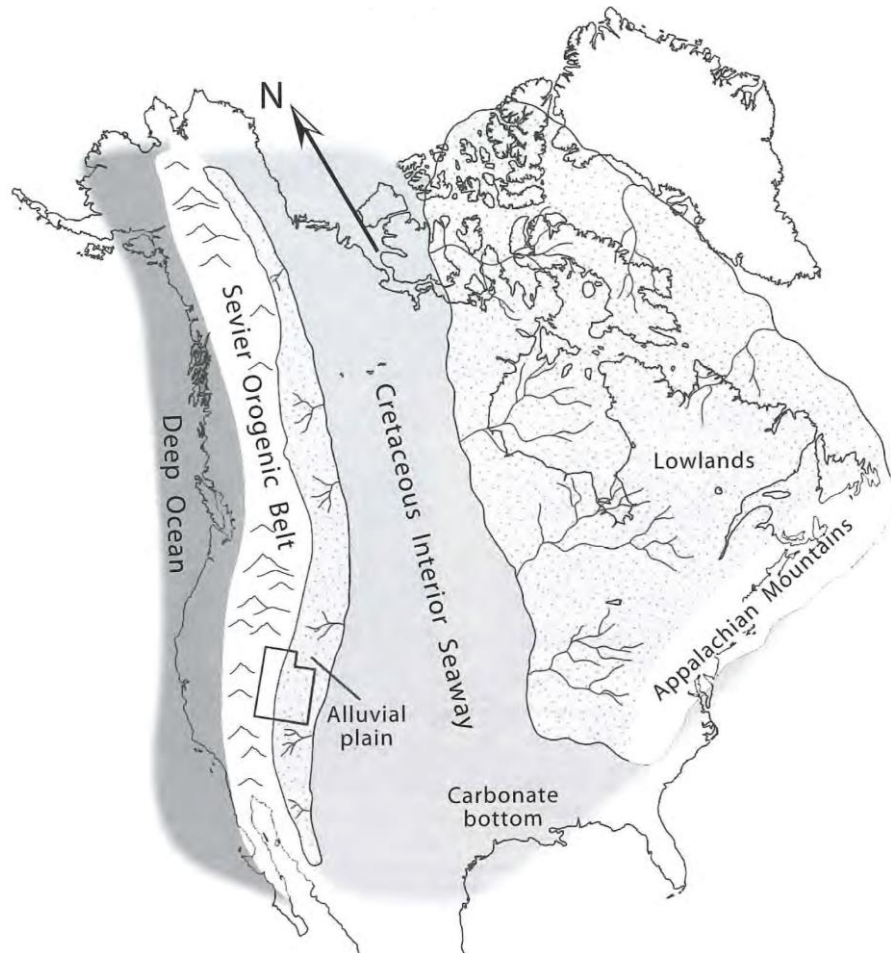


Figure 2.8. Palaeogeography and depositional environment map of North America during the late Cretaceous (80–100 Ma; from Hintze & Kowallis, 2009). Note the Late Cretaceous Interior Seaway dividing North America into two landmasses, and the Sevier Orogenic Belt to the west. Outline of Utah is highlighted in black.

2.2.5. Early- to mid-Cretaceous (145 to 80 Ma)

The era of relative tectonic quiescence in western N. America came to an end in the Jurassic with the onset of the Sevier orogeny (~ 140–50 Ma; Armstrong, 1968), and marks the transition to **Phase 6** of Hintze and Kowallis (2009; Fig. 2.4). Opening of the Atlantic Ocean to the east (Fig. 2.2a) caused a significant increase in the horizontal compressive stress (far-field stress) on the west coast subduction zone (Figs 2.2a & 2.3; Coney & Evenchick, 1994). This increased compressive stress initiated the rise of the Cordilleran thrust belt along the west coast (Fig. 2.5), which in turn accreted various arcs and continental fragments onto the western edge of the N. American continent (Figs 2.2a & 2.3; Coney & Evenchick, 1994). The Cordilleran thrust belt continued to grow over a period of about 100 million years from the Jurassic to the Eocene, eventually forming the high altitude mountain chain that exists today, running the entire length of the west coast of Canada, N. America and Mexico (Figs 2.2a, 2.3 & 2.5). Over the course of the Sevier

orogeny, frontal thrusts propagated progressively in an easterly direction, ceasing at a point just to the east of the former Neoproterozoic passive margin hinge line (Fig. 2.4, Phase 6). In Utah, this point is known as the Sevier thrust belt (Armstrong, 1968; DeCellas & Coogan, 2006) or the Sevier Orogenic Mountains (Figs 2.4, 2.8 & 2.9; Hintze & Kowallis, 2009), which is entirely thin skinned.

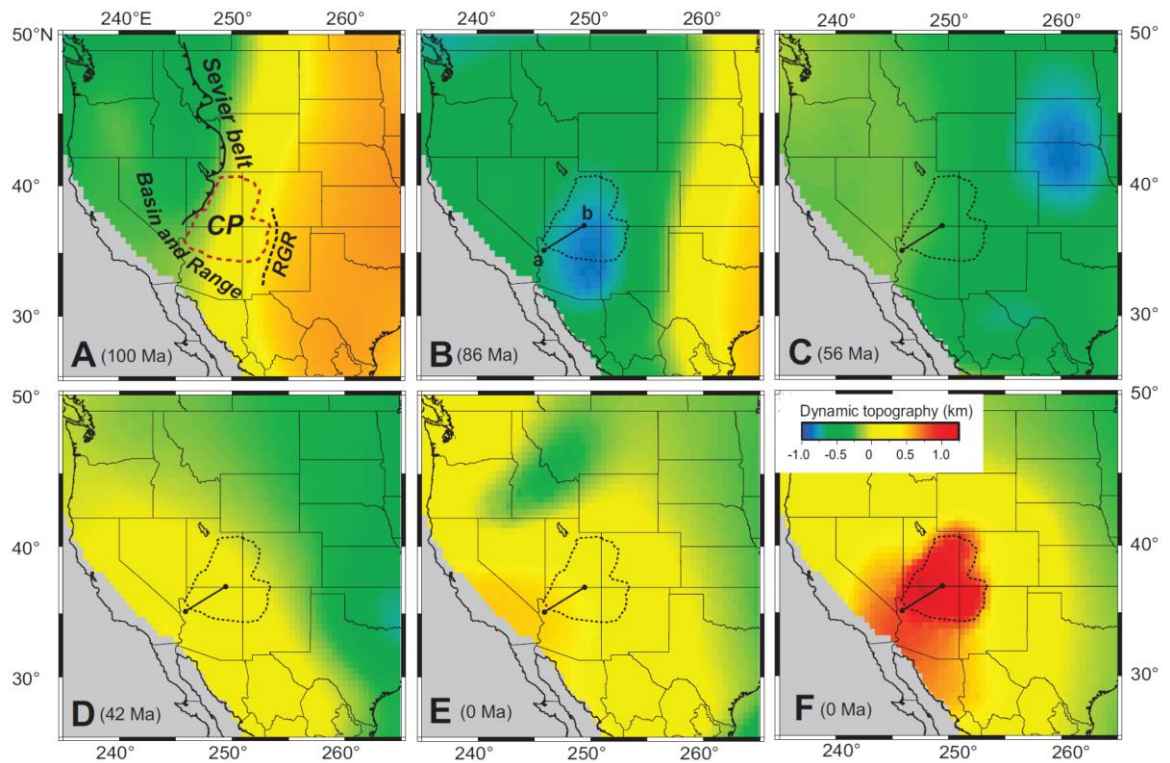


Figure 2.9. A–E show predicted dynamic topography over western USA showing subsidence and uplift of the Colorado Plateau, based on a model of Farallon slab subduction (from Liu & Gurnis, 2010). F shows a model for present-day topography which includes active mantle upwelling (note, this model closest resembles present-day elevation of the Plateau; from Liu & Gurnis, 2010). Reds and yellows are indicative of positive dynamic topography.

In response to the development of the Sevier Orogeny, a seaway developed across N. America, known as the Cretaceous Interior Seaway (Figs 2.3 & 2.8): dividing the continent into two large landmasses (Fig. 2a; Kauffman, 1984; Weimer, 1986; Hintze & Kowallis, 2009). This epicontinental seaway extended from Arctic Canada to Texas. Clastic influx was predominantly from the west, draining the western Cordilleran Mountain Chain of the Sevier Orogenic Belt (Fig. 2.8). In Utah, these deposits include the Cedar Mountain Formation and the dominant bluish-grey Mancos Shale (which includes the Ferron and Muley Canyon/ Emery sandstone members; Hintze & Kowallis, 2009; Fig. 2.7f). Much of the Cretaceous sedimentary record has been stripped from eastern and southern Utah

through erosion by the Colorado River and its many tributaries (Hintze & Kowallis, 2009). This erosion has created some of Utah's most distinctive erosional features, including the buttes and mesas of the badlands (e.g. Factory Butte, Fig. 2.7f) and the Book Cliffs.

2.2.6. Late Cretaceous to Palaeogene (80 to 35 Ma)

By the late Cretaceous, plate boundary conditions on the western margin of the N. American continent were in a state of flux, as the arrival of a buoyant oceanic plateau (Liu & Gurnis, 2010) resulted in flattening of the previously steep-angle of the subducting Farallon plate (Severinghaus & Atwater, 1990; Liu & Gurnis, 2010). Consequently, the Farallon plate began to scrape along the base of the N. American lithosphere. Tracking the leading edge of the subducting plate, magmatism swept inboard to the east (ceasing abruptly along the Sierra Nevada arc; Humphreys et al., 2003). Coincident with the flattening of the Farallon Plate, basement-cored uplifts (Fig. 2.10) started to rise in the foreland of the Cordilleran thrust belt, creating the Southern Rocky Mountains of Wyoming, Colorado, and New Mexico (Figs 2.2a & 2.3); this event is known as the Laramide Orogeny (Fig. 2.4, **Phase 7**; Armstrong, 1968; Bump & Davis, 2003; Hintze & Kowallis, 2009; Davis & Bump, 2009). The uplifts reactivated older structures and fabrics in the basement, including some of the Proterozoic normal faults (compare Proterozoic basement trends in Figure 2.6 with Laramide fold structures in Figure 2.10; Marshak et al., 2000; Bump & Davis, 2003; Davis & Bump, 2009). Timings of the Laramide Orogeny are a matter of some debate, with the event beginning in the late Cretaceous, ~80–70 Ma, and ceasing in the Eocene ~55–35 Ma (Davis & Bump, 2009).

On the Colorado Plateau, the Laramide Orogeny resulted in the creation of large monoclinical structures (Fig. 2.10; Bump & Davis, 2003; Davis & Bump, 2009; Fillmore, 2011). In south-eastern Utah, these include the Comb Ridge, Escalante, San Rafael, Teasdale, Uncompahgre, Upper Valley and Waterpocket monoclines (Fig. 2.10b ; Bump & Davis, 2003; Davis & Bump, 2009; Hintze & Kowallis, 2009; Fillmore, 2011). Dynamic uplift of the Colorado Plateau commenced ~80 Ma (Fig. 2.9; Liu & Gurnis, 2010; Roberts et al., 2012), raising the plateau by ~1 km over a period of approximately 30 million years (Roberts et al., 2012).

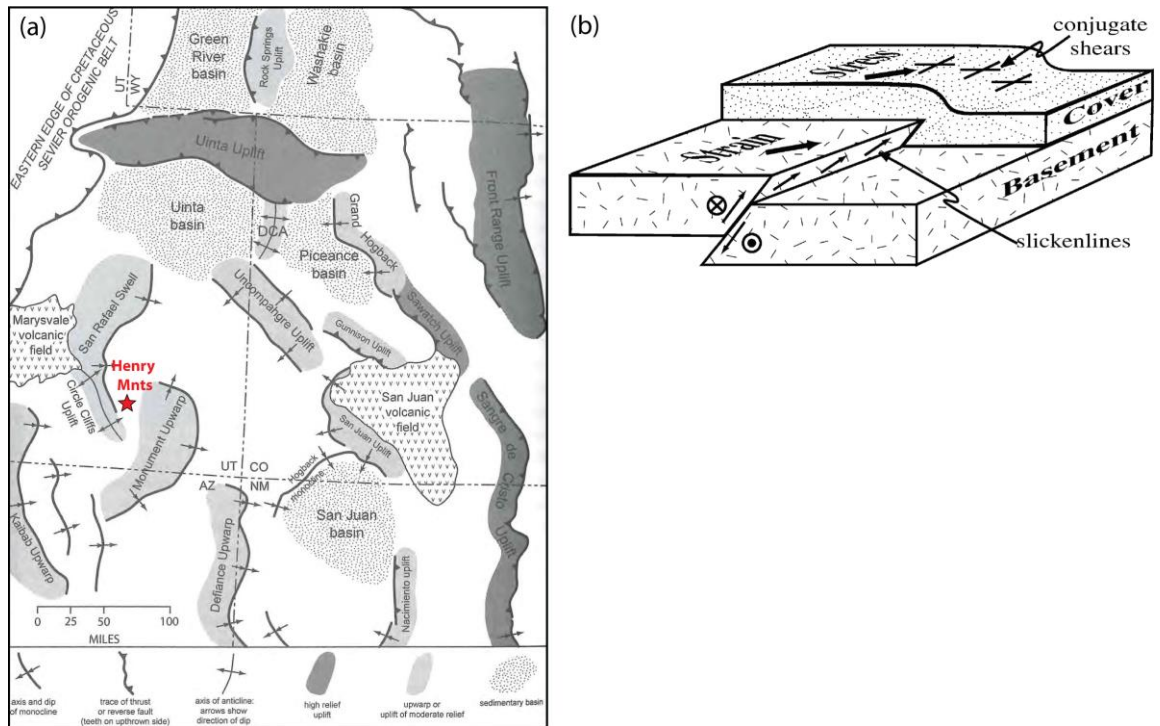


Figure 2.10. Laramide folding on the Colorado Plateau. (a) Structural map showing Laramide tectonic elements of the Four Corners area on the Colorado Plateau (from Fillmore, 2011). Location of the Henry Mountains shown by a red star. (b) Schematic block diagram showing the proposed relationship between structures in the basement and cover (from Bump & Davis, 2003).

2.2.7. Latest-Palaeogene to Present (~35 to 0 Ma)

Thrusting in both the Cordillera Mountains and the southern Rocky Mountains ceased during the Eocene, as the next change in the plate boundary conditions brought to an end the Sevier and Laramide orogenies respectively. This change was the result of the spreading centre between the Pacific Plate and the already subducting Farallon Plate coming into contact with the subduction zone (Fig. 2.11; Irwin, 1990). The spreading centre (or ridge), a system of spreading segments and transform faults, was at an oblique angle to the ~N–S trending subduction zone (Atwater, 1970; Severinghaus & Atwater, 1990).

At ~30 Ma, the westward moving North American Plate began to override the spreading ridge between the Farallon and Pacific plates (Atwater, 1970), and the Farallon Plate was divided into two smaller plates: the northern Juan de Fuca Plate; and the southern Cocos Plate (Fig. 2.11; Irwin, 1990). With continued subduction, triple junctions (intersections of three tectonic plate boundaries) developed and began to migrate apart. The zone between the two triple junctions displayed strike-slip movement (i.e. the San Andreas Fault), while the segments to the north and south remained as convergent subduction

zones (Fig. 2.11; Irwin, 1990). In this zone between the two triple junctions (i.e. where the spreading centre had been subducted), spreading ceased, creating a window in the subducting slab (this expanded to form a slab gap with continued subduction of the spreading centre; Fig. 2.11; Severinghaus & Atwater, 1990). This allowed upwelling of hot asthenosphere to come into contact with the continental lithosphere of the overriding N. American plate (Dickinson, 1997). The addition of heat to the freshly hydrated lithosphere produced a significant burst of magmatism that followed the track of the subducting slab window (Figs 2.12 & 2.13; Humphreys et al., 2003; McQuarrie & Oskin, 2010). At the surface, explosive andesitic and dacitic volcanics erupted along the Reno-Marysville, San Juan and Mogollon-Datil belts, producing voluminous ($\sim 5 \times 10^5 \text{ km}^3$; Johnson, 1991) ignimbrite and tuff deposits (the ignimbrite flare-up of the Oligocene; Nelson & Davidson, 1997).

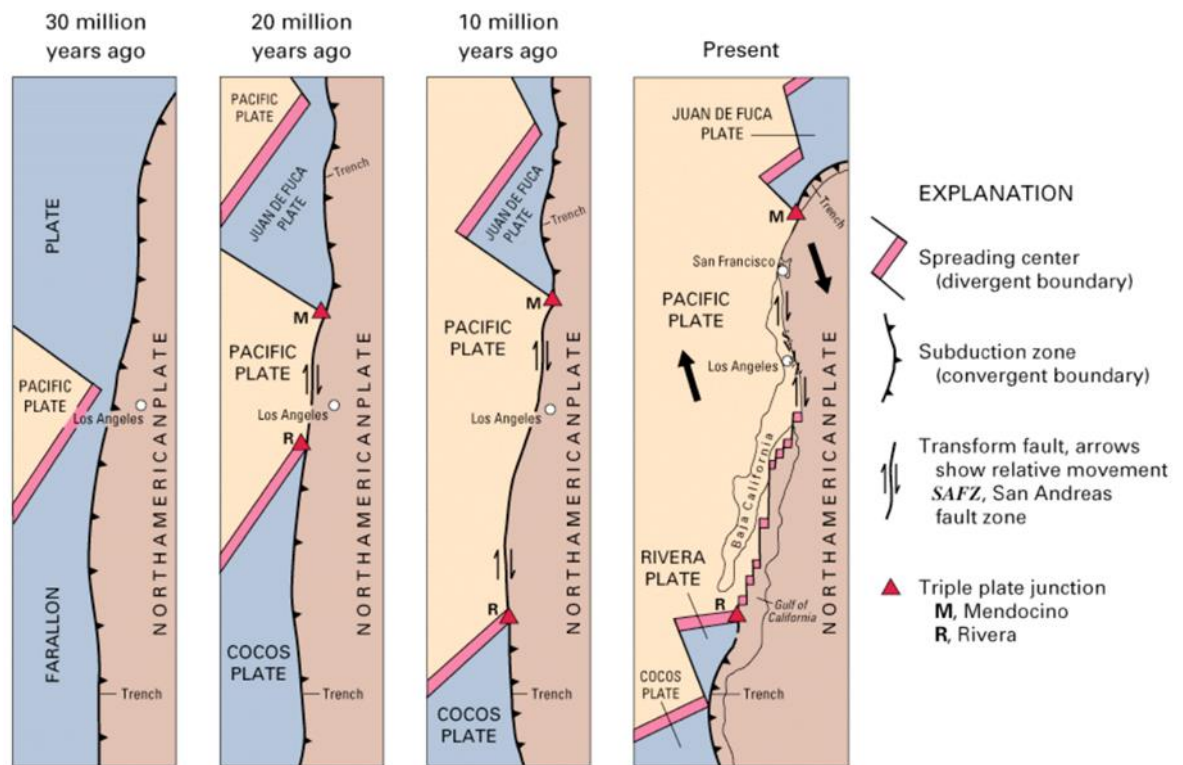


Figure 2.11. The geological evolution of the San Andreas Fault along the western coast of North America from ~ 30 Ma to present (modified after Irwin, 1990; re-drawn by USGS <http://pubs.usgs.gov/gip/dynamic/Farallon.html>).

As a combined result of lithospheric heating and the removal of compressive stress, the over-thickened crust of the Cordilleran hinterland (to the west of the Sevier fold-thrust belt) began to collapse, extending in a westerly direction, creating the Basin and Range

Province of western Utah and Nevada (Figs 2.1–2.3; Stewart, 1998; Stewart et al., 1998; Sonder & Jones, 1999; Dickinson, 2002).

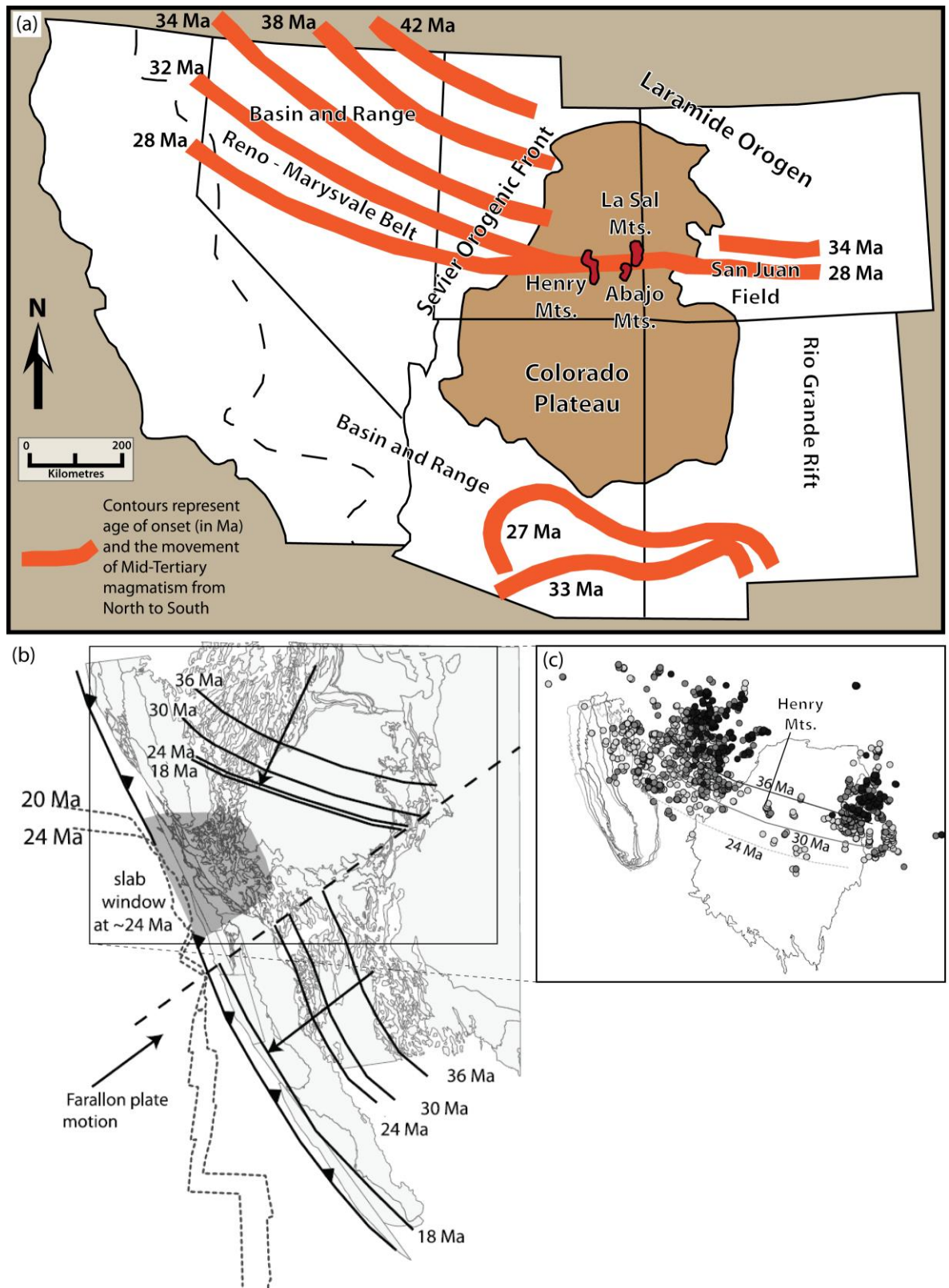


Figure 2.12. A series of maps depicting magmatism and volcanism across western North America from 42 Ma to the present. (a) Simplified map showing the location of the Henry, La Sal and Abajo Mountains and their relationship to tectono-magmatic elements in south-western USA (modified from Nelson et al., 1992). (b) Map showing plate boundary volcanism for SW USA (from 36 to 18 Ma) based on plate reconstruction

models of McQuarrie and Oskin (2010). SW movement of magmatic systems linked to slab roll-back of the subducting Farallon plate. Dashed lines show location of Farallon plate spreading axis at 24 and 20 Ma, while grey areas depicts the proposed slab window. Image from McQuarrie and Oskin (2010). (c) Map showing south-westward migration of magmatism (36 to 24 Ma; from McQuarrie & Oskin, 2010). Outlines of the Sierra Nevada–Great Valley block (left) and Colorado Plateau region (right) are shown.

During the Oligo–Miocene (~34–15 Ma), the Colorado Plateau underwent a second phase of uplift (Fig. 2.9; Liu & Gurnis, 2010; Roberts et al., 2012), raising the plateau by a further ~1.5 km (Roberts et al., 2012). This was coincident with the emplacement of the magmatic intrusions on the plateau (Fig. 2.4, **Phase 8** and Fig. 2.14; Hintze & Kowallis, 2009), including the emplacement of the Henry Mountains igneous centres (Nelson et al., 1992).

During the Neogene (~17 Ma), the extensional Wasatch Fault Zone (still active today) developed in Utah, following the Cambrian shelf/ hinge line (old passive margin), resulting in westward extension (Fig. 2.4, **Phase 9**; Hintze & Kowallis, 2009). This was accompanied by further uplift and erosion of the plateau. Most of the Utahn landforms that we see today developed over the last 5 million years, partly in response to this most recent uplift (Hintze & Kowallis, 2009).

Figure 2.13. (*overleaf*)

A series of map view reconstructions of volcanism across western North America from 36 Ma to the present (McQuarrie & Oskin, 2010). Underlying map grid is a palinspastic reconstruction showing plate deformation through time. Blue line depicts active plate boundary (spreading centre) of subducting Farallon plate. Various coloured dots show the locations of volcanic deposits of varying geochemistry through time. Note the relative lack of volcanism on the Colorado Plateau (CP) with respect to surrounding regions, with the exception of 24 Ma and 18 Ma maps.

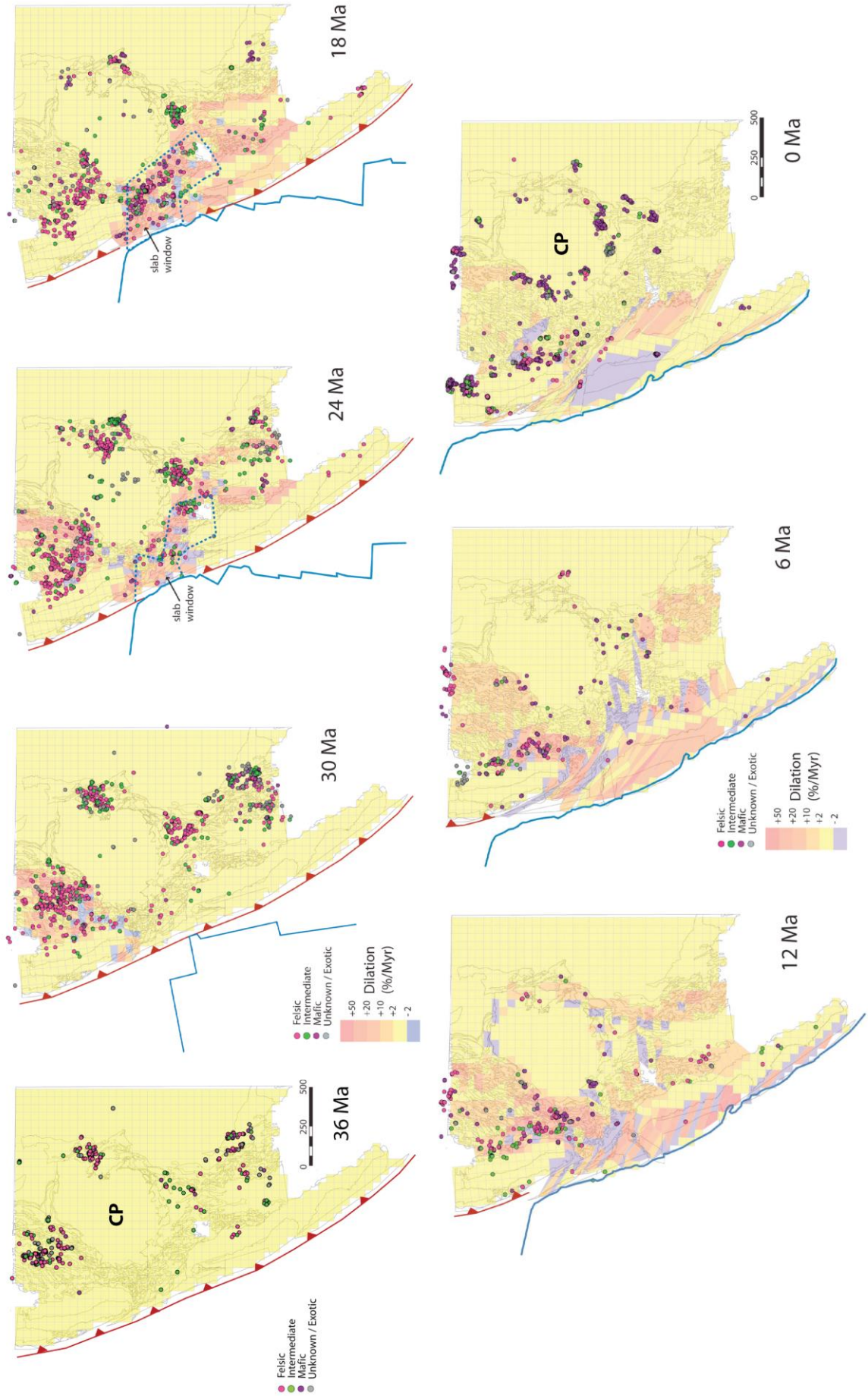


Fig. 2.13

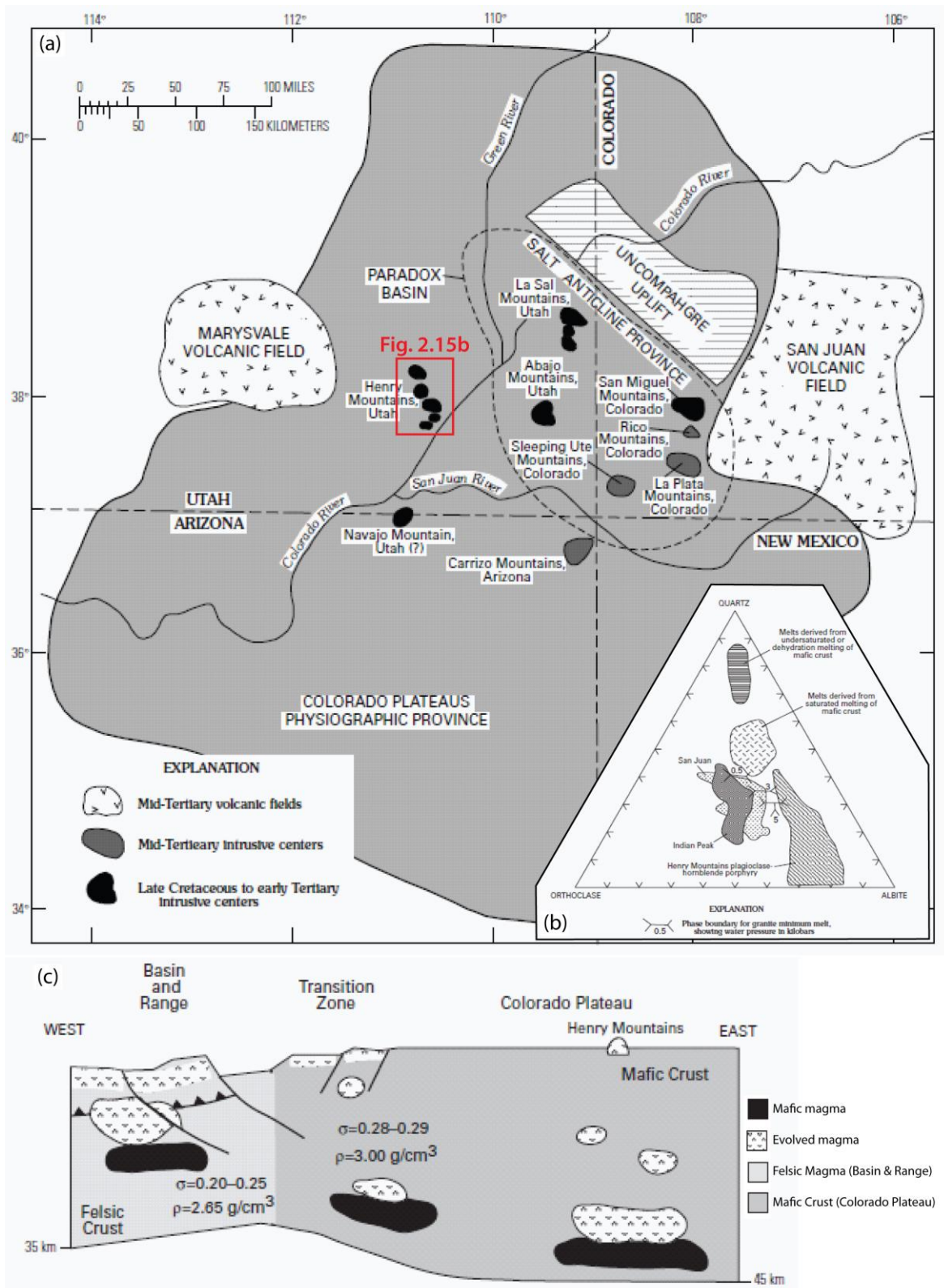


Figure 2.14. Magmatism of the Colorado Plateau. (a) Simplified map showing selected magmatic and structural features on the Colorado Plateau (Ross, 1997). (b) Ternary diagram plotting normative compositions of laccolith complexes of southeastern Utah, including the Henry Mountains (from Nelson & Davidson, 1997). (c) Cartoon diagram highlighting differences in crustal structure, composition and magma volumes across south-western USA (the Basin and Range province, across the transition zone, and the Colorado Plateau interior; from Nelson & Davidson, 1997).

2.3. Uplift and Magmatism on the Colorado Plateau

2.3.1. Dynamics (uplift) of the Plateau

The geological and tectonic history of the Colorado Plateau during the last 80 million years (late Cretaceous through to present) has been dominated by dynamic uplift and magmatism. The present elevation of the Colorado Plateau is ~2 km (Roy et al., 2009; Liu & Gurnis, 2010, Roberts et al., 2012). Timing of the uplift has remained the subject of debate: Wolfe et al. (1998) proposed that the present elevation was attained in the Eocene (from palaeobotanical studies); whereas Sahagian et al. (2002) suggested a much later Miocene timing (from basalt vesicularity). A recent exhumation study by Flowers et al. (2008), carrying out (U-Th)/He apatite thermochronology, potentially provides the most accurate date for uplift yet, with ~1 km of elevation over the SW Colorado Plateau by the latest Cretaceous. Roberts et al. (2012) have also published timings for uplift based on the inversion of river profiles (the assumption being that the resultant profiles are controlled by uplift rate and moderated by erosion) and correlation with field observations and dating of stratigraphy. They proposed that a first phase of uplift occurred between 80 and 50 Ma, with 1 km of uplift at a rate of ~0.03 mm/yr. Their river profiles also identify a second phase of uplift between 35 and 15 Ma (~1.5 km uplift at ~0.06 mm/yr), followed by a final phase of uplift over the last 5 million years.

The mechanical reasons for the dynamic uplift of the plateau have also been hotly debated over the decades, and have been the focus of a number of publications in recent years, with various models proposed in order to explain the vertical motion, including: crustal thickening (Bird, 1988; McQuarrie & Chase, 2000); removal of mantle lithosphere (England & Houseman, 1988; Spencer, 1996; Roberts et al., 2012); chemical alteration of the continental lithosphere (Humphreys et al., 2003; Roy et al., 2004); and active mantle upwelling and dynamic topography (Parson et al., 1994; Moucha et al., 2009; Liu & Gurnis, 2010). Recent estimates for crustal thickness across the Colorado Plateau do not appear to support the thicker than normal crust estimates (i.e. 45 km) previously proposed (e.g. McQuarrie & Chase): therefore the present elevation of the Colorado Plateau cannot be explained by crustal thickening (Roberts et al., 2012). Liu and Gurnis (2010) used inverse models of mantle convection to predict the impact of the subducting Farallon plate on the vertical motion on the plateau. In the model of Liu and Gurnis (2010), the arrival of the flat-lying Farallon slab ~100 Ma results in dynamic subsidence of the continental crust, sweeping from west to east, reaching a maximum at ~86 Ma (Fig. 2.9). Subsidence is followed by two stages of dynamic uplift in the early Palaeogene (~56

Ma; Fig. 2.9) and in the mid-Palaeogene (Eocene, ~42 Ma; Fig. 2.9), following the removal of the Farallon slab below the plateau and buoyant upwellings, resulting in an overall uplift of ~1.2 km, suggesting that the Colorado Plateau attained its present-day elevation during the Oligocene (Fig. 2.9; Liu & Gurnis, 2010). In contrast, Roberts et al. (2012) suggested that the uplift history is likely to be consistent with episodic convective removal of lower lithospheric mantle beneath the region, and associated with the hot spot currently beneath Yellowstone.

2.3.2. Magmatism

Accompanying the uplift of the Colorado Plateau have been three periods of magmatism, though in comparison to surrounding areas in western N. America, the volumes have been minor (Fig. 2.13; Nelson & Davidson, 1997; McQuarrie & Oskin, 2010). The first event was the mid-Tertiary intrusive andesite/ diorite magmatism between ~30 and 23 Ma, creating the Henry, La Sal and Abajo Mountains of south-eastern Utah (Figs 2.12 and 2.14; Nelson & Davidson, 1997). This period of intrusive magmatism was followed in the late Cenozoic (<17 Ma) by a period of basaltic magmatism around the margins of the plateau (Fig. 2.13; Nelson & Davidson, 1997; McQuarrie & Oskin, 2010) associated with extension in the Rio Grande and Basin and Range rift systems. A final period of basaltic volcanism, including the San Rafael Dyke Swarm to the north of the Henry Mountains, occurred over the last ~ 5 Ma (Steve Nelson, personal comments). The San Rafael Dyke System has a distinct N–S trend, suggesting E–W extension: this is both kinematically and temporally consistent with the presently active Wasatch fault zone (see Fig. 2.4, **Phase 9**).

Igneous activity of the Colorado Plateau has been, along with greater magmatism in western N. America, the subject of much discussion over the last 40 years: the tectonic processes that gave rise to the voluminous Cenozoic magmatism still the subject of hot debate (Nelson & Davidson, 1993; McQuarrie & Oskin, 2010 and references therein). Cenozoic volcanism in western N. America must account for the significant changes along the Pacific plate boundary (Fig. 2.11; McQuarrie & Oskin, 2010). McQuarrie & Oskin (2010) made the observation that magmatism in the Basin and Range province is strongly linked to plate boundary effects relating to the subduction of the Farallon plate and its developing slab window (Figs 2.12b & 2.13; McQuarrie & Oskin, 2010).

Mid-Tertiary magmatic fronts swept across the western United States (Fig. 2.12; Cross & Pilger, 1978; Burke & McKee, 1979; Glazner & Bartley, 1984; Nelson & Davidson, 1997): from the north, in a south-westerly direction (from 36 to 24 Ma; Fig. 2.12c; McQuarrie & Oskin, 2010); and the from the south in a westerly direction (from 36 to 18 Ma; Fig. 2.12b; McQuarrie & Oskin, 2010). McQuarrie & Oskin (2010) suggested that the most logical explanation for these patterns can be related to slab roll-back and steepening of the subducting Farallon Plate. Roll-back of the once flat subducting slab not only explains the movement of the magmatic fronts, but is also a key driver for the extension seen in western US (Dickinson, 2002), as well as the later influx of basaltic magmatism (Harry et al., 1993).

Using geochemical signatures, Nelson and Davidson (1993, 1997) suggested that both the Cenozoic intrusive rocks of the Colorado Plateau and the volcanic rocks in the surrounding region to the west have strong affinities to arc rocks. They proposed that the intrusions of the Colorado Plateau are part of an E–W oriented magmatic belt (Fig. 2.12), and the relatively minor volumes of magma on the plateau are due to a thickened crust beneath the plateau (Fig. 2.14).

The Yellowstone–Snake River Plain (YSRP) system to the north of the Colorado Plateau is believed to be related to a hotspot plume (Armstrong et al., 1975; Pierce & Morgan, 2009), though the exact mechanisms are still unresolved (Fouch, 2012). Rhyolitic volcanics of the YSRP began erupting ~12 Ma (Puskas et al., 2007; Shervais & Hanan, 2008) and young eastwards. This migration pathway corresponds to the present-day movement of the North American plate (Puskas et al., 2007; Pierce & Morgan, 2009; Fouch, 2012). There appears to be little expression of the YSRP magmatism on the Colorado Plateau (Fig. 2.13; McQuarrie & Oskin, 2010), though time equivalent basaltic magmatism is present locally (e.g. San Rafael dyke swarm). Roberts et al. (2012) did however link most recent uplift of the plateau to potential plume related activity.

2.4. Geology of the Henry Mountains

The Henry Mountains are located in south-eastern Utah (Figs 2.12, 2.14 & 2.15), and are one of more than ten mountain ranges located on the central and eastern Colorado Plateau (Fig. 2.14) that are composed of sedimentary domes with igneous cores, encircled by satellite dykes, sills and laccoliths (Fig. 2.16; Hunt, 1953; Engel, 1959; Jackson &

Pollard, 1988; Nelson et al., 1992; Nelson & Davidson, 1993; Horsman et al., 2005). The Henry Mountains range trends north–south and is about 60 km in length (Fig. 2.15; Jackson & Pollard, 1988). West of the Henry Mountains lies the Circle Cliffs Uplift and Waterpocket Monocline, to the north the San Rafael Swell, and to the southeast and east Monument Uplift and the Canyonlands (Figs 2.15 and 2.17). The range consists of 5 principal peaks reaching heights greater than 3350 m (the elevation of the plateau ~1525 m), from north to south these are: Mt Ellen; Mt Pennell; Mt Hillers; Mt Holmes; and Mt Ellsworth (Figs 2.15 & 2.16c). Each peak represents a distinct intrusive centre emplaced into nearly flat-lying stratigraphy on a gently dipping (~2°) eastern limb of an asymmetrical syncline that also trends north–south (Jackson & Pollard, 1988). The Waterpocket Monocline, part of the Laramide Circle Cliffs Uplift (Figs 2.10, 2.15a & 2.16b), forms the western limb of the basin (Figs 2.15a & 2.18; Hunt, 1953), trending sub-parallel to the range.

Figure 2.15. (*overleaf*)

Location and geology of the Henry Mountains, Utah. (a) Topographic map of the Henry Mountains region in south-eastern Utah. Key geological structures and features are highlighted. (b) Simplified geological map of the Henry Mountains and their location within Utah (map to the right; adapted from Morgan et al., 2008). $^{40}\text{Ar}/^{39}\text{Ar}$ age determinations are the various Henry Mountains igneous intrusions are provided (from Nelson et al., 1992).

Figure 2.16. (*overleaf*)

Contour maps for the Henry Mountains (excluding Mount Ellen) and Navajo Mountain, accompanied by a series of diagrams illustrating the space occupied by intrusive stocks and the theoretical space available for them (from Hunt, 1953).

Figure 2.17. (*overleaf*)

Photographs showing significant geological structures of the Henry Mountains area in south-eastern Utah, including the: (a) San Rafael Swell Uplift, to the north of the Henry Mountains; (b) Waterpocket Fold, part of the Circle Cliffs Uplift, just to the west of the Henry Mountains; and (c) Five peaks (intrusive centres) of the Henry Mountains.

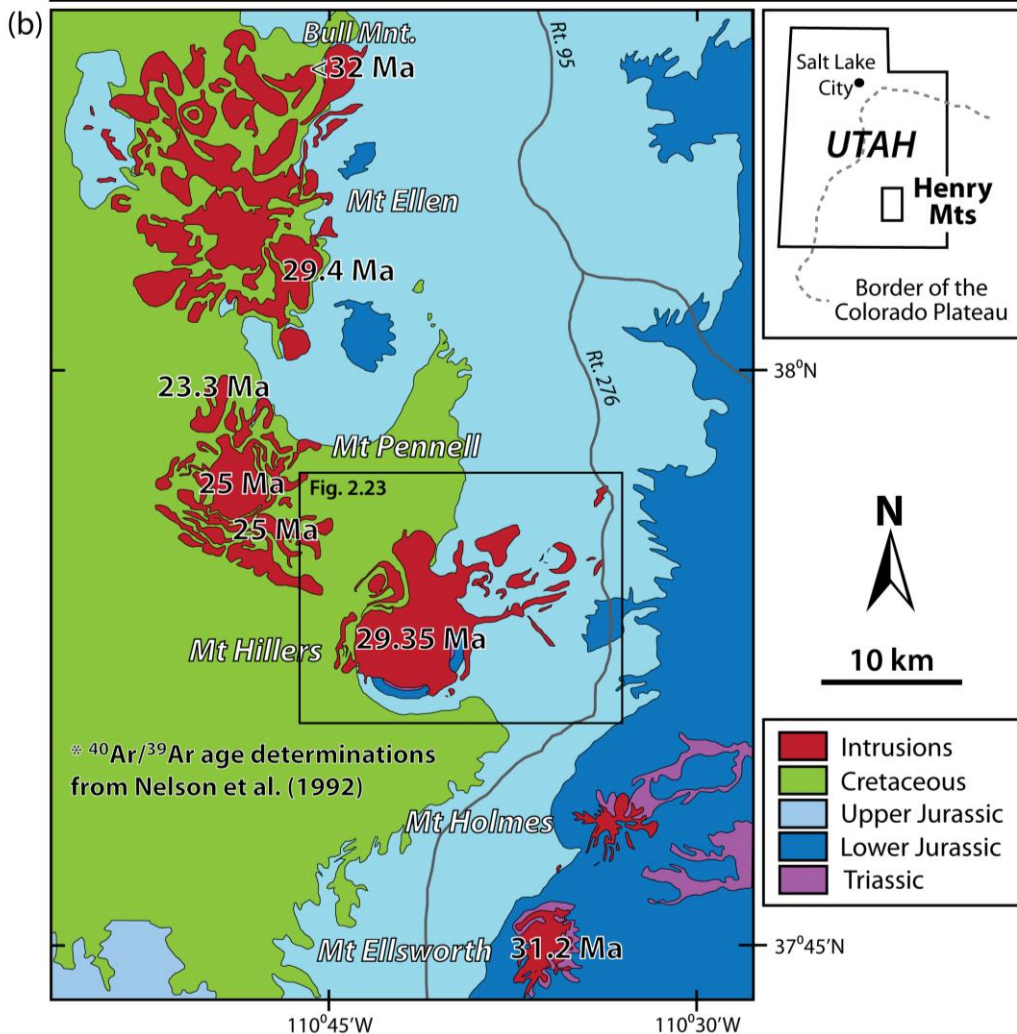
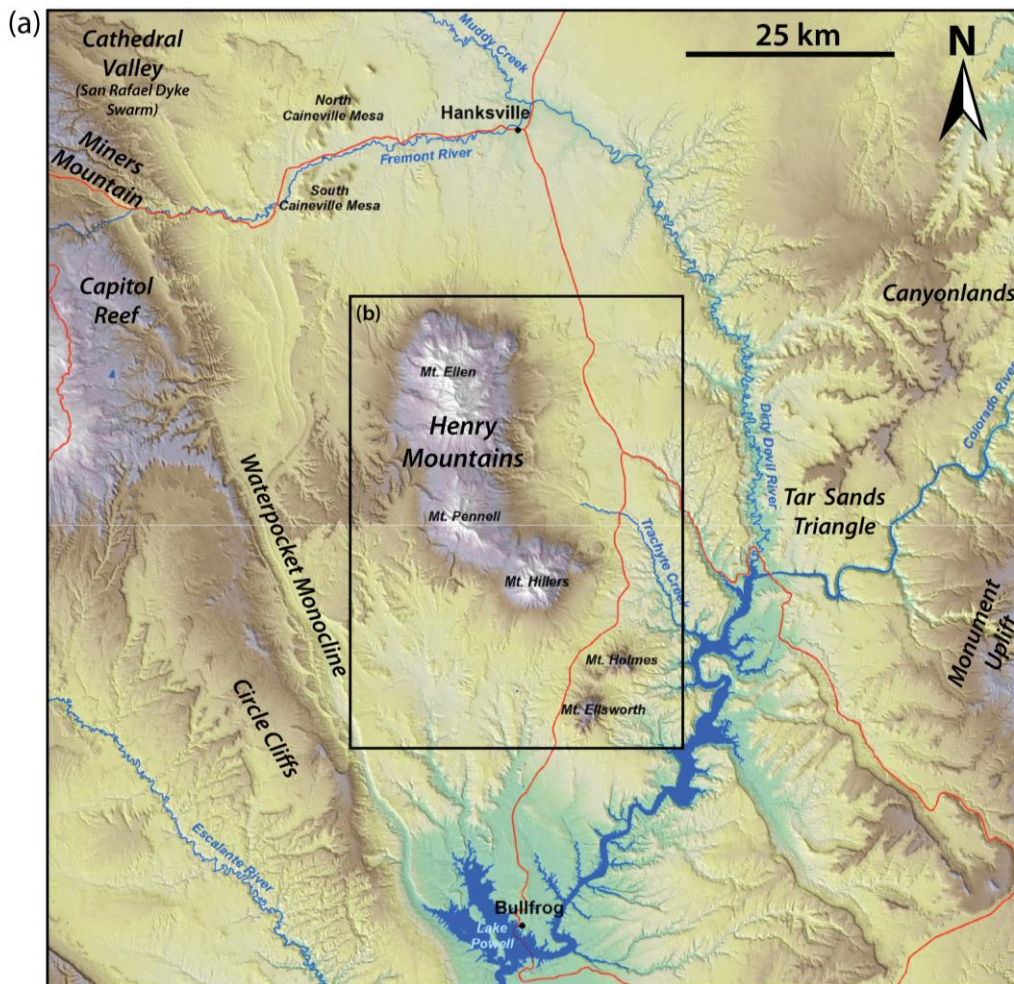
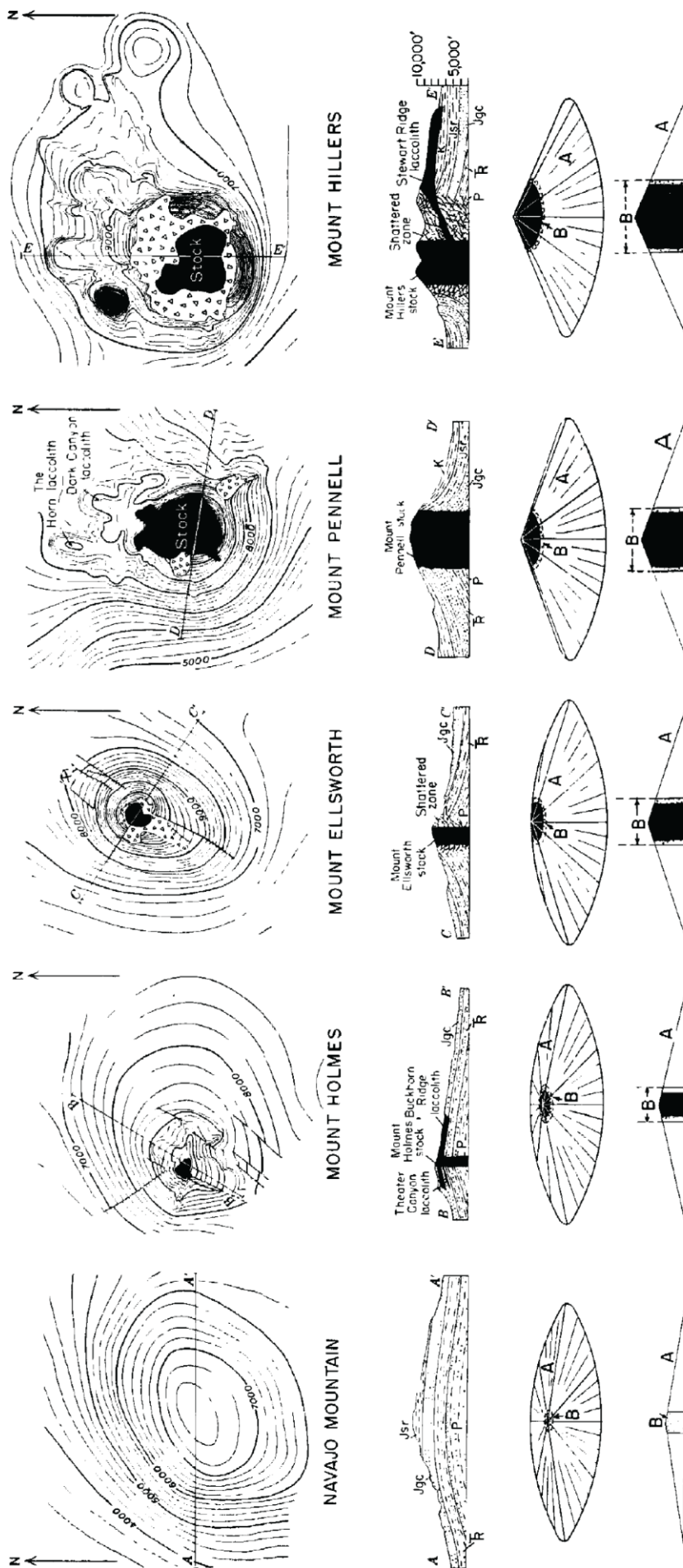


Fig. 2.15



K, Cretaceous rocks, Jsr, rocks of San Ratael group, Jgc, rocks of Glen Canyon group, K, Triassic rocks, P, Permian rocks, R, Perman ricks. Structure contours drawn on base of Ferron sandstone member of Mancos shale. Contour interval is 200 feet, datum is sea level.

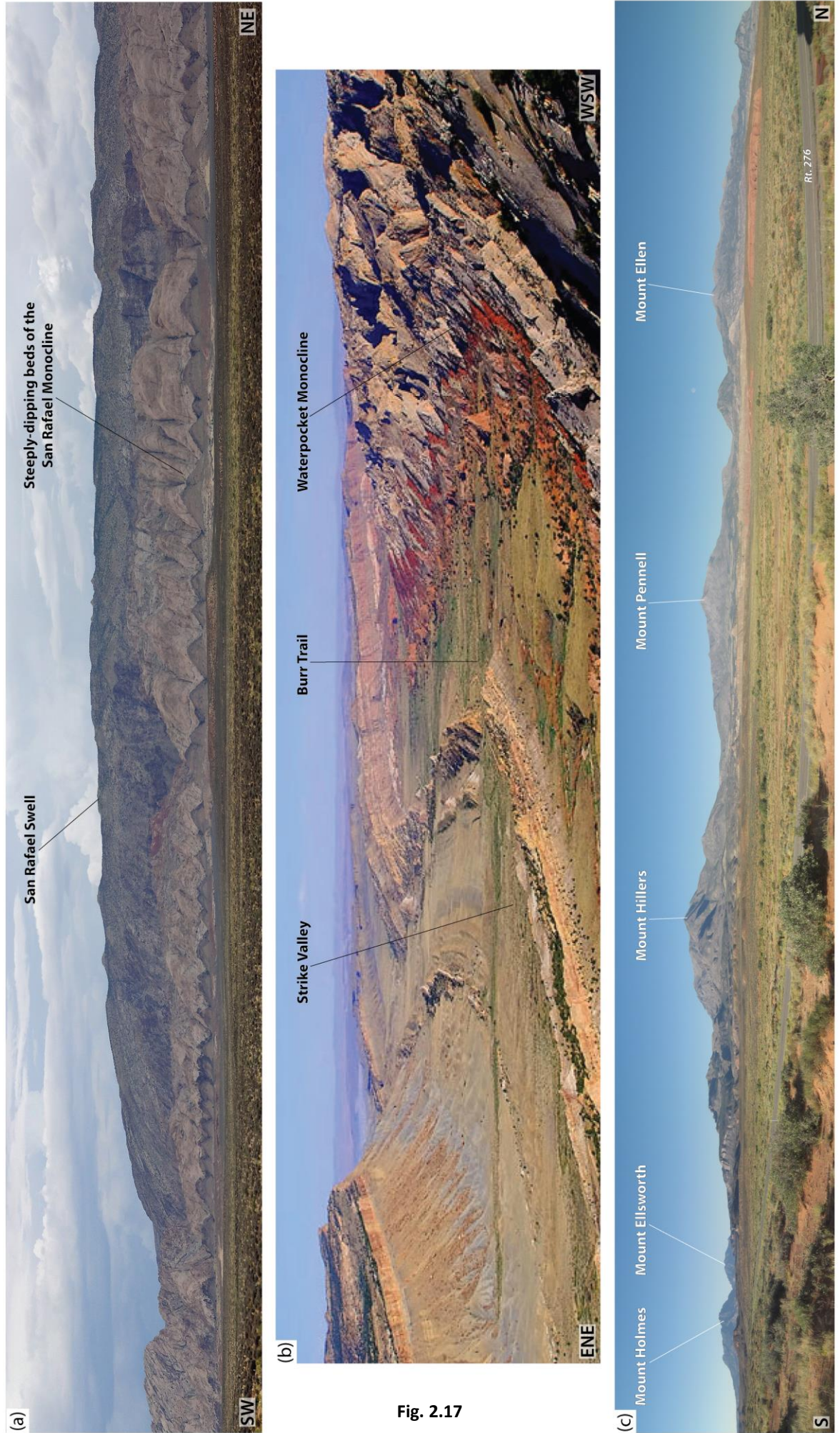


Fig. 2.17

2.4.1. Stratigraphy

The stratigraphy of the Henry Mountains region is dominated by an approximately 3–6 km thick succession of Permian to Cretaceous sandstones and shales (Fig. 2.19; Hunt, 1953; Hintze, 1963; Peterson et al., 1980; Stokes, 1980; Jackson & Pollard, 1988;). The exposed sedimentary succession starts at the base of the Permian Cutler Formation and ends with the Cretaceous (Campanian) Mesa Verde Formation (Fig. 2.19; Jackson & Pollard, 1988). About 100 km to the west of the Henry Mountains, in western Garfield County, an approximately 1 km thick sequence of lower- to mid-Palaeogene (lower Tertiary) sediments overlies the Mesa Verde Formation (Fig. 2.19a; Doelling, 1975). Therefore, a maximum of about 3.7 km of sedimentary strata are estimated to have overlain the Permian Cutler Formation during the late Palaeogene (Oligocene) at the time of emplacement of the Henry Mountains intrusions (Hunt, 1953; Hintze, 1963; Doelling, 1975; Peterson et al., 1980; Stokes, 1980; Jackson & Pollard, 1988). Roughly 1.3 to 1.9 km of stratified sediments are estimated to lie between the base of the Permian Cutler Formation and crystalline basement rocks (from stratigraphic sections; Fig. 2.19; Hintze, 1963; Doelling, 1975; Jackson & Pollard, 1988).

The intrusions of the Henry Mountains are emplaced at various levels in the Permian to Upper Jurassic stratigraphy (Fig. 2.19a). The base of the main intrusive bodies lie within the Permian stratigraphy (e.g. in the Cedar Mesa Formation for Mount Hillers; Figs 2.18 and 2.19a; Jackson & Pollard, 1988), whilst the satellites to the NE of Mount Hillers are hosted within shallower strata (e.g. Jurassic Entrada, Summerville and Morrison Formations; Fig. 2.19a; Jackson & Pollard, 1988). The following sections provide a basic summary of these key host rock intervals.

Figure 2.18. *(overleaf)*

Simplified geological cross-section through the Circle Cliffs Uplift, Capitol Reef National Park, and the Henry Mountains (from the USGS; poster available in the Capitol Reef National Park Information Centre).

Geological Cross Section of Capitol Reef National Park

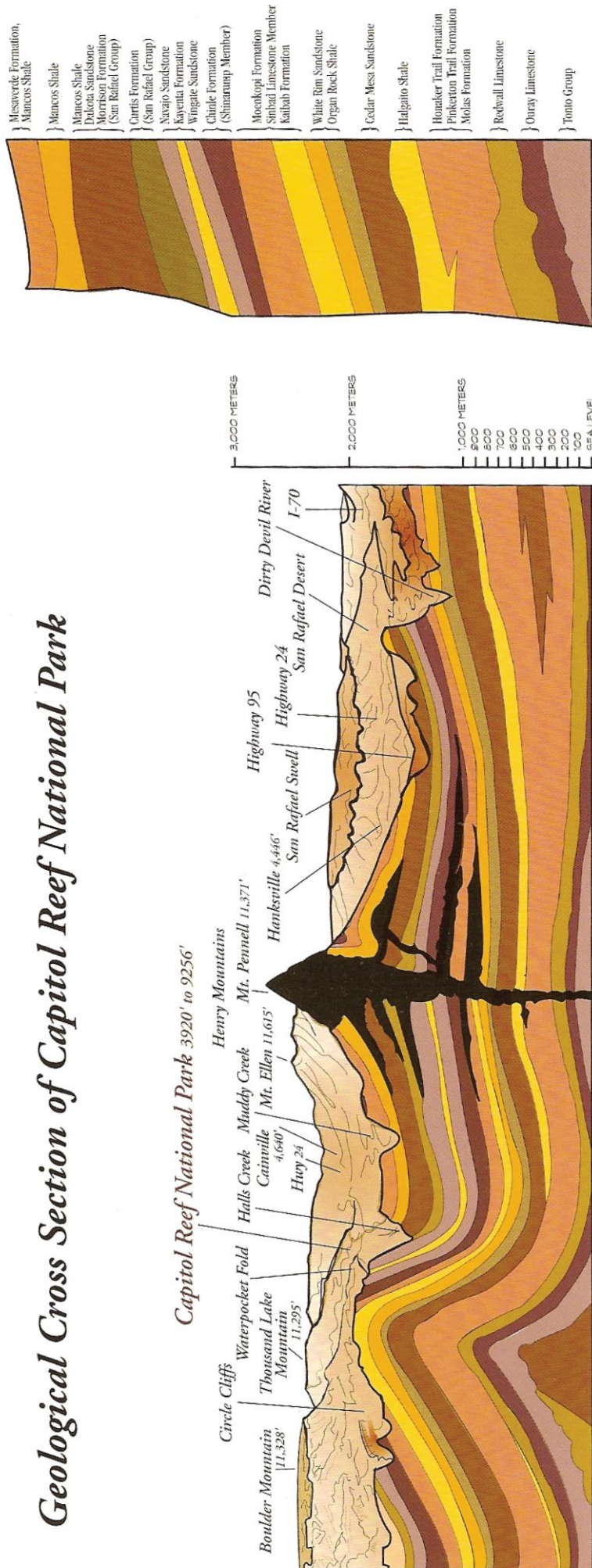


Fig. 2.18

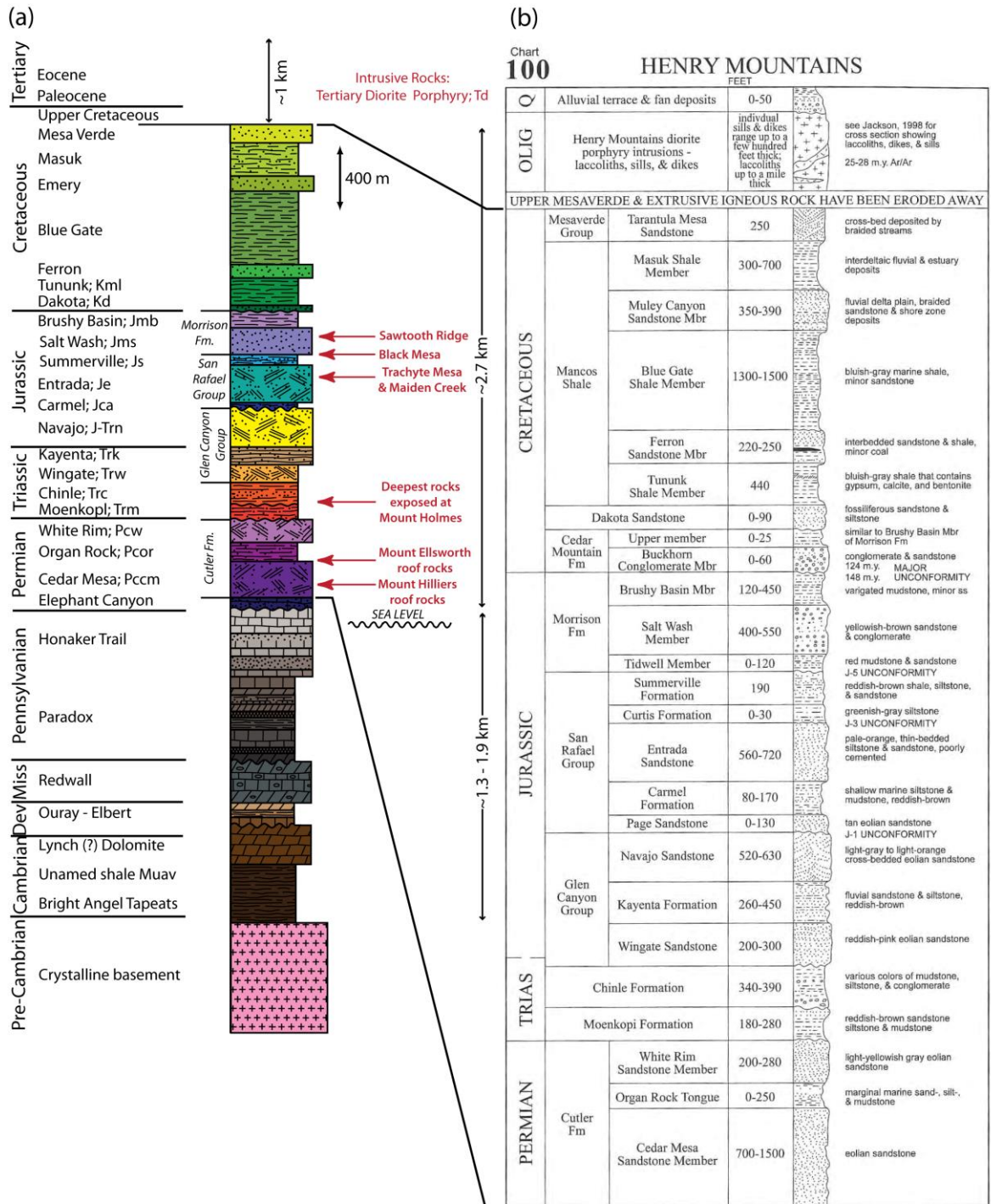


Figure 2.19. Stratigraphy of the Henry Mountains region. (a) Stratigraphic column for SW Utah and the Henry Mountains region (modified from Jackson & Pollard, 1988). (b) Stratigraphic column for the Henry Mountains, with ages and thicknesses of units (from Hintze & Kowallis, 2009).

2.4.1.1. *Cutler Formation (Roof Rocks to Mount Hilliers)*

The Cutler Formation is Permian in age, consisting of a heterogeneous sequence of dominant arkosic conglomerates, and lesser amounts of arkosic sandstones, siltstones and mudstones (Condon, 1997). The Cutler Formation was deposited by dominantly west-flowing rivers, draining the Uncompahgre Mountains to the East (Condon, 1997; Fillmore,

2011). In the Henry Mountains region, the Cutler Formation can be divided into three distinct units: Lower Cutler beds and Cedar Mesa Sandstone Member (~200 to 460 m thick); Organ Rock Tongue (<80 m thick); and White Rim Sandstone Member (~60–85 m thick; Fig. 2.19b; Hintze & Kowallis, 2009; Fillmore, 2011). The Cedar Mesa Sandstone consists largely of red and white cross-bedded aeolian (wind-driven) sandstones deposited in a vast (>50 km²; Condon, 1997) dune field (Stanesco & Campbell, 1989; Condon, 1997; Fillmore, 2011). The sandstones are predominantly quartz arenite/ sub-arkosic sandstones and exhibit large-scale cross-bedding. In stark contrast to the underlying, lighter-coloured, Cedar Mesa Sandstone Member, the Organ Rock Formation has a dark brown-red colour. Organ Rock is composed of mostly silty sandstones and sandy siltstones, with lesser amounts of limestone-nodule conglomerate and mudstone (Condon, 1997; Fillmore, 2011). Alternating resistant and less resistant beds result in distinctive horizontal banding (Condon, 1997). Until the recent studies of Stanesco, Dubiel, Condon and others (including: Stanesco & Dubiel, 1992; Dubiel et al. 1996; Condon, 1997; Stanesco et al., 2000), the depositional environment of the Organ Rock Formation was poorly understood. Deposition occurred in a variety of fluvial, alluvial, and aeolian environments, changing considerably with location: southwest-flowing rivers (draining the Uncompahgre Mountains) separating various ergs (see fig. 22 in Condon, 1997). The White Rim Sandstone Member (the uppermost unit of the Cutler Formation) consists of fine- to coarse-grained, greyish-white to white sandstones (Condon, 1997; Fillmore, 2011). These sandstones were also deposited in an aeolian dune environment and display large-scale, high-angle cross-beds and flat beds (Condon, 1997).

2.4.1.2. *Entrada Sandstone (Host Rocks to Trachyte Mesa and Maiden Creek)*

The Entrada Sandstone is Late Jurassic in age, constituting the central part of the San Rafael Group (Fig. 2.19). The Entrada extends over a vast area, making it the largest of the Colorado Plateau ergs; the only one to extend eastwards of the Uncompahgre Highlands (Kocurek & Dott, 1983). The Entrada Sandstone ranges in thickness from 170 to 220 m (560–720 ft; Fig. 2.19b; Hintze & Kowallis, 2009) and is composed of white to red cross-bedded aeolian sandstone and red/ brown silty sandstone beds, interlayered with thin siltstone and shale beds (Figs 2.7d & 2.20a; Aydin, 1978). It weathers to form vertical cliffs and steep-rounded mounds of 'slick rock' (Fig. 2.20a; Wright et al., 1962; Fillmore, 2011). The average grain size of the quartz-dominated Entrada Sandstone is ~0.15 mm (Fig. 2.20b, c), although larger grain sizes are measured in some layers (Aydin, 1978). The

Entrada Sandstone is poorly cemented and therefore relatively friable in character (Aydin, 1978; Hintze & Kowallis, 2009). Calcite is the most common cement, although siliceous and pelitic (mud) cements are abundant in some layers (Aydin, 1978).

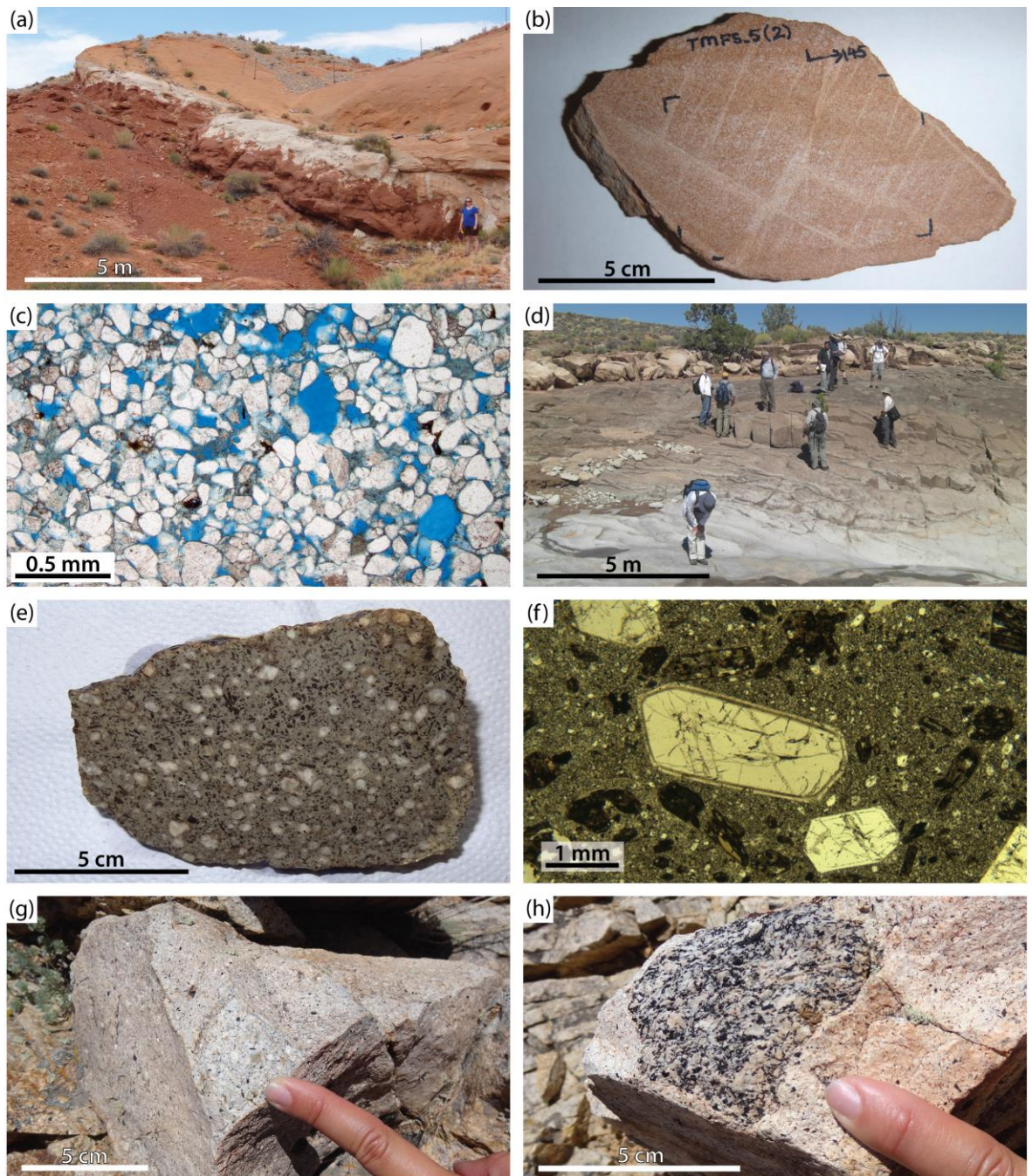


Figure 2.20. Rock types of the Henry Mountains. (a) Example outcrop of the Entrada Sandstone Formation of the Glen Canyon Group, showing range of lithological types (muddy, friable red sandstones at base; bleached sandstone unit; and more indurated, red-stained, quartz-arenite sandstones above). (b) Hand specimen of red-stained, quartz-arenite (Entrada) sandstone with deformation banding (sample from Trachyte Mesa). (c) Photomicrograph of thin section of Entrada Sandstone, seen through plane polarised light. Note, well-sorted, sub-angular to sub-rounded grains; ranging in the size from 50–250 μm . Grain composition almost 100% quartz (black colour in thin section reflects Fe-staining around grains). The thin section has been impregnated with blue dye to highlight the significant pore space within the Entrada

sandstone (18-20% in this sample). (d) Outcrop example of intermediate (diorite) intrusive rocks which comprise most (~98%) of the Henry Mountain intrusions (locality example from the Trachyte Mesa intrusion). (e) Hand specimen of plagioclase-hornblende porphyry (sample from Trachyte Mesa intrusion). (f) Photomicrograph of thin section of sample shown in (e). Note zoning within plagioclase phenocrysts. (g) Hand specimen of the rare syenite (more rhyolitic/ acidic) intrusive rocks of the Horn intrusion, Mount Pennell. (h) Hand specimen example of cm-scale mafic xenolith; these commonly found throughout the various intrusions of the Henry Mountains.

The Entrada Sandstone is typically highly porous (Fig. 2.20c) and, as a result, is the ideal lithology for the formation of deformation bands (see section 2.5.1 for more on the formation of deformation bands). As a result, along with the Navajo Sandstone (Fig. 2.19), it has been the focus of studies on such structures (including: Aydin, 1978; Aydin & Johnson, 1978; Aydin & Johnson, 1983; Fossen et al., 2007). The typical thickness of deformation bands within the Entrada Sandstone is about 1–1.2 mm (Aydin, 1978). Displacement along the deformation bands is usually only a few millimetres (Aydin, 1978). The deformation bands are mostly easily identifiable in the field as they are usually lighter in colour than the surrounding parent rock (Fig. 2.20b) and stand proud of the parent rock as thin ribs; this is due to compaction of grains resulting in relatively higher resistance to erosion (Aydin, 1978).

2.4.1.3. *Summerville Formation (Host Rocks to Black Mesa).*

The Summerville Formation is the uppermost member of the Upper Jurassic San Rafael Group, lying above the Entrada Sandstone in the stratigraphic column (Fig. 2.19; Bazard & Butler, 1992). A thinner unit than the Entrada at ~58 m (190 ft; Fig. 2.19b; Hintze & Kowallis, 2009), the Summerville Formation consists of heterolithic red beds comprised of alternating reddish-brown shale, siltstone and sandstone layers (Fig. 2.19; Blakey, 1989; Hintze & Kowallis, 2009). Interbeds of white gypsum are also common and contribute to its needle-like appearance (Kowallis, 2011). The Summerville Formation was deposited in a tidal-influenced, low-relief coastal plain environment (Caputo & Pryor, 1991), and commonly exhibits symmetrical ripples and mudcracks.

2.4.1.4. *Morrison Formation (Host Rocks to Sawtooth Ridge)*

The Morrison Formation, the youngest of the Jurassic sediments, is comprised of three members, from base to top these are: the Tidwell Member; the Salt Wash Sandstone Member; and the Brushy Basin Shale Member (Fig. 2.7e & 2.19; Peterson et al., 1980; Robinson & McCabe, 1997; Hintze & Kowallis, 2009). The rocks of the Morrison Formation unconformably overlie the older Jurassic sediments of the San Rafael Group (J-5 Unconformity in Fig. 2.19; Bazard & Butler, 1992; Hintze & Kowallis, 2009). The Tidwell Member, not present in the stratigraphy for much of the Henry Mountains region (varying thickness between 0 and 37 m (0–120 ft); Fig. 2.19b; Hintze & Kowallis, 2009), is composed of heterolithic lacustrine and fluvial red mudstones and sandstones (Fig. 2.19; Peterson, 1980; Robinson & McCabe, 1997; Hintze & Kowallis, 2009).

The Salt Wash Sandstone Member is comprised of yellowish-brown sandstone, mudstones and conglomerates of fluvial origin (Peterson, 1980; Robinson & McCabe, 1997; Hintze & Kowallis, 2009). The thickness for this unit varies between 122 and 152 m (400–550 ft; Fig. 2.18b; Hintze & Kowallis, 2009). In the Henry Mountains region, the Salt Wash Member is comprised of well-bedded, resistant sandstone beds ranging in thickness from 0.5 to 5 m, interlayered with thinner beds of sandy shale and shale (Johnson & Pollard, 1973).

The youngest member of the Morrison Formation, the Brushy Basin Member, is composed of a mixture of variegated mudstone and conglomerate units of lacustrine and fluvial origin, with minor sandstone (Figs 2.7e & 2.19; Peterson, 1980; Robinson & McCabe, 1997; Hintze & Kowallis, 2009;). The Brushy Basin Member is a highly distinctive unit, forming ‘tie-dyed’ mounds of maroon and cream in the dry (Fig. 2.7e), and a deep purple and cream in the wet. The Brushy Basin Member varies in thickness from 37 to 137 m (120–450 ft; Fig. 2.19b; Hintze & Kowallis, 2009).

Only very slight contact metamorphism of the sediments occurs as a result of the emplacement of the Henry Mountains intrusions (Hunt, 1953; Engel, 1959; Horsman et al, 2010). Some of the shales and siltstones adjacent to intrusions appear to have baked margins and are reconstituted at, and within, ~0.5 to 1 m of the contact (Engel, 1959). This metamorphism is weak and there is no significant increase in grain size.

2.4.2. Henry Mountains Intrusions

Igneous rock composition throughout the Henry Mountains is incredibly consistent with ~95% comprising of a bulk diorite composition (58–63% SiO₂), the remaining ~5% largely rhyolite porphyry and syenite and found cross-cutting earlier diorite on Mount Pennell (Fig. 2.20e–h; Hunt, 1953, 1988; Engel, 1959; Nelson & Davidson, 1992). The diorite has a porphyritic texture with phenocrysts constituting 25–55% of the rock: 20–40% plagioclase feldspar (An₂₀ to An₆₀); 5–15% hornblende; and 1–3% epidote or clinopyroxene, titanite and oxides (Fig. 2.20e, f; Engel, 1959; Nelson & Davidson, 1992; Horsman et al., 2005, 2010). The matrix accounts for 45–75% of the rock and is a fine-grained, equigranular groundmass comprised of plagioclase, hornblende, quartz, alkali feldspar, oxides, and trace apatite and titanite (Nelson & Davidson, 1992; Horsman et al., 2005, 2010). Xenoliths are largely mafic (amphibolite, garnet amphibolite and tonalite; Fig. 2.19h) in composition, although rare felsic xenoliths occur (Nelson & Davidson, 1992; Horsman et al., 2005, 2010). Occurrences of sedimentary xenoliths are rare, suggesting that stoping is not a significant emplacement mechanism (Horsman et al., 2010). Despite the consistent bulk dioritic composition throughout the Henry Mountains, significant textural variations (in particular phenocryst size and phenocryst: matrix modal abundance ratio) can be used to characterise the diorite of the different intrusions and, in places, to identify distinct magma pulses within an intrusion.

The intrusions of the Henry Mountains are Oligocene (late-Palaeogene) in age (Nelson & Davidson, 1992; Paquette et al., 2010). Hornblende ⁴⁰Ar-³⁹Ar and fission-track data for the Henry Mountains intrusions give ages ranging from 31.2 to 23.3 Ma (Nelson & Davidson, 1992; Fig. 2.15b). Preliminary U/Pb ages for zircons from Mount Hillers cluster around 24.75 ± 0.50 Ma suggesting that assembly of this entire intrusive centre occurred in less than ~1 Myr (Paquette et al., 2010). The preliminary U/Pb zircon ages of Paquette et al. (2010) are in good agreement with published fission track ages on zircon and sphene from the same Mount Hillers laccolith intrusion of 21 to 29 Ma (Sullivan, 1997). However, the U/Pb zircon age of 24.75 ± 0.50 Ma is significantly younger than, and therefore in poor agreement with, the ⁴⁰Ar-³⁹Ar age of 29.35 ± 0.33 Ma published by Nelson et al. (1992) and Nelson and Davidson (1997). On the other hand, this poor agreement of results can be accounted for by the presence of excess argon and xenocryst contamination, as emphasised by Nelson et al. (1992) and Nelson and Davidson (1997).

Throughout the Henry Mountains, the diorite igneous rocks show extensive alteration, the effects of which are either deuteric or hydrothermal (Engel, 1959). The alteration is principally of the phenocryst population with sericitisation of feldspars and replacement of hornblende by chlorite, calcite, epidote, iron oxides and minor serpentine (Engel, 1959). The degree of alteration varies spatially and is greatest in parts of the central stocks (intrusive centres/ domes) and surrounding shattered zones, in the roof sections of laccolith satellite intrusions, and in some of the dykes forming outlying intrusive bodies (Engel, 1959). Minor to moderate alteration only is observed in many of the internal parts of the central stocks, laccoliths and bysmaliths (cylindrical intrusions bounded by vertical faults) collectively.

2.4.2.1. *The Five Igneous Centres*

2.4.2.1.1. *Mount Ellen*

Mount Ellen is the most northern of the five intrusive centres comprising the Henry Mountains (Figs 2.15, 2.17c & 2.21). Having a maximum elevation of 3512 m (with a prominence above the plateau of 1786 m) and a diameter of ~20 km, the Mount Ellen intrusive complex is the largest of the five Henry Mountains. The central/ main intrusive centre and shattered zone are situated along the southern section of the complex, with satellite intrusions being localised in the north-east (Engel, 1959). Hunt (1953) reported that the central 'stock' of Mount Ellen is roughly circular in map view, surrounded by a shattered zone consisting of sedimentary breccias variously injected by igneous rocks, with proportions of sedimentary to igneous rocks varying widely in this zone. The Mount Ellen intrusive centre is locally well exposed, but the majority is covered in brush and forest and, therefore, poorly exposed.

The Bull Creek laccolith is situated at the north-eastern edge of Mount Ellen (Fig. 2.21b). The laccolith is exposed for ~2.7 km along Bull Creek, in a valley or depression ~275 m deep at the bulged northeast part of the intrusion (Fig. 2.21b; Engel, 1959). Bull Creek laccolith adjoins with Bull Mountain bysmalith (Fig. 2.21b, c). In contrast to the consistent diorite igneous rock of the Henry Mountains, quartz is fairly abundant in samples collected along the floor of Bull Creek, which contain euhedral quartz phenocrysts large enough to be identified in hand specimen (Engel, 1959).

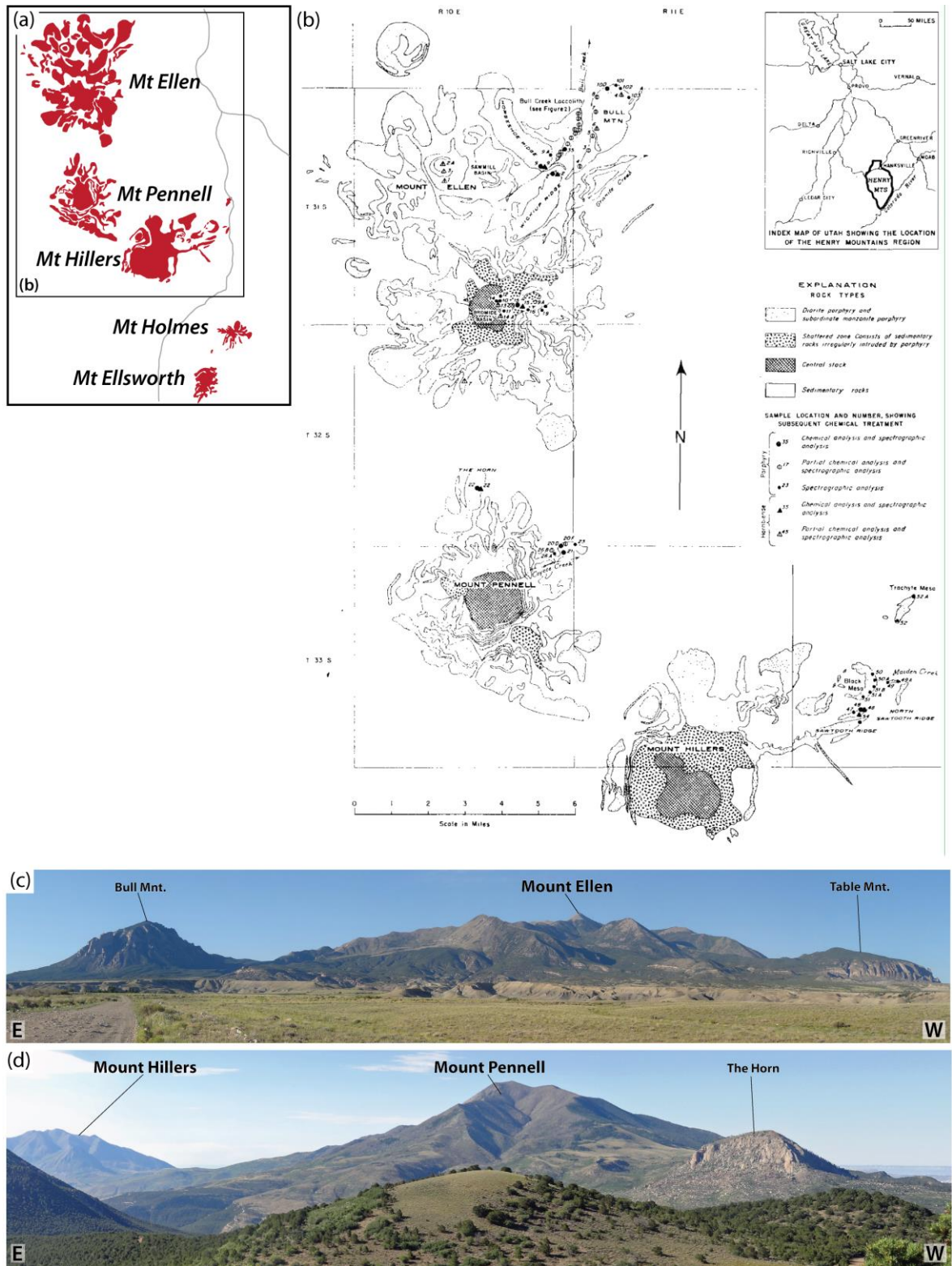


Figure 2.21. A series of figures relating to the northern three Henry Mountains: Mt Ellen; Mt Pennell; and Mt Hillers. (a) Simplified igneous map of the five Henry Mountains (adapted from Morgan et al., 2008). Map area for (b) highlighted. (b) Generalised geological map showing the northern intrusive centres and key satellite intrusions of the Henry Mountains (from Engel, 1959; after Hunt, 1953). (c) Photograph of Mount Ellen and its northern satellite intrusions. (d) Photograph of Mount Pennell and its northern satellite intrusions.

Bull Mountain bysmalith (Fig. 2.21b, c) is a prominent topographic landmark and stands in isolation between Bull Creek to the west and Granite Creek to the south-east (Fig. 2.21b; Engel, 1959). The bysmalith rises ~610 m above the creeks. The western margin of Bull Mountain and the contact between the intrusion and the sedimentary country rock is poorly exposed. However, a steep cliff face defines the northern margin of Bull Mountain (Fig. 2.21c), and here the intrusion can be observed to be emplaced against steeply dipping beds of the Morrison Formation (Engel, 1959). The floor of the bysmalith is not exposed.

Adjacent to Bull Creek laccolith and Bull Mountain bysmalith are Horseshoe Ridge and the Wickiup Ridge laccoliths (Fig. 2.21b). The Horseshoe Ridge laccolith adjoins Bull Creek laccolith on the west, but is poorly exposed and fairly inaccessible (Engel, 1959). Wickiup Ridge laccolith lies between the Mount Ellen central intrusive centre and both the Horseshoe Ridge and Bull Creek laccoliths. Table Mountain, a large bysmalith, is the most north-westerly satellite intrusion (Fig. 2.21c).

2.4.2.1.2. *Mount Pennell*

Mount Pennell is the second highest of the Henry Mountains, at 3467 m, and is situated directly south of Mount Ellen (Figs 2.15, 2.17c & 2.21). Similar to Mount Ellen, Mount Pennell is comprised of a central intrusive centre and shattered zones, surrounded by laccoliths and numerous dykes and sills radiating from the centre (Figs 2.16 & 2.21b; Engel, 1959; Nelson and Davidson, 1993). However, in contrast to Mount Ellen and the southern Henry Mountain intrusive centres, several igneous rock types (Fig. 2.20e–h) are found here (Hunt, 1953; Nelson, 1991; Nelson et al., 1992; Nelson & Davidson, 1993; Horsman et al., 2010). In addition to the typical plagioclase-hornblende porphyritic diorite accounting for ~95% volume of the igneous rock of the Henry Mountains, a nepheline (Ne-) to quartz (Q-) bearing normative sodium-rich (Na-) syenite and a number of rhyolite porphyries (Fig. 2.19g, h) are also found at Mount Pennell, occurring in a composite stock that cross-cuts the dominant plagioclase-hornblende porphyry (Nelson & Davidson, 1993). This cross-cutting intrusive body exhibits intricate internal intrusive relationships with a variety of petrographic types (Hunt, 1988; Nelson, 1991; Nelson & Davidson, 1993).

The Horn laccolith is the most northerly satellite intrusion of Mount Pennell (Fig. 2.21b, d; Engel, 1959). The Coyote Creek laccolith is also located to the north of the intrusive centre, extending north-east from Mount Pennell (Fig. 2.21b).

2.4.2.1.3. Mount Hillers

Mount Hillers (Figs 2.15, 2.16, 2.17c, 2.21b, 2.22, & 2.23) displays the best exposure of the five Henry Mountains intrusive centres, and as a result is also the most studied. The intrusions of Mount Hillers have resulted in an approximately 2.5 km cumulative vertical displacement of the surrounding country rock (Figs 2.22b & 2.24; Hunt, 1953; Jackson & Pollard, 1988; Horsman et al., 2005). Presently, the dome of Mount Hillers has a diameter of ~15 km (Hunt, 1953; Jackson & Pollard, 1988; Horsman et al., 2005). Cross-sections through many intrusions that radiate away from the centre of the Mount Hillers dome exist as a result of several steep, narrow canyons that cut into the mountain (e.g. Gold Creek Overlook; Fig. 2.23b).

Figure 2.22. (overleaf)

Mount Hillers and its satellite intrusions. (a) Simplified geological map of Mount Hillers and its satellite intrusions (modified from Larson et al., 1985). Line A–A' shows the location of the cross-section (b). In (a), the various intrusions that comprise the Mt Hillers intrusive complex are numbered, using the names given by Hunt (1953): 1 – Mt Hillers central complex; 2 – Bulldog Peak intrusion; 3 – Stewart Ridge intrusion; 4 – Specks Ridge intrusion; 5 – Chaparral Hills Laccolith; 6 – Specks Canyon; 7 – speculated feeder system to the Trachyte Mesa intrusion; 8 – Sawtooth Ridge intrusion; 9 – Black Mesa intrusion; 10 – Maiden Creek intrusion; and 11 – Trachyte Mesa intrusion. (b) Interpretative geological cross-section through Mount Hillers and the Black Mesa satellite intrusion, based on geological maps of Hunt (1953) and Larson et al., (1985; see (a)). Adapted from de Saint Blanquat et al., 2006. (c) Topographic aerial image from Google Earth™ of the north-eastern satellite intrusions to the Mount Hillers complex. Area highlighted on map (a). Map areas for Figures 2.26, 2.30 and 2.32 are shown.

Figure 2.23. (overleaf)

Photographs of Mount Hillers. (a) Photograph of Mount Hillers and its satellite intrusions to the north and north-east. (b) Photograph of the eastern side of the Mount Hillers intrusive complex. (c) Photograph of the southern side of Mount Hillers showing the 'teeth' (near-vertical sediments).

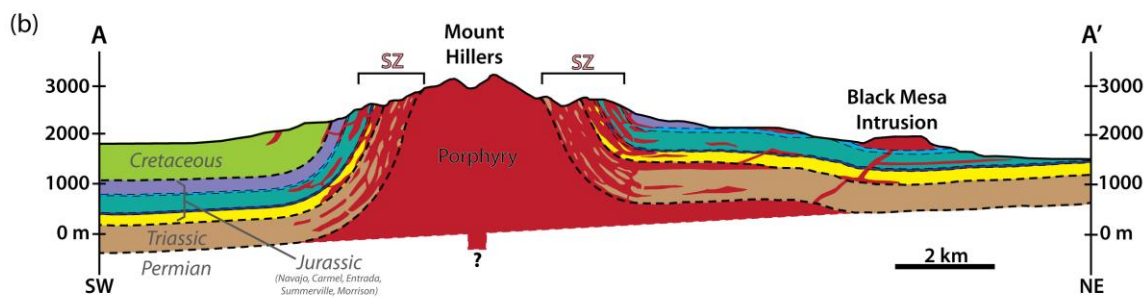
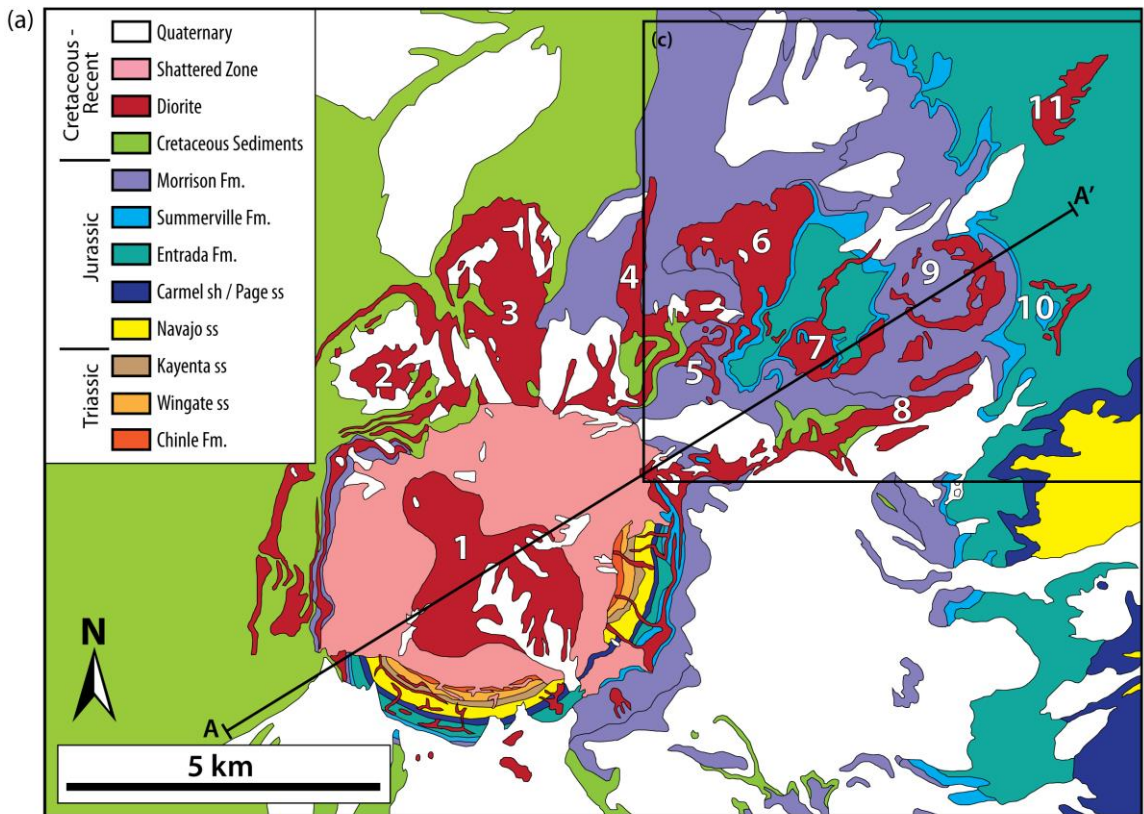


Fig. 2.22

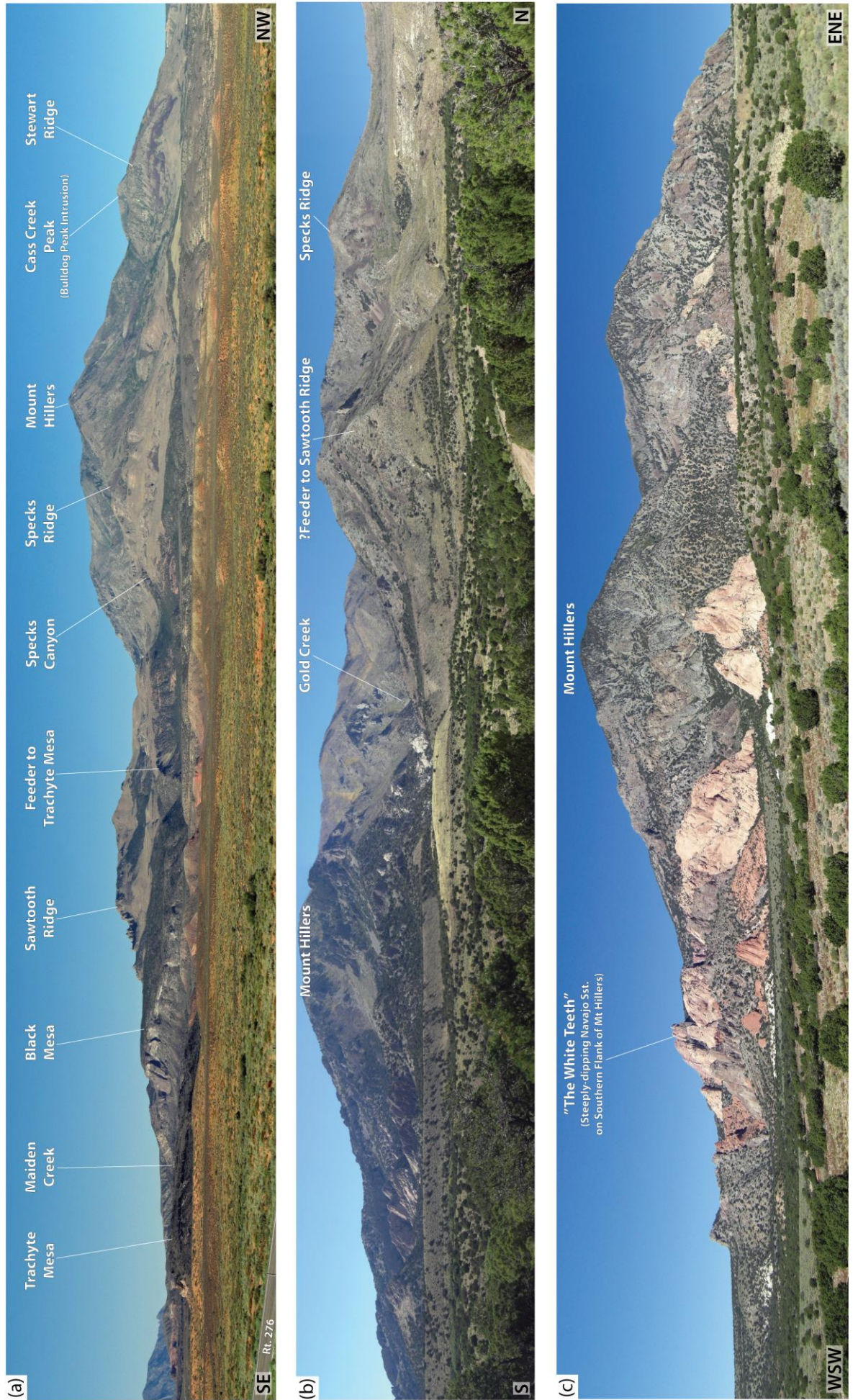


Fig. 2.23

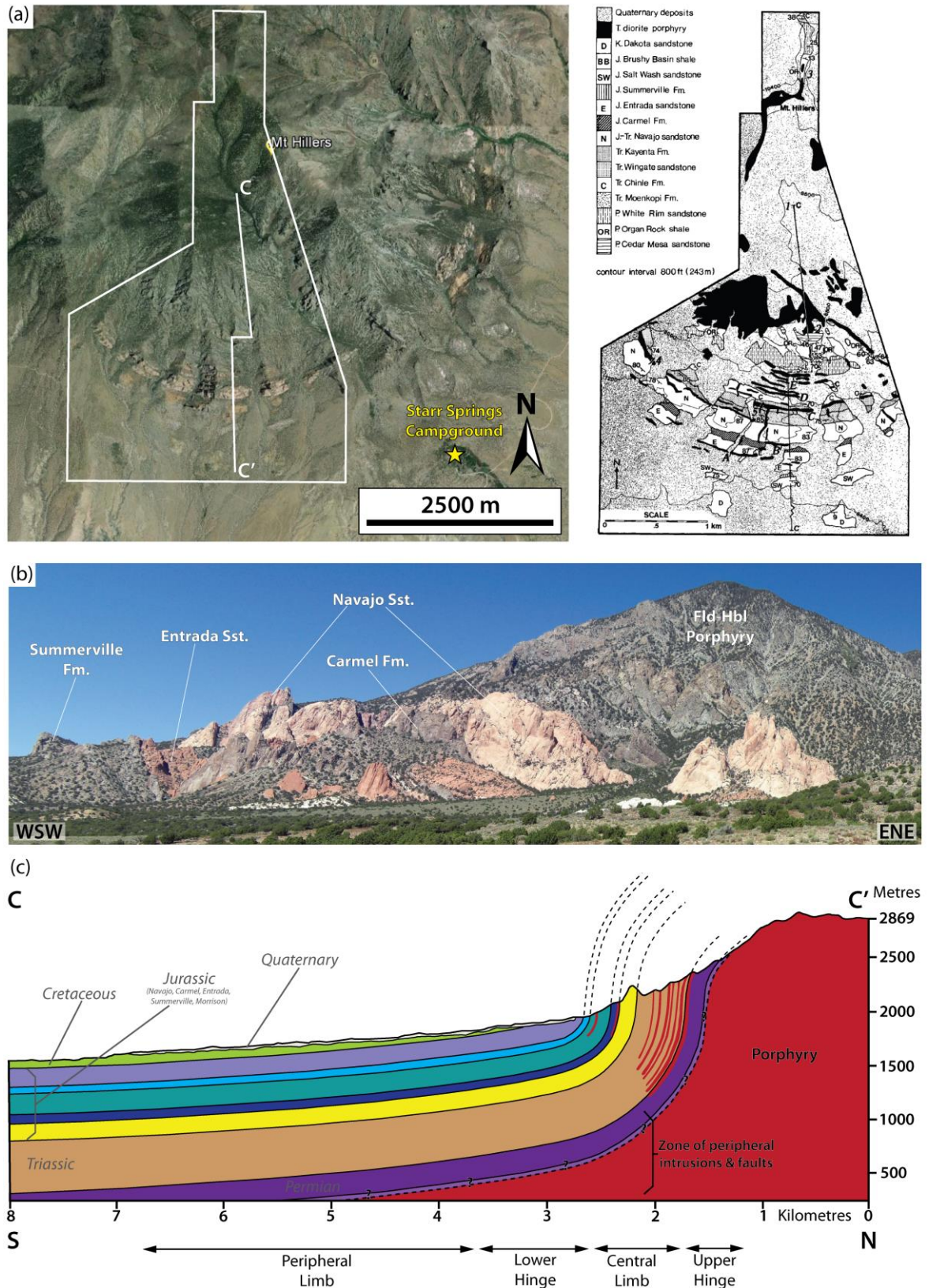


Figure 2.24. Southern margin of Mount Hillers. (a) Aerial photograph (left; from Google Earth™) and geological map (right; from Jackson & Pollard, 1988) of southern Mount Hillers. Note radial outcrop pattern of host rocks around the intrusion. (b) Photograph of the sub-vertically dipping host rocks to Mount Hillers forming “teeth” like outcrops. (c) Geological cross-section through southern Mount Hillers, showing steepening of host rock bedding around the intrusion margin (adapted from Jackson & Pollard, 1988). For location, see line C–C’ in (a).

Small satellite intrusions outcrop on the north and north-eastern flank of Mount Hillers, up to 10 km from the centre of the mountain (Figs 2.22 & 2.23a; Horsman et al., 2005). These are: Bulldog Peak intrusion; Stewart Ridge intrusion; Specks Ridge intrusion; Chaparral Hills Laccolith; Specks Canyon; Black Mesa intrusion; Sawtooth Ridge intrusion; Maiden Creek intrusion; and Trachyte Mesa intrusion and its speculated feeder (names after Hunt, 1953; Figs 2.22 & 2.23a). According to their three dimensional geometries, Hunt (1953) and Johnson and Pollard (1973) characterised Sawtooth Ridge as an elongate laccolith, Black Mesa as a bysmalith or “punched” laccolith, Maiden Creek as a sill, and Trachyte Mesa as a transitional sill-laccolith.

2.4.2.1.4. *Mount Holmes*

Mount Holmes is located to the south east of Mount Hillers (Figs 2.15, 2.16, 2.17c, & 2.25) and is significantly smaller than the three more northern Henry Mountains peaks (Fig. 2.15), with a height of 2438 m and a significantly smaller diameter (<10 km; Hunt, 1953; Fig. 2.16). Mount Holmes comprises two domes, both capped by Jurassic sediments that dip outwards in a symmetrical manner (Jackson & Pollard, 1988). The larger of the domes forms the mountain summit and comprises three vertical diorite dykes that are between 20 and 30 m thick and strike radially that can be observed as outcrops that extend down the flanks of the mountain (Jackson & Pollard, 1988). The dykes crop out in discrete segments, the edges of which plunge steeply, suggesting upward propagation of the dykes along steeply inclined trajectories (Pollard et al., 1975). Porphyritic sills and small laccoliths intrude the stratigraphy of the more steeply dipping (~20°) central limb of the flexure, such as Buckhorn Ridge (Figs 2.16 & 2.25; Hunt, 1953; Jackson & Pollard, 1988;) and Theater Canyon Laccolith (Fig. 2.16; Hunt, 1953)

It is important to note that no large central igneous body crops out at the top of the dome (Fig. 2.25b; Jackson & Pollard, 1988). Furthermore, the location of an intrusion that might core the intrusive centre can only be inferred. Dip directions of beds, collected largely on truncated surfaces of large sandstone dunes, are radially symmetric about the western half of the mountain. Jackson and Pollard (1988) combined this structural dataset with the structure contour map of Hunt (1953) to suggest that at least the western part of the Mount Holmes intrusive complex underlying the dome is roughly circular in plan.

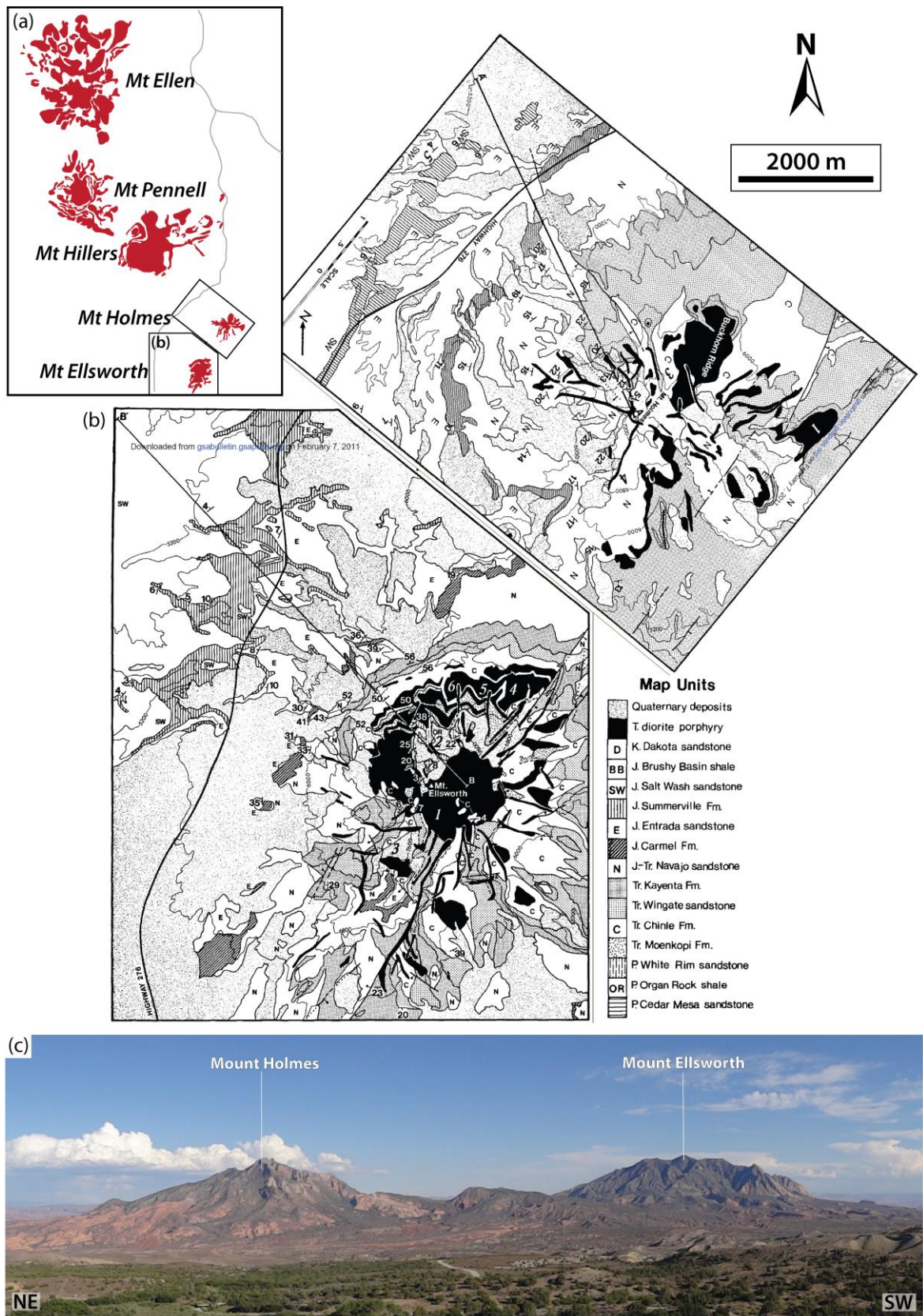


Figure 2.25. A series of figures relating to the southern two Henry Mountains: Mt Holmes; and Mt Ellsworth. (a) Simplified map of the five Henry Mountains intrusive complexes (adapted from Morgan et al., 2008). Map area for (b) highlighted. (b) Geological maps of Mt Holmes and Mt Ellsworth (from Jackson & Pollard, 1988). (c) Photograph of Mounts Holmes and Ellsworth, viewed from the NW (Starr Springs campsite, Mount Hillers).

The deepest stratigraphic unit exposed on Mount Holmes is the Triassic Chinle Formation (Jackson & Pollard, 1988). The Jurassic Navajo Sandstone is observed outcropping near the mountain summit. The Navajo Sandstone is continuous over the dome, apart from where it is cut by dykes and locally eroded. The intrusions of Mount Holmes have resulted in an approximately 1.2 km cumulative vertical displacement of the surrounding country rock (Jackson & Pollard, 1988).

2.4.2.1.5. *Mount Ellsworth*

Mount Ellsworth (Figs 2.15, 2.16, 2.17c, & 2.25) is the most southerly of the five Henry Mountains peaks, lying just to the south-west of Mount Holmes (Fig. 2.25). Mount Ellsworth, similar to Mount Holmes, is significantly smaller than Mounts Ellen, Pennell and Hillers (Fig. 2.15). It has a diameter of <10 km (between 5 and 7 km; Figs 2.16 & 2.25b; Hunt, 1953; Jackson & Pollard, 1988) and a height of 2543 m. The intrusions of Mount Ellsworth have resulted in an approximate 1.8 km cumulative vertical displacement of the surrounding country rock (Jackson & Pollard, 1988).

2.4.2.2. *North-eastern Satellite Intrusions to Mount Hillers*

2.4.2.2.1. *Sawtooth Ridge*

Sawtooth Ridge is the closest of the satellite intrusions to the intrusive centre (Figs 2.22, 2.26 & 2.27). The intrusion is a highly elongate and narrow body, trending roughly ENE–WSW (Figs 2.26 & 2.27) and has a jagged topography from which it gets its name: Sawtooth (Figs 2.27b; Hunt, 1953; Johnson & Pollard, 1973; Horsman et al., 2005). Sawtooth Ridge intrudes the Upper Jurassic Morrison Formation (Fig. 2.26; Hunt, 1953; Johnson & Pollard, 1973). A significant amount of the intrusion has been removed by erosion and weathering (Johnson & Pollard, 1973). However, the north-eastern distal margin of Sawtooth Ridge is exposed along a cliff face about 30 m high (Fig. 2.27c). This cliff face exposes and displays the complex cross-sectional shape of the intrusion.

Both the bottom and top contacts of Sawtooth Ridge are locally concordant (Johnson & Pollard, 1973). However, the contact at the periphery cross-cuts the Morrison Formation to become a vertical fault (slickensides in the vertical direction), continuing upwards vertically for ~25 m before flattening out to form the top of the intrusion (Johnson & Pollard, 1973). There is a strong correlation between jointing in the main body of the

Figure 2.26. (previous page)

Fence diagram showing the subsurface geometries around Sawtooth Ridge, Black Mesa and Maiden Creek, as envisaged by Hunt (1953). (a) Map showing the location of cross-sectional fences shown in (b). (b) Isometric fence diagram of the Sawtooth Ridge, Black Mesa and Maiden Creek satellite intrusions (adapted from Hunt, 1953). (c) Stratigraphic column, as in Fig. 2.19a, and key to colours in (b).

2.4.2.2.2. *Black Mesa*

The Black Mesa intrusion is located on the north-eastern flank of Mount Hillers, similar to Sawtooth Ridge (Figs 2.22, 2.26 & 2.28). It intrudes just below the Morrison Formation within the upper section of the Summerville Formation (Fig. 2.26; Hunt, 1953; de Saint-Blanquat et al., 2006). The Black Mesa intrusion is a cylindrical body (Fig. 2.28), 1.7 km in diameter, increasing in thickness from ~150 m in the north-west to ~250 m in the south-east (de Saint-Blanquat et al., 2006). Sub-horizontal strata surrounding the intrusion abruptly change orientation close to the contact with the intrusion to become steeply dipping to sub-vertical (de Saint-Blanquat et al., 2006). To the west of Black Mesa, this folding is evident by a synclinal structure (Fig. 2.28b, c). In contrast, the eastern contact of the intrusion is defined by vertical faults and morphologically by a cliff face, approximately 130 m high (Fig. 2.28; de Saint-Blanquat et al., 2006). The roof of the intrusion is relatively flat, dipping slightly to the north, and is largely covered by concordant sedimentary beds of the Morrison Formation (Fig. 2.28b, c; de Saint-Blanquat et al., 2005). Hunt et al. (1953) concluded that the floor of the Black Mesa intrusion must be close to the current bottom exposure due to the presence of the Morrison Formation both at the base and top of the exposed intrusive rock. If this statement is correct, then the volume of intrusive rock can be estimated between 0.3 and 0.5 km³ assuming a cylindrical geometry (de Saint-Blanquat et al., 2006).

The Black Mesa intrusion is complicated to define with regards to intrusion terminology, in that it is not strictly a laccolith or a bysmalith, neither in terms of its shape nor its growth mechanisms (de Saint-Blanquat et al., 2006). Following the terminology of Corry (1988), de Saint-Blanquat et al. (2006) described Black Mesa as a hybrid between a punched and sheeted laccolith.

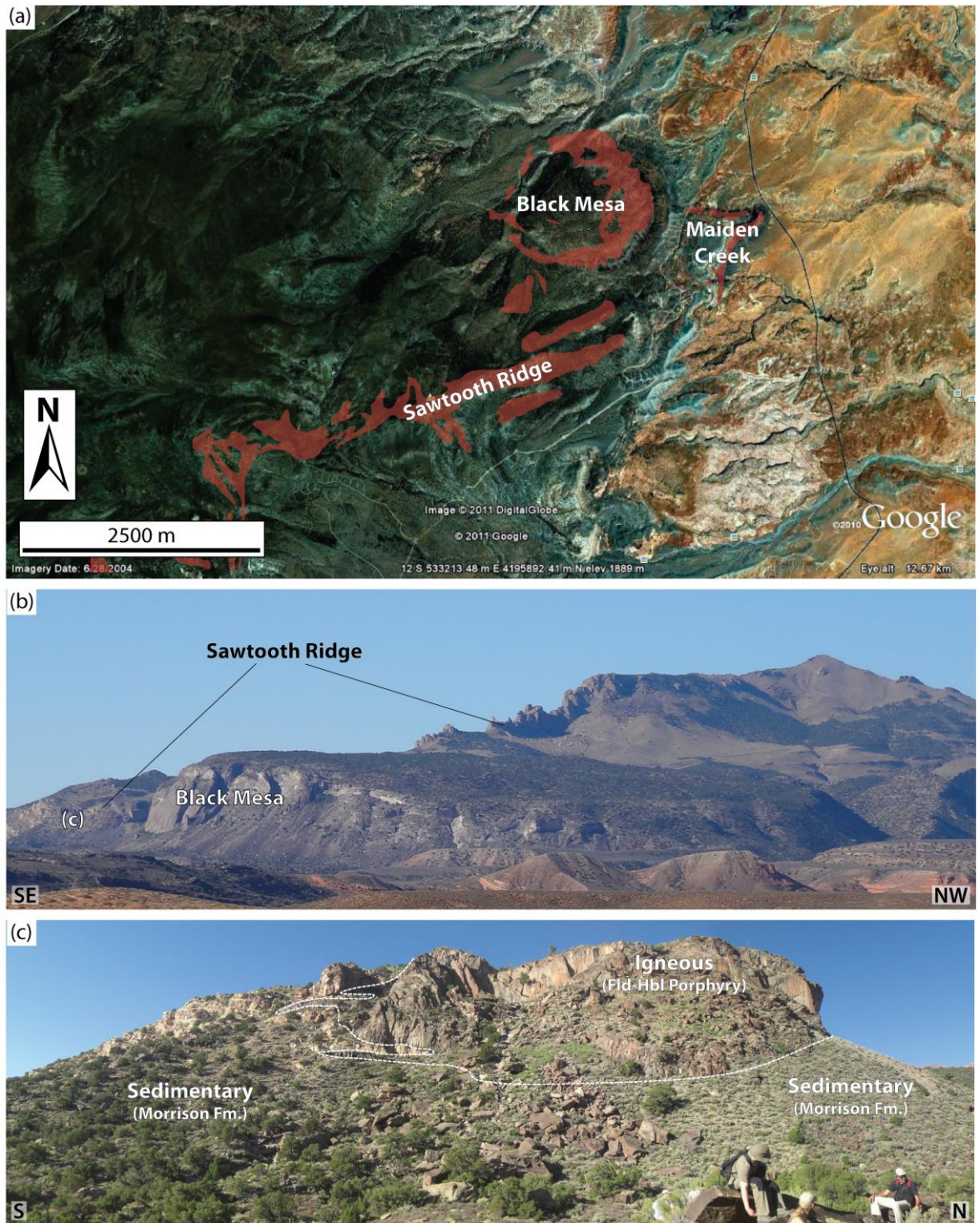


Figure 2.27. Sawtooth Ridge intrusion. (a) Map showing igneous outcrop to the NE of Mount Hillers. (b) Photograph of the Sawtooth Ridge intrusion, showing its elongate geometry and jagged top. (c) Photograph of the eastern end of the Sawtooth Ridge intrusion showing a faulted periphery against the Morrison Formation (outline of igneous intrusion modified from Johnson & Pollard, 1973).

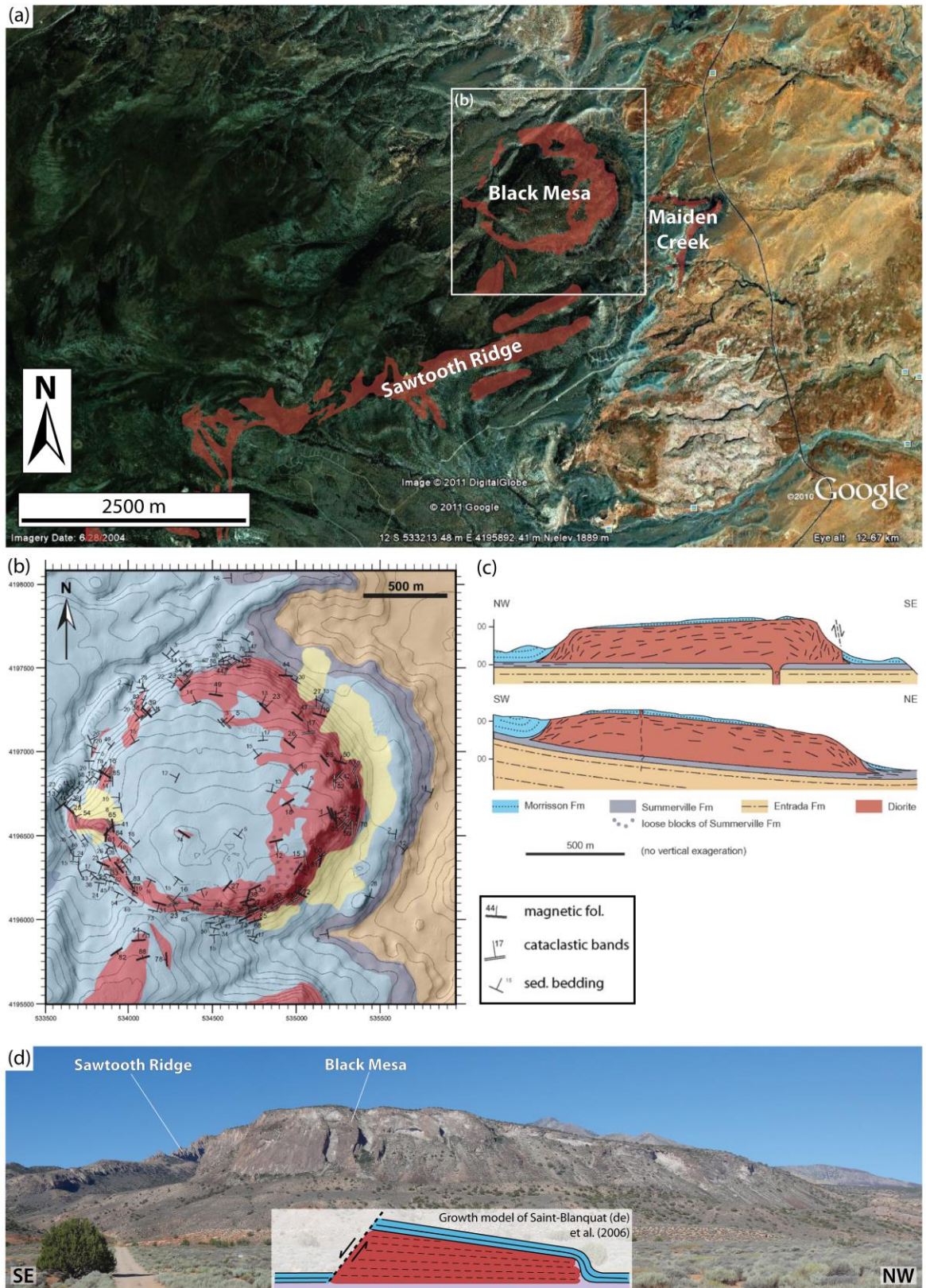


Figure 2.28. Black Mesa intrusion. (a) Map showing igneous outcrop to the NE of Mount Hillers. (b) Geological map and (c) two perpendicular cross-sections of the Black Mesa intrusion (from de Saint Blanquat et al., 2006). (d) Photograph of the Black Mesa intrusion. Inset: growth model of de Saint Blanquat et al., (2006).

2.4.2.2.3. *Maiden Creek*

The Maiden Creek intrusion, characterised as a sill (Hunt, 1953; Johnson & Pollard, 1973; Horsman et al., 2005), is a small intrusion ($\sim 1 \text{ km}^2$ in map view) and one of the most distal of the satellite intrusions of the Mount Hillers intrusive centre (Figs 2.22, 2.26 & 2.29). Maiden Creek intrudes the Entrada Sandstone of the Jurassic San Rafael Group (Fig. 2.26; Gilbert, 1877; Hunt, 1953; Johnson & Pollard, 1973; Horsman et al., 2005).

From the abundance of lateral contacts of the Maiden Creek intrusion with surrounding wall rocks, it can be inferred that the current map pattern of the intrusion corresponds closely to the original geometry of the intrusion. Horsman et al. (2005) divided this original intrusive geometry into two discrete parts: the main body of the intrusion; and finger-like lobes projecting outwards from the main body of the intrusion (Fig. 2.29b). The main body of the Maiden Creek sill has a somewhat elliptical shape when considered in terms of its map view (Fig. 2.29b). This geometry is one that is commonly associated with laccolithic intrusions (Corry, 1988; Horsman et al., 2005). A tabular shape, concordant with the bedding in the surrounding Entrada Sandstone, is observed in cross-sectional view. Horsman et al. (2005) have suggested the presence of three large finger-like lobes and provide evidence for the existence of a fourth lobe (Fig. 2.29b, e).

Further detailed analysis of Maiden Creek is the focus of Chapters 5 and 6.

Figure 2.29. *(overleaf)*

Maiden Creek intrusion. (a) Map showing igneous outcrop to the NE of Mount Hillers. (b) Geological map of the Maiden Creek intrusion and the inferred map view geometry with a circular shaped main body (sill) and four finger-like intrusive lobes (from Horsman et al., 2005). (c) Photograph along the top surface of south-eastern igneous lobe. (d) Photograph of the same igneous lobe seen in (c), from within Secret Nap Gorge (height of cliff face $\sim 40 \text{ m}$). (e) A series of cross-sections through the Maiden Creek intrusion (from Horsman et al., 2005). No vertical exaggeration to the cross-sections. Note, location of photos (c) and (d) shown on section D–D'. (f) Panoramic photograph of the eastern margin of the Maiden Creek intrusion.

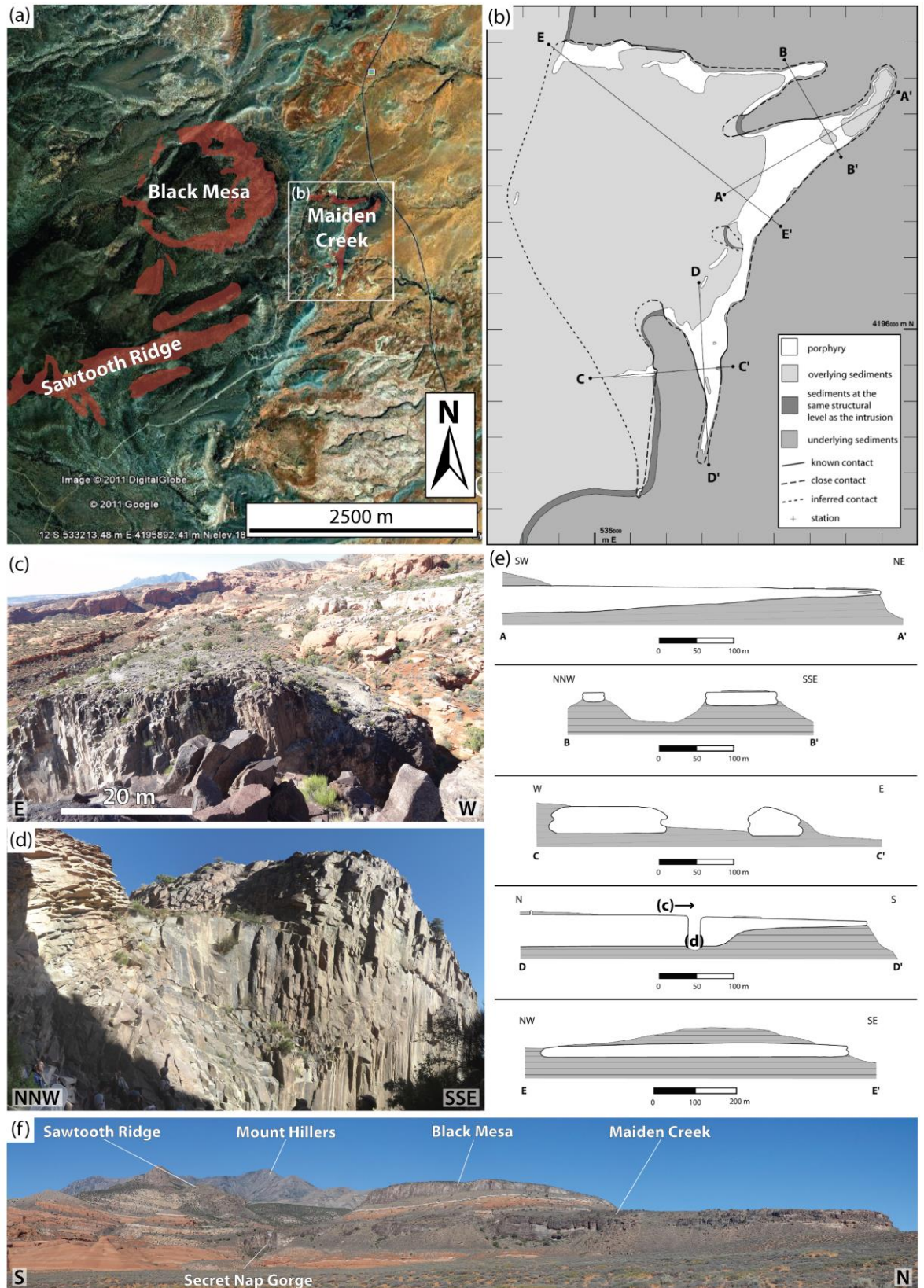


Fig. 2.29

2.4.2.2.4. *Trachyte Mesa*

Trachyte Mesa (Figs 2.22, 2.30 & 2.31) is roughly 1.5 km long and 0.6 km wide, trending NE–SW, varying in thickness between 5 m in the northeast to greater than 50 m in the SW (Morgan et al., 2008). The intrusion trends along a line that can be traced 12.6 km southwest to the peak of Mount Hillers (Fig. 2.22), Trachyte Mesa being the most distal of

the Mount Hillers satellite intrusions. The intrusion is generally concordant with the Entrada Sandstone, into which it intrudes (Fig. 2.30; Hunt, 1953; Johnson & Pollard, 1973; Morgan et al., 2008). The intrusion defines both the top and the edges of the Mesa, with the exception being in the southwest where the intrusion margin is covered by sediments (Figs 2.30 & 2.31). The top is mostly flat. However, the northeast section of Trachyte Mesa can be divided into three geomorphic regions: a long plateau on the northeast margin; a central plateau (2 to 3 m higher than the NE plateau, its border defined by a cliff); and a northwest region that slopes downwards towards the NW (Morgan et al., 2008). The southwest section of Trachyte Mesa has a more irregular topography, with a greater amount of country rock covering the top, the intrusion rising up gently from where it is buried by sediments to the SW (Figs 2.30 & 2.31d; Morgan et al., 2008). Similar to many of the satellite intrusions to intrusive centres of the Henry Mountains, field observations and mapping suggest that the present exposure of the Trachyte Mesa corresponds closely to its original intrusive geometry (e.g. Horsman et al., 2005; de Saint-Blanquat et al., 2006; Morgan et al., 2008).

Originally named Howell Laccolith, Gilbert (1877) first described Trachyte Mesa as a laccolith. All subsequent workers have continued to use this term to describe the intrusion (e.g. Hunt, 1953; Johnson & Pollard, 1973). However, more recently, Morgan et al. (2008) refer to the Trachyte Mesa intrusion (TMI) and do not use the term laccolith as they propose (similar to Johnson & Pollard, 1973) that Trachyte Mesa has features that are transitional between both a sill and a laccolith, in that the body has the characteristic convex upper surface of a laccolith, but appears to be comprised of multiple stacked thin sills (Fig. 2.31b). Furthermore, Morgan et al. (2008) proposed that structural and rock magnetic data (anisotropy of magnetic susceptibility; AMS) indicate that the intrusion grew vertically and horizontally by the accumulation of multiple smaller horizontal magma sheets ('Christmas tree' structure; Fig. 2.31b, d), thin (2–3 cm) cataclastic shear bands defining the contact between sheets.

Figure 2.30. *(overleaf)*

Fence diagram showing the subsurface geometries at Trachyte Mesa, as envisaged by Hunt (1953). (a) Map showing the location of cross-sectional fences shown in (b). (b) Isometric fence diagram of the Trachyte Mesa satellite intrusion (adapted from Hunt, 1953).

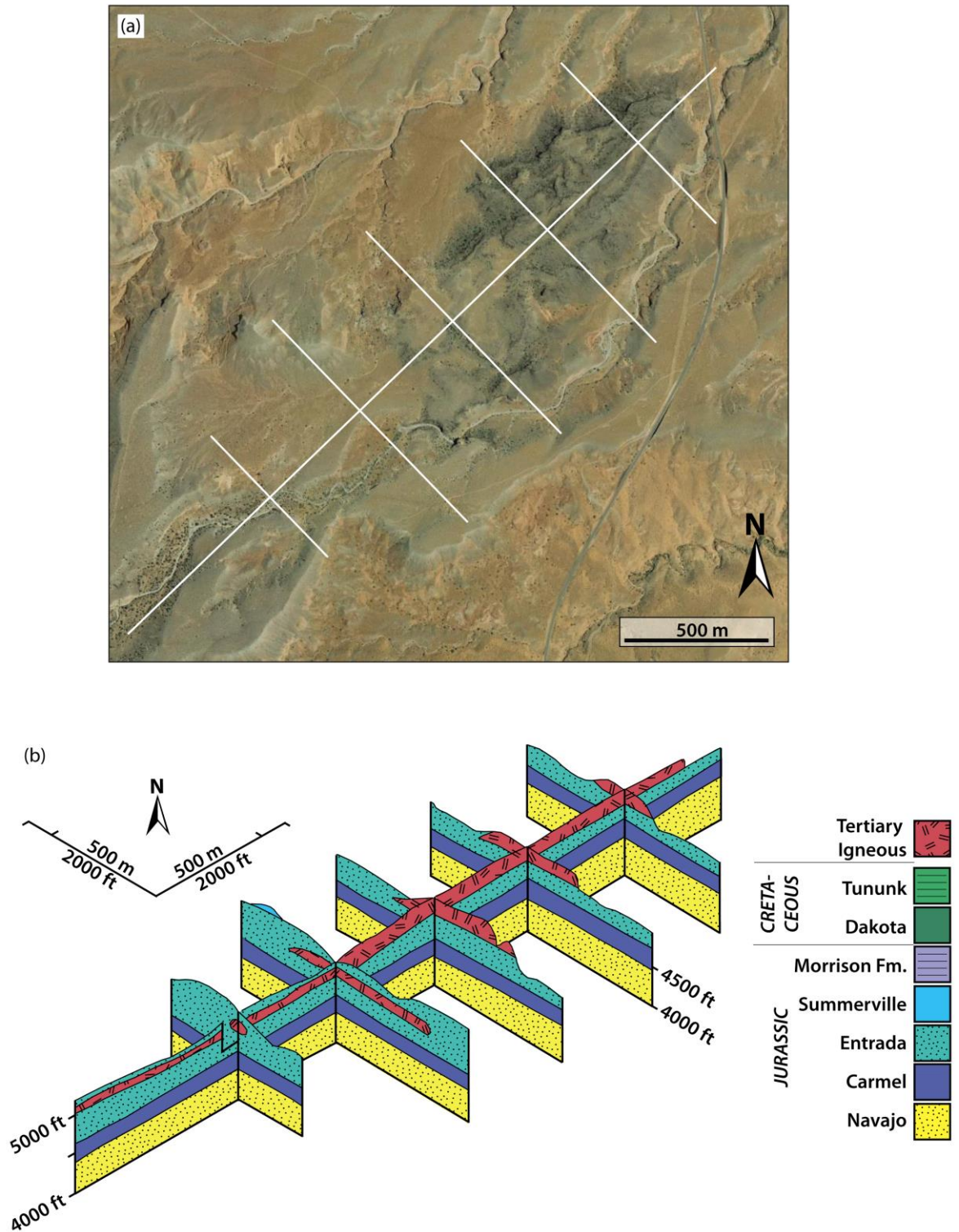


Fig. 2.30

Similar to Morgan et al. (2008), Wetmore et al. (2009) also referred to the Trachyte Mesa intrusion (rather than laccolith) in their publication on the geometry of the intrusion and implications for the emplacement of small melt volume into the shallow crust. Wetmore et al. (2009) used a combination of structural and geophysical data sets to re-evaluate the proposed geometry of the intrusion. In contrast to most previous studies that assumed a blister-shaped magma body intruded into flat and gently north-west dipping stratigraphy,

Wetmore et al. (2009) proposed that the Trachyte Mesa intrusion instead intruded along a series of NE-trending, upright and open folds that formed within the Jurassic Entrada Formation (suggesting a Middle Jurassic age for the folds, as they are truncated at the contact with the overlying Curtis/ Summerville Formations). Furthermore, Wetmore et al. (2009) also provided a reassessment of the size of the intrusion, using magnetic and two-dimensional resistivity survey data (Fig. 2.31d) alongside mapping (outcrop) data. They proposed that the intrusion is 2.2 km long and 0.7 km wide with an average thickness of ~15 m (maximum ~40 m), and is confined within the axis of a syncline bound to the north-west and south-east by anticlines. In cross-section the intrusion largely has concave-up top and bottom surfaces (characteristic of a laccolith body). Wetmore et al. (2009) concluded that the geometry and structural position of the Trachyte Mesa intrusion support the idea that the emplacement of the intrusion was fundamentally controlled by both pre-existing country rock structures and the density of the magma relative to that of the hot rocks. Hunt (1953) proposed that the feeder system to Trachyte Mesa is exposed as a narrow NE–SW trending ridge to the north of Black Mesa (Fig. 2.32)

Further detailed analysis of Trachyte Mesa is the focus of Chapters 3 and 4.

Figure 2.31. *(overleaf)*

Trachyte Mesa intrusion. (a) Satellite image showing mapped extent of the Trachyte Mesa intrusion (after Morgan et al., 2008) and location of cross-section shown in (b). (b) Interpretative geological cross-sections of the Trachyte Mesa intrusion (from Morgan et al., 2008). (c) Bulbous termination to an intrusive sheet on the south-western margin of the Trachyte Mesa intrusion. (d) Geological map of the Trachyte Mesa intrusion (from Morgan et al., 2008) with magnetic map (from Wetmore et al., 2009) overlain. (e) Photograph of the classic outcrop from the south-western margin of Trachyte Mesa, used in the papers of Gilbert (1887), Hunt (1953), Johnson and Pollard (1973), Morgan et al., (2008) and Wetmore et al. (2009). Photograph corresponds to the cross-section in (b). (f) Panoramic photograph of the western margin of the Trachyte Mesa intrusion.

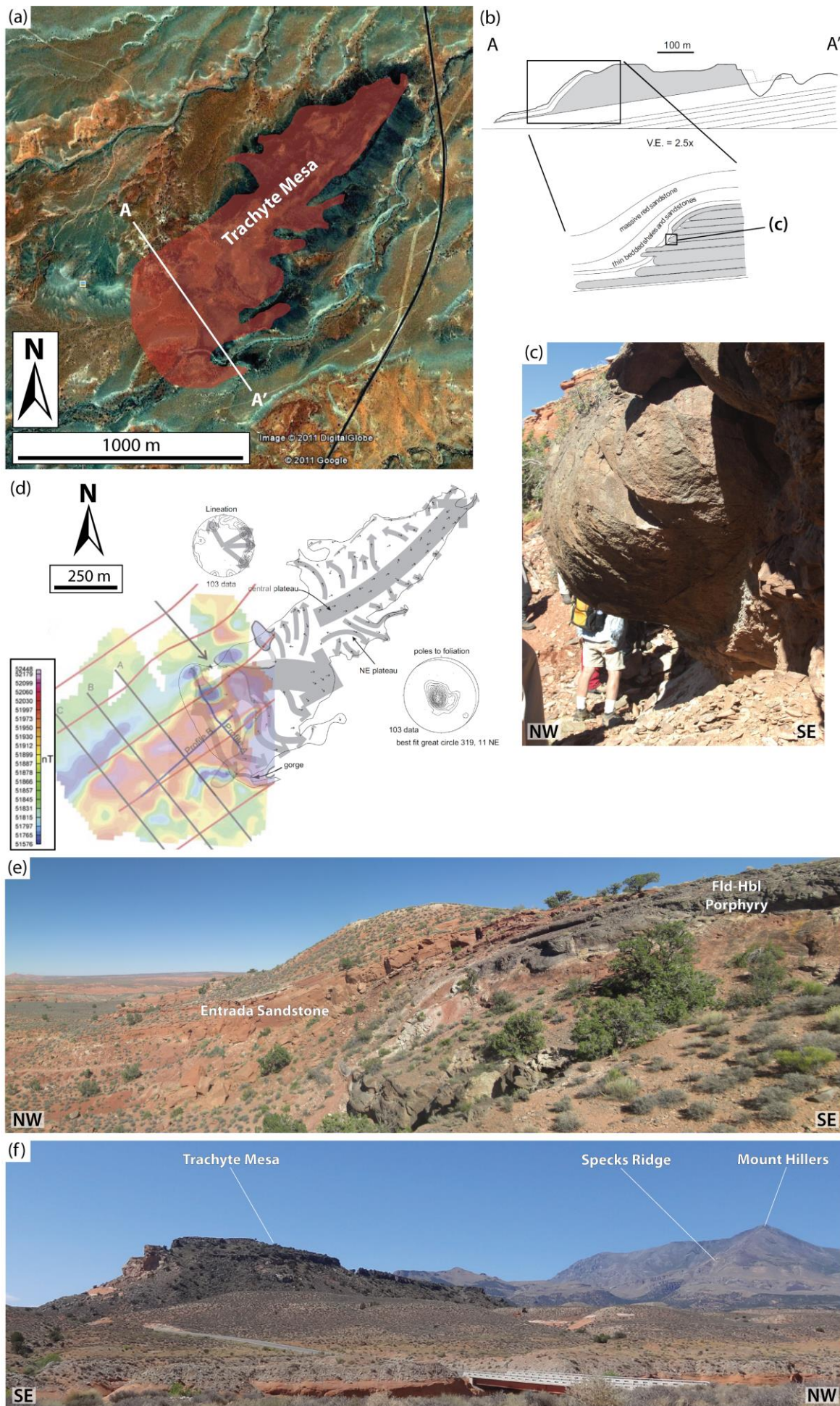


Fig. 2.31

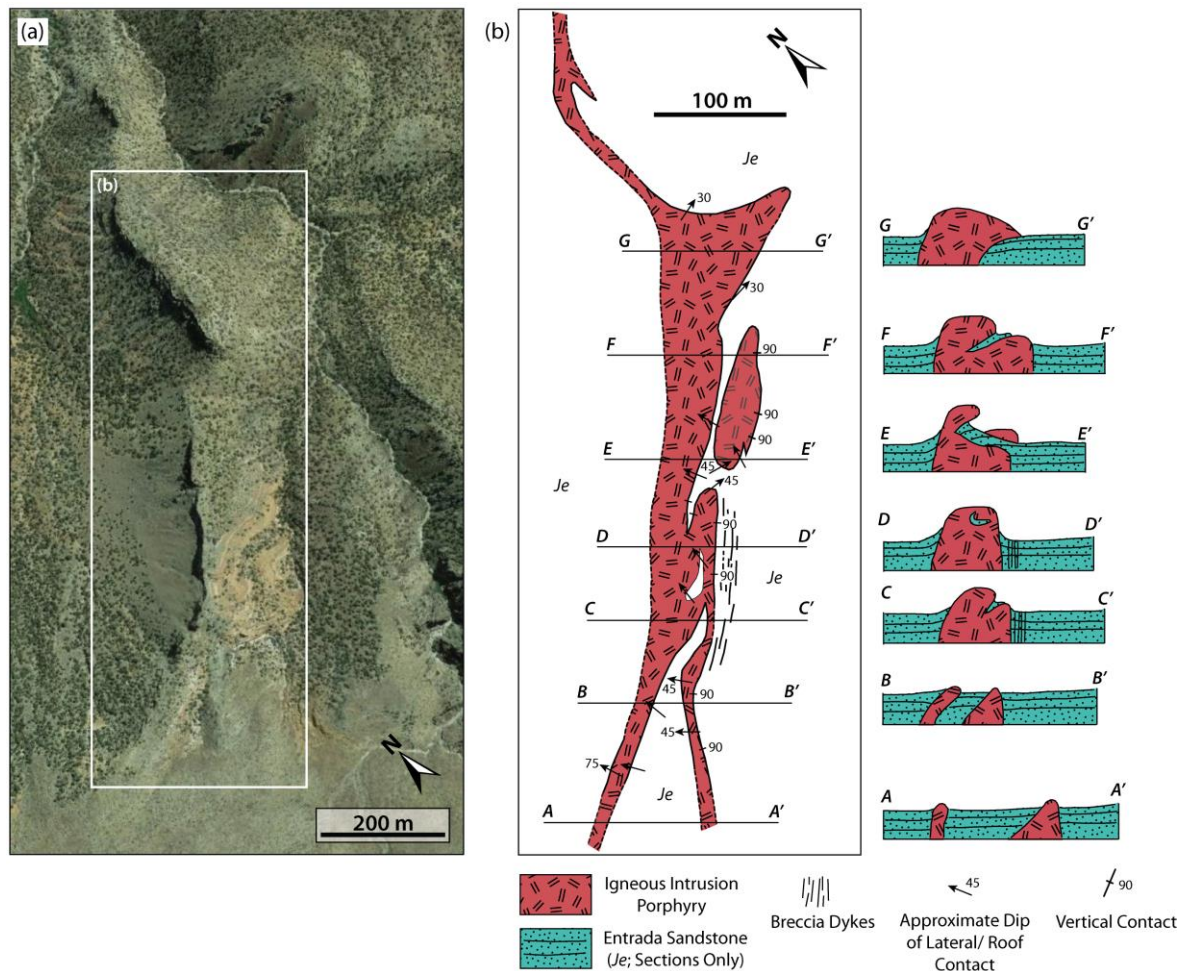


Figure 2.32. Trachyte Mesa Feeder system. (a) Topographic aerial image from Google Earth™ of the proposed Trachyte Mesa feeder. (b) Sketch geological map and diagrammatic cross-sections of the dyke feeder of the Trachyte Mesa intrusion (modified from Hunt, 1953).

2.5. Deformation Structures in the Entrada Sandstone

The two satellite intrusions that will be the primary focus of this study are Trachyte Mesa and Maiden Creek, both of which intrude the Entrada Sandstone. The Entrada, and underlying Navajo sandstones, have both long been studied for their reservoir properties and the abundant deformation structures (Aydin, 1978; Aydin & Johnson, 1978, 1983; Fig. 2.33). These aeolian sandstones are weakly cemented and highly porous (>10%), making them ideal candidates for the development of deformation bands (Aydin, 1978; Shipton & Cowie, 2001; Fossen et al., 2007).

2.5.1. Deformation Bands and their Classification

The term deformation band was first used in the context of sandstones by Aydin and co-workers in the late 1970s (Aydin, 1978; Aydin & Johnson, 1978, 1983) while studying the deformation structures hosted by the Entrada and Navajo sandstones exposed in SE Utah.

Since then, the term has been more widely incorporated to refer to small (sub-cm) zones of strain localisation formed by grain re-organization and/or grain crushing (Fossen et al., 2007, and references therein). The processes that result in the formation and evolution of deformation bands include grain rotation and translation (Fossen et al., 2007). Both of these processes, regardless of whether they include grain crushing or rotation and frictional sliding along grain boundaries, require a degree of porosity. In highly porous materials, deformation bands will result from strain localisation, whereas in materials with a low porosity, tension fractures, slip surfaces and/or stylolites will occur (Fossen et al., 2007).

Deformation bands in porous rocks (such as the Entrada and Navajo sandstones) are generally low-displacement deformation zones of mm- to cm-thickness (Fig. 2.33) that tend to have enhanced cohesion and reduced permeability compared with ordinary fractures (Fossen et al., 2007; Skurtveit et al., 2015). Strain in such highly porous rocks and sediments cannot be initially accommodated by fracture or slip surfaces. Instead, deformation bands form in areas of strain localisation. Subsequent faults and slip surfaces may then develop due to strain-hardening and brittle failure of the deformation band zone (i.e. formation of principal slip-surfaces, PSS; Aydin & Johnson, 1978; Shipton & Cowie, 2001, 2003). Offsets along individual deformation bands are rarely greater than a few centimetres regardless of the length of the deformation band, which sometimes is in excess of 100 m long (Fossen et al., 2007).

Fossen et al. (2007) discussed the various classification schemes used for describing deformation bands: (1) kinematic-based classification; and (2) deformation-mechanism classification (Fig. 2.34a, b).

2.5.1.1. *Kinematic-based Classification*

Kinematically, deformation bands can fall into the following types: dilation bands; shear bands; compaction bands; or hybrids of these (Fig. 2.34a; Aydin et al., 2006). The most commonly described deformation bands are compactional shear bands, caused by grain reorganization, with or without cataclasis (Fossen et al., 2007). This compaction contributes to strain hardening and the creation of a localised band network or zone that precedes faulting (e.g. Shipton & Cowie, 2003).

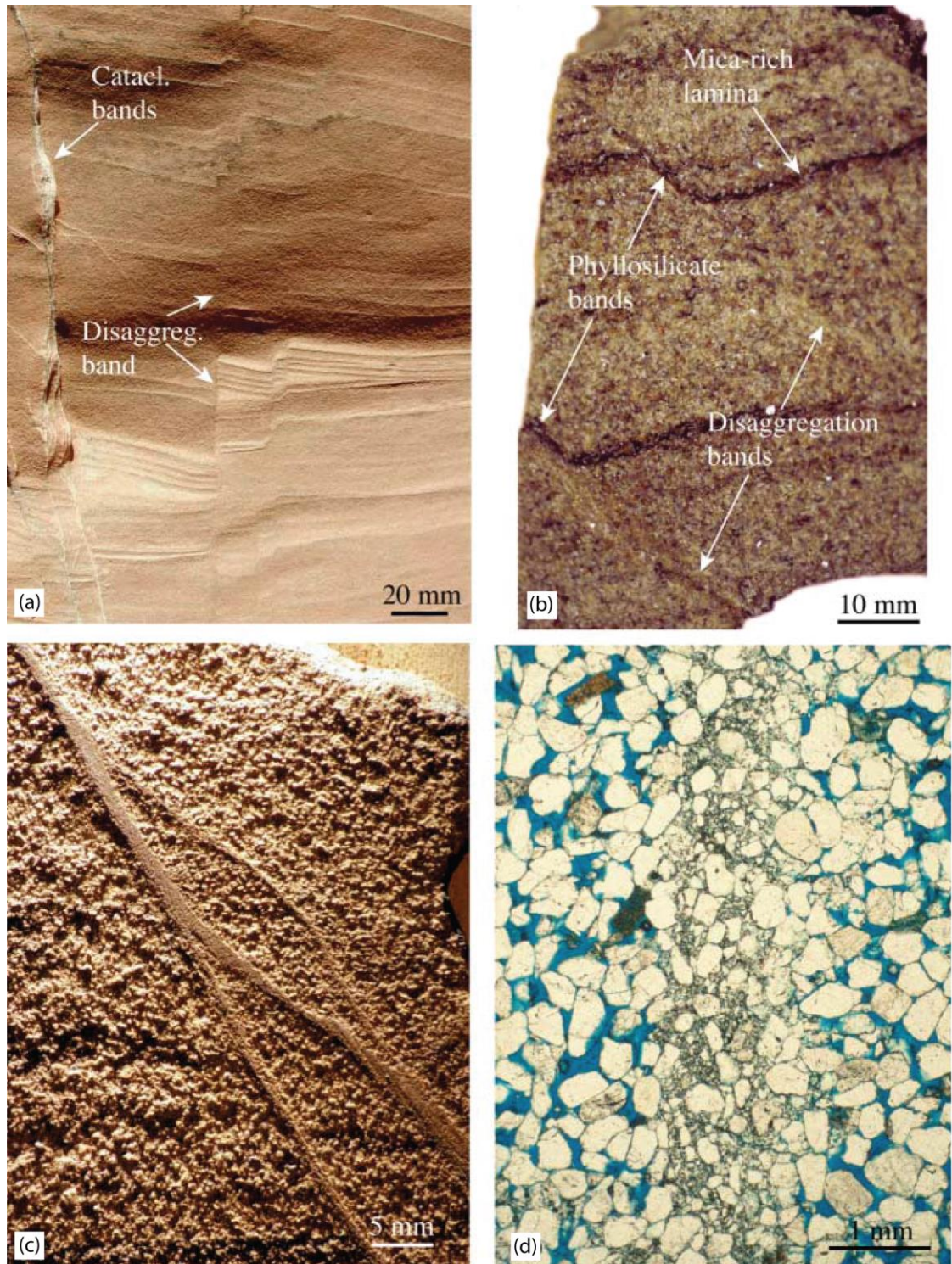


Figure 2.33. Photographic examples of deformation bands (Fossen et al., 2007). (a) Disaggregation bands and cataclastic deformation bands in the Navajo Sandstone, Utah. (b) Phyllosilicate – disaggregation bands in Jurassic sandstone (Gullfaks Field, North Sea). (c) Phyllosilicate band, Brent Group, Gullfaks Field. Note the positive relief (increase of cohesion) and loss of porosity. (d) Photomicrograph of a single cataclastic deformation band, showing a low-porosity cataclastic core mantled by a zone of compaction. Blue indicates pore space.

2.5.1.2. Deformation-mechanism Classification

Although it is good to classify deformation bands by the kinematics of formation, this may not always be easy to define. An alternative is to use dominant deformation mechanism

(Fig. 2.34b; Fossen et al., 2007). The benefit of this classification is that different mechanisms produce bands with different petrophysical properties, which is of particular interest to industries (e.g. petroleum, hydrology) where permeability and fluid flow are a key issue. The dominant deformation mechanisms are: (1) granular flow (grain boundary sliding and grain rotation); (2) cataclasis (grain fracturing and grinding or abrasion); (3) phyllosilicate smearing; (4) dissolution and cementation (Fig. 2.34b; Fossen et al., 2007).

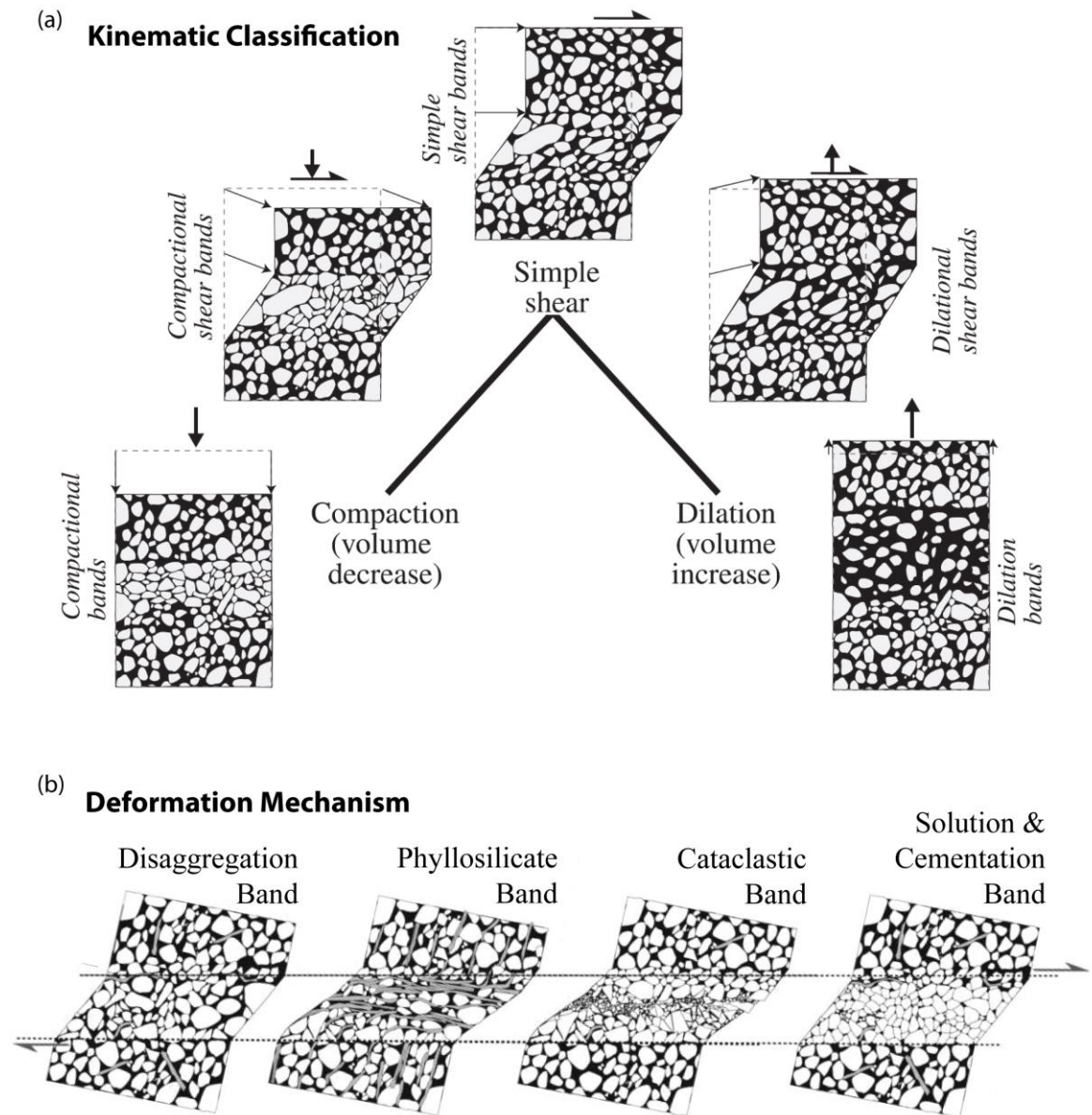


Figure 2.34. Classification of deformation bands. (a) Kinematic classification of deformation bands (Fossen et al., 2007). (b) Deformation bands classified by deformation mechanism (Fossen et al., 2007).

Disaggregation bands (Fig. 2.34b) develop by shear-related disaggregation of grains by granular flow or particulate flow (Rawling & Goodwin, 2003; Fossen et al., 2007). These are commonly found in sands and poorly consolidated sandstones and are therefore a

common structure that form during sand-box modelling experiments (Mandl et al., 1977; McClay & Ellis, 1987; Bense et al., 2003).

Phyllosilicate bands (Knipe et al., 1997) form in sandstone where the content of platy (phyllosilicate) minerals exceeds 10–15%. The platy minerals promote frictional grain boundary sliding rather than grain fracturing (i.e. cataclasis). Phyllosilicate bands can accumulate greater offsets than other types of deformation bands as the platy minerals inhibit strain hardening, and form weak slip surfaces. If the clay content is high enough (e.g. >40%; Fisher & Knipe, 2001), then these structures become clay smears (Fisher & Knipe, 2001; Fossen et al., 2007).

The classic deformation bands described by Aydin (1978) and Aydin and Johnson (1983) fall within the cataclastic deformation band category of Fossen et al. (2007; Fig. 2.34b), where mechanical grain fracture is a significant deformation mechanism. Aydin (1978) identified two distinct zones within these cataclastic deformation bands: an outer zone where the matrix, including pores and matrix material, deforms; and an inner low-porosity zone, <1 mm thick, where the sand grains fracture and further consolidation takes place (Figs 2.33 and 2.34; Aydin, 1978; see also fig. 1d in Fossen et al., 2007).

Dissolution and cementation may occur preferentially along a deformation band during or, more commonly, after deformation. Solution bands (Gibson, 1998) typically consist of tightly packed grains smaller in size than the matrix, but showing little evidence of cataclasis.

Deformation structures, such as those outlined above, can develop in response to both regional (tectonic) and local stresses. In this study, we focus on local host rock deformation structures that developed in response to the emplacement of igneous intrusions. These shall be described in more detail in the following chapters, with particular reference to the emplacement of the Trachyte Mesa and Maiden Creek Intrusions.



3. Chapter 3: A synopsis of the deformation structures associated with the Trachyte Mesa intrusion, Henry Mountains, Utah: implications for emplacement mechanisms.

| | | | |
|----------------|---------------|--|---------------|
| <i>Layout:</i> | 3.1. | Introduction | p. 112 |
| | 3.2. | Geological Setting | p. 114 |
| | 3.2.1. | <i>Henry Mountains</i> | p. 114 |
| | 3.2.2. | <i>Trachyte Mesa Intrusion</i> | p. 115 |
| | 3.3. | Field Observations | p. 117 |
| | 3.3.1. | <i>Intrusion Geometry</i> | p. 118 |
| | 3.3.2. | <i>Deformation Structures</i> | p. 120 |
| | 3.3.2.1. | <i>Structural types and geometry</i> | p. 120 |
| | 3.3.2.2. | <i>Structural Phases</i> | p. 123 |
| | 3.4. | Spatial distribution of structures | p. 127 |
| | 3.4.1. | <i>Structural transect profiles</i> | p. 127 |
| | 3.4.2. | <i>Variations with intrusion margin trend</i> | p. 132 |
| | 3.4.3. | <i>Deformation structures at the intrusion contact</i> | p. 132 |
| | 3.5. | Kinematics | p. 134 |
| | 3.6. | Discussion | p. 135 |
| | 3.6.1. | <i>Deformation phases (pre-, syn-, and late-stage emplacement)</i> | p. 135 |
| | 3.6.1.1. | <i>Phase 1 – Pre-emplacment deformation</i> | p. 137 |
| | 3.6.1.2. | <i>Phase 2 – Syn-emplacment deformation</i> | p. 137 |
| | 3.6.1.3. | <i>Phase 3 – Late-stage emplacement deformation</i> | p. 138 |
| | 3.6.2. | <i>Modes of Emplacement</i> | p. 138 |
| | 3.6.3. | <i>Emplacement and structural evolution</i> | p. 140 |
| | 3.6.3.1. | <i>Stage 1 - Onset of sheet emplacement and radial growth of a thin “proto-sill” sheet</i> | p. 141 |
| | 3.6.3.2. | <i>Stage 2 - Vertical inflation of sill sheet</i> | p. 143 |
| | 3.6.3.3. | <i>Stage 3 - Emplacement of additional sill sheets</i> | p. 145 |
| | 3.6.3.4. | <i>Stage 4 - Onset of sill-climbing</i> | p. 145 |
| | 3.6.3.5. | <i>Stage 5 - Cooling and relaxation of intrusion</i> | p. 146 |
| | 3.6.4. | <i>Sequence of stacking</i> | p. 147 |
| | 3.6.5. | <i>Faulting at sill terminations</i> | p. 148 |
| | 3.7. | Conclusions | p. 148 |

Deformation structures associated with the Trachyte Mesa intrusion, Henry Mountains, Utah: implications for sill and laccolith emplacement mechanisms.

This chapter is written for submission to Journal of Structural Geology

Co-Authors*: **Penelope I.R. Wilson**, Ken J.W. McCaffrey, Robert. W. Wilson, Ian Jarvis, Robert E. Holdsworth

*(*note: all scientific work was undertaken by the student/ principal author P. Wilson, and input from co-authors on this work was at an advisory/ editorial level only)*

Abstract

Deformation structures in host rocks of shallow crustal igneous intrusions may record how magma was emplaced and accommodated within the shallow crust. Trachyte Mesa, a small intrusion in the Henry Mountains, Utah, is comprised of a series of stacked sheets. However, new structural analysis of the kinematic, spatial and temporal distribution of deformation structures in the host rocks of the intrusion has enabled the recognition of three distinct phases, interpreted to represent pre-, syn-, and late-stage-emplacement deformation. We present a new 5-stage model for the emplacement of Trachyte Mesa, following a two-stage growth mechanism for individual sheets, with radial growth of a thin sheet followed by vertical inflation. Syn-emplacement structures localised to the intrusion lateral margins consist of: prolific deformation bands widespread over the margin; and dip-slip faults restricted to the tips of individual sheets due to strain localisation during vertical inflation. Magma preferentially exploited these faults, initiating sill climbing. The order in which sheets are stacked impacts on the intrusion geometry and associated deformation. Our results offer new insights into the incremental intrusion geometries of shallow crustal magmatic bodies and the potential impact of their emplacement on surrounding sedimentary rocks.

Keywords:

Deformation Bands; Faults; Intrusion; Sill; Laccolith; Emplacement Mechanism

3.1. Introduction

Shallow-level (<5 km depth) sill and laccolith complexes typically consist of a series of sub-horizontal tabular sheet-like intrusions and form an integral part of sub-volcanic plumbing systems (Cruden & McCaffrey, 2001). Understanding the formation of these networks of sub-horizontal intrusions is, therefore, key to assessing volcanic and sub-volcanic processes such as magma supply and storage in the upper crust (Bachmann & Burgantz, 2008). To-date, significant insights into sill and laccolith emplacement have been made through the characterisation of their geometry and internal architecture using field- and seismic-based data (Du Toit, 1920; de Saint Blanquat & Tikoff, 1997; Thomson, 2004; Thomson & Hutton, 2004; Horsman et al., 2005; Stevenson et al., 2007a, b; Thomson & Schofield, 2008; Magee et al., 2012). A number of studies have examined the important role played by active faults and shear zones and pre-existing host rock structures in controlling the emplacement and growth of mid-crustal granitic intrusions (e.g. Hutton et al., 1990; McCaffrey, 1992; Neves et al., 1996; Holdsworth et al., 1999; Passchier et al., 2005). Several studies have examined emplacement-related deformation structures associated with the intrusions of the Henry Mountains (Johnson & Pollard, 1973; Pollard et al., 1975; Morgan et al., 2008), but a complete analysis of the geometry, kinematics and sequential development of the wall rock structures has not yet been published.

The Henry Mountains, located in SE Utah on the Colorado Plateau (Fig. 3.1a), are a type locality for the study of shallow-level igneous intrusions and their emplacement. It was here that Gilbert (1877) famously first described and named laccoliths (coining the term “laccolite”; Gilbert, 1896). Since the ground-breaking work of Gilbert (1877, 1896), a number of studies have examined the geometries, geochronology and emplacement of intrusions in the Henry Mountains (e.g. Hunt, 1953; Johnson & Pollard, 1973; Jackson & Pollard, 1988; Nelson & Davidson, 1993; Habert & de Saint Blanquat, 2004; Horsman et al., 2005; Morgan et al., 2005; de Saint-Blanquat et al., 2006; Wetmore et al., 2009; Wilson & McCaffrey, 2013).

Following numerous field studies of the Henry Mountains, Hunt (1953) outlined three general emplacement models for shallow level intrusions (see Fig. 1.6 in Chapter 1): (1) radial growth only, with magma emplaced at a constant thickness, and country rocks displaced both vertically and laterally (i.e. a “bulldozing” mechanism; Model B of Hunt, 1953, fig. 70, p. 142); (2) two-stage growth, comprising radial growth of a thin sheet,

followed by dominantly vertical growth and associated vertical uplift of the overriding host rocks (i.e. a “two-stage growth” mechanism; Model A of Hunt, 1953); and (3) simultaneous vertical and horizontal growth (Model C of Hunt, 1953). Mounting evidence suggests that many shallow-level crustal intrusions are emplaced and grow through the incremental addition of small volumes of magma, and the amalgamation and stacking of sill sheets (e.g. Pitcher, 1970; Mahan et al., 2003; Glazner et al., 2004; Menand, 2008; Morgan et al., 2008). Therefore, the two-stage growth model (i.e. model A of Hunt) appears most applicable for larger shallow level intrusions (i.e. vertical inflation with stacking of sill sheets though under- and over-accretion; Menand, 2008; Menand et al., 2011). However, for the emplacement of individual sill sheets all three of Hunt’s models (1953) may still be viable.

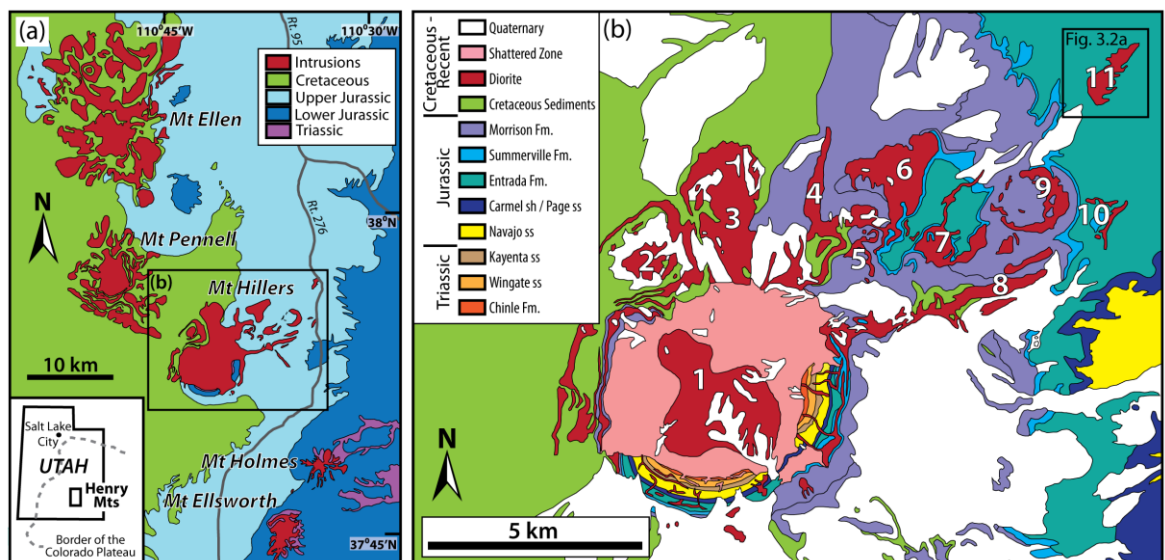


Figure 3.1. Simplified geological maps of the study area. (a) The Henry Mountains region (adapted from Morgan et al., 2008) and its location within Utah (inset map). (b) Mount Hillers and its satellite intrusions (modified from Larson et al., 1985). In (b), the various intrusions that comprise the Mt Hillers intrusive complex are numbered, using the names given by Hunt (1953) : 1 – Mt Hillers central complex; 2 – Bulldog Peak intrusion; 3 – Stewart Ridge intrusion; 4 – Specks Ridge intrusion; 5 – Chaparral Hills Laccolith; 6 – Specks Canyon; 7 – speculated feeder system to the Trachyte Mesa intrusion; 8 – Sawtooth Ridge intrusion; 9 – Black Mesa intrusion; 10 – Maiden Creek intrusion; and 11 – Trachyte Mesa intrusion.

Corry (1988) further adapted the emplacement models of Hunt (1953), highlighting that deformation structures associated with emplacement are strongly linked to the mechanism of emplacement (Fig. 1.6 in Chapter 1). A few notable studies of emplacement-related host rock deformation have focused on intrusions of the Henry

Mountains; these include Johnson and Pollard (1973), Jackson and Pollard, (1988), and Morgan et al. (2008). However, even in these cases, little consideration has been given to the kinematic pathways and associated strains that can potentially preserve information concerning the emplacement mechanism and magma movement (i.e. flow directions).

This paper presents a new structural analysis of the geometry, spatial distribution, kinematics, and relative time sequences of host-rock deformation structures surrounding the Trachyte Mesa intrusion, a small satellite intrusion adjacent to the Mount Hillers intrusive complex, Henry Mountains, Utah, USA (Fig. 1b, intrusion 11). By integrating observations of the host-rock structures with the sequential intrusion history, we have created an improved model for the emplacement of Trachyte Mesa that builds on the pioneering studies of Gilbert (1877), and the more recent work of Johnson and Pollard (1973), Morgan et al., (2008) and Wetmore et al. (2009). The results offer new insights into the incremental evolution of intrusion geometries in shallow-level magmatic bodies and how their emplacement leads to deformation of the surrounding sedimentary host rocks.

3.2. Geological Setting

3.2.1. Henry Mountains

The Henry Mountains Complex consists of five intrusive centres that form the principal mountain peaks in the area. From north to south these are: Mt Ellen; Mt Pennell; Mt Hillers; Mt Holmes; and Mt Ellsworth (Fig. 3.1a). Most of the intrusions have an intermediate (diorite) composition (58–63% SiO₂; Hunt, 1953; Engel, 1959; Nelson et al., 1992) and a porphyritic texture, with dominant feldspar (An₂₀–An₆₀; 20–40%) and hornblende (5–15%) phenocrysts (i.e. plagioclase-hornblende porphyry). The textural characteristics vary significantly from one intrusion to another (Hunt, 1953; Nelson et al., 1992). The intrusions are Oligocene in age (31.2–23.3 Ma K-Ar ages; Nelson et al., 1992), and were emplaced within a ~2.7 km thick section of late Palaeozoic–Mesozoic sedimentary rocks (dominantly aeolian to shallow-marine sandstones, siltstones and mudstones) overlying Precambrian crystalline basement (Jackson & Pollard, 1988). Although Laramide structures, such as the N–S trending Waterpocket Fold (Davis, 1978; Jackson & Pollard, 1988; Bump & Davis, 2003) occur locally, the strata into which the Henry Mountains intrusions were emplaced are relatively flat lying (Jackson & Pollard,

1988). The intrusions post-date this minor Late Cretaceous to Palaeogene Laramide orogenic activity on the Colorado Plateau (Davis, 1978, 1999). Lack of significant pre- and post-emplacement tectonism aids the identification of emplacement-related deformation structures and has preserved the original magmatic and solid-state fabrics within the intrusive bodies.

3.2.2. Trachyte Mesa Intrusion

The Trachyte Mesa intrusion, referred to as the “Howell laccolith” by Gilbert (Hunt, 1988) is the most distal satellite intrusion of the Mount Hillers intrusive complex, located 12 km to the NE (Fig. 3.1b). The intrusion has an elongate (~2.2 km long and 0.7 km wide) laccolithic geometry, trending NE–SW (Fig. 3.2). Thicknesses observed in cliff exposures range from 5–50 m (Morgan et al., 2008), with an average thickness, estimated from magnetic and resistivity studies, of ~15 m (Wetmore et al., 2009). The intrusion is generally concordant with the Entrada Sandstone Formation, within which it is emplaced (Johnson & Pollard, 1973; Morgan et al., 2008; Wetmore et al., 2009). The Entrada Sandstone Formation (part of the San Rafael Group) is Jurassic (Callovian) in age and comprises a mixture of white cross-bedded sandstones, reddish-brown silty sandstones, siltstones, and shale beds (Aydin, 1978).

Various models have been suggested for the geometry and internal architecture of the intrusion, ranging from a single domal “laccolitic” body (Gilbert, 1887; Hunt, 1953; Wetmore et al., 2009), to a series of stacked intrusive sheets and lobes (Fig. 3.2d, e; Johnson & Pollard, 1973; Morgan et al., 2005, 2008). In the exposures described by Morgan et al. (2008), a complex stacking history may be interpreted, with earlier sub-horizontally stacked intrusive sheets at the top of the sequence being flexed and arched by the emplacement of later sub-horizontally stacked tongue-like sheets beneath (i.e. under- and mid-accretion of Menand, 2008; Fig. 3.2d, e). These were evaluated further in the present study.

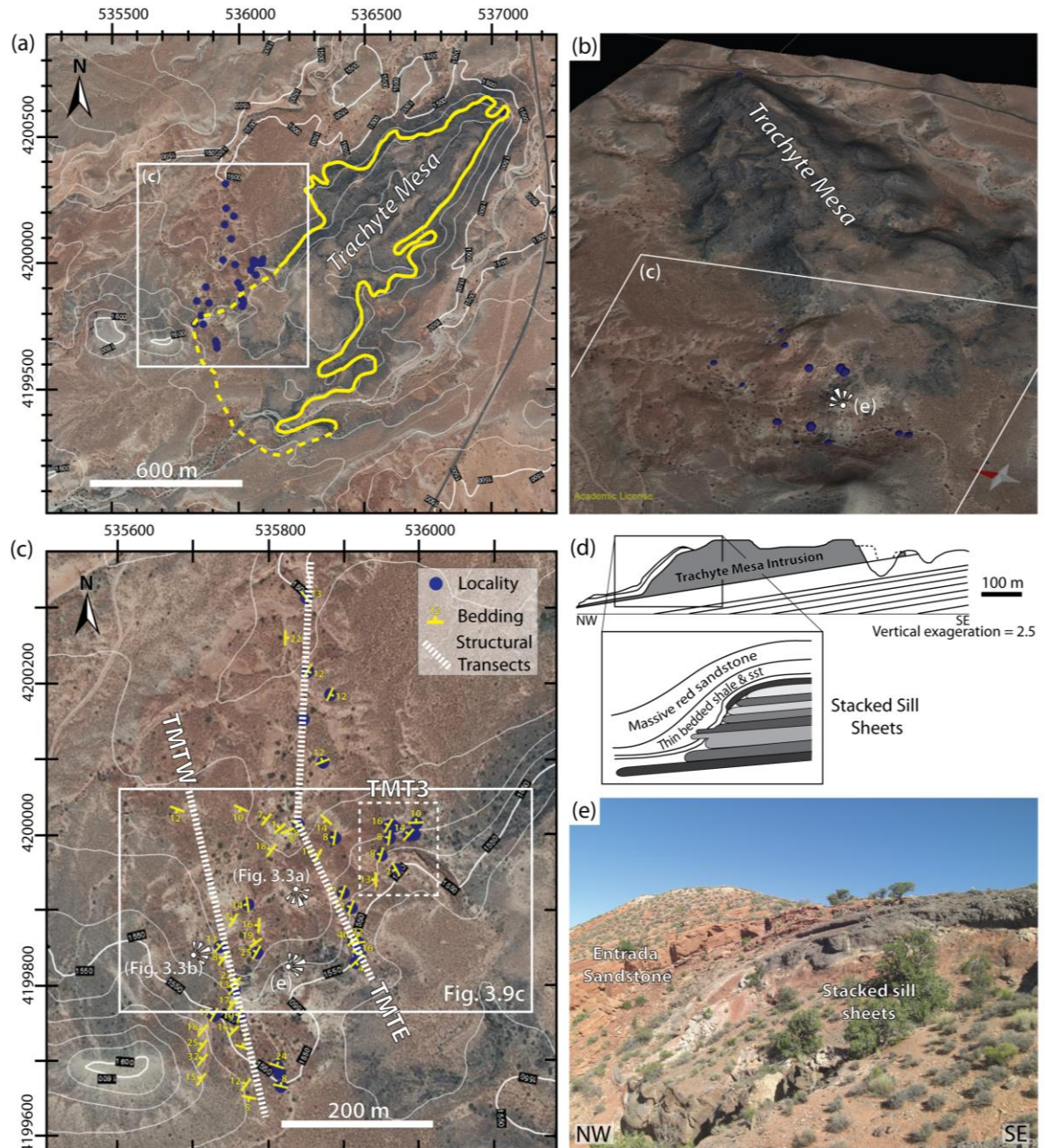


Figure 3.2. Location of the study sections. (a) Contoured and georeferenced aerial image of the Trachyte Mesa area showing the intrusion outline of Morgan et al. (2008). Locations of structural stations are shown by the blue filled circles. (b) Perspective view of DEM model of the Trachyte Mesa area, looking NE. Note viewpoint location for photo (e). (c) Contoured (heights in metres) and georeferenced aerial image (source: <http://gis.utah.gov/data/aerial-photography/>) of field study area, located on the southern end of the NW margin of the intrusion. Structural station localities, bedding measurements, structural transect lines (TMTE, TMTW) and detailed study area (TMT3) are shown. Also see Appendices for locations of structural stations mentioned within the paper. Note viewpoint location for photo (e). (d) Schematic cross-sections (NW–SE) across the Trachyte Mesa intrusion, showing stacked sill sheets (after Morgan et al., 2008). (e) Field photograph showing monoclinial upper contact and stacked intrusive sheets observed at NW margin of intrusion. Note zoom-in image in (d) is based on the field observations at this outcrop locality.

The present-day local geomorphology is controlled by the intrusion (Fig. 3.2a–b). This assertion is supported by the presence of multiple intrusion–host-rock contacts on the top and NW margins of the intrusion, although the SE margin is less well constrained (Morgan et al., 2008). The mesa has a relatively flat top with steeper NW and SE lateral margins. Where exposed, the base of the overall intrusion appears to be relatively concordant with the underlying sandstones, dipping $<10^\circ$ to the NW. Wetmore et al. (2009) suggested that the trend of the intrusion was controlled by a series of NE–SW trending pre-existing (Laramide?) folds, with the axis of the intrusion located within a synform. However, the local bedding and base intrusion contact exposures do not support the model for a tight syncline along the axis of the Trachyte Mesa intrusion (Morgan et al., 2008).

In contrast to the sub-horizontal stratigraphy below the intrusion, the host-rock units above show significant distortion and deformation (Johnson & Pollard, 1973; Morgan et al. 2008). At the NW margin of the intrusion, a clear monoclinical bending of the overlying beds is apparent (Fig. 3.2e), which is interpreted to be the result of vertical and lateral growth of the intrusion (Gilbert, 1887; Hunt, 1953; Johnson & Pollard, 1973; Morgan et al., 2008).

3.3. Field Observations

This field study focused on the southern end of the NW lateral intrusion margin (outlined in Fig. 3.2) as this area offers the best exposure of the intrusion and its contact with overlying host rocks (Fig. 3.2b, e). Detailed kinematic and geometrical studies were carried out at numerous outcrops, regularly spaced along two structural transects across the NW margin (Fig. 3.2c; for individual field localities see kmz file in the Appendices), Trachyte Mesa Transect East (TMTE) and West (TMTW); and at additional outcrops close to intrusion contacts (including area TMT3; Fig. 3.2c). At each structural station, a representative structural dataset (including: deformation type; geometry; kinematics; phase (i.e. cross-cutting relationships/ relative timing; character) was collected (minimum of 30 measurements per station; >50 in areas of high intensity deformation).

3.3.1. Intrusion Geometry

Figure 3.3 provides an overview of the intrusion contact relationships on the NW margin where structural transects were performed (TMTE and TMTW; Fig. 3.2c). Multiple stacked sill sheets and sheet terminations can be observed and comprise the overall intrusive body (Fig. 3.2d, e). Along the eastern transect (TMTE; Fig. 3.2c) from the NW to SE, the upper sill sheets and the overriding sandstone beds display a distinct monoclinial geometry with maximum dips of $\sim 40^\circ$ NW (Figs. 3.2c & 3.3a). Lower sub-horizontal sill sheets are also apparent (Fig. 3.3a). Sandwiched between these upper and lower sill sheets is a zone of highly deformed sandstone with little to no depositional characteristics preserved (Fig. 3.3a). A number of sill sheets exhibit “bulbous” terminations (Fig. 3.3); though others display a more planar, sub-vertical sheet termination (Fig. 3.3). Morgan et al. (2008) provided a comprehensive review of the stacked sill sheet geometries in this area.

The monoclinial geometry appears to be discontinuous along the margin. Along the western transect (TMTW; Fig. 3.2c), ~ 200 m SE of where the monocline is well exposed, multiple sub-horizontal sheets can be seen to be stacked one on top of the other (Fig. 3.3b, c), with terminations stepping back onto the top of the overall intrusive body, forming a “staircase geometry”. Here, the morphology of the bedding in the overlying sandstone appears more complex and step-like, mimicking the sill sheet geometry below (Fig. 3.3c). In this same area, an upward-inclined sheet can also be seen, which possibly reflects sill climbing during emplacement (Fig. 3.3b). In area TMT3 (Fig. 3.2c), intrusion geometries are less well exposed, however, the overlying sandstone units resemble the more step-like/ terrace geometry seen along the western transect.

Figure 3.3. (overleaf)

Photographs and interpretative sketches showing outcrop geometries of stacked sill sheets on the southern NW margin of Trachyte Mesa. (a) View looking SE from station TMTE-6 along structural transect TMTE (viewpoint location shown in Fig. 3.2c and (d)). (b) View looking NE from station TMTW-2 onto structural transects TMTW (foreground) and TMTE (in distance) (viewpoint location shown in Fig. 3.2c and (d)). (c) View looking SW at TMTW-3 (viewpoint location see (d)). Key observations include: monoclinial geometry of overriding sandstone units, (a) and (b); flexed/ monoclinial upper sill sheets (a) vs. sub-horizontal stacked sill sheets (b, c); sub-horizontal lower sill sheets with “bulbous” terminations (a) and (b); sill climbing in upper sill sheet, propagating along reverse dip-slip fault (b). (d) Aerial photograph of areas highlighted in photos (a)–(c). Note contrasting intrusion margin geometries along strike of the intrusion margin, vertically stacked-sheets in east of study area (i.e. around TMTE), and stepped stacked sheets in the west (TMTW).

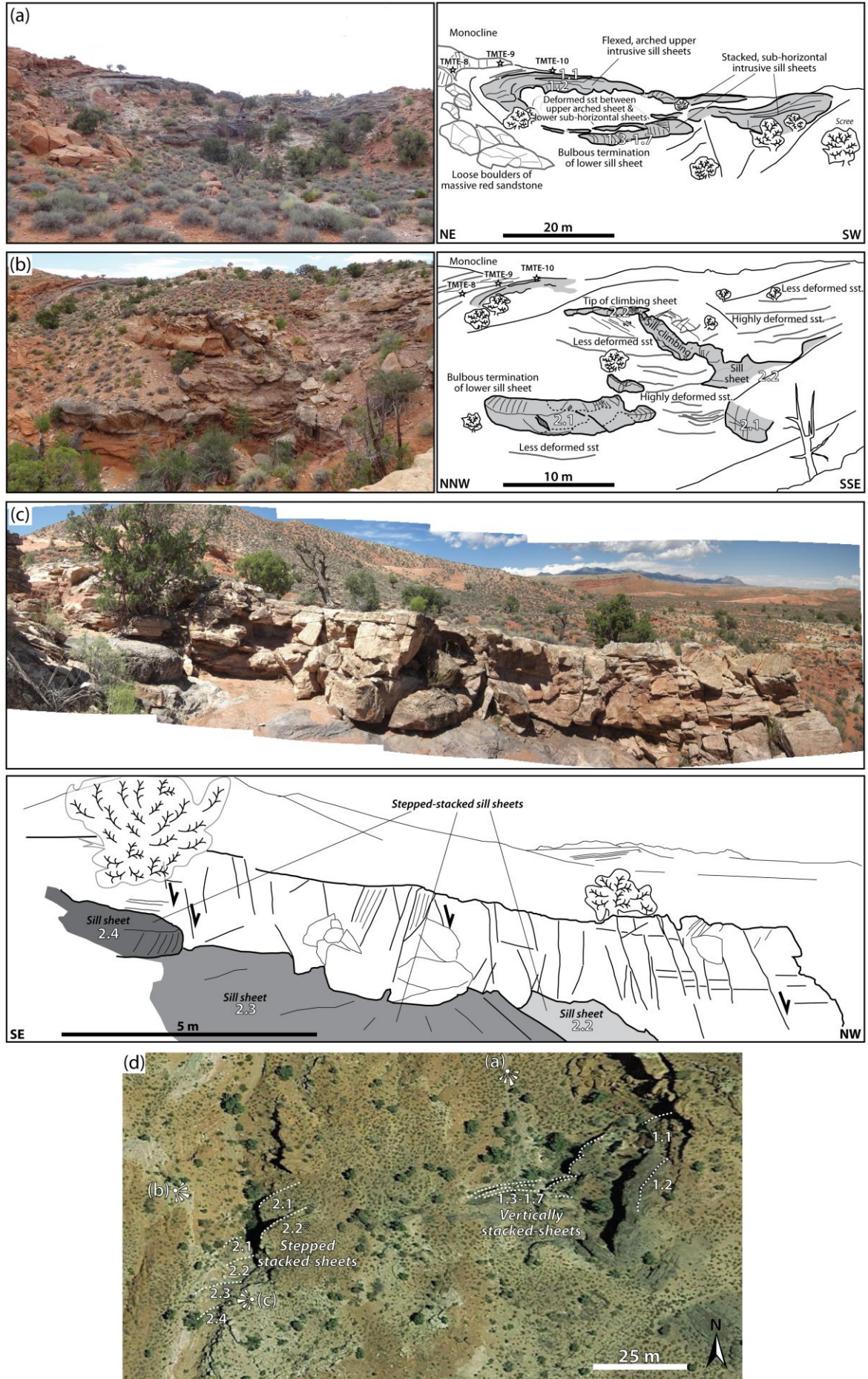


Fig. 3.3

3.3.2. Deformation Structures

3.3.2.1. Structural Types and Geometry

As noted above, locally, bedding has been deformed to form a monoclinial fold across the NW lateral margin of the intrusion, with dips ranging from sub-horizontal to $\sim 40^\circ$ NW on the steep limb (Figs 3.2 & 3.4a). Deformation structures observed within the Entrada Sandstone host rock include: prolific deformation bands; dip-slip faults; and tensile (Mode 1; Price, 1966) joints (Figs 3.4b–d & 3.5). Most of the deformation bands are porosity reducing and cataclastic in character (Fig. 3.6), showing small (mm- to cm-scale) offsets. There is a wide variation in deformation band orientation, with a dominant NE–SW trend, paralleling that of the intrusion (Figs 3.2a & 3.4b). Locally, small populations of dip-slip faults are observed (Fig. 3.4c), that trend parallel to the intrusion margin (NE–SW and ESE–WNW locally). A more widely distributed system of tensile joints, striking both parallel and perpendicular to the intrusion margin, is also observed (Fig. 3.4d). These joints commonly show evidence for fluid migration, with fine white carbonate precipitates and/or well-developed calcite crystals (Fig. 3.5g) on joint surfaces. Furthermore, highly altered (i.e. rich in hydrous minerals) vertical igneous lenses (note, original phenocrysts can still be identified) can be seen exploiting joints on the top surface of the intrusion (Fig. 3.5h). The highly altered nature of the plagioclase-hornblende porphyry suggests that these joint sets were also utilised by hydrothermal fluids.

Various shear zones are observed within and on the top surface of the intrusion (a number of which were described by Morgan et al., 2008). Within the host-rock these are restricted to the reddish-brown silty sandstone and shale unit that is commonly observed immediately above the intrusion, and are not apparent in the more massive red sandstone units above (Fig. 3.5b). In the upper few centimetres of individual intrusive sheets, and at the interface between the intrusive sheets, a strongly foliated (sub-horizontal foliation) zone occurs with significant stretched plagioclase phenocrysts (see fig. 3a in Morgan et al., 2008). The shear sense on structures on the top surface of the intrusion indicate a top-to-the-SE movement (i.e. reflecting the outward, NW-oriented, horizontal motion of the underlying intrusive sheet; Fig. 3.5b).

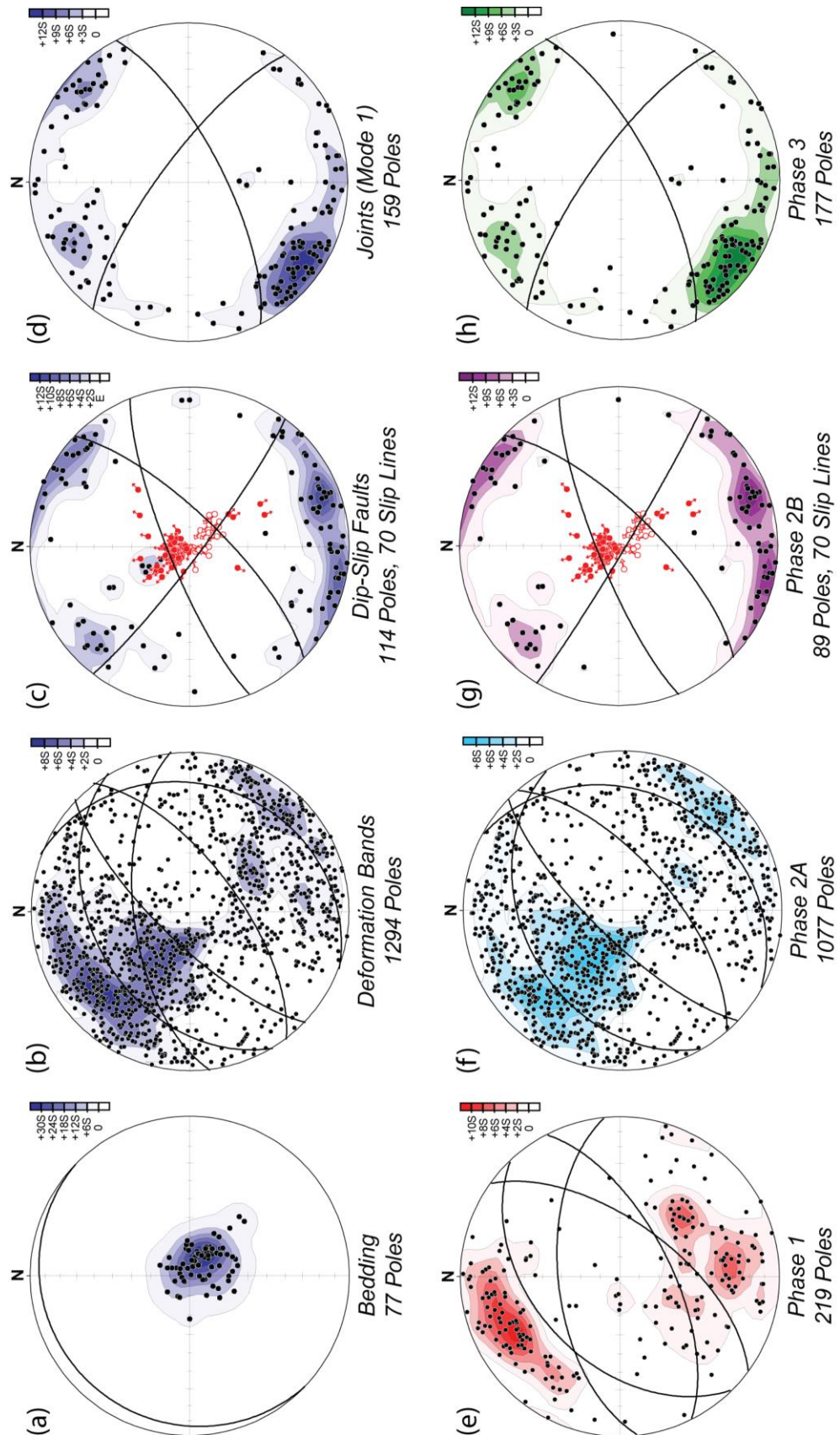


Figure 3.4. Summary stereoplots of field structural data. Equal area, lower hemisphere stereoplots of data showing poles to planes (contoured) sorted by structural type: (a) bedding, (b) deformation bands, (c) faults, (d) opening ‘Mode 1’ joints; and structural phase: (e) Phase 1, (f) Phase 2A, (g) Phase 2B, (h) Phase 3. Mean planes for distinct cluster populations are shown for each plot. Plots (c) and (g) also show fault slip lines with movement direction indicated (solid fill = normal fault slip; white fill = reverse slip).

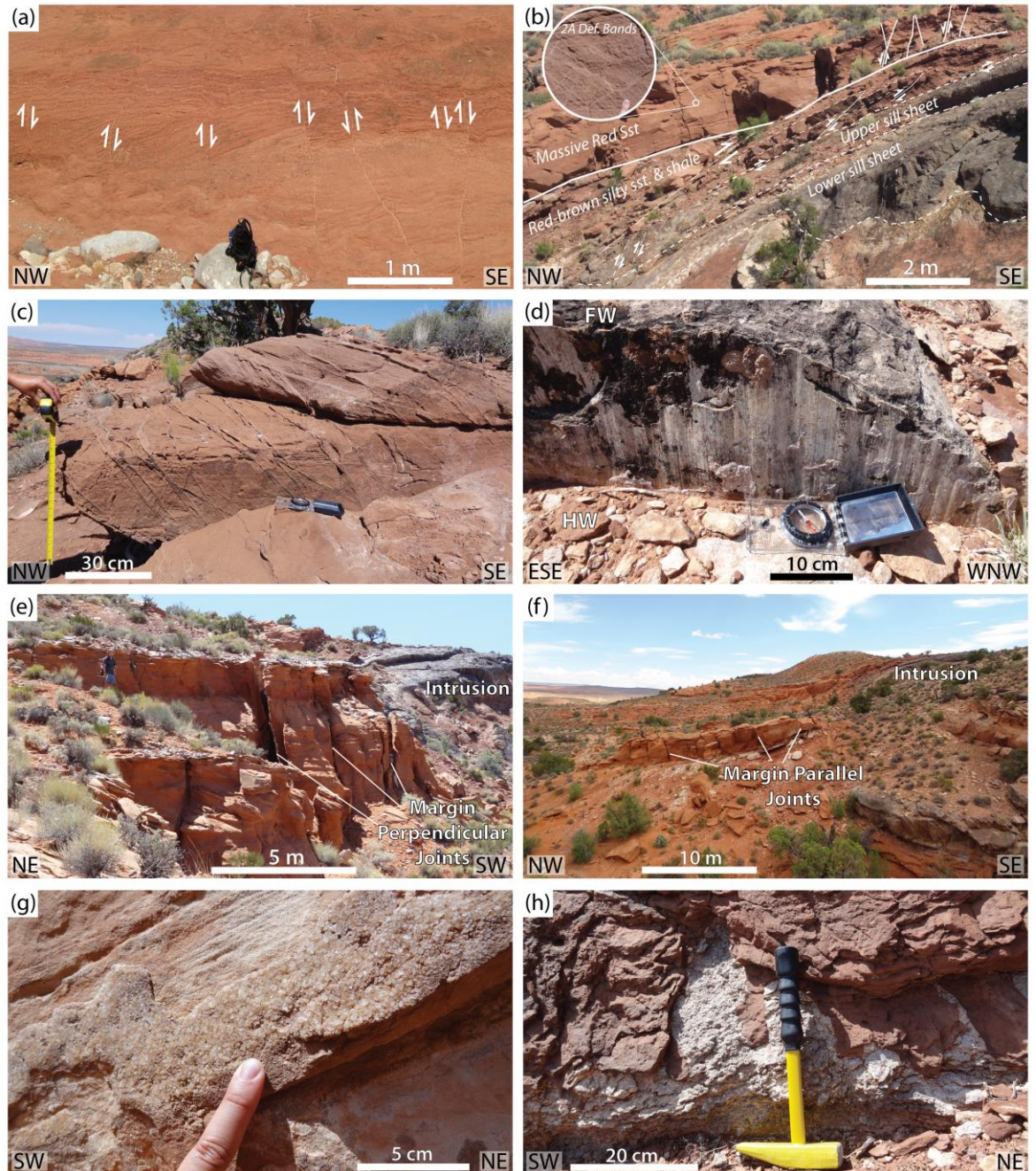


Figure 3.5. Annotated field photographs showing examples of Phase 1 (a), Phase 2 (b–d), and Phase 3 (e–h) deformation structures. (a) Background deformation bands cutting the Entrada Sandstone distal to the intrusion (0.2–2m spacing). (b) Deformation structures at intrusion contact, locality TMTE-9 in Fig. 3.3. Low angle shear and reverse faults (top-to-the-SE) on top surface of the intrusion and within the highly deformed shaley red sandstone layer adjacent to the contact. Extensional conjugate deformation bands in massive red sandstone (also see fig. 9 in Morgan et al., 2008). (c) Closely spaced porosity reducing deformation bands in massive red sandstone, localised to intrusion margin and host-rock overlying the top surface of the intrusion (0.5–5cm spacing). (d) Dip-slip normal fault (down-to-the-NW) with well-preserved slickenlines on principal slip surface. (e) Opening ‘Mode I’ joints trending perpendicular to the intrusion margin (NW–SE), 0.5–2m spacing. (f) Opening ‘Mode I’ joints trending parallel to the intrusion margin (NE–SW), 1–2m spacing. (g) Calcite crystals precipitated on margin parallel joint surfaces in (f). (h) Highly altered (hydrous minerals) plagioclase-hornblende porphyry (note, original phenocrysts still identifiable) exploiting joints on top surface of intrusion.

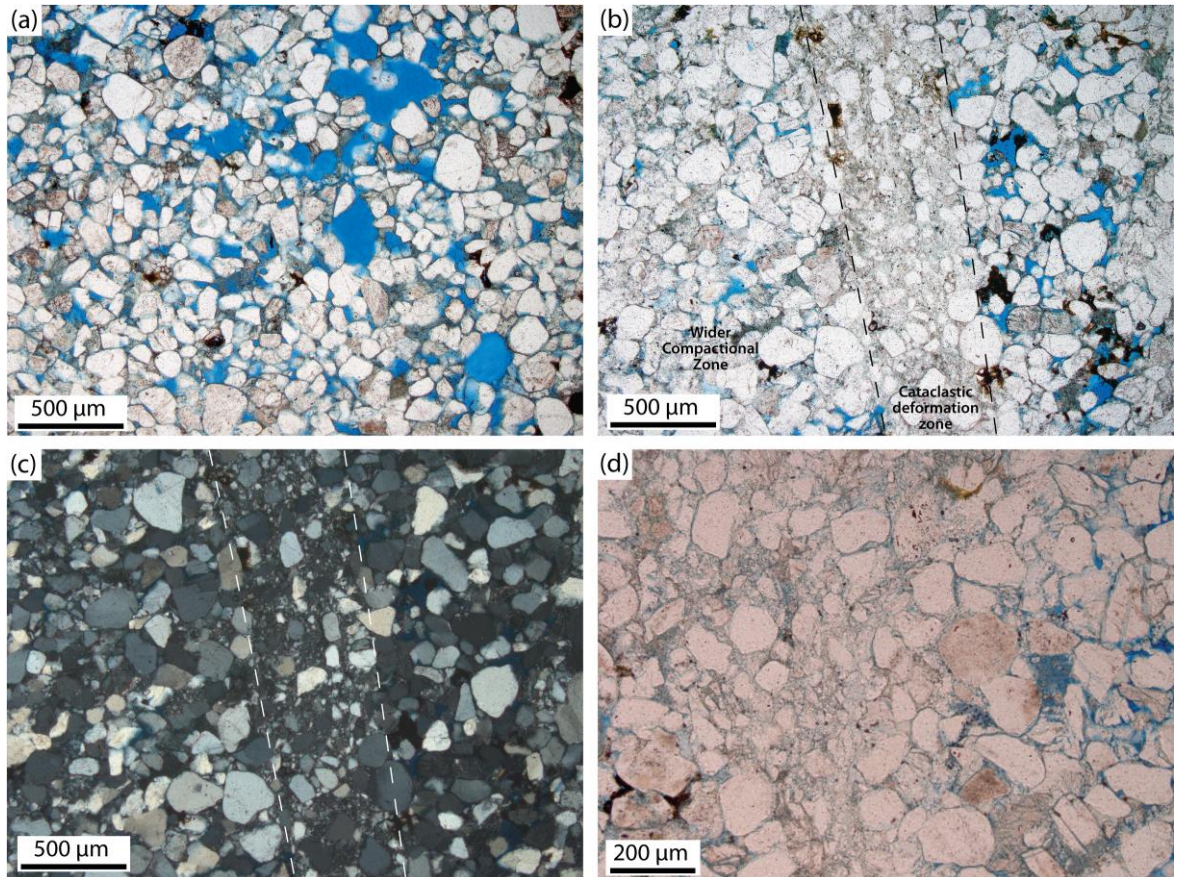


Figure 3.6. Photomicrographs of Entrada sandstone (blue dye infilling pore space). (a) Relatively undeformed parent host rock showing significant pore space, 18–20%. Photo taken using plane polarized light (ppl) at x5 magnification. (b) Section across deformation band showing two distinct zones: a narrow (0.5 mm) cataclastic deformation zone characterised by a wide range of grain sizes, angular grains and a fine-grained matrix resulting from grain size reduction; and a wider compactional zone. Porosity reduction is nearly 100% within the cataclastic deformation zone, while within the compactional zone reduction ranges from 50–90% (i.e. <5% porosity). Photo taken using ppl at x5 magnification. (c) Same view as (b) using cross-polarised transmitted light (xpl). (d) Close-up (x10 magnification, in ppl) of microstructure within a cataclastic deformation band highlighting angular fractured grains and significant reduction in both grain size and porosity. Note also the increase in calcite cement within the deformation band zone.

3.3.2.2. Structural Phases

Deformation structures observed within the host rocks to the intrusion may be categorised into three distinct phases (Figs 3.4e–h & 3.5 & Table 1), according to: structural type; deformation character; geometry; kinematics; spacing/ intensity; and cross-cutting relationships observed in the field (Fig. 3.7).

| Phase | 1 | 2 | 3 |
|-----------------------|---|--|--|
| Structures | Deformation bands and extensional faults (no infill or slickenlines on surfaces) | 2A - Deformation bands (conjugate sets); 2B - Dip-slip (normal & apparent reverse faults) with well developed slickenlines, and white (calcareous?) precipitate | Opening mode joints |
| Geometry | ENE-WSW (NE-SW to E-W) | NE-SW (N-S to E-W) | NE-SW (margin parallel) and NW-SE (margin perpendicular) |
| Kinematics | NW-SE extension? | NW-SE extension? Local flexure around intrusion (down to NW) | Tensile (σ_1 vertical) |
| Spacing/ Intensity | Low-moderate (50 cm to 5 m); High intensity (cm spacing) ladder structures/ deformation corridors | High (mm to 10 cm); Increasing intensity across the edge of the intrusion | Low-moderate (50 cm - 5 m) |
| Timing | Early | Mid; Cross-cut Phase 1 extensional faults | Late; Cross-cut all other structures (including Phase 2 normal faults) |
| Comments | Apparent background deformation; not directly linked to intrusion of Trachyte Mesa (but may still have developed during the same event) | Phase 1 and 2 deformation bands are difficult to differentiate and may be linked (differences due to local variations associated with intrusion) | Calcite infill and crystal growth on many surfaces |

Table 1. Summary table of deformation phases observed in the host rocks to the Trachyte Mesa intrusion (see text for more details).

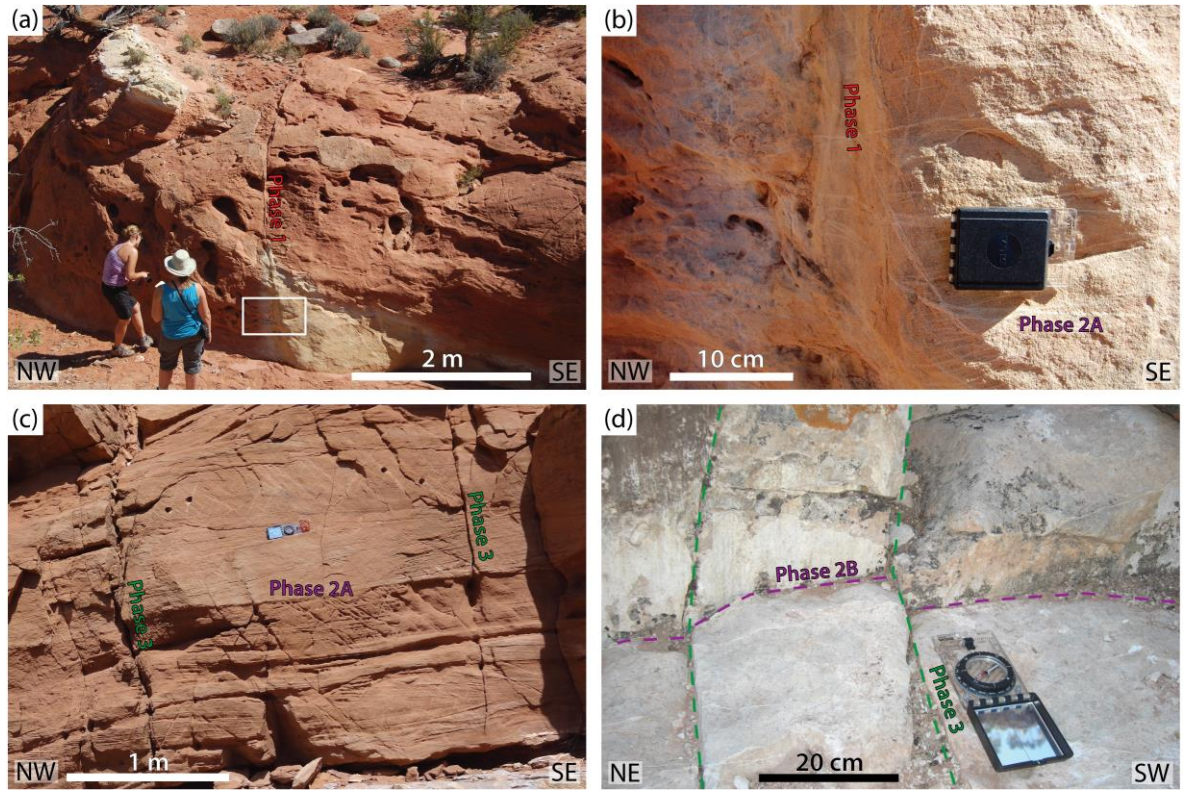


Figure 3.7. Cross cutting relationships between structural phases. (a) Example of large phase 1 deformation band observed at structural station TMTE-4. (b) Zoom-in on deformation band shown in (a), note the second system of deformation bands (phase 2A) cross cutting the steeply dipping phase 1 set. (c) Conjugate deformation bands (phase 2A) cross cut by steeply-dipping phase 3 joints (TMTE-9). (d) Steeply dipping extensional faults (phase 2B) cross cut by phase 3 joints (TMTW-3).

Phase 1 consists of a set of deformation bands and extensional faults, trending oblique (ENE–WSW) to the NE–SW trend of the intrusion (Figs 3.4e & 3.5a), and were found over a wide area away from the intrusion (>500 m). Phase 1 deformation bands are discrete and are often identified by offsets on bedding and cross-beds. Where significant offsets (cm- to m-scale) are seen, the sense of shear is largely consistent with extension. Phase 1 structures display a low- to moderate-intensity, with spacing between 50 cm to 100 cm. However, high intensity (cm-scale spacing) ladder structures/ deformation corridors also occur, similarly trending ENE–WSW. Phase 1 structures are interpreted as being related to the regional strain that predated the intense deformation that was associated with emplacement of the intrusion because they occur at significant distances (>500 m) away from the intrusion.

Phase 2 comprises a second set of deformation bands and faults (Figs 3.4f–g, 3.5b–d & 3.8) that overprint the earlier Phase 1 structures (Fig. 3.7b). Both the deformation bands and the faults trend NE–SW, parallel to the NW lateral margin and overall trend of the intrusion (Figs 3.4f, g & 3.9). In contrast to Phase 1 deformation bands, Phase 2 structures are much more obvious in exposures, often occurring as resistant ridges standing proud of the host Entrada Sandstone (Fig. 3.5c). Microstructural analysis of these Phase 2 deformation bands shows that they are the result of cataclasis and compaction, with significant (almost 100%) porosity reduction along the deformation bands (Fig. 3.6). The intensity (fracture density) of Phase 2 deformation bands is significantly higher than that of Phase 1, with fracture spacing in the order of 0.5 cm to 5 cm, although intensity decreases rapidly as you move off the intrusion margin. Phase 2 deformation bands form conjugate sets with extensional offsets (Fig. 3.8a, b). Phase 2 faults are dip-slip in character, showing both normal and reverse movements (Fig. 3.4c, g), but with a common down-to-the-NW offset (Fig. 3.8c–e). Unlike Phase 1 extensional faults, these often show a distinct principal slip surface (PSS; Fig. 3.8e), and slickenlines are commonly observed (Figs 3.4g, 3.5d and 3.9). Phase 2 structures can be sub-divided further according to their cross-cutting relationships. Deformation bands (Phase 2A) are consistently cross-cut by the dip-slip faults (Phase 2B), as well as steeply dipping ladder zones (Fig. 3.8c–e).

Phase 3 comprises a system of tensile joints, often infilled with sparry calcite, which overprint all other deformation structures (Figs 3.4h & 3.5e–h). The system of joints consists of two sets: a NW–SE trending set, perpendicular to the intrusion margin (Fig. 3.5e); and a NE–SW trending set, sub-parallel to the intrusion margin (Fig. 3.5f). No clear cross-cutting relationship is apparent between these two joint sets.

Figure 3.8. (*overleaf*)

Annotated field photographs showing additional examples of Phase 2A (a–b) and 2B (c–e) structures and kinematics. (a) Monoclinial bedding geometries in sandstone units ~30 m above the intrusion showing conjugate fault/ deformation band geometries consistent with flexure (note offset on bedding in paler sandstone unit). (b) Outcrop example (~5 m above intrusion) of conjugate deformation banding showing consistent offsets to those seen in (a). (c) Steep ladder zone (down-to-the-NW shear) overprinting conjugate deformation bands. Note kinematics of background deformation bands and ladder zone are the same. (d) Outcrop example of normal faults developed at the termination of sill sheets. Note total throw on normal faults is consistent with the thickness of the individual sill sheet, implying that the faults may be induced by sill sheet inflation. (e) Zoomed-in area outlined in (d) showing ~50 cm normal (down-to-the-NW) offset of bedding contact (PSS – Principal Slip Surface; DZ – Damage Zone).

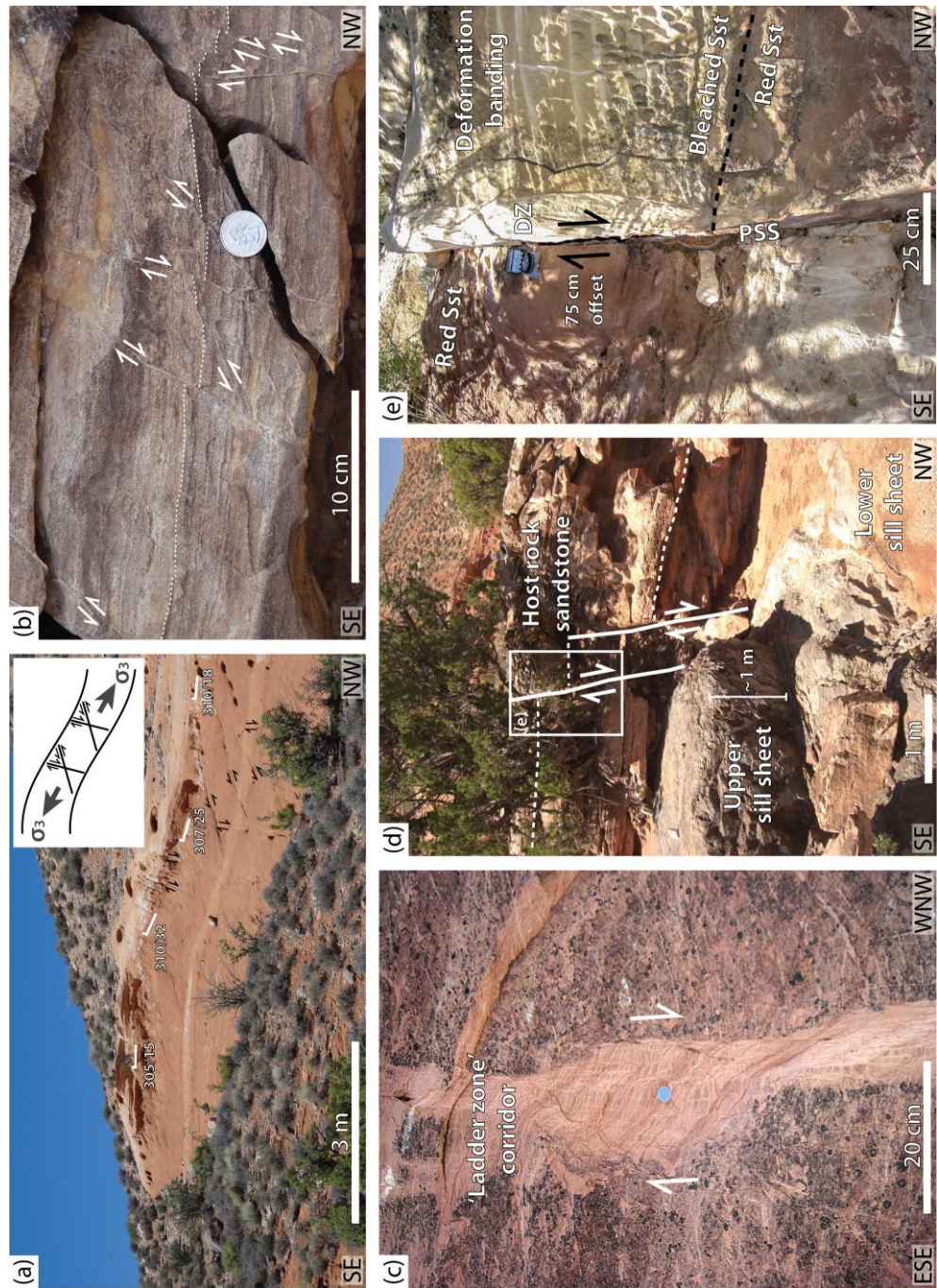


Fig. 3.8

3.4. Spatial Distribution of Structures

3.4.1. Structural Transect Profiles

Distinct structural domains were identified along the two structural transects (TMTW and TMTE; Figs 3.10 & 3.11) within the host rock that reflect both temporal and kinematic variations in deformation. The structural data at individual stations are plotted on two composite cross sections created in Move™ (Figs 3.10 & 3.11; see also kmz file in Appendices for locations of structural stations and transects). It is clear from these cross sections that Phase 1 deformation structures are only identifiable at more distal

structural stations to the intrusion margin, and are overprinted by Phase 2A, 2B and 3 deformation structures with increased proximity to the intrusion. Phase 2 structures increase in intensity from just outboard of the intrusion margin, and onto the top surface of the intrusion. Phase 2A conjugate deformation bands appear to rotate about a horizontal axis in the vicinity of the flanking monocline (Figs 3.8a, 3.10 & 3.11).

Figure 3.9. *(overleaf)*

Field photographs and structural data demonstrating the arcuate trend of Phase 2B faults. (a–b) Equal area lower hemisphere stereoplots, showing all fault trends of Phase 2B faults. Faults show dip-slip normal and reverse movements, consistent with NW–SE extension (note inclination of σ_3 , associated with flexure along the intrusion margin). (c) Map showing the distribution of the main outcrop localities at which Phase 2B fault data were collected. The change in geometry and kinematics of the faults with the changing trend of the intrusion margin can be seen from the equal area lower hemisphere plots for each outcrop showing poles to planes, slickenlines and interpreted kinematics. Solid white lines depict areas where intrusion margin is exposed in outcrop, dashed white lines show inferred continuation of margin beneath sandstone beds (note, magnetic data from Wetmore et al. (2009) was used to guide this subsurface geometry). See Fig. 3.2c for location in context of wider area. (d)–(f) Field photographs showing outcrop examples of Phase 2 dip-slip normal faults. Although individual faults are quite linear, a clear rotation in fault trend may be seen when walking along strike. Many fault surfaces have well-developed slickenlines showing almost pure dip-slip kinematics.

Figure 3.10. *(overleaf, fold-out)*

Structure along Trachyte Mesa transect TMTW. Cross section constructed in 2D Move™ (for location, see Fig. 3.2c and Google Earth™ kmz project in Appendices). Equal area, lower hemisphere plots of poles to planes highlight deformation structure populations collected at each station (white stars; bedding planes highlighted in yellow). Note the stepped/ terraced geometry of the margin. Colour bars across the lower part of the section show the spatial distribution of the different deformation phases.

Figure 3.11. *(overleaf, fold-out)*

Structure along Trachyte Mesa transect TMTE. (a) Cross section constructed in 2D Move™ (for location, see Fig. 3.2c and Google Earth™ kmz project in Appendices). See Figure 3.10 for key. Note, the main intrusion is in the SE (to the right) of the section, while a smaller distal intrusion fan be seen further outboard. (b) Close-up of the area around the intrusion margin and corresponding field photograph of the same outcrops. Numbers 1–5 indicate the possible timing of sheet emplacement, with 1 being the earliest sheet. Note the monoclinical geometry of the upper sill sheets and overriding massive sandstone.

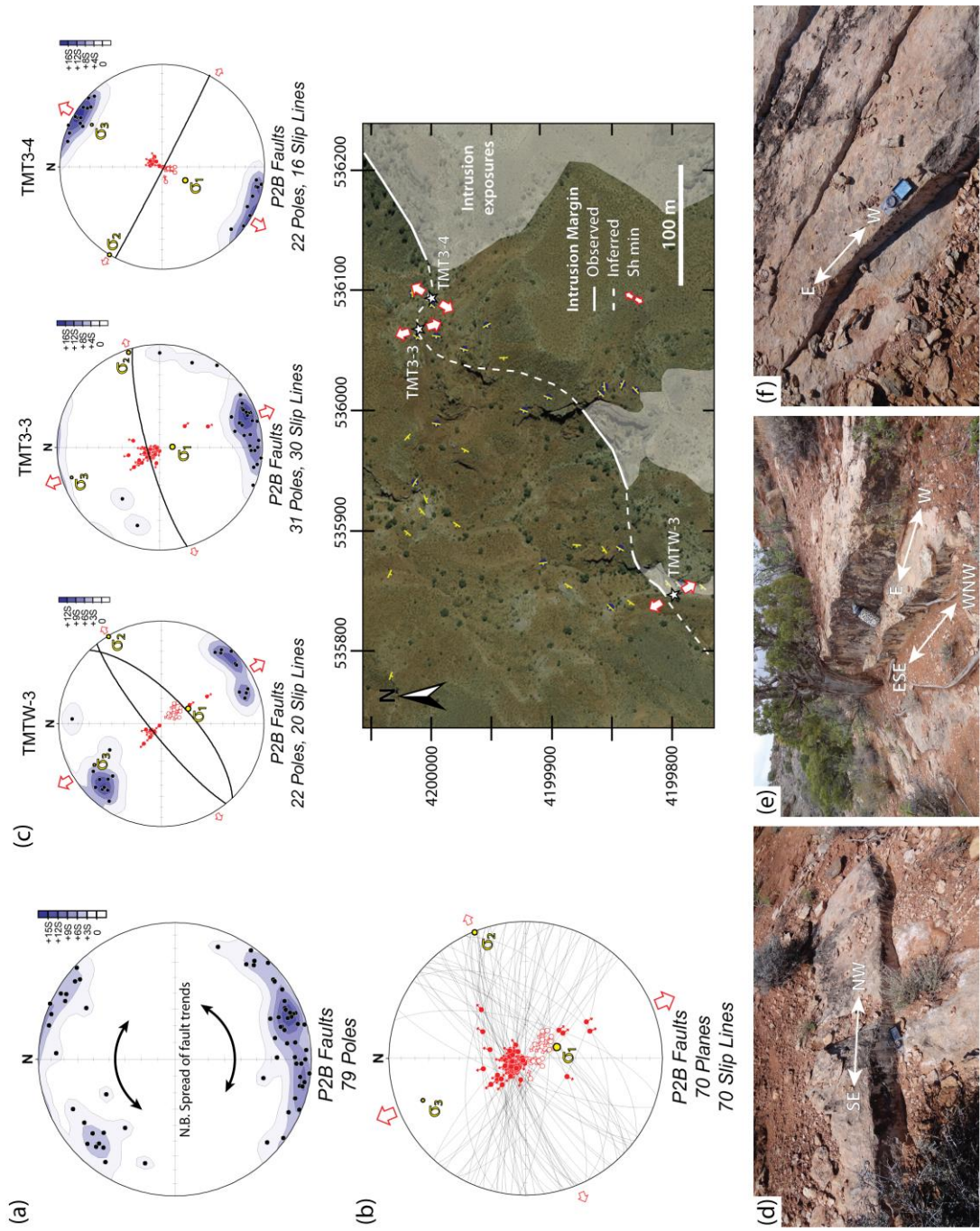


Fig. 3.9

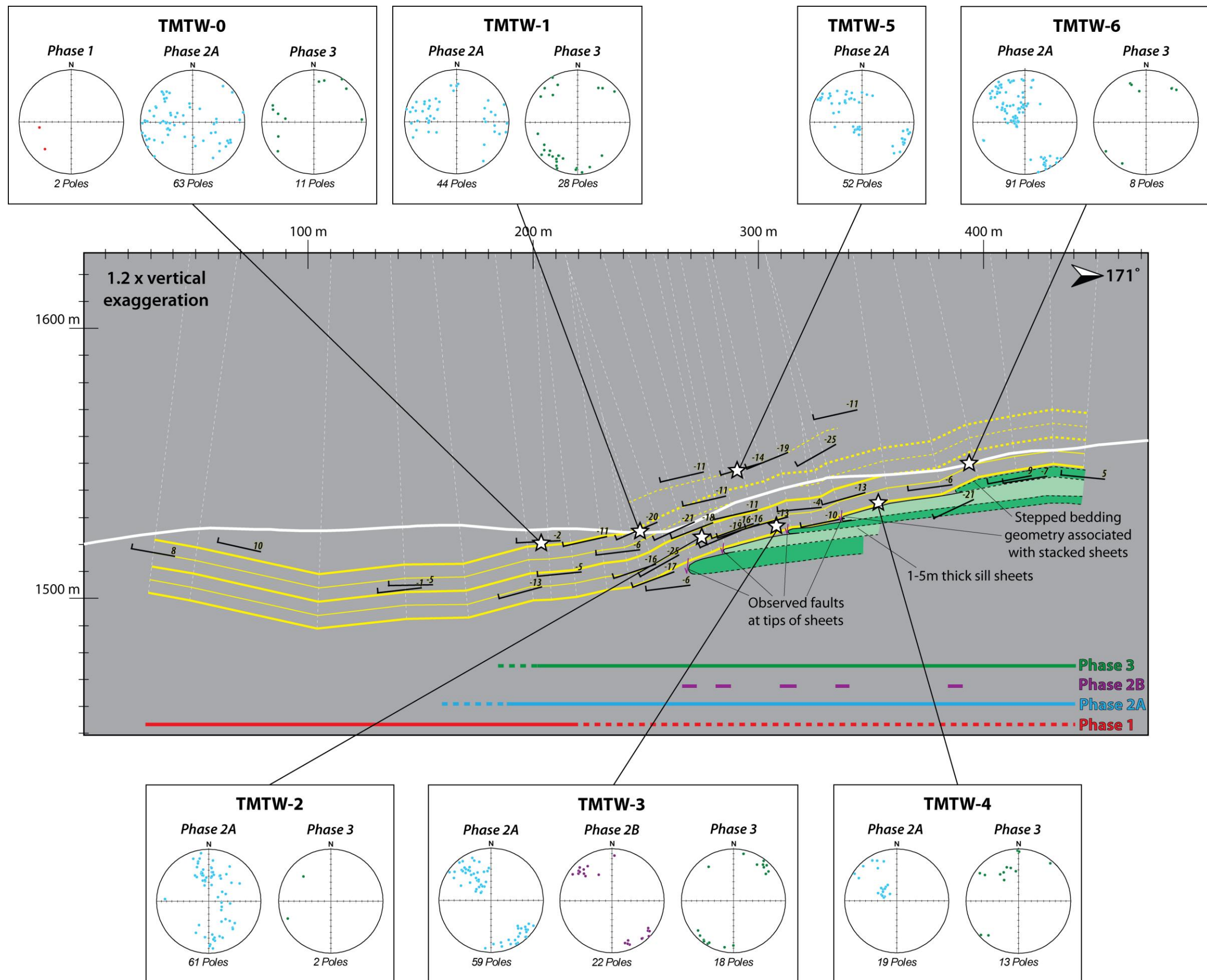


Fig. 3.10

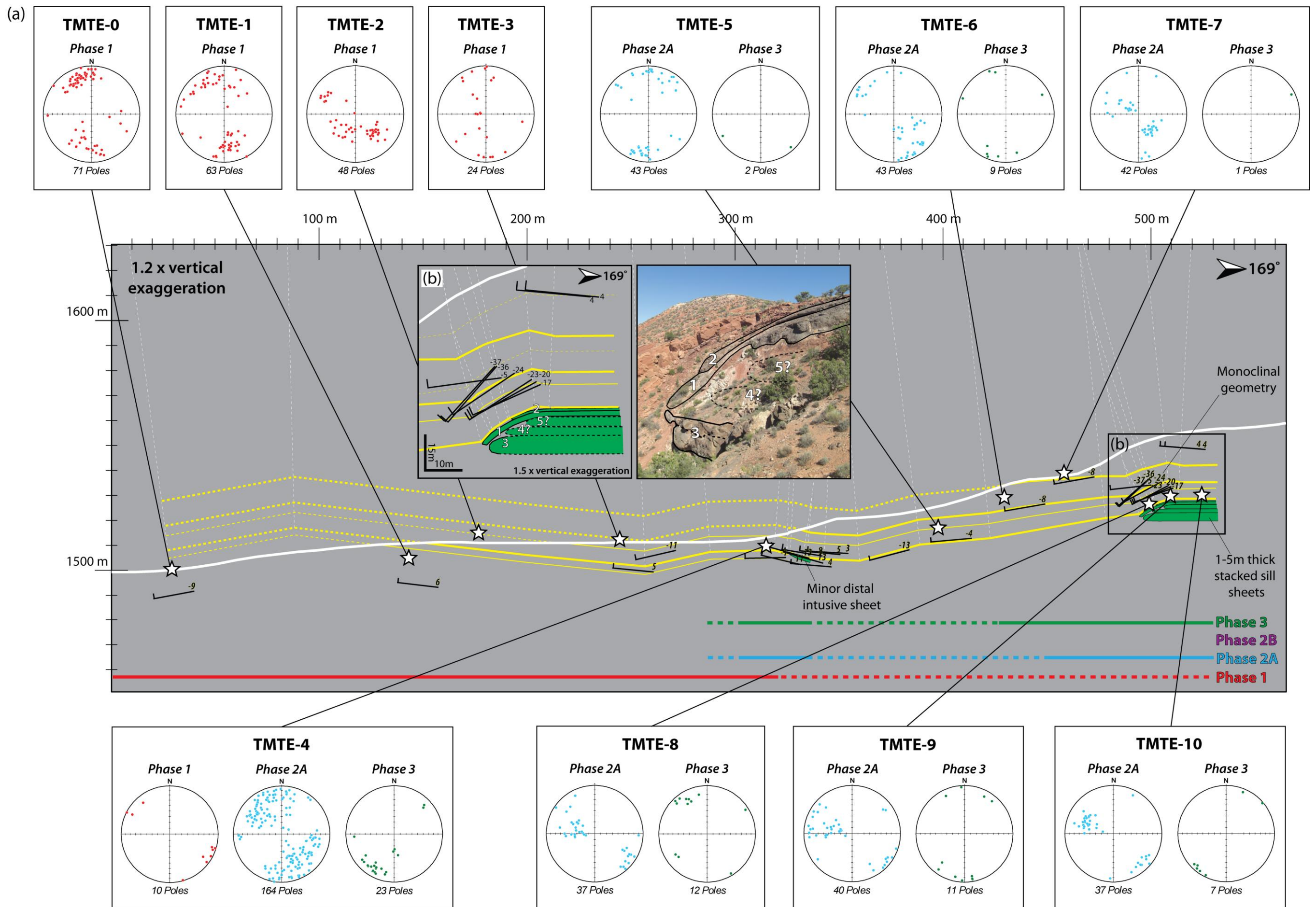


Fig. 3.11

Bedding along the western transect (TMTW) displays a stepped ('staircase') geometry with each step appearing to be associated with a new intrusive sill sheet (Fig. 3.10). Deformation structures vary across these 'stepped' zones, with Phase 2B (faults and steep deformation corridors/ ladder zones) appearing localised to sill sheet terminations (Figs 3.8d & 3.10). In contrast, bedding geometry appears simpler along the eastern section (TMTE), the monoclinical structure lacking the 'steps' observed for TMTW. Accordingly, Phase 2B faults are also rare in the outcrops along the eastern transect (Fig. 3.11).

3.4.2. *Variations with Intrusion Margin Trend*

Phase 2B, steep dip-slip (normal and reverse) faults are most commonly observed on the intrusion margin, associated with the tips/ terminations of intrusive sheets (Fig. 3.8d, e). Phase 2B faults are largely observed only at structural station outcrops on the western transect (TMTW) and additional TMT3 outcrops (Figs 3.2c & 3.9). Mapping of these faults along strike reveal an arcuate trend that appears to match the proposed curved nature of the 'lobe'/ promontory of stacked intrusive sheets (Morgan et al., 2008; Wetmore et al., 2009) emanating from the main intrusion (Fig. 3.9). There is a distinct lack of Phase 2B faults in the vicinity of eastern transect (TMTE; Fig. 3.11). This may be due to the style of emplacement in this area.

3.4.3. *Deformation Structures at the Intrusion Contact*

Deformation microstructures within the sheared upper contact of the intrusion show predominantly brittle, and to a lesser extent brittle-ductile, deformation structures (Figs 3.12 & 3.13). At the tip and frontal edge of the intrusion contact, sub-vertical fractures and shear bands (with down-to-the-NW kinematics) may be seen (Fig. 3.12a, d). Similar to those observed at outcrop, stepped/ staircase intrusion geometries are observed at the micro scale, with steps appearing to be associated with sub-vertical shear-fractures within the host rock (Fig. 3.12a). These fractures do not appear to extend into the intrusion and are therefore likely to be linked to the emplacement of the magma. Furthermore, magma can also be seen exploiting these sub-vertical shear-fractures (Fig. 3.12b).

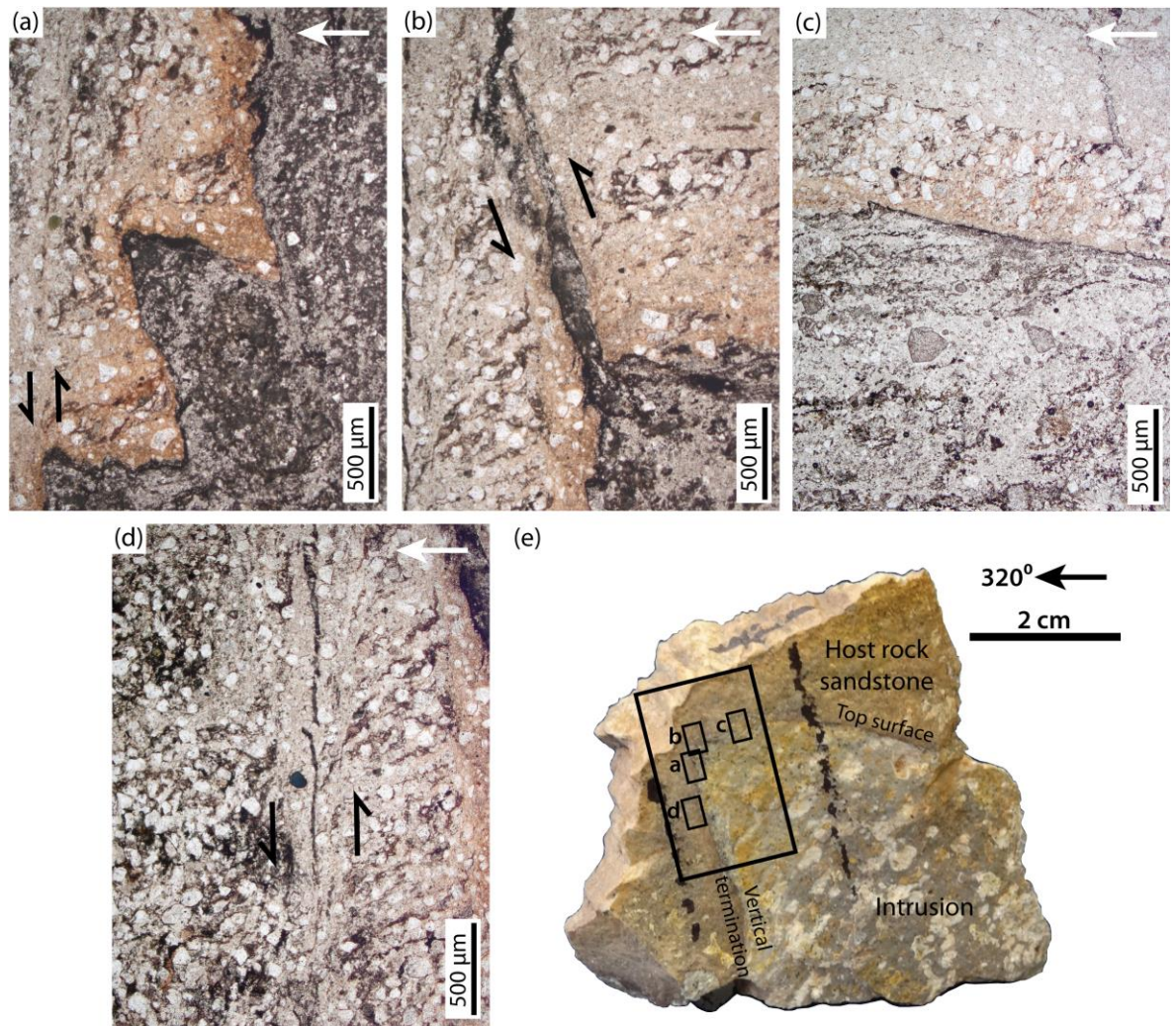


Figure 3.12. Photomicrographs of microstructures observed at the intrusion–sandstone contact. (a) Stepped vertical contact at the tip of an intrusive sill sheet. (b) Magma injecting upwards along an extensional fracture. (c) Top surface of intrusion showing sharp contact and narrow altered margin. (d) Sub-vertical fracture within host rock adjacent to contact, showing down-to-the-NW movement. (e) Oriented sample highlighting area of thin section and location of images (a)–(d).

Further deformation structures can be found on the top surface of the intrusion. Where the contact between intrusive sheets and the host rock can be observed, three distinct layers can be defined (Fig. 3.13): (1) a 5–10 cm thick baked sandstone layer; (2) a <1 cm thick chilled intrusion margin; and (3) a 1–2 cm zone of aligned (NW–SE) stretched plagioclase phenocrysts, beneath which mineral alignment decreases significantly. Low-angle fracture planes bisect the baked sandstone horizon (Fig. 3.13a) but do not appear to extend into the intrusion. These fracture planes trend parallel to the intrusion margin (NE–SW), and dip shallowly ($\sim 20^\circ$) to the SE (Fig. 3.13a). Slickenlines are preserved on the shear planes in the baked sandstone horizon of the intrusion–host rock contact, showing down-to-the-SE kinematics.

These structures are interpreted to be Riedel shear (R_1) fractures consistent with a top-to-the-SE shear sense. Microstructural analysis of the stretched feldspar phenocrysts on the top surface of the intrusive sill sheets (Fig. 3.13b) indicates significant brittle deformation with shearing of the phenocrysts along multiple fracture planes (Fig. 3.13c, d). Kinematics of these fracture planes are also consistent with Riedel shear fractures associated with top-to-the-SE (140°) shear (Fig. 3.13d–f).

3.5. Kinematics

Kinematic indicators on Phase 2B dip-slip faults include offsets of bedding plane markers, and steps on slickenlines preserved on fault surfaces (Figs 3.4g, 3.8 & 3.9). The dip-slip faults record both normal and reverse shear sense, with a predominant down-to-the-NW movement, consistent with an overall NW–SE extension or flexure across the margin of the intrusion (Fig. 3.8c–e). Sense of slip on Phase 2A deformation bands mirrors the kinematics of the Phase 2B faults (Fig. 3.8a, b), although they are distributed more widely across the intrusion margin. Conjugate sets of extensional deformation bands commonly have an inclined acute bisector axis, consistent with either an original moderately inclined σ_3 axis dipping towards the NW, or alternatively rotation about a broadly horizontal axis post-formation. In either case, the Phase 2B fault kinematics are consistent with accommodation of down-to-the-NW extension and rotation.

Strain inversion has been carried out following the Minimized Principal Stress Variation method developed by Reches (1987) using MyFault™ software. This method assumes that the stress required to cause fault slip obeys a Coulomb yield criterion. It is reasonable to use such an approach as the overall finite strains recorded here are low, meaning that any rotations of stress axes will be relatively minor (e.g. De Paola et al. 2005). Figure 3.9 shows the bulk inversion for all Phase 2B faults (Fig. 3.9b), as well as each individual structural station where faults were observed (Fig. 3.9c). However, it should be noted that significant populations of dip-slip faults were only observed at a limited number of locations (TMTW-3, TMT3-3, TMT3-4, Fig. 3.9). Bulk inversion suggests that the main stress acting on these faults was extensional (i.e. sub-vertical σ_1), with NW–SE (margin perpendicular) oriented extension. Inclination of the stress axes also reflects the flexural component of this extension ($\sigma_3 = 338/20$; $\sigma_1 = 160/70$), with extension inclined down

towards the NW. Comparisons of the strain inversion at individual structural stations highlight distinct local variations. Spatial variation is observed in the orientation of dip-slip faults, and the kinematic inversion of these individual fault populations reveals a change in the local extensional strain along the intrusion margin (extension varying from NW–SE to NNE–SSW; Fig. 3.9c). Local variations appear to reflect changes in the stress field, mimicking changes in the orientation of the intrusion margin.

3.6. Discussion

3.6.1. Deformation Phases (*pre-, syn-, and late-stage emplacement*)

The three distinct deformation phases (Table 1) identified on the north-western margin of the Trachyte Mesa intrusion may be directly linked to specific stages in an emplacement model (pre- Phase 1, syn- Phase 2A and 2B, and late-stage- Phase 3 emplacement).

Figure 3.13. (*overleaf*)

Flow generated fabrics at the intrusion margin. (a) Outcrop photograph showing low-angle brittle extensional faults (see inset stereoplot) cutting baked sandstone unit on top surface of an intrusive sheet. These are interpreted to be equivalent to R_1 Riedel shear planes, depicted in (d). The faults are only apparent in the baked sandstone and appear to terminate at the intrusion–host rock interface. (b) Stretched plagioclase phenocrysts within a strongly sub-horizontal foliated zone (2–3 cm) on the top surface of an intrusive sheet. Note also the thin (<1 cm) chilled margin zone above the stretched phenocryst/foliated layer. (c) Photograph of thin section across sheared intrusion top surface. (d) Photomicrograph of deformed, elongate plagioclase phenocryst within the uppermost 2–3 cm of an intrusive sheet (note section is cut along a vertical plane oriented parallel to the stretching direction, 140°–320°). The phenocryst is deformed mainly by brittle deformation and a series of preferred deformation planes, with offset, can be identified. The movement and orientation of these planes are consistent with Riedel fractures associated with top-to-the-right (SE) sub-horizontal shear. (e) Diagram illustrating incremental strain associated with simple-shear deformation. Image on left shows initial configuration of Riedel shear fractures, while image on right shows orientations after continued simple shear and flattening (20% pure shear). Note clockwise rotation of fractures. (f) Schematic cartoon depicting the deformation structures observed at outcrop and in thin section on the top surface of an intrusive sheet. The structures and kinematics are consistent with top-to-the-SE sub-horizontal shear. This shearing is likely driven by magmatic flow within the underlying sheet, leading to sub-horizontal shortening and shear at the intrusion contact.

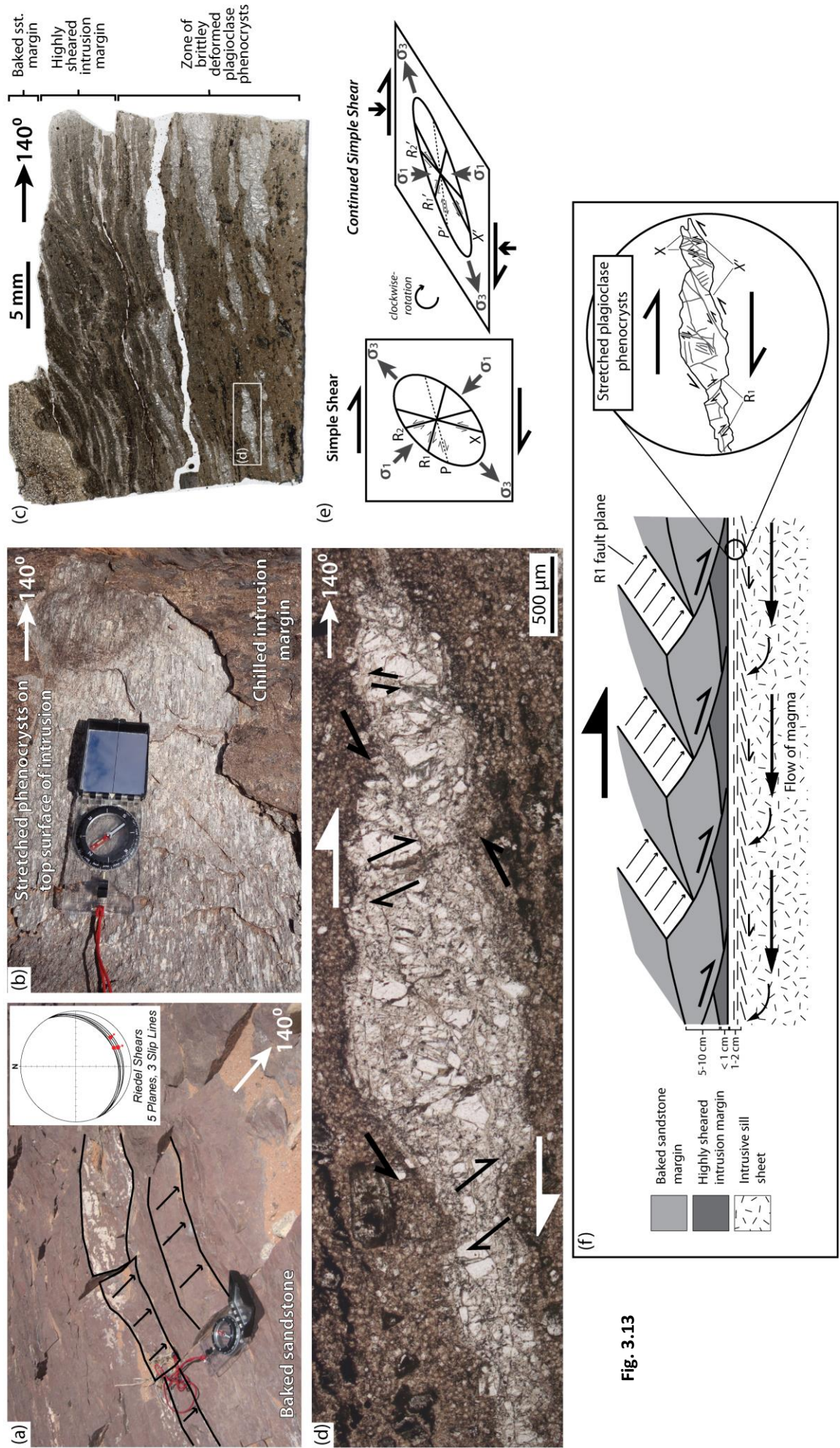


Fig. 3.13

3.6.1.1. Phase 1 – Pre-emplacement Deformation

Phase 1 deformation structures are found throughout the Trachyte Mesa area, including regions that are significantly distal to the intrusion (Figs 3.11 & 3.12). As Phase 1 structures do not show any significant spatial or geometric affinity to the Trachyte Mesa intrusion, we suggest that these are likely to have developed prior to emplacement. This is also supported by the consistent cross-cutting relationship observed in the field (i.e. Phase 2 overprinting Phase 1; Fig. 3.7b).

Phase 1 deformation structures could be attributed to one or more of a number of late Cretaceous to early Tertiary Laramide uplift deformation events (including the San Rafael Swell, Uncompahgre, Monument, Kaibab, Circle Cliffs, and Miners Mountain uplifts) which resulted in the formation of a series of asymmetrical anticlines (Fig. 2.10 in Chapter 2; Bump & Davis, 2003), prior to the emplacement of the Trachyte Mesa intrusion. Phase 1 deformation structures appear to have a preferred ENE–WSW trend, although regional analysis reveals a wider spread of orientations (this study, see regional structural data and stereoplots in Appendices; Bump & Davis, 2003), which imply a complicated pre-intrusion deformation history, or that early deformation in the sedimentary cover may have been controlled locally by underlying basement trends (Bump & Davis, 2003).

3.6.1.2. Phase 2 – Syn-emplacement Deformation

Strong spatial, geometric and kinematic relationships between the Phase 2 structures and the intrusion margin lead to the interpretation that this deformation is related to the emplacement of the Trachyte Mesa intrusion (cf. Morgan et al., 2008). The relative timings of Phase 2 deformation structures may be further refined through their cross-cutting relationships: Phase 2B faults and ladder zones overprint the more widespread 2A deformation bands. We suggest that this is a result of strain localisation within the overburden during vertical inflation of the underlying sill sheet. The observed monoclinial geometry, and distribution and style of deformation, matches closely to mechanical models of steeply dipping forced folds (Withjack et al., 1990; Johnson & Johnson, 2002). As outlined for the western transect (TMTW; Fig. 3.10), Phases 2A and 2B deformation appear to alternate across each individual sill sheet termination. We therefore interpret this to indicate that this 2A–2B strain localisation may be related to the emplacement of each individual sheet rather than the overall intrusion.

3.6.1.3. Phase 3 – Late-stage Emplacement Deformation

Phase 3 tensile (Mode 1; Price, 1966) joints consistently overprint all other structures in the study area. Phase 3 tensile joints are interpreted to represent late-stage emplacement deformation, rather than post-emplacement deformation. The joints are most likely associated with deflation of the host rocks as the magma body beneath cooled, crystallised and contracted. During vertical inflation of the intrusive sill sheets and overall intrusion, vertical stresses are exerted on the overriding strata. Following cessation of magma flow and contraction of the sheets, this stress is removed, and the overriding host rocks relax and tensile joints (relaxation cooling joints) open. This origin for the Phase 3 joints fits with their wide spatial distribution over the intrusion, in contrast to the Phase 2B faults, which are localised around sill sheet terminations. A late-stage emplacement timing for the formation of the joints, rather than post-emplacement, is supported by the presence of calcite crystals on the joint surface (Fig. 3.5g) and ‘flame-like’, magma and hydrothermal fluid escape structures (Fig. 3.5h) observed on the top surface of some intrusive sheets, suggesting that these joint sets must have developed while hydrothermal fluids associated with the intrusion were still circulating.

3.6.2. Modes of Emplacement

Davis (1925) first proposed a model for a proto-laccolith spreading to its full lateral extent as a thin sheet before vertical inflation. Hunt (1953) proposed two end-member models (“bulldozing” and “two-stage growth”) for laccolith emplacement and growth from a central feeder system. In his general description of the emplacement and growth of laccoliths, Corry (1988) clearly favoured a “two stage growth” model (i.e. radial growth to full lateral extent, followed by vertical growth) and stated that there is no reported field evidence for the remnant hinge zones expected for a radial growth model. Koch et al. (1981), Jackson and Pollard (1988, 1990), Kerr and Pollard (1998), Galland et al. (2009), and others have suggested that the radial extent of the intrusion may be controlled by the effective thickness of the overburden and the elastic properties of the overlying sandstone. However, as discussed by Corry (1988), other factors such as magma viscosity, strain rate and sheet thickness should also be considered. Although the models of Hunt

(1953) and Corry (1988) refer to the emplacement and growth of laccoliths, the concepts are just as applicable to a small sill sheet as they are for larger tabular intrusive bodies.

Corry (1988) made predictions on the likely deformation associated with Hunt's (1953) emplacement models, suggesting that deformation associated with a "bulldozing mechanism" (i.e. radial growth of a full thickness intrusive body) will likely be more complex and distributed than in the "two-stage growth" model. As magma "bulldozes" its way through the host rock, it leaves in its wake a series of remnant deformation "hinge zones" that reflect the propagating deformation front. In contrast, with a "two-stage growth" model, most of the deformation is localised within the high-strain hinge zones at the lateral termination. This is because only minor deformation occurs with the initial radial growth of a thin sheet, and more intense strain developing during the secondary inflation/ vertical growth stage.

The kinematics and spatial distribution of these deformation structures may therefore be closely related to the mode of emplacement. Thus deformation is either focused in the area around the periphery of an intrusion, and is less pronounced in the roof zone above the intrusion (Corry, 1988), or, as in the classic beam-bending model for a domal intrusion (Pollard & Johnson, 1973; Kerr & Pollard, 1998), tensile deformation is likely to be distributed across the wider roof area due to flexure. Corry (1988) also suggested that deformation/ accommodation structures associated with a "bulldozing mechanism" for emplacement are likely to be compression-dominated.

At Trachyte Mesa, this study has demonstrated that the host-rock deformation structures are strongly localised in the region at the lateral margin of the intrusion, an observation that confirms previous studies of others (Koch et al., 1981; Corry, 1988; Morgan et al., 2008). Although thermal alteration and compaction are apparent in host-rock exposures on the roof of the intrusion, brittle deformation structures such as those described herein on the NW margin are not observed above the intrusion. This, and the fact that there is no evidence for remnant hinge zones formed by an outward propagating intrusion margin, would suggest that Trachyte Mesa is likely to have formed by "two-stage" growth. The term "punched laccolith" (first used by Gilbert, 1877) has been used to describe relatively flat-topped tabular intrusions, a common characteristic of many laccoliths (including Trachyte Mesa; Morgan et al., 2008), which have formed through

two-stage growth. In contrast, extension-dominated deformation and accommodation structures are predicted to occur with a “two-stage”/ incremental vertical growth mechanism. As all of the emplacement-related deformation structures observed in this study reflect overall extensional strain, our model for emplacement clearly favours the “two-stage” emplacement mechanism.

Morgan et al. (2008) proposed an incremental growth model for the Trachyte Mesa intrusion, through vertical and horizontal growth by the accumulation of multiple horizontal magma sheets. Their emplacement model has strong similarities to the hybrid case of Corry (1988), as both include vertical stacking and lateral sheet propagation (and an outward propagating hinge). In their model, a series of stacked sill sheets are emplaced, with newer sheets emplaced on top of older. This vertical stacking leads to uplift and monoclinial bending of the overlying sandstone units, while in front of the sill sheet terminations a low-pressure triangular zone develops. Key to the development of this low-pressure zone is the contrasting rock properties of the thinly bedded shaley units (i.e. more deformable) along which the sills are emplaced, and the mechanically strong (and more resistant to bending) overlying massive sandstones (e.g. Fig. 3.2d). It is envisaged that tongue-like magma sheets would then fill this low-pressure zone, with this process subsequently leading to lateral propagation of the intrusion (and also the outward propagation of a deformation hinge).

The observations presented here are consistent with an incremental, “stacked sill sheet” growth model for the overall intrusion (cf. Morgan et al., 2008). However, in contrast to that interpretation, evidence for a “two stage” incremental growth mechanism is observed for the emplacement of individual sheets. Furthermore, although contrasting styles of deformation may be observed in the shaley and more massive red sandstone host rock units, no strong evidence exists for incremental lateral sill propagation. Instead we envisage that individual sill sheets were emplaced close to their full radial extent as thin sheets that then vertically inflated through additional magma influx.

3.6.3. Emplacement and Structural Evolution

Based on the work of previous authors (Corry, 1988; Morgan et al., 2008) and our new field observations of intrusion geometries and deformation structures on the NW margin,

a new multistage model for the emplacement of Trachyte Mesa intrusion is proposed. This emplacement model is shown in Figure 3.14 and discussed in the following sections.

3.6.3.1. Stage 1 - Onset of Sheet Emplacement and Radial Growth of a Thin “proto-sill” Sheet

A magma feeder system propagated vertically through the sedimentary pile until it reached a suitable interval for a horizontal sheet to propagate laterally. In the case of Trachyte Mesa this is a thin, mechanically weak, reddish-brown silty sandstone and shale layer occurring between thicker, massive sandstone units (Fig. 3.5b; Morgan et al., 2008). The “proto-sill” propagated as a thin sheet, with minor inflation, to its maximum lateral extent (Fig. 3.14). In contrast, Morgan et al. (2008) suggested that lateral sill propagation and thickening may have been episodic [i.e. similar to the hybrid model of Hunt (1953) and Corry (1988)]. However, the lack of observable remnant deformation hinge zones on the roof of the intrusion (and others like it; Corry, 1988) favours propagation of a thin proto-sill sheet rather than one with significant inflation. The lateral extent of the sill was likely governed by viscosity of the magma and the properties of the host rock (Thomson & Schofield, 2008).

Figure 3.14. (overleaf)

Schematic diagram outlining a two-stage growth model for sill emplacement at the Trachyte Mesa intrusion and associated deformation structures. (a) Conventional stacking model (as observed at TMTW study area; Fig. 3.10). Stages of emplacement, as discussed in text, are: Stage 1 – Sill initiation and radial growth as a thin “proto-“ sill sheet; Stage 2 – Thickening of the sill sheet, resulting in roof uplift and strain localisation in the host rock at the sill sheet termination; Stage 3 – Emplacement of a second sill sheet (repetition of stages 1 and 2 for 2nd sheet); Stage 4 – Sill climbing through the exploitation of faults developed during Stage 2; Stage 5 – Sill flattening (not observed at Trachyte Mesa) and late stage cooling and relaxation of the intrusion. (b) Schematic illustration highlighting the impact of out-of-sequence stacking (equivalent to Stage 2 in (a)) on margin geometry and deformation structures (as observed in TMTE study area; Fig. 3.11).

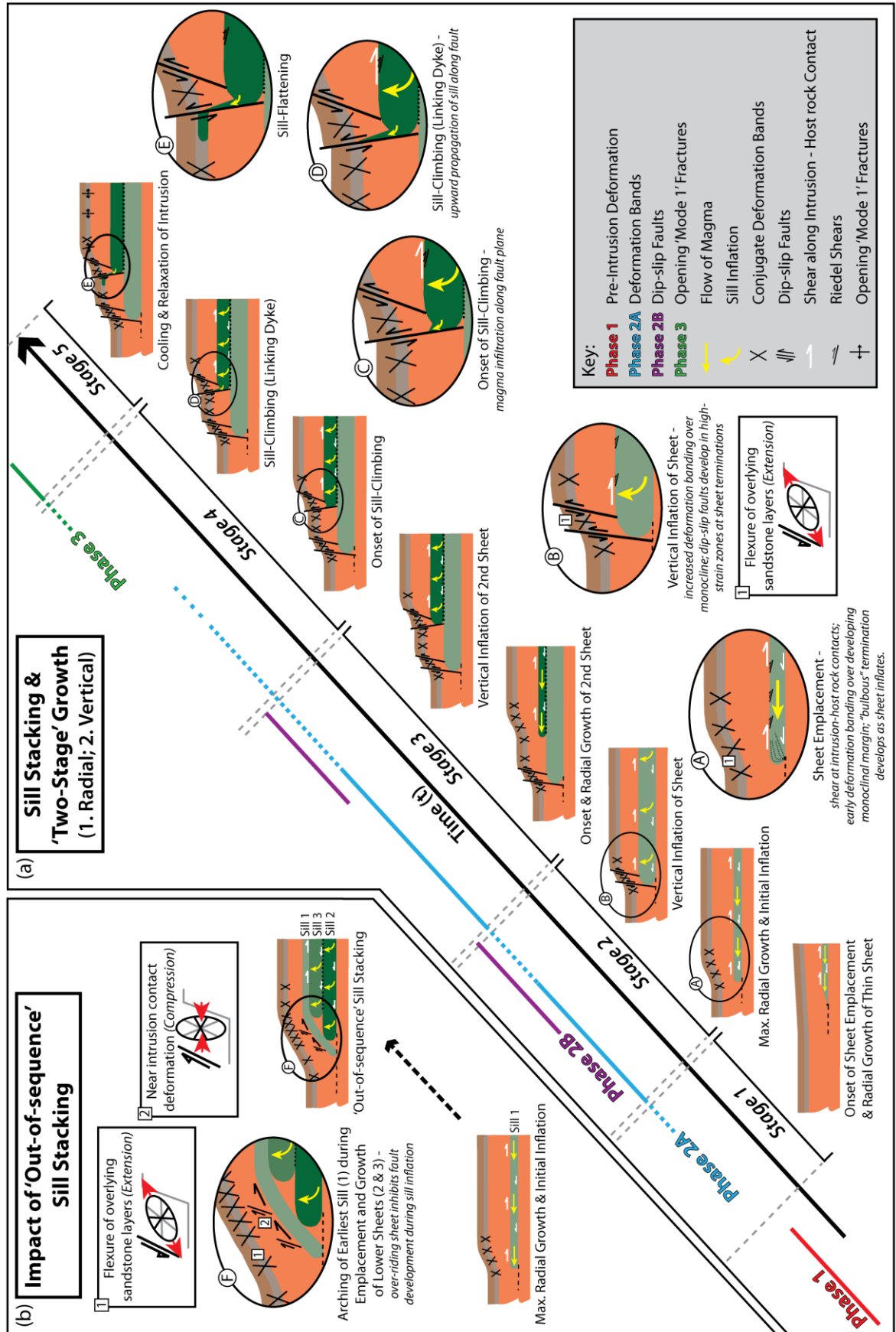


Fig. 3.14

Deformation associated with this early emplacement is likely to have been minor, and dominated by shear at the proto-sill sheet contacts (e.g. stretched plagioclase feldspars; Fig. 3.13). As magma flowed in a NE direction, spreading out radially to the NW and SE, shear zones developed on the top and base surfaces of the intrusion and its contact with the surrounding host rock. These shear structures show both brittle and plastic deformation characteristics due to the effects of hot magma being emplaced into a cold host rock. Vergence on these shear structures is opposite to the flow direction of the magma sheet (i.e. on the NW margin, top-to-the-SE-verging shear fabrics occur on the top surface of the intrusion). These shear fabrics may be seen both at outcrop and in thin section (Fig. 3.13), and have also been defined by AMS (Anisotropy of Magnetic Susceptibility) studies (Morgan et al., 2008). Shear at the intrusion margin is likely to be the first accommodating structure related to the onset of sheet emplacement.

3.6.3.2. Stage 2 - Vertical Inflation of Sill Sheet

Once the magma had reached its maximum radial extent, vertical inflation commenced as magma supply continued. The thickness of the sill will be governed by the thickness of the overburden (i.e. lithostatic pressure) and the magma pressure (Corry, 1988; Thomson & Schofield, 2008). Thickening of the sill sheet resulted in roof uplift and deformation (e.g. fractures and deformation bands associated with forced folding and flexural bending) of the overlying strata (Sterns, 1978; Cosgrove & Hiller, 1999; Galland et al., 2009; Magee et al., 2014). This is manifest as conjugate sets of extensional cataclastic deformation band structures (Phase 2A; Figs 3.4, 3.5, 3.6 & 3.8), formed in the overlying massive sandstone beds, localised to the developing lateral margin, increasing in intensity around the monoclinial flank above the sill termination (Figs 3.10, 3.11 & 3.14). This is consistent with extensional deformation structures forming in the outer arc areas of monoclinial flexural folds, while we might expect contractional structures to predominate on the inner arc areas (Frehner, 2011). This extension and contraction in the outer and inner arcs respectively may help to explain the observation that deformation within the blocky sandstone unit is predominantly extensional, while in the more shaley unit at the intrusion contact reverse faults are apparent (Fig. 3.5b, and also noted by Morgan et al., 2008).

Although lateral propagation of the sill is likely to have ceased during this inflation phase of emplacement, shear structures still continued to develop on the top surface of the intrusion as magma flowed along the sill. Figure 3.13 shows examples of shear structures on the intrusion top surface (and overlying baked sandstone). As these brittle structures clearly deform the already cooled rock, this shear deformation is post initial emplacement. However, in order to accommodate the additional volume of magma, shear strain on the top surface will have become dominated by flattening (vertical shortening). This is apparent in the stretching and flattening of plagioclase crystals within the upper 2-5cm of the sill sheet (Fig. 3.13c, d). As vertical inflation continued, strain becomes localised at the sill sheet termination resulting in the formation of Phase 2B structures (Figs 3.8, 3.9 & 3.14). This strain localisation led to the development of steep deformation corridors cross-cutting earlier conjugate deformation bands (Fig. 3.8c) and eventually the development of principal slip surfaces and ultimately dip-slip faults (Figs 3.8, 3.9 & 3.14). These Phase 2B dip-slip faults observed at Trachyte Mesa therefore played a significant role in accommodating the extra volume of magma within the crust.

In the emplacement model of Morgan et al. (2008), sill sheets intruded along a thinly bedded muddy red sandstone and shale unit as full thickness (~1–5 m thickness) tongue-shaped sheets with “bulbous” terminations. A temporary zone of low-pressure was created in front of the intrusion margin as the angle between the stronger massive red sandstone and the weaker silty sandstone and shale unit beneath increased during vertical growth of the intrusion through the accumulation of stacked sheets. In this scenario, magma pressure exceeds lithostatic load, and tongue-like sheets, fed from the stacked sheets, fill the zone of low-pressure, continuing lateral propagation of the intrusion. However, this explanation is inconsistent with the structural evidence, as a zone of low-pressure is unlikely to develop where normal faults accommodate the strain. Instead, it is suggested here that the smooth, curved nature of the “bulbous” sill sheet terminations (Fig. 3.3a) are the result of inflation (akin to that of the rounded surface of a balloon; Fig. 3.14a). Had this rounded geometry formed during the sill propagation, we might expect to see more evidence for magma infiltrating the host rock in front of the intrusion, rather than the presence of sheared, steeply-dipping, shaley red sandstone.

Smart et al. (2010) modelled the strain distribution of monoclinaly deformed beds overlying a steeply dipping extensional fault. In their finite element model, Smart et al.

(2010) noted the outer and inner arc strain domains discussed above (e.g. Frehner, 2011) within the overlying folded units, and also identified a zone of high sub-horizontal extensional strain within the footwall block (see fig. 11 in Smart et al., 2010). This local extensional strain domain may provide a mechanism for the “ballooning” inflation at the sill tip to form the observed bulbous terminations. In contrast, formation of extensional faults at the sill tips will impede the development of bulbous terminations as this extensional strain will be accommodated by fault extension. This model is supported by the observation that sill sheets with a bulbous character show little evidence for fault development (Morgan et al., 2008), while those with faults at their tips do not exhibit bulbous terminations (e.g. Fig. 3.3c; this study).

3.6.3.3. Stage 3 - Emplacement of Additional Sill Sheets

Successive sheets were emplaced through the same two-stage emplacement (i.e. radial followed by vertical growth) as for the first sill sheet. Along the western transect (TMTW; Fig. 3.10), the sequence of sill sheet stacking largely appears to have occurred from the bottom of the intrusion upwards, as each successive sill sheet was emplaced on top of the underlying sheet, and hence creating a ‘Christmas-tree’-type laccolith. However, the sequence and level at which successive sheets were emplaced varies significantly (the impact of out-of-sequence stacking is discussed below).

3.6.3.4. Stage 4 - Onset of Sill-Climbing (transgression)

Following the formation of Phase 2B faults during the vertical inflation stage, magma was able to utilise these faults and sill-climbing commenced (Figs 3.14 & 3.15; Thomson & Schofield, 2008). If the fault plane was able to open, magma was able to propagate along the fault (Figs 3.3b, 3.14 & 3.15). At Trachyte Mesa, examples of sill climbing can be observed at both outcrop (Fig. 3.3b) and in thin section (Fig. 3.12b). This sill climbing preferentially exploited reverse dip-slip faults (Figs 3.3b & 3.15). There are two likely reasons for the magma preferentially exploiting these faults. The first is that the geometry of the reverse faults, dipping towards the sill termination, allowed the magma to continue its outward radial flow up along the fault plane and up through the host stratigraphy. However, probably the most important factor controlling sill climbing along these faults is the stresses induced on the fault due to roof uplift (Fig. 3.15). If the Phase

2B faults have a normal geometry (i.e. dipping away from the sill sheet), vertical compressive stress associated with uplift of the underlying footwall block (i.e. vertical inflation of sill sheet) will keep the plane closed and prevent migration of magma along its path (Fig. 3.15). In contrast, if the fault has a reverse geometry (i.e. dipping towards the sill sheet) uplift of the hangingwall block reduces the vertical effective stress, thus enabling magma to exploit the fault plane (Fig. 3.15).

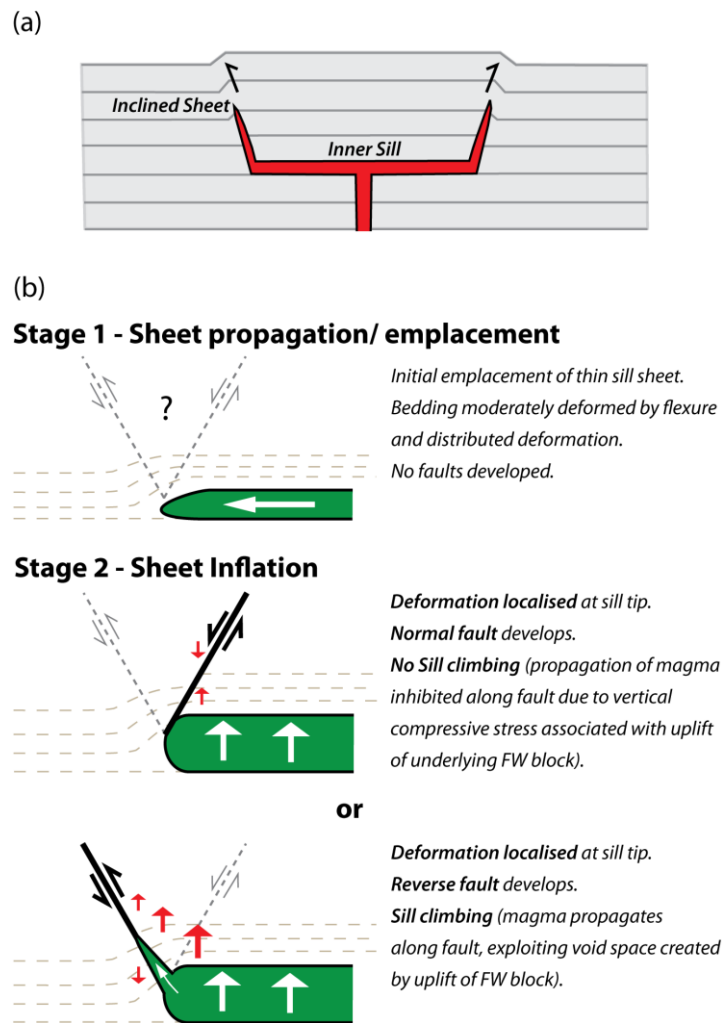


Figure 3.15. Faulting accompanying sill emplacement. (a) Schematic diagram showing the development of a saucer-shaped sill (after Galland et al., 2009). (b) Development of dip-slip faults at sill tips during two-stage growth model and implications for sill climbing and vertical propagation.

3.6.3.5. Stage 5 - Cooling and Relaxation of Intrusion

As the intrusive sheets (and overall intrusive body) started to cool and contract with the cessation of magma flow, the host rocks above also relaxed. During this relaxation of the overriding strata, and the removal of the vertical compressive stresses that had been exerted on the overlying sediments during vertical inflation of the intrusive sheets, tensile

joints formed and opened, allowing magma and hydrothermal fluids to circulate (Figs 3.5g, h & 3.14).

3.6.4. Sequence of Stacking

The sequence in which intrusive sill sheets are stacked plays a significant role in the resulting geometry of the intrusion and the overlying stratigraphy, as well as the types of deformation structures observed in the host rocks. In the two structural transects carried out here (Figs 3.2, 3.10 & 3.11), two contrasting styles of intrusion geometry are observed that appear to be the result of different orders of sill stacking. On the western transect, the margin of the intrusion is characterised by a series of sub-horizontal sill sheets of varying thickness (0.5–3 m) stacked one on top of the other (Fig. 3.10). This conventional stacking sequence would be consistent with the order of stacking discussed above and outlined in Figure 3.14a. In contrast, on the eastern transect the order of sill stacking appears out-of-sequence. As discussed by Morgan et al. (2008) and highlighted in Figure 3.11b, it appears that the lower sub-horizontal sheets were actually emplaced later than upper sheets (under- and/ or mid-accretion of Menand, 2008). The main evidence for this out-of-sequence stacking is the fact that the upper sill sheets have been arched and rotated upwards in a similar monoclinial geometry to the overlying sandstone beds due to the emplacement of sub-horizontal sheets beneath. Not only does the sequence of stacking affect the geometry of the intrusion, it also has a significant impact on the style of deformation occurring in the overriding host rock (compare Figs 3.10 and 3.11). In a sequentially stacked sequence (e.g. TMTW; Fig. 3.10) a “stepped” bedding profile is developed (i.e. terraces associated with individual sill sheets), and dip-slip faults (Phase 2B) occur at the tips of successive intrusive sheets. In areas where out-of-sequence emplacement is apparent (e.g. TMTE; Fig. 3.11), the intrusion margin is distinctly monoclinial (i.e. one single step), and due to the presence of the overriding sill sheets, development of Phase 2B faults is inhibited (Fig. 3.14b). Close to the intrusion contact, compressional deformation structures including small reverse faults are observed, although in the more competent sandstone beds extension-dominated deformation structures still prevail (Fig. 3.5b).

3.6.5. Faulting at sill terminations

A significant observation from this study, previously undocumented at Trachyte Mesa, is the presence of dip-slip faults associated with individual sill terminations (i.e. Phase 2B structures). Thomson and Schofield (2008) suggested that the main control on the development of faults at sill sheets terminations is the depth of formation. At shallower depths, cohesive strength along bedding planes is less, and so favours the development of flexural slip folding. As depth increases, higher shear stresses are required for flexural slip, thus favouring mechanical failure of the rock through fracture/ faulting (Stearns, 1978). The overburden thickness estimated for the Trachyte Mesa by Hintze and Kowallis (2009) suggests that the Entrada Sandstone would have been at a paleodepth of ~3 km at the time of magma emplacement, therefore placing it within the brittle zone (as defined by Schofield et al., 2012).

Pollard and Johnson (1973) presented a conceptual model for the formation of peripheral dykes located at the tips of laccolith bodies from field observations. It was suggested that the dykes formed at the periphery of the intrusions as a result of flexural/ elastic bending of the overburden layers (contractional over the centre and extensional over the periphery). Evidence for sill-climbing at Trachyte Mesa is in agreement with such extensional strain at the periphery. However, instead of the strain being accommodated by simple tensile joints, it is proposed that it was the Phase 2B faults that were exploited by the magma (Fig. 3.3b). Sill climbing associated with the exploitation of peripheral faults is likely to play a significant role in the development of saucer-shaped sills (Fig. 3.15; Galland et al., 2009).

3.7. Conclusions

Trachyte Mesa intrusion, the most distal satellite intrusion of the Mount Hillers intrusive complex in the Henry Mountains Utah, comprises a series of stacked sill sheets. Deformation structures (geometry, kinematics, and spatial distribution) associated with the emplacement of the intrusion vary in style and intensity along the intrusion margin. Detailed analysis of the host rock deformation structures and their cross-cutting relationships enables the recognition of three distinct phases, interpreted to represent pre- (Phase 1), syn- (Phase 2), and late-stage (Phase 3) emplacement deformation stages. Spatial and kinematic association of Phase 2 structures (deformation bands and dip-slip

faults) indicate extensional strain normal to the intrusion margin during emplacement, with the inclination of the σ_3 axis reflecting the flexural nature of the margin.

The preferred emplacement model of a series of stacked sill sheets is in agreement with previous studies (Morgan et al., 2008), but a different mechanism for the emplacement of individual sill sheets is envisaged in which dip-slip faults accommodate sill inflation/vertical growth. All emplacement-related deformation structures observed reflect extensional strain-dominated deformation. Each individual sill sheet is believed to have grown to its maximum radial extent as a thin sheet, and then in a second stage, to inflate vertically to its present thickness. It is likely that most deformation of the host rock took place during this second stage, with faults developing at the sill terminations due to strain localisation.

Magma preferentially exploited the faults that developed at the periphery of sill sheets, initiating sill climbing. Extensional roof faulting and sill climbing support a two-stage growth history for the overall intrusion. These observations are consistent with theoretical models of sill emplacement (e.g. Pollard & Johnson, 1973; Koch et al., 1981; Thomson & Schofield, 2008).

The order in which sill sheets are stacked has impacted on the intrusion geometry and associated deformation. In conventionally stacked sequences (i.e. base upwards) a “stepped”/ terraced bedding profile develops, with the presence of dip-slip faults localised at the tips of successive intrusive sheets. By contrast, where intrusive sheets are emplaced beneath earlier intruded sheets (i.e. out-of-sequence stacking), the resulting intrusion and host rock geometries and emplacement-related deformation structures are significantly different, having a monoclinical rather than stepped profile, with no dip-slip faults at sill terminations.

Not only do the deformation structures record the strain evolution, and thus mode of emplacement of the intrusion, they also controlled the subsequent propagation of the intrusive body (e.g. in the form of sill climbing). These observations provide new insights on the emplacement mechanisms of sills and laccoliths, how magma is accommodated in the subsurface, and how emplacement of high-level intrusions can affect sedimentary host rocks. Furthermore, the structural similarities we observe at multiple scales (i.e. thin

section, individual intrusive sheets and the overall intrusion) may reflect a scale-invariance which may make our models applicable to larger-scale intrusions (i.e. laccoliths and plutons; cf. Rocchi et al., 2002).



4. Chapter 4: Fracture analysis of deformation structures associated with the Trachyte Mesa intrusion, Henry Mountains, Utah: implications for reservoir connectivity and fluid flow around sill intrusions.

| | | | |
|----------------|---------------|--|---------------|
| <i>Layout:</i> | 4.1. | Introduction | p. 151 |
| | 4.2. | Geological Setting | p. 153 |
| | 4.2.1. | <i>Trachyte Mesa Intrusion</i> | p. 154 |
| | 4.2.2. | <i>The Entrada Sandstone Formation</i> | p. 154 |
| | 4.3. | Study zone, sampling and analysis methods | p. 155 |
| | 4.3.1. | <i>Outcrop traverse</i> | p. 159 |
| | 4.3.2. | <i>Fracture analysis methods</i> | p. 160 |
| | 4.3.2.1. | <i>Fracture network map</i> | p. 160 |
| | 4.3.2.2. | <i>Measuring lengths and quantities</i> | p.160 |
| | 4.3.2.3. | <i>Node counting</i> | p.160 |
| | 4.3.3. | <i>Sample collection</i> | p. 162 |
| | 4.4. | Results | p. 164 |
| | 4.4.1. | <i>Outcrop fracture analysis</i> | p. 164 |
| | 4.4.2. | <i>Hand specimens</i> | p. 172 |
| | 4.4.3. | <i>Thin section analysis</i> | p. 173 |
| | 4.4.3.1. | <i>Sample TMFS-1</i> | p. 173 |
| | 4.4.3.2. | <i>Sample TMFS-2</i> | p. 173 |
| | 4.4.3.3. | <i>Sample TMFS-3</i> | p. 176 |
| | 4.4.3.4. | <i>Sample TMFS-4</i> | p. 176 |
| | 4.4.3.5. | <i>Sample TMFS-5</i> | p. 176 |
| | 4.4.3.6. | <i>Sample TMFS-6</i> | p. 177 |
| | 4.5. | Interpretations and Discussion | p. 178 |
| | 4.5.1. | <i>Fracture intensity and Topology variations across margin</i> | p. 178 |
| | 4.5.2. | <i>Microstructural interpretations</i> | p. 181 |
| | 4.5.3. | <i>Wider implications</i> | p. 182 |
| | 4.6. | Conclusions | p. 183 |

Fracture analysis of deformation structures associated with the Trachyte Mesa intrusion, Henry Mountains, Utah: implications for reservoir connectivity and fluid flow around sill intrusions.

This chapter is written for submission to Petroleum Geoscience

Co-Authors: Penelope I.R. Wilson, Robert. W. Wilson, David J. Sanderson, Ken J.W. McCaffrey, Ian Jarvis*

*(*note: all scientific work was undertaken by the student/ principal author P. Wilson, and input from co-authors on this work was at an advisory/ editorial level only)*

Abstract

Shallow level intrusions are a common feature of many basins currently being explored for hydrocarbon potential. However the sub-seismic structure and reservoir scale implications of igneous intrusions are poorly understood. The Trachyte Mesa intrusion is a small (~1.5 km²), NE–SW trending satellite intrusion to the Mount Hillers intrusive complex in the Henry Mountains, Utah. It is emplaced within the highly porous, aeolian Entrada Sandstone Formation. A conjugate set of NE–SW striking deformation bands trend parallel to the intrusion margins. A small study of fracture connectivity has been carried out at 6 sample stations along a ~100 m long, NW–SE trending transect across the north-western lateral intrusion margin. Following the methodology of Sanderson and Nixon (2015), this chapter presents results of various fracture network characteristics, including: total number of fractures (and branch lines); total fracture (branch) length; frequency; density (intensity); spacing; characteristic fracture length; and dimensionless intensity. Nodal analyses were also applied to the sample areas. These quantitative fracture studies are supplemented with petrological, porosity and microstructural analyses. Results show a marked increase in deformation band intensity and significant porosity reduction with proximity to the intrusion. These deformation bands are likely to impede fluid flow, and potentially form baffles in a reservoir. A corresponding increase in Y- and X- nodes highlights the significant increase in deformation band interconnectivity, which in turn will significantly reduce the network connectivity and permeability pathways of the sandstone. This study highlights that fluid flow in deformed host rocks around igneous bodies may vary significantly from that of the undeformed host rock reservoir. Therefore, a better understanding of the variability of deformation structures, and their association with intrusion geometry, will have important implications for hydrocarbon reservoir deliverability and CO₂ sequestration. Building digital field analogues can bridge the gap between thin section- (pore), outcrop- (sub-seismic), and regional (seismic) scales.

Keywords

Deformation bands; Fractures; Intrusions; Reservoir Connectivity; Fluid Flow

4.1. Introduction

Numerous studies have shown that deformation bands can have a significant influence on fluid flow (Fossen & Bale, 2007). Deformation bands are a common deformation structure in many reservoir sandstones. In particular, weakly cemented and highly porous (>10%) sandstones are ideal candidates for the development of deformation bands (Aydin, 1978; Shipton & Cowie, 2001; Fossen et al., 2007). Due to their mode of formation (i.e. mainly cataclasis and compaction; Fossen et al., 2007) deformation bands tend to have lower permeabilities than their host rock sandstones and, in turn, negatively affect fluid flow (Sterlof et al., 2004; Fossen & Bale, 2007; Rotevatn et al., 2013). Porosity and permeability reductions due to deformation bands may significantly reduce reservoir connectivity by creating baffles to fluid flow and even, in some cases, act as seals to hydrocarbon accumulations (e.g. Knipe et al., 1997; Ogilvie & Glover, 2001; Parnell et al., 2004).

Deformation bands have been documented to develop in most structural and tectonic settings provided the host rock is susceptible to their formation (Fossen et al., 2007). Deformation bands preferentially develop in more poorly lithified layers within arenitic to arkosic sandstones (i.e. those lacking in lithics) at shallow depths (1–3 km; Fossen, 2010). This depth regime is coincident with the emplacement of shallow-level intrusions, and there is good field evidence to suggest that deformation bands do develop as accommodation structures associated with sills and laccoliths (e.g. Morgan et al. 2008; this study).

These deformation structures may have important implications on the compartmentalisation and fluid flow within reservoirs hosting intrusions. Quantitative studies have previously been carried out to analyse the deformation structures associated with salt movement (e.g. Antonellini & Aydin, 1995), but as yet no such studies exist for igneous intrusions. This research therefore aims to carry out detailed kinematic, geometric and spatial analyses of fracture networks in host rock sandstone, associated with emplacement of the Trachyte Mesa igneous intrusion, Henry Mountains, Utah (Fig. 4.1).

A fracture network can be regarded as a system of fractures developed within the same rock volume and may be made up of multiple fracture sets (Adler & Thovert, 1999). Fractures are generally described by their geometry (e.g. orientation and length) and

characteristic attributes (e.g. fracture type, morphology and mineral fill). These attributes may be used to define fracture sets (Priest, 1993; Adler & Thovert, 1999; Sanderson & Nixon, 2015) which are often used to define distinct structural events within the evolution of a wider fracture network. In Chapter 3 the term ‘phases’ was used to describe what are in effect the various fracture sets observed in the Trachyte Mesa study area. Through these attributes we can gain a good understanding of the various fracture sets and networks, however the relationships between these systems (e.g. connectivity) requires further analysis. Sanderson and Nixon (2015) highlight the use of ‘topology’ for describing the relationships between geometrical objects, and outline a workflow for fracture analysis, building on the work of others (including: Mauldon, 1994; Manzocchi, 2002, Rohrbaugh et al., 2002; Mäkel, 2007). This workflow has been applied as part of the present study and is described in detail in Section 4.3.

4.2. Geological setting

4.2.1. Trachyte Mesa Intrusion

The Trachyte Mesa intrusion is a small (1.5 km²) satellite intrusion to the Mount Hillers intrusive complex in the Henry Mountains, SE Utah (Fig. 4.1). The Henry Mountains intrusions are Oligocene in age (31.2 to 23.3 Ma; Nelson et al., 1992). These intrusions, therefore, post-date the minor Laramide structuration observed on the Colorado Plateau. The intrusions are emplaced within an approximately 3–6 km thick section of late Palaeozoic–Mesozoic strata overlying Precambrian basement; the Trachyte Mesa intrusion was likely emplaced at a paleo-depth of ~3 km (Jackson & Pollard, 1988; Hintze & Kowallis, 2009).

Trachyte Mesa has an elongate, laccolithic geometry, trending NE–SW (Fig. 4.1b) with thicknesses varying from 5–50 m (Morgan et al., 2008). There is strong evidence to suggest that the intrusion formed by the amalgamation and stacking of multiple thin (~1–5 m thick) sill sheets (Johnson & Pollard, 1973; Menand, 2008; Morgan et al., 2008; this study, Chapter 3). The intrusion is generally concordant with the Entrada Sandstone Formation, within which it is emplaced (Johnson & Pollard, 1973; Morgan et al., 2008; Wetmore et al., 2009). The best exposures of the intrusion, contact and overlying host rock can be found on the southern end of the north-western lateral margin (Fig. 4.1c, d).

4.2.2. The Entrada Sandstone Formation

The Entrada Sandstone Formation (part of the San Rafael Group) is Jurassic (Callovian) in age and is composed of a mixture of white cross-bedded sandstones, reddish-brown silty sandstones, siltstones, and shale beds (Aydin, 1978; Fig.4.2). The Entrada was deposited in an aeolian environment and extends over a vast area, making it the largest of the Colorado Plateau ergs (Hintze & Kowallis, 2009). Entrada Sandstone is generally quartz-dominated (Aydin, 1978), although a subarkosic composition for rock units studied around the Trachyte Mesa intrusion may be a more appropriate lithological description (Fig. 4.3). Calcite is the most common cement, although siliceous and pelitic cements are abundant in some layers (Aydin, 1978).

Figure 4.1. (overleaf)

Geological setting and study area. (a) Simplified maps showing location of the Henry Mountains with respect to Utah, and the Trachyte Mesa (TM) Intrusion with respect to the Henry Mountains intrusive complex. The Henry Mountains regional map is adapted from Morgan et al. (2008). (b) Geological map of the Trachyte Mesa intrusion showing surface map extent and proposed magma flow directions during emplacement (from Morgan et al., 2008) overlain with magnetic map (from Wetmore et al., 2009) to show subsurface extent to the SW. Arrow points to study area. (c) Aerial photograph (from Google Earth™) over the study area (NW margin of the Trachyte Mesa intrusion). Sample stations for fracture studies highlighted. Red lines show mappable northern limit of intrusive rocks (i.e. the northern margin). (d) Field photograph showing monoclinical geometry of the NW intrusion margin. Note blocky, red Entrada Sandstone units concordant with the underlying intrusion top surface, and stacked intrusive sheets below. Viewpoint location shown in (c).

Figure 4.2. (overleaf)

(a) Panoramic photograph of study area (sampling traverse across lateral margin of the Trachyte Mesa intrusion). Note red, cross-bedded Entrada Sandstone unit, and Trachyte Mesa intrusion outcropping to the right. (b) Annotated sketch of (a) with sample station (TMFS-1, etc.) locations, discussed in this study, highlighted with white stars. Note, sample stations are all within the same more massive, cross-bedded sandstone unit. (c) Cross-section from Morgan et al. (2008) showing measured bed thickness and corresponding reduction in porosity across the intrusion margin (see fig. 8 in Morgan et al. (2008) for associated porosity and strain ratio plots).

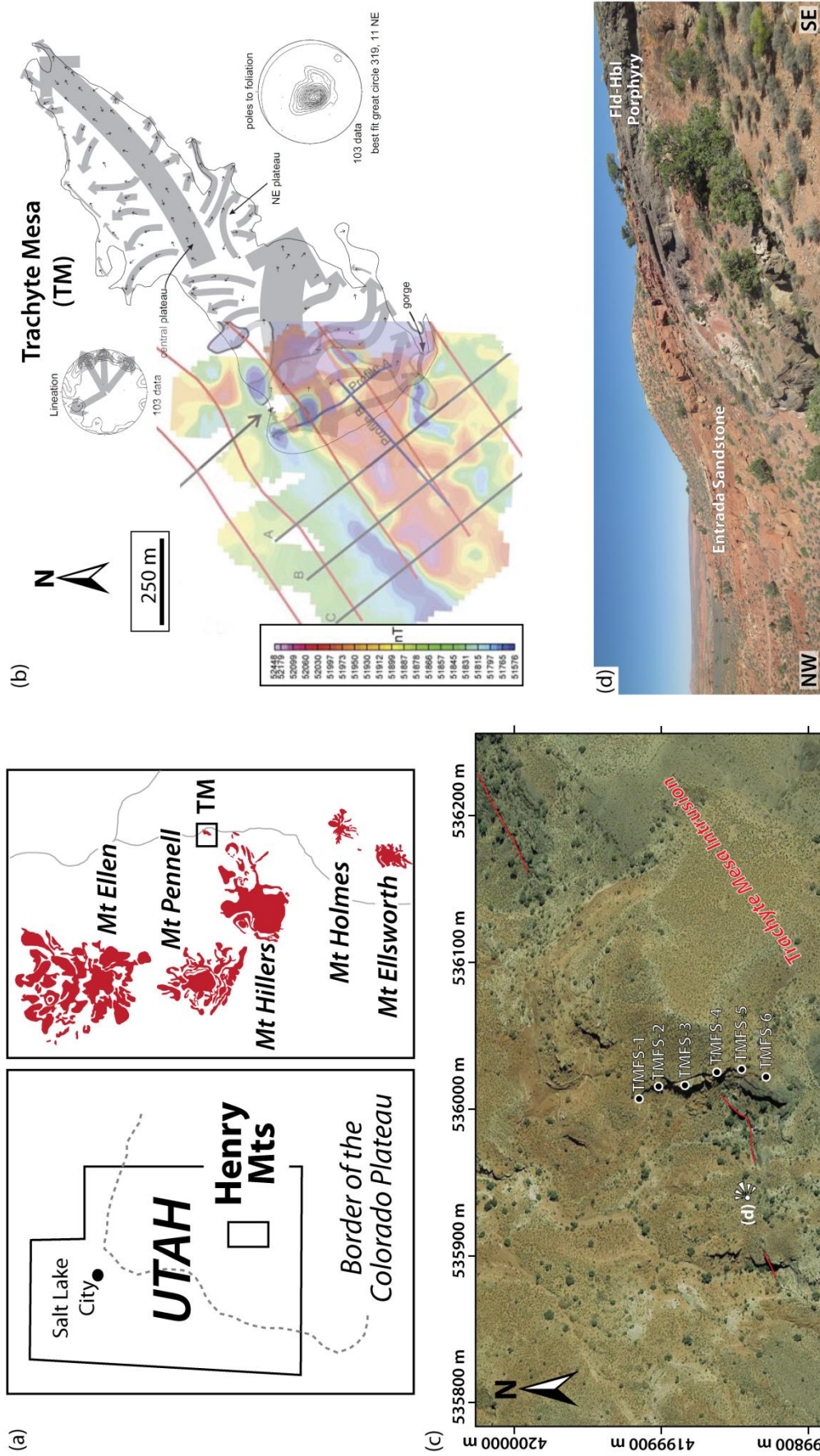


Fig. 4.1

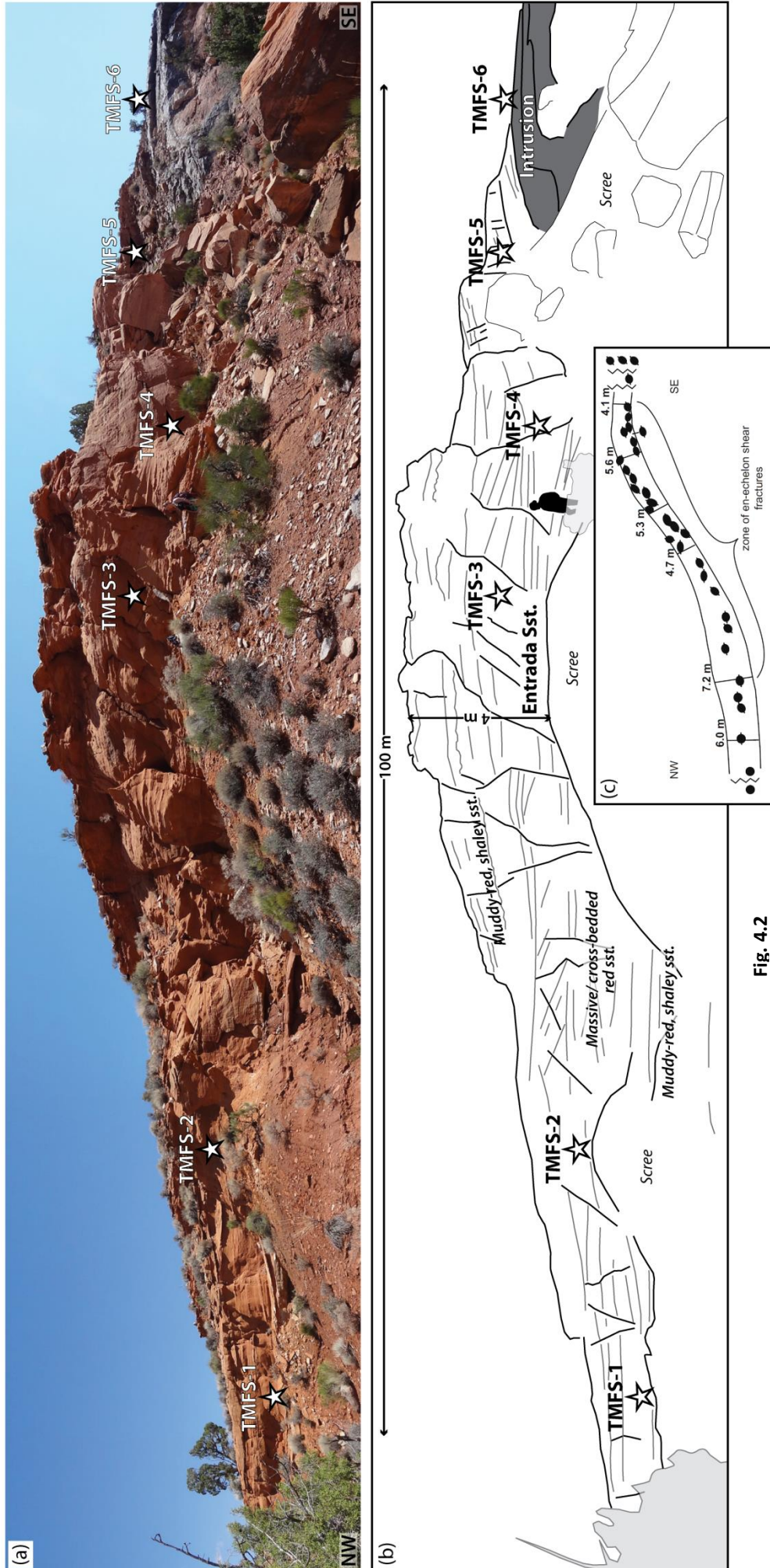


Fig. 4.2

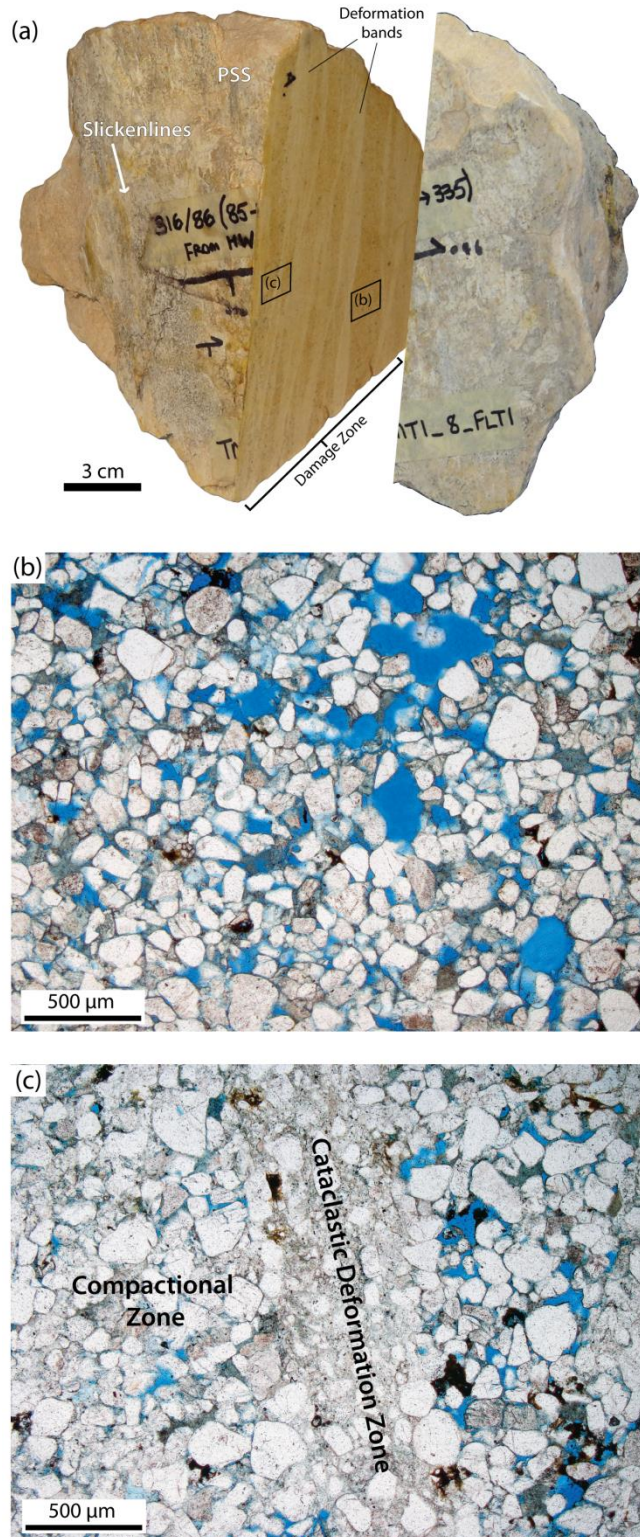


Figure 4.3. Photograph of a hand specimen (a) and photomicrographs of thin sections (b, c) showing deformation bands. Note principal slip surface (PSS) and associated deformation zone in (a). Impregnation of pores with blue resin has been used to highlight pore space in thin sections (b, c). Note, ~15% porosity (visually estimated using percentage estimation comparison charts of Tucker, 2001) in less deformed zone between deformation bands (b), and almost 0% porosity in cataclastic deformation band (c). Pre-intrusion porosity was likely to be >30% (Morgan et al., 2008). Note this sample is a Phase 2B fault (discussed more in Chapter 3).

The Entrada Sandstone, being highly porous (e.g. Fig. 4.3b), is the ideal lithology for the formation of deformation bands and, as a result (along with the Lower Jurassic Navajo Sandstone, also found on the Colorado Plateau and stratigraphically below the Entrada; Jackson & Pollard, 1988), has been the focus of several studies on such structures (Aydin, 1978; Aydin & Johnson, 1978, 1983; Shipton & Cowie, 2001; Fossen & Bale, 2007; Fossen et al., 2007). Although deformation bands are common throughout the Entrada Sandstone, local to the Trachyte Mesa intrusion, there appears to be a strong increase in deformation bands aligned parallel to the intrusion margin. This spatial and geometric correlation leads to the proposal that these structures formed directly in response to the emplacement of the intrusion (this study, Chapter 3). Deformation bands in the vicinity of Trachyte Mesa generally form as conjugate sets trending roughly NE–SW and individual bands are relatively discrete (<0.5 mm; Fig. 4.3c), though a few wider deformation zones have developed which are cored by principal slip surfaces (e.g. Fig. 4.3a). In contrast, much wider deformation band clusters (>20 cm) can be found hosted by the Entrada Sandstone elsewhere on the Colorado plateau (e.g. see figs 1, 7 & 9 in Fossen & Bale, 2007).

4.3. Study zone, sampling and analysis methods

4.3.1. Outcrop traverse

A small study of fracture spacing was carried out along part of Structural Transect TMTE (Fig. 4.2; for details on TMTE see Chapter 3; see also Google Earth™ project (kmz file) in Appendices for locations) in order to try and quantify the change in fracture intensity observed across the lateral margin of the intrusion. The study consists of six outcrops, relatively evenly spaced, from ~80 m outboard of the exposed intrusion margin (sample station TMFS-1; Figs 4.1c & 4.2), and up over the monoclinical lateral intrusion margin, onto the top surface of the intrusion (TMFS-6). At each outcrop, a 1.5 m box (where possible) was marked onto the surface of the sandstone. A metre ruler was also used for scaling purposes. A suite of photographs were then collected for each outcrop. These photographs were subsequently used to map out the fracture networks at each sample station post-fieldwork using a graphics package (*Adobe Illustrator*).

As roughly NE–SW trending deformation bands are the dominant structural type identified along transect TMTE (see Chapter 3), care was taken to ensure that the surfaces

photographed, and subsequently analysed, were oriented in a similar, optimal (NW–SE) orientation in order to sample the fracture network most appropriately. Note, due to this sampling technique results will only be appropriate for analysing fluid flow across (perpendicular to) the intrusion margin (i.e. NW–SE), and are not likely to be appropriate for flow parallel to the intrusion margin (i.e. NE–SW). Further studies of other oriented surfaces will be required for a full 3D framework to be defined.

4.3.2. Fracture analysis methods

Various analytical techniques have been proposed for the investigation of fracture networks (e.g. Walsh & Watterson, 1993; Berkowitz, 1995; Adler & Thovret, 1999). In this study the method of Sanderson and Nixon (2015) has been applied. The method is described in detail by Sanderson and Nixon (2015), and only a brief description is given here. The basic principal is outlined in Figure 4.4, and is comprised of mapping out a fracture network, measuring fracture (or branch) lengths and quantities, and node counting.

4.3.2.1. Fracture Network Map

Using the acquired outcrop photographs, fracture networks were mapped to the highest level of detail attainable from the image resolution. Areas were then selected in order to sample the fracture networks at each sample site with as little bias as possible. In areas of more heterogeneous deformation, multiple areas were sampled at a range of scales (ranging from 20–100 cm diameter circles) in order to capture the variability. Circular scan-lines/ areas were used rather than squares (e.g. after Mauldon, 1994; Rohrbaugh et al., 2002; Sanderson & Nixon, 2015) as these provide the least orientation bias, with an equal likelihood of sampling any given fracture orientation on a 2-D surface.

4.1.1.1. Measuring Lengths and Quantities

For each sample circle, the total number of fractures and total fracture length were recorded. In addition, the total number of fault branches (i.e. segments between intersecting fracture points or nodes) was also recorded. Sanderson and Nixon (2015) show preference to the use of branches as it is often difficult to recognise an individual,

continuous fracture trace within a fracture network, whereas branches are uniquely identifiable. Furthermore, as exposures and sampling areas are of finite size, many fractures may extend beyond the sample area. Therefore, the frequency and length of fractures will be subject to a sampling bias (Riley, 2005). In contrast the length of branch lines is likely to be less, thus reducing this sampling bias issue.

Using sample area, total number of fractures (or branches) and total fracture (branch) length, a number of fracture network characteristics can be defined. These include: frequency (total number/ area); density (also termed fracture intensity; total length/ area); spacing (the inverse of density, i.e. area/ total length); characteristic fracture length (mean length; total fracture length/ total number of fractures); and dimensionless intensity (multiplying fracture density by the characteristic length). More details on the derivation of these are outlined in Sanderson and Nixon (2015).

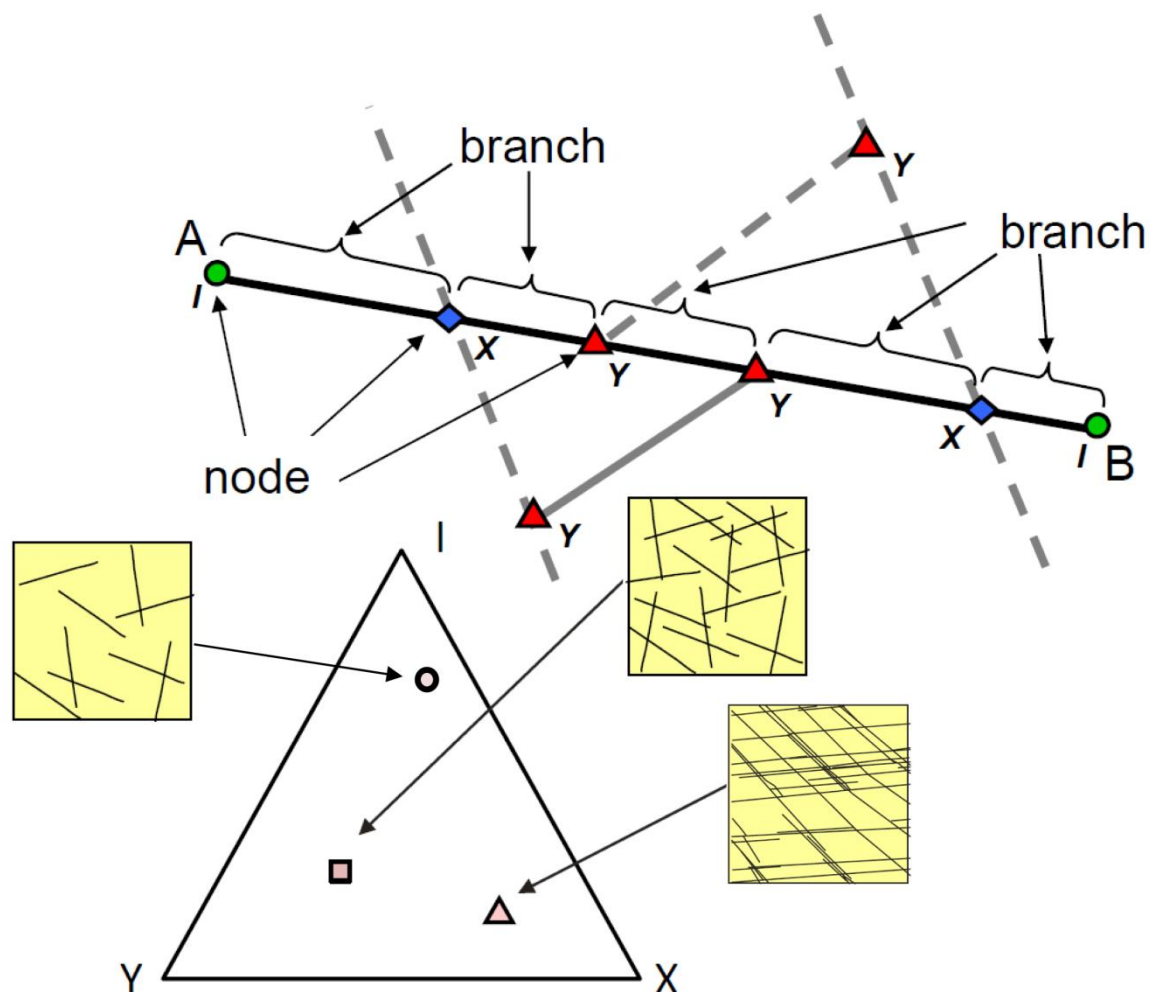


Figure 4.4. Schematic image outlining principal method applied for fracture analysis (Sanderson & Nixon, 2015). Fracture trace (A–B), with associated intersecting fractures (dashed), showing arrangement of nodes and branches: I-nodes (circles); Y-nodes (triangles); X-nodes (diamonds). Proportions of I-, Y- and X-nodes may be plotted on a triangular plot to visualise different fracture network types (after Manzocchi, 2002).

4.1.1.2. Node Counting

A given fracture network consists of lines, nodes and branches (Fig. 4.4). As outlined above, lines will consist of one or more branches, with nodes (i.e. fracture intersections) at either end of each branch. Three main types of nodes exist: I-nodes (isolated fracture terminations within the host rock); Y-nodes (where one fracture terminates against another); and X-nodes (where two fractures cross-cut one another). Within a sample area, a fourth type of node may also be recorded, where fractures intersect the outer perimeter of the sample area (termed E-nodes; Sanderson & Nixon, 2015).

The proportion of I-, Y- and X-nodes have been used by various authors to characterize a fracture network (e.g. Manzocchi, 2002, Mäkel, 2007) and the results plotted on a triangular plot (Fig. 4.4). As this nodal relationship will remain unchanged by any continuous transformations (i.e. strains), this is termed a topological classification (Sanderson & Nixon, 2015).

4.3.3. Sample Collection

A selection of rock samples were also collected at each sample station (Fig. 4.5) in order to carry out hand specimen and thin section (i.e. petrological, porosity and microstructural) studies. Samples were oriented in the field in order to enable thin sectioning in a similar vertical, NW–SE oriented plane to the outcrop photo/ scan surfaces. Ensuring that similarly orientated sample areas are studied at all scales increases the chances of sampling the same fracture systems (i.e. NE–SW trending fracture networks) as observed in outcrop, and thus the resulting scalar statistics should be more appropriate.

Figure 4.5. (overleaf)

Hand specimen photos and fracture analysis (circles). (a) Sample TMFS-1. (b) Sample TMFS-2. (c) Sample TMFS-3. (d) Sample TMFS-4. (e) Sample TMFS-5. (f) Sample TMFS-6. Fracture analysis was carried out on freshly cut surfaces. Circular scans show the fracture network and associated I-, Y-, and X-nodes. Statistics show total number of fractures (N), total fracture length (L), fracture density/ intensity (D), and dimensionless intensity. Note, a wider set of statistical results (including those for branch line studies) is shown in Table 1.

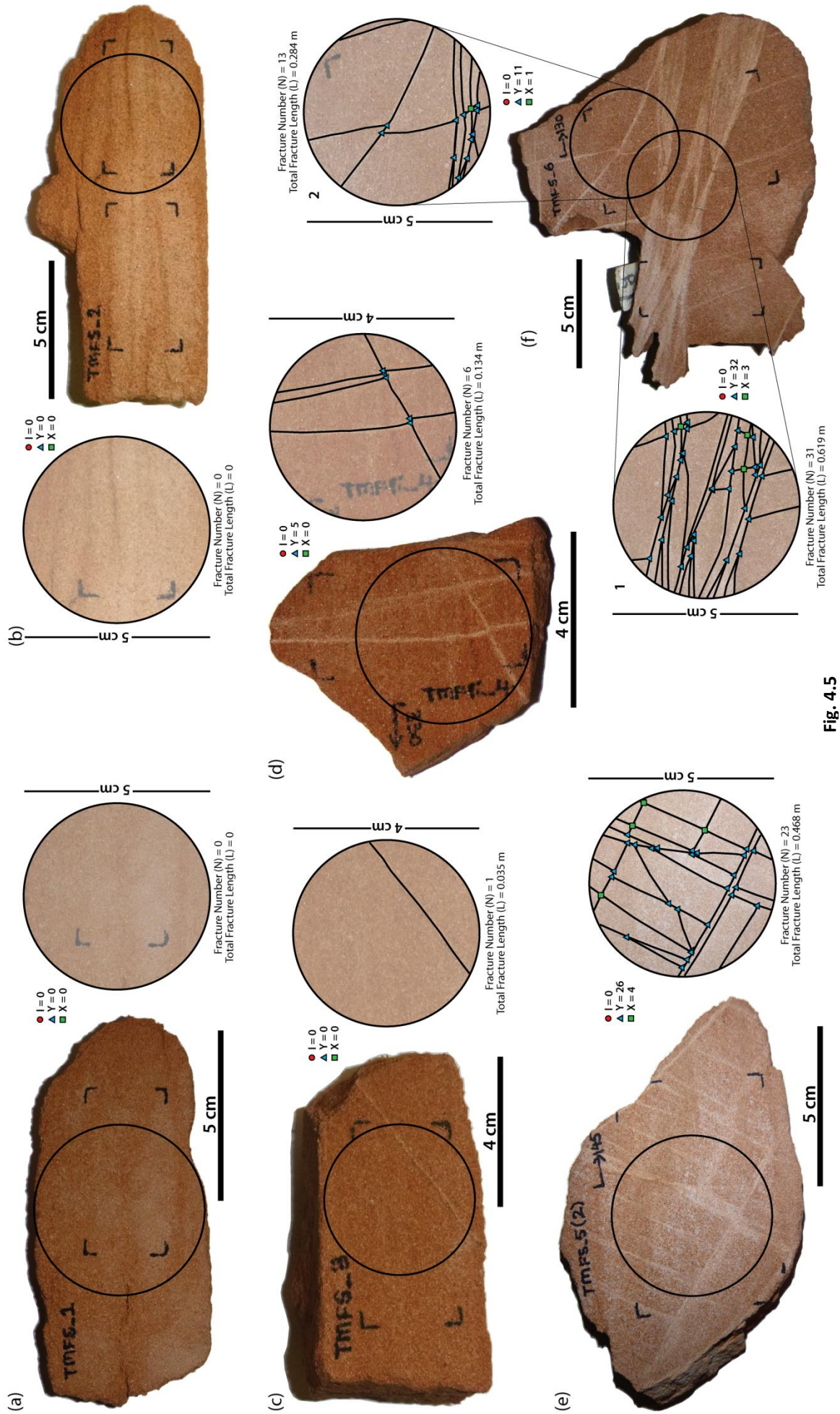


Fig. 4.5

It is acknowledged that by only carrying out fracture studies in one orientation we are invoking an orientation bias into our results. However by having a common sample orientation, the results between each sample location should at least be consistent.

4.4. Results

4.4.1. Outcrop Fracture Analysis

Figures 4.6 to 4.11 show the photographs and associated mapped fracture networks for each sample station respectively. Each locality lies within the same red, cross-bedded massive sandstone unit (Fig. 4.2). Various sample areas were used at each sample station, limited in part by outcrop extent; however a consistent 20 cm diameter circular scan area was sampled for each locality. Table 4.1 summarises the various fracture network characteristics derived for each scan area. These are also depicted in Figures 4.6 to 4.11.

Table 4.1. (overleaf)

Summary data table showing results of circular scan fracture analyses carried out in this study.

Figure 4.6. (overleaf)

Outcrop photographs and corresponding fracture interpretations for locality TMFS-1. (a) NW–SE oriented, sub-vertical outcrop surface with five circular scan areas defined (ranging in size from 100 cm to 20 cm). Tape measure is extended to 1 m. (b) Zoom in to area lower left of (a). Circular scan 6 is 30 cm in diameter. (c) Circular scans showing fracture network and associated I-, Y-, and X-nodes. Statistics show total number of fractures (N), total fracture length (L), fracture density/ intensity (D), and dimensionless intensity for each scan area. Note, a wider set of statistical results (including those for branch line studies) is shown in Table 1.

Figure 4.7. (overleaf)

Outcrop photographs and corresponding fracture interpretations for locality TMFS-2. (a) NW–SE oriented, sub-vertical outcrop surface with seven circular scan areas defined (ranging in size from 100 cm to 20 cm). Tape measure is extended to 1 m. Note, the six smaller scans are all 20 cm diameter, and the variations in size on the photo are due to the oblique perspective of the photograph. (b) Circular scans showing fracture network and associated I-, Y-, and X-nodes. Statistics show total number of fractures (N), total fracture length (L), fracture density/ intensity (D), and dimensionless intensity for each scan area. Note, a wider set of statistical results (including those for branch line studies) is shown in Table 1.

| Locality | Scale | Circle radius m | Sample Area m ² | Fractures | | | | Branch lines | | | | Fracture Nodes | | | | | | | | |
|-----------|---------|--------------------|-------------------------------|-----------|-----------------|-----------|---------|--------------|------|--------|-----------------|----------------|---------|------|------|------|----|-----|-----|---------------|
| | | | | Number | Total Length, m | Frequency | Density | CL | DI | Number | Total Length, m | Frequency | Density | CL | DI | E | I | Y | X | Total I, Y, X |
| TMFS_1(1) | Outcrop | 0.50 | 0.79 | 16 | 5.85 | 20.37 | 7.45 | 0.37 | 2.72 | 34 | 5.852 | 43.29 | 7.45 | 0.17 | 1.28 | 12 | 11 | 9 | 4 | 24 |
| TMFS_1(2) | Outcrop | 0.25 | 0.20 | 6 | 1.91 | 30.56 | 9.71 | 0.32 | 3.08 | 13 | 1.906 | 66.21 | 9.71 | 0.15 | 1.42 | 8 | 3 | 1 | 3 | 7 |
| TMFS_1(3) | Outcrop | 0.10 | 0.03 | 3 | 0.49 | 95.49 | 15.61 | 0.16 | 2.55 | 5 | 0.490 | 159.15 | 15.61 | 0.10 | 1.53 | 6 | 0 | 0 | 1 | 1 |
| TMFS_1(4) | Outcrop | 0.10 | 0.03 | 8 | 0.74 | 254.65 | 23.52 | 0.09 | 2.17 | 15 | 0.739 | 477.46 | 23.52 | 0.05 | 1.16 | 7 | 4 | 5 | 1 | 10 |
| TMFS_1(5) | Outcrop | 0.10 | 0.03 | 0 | 0.00 | | | | | 0 | 0.000 | | | | | | | | | |
| TMFS_1(6) | Outcrop | 0.15 | 0.07 | 17 | 2.24 | 240.50 | 31.74 | 0.13 | 4.19 | 42 | 2.244 | 594.18 | 31.74 | 0.05 | 1.70 | 15 | 3 | 18 | 8 | 29 |
| TMFS_1(7) | Sample | 0.03 | 0.00 | 0 | 0.00 | | | | | 0 | 0.000 | | | | | | | | | |
| TMFS_2(1) | Outcrop | 0.50 | 0.79 | 5 | 1.96 | 6.37 | 2.50 | 0.39 | 0.98 | 6 | 1.961 | 7.64 | 2.50 | 0.33 | 0.82 | 7 | 2 | 1 | 0 | 3 |
| TMFS_2(2) | Outcrop | 0.10 | 0.03 | 3 | 0.59 | 95.49 | 18.65 | 0.20 | 3.64 | 4 | 0.586 | 127.32 | 18.65 | 0.15 | 2.73 | 5 | 0 | 1 | 0 | 1 |
| TMFS_2(3) | Outcrop | 0.10 | 0.03 | 1 | 0.20 | 31.83 | 6.32 | 0.20 | 1.25 | 1 | 0.198 | 31.83 | 6.32 | 0.20 | 1.25 | 2 | 0 | 0 | 0 | 0 |
| TMFS_2(4) | Outcrop | 0.10 | 0.03 | 1 | 0.20 | 31.83 | 6.40 | 0.20 | 1.29 | 1 | 0.201 | 31.83 | 6.40 | 0.20 | 1.29 | 2 | 0 | 0 | 0 | 0 |
| TMFS_2(5) | Outcrop | 0.10 | 0.03 | 0 | 0.00 | | | | | 0 | 0.000 | | | | | 0 | 0 | 0 | 0 | 0 |
| TMFS_2(6) | Outcrop | 0.10 | 0.03 | 3 | 0.34 | 95.49 | 10.72 | 0.11 | 1.20 | 3 | 0.337 | 95.49 | 10.72 | 0.11 | 1.20 | 4 | 2 | 0 | 0 | 2 |
| TMFS_2(7) | Outcrop | 0.10 | 0.03 | 3 | 0.39 | 95.49 | 12.38 | 0.13 | 1.61 | 4 | 0.389 | 127.32 | 12.38 | 0.10 | 1.20 | 5 | 0 | 1 | 0 | 1 |
| TMFS_2(8) | Sample | 0.03 | 0.00 | 0 | 0.00 | | | | | 0 | 0.000 | | | | | | | | | |
| TMFS_3(1) | Outcrop | 0.25 | 0.20 | 24 | 3.46 | 122.23 | 17.63 | 0.14 | 2.54 | 82 | 3.461 | 417.62 | 17.63 | 0.04 | 0.74 | 11 | 5 | 32 | 19 | 56 |
| TMFS_3(2) | Outcrop | 0.25 | 0.20 | 13 | 2.47 | 66.21 | 12.55 | 0.19 | 2.38 | 21 | 2.465 | 106.95 | 12.55 | 0.12 | 1.47 | 11 | 8 | 7 | 0 | 15 |
| TMFS_3(3) | Outcrop | 0.25 | 0.20 | 22 | 2.94 | 112.05 | 14.99 | 0.13 | 2.00 | 49 | 2.943 | 249.55 | 14.99 | 0.06 | 0.90 | 17 | 9 | 20 | 4 | 33 |
| TMFS_3(4) | Outcrop | 0.10 | 0.03 | 18 | 1.38 | 572.96 | 43.82 | 0.08 | 3.35 | 67 | 1.377 | 2132.68 | 43.82 | 0.02 | 0.90 | 12 | 3 | 21 | 17 | 41 |
| TMFS_3(5) | Outcrop | 0.10 | 0.03 | 4 | 0.64 | 127.32 | 20.35 | 0.16 | 3.25 | 5 | 0.639 | 159.15 | 20.35 | 0.13 | 2.60 | 5 | 2 | 1 | 0 | 3 |
| TMFS_3(6) | Outcrop | 0.10 | 0.03 | 6 | 0.55 | 190.99 | 17.57 | 0.09 | 1.62 | 9 | 0.552 | 286.48 | 17.57 | 0.06 | 1.08 | 8 | 1 | 3 | 0 | 4 |
| TMFS_3(7) | Outcrop | 0.10 | 0.03 | 0 | 0.00 | | | | | 0 | 0.000 | | | | | | | | | |
| TMFS_3(8) | Outcrop | 0.50 | 0.79 | 42 | 8.67 | 53.48 | 11.03 | 0.21 | 2.28 | 135 | 8.666 | 171.89 | 11.03 | 0.06 | 0.71 | 24 | 15 | 44 | 22 | 81 |
| TMFS_3(9) | Sample | 0.02 | 0.00 | 1 | 0.04 | 795.77 | 28.22 | 0.04 | 1.00 | 0 | 0.035 | 0.00 | 28.22 | | | 0.00 | 0 | 0 | 0 | 0 |
| TMFS_4(1) | Outcrop | 0.25 | 0.20 | 47 | 5.79 | 239.37 | 29.47 | 0.12 | 3.63 | 131 | 5.786 | 667.18 | 29.47 | 0.04 | 1.30 | 21 | 15 | 56 | 13 | 84 |
| TMFS_4(2) | Outcrop | 0.25 | 0.20 | 35 | 4.19 | 178.25 | 21.32 | 0.12 | 2.55 | 68 | 4.187 | 346.32 | 21.32 | 0.06 | 1.31 | 23 | 22 | 25 | 6 | 53 |
| TMFS_4(3) | Outcrop | 0.10 | 0.03 | 12 | 0.90 | 381.97 | 28.65 | 0.08 | 2.15 | 26 | 0.900 | 827.61 | 28.65 | 0.03 | 0.99 | 11 | 2 | 10 | 2 | 14 |
| TMFS_4(4) | Outcrop | 0.10 | 0.03 | 13 | 1.33 | 413.80 | 42.32 | 0.10 | 4.33 | 15 | 1.330 | 477.46 | 42.32 | 0.09 | 3.75 | 13 | 11 | 2 | 0 | 13 |
| TMFS_4(5) | Sample | 0.02 | 0.00 | 6 | 0.13 | 4774.65 | 106.57 | 0.02 | 2.38 | 0 | 0.134 | 0.00 | 106.57 | | | | 0 | 5 | 0 | 5 |
| TMFS_5(1) | Outcrop | 0.50 | 0.79 | 278 | 32.60 | 353.96 | 41.51 | 0.12 | 4.87 | 877 | 32.598 | 0.00 | 41.51 | | | | 97 | 372 | 176 | 645 |
| TMFS_5(2) | Outcrop | 0.10 | 0.03 | 95 | 4.10 | 3023.94 | 130.57 | 0.04 | 5.64 | 320 | 4.102 | 10185.92 | 130.57 | 0.01 | 1.67 | 44 | 0 | 143 | 39 | 182 |
| TMFS_5(3) | Outcrop | 0.10 | 0.03 | 109 | 4.92 | 3469.58 | 156.55 | 0.05 | 7.06 | 403 | 4.918 | 12827.89 | 156.55 | 0.01 | 1.91 | 45 | 2 | 169 | 67 | 238 |
| TMFS_5(4) | Sample | 0.03 | 0.00 | 23 | 0.47 | 11713.80 | 238.54 | 0.02 | 4.86 | 0 | 0.468 | 0.00 | 238.54 | | | | 0 | 26 | 4 | 30 |
| TMFS_6(1) | Outcrop | 0.10 | 0.03 | 108 | 4.42 | 3437.75 | 140.64 | 0.04 | 5.75 | 355 | 4.418 | 11300.00 | 140.64 | 0.01 | 1.75 | 39 | 1 | 169 | 41 | 211 |
| TMFS_6(2) | Outcrop | 0.10 | 0.03 | 75 | 3.78 | 2387.32 | 120.39 | 0.05 | 6.07 | 261 | 3.782 | 8307.89 | 120.39 | 0.01 | 1.74 | 33 | 1 | 114 | 37 | 152 |
| TMFS_6(3) | Outcrop | 0.25 | 0.20 | 117 | 12.76 | 595.88 | 65.00 | 0.11 | 7.09 | 363 | 12.763 | 1848.74 | 65.00 | 0.04 | 2.29 | 59 | 0 | 152 | 36 | 188 |
| TMFS_6(4) | Sample | 0.03 | 0.00 | 31 | 0.62 | 15788.17 | 315.24 | 0.02 | 6.29 | 0 | 0.619 | 0.00 | 315.24 | | | | 0 | 32 | 3 | 35 |
| TMFS_6(5) | Sample | 0.03 | 0.00 | 13 | 0.28 | 6620.85 | 144.52 | 0.02 | 3.15 | 0 | 0.284 | 0.00 | 144.52 | | | | 0 | 11 | 1 | 12 |

Table 4.1

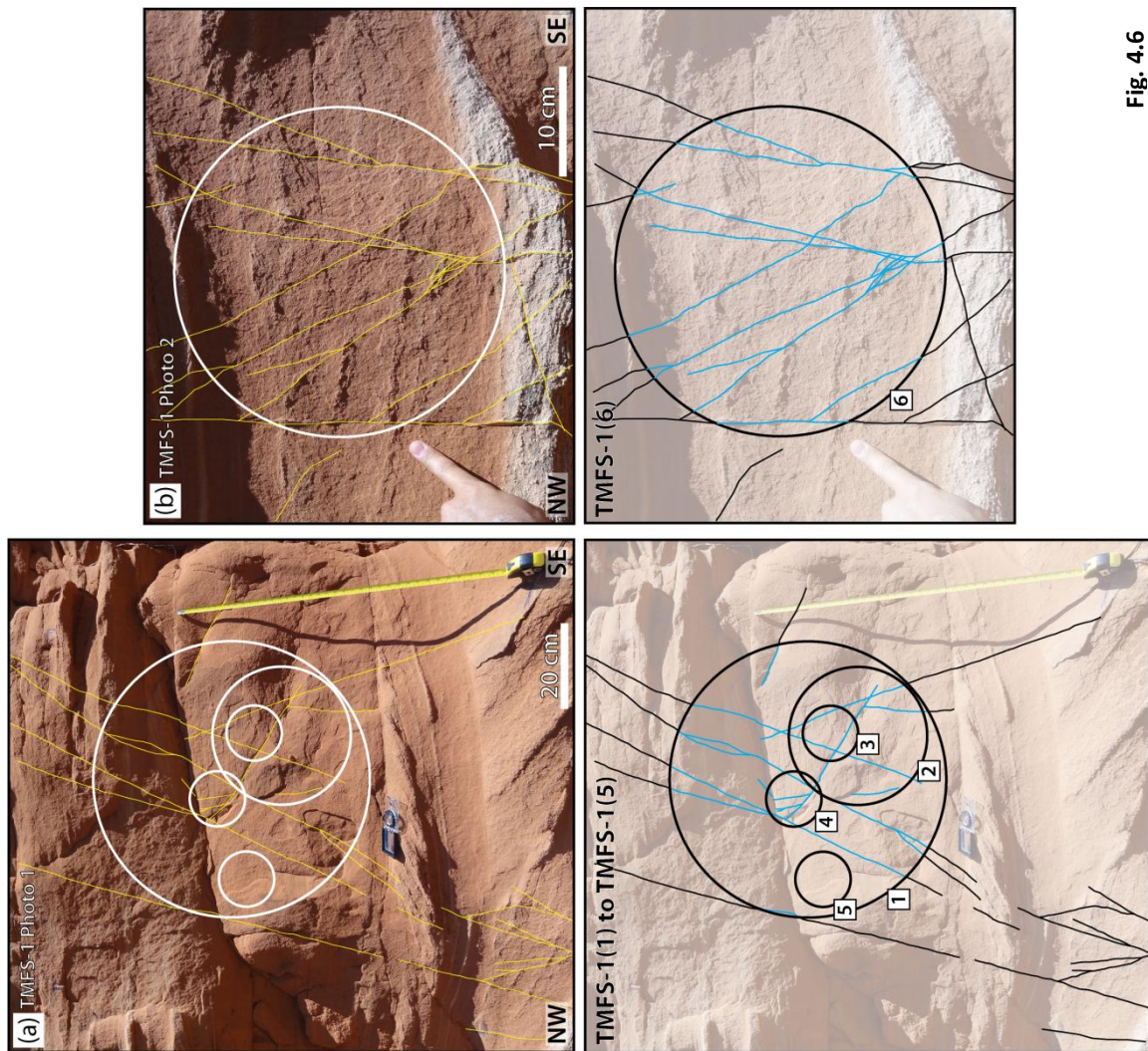


Fig. 4.6

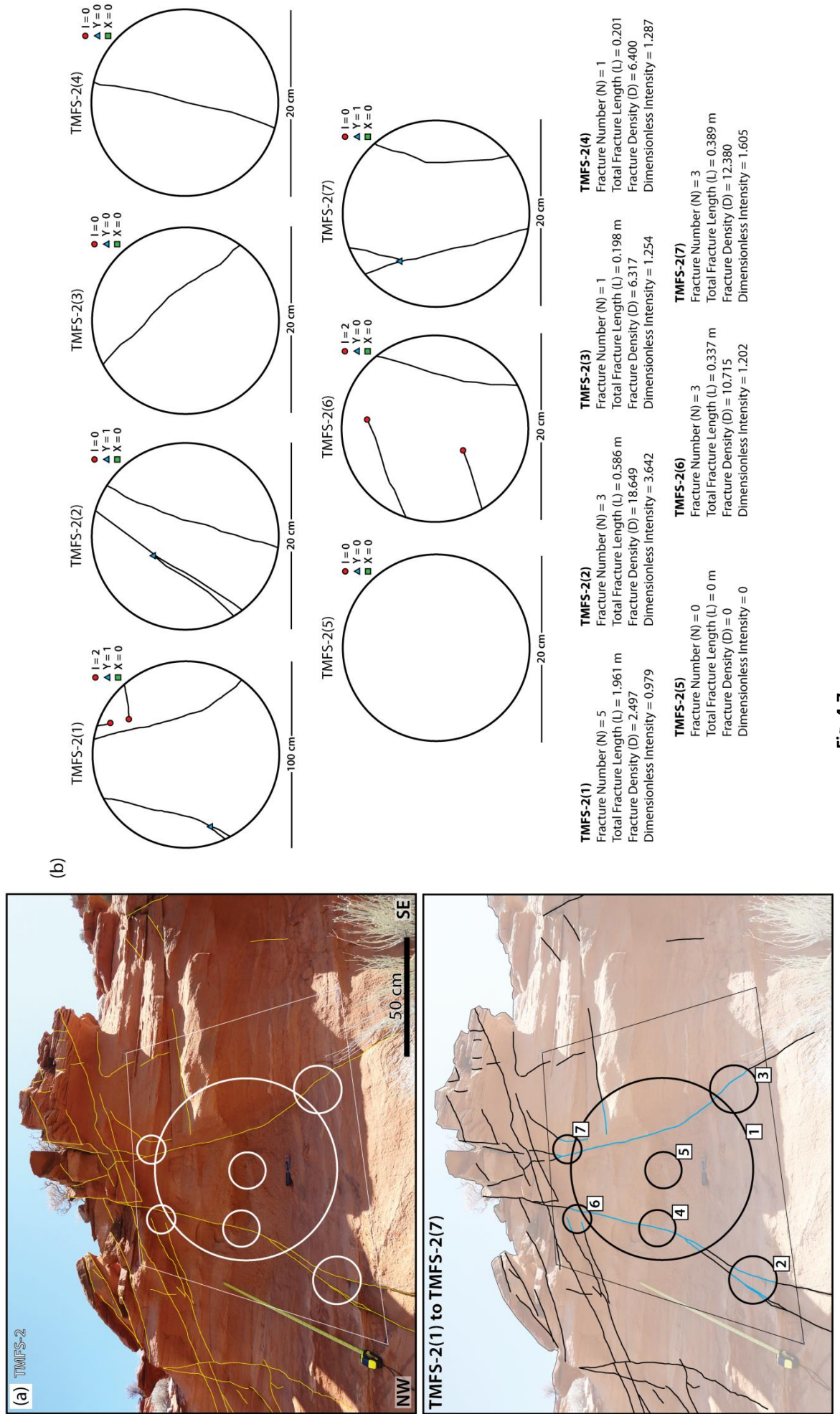


Fig. 4.7

Figure 4.8. *(overleaf)*

Outcrop photographs and corresponding fracture interpretations for locality TMFS-3. (a) NW–SE oriented, sub-vertical outcrop surface with eight circular scan areas defined (ranging in size from 100 cm to 20 cm). Tape measure is extended to 1 m. (b) Circular scans showing fracture network and associated I-, Y-, and X-nodes. Statistics show total number of fractures (N), total fracture length (L), fracture density/ intensity (D), and dimensionless intensity for each scan area. Note, a wider set of statistical results (including those for branch line studies) is shown in Table 1.

Figure 4.9. *(overleaf)*

Outcrop photographs and corresponding fracture interpretations for locality TMFS-4. (a) NW–SE oriented, sub-vertical outcrop surface with a 50 cm circular scan area defined. (b) Outcrop surface adjacent to (a) with three further scan circles defined (scan circle 2 is 50 cm, while 3 and 4 are both 20 cm). (c) Circular scans showing fracture network and associated I-, Y-, and X-nodes. Statistics show total number of fractures (N), total fracture length (L), fracture density/ intensity (D), and dimensionless intensity for each scan area. Note, a wider set of statistical results (including those for branch line studies) is shown in Table 1.

Figure 4.10. *(overleaf)*

Outcrop photographs and corresponding fracture interpretations for locality TMFS-5. (a) NW–SE oriented, sub-vertical outcrop surface (~1.5 x 1.5 m) with a 100 cm diameter scan area defined. Visible tape measure extent is 0.92 m. (b) Zoom-in to area in lower right of (a) for more detailed fracture interpretation (better resolution image) in a 20 cm scan area. (c) Zoom-in to area in upper middle of (a) for more detailed fracture interpretation (better resolution image) in a 20 cm scan area. Note sample core holes are those collected by Morgan et al. (2008) for their study. (d) Circular scans showing fracture network and associated I-, Y-, and X-nodes. Statistics show total number of fractures (N), total fracture length (L), fracture density/ intensity (D), and dimensionless intensity for each scan area. Note, a wider set of statistical results (including those for branch line studies) is shown in Table 1.

Figure 4.11. *(overleaf)*

Outcrop photographs and corresponding fracture interpretations for locality TMFS-6. Circular scan areas for fracture studies highlighted in (a) and (b). Circles 1 and 2 are 20 cm diameter areas sampling a NW–SE trending vertical rock surface, while circle 3 samples a sub-horizontal surface (note, elliptical shape of this sample area is to account for the perspective view in the photograph). (c) Circular scans showing fracture network and associated I-, Y-, and X-nodes. Statistics show total number of fractures (N), total fracture length (L), fracture density/ intensity (D), and dimensionless intensity. Note, a wider set of statistical results (including those for branch line studies) is shown in Table 1.

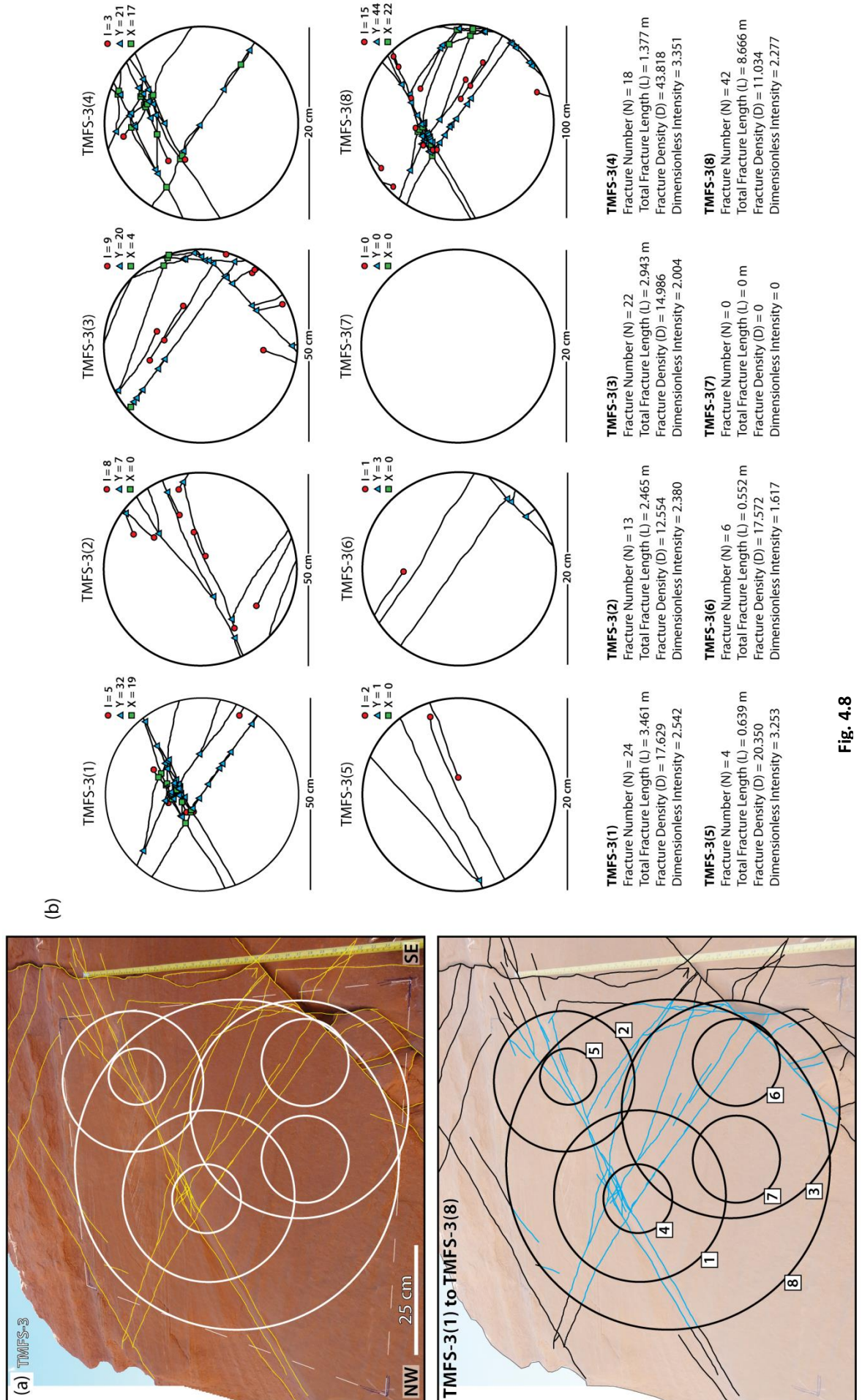


Fig. 4.8

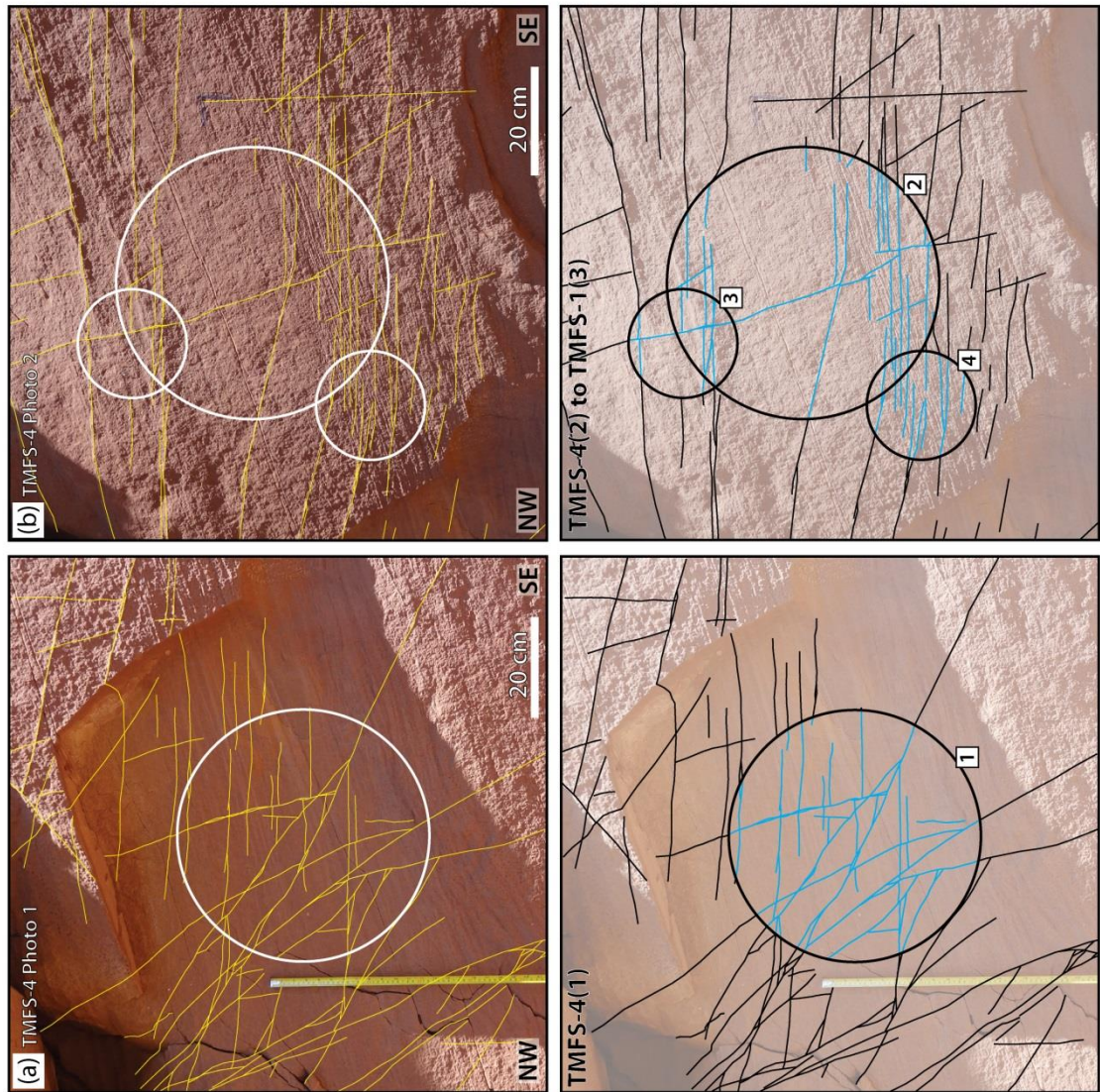


Fig. 4.9

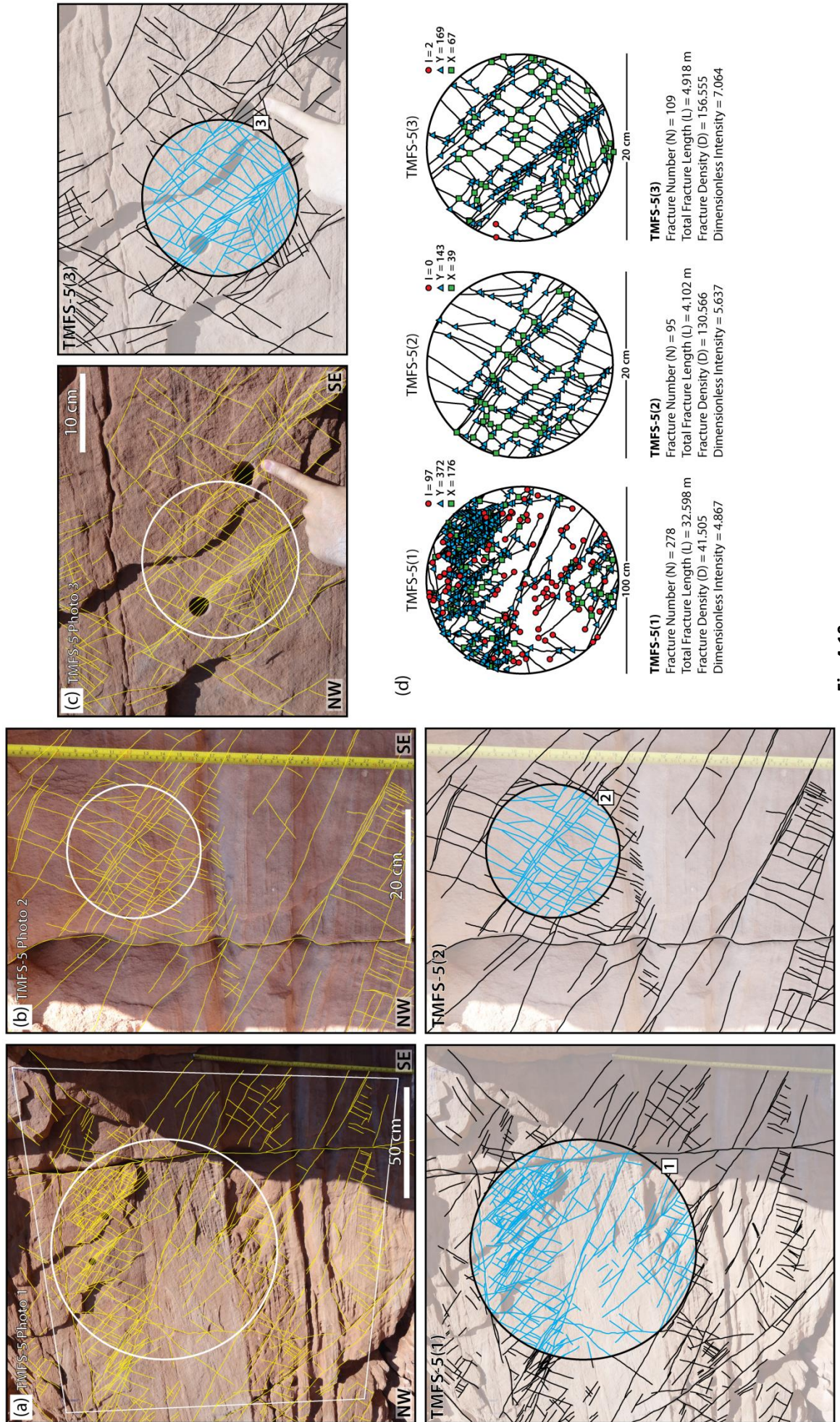


Fig. 4.10

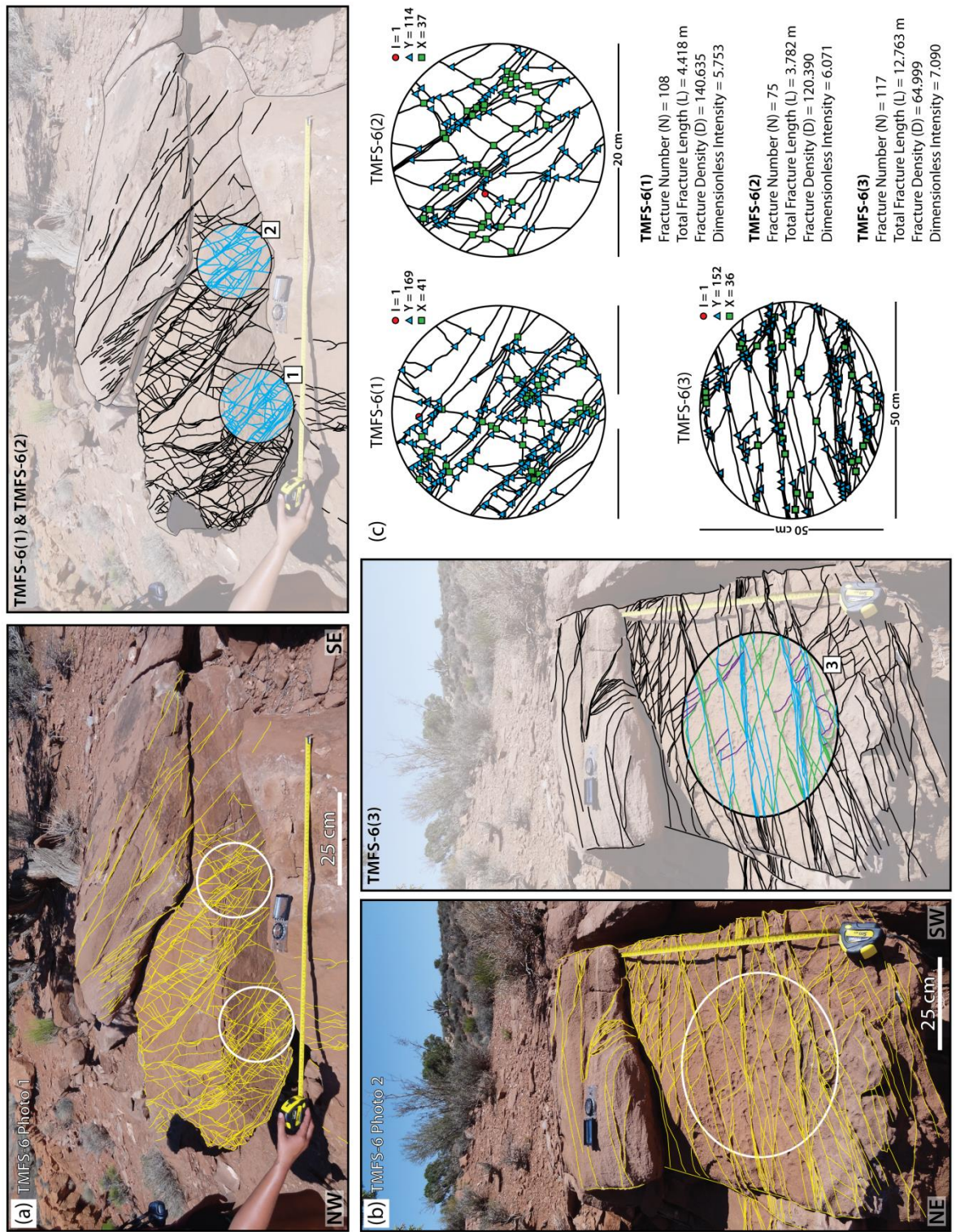


Fig. 4.11

4.4.2. Hand Specimens

Similar fracture analysis methods were also applied at the hand specimen scale (Fig. 4.5). Oriented samples were cut along a similar NW–SE sample plane to reveal a smooth freshly exposed sample surface. Digital photographs were taken and similar to the

method outlined above, deformation bands and fractures were interpreted. Circular sample areas were again defined (4 or 5 cm diameter circles used depending on the size of the sample) and fracture statistics recorded. Results are again documented in Table 4.1 and also shown on Figure 4.5.

4.4.3. Thin Section Analysis

Optical microscopy petrographical, porosity and microstructural analyses were carried out on thin sections cut from each hand specimen (Fig. 4.12). Sections were impregnated with blue dye in order to highlight porosity. Both compositional and porosity percentages were visually estimated using percentage estimation comparison charts (Tucker, 2001).

4.4.3.1. Sample TMFS-1

Sample TMFS-1 is a well sorted, medium to fine grain (~250 µm) sandstone, dominated by quartz (>80%) and feldspar (plagioclase and microcline). Using the classification of sandstones in Tucker (2001), the rock is therefore a subarkosic sandstone. Haematite can be seen coating quartz grains. No distinct cross-laminations are apparent when viewing the thin section under the microscope, although weak layering is visible when viewing the whole thin section (Fig. 4.12a). The sample shows relatively high porosity (Fig. 4.12a), however zonal variations are apparent; an average porosity of ~20%, and up to 30% in places. The sample is relatively poorly cemented with patchy calcite spar (Fig. 4.12a).

No deformation bands are apparent within sample TMFS-1. However, the sandstone is relatively well compacted, with embayed contacts apparent at grain contacts.

4.4.3.2. Sample TMFS-2

TMFS-2 appears to sample a slightly more coarse-grained bed within the sandstone horizon. Laminations are clearly apparent at both the hand specimen (Fig. 4.5b) and thin section scale (Fig. 4.12b). Thin section analysis shows a well sorted sample with similar subarkosic grain composition to TMFS-1. Sub-rounded grains suggest that this sandstone is relatively mature. Large patches of sparry calcite are present.

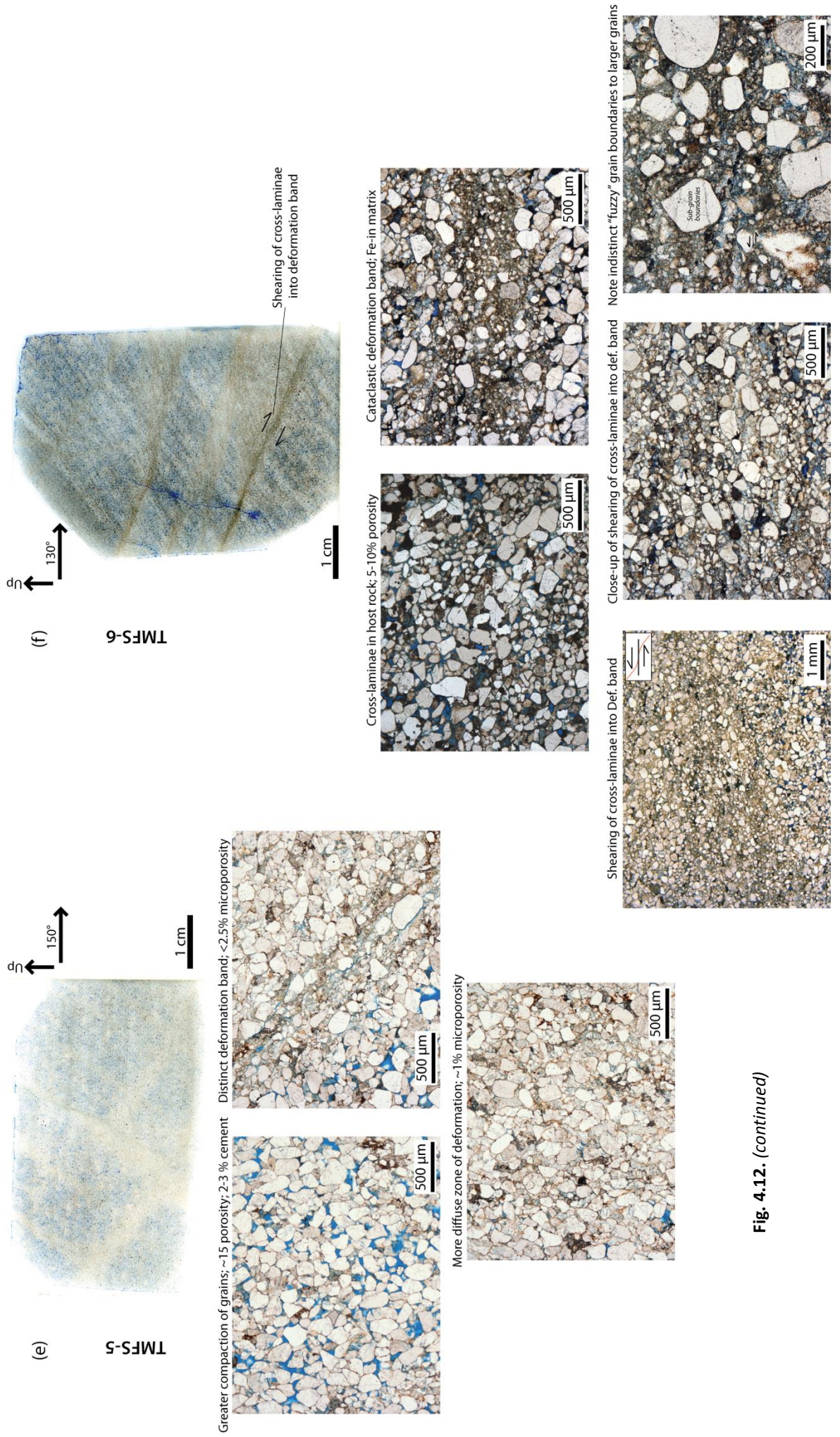


Fig. 4.12. (continued)

Similar to TMFS-1, this sample also contains no deformation bands. However, porosity is lower than that of TMFS-1, with an average porosity of ~15%. Calcite cementation reduces porosity significantly across the whole sample with porosity for some laminations <10%.

4.4.3.3. *Sample TMFS-3*

Sample TMFS-3 appears to be a very porous sample showing up to 30–35% porosity, again displaying only patchy calcite spar cementation (Fig. 4.12c). The sample exhibits minor deformation, though only one deformation band was sampled. This deformation band is not well developed and shows weak deformation and grain crushing (cataclasis). The deformation band shows significant porosity reduction (<5% porosity in the deformation band zone), with the majority of the porosity reduction appearing to be due to the development of the dominant carbonate cement within the deformation band.

4.4.3.4. *Sample TMFS-4*

The petrology of sample TMFS-4 remains similar to that of samples TMFS-1 to -3. Background (host rock) porosity is variable from lamina to lamina, although the average is relatively high at ~25% (Fig. 4.12d).

TMFS-4 samples three discrete (~1 mm wide) deformation bands (Figs. 4.5d & 4.12d). Microstructural analysis of these deformation bands shows evidence for cataclasis (grain crushing and grain size reduction). The grain size of the undeformed rock is medium to coarse (>250 μm), while within deformation bands this is significantly reduced (<50 μm). Although porosity is considerably reduced, micro-porosity (<5%) is still apparent within deformation bands (Fig. 5.12d). Calcite is also present within the deformation band, accounting for some of the porosity reduction.

4.4.3.5. *Sample TMFS-5*

Sample TMFS-5 displays significant deformation zones. Background (host rock) porosity within sample TMFS-5 is lower than the less deformed samples described above (~15%;

Fig. 4.12e). This is due to greater compaction, as evidenced by greater interlocking (tightly packed) grains, embayed contacts and possible pressure solution. Calcite cementation within the background rock is patchy, with calcite spar accounting for only 2–3% of porosity reduction.

Sampling several deformation bands, these appear more diffuse (up to 1 cm wide) than those sampled in TMFS-4. Although not well established, distinct slip zones may be identified within deformation bands (Fig. 4.12d). Micro-porosity within the deformation band is extremely low (~1%; Fig. 4.12e). Clear cataclasis and associated grain size reduction can be seen within deformation bands. Although larger grains are still present within the deformation bands, these show evidence for significant micro-fracturing and early development of sub-grain boundaries.

4.4.3.6. *Sample TMFS-6*

Sample TMFS-6 shows a clear system of moderately-dipping cross-laminations (Fig. 4.12f). Again a subarkosic grain composition is apparent (quartz grains with lesser plagioclase- and microcline-feldspars). Embayed contacts are visible. Background porosity is significantly reduced in TMFS-6 compared to the other 5 samples, at 5 to 10% (Fig. 4.12f). This is largely due to both compaction and greater calcite cementation.

Multiple diffuse and discrete, anastomosing deformation bands are identifiable. Micro-porosity within the deformation bands is <2%, again the result of cataclasis (grain size reduction), compaction and cementation. Shearing of cross-laminations into deformation bands can be clearly identified (Fig. 4.12f). Within deformation bands larger quartz grains are still evident within a finer-grained cataclastic matrix. However, some of these larger grains have ‘fuzzy’ grain boundaries which may reflect cataclasis along the boundary, while other grains show clear sub-grain boundaries parallel to deformation band orientations. Weakly developed slip planes are apparent within deformation bands, while at a grain-scale, shear can also be identified (Fig. 4.12f). Haematite is also incorporated into the matrix within deformation bands as a result of quartz grain crushing. Note the brownish-staining of deformation bands in Figure 4.12f.

4.5. Interpretations and Discussion

4.5.1. Fracture Intensity and Topology Variations Across Margin

Six sample stations have been analysed across an approximately 100 m long transect over the north-western intrusion margin (Figs 4.1c & 4.2). Nodal populations for each station have been recorded and populated on triangular plots (Fig. 4.13; after Manzocchi, 2002). The outcrops studied show a clear dominance of I- and Y- nodes (Fig. 4.13a), although the dominance of these nodes varies spatially. Samples stations more distal to the intrusion (i.e. TMFS-1 to -3) show a greater proportion of I-, and to a lesser extent, X-nodes (Fig. 4.13b, c). In contrast, there is a general increase in the dominance of Y-nodes with proximity to the intrusion (Fig. 4.13b, c). At sample stations TMFS-5 and -6 overlying the intrusion, I-nodes are negligible, and the nodal populations are dominated by Y- and X-nodes. These results reflect the overall increase in conjugate deformation bands observed at the intrusion margin (Morgan et al., 2008; this study, Chapter 3).

A clear increase in fracture abundance can be observed through a brief, visual overview of each sample site (Figs. 4.6–4.11). Quantitative analysis supports this observation (Fig. 4.14). Results from scan station analyses show a significant increase in fracture (line) frequency and density (intensity) with proximity to the intrusion (Fig. 4.14a). This increase in fracture frequency and density is also observed when analysing branches (Fig. 4.14b). Sanderson and Nixon (2015) proposed that fracture density (intensity) is the most fundamental measure of fracture abundance and provides an unbiased estimate for comparing fracture networks. Characteristic lengths appear to decrease towards the intrusion margin as a consequence of the increased fracture/ branch density (Fig. 4.14a, b). Although fracture length is somewhat dependent on the size of the sample area (Sanderson & Nixon, 2015), this decrease in characteristic length with proximity to the intrusion can be observed when comparing the consistent 20 cm scan areas. This relationship is also supported by analysis of characteristic branch lengths, which are less susceptible to sampling bias (Sanderson & Nixon, 2015). Dimensionless intensity (viewed as a scalar invariant characteristic) has also been calculated for each scan station population. This can be seen to increase markedly with proximity to the intrusion when analysing fractures (Fig. 4.14a). This increase is still apparent when analysing branches, however, the increase is less pronounced (Fig. 4.14b). The ratio of dimensionless intensity values for faults versus branches appears to be about 2:1 (Fig. 4.15).

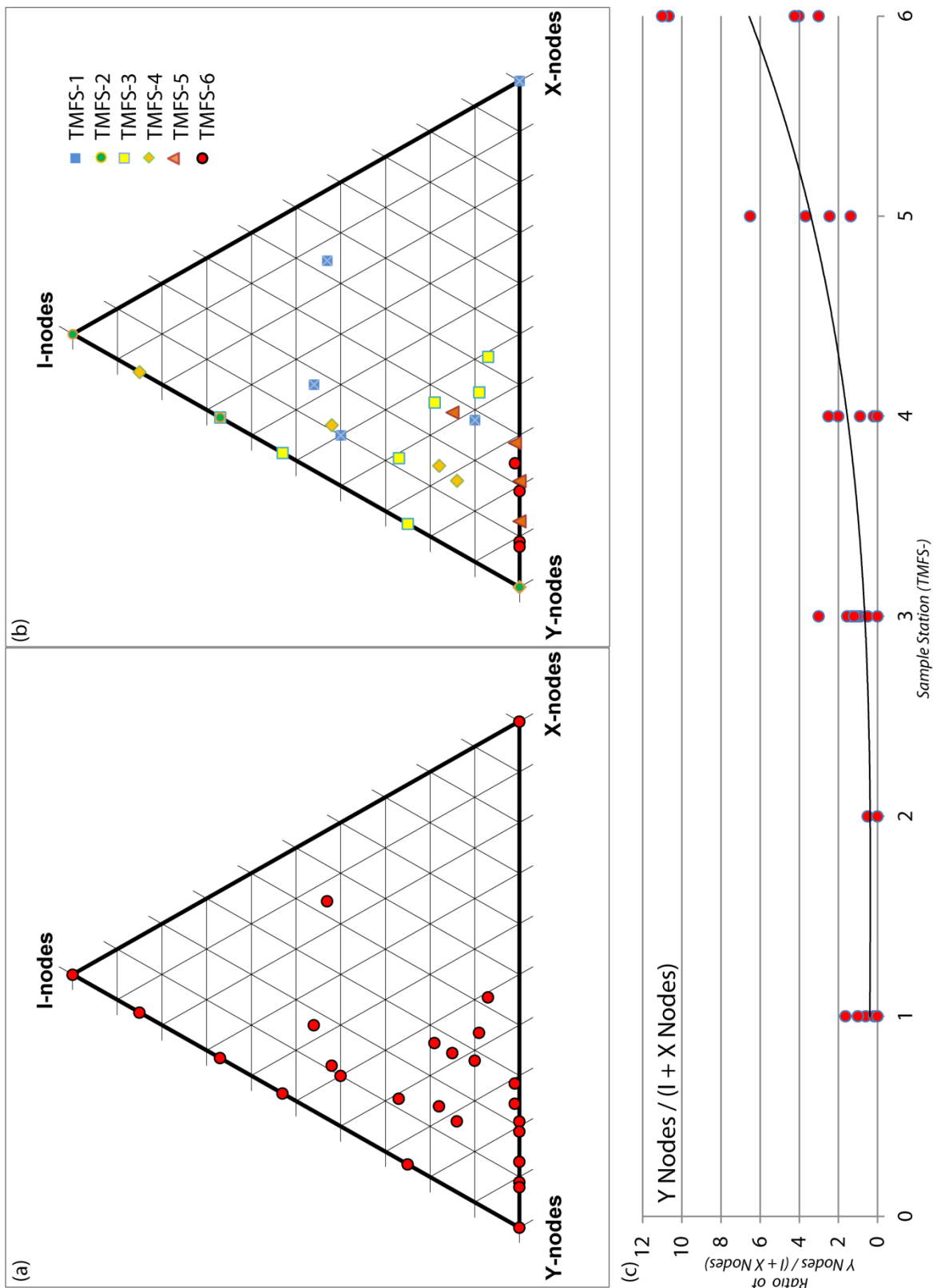


Figure 4.13. Fracture statistic triangular plots. (a) Triangular plot showing ratio of I-, Y- and X-nodes. (b) As in (a) with each sample location defined. (c) Scatter graphs showing ratio of Y-nodes to other nodes (i.e. I- and X-) across the study area. Note the increase in the ratio of Y-nodes onto the intrusion. Triangular plots created using Excel spreadsheet method of Graham & Midgley (2000).

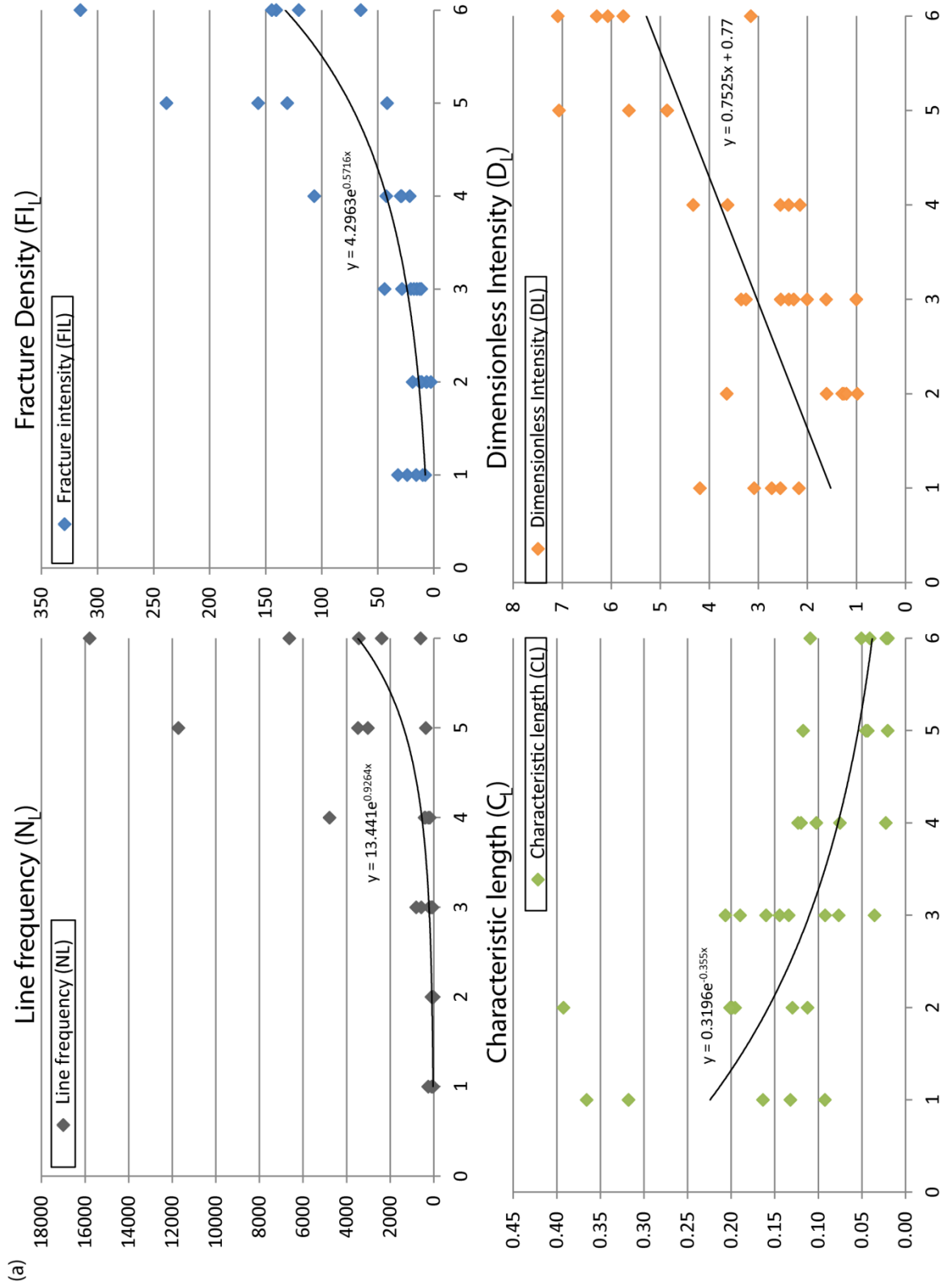


Figure 4.14. (continues overleaf)

Fracture statistics and their variation with location for: (a) fracture line; and (b) branch line statistics. Scatter graphs showing variations in Fracture Frequency (F_L , F_B), Fracture Intensity (FI_L , FI_B), Characteristic Length (C_L , C_B) and Dimensionless Intensity (D_L , D_B). X-axis refers to sample location (i.e. 1=TMFS-1, etc.).

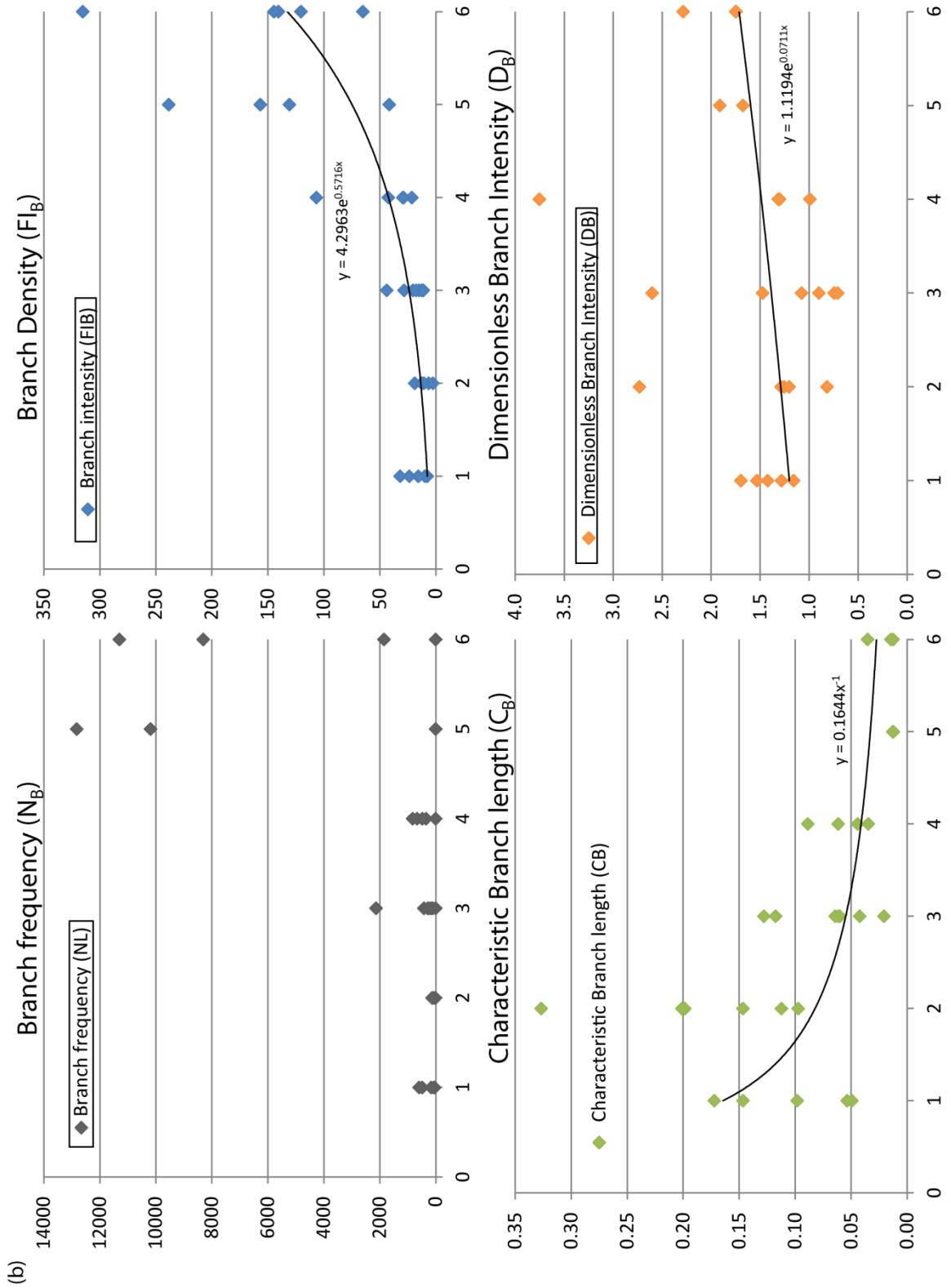


Figure 4.14. (continued)

4.5.2. Microstructural Interpretation

Microstructural analysis of deformed samples (i.e. TMFS-4, -5 and -6; Figs 4.5 and 4.12) shows dominantly brittle deformation with cataclastic flow and compaction occurring within deformation bands. Despite significant porosity reduction from undeformed host

rock (typically 20–30%) to within deformation bands, micro-porosity of <2% is still apparent within deformation bands. This porosity reduction is largely the result of this cataclasis and compaction, however, calcite cementation also plays a significant role in many of the sample deformation bands. Of significance, a reduction in host rock porosity is also apparent within samples TMFS-5 and TMFS-6, from sandstone beds overlying the intrusion (>25% in samples TMFS-1 to -3 compared to <15% in samples TMFS-5 and -6). This reduction appears to be the result of greater compaction of grains (and to a lesser extent, an increase in cementation). This is consistent with the observed porosity reduction and thinning of beds over the monoclinical intrusion margin of Morgan et al. (2008).

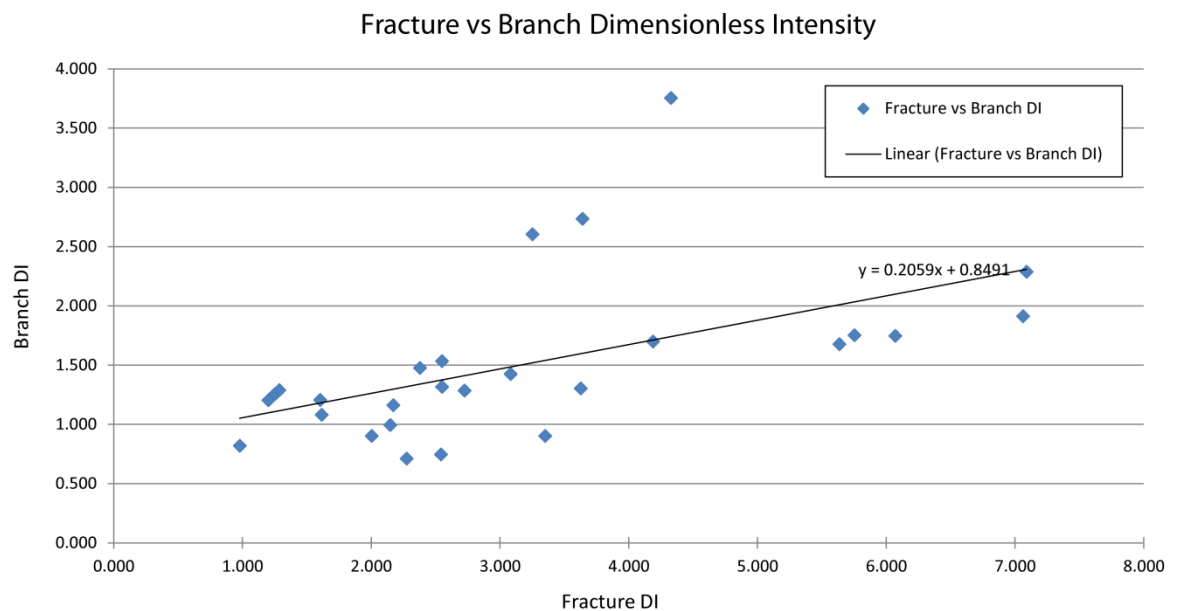


Figure 4.15. Plot showing the difference between fracture and branch line dimensionless intensity values. Note the approximately 2:1 ratio.

4.5.3. *Wider Implications*

Shallow level intrusions are a common feature of many basins currently being explored for hydrocarbon potential, including: NE Atlantic margin (e.g. Malthe-Sørrensen et al., 2004; Hansen & Cartwright 2006); West of Shetland (e.g. Rateau et al., 2013); and the southern and north-western margins of Australia (e.g. Holford et al., 2012; Magee et al., 2013). This quantitative study of fractures highlights the significant impact magma emplacement can have in highly porous clastic reservoir systems. Although only a small study, results show that fracture abundance and intensity increase markedly across the

NW margin of the Trachyte Mesa intrusion. The methods applied provide a means of quantifying this increase in deformation intensity across the intrusive margin.

The deformation bands show significant porosity reduction that is most apparent in the sandstones overlying the intrusion. These deformation bands are likely to impede (though not completely prevent) fluid flow and form baffles in a reservoir. The increase in Y- and X- nodes highlights the significant increase in deformation band interconnectivity, which in turn will significantly reduce the network connectivity and permeability pathways of the sandstone.

The deformation aureole around intrusions has not been analysed as part of this study. However, this is an important factor to consider when assessing the likely impact this intrusion-related deformation may have on a wider reservoir system. At Trachyte Mesa, deformation structures decrease markedly from ~5 to 10 m above the intrusion margin (although limited outcrop extent prevents a more detailed quantification of this). However, considering an intrusion the size of Trachyte Mesa (~1.5 km²), this ~10 m thick zone of deformation may reduce the exploitable reservoir volume noticeably.

Although further analyses are required in order to understand the 3D connectivity of these fracture systems, this study emphasises the potential importance of understanding the impact of syn-emplacement deformation to localised fluid flow around igneous intrusions. Gaining a better understanding of these emplacement-related deformation structures will therefore have important implications for fluid flow, hydrocarbon reservoir connectivity/ deliverability, and CO₂ sequestration.

4.6. Conclusions

Although deformation structures vary in style and intensity across the lateral “monoclinal” margin of the Trachyte Mesa intrusion (Chapter 3, this study), there is a clear relationship between deformation and proximity to the intrusion margin. This has therefore led a number of authors to propose that these deformation structures developed in response to emplacement of the intrusion (e.g. Johnson & Pollard, 1973; Morgan et al., 2008; this study).

Although only a small study, results show that fracture abundance and intensity increases markedly across the NW margin of the Trachyte Mesa intrusion. The methods applied provide a means of quantifying this increase in deformation intensity across the intrusive margin. Furthermore, the application of topologic analysis (i.e. in the form of nodal analysis) provides a means of understanding the network connectivity of deformation structures, and thus their negative impact on reservoir permeability. The increase in Y- and X-nodes with proximity to the intrusion likely creates a baffle or barrier to flow perpendicular to the intrusion margin, as well as potentially forming non-productive reservoir zones.

This study highlights that fluid flow in deformed host rocks around igneous bodies may vary significantly from that of the undeformed host rock reservoir. Therefore, a better understanding of the variability of deformation structures, and their association with intrusion geometry, will have important implications for hydrocarbon reservoir deliverability and CO₂ sequestration. Building digital field analogues can bridge the gap between thin section- (pore), outcrop- (sub-seismic), and regional (seismic) scales.



5. Chapter 5: Intrusion – host rock deformation and contact geometries, Maiden Creek, Henry Mountains, Utah

| | | |
|----------------|---|---------------|
| <i>Layout:</i> | 5.1. Introduction | p. 187 |
| | 5.2 Geological Setting | p. 189 |
| | 5.2.1. Maiden Creek intrusion | p. 192 |
| | 5.3 Intrusion geometries and deformation structures by domains | p. 194 |
| | 5.3.1. Zone 1: NE intrusion | p. 194 |
| | 5.3.1.1. Intrusion and host rock geometries | p. 194 |
| | 5.3.1.2. Syn-emplacment deformation structures | p. 194 |
| | 5.3.2. Zone 2: Eastern margin and ‘Whispering Wind Gully’ | p. 198 |
| | 5.3.2.1. Intrusion and host rock geometries | p. 198 |
| | 5.3.2.2. Syn-emplacment deformation structures | p. 204 |
| | 5.3.2.2.1. Zone 2a | p. 204 |
| | 5.3.2.2.2. Zone 2b | p. 205 |
| | 5.3.3. Zone 3: Southern intrusion and ‘Rattlesnake Gully’ | p. 209 |
| | 5.3.3.1. Intrusion and host rock geometries | p. 209 |
| | 5.3.3.2. Syn-emplacment deformation structures | p. 214 |
| | 5.3.4. Zone 4: NW margin | p. 217 |
| | 5.3.4.1. Intrusion and host rock geometries | p. 217 |
| | 5.3.4.2. Syn-emplacment deformation structures | p. 225 |
| | 5.3.4.2.1. Zone 4a | p. 225 |
| | 5.3.4.2.2. Zone 4b | p. 226 |
| | 5.3.5. Zone 5: SW Maiden Creek | p. 227 |
| | 5.3.5.1. Intrusion and host rock geometries | p. 227 |
| | 5.3.5.2. Syn-emplacment deformation structures | p. 227 |
| | 5.4. Discussion | p. 227 |
| | 5.4.1. Eastern margin (Zones 1, 2 and 3) | p. 232 |
| | 5.4.1.1. Lobes, Steps and Bridges | p. 236 |
| | 5.4.1.2. Kinematic partitioning | p. 237 |
| | 5.4.2. NW margin (Zone 4) | p. 237 |
| | 5.4.3. Unexposed SW margin (Zone 5) | p. 240 |
| | 5.4.4. A new model for development of the Maiden Creek intrusion | p. 241 |
| | 5.5. Conclusions | p. 246 |

Intrusion–host rock deformation and contact geometries, Maiden Creek, Henry Mountains, Utah

Abstract

The Maiden Creek intrusion is a small satellite intrusion to the Mount Hillers intrusive complex of the Henry Mountains, SE Utah. Emplaced within sandstones in the shallow crust, deformation structures in host rocks to the intrusion imply dominantly brittle deformation and, by proxy, intrusion emplacement mechanisms. Intense zones of compressional deformation are associated with host rocks adjacent to and ‘squeezed’ by lateral margins of converging intrusive bodies. In contrast, extensional deformation structures are associated with deformation in overlying sandstones and peripheral lateral margins. A thin (<1 m thick) shaley-siltstone horizon immediately overlies much of the top surface of the intrusion, acting as a detachment surface, above which syn-emplacement deformation is seemingly lacking. Detailed analysis from field studies of intrusion contacts and syn-emplacement host rock deformation structures to the intrusion has highlighted a complex intrusion geometry, including: lobate morphologies; steps and broken bridges; inclined sill sheets; and concave-upwards ‘laccolithic’ morphologies. A new model is proposed for the emplacement, evolution and final geometry of the intrusion, with a central elongate NE–SW lobe resulting from a principal north-easterly propagating magma flow. It is suggested that a feeder is located to the south-west of the Maiden Creek intrusion, in line with the termination of the neighbouring NE–SW trending Sawtooth Ridge satellite intrusion. Lateral growth of the Maiden Creek intrusion resulted from radial spreading of magma from this main north-easterly flow trend towards the east and north-west. This study suggests that much can be learnt about intrusion geometries and emplacement mechanisms through detailed structural and kinematic analyses of the host rocks and intrusion–host rock contact.

Keywords

Intrusion morphologies, Accommodation structures; Sill emplacement; Henry Mountains

5.1. Introduction

Our understanding of shallow level igneous intrusions, their emplacement mechanisms and morphologies, has developed significantly over the last 138 years since the pioneering work of G. K. Gilbert (1877) on the intrusions of the Henry Mountains, Utah. Mounting evidence from numerous studies focusing on the geometry and internal architecture of sills, laccoliths and plutons suggests that intrusions grow as a result of multiple magma pulses and through the amalgamation of numerous intrusive bodies (Pitcher, 1970; Hutton, 1996; Cruden & McCaffrey, 2001; Mahan et al., 2003; Glazner et al., 2004; Menand, 2008, 2011). The supporting evidence includes: field mapping of internal contacts and external margins (e.g. Morgan et al., 2008; Magee et al., 2012); geochronological studies (e.g. Coleman et al., 2004; Westerman et al., 2004); and magnetic and macroscopic fabric analyses (e.g. de Saint Blanquat & Tikoff, 1997; Horsman et al., 2005; Stevenson et al., 2007b).

Horsman et al. (2009), in their synopsis of the various studies of satellite intrusions in the Henry Mountains, Utah (Horsman et al., 2005; de Saint Blanquat et al., 2006; Morgan et al., 2008), suggested that the various forms of sill and laccolith geometries lie on a hypothetical evolutionary timeline reflecting the addition of successive sill sheets. In this scheme, sills (e.g. Maiden Creek) evolve to form laccoliths (e.g. Trachyte Mesa), laccoliths grow to become bysmaliths or punched laccoliths (e.g. Black Mesa), and these eventually grow to form plutonic scale intrusions.

Sills with tabular and concave upwards morphologies have been commonly observed in the field (e.g. Du Toit, 1920; Leaman, 1975), and stepped- and saucer-shaped morphologies observed in seismic sections (e.g. Francis, 1982; Cartwright & Hanson, 2006; Thomson & Schofield, 2008; Schofield, 2009). Furthermore, recent studies have shown that tabular and saucer-shaped sill intrusions are often emplaced by the amalgamation of magma fingers, sheets and lobes (Pollard et al., 1975; Malthe-Sørenssen et al., 2004; Thomson & Hutton, 2004; Horsman et al., 2005; Stevenson et al., 2007a; Morgan et al., 2008; Schofield et al., 2010, 2012a, b).

Pollard et al. (1975) first reported finger-like geometries for a number of intrusions on the Colorado Plateau, USA. Magma fingers typically display short lengths, between 1 and 10 metres (Pollard et al., 1975; Horsman et al., 2005), whereas lobate bodies range in size

from hundreds of metres to kilometres in scale (Schofield et al., 2012a). For this reason, Schofield et al. (2012a) highlighted that magma fingers are a sub-seismic resolution feature, whereas lobes can be resolved. Schofield (2009) and Schofield et al. (2012a) proposed that fingers are an integral part of sill intrusions, with magma fingers growing to form lobes, and lobes coalescing to form sills (Fig. 5.1a). Structural steps, parallel to the magma transport direction, are commonly identified on the top surfaces of sills (Rickwood, 1990; Schofield et al., 2012a). The development of steps has also been described in terms of hackle steps on dykes and joint surfaces (Pollard et al., 1975; Rickwood, 1990; Frid et al., 2005) and the interconnection of sill sheets propagating at slightly different stratigraphic levels (Schofield et al., 2012a). In the case of overlapping sill sheets, a host rock bridge or relay develops between the sheets. As these sheets inflate, fractures develop due to flexure, which may then be exploited by magma and results in the sheets coalescing (Fig. 5.1.b; Nicholson & Pollard, 1985; Hutton, 2009). The remnant bridges are termed 'broken bridges'. Schofield et al. (2012a) proposed that stepped geometries are characteristic of brittle emplacement mechanisms, whereas magma fingers and lobes are associated with ductile (or fluidisation) emplacement processes. They also suggested that these brittle and ductile end member processes may be linked both to rock rheology and depth (i.e. brittle – deeper; ductile – shallower), acknowledging that a transition zone may exist where both processes and resulting geometries may occur.

This study focuses on the intrusion geometries and their associated host-rock deformation structures of the Maiden Creek intrusion in the Henry Mountains, Utah. Here, Horsman et al. (2005) interpreted the intrusion to have elongate finger-like lobe geometries, while Johnson and Pollard (1973) described intense host-rock deformation structures within the sandstones immediately adjacent to and above intrusion outcrops. The abundance of preserved intrusion–host rock contacts makes Maiden Creek an excellent study area. Using detailed structural and kinematic studies of the host rock deformation, the aim is to test the hypothesis that host rock deformation structures are intrinsically linked to intrusion geometries, and their emplacement. This approach has led to a reinterpretation of the finger-lobe model for the Maiden Creek intrusion and the results are presented and discussed below.

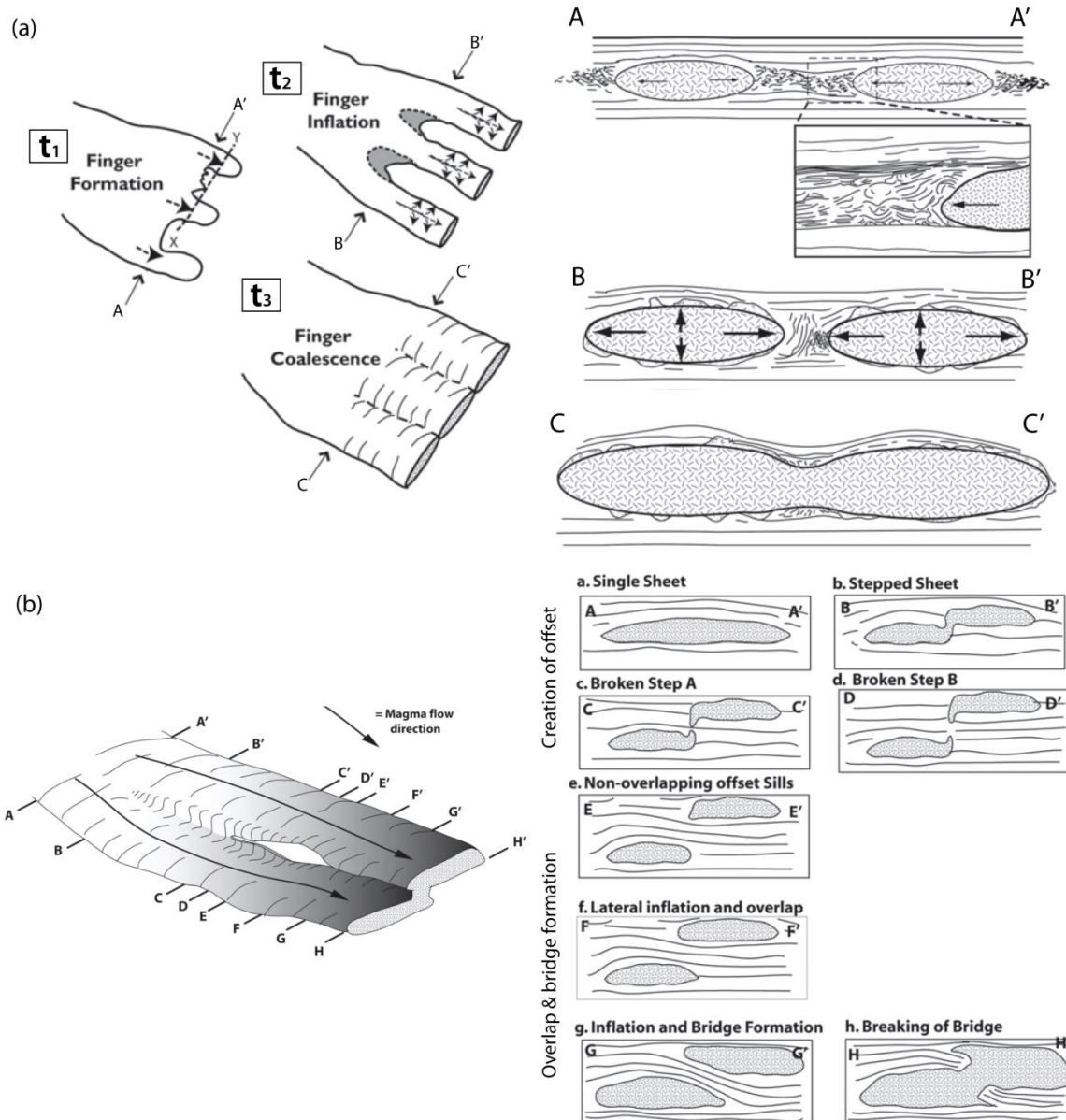


Figure 5.1. Schematic sketches illustrating geometries and evolution of: (a) magma fingers and lobes; and (b) steps and broken bridges. Images from Schofield (2009) and Schofield et al. (2012).

5.2. Geological Setting

Emplaced within an ~3–6 km thick section of late Palaeozoic–Mesozoic sedimentary rocks overlying Precambrian basement (Jackson & Pollard, 1988; Hintze & Kowallis, 2009), the Henry Mountains are located in south-eastern Utah (Fig. 5.2a) and are one of more than ten mountain ranges on the central and eastern Colorado Plateau that are comprised of sedimentary domes with igneous cores, encircled by smaller satellite intrusions (dykes, sills and laccoliths; Gilbert, 1877; Hunt, 1953; Jackson & Pollard, 1988; Nelson et al., 1992). The range consists of five principal peaks (Fig. 5.2a), from north to south these are: Mt Ellen; Mt Pennell; Mt Hillers, Mt Holmes; and Mt. Ellsworth. Igneous rock composition throughout the Henrys is very consistent with ≥95% comprising of an intermediate, bulk

diorite composition (58–63% SiO₂; Hunt, 1953, 1988; Engel, 1959; Nelson & Davidson, 1993). The diorite has a porphyritic texture with dominant plagioclase and hornblende phenocrysts constituting 25–55% of the rock (Engel, 1959; Nelson & Davidson, 1993; Horsman et al., 2005). Despite the consistent bulk dioritic composition throughout the Henry Mountains, significant textural variations (in particular phenocryst size and phenocryst:matrix modal abundance ratio) can be used to characterise the diorite of the different intrusions and, in places, to identify distinct magma pulses within an intrusion (Horsman et al., 2005).

Mount Hillers (Figs 5.2a) displays the best exposure of the five Henry Mountains intrusive centres, and as a result is also the most studied (e.g. Gilbert, 1877; Hunt, 1953; Johnson & Pollard, 1973; Jackson & Pollard, 1988; Horsman et al., 2005, 2009; de Saint Blanquat et al., 2006; Morgan et al., 2008). Numerous satellite intrusions outcrop to the north and north-east (Fig. 5.2). Interestingly, Sawtooth Ridge, Black Mesa and Maiden Creek satellite intrusions are situated in close proximity to one another and yet all display very different geometries (Fig. 5.2b). Sawtooth Ridge is the closest of the three satellite intrusions to Mount Hillers. The intrusion is a highly elongate and narrow body, trending roughly ENE–WSW (Figs 5.2) and has a jagged topography from which it gets its name: Sawtooth (Hunt, 1953; Johnson & Pollard, 1973; Horsman et al., 2005). Situated just to the north of the tip of Sawtooth Ridge is Black Mesa (Fig. 5.2). Described as a punched laccolith or bysmalith, Black Mesa is characterised by a circular shape in map view (Fig. 5.2b) and a faulted cliff face ~130 m high constitutes its eastern margin (Hunt, 1953; Habert et al., 2004; de Saint Blanquat, 2006; Horsman et al., 2009). Both Sawtooth Ridge and Black Mesa intrude at the same stratigraphic level, within the upper Summerville Formation (Jurassic reddish, brown shales, siltstones and sandstones; Hintze & Kowallis, 2009). Maiden Creek, described as a sill for the most part (Hunt, 1953; Johnson & Pollard, 1973; Horsman et al., 2005), is situated just to the north-east of Sawtooth Ridge and at the foot of the domineering faulted cliff face of Black Mesa (Fig. 5.2b). Dissimilar to its neighbouring satellite intrusions, however, Maiden Creek is intruded stratigraphically lower, within the Entrada Sandstone Formation of the Jurassic San Rafael Group (Hunt, 1953; Hintze & Kowallis, 2009).

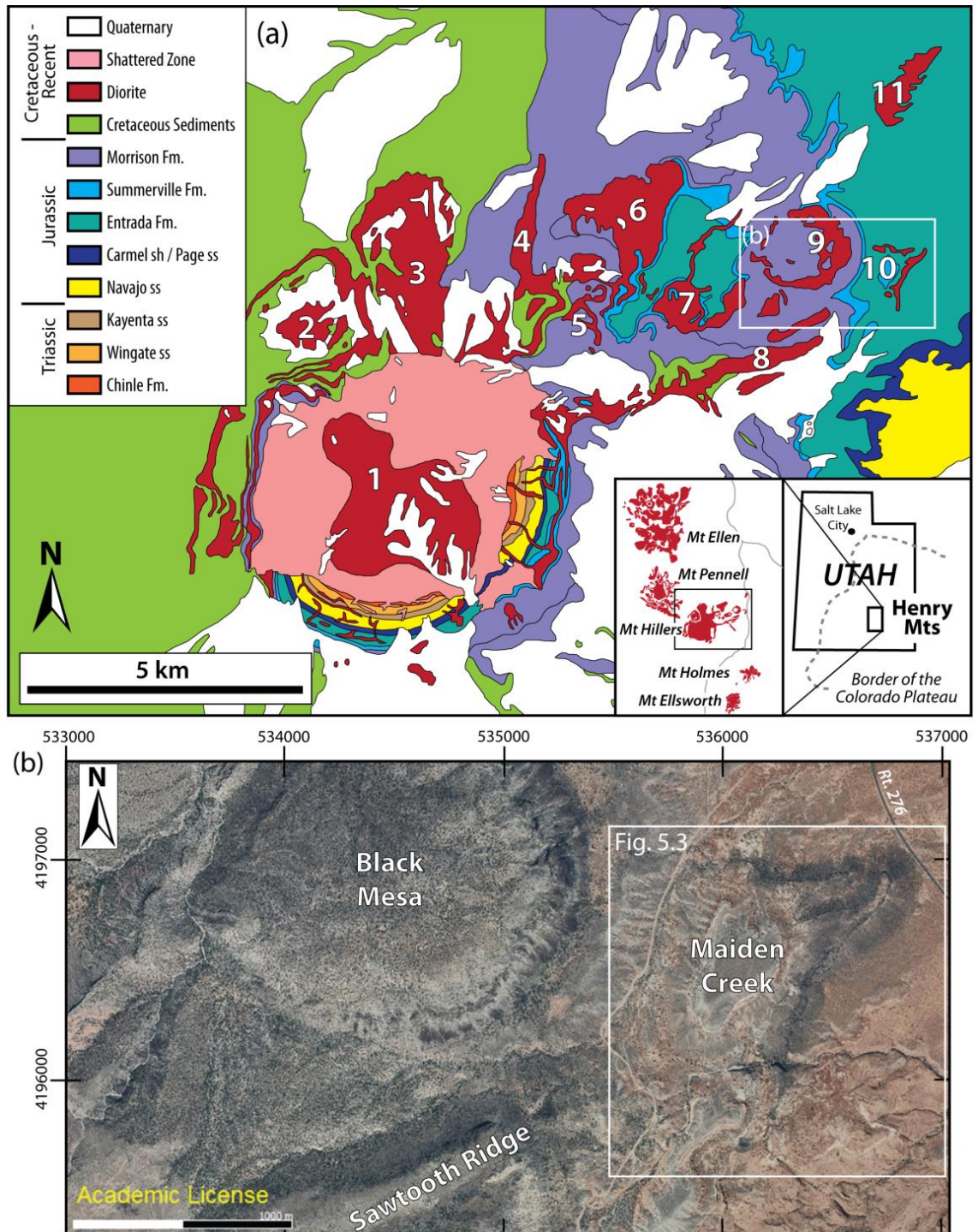


Figure 5.2. Location and geology maps of the Mount Hillers intrusive complex, Henry Mountains, Utah. (a) Simplified geological map of Mount Hillers and its satellite intrusions (modified from Larson et al., 1985). The various intrusions that comprise the Mt Hillers intrusive complex are numbered, using the names given by Hunt (1953): 1 – Mt Hillers central complex; 2 – Bulldog Peak intrusion; 3 – Stewart Ridge intrusion; 4 – Specks Ridge intrusion; 5 – Chaparral Hills Laccolith; 6 – Specks Canyon; 7 – speculated feeder system to the Trachyte Mesa intrusion; 8 – Sawtooth Ridge intrusion; 9 – Black Mesa intrusion; 10 - Maiden Creek intrusion; 11 – Trachyte Mesa intrusion. Inset maps show location of Mount Hillers with respect to Utah and the Henry Mountains as a whole. (b) Aerial photograph showing location and geomorphology of the Maiden Creek intrusion and neighbouring intrusions (Black Mesa and Sawtooth Ridge). Image from Google Earth™.

5.2.1. Maiden Creek Intrusion

The Maiden Creek intrusion (originally Laccolite D of Gilbert, 1877) is a small intrusion (~1 km² in map view; Fig. 5.3). From the abundance of lateral contacts of the Maiden Creek intrusion with the surrounding host rocks, it can be inferred that the current map pattern of the intrusion corresponds closely to the original geometry of the intrusion (Horsman et al., 2005). Johnson and Pollard (1973) provided a short summary of the intrusion and host rock deformation in their report on the mechanics of laccolith intrusions in the Henry Mountains from field observations. They noted its irregular shape in map view (Figs 5.2b & 5.3).

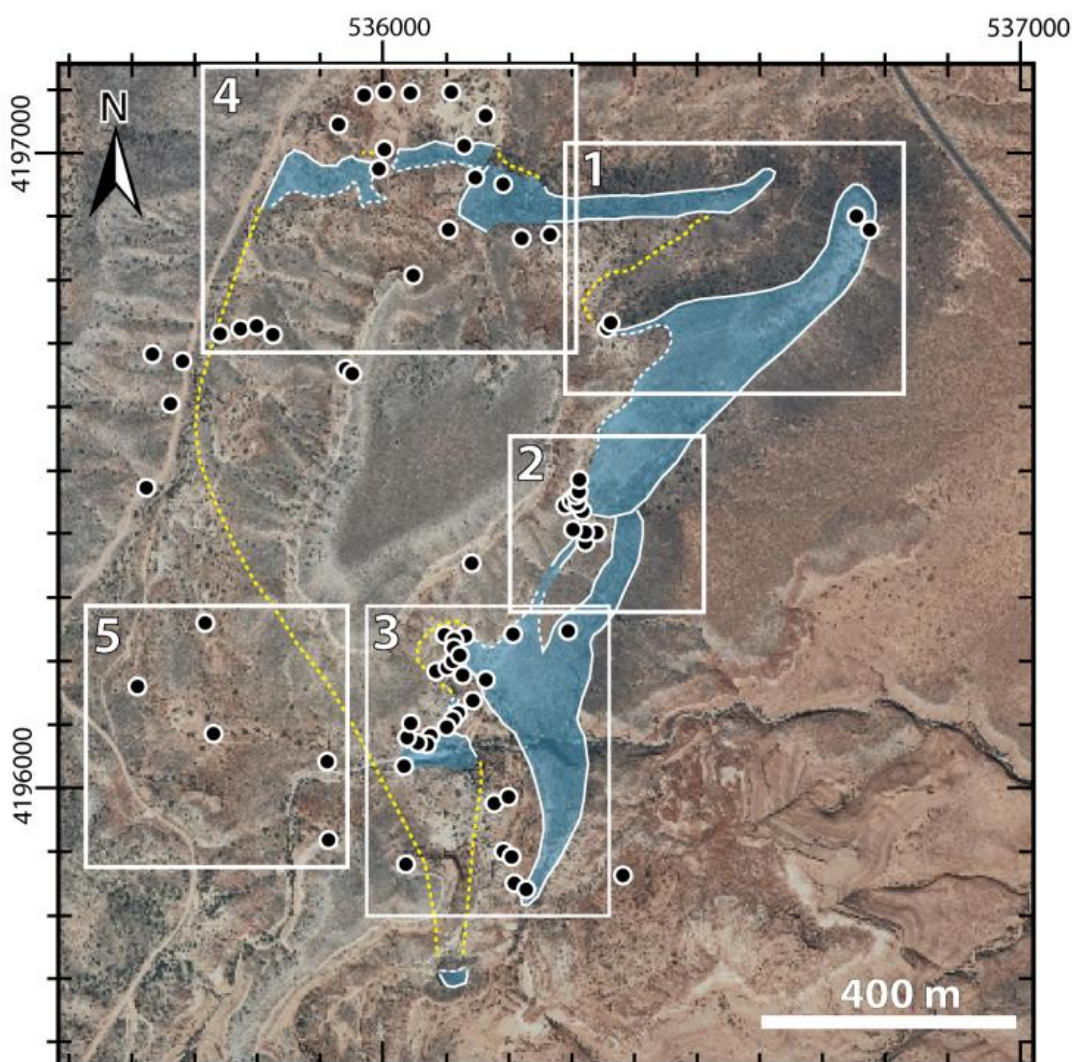


Figure 5.3. Map of the Maiden Creek intrusion and study areas. Zoomed-in aerial photograph (source: <http://gis.utah.gov/data/aerial-photography/>) of the Maiden Creek intrusion. Intrusion outcrop extent shown in blue (modified after Horsman et al., 2005). Yellow dashed line depicts subsurface intrusion extent proposed by Horsman et al., 2005. Black circles with white outlines show structural stations analysed in this study (also see Google Earth™ kmz file in Appendices for structural station locations). Mapped white boxes show structural zones discussed in this paper: 1 – NE Intrusion; 2 – Eastern margin and ‘Whispering Wind Gully’; 3 – Southern Intrusion and ‘Rattlesnake Gully’; 4 – NW Maiden Creek; and 5 – SW Maiden Creek.

Horsman et al. (2005), using a combination of field mapping and fabric studies (both field lineation and AMS measurements), divided this original intrusive geometry into two discrete parts: the main body of the intrusion; and interpreted finger-like lobes projecting outwards from the main body of the intrusion (outline in Fig. 5.3). The main body is described as having a simple sill-like morphology, while three finger-like lobes (100 m scale) emanate from this main sill, two in the north-east and one to the south (Horsman et al., 2009). A fourth finger-like lobe is inferred from outcrops observed to the west of the southern finger-like lobe (Horsman et al., 2005). Horsman et al. (2009) suggested that these lobes cut up through the stratigraphy in the direction of magma flow with the southern one of the NE pair cutting up gradually whereas the southern lobe, in comparison, shows a stepped basal contact. Reporting field observations of two vertically stacked bulbous terminations, along with a narrow band of solid-state fabrics within the intrusion, Horsman et al. (2005, 2009) proposed that the intrusion is comprised of two vertically stacked sheets, the second sheet intruded above the first and having an almost identical thickness and extent to the first. Based on the relatively small volume of the intrusion ($<0.03 \text{ km}^3$) Horsman et al. (2005) proposed that the Maiden Creek intrusion represents the initial stages of emplacement.

Johnson and Pollard (1973) described intrusion–host rock geometries at an outcrop on the NE edge of Maiden Creek. Here they observed an intense zone of cataclastic deformation (~10 m wide) adjacent to a blunt intrusion margin. In contrast to this intensely deformed lateral margin, they noted that deformation dies out quickly (within 1 m) on the top surface of the intrusion. However, there are few other documented descriptions of host rock deformation structures associated with the Maiden Creek intrusion.

Detailed kinematic and geometrical studies were carried out at a total of 80 structural stations dispersed over the entirety of the intrusion (see spreadsheets and Google Earth™ kmz file in Appendices for locations of structural stations). At each structural station, a representative structural dataset (including: deformation type; geometry; kinematics; character; and cross-cutting relationships) was collected (minimum of 30 measurements per station; >50 in areas of high intensity deformation). In total, 3986 structural measurements were collected. This dataset enabled a detailed structural analysis of the

intrusion. The results suggest a highly complex intrusion geometry accompanied by equally complex and varied host rock and contact deformation structures. Consequently, for ease of description, the intrusion has been divided into 5 separate zones (Fig. 5.3): Zone 1 – NE intrusion; Zone 2 – Eastern margin and ‘Whispering Wind Gully’; Zone 3 – Southern intrusion and ‘Rattlesnake Gully’; Zone 4 – NW margin; Zone 5 – SW Maiden Creek. Each of the areas will be discussed in detail in the following sections.

5.3. Intrusion Geometries and Deformation Structures by Domain

5.3.1. Zone 1: NE Intrusion

5.3.1.1. Intrusion and Host Rock Geometries

Zone 1 comprises two distinct elongate intrusive bodies, separated by a sandstone gully (Fig. 5.4). The main intrusive body (main lobe) displays a lobate morphology trending NE–SW, bending to a more N–S trend at the tip (Fig. 5.5a–c). The exposed lobe is ~500 m long, >30 m thick (basal contact is not clearly visible, though Horsman et al. (2005) implied a vertical thinning towards the NE tip), and thins laterally from ~150 m wide in the SW to ~45 m at the tip. The top surface is flat with convex, upper lateral margins. Lateral margins are relatively steep, with the NW lateral margin in the sandstone gully showing a jagged and stepped geometry (Fig. 5.5). A distinct NE–SW trending fabric is identifiable from aerial images (Fig. 5.4b, d). This is confirmed by AMS and fabric studies by Horsman et al. (2005).

The second intrusive body (northern ridge) appears smaller and trends approximately E–W (Fig. 5.4a). Only the northern lateral margin is exposed, except at the tip of the intrusion, and no basal contact is identifiable. Unlike the adjacent lobe, this body does not exhibit a flat top surface, and its true sub-surface geometry is not well constrained.

5.3.1.2. Syn-emplacement Deformation Structures

Deformation structures were observed in both sandstones on the top surface (Fig. 5.4e, f) and on the NW-lateral margin of the main lobe (structural stations MCSS-39, 40, 41 & 43; Fig. 5.5), as well as in the intrusion itself (Fig. 5.5b, d, g). Deformation structures within the host rock sandstone dominantly trend NE–SW (Fig. 5f), parallel to the main trend of the larger of the two intrusive bodies (main lobe; Fig. 5.4a, b).

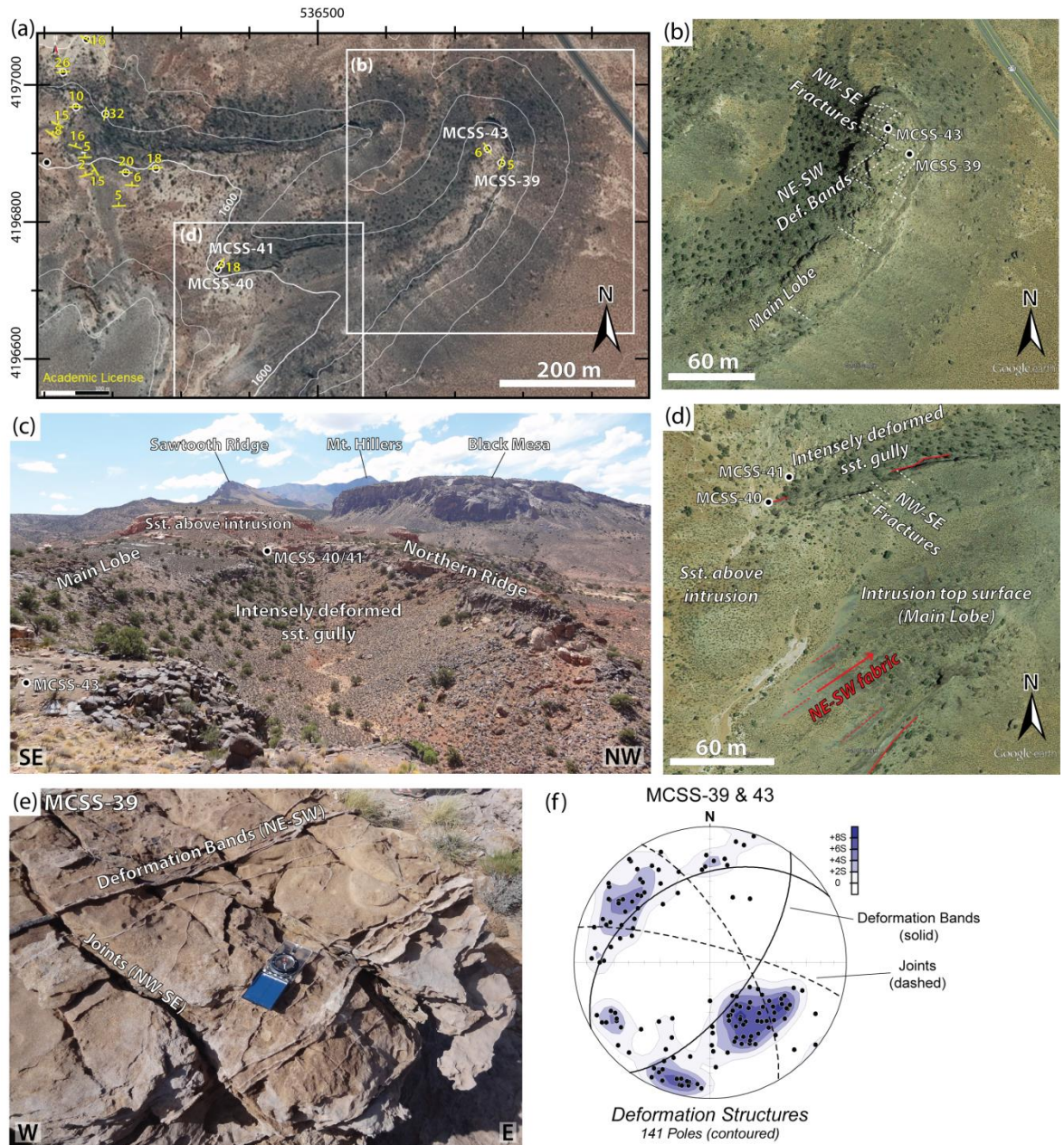


Figure 5.4. NE Maiden Creek Intrusion (Zone 1). (a) Aerial photograph over NE Maiden Creek. Grey outcrops are igneous, brownish outcrops are sandstone. Note NE–SW trending “Main” Lobe and E–W trending northern ridge. Bedding strike and dip in yellow. (b) NE tip of the main lobe (structural stations MCSS-39 and -43) as seen in Google Earth™. Note, change in trend of the lobe from NE–SW to NNE–SSW towards the tip. (c) View looking south-west from structural station MCSS-43. Note the sandstone gully between elongate igneous bodies (Main Lobe and northern ridge). (d) NE–SW fabrics on intrusion top surface of Main Lobe, as seen in Google Earth™. (e) Field photograph of NE–SW deformation bands and NW–SE joints (structural station MCSS-39). (f) Lower hemisphere equal area stereoplot for planar structures recorded at structural stations MCSS-39 and -43. Poles to planes are contoured and mean planes are shown for each plot (black lines).

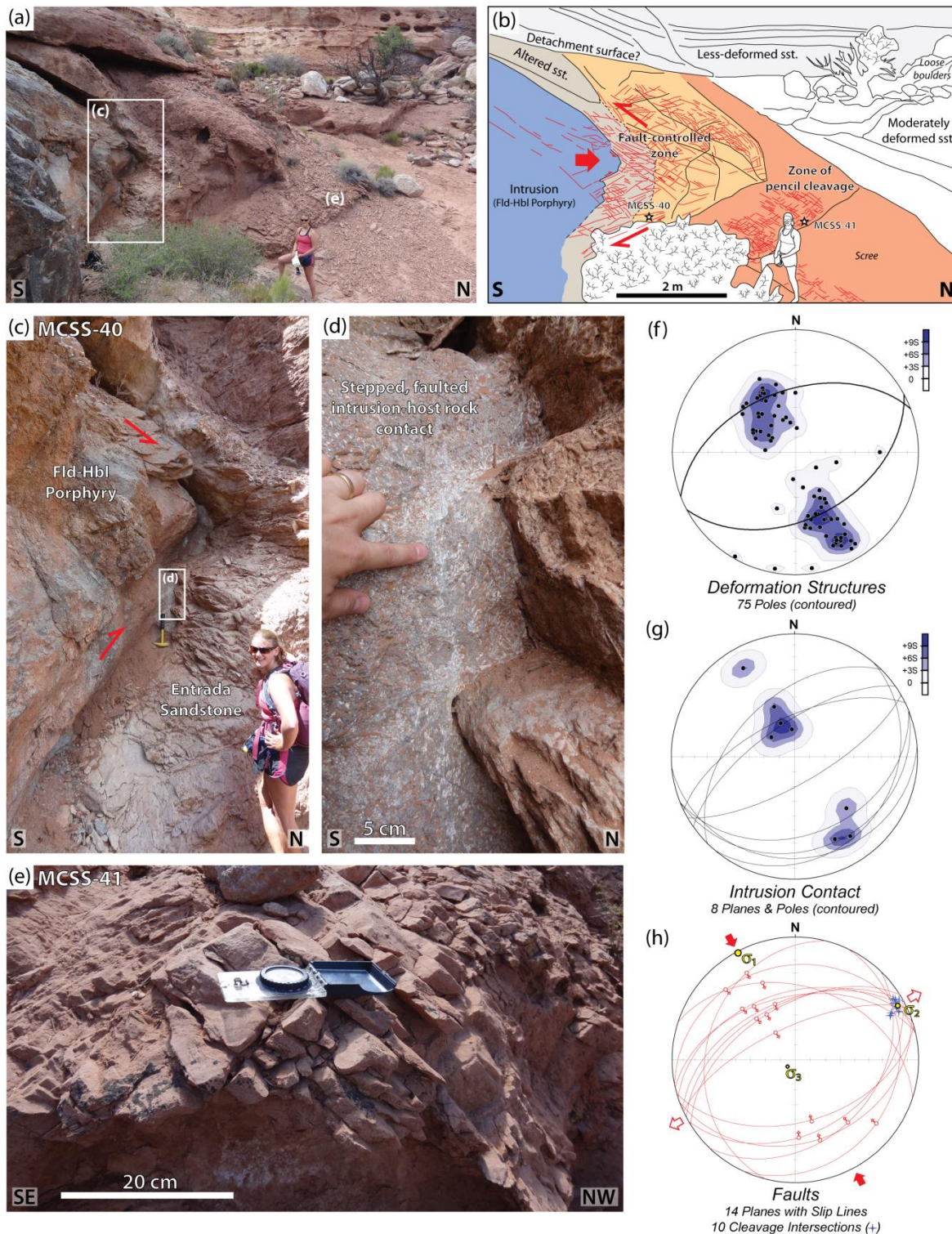


Figure 5.5. Structural stations MCSS-40 and -41 in Zone 1. (a) Outcrop photo, and (b) schematic sketch of the north-western lateral margin of the Main Lobe, highlighting intrusion-related deformation at the intrusion–host rock contact and within the adjacent host sandstones (compare to fig. 13 in Johnson & Pollard, 1973). (c) Field photograph showing the stepped, faulted intrusion–host rock contact. (d) Zoom-in of the stepped intrusion–host rock contact. Note, fractures extending into intrusion, parallel the intrusion. Also note the stretched, elongate feldspar phenocrysts and resulting fabrics showing drag into fault surfaces. (e) Pencil cleavage. (f)–(h) are a series of lower hemisphere equal area stereoplots, showing poles to planes (contoured) for: (f) NE–SW trending deformation structures (faults, deformation bands and pencil cleavage); (g) stepped surfaces of the intrusion–host rock contacts shown in (d); and (h) reverse faults (red planes), kinematics (red slip symbols) and pencil cleavage intersections (blue crosses). Stress axes and

Shmin/ SHmax orientations calculated using kinematic inversion method of Reches (1987). Mean planes are shown for each plot (black lines).

On the top surface of the main lobe, a conjugate set of deformation bands dip steeply (>70°) to the SE and moderately (~40°) to the NW (Fig. 5.4f). Deformation bands (Fig. 5.4e) are very prominent (positive relief) and thick (up to 1 cm for an individual band; 5 cm for an anastomosing system; Fig. 5.4e). These deformation bands are cross-cut by steeply-dipping tensile joints trending roughly NW–SE, perpendicular to the intrusion trend and the deformation bands (Fig. 5.4e, f). These tensile joints are also apparent within the intrusive body, and are identifiable in aerial photographs (Fig. 5.4b, d).

The NW lateral margin of the main intrusive lobe shows a stepped and faulted geometry, with zones of high intensity deformation in the adjacent host-rock sandstone (Fig. 5.5). The deformed sandstone can be divided into three areas (A, B, C) with distance from the intrusion–host rock contact (Fig. 5.5b):

- **A** 0–1 m (fault controlled zone): altered, whitish-grey sandstone, intensely deformed by abundant NE–SW trending, reverse faults dipping moderately to both the SE and the NW (Fig. 5.5a–c, f, h). Offsets on deformation bands and other faults, in addition to slickenlines, provide the kinematic data (Fig. 5.5h).
- **B** 1–3m (fault controlled zone): reddish sandstones also deformed by reverse faults and deformation bands.
- **C** ≥3 m (zone of pencil cleavage): intense (mm- to cm- spacing) conjugate deformation banding forming distinct planes (Fig. 5.5e,f, h). This area is characterised by a zone of loose scree formed by pencil cleavage shards (Fig. 5.5a).

The geometries of deformation fabrics are similar in all three zones and the stepped intrusion–host rock contact also exhibits these same orientations (Fig. 5.5f, g). Similar conjugate faults/ shear fabrics can also be seen within the intrusion, although none appear to cross-cut the contact. These shear fabrics show similar reverse kinematics to the faults observed in the adjacent country rock (Fig. 5.5d). Kinematic inversion (Reches, 1987 method) of faults confirms a compressional system with a NNW–SSE SHmax and an ENE–WSW Shmin (Fig. 5.5h). Cleavage intersection from area C is coincident with σ_2 (Fig. 5.5h).

An apparent sub-horizontal surface is found above the deformed sandstones in subzones A, B, and C (Fig. 5.5a, b). Sandstone beds above this within the gully show less deformation than those below. This detachment surface is traceable onto the top surface of the main intrusive lobe on the NW lateral margin, and is found within a more shaley-sandstone unit.

5.3.2. Zone 2: Eastern Margin and ‘Whispering Wind Gully’

5.3.2.1. Intrusion and Host Rock Geometries

Intrusion geometries along the eastern margin are somewhat complex (Figs 5.6 & 5.7). Zone 2 and Whispering Wind Gully mark a change in trend of the eastern margin of Maiden Creek (Figs 5.3 & 5.6), from trending NE–SW in the north (Zone 1) to roughly NNE–SSW to N–S in the south (Zone 3). The outer (eastern) lateral margin is steeply dipping and forms a cliff up to 30 m high (Fig. 5.7a). For ease of description, Zone 2 has been further divided into two subareas: Zone 2a to the south; and Zone 2b (including Whispering Wind Gully) to the north (Fig. 5.6b). North of Whispering Wind Gully, the intrusion top surface is relatively flat and appears to be a continuation of the main, NE–SW trending lobe in Zone 1 (Figs 5.3, 5.6a–c & 5.7a).

Figure 5.6 (overleaf)

Eastern margin and ‘Whispering Wind Gully’ (Zone 2). (a) Aerial photograph of the Eastern Margin of Maiden Creek (Zone 2). Bedding strike and dip in yellow. (b) Panorama field photograph of Zones 2a and 2b, view looking north-west. Viewpoint location provided on (d). Note the outcrop of igneous intrusion higher than the intrusion in the foreground, with sandstones outcropping between. (c) Panorama field photograph of Zone 2a, view looking ESE. Viewpoint location provided on (d). Note the elongate igneous ridge denoting the edge of the intrusion. (d) Spatial distribution of deformation structures across the eastern margin of the Maiden Creek intrusion and Whispering Wind Gully (Zone 2). Structural stations highlighted by white circles with black outlines, sandstone–igneous contacts in red, and detachment surfaces in pink. Red and white arrows depict inferred SHmax and Shmin orientations, based on fault and deformation band trends. Fault/deformation band geometries are depicted in lower hemisphere equal-area stereoplots. Poles to planes are contoured and mean planes are shown for each plot (black lines).

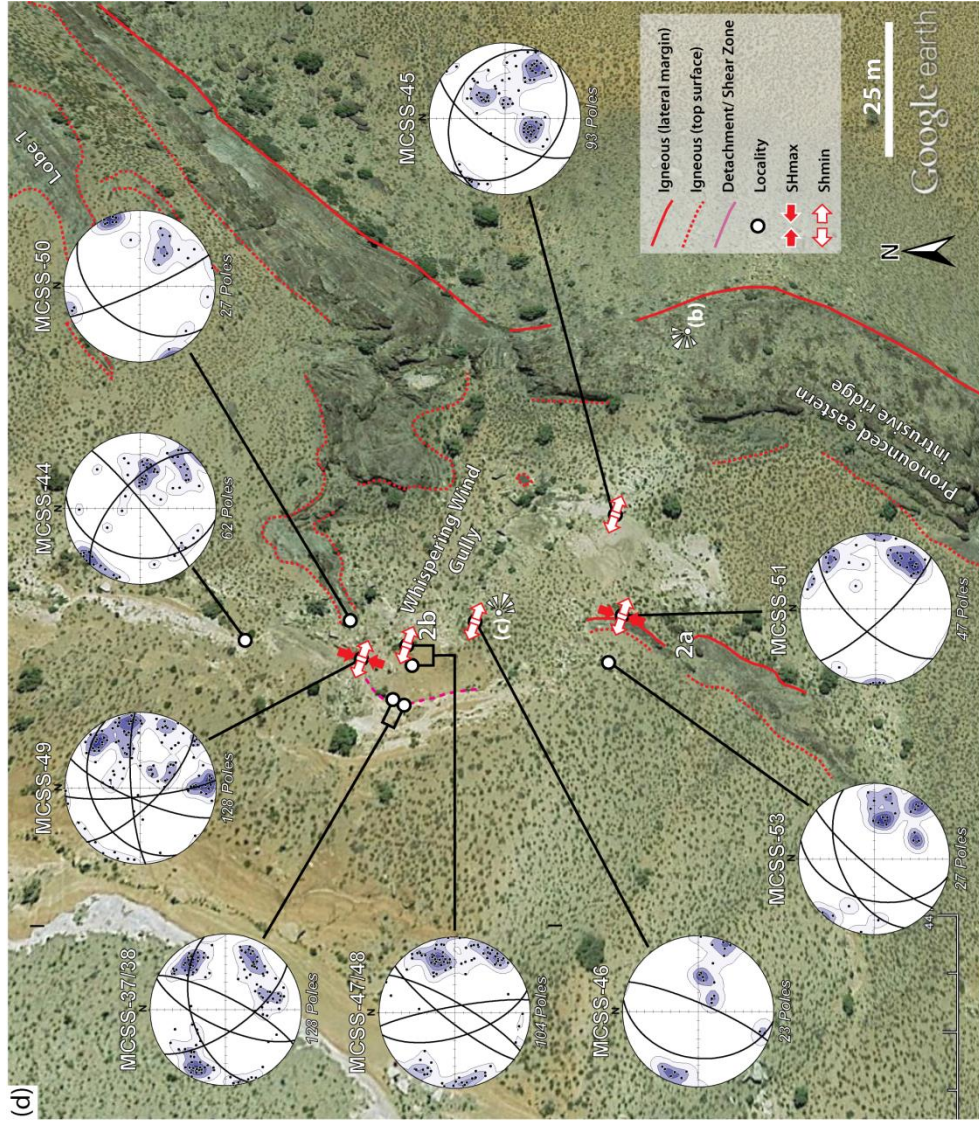


Fig. 5.6



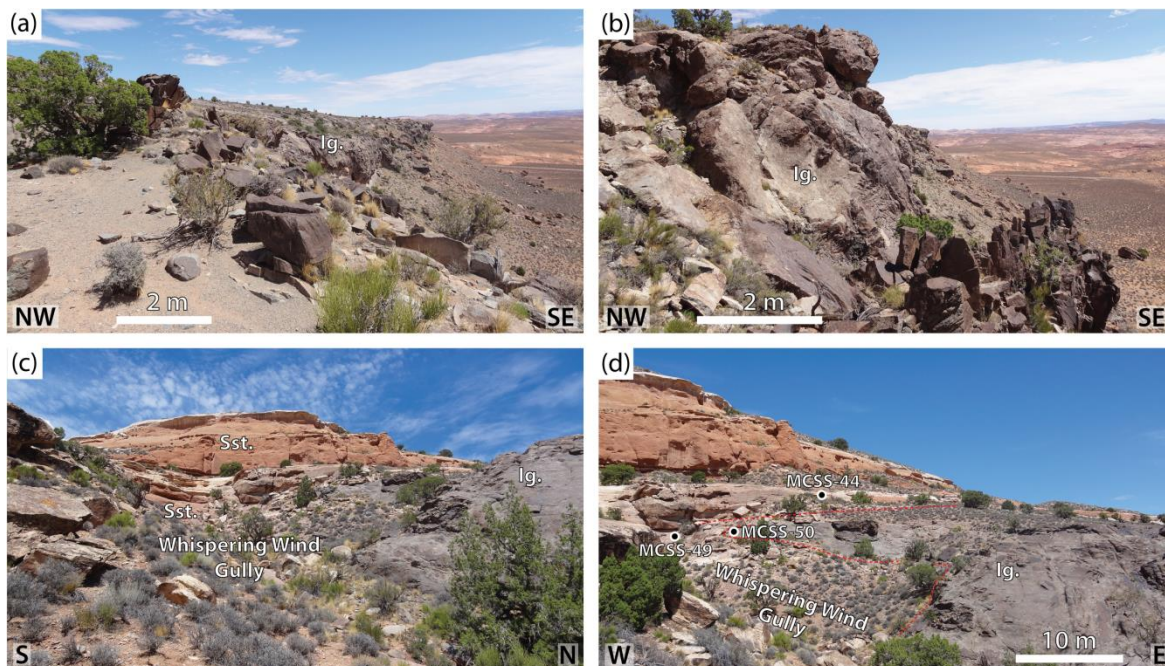


Figure 5.7. Series of field photographs showing various intrusion geometries in Zone 2. (a) View looking north-east along the eastern margin of the Maiden Creek intrusion. (b) View looking north-east from the eastern edge of Whispering Wind Gully, Zone 2b. Note the NE–SW trending ridge of columnar jointed intrusion in the foreground. (c) View looking west along the length of Whispering Wind Gully in Zone 2b. Intrusion outcrops are observed on the northern flank of the gully, but are absent in the south and central gully. Here, lateral margins and an inclined top surface to the intrusion are visible. (d) View looking north across Whispering Wind Gully. Note flat top surface to intrusion to the north, undeformed sub-horizontal sandstones above, and deformed sandstones in gully at same level as intrusion.

South of Whispering Wind Gully (Zone 2a) the intrusion top surface appears to be more undulatory. Two distinct elevated elongate exposures of intrusive rocks can be observed, separated by lower-lying sandstone outcropping in-between (Fig. 5.6). The outcrops to the east form a pronounced ridge (Fig. 5.6c) running along the eastern margin of the intrusion, and appear to be onlapped by sub-horizontal sandstone beds to the west (Fig. 5.6b, c). Slightly further up the slope, we pass into another intrusive zone, lying topographically higher than the ridge to the east (Fig. 5.6b, d). The outcrop is ~80 m long and up to 3 m high (Fig. 5.6a), disappearing beneath sandstones to the north and south (Fig. 5.6b–d). The upper contact of this outcrop appears relatively flat-lying and concordant with the sandstone horizons above. This was interpreted in the field as an intrusion top surface. The lower contact has a stepped geometry and is offset by faults (Fig. 5.8). This contact was interpreted in the field to be a lateral (or basal?) contact. This contact strikes NNE–SSW (289/62).

Whispering Wind Gully (Zone 2b) is a topographic incision (Figs 5.6b & 5.7c, d), covering an area ~90 m long by 50 m wide, trending ~NW–SE (Fig. 5.6d). Igneous outcrops form the northern edge of the gully, while sandstones are present in the central and southern areas (Figs 5.6d & 5.7c, d). The sandstone within the gully lies topographically below and adjacent to the intrusion top surfaces to the northeast, and south (Fig. 5.7c, d). The northern edge of the gully exhibits a steep (S-dipping) intrusion–host rock contact (Fig. 5.7d). At the head of the gully, a steep, faulted western intrusion–host rock contact can also be observed: although the extent of this contact is poorly constrained (Fig. 5.9b). At the head of the gully, a sub-horizontal, shaley-sandstone horizon is apparent, traceable onto the top surface of the intrusion on the northern side. This marks a change in sandstone bedding geometries from layered sub-horizontal sandstones above, to moderately dipping (16–50°) below and within the gully (Figs 5.7c & 5.9). The intrusion morphology of the eastern margin within Whispering Wind Gully appears somewhat different to the neighbouring areas to the north and south. A steep ENE–WSW trending intrusive wall can be seen (Fig. 5.7b) exhibiting columnar-style jointing. This structure and variations in geomorphic character make it difficult to link the intrusion outcrops to the south of the Whispering Wind Gully, to those in the north, as one continuous body.

Figure 5.8 (*overleaf*)

Geometries and deformation structures in Zone 2a. (a) Field photograph and schematic sketch showing a complex intrusion margin with a jagged intrusion–host rock contact. (b) Zoomed-in field photograph and schematic sketch showing faulted intrusion margin in Zone 2a. Note sinistral and normal movements on fault planes. Faults can be seen continuing from the sandstone into the adjacent intrusion, and appear to control the geometry of the intrusion–host rock contact. A sheared margin (≤ 10 cm) can be seen within the intrusion at the contact, while a wider (15 to 30 cm) zone of altered/ baked sandstones are found at the contact. (c) Lower hemisphere equal area stereoplots showing: left – poles to planes (contoured) for planar structures recorded at structural stations MCSS-43, -51, and -53; and right – extensional faults (red planes) and kinematics (red slip symbols) in Zone 2a. Mean planes are shown for each plot (black lines). (d) Photograph of a faulted intrusion–host rock contact. Note stretched plagioclase phenocrysts in the sheared/ chilled intrusion margin, and the resulting fabric being dragged into the sinistral fault plane. (e) Faulted intrusion margin and zoom-in of normal fault. (f) Zoom-in of a dip-slip fault plane within the intrusion. Note black glassy surface (pseudotachylite?). (g) Zoom-in showing drag on sheared contact fabrics into a sinistral fault. (h) Intrusion–sandstone interaction along sheared contact. Note thin baked aureole in sandstone and chilled intrusion margin showing ductile shear fabrics in intrusion.

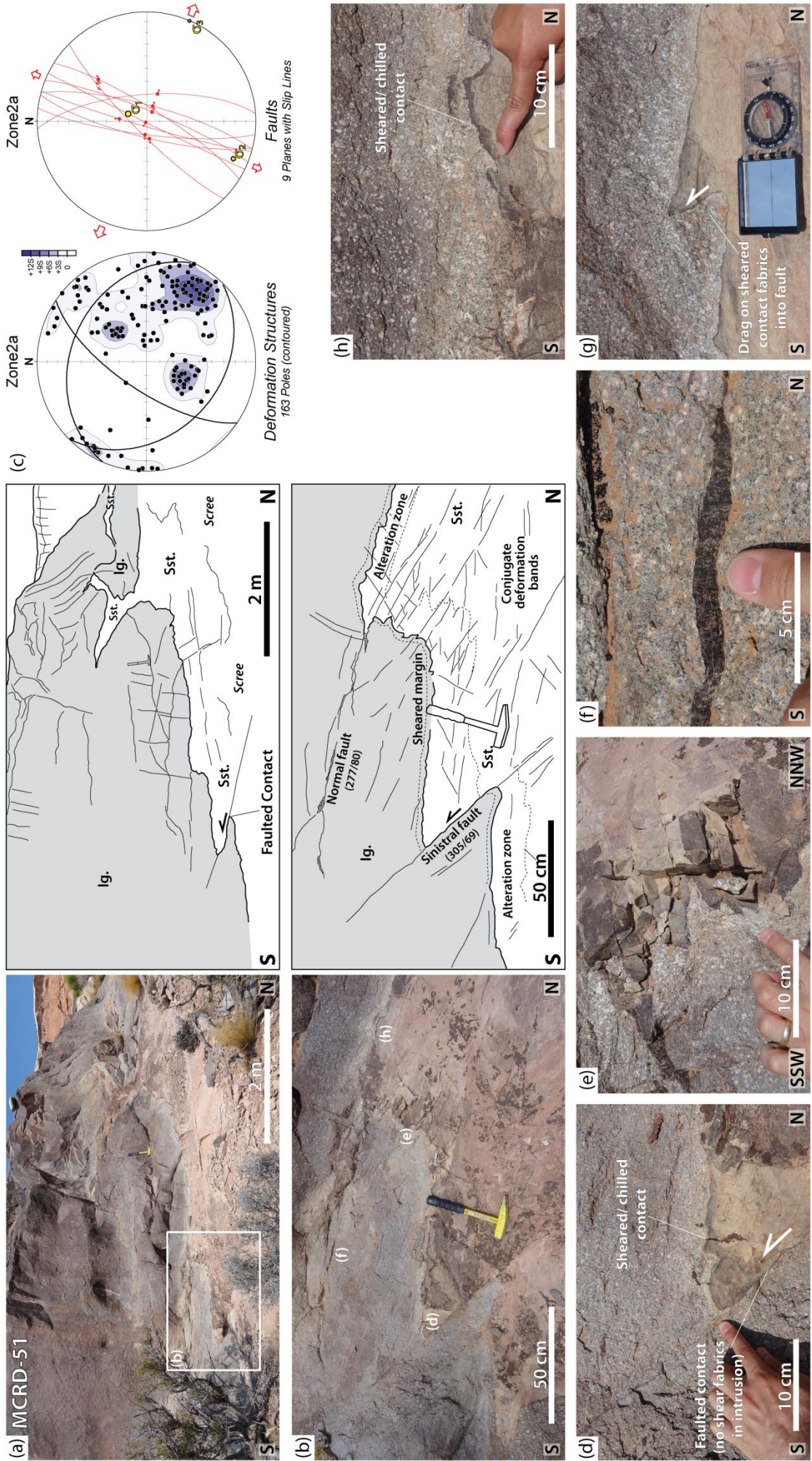


Fig. 5.8

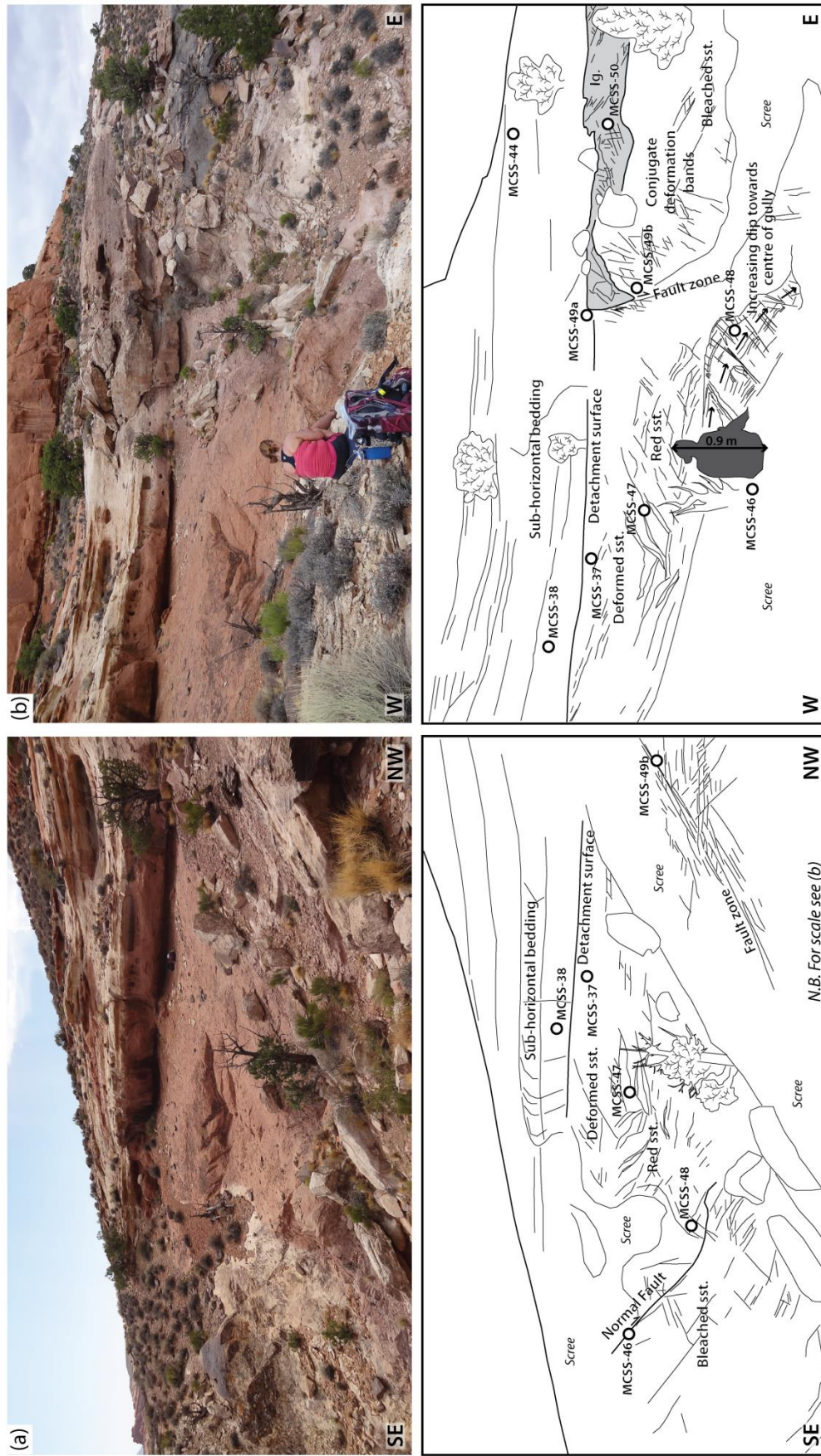


Figure 5.9. Overview field photographs and corresponding sketches of Whispering Wind Gully and Zone 2b, highlighting key geometries, structures and locations of structural stations (white with black outline circles). (a) View looking north. Note presence of intrusion on the northern flank of the gully, and the detachment surface in line with the top surface of this intrusion. (b) View looking south-west. Note the detachment surface separating sub-horizontal beds above from folded and faulted beds below.

5.3.2.2. *Syn-emplacement Deformation Structures*

5.3.2.2.1. *Zone 2a*

MCSS-45 is a zone of bleached sandstone outcropping between the two intrusive exposures in Zone 2a (Fig. 5.6a, d). Two main deformation trends are apparent: ~NW–SE and ~NNE–SSW (Fig. 5.6d). A conjugate set of deformation bands trending ~NW–SE dip moderately (~30°) to the NE and SW. The second set of structures consists of deformation bands, faults and fractures trending ~NNE–SSW and dipping steeply to the NW (Fig. 5.8c). Movement on this latter set appears to be dip-slip (kinematics not easily identifiable).

Structural stations MCSS-51 and -53 (Fig. 5.6a, d) are located at the intrusion–host rock contacts of the western intrusive body (Fig. 5.8). Deformation structures at the upper contact (MCSS-53) lie solely within the overlying host rock, and the intrusion–host rock contact appears relatively flat lying. Deformation structures include deformation bands and minor faults, trending roughly NE–SW and dipping moderately (~45°) to the NW (Figs 5.6d & 5.8c). Faults again show dip-slip movement with kinematics poorly constrained.

In contrast, the lower contact (MCSS-51) appears more structurally complex (Fig. 5.8a, b). The contact is highly irregular, showing multiple stepped geometries with fingers of highly-deformed sandstone within the igneous body (Fig. 5.8a, b). The intrusion contact appears to exhibit two distinct trends: ~N–S and ~NE–SW (Figs 5.6d & 5.8c). Both trends are consistent with faults observed in both the host-rock and the intrusion (Fig. 5.8). A further set of NW–SE trending deformation bands can also be observed in the host-rock sandstone (Figs 5.6d & 5.8b, c). A number of fault surfaces can be traced from the host rock sandstone into the intrusion, and appear to displace the intrusion–host rock contact (Fig. 5.8a, b, d), with m- to mm- scale offsets. An ultrafine, black rock (pseudotachylite?) can be observed on some larger faults that extend from the host rock into the intrusion (Fig. 5.8f).

The intrusion–host rock contact separates a sheared margin (up to 10 cm wide) within the intrusion from a zone of altered sandstone and baked sandstone (up to ≤10 cm wide) (Fig 5.8b, e). Brittle and plastic(?) deformation fabrics can be seen within the chilled margin, characterised by aligned, stretched, elongate feldspar phenocrysts (Fig. 5.8e–h). This fabric parallels the intrusion–host rock contact in many places (Fig. 5.8d–h): the exception being where the contact is faulted. Here, the fabrics terminate at the fault, and show drag

into the shear surface (Fig. 5.8d, h). Shear fabrics on the N–S segments of the intrusion–host rock contact show evidence for weak dextral shear (though slickenlines on fault surfaces suggest predominantly dip-slip movements; Fig. 5.8f), while fault offsets and associated drag on NE–SW segments show sinistral shear (Fig. 5.8d, g, h).

5.3.2.2.2. Zone 2b

Structurally, Zone 2b is best described according to structures above and below a continuous sub-horizontal surface (dipping shallowly, $<10^\circ$, to the SE) that can be traced onto the top surface of the intrusion in the north (Fig. 5.9). Deformation structures below this surface are steeply dipping (Fig. 5.10); while in contrast, those above display shallow- to moderate-dips (Figs 5.6d, 5.9 & 5.11). There is also a contrast in deformation intensity (i.e. fracture spacing): beds above this surface are less deformed than those below. Weak shear fabrics can be observed on this sub-horizontal surface (Fig. 5.11b), which are developed within a more muddy-sandstone unit than those above and below. These shear fabrics are most pronounced with proximity to the intrusion top surface (MCSS-49a). Outcrop exposures were not conducive to the collection of kinematic data. Some low-angle faults above this surface appear to shallow-out and detach into this zone (Fig. 5.11a).

Figure 5.10 (overleaf)

Zone 2a deformation. (a) Series of lower hemisphere equal area stereoplots for deformation structures (contoured poles to planes) observed in Whispering Wind Gully (i.e. Zone 2b), by structural station. Note structural station MCSS-49 has been further divided into structures above (-49a) and structures below (-49b) the detachment surface. For corresponding locations see Figure 5.6a, d, and 5.9 and the Google Earth™ kmz file in the Appendices. (b) Series of lower hemisphere equal area stereoplots for faults within Whispering Wind Gully, by structural station. Faults planes (red lines) and kinematics (red slip symbols) indicate dominantly extensional deformation within the gully. Mean planes are shown for each plot (black lines). (c)–(h) Series of field photographs showing: (c) large fault plane at structural station MCSS-46; (d) zoomed-in photo of fault plane shown in (c) highlighting lunate fractures indicating normal dip-slip kinematics; (e) highly deformed sandstones within the centre of the gully (note steeply-dipping NE–SW trending deformation corridors acting as hinge lines to steepening bedding); (f) differing lateral intrusion–host rock contacts, one faulted and one chilled; (g) Zoom-in of chilled intrusion margin with some evidence for shear from slightly undulatory contact; and (h) fault plane with strike-slip slickenlines and shear fabrics indicating dextral kinematics.

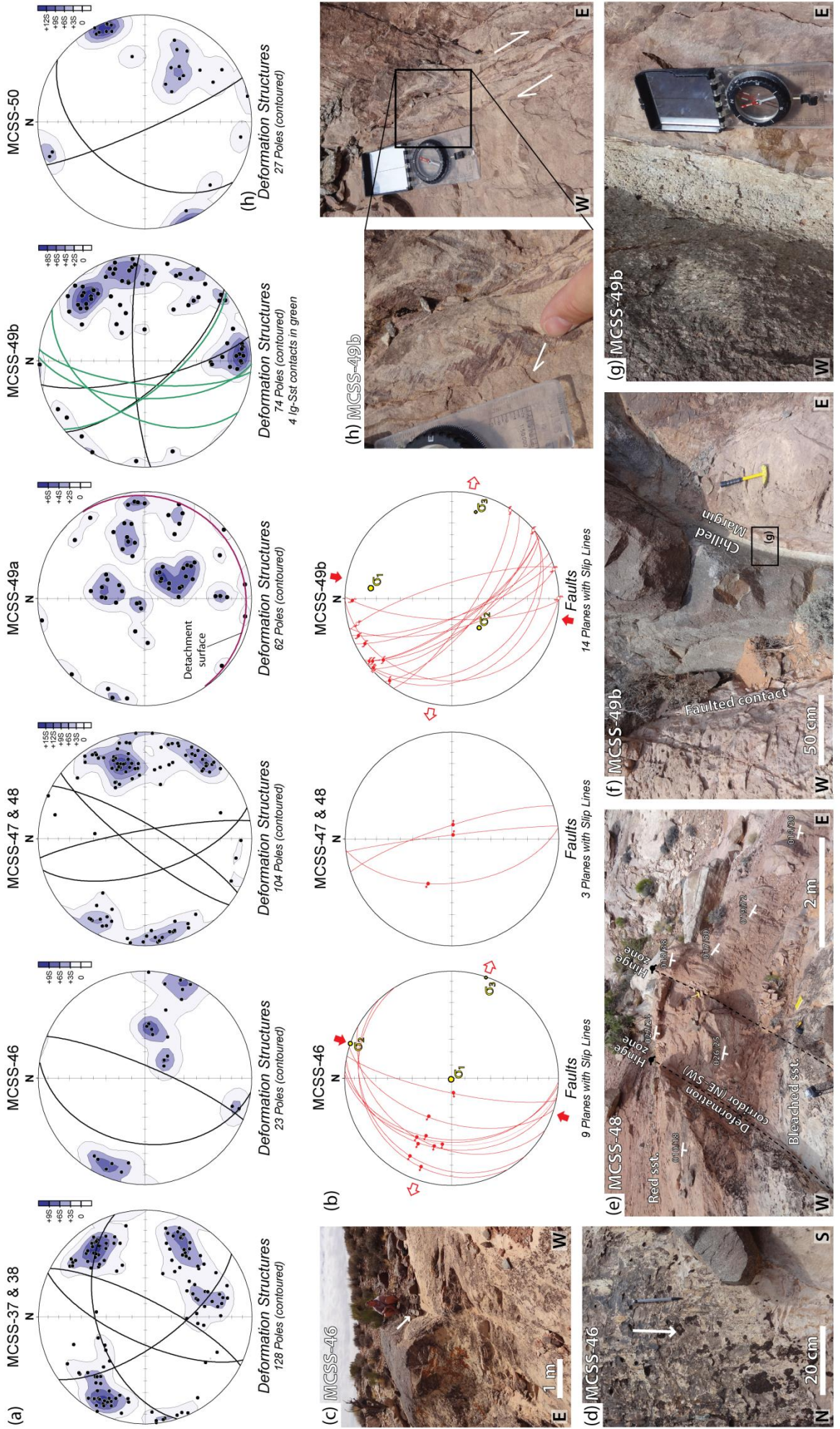


Fig. 5.10

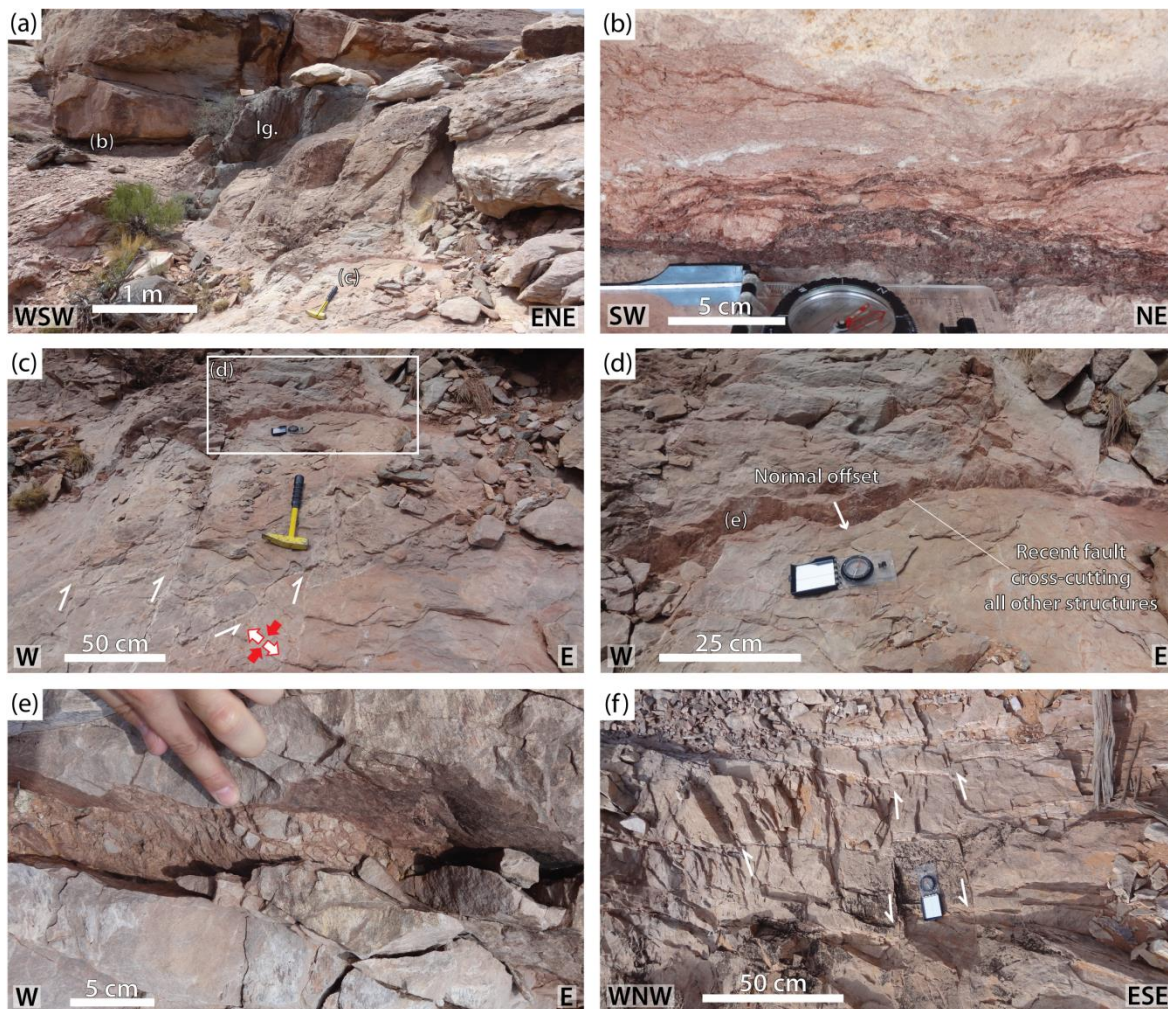


Figure 5.11. Deformation structures in Zone 2a. Field photographs showing: (a) igneous outcrop in the NW section of Whispering Wind Gully and detachment surface in line with the intrusion top surface, separating moderately deformed, sub-horizontal beds above from intensely deformed, folded beds below; (b) close-up of the detachment surface showing weak shear fabrics; (c) deformed host rock sandstones adjacent to intrusion showing strike-slip displacements along faults; (d) recent E–W trending fault cross-cutting all other structures, showing normal offsets on modern day topography; (e) zone of breccia associated with the normal fault shown in (d); and (f) fault patterns in the host rocks sandstones adjacent to the intrusion with dominant sinistral strike-slip displacements.

Deformation structures within the gully include deformation bands, faults, fractures and veins (Fig. 5.10). The gully is characterised by a SE-plunging syncline, which can be easily distinguished in outcrop by layered bleached and red-stained sandstone beds (Fig. 5.9b). Deformation structures and kinematics vary across the gully from south to north, as one approaches the intrusion–host rock contact (compare structural stations MCSS-46, -47/48, -49b, and -50 in Fig. 5.6d).

On the south side of the gully, an outcrop of bleached sandstone (MCSS-46; Figs 5.6a, d & 5.9) is highly deformed with abundant deformation bands (cm-spacing) and faults trending NNE–SSW (Fig. 5.10a–d). Deformation bands form a conjugate NNE–SSW trending set, dipping steeply ($\sim 80^\circ$) to the ESE and moderately ($\sim 40^\circ$) to the WNW (Fig. 5.10a). Faults also trend \sim NNE–SSW and dip predominantly to the west (Fig. 5.10b, c). Slickenlines and kinematic indicators on slip surfaces (e.g. R-M shear sense criteria of Petit, 1987) indicate normal movement on dip-slip fault planes (Fig. 5.10d).

Moving into the centre of the gully (structural stations MCSS-47- and 48; Figs 5.6a, d & 5.9), red sandstone outcrops within the syncline appear highly deformed, with deformation bands and faults (cm-spacing; Fig. 5.10e). Here, two fault/ deformation band systems are present, trending NE–SW and NNW–SSE. Both systems consist of steep ($>65^\circ$) structures dipping both to the east and west (Fig. 5.10a, e). The main fault planes (exhibiting clear slip surfaces) dominantly trend NNW–SSE (Fig. 5.10b). Slickenlines and offsets on bedding indicate normal, dip slip movement; kinematics consistent with those at MCSS-46 (Fig. 5.10b, e). Approaching the syncline axis bedding steepens to $\sim 50^\circ$; with NE–SW trending deformation corridors appearing to act as hinge zones as the bedding steepens (Fig. 5.10e).

A wider array of structures and trends are apparent on the northern side of the gully, adjacent to the intrusion contact. Here, the outcrop appears to provide a window into the intrusion to the north, with steep intrusion–host rock contacts identifiable on two sides (Fig. 5.10f). Deformation structures in the adjacent host rocks consist of deformation bands, faults, fault-related zones of cataclasite and breccia, and mineralised veins (Figs 5.10h & Fig. 11c–f). Deformation structures can be separated into three general orientations: NW–SE; NNE–SSW; and E–W (Fig. 5.10a). The most pronounced systems of faults trend roughly NW–SE, dipping steeply ($>60^\circ$) to the SW (Fig. 5.10b). Kinematic indicators include sub-horizontal slickenlines, shear fabrics and off-sets on other faults and deformation bands (Figs 5.10h & 5.11c). These consistently imply a dominantly dextral strike-slip movement (Figs 5.10b, h & 5.11c). The largest of these faults also defines a sheared intrusion–host rock contact (Fig. 5.10f). Deformation structures trending NNE–SSW dip steeply ($>70^\circ$) to the west, and show both sinistral and normal offsets on adjacent structures (Fig. 5.11c, f). These structures are also mimicked by the intrusion–host rock contact: NNE–SSW intrusion–host rock contacts showing both chilled

(intrusion) and altered/ (?) baked (sandstone) margins (Fig. 5.10g). There appears to be a mutual cross-cutting relationship between both the NNE–SSW and the NW–SE trending structures, and both sets clearly define/ control the intrusion geometry (Fig. 5.10a, b, f).

A system of roughly E–W faults, fractures and veins are also apparent, predominantly dipping steeply ($\sim 80^\circ$) to the north (Figs 5.10a & 5.11a, f). One exception to this is an up to 5 cm wide brecciated fault zone that dips steeply to the SSE (151/83; Fig. 5.11b–d). The N-dipping faults, fractures and veins are commonly cross-cut and offset by the NW–SE and NNE–SSW trending fault sets (Fig. 5.11f). In contrast, the S-dipping breccia zone appears to cross-cut all other structures and also appears to displace present-day topography (Fig. 5.11a, b–d). Kinematics on the N-dipping structures indicate a dextral shear sense (see fault relay in Fig. 5.11f); while the S-dipping breccia zone shows normal displacements (Fig. 5.11c, d).

Within the intrusion to the north (MCSS-50; Figs 5.6a, d & 5.9b) abundant fractures (dm-spacing) are apparent, trending similarly to the structures in the adjacent host rock (i.e. \sim NNW–SSE and \sim NE–SW; Fig. 5.10a).

5.3.3. Zone 3: Southern Intrusion and ‘Rattlesnake Gully’

5.3.3.1. Intrusion and Host Rock Geometries

The morphology of the southern Maiden Creek intrusion (Zone 3; Fig. 5.3) is dominated by a ~ 400 m long, roughly N–S trending ridge of igneous rock; seemingly a continuation of the eastern margin in Zone 2 (Figs 5.12 & 5.13a, b). To the west of this ridge is a deep (>30 m), steep-sided gully (Rattlesnake Gully; Fig. 5.12a–c) comprised of highly deformed sandstones, outcropping at the same topographic level as the adjacent igneous rocks (Fig. 5.13a, c). Further igneous intrusion can be found outcropping along the western border of the gully (Fig. 5.12a, c). Two separate bodies can be inferred from the presence of both identifiable lateral contacts, and sandstones at the same level in-between. These igneous outcrops flanking either side of the sandstone gully represent the southern pair of finger-like lobes of Horsman et al. (2005).

Figure 5.12 (*overleaf*)

Zone 3: Southern Intrusion and 'Rattlesnake Gully'. (a) Aerial photograph of the southern Maiden Creek intrusion and Rattlesnake Gully (Zone 3). Bedding strike and dip in yellow. Black points show structural stations analysed in this study. Note igneous rock appears dark-grey in comparison to the light grey to brown colours of the host rock sandstone. (b) Zoom-in of complex zone of folded bedding from map in (a). Note steeply-dipping folded beds in sandstones between intrusive lobes, in contrast to shallowly-dipping ($<15^\circ$) beds in sandstones above. Inset stereoplots show poles to planes (contoured) for bedding above and below the Maiden Creek Shear Zone (MCSZ) detachment surface. (c) Spatial distribution of deformation structures in the host rock sandstones within Rattlesnake Gully (Zone 3). Structural stations highlighted by white circles with black outlines, sandstone–igneous contacts in red, and shear zone in pink. Red and white arrows depict inferred SHmax and Shmin orientations, based on fault and deformation band trends. Fault/deformation band geometries are depicted in lower hemisphere equal-area stereoplots. Poles to planes are contoured and mean planes are shown for each plot (black lines). (d) Panorama field photograph showing the entire eastern margin of the Maiden Creek intrusion, viewed from the ESE (see map (c) for photo location). Note the bleached sandstone horizon in the foreground, dipping to the NE, is the same sandstone unit that overlies the intrusion top surface. Offset on this sandstone horizon is <10 m at the southern tip of the eastern lobe and increases northwards along the intrusion margin towards Zone 2 (N.B. horizon offset geometry is similar to that of the throw on a fault, with offset increasing towards its centre).

Figure 5.13 (*overleaf*)

Intrusion and host rock geometries in Zone 3. (a) The western margin of the Eastern Lobe (view looking east). Here outcropping intrusion is ~ 35 m at its thickest. Note the relatively flat intrusion top surface, and narrowing towards the south. Location of Secret Nap Gorge highlighted. (b) View looking south along the trend of the Eastern Lobe. (c) The western margin of the Eastern Lobe at the head of Rattlesnake Gully, view looking north-east. Note the detachment/ shear surface separating less deformed sub-horizontal sandstones above, from deformed and folded beds below and adjacent to the intrusion margin. (d) View into Secret Nap Gorge and the Eastern Lobe, as seen from the ESE. This is the only basal (lower) contact that can be observed. Note the irregular, hour-glass geometry to lateral intrusion margin. Beds below are sub-horizontal and concordant with the lower intrusion contact, but are discordant (truncated) against the lateral margin. (e) Zoom-in of sub-horizontal basal contact. (f) The eastern margin of the western intrusive lobe, within Rattlesnake Gully. A water-cut incision provides a window into the internal architecture of the intrusive body. Note the irregular (hour-glass) geometry to the lateral intrusion margin, and relatively flat top surface. Deformed sandstone beds are folded and sheared into a faulted intrusion–host rock contact. The detachment/ shear surface, MCSZ can also be identified, in line with the top surface of the intrusion. (g) Structural zonation within the Western Lobe resulting from dominant low-angle faults and fractures in the uppermost few metres, and predominate sub-vertical 'cooling' fractures below.

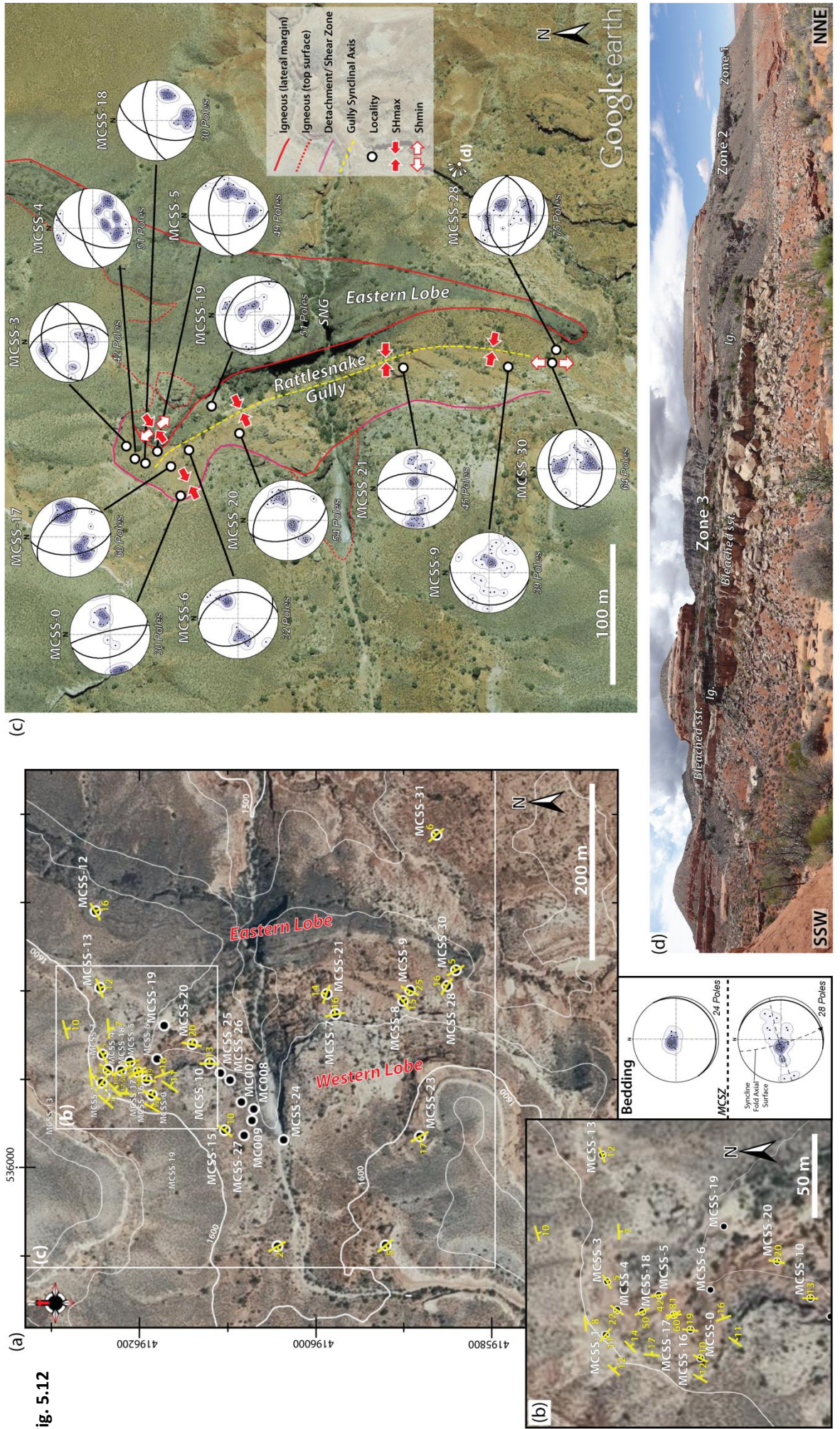


Fig. 5.12



Fig. 5.13

The 3D geometry of the eastern intrusive lobe is well constrained, with both lateral margins and top surface clearly identifiable (Figs 5.12d & 5.13a–c). A deep erosional incision (~35 m) truncates the ridge about half way along its length (known locally as “Secret Nap Gorge”; Fig. 5.13a, d), providing a window into the internal architecture of the intrusive body. The floor of Secret Nap Gorge lies within the intrusion. However, on

the outer eastern-most section, a sub-horizontal basal intrusive–host rock contact can be observed (Fig. 5.13d, e). The width of the eastern lobe narrows from ~160 m in the north to <30 m wide in the south (Fig. 5.12). A contrast in vertical thickness can also be observed, from ≥ 35 m in the north to ~10 m at its southern-most tip (Figs 5.12d & 5.13a). Although the overall trend of the ridge is roughly N–S, a clear arcuate geometry can be defined when mapping both margins of the eastern intrusive ridge in detail (Fig. 5.12c).

The geometries of the western intrusive outcrops are more poorly constrained due to lack of exposure. The architecture is best observed within a similar erosional cut to that in Secret Nap Gorge (Fig. 5.12a, c). Here, an eastern lateral margin and intrusion top surface can both be defined. The lateral contact in this area shows a distinct angular hour-glass geometry (Fig. 5.13f, g), with upper and lower portions of the intrusion protruding further into the adjacent host rock than the middle portion of the intrusion. The intrusion top surface is relatively flat lying; ~300 m to the south, a small, jagged outcrop (~20 m² and ~5 m thick) of intrusion can be found (Fig. 5.12a). Although no intrusive rocks can be observed elsewhere along the western gully-side, similar overlying bedding geometries support the inference that a continuous intrusive body may be present in the sub-surface. A western limit of this intrusive body cannot be defined as it is hidden by the overlying sandstones.

A similar distinct sub-horizontal surface within the sandstone to that observed in Zones 1 and 2 can be traced onto the top surfaces of both intrusive bodies (Fig. 5.13c, f). This surface (labelled MCSZ in Fig. 5.13b,c,f, g) marks a distinct change in the geomorphological and structural character of the sandstones above and below (i.e. within the gully). Above this surface, sandstone beds are relatively flat-lying, and concordant with the intrusion top surfaces (Figs 5.12b & 5.13c, f). Whereas below this surface, sandstone beds within Rattlesnake Gully appear folded and highly deformed (Figs 5.12b & 5.13c, f). Sandstone beds are also truncated by steep igneous contacts at the lateral margins (i.e. the intrusion margins are discordant to bedding; Fig. 5.13a, f). The sandstone gully also trends roughly NW–SE to N–S, reflecting the arcuate trend of the western margin of the eastern igneous lobe (Fig. 5.12a, c). No basal contacts to the igneous bodies can be observed within the gully (Fig. 5.13a).

A distinct bleached white sandstone horizon can be mapped from the intrusion top surface in the west to outboard (to the east) of the intrusion (Fig. 5.12d). On the intrusion top surface this bleached horizon is sub-horizontal and concordant with the intrusion–host rock contact. However, to the east of the Maiden Creek intrusion, beds dip shallowly to the north-east (away from the intrusion), and terminate against/ are discordant with the steep intrusive margin (Fig. 5.12d). Displacements of this sandstone horizon increase northwards along the outer intrusive margin of the eastern lobe (Fig. 5.12d). No evidence for monoclinial flexure can be observed over this margin.

5.3.3.2. *Syn-emplacment Deformation Structures*

Similar to Zone 2b (Whispering Wind Gully) and to a lesser extent the gully in Zone 1, deformation structures in Zone 3 (Fig. 5.14a) can be separated into those above, and those below the observed sub-horizontal detachment surface (Fig. 5.14b). Again this detachment surface appears to lie within a more muddy/ shaley unit than the coarser sandstone units above and below (Fig. 5.14b, c). However, in contrast to the detachment surfaces in Zones 1 and 2b, the structure here exhibits well-developed cataclastic shear fabrics showing top-to-the-WNW movements (Fig. 5.14a, c; *note, this shear zone is examined in more detail in Chapter 6*).

Figure 5.14 (*overleaf*)

Deformation structures within Rattlesnake Gully in Zone 3. (a) Series of lower hemisphere equal angle stereoplots of planar deformation structures. Plots show poles to planes (contoured) and mean planes are shown for each dominant set (black lines). Red planes show faults and shear surfaces with slickenlines and movements depicted by slip symbols. Results of kinematic strain inversion (using inversion method of Reches (1987) in MyFault™ software) are shown (yellow dots show inferred stress axes and arrows show S_{\min}/S_{\max} orientations). (b)–(g) Field photographs of: (b) head of Rattlesnake Gully, view looking NW, showing low- to moderately-deformed sub-horizontal sandstone beds above the detachment/ shear surface, MCSZ, with intensely deformed and folded sandstone beds below; (c) zoom-in of the well-developed shear zone (MCSZ) outcrop (structural station MCSS-0); (d) ‘kink-band’ geometry to deformed sandstone beds flanking the western intrusive ‘lobe’, and increasing deformation banding with steepening of bedding into the gully and central zone of pencil cleavage; (e) conjugate dextral and sinistral strike-slip faults and deformation bands in sandstone beds flanking the eastern lobe; (f) zoom-in of pencil cleavage (discrete planes) seen running along the centre of Rattlesnake Gully; and (g) stepped (jagged) intrusion–host rock contact controlled by syn-emplacment strike-slip faulting.

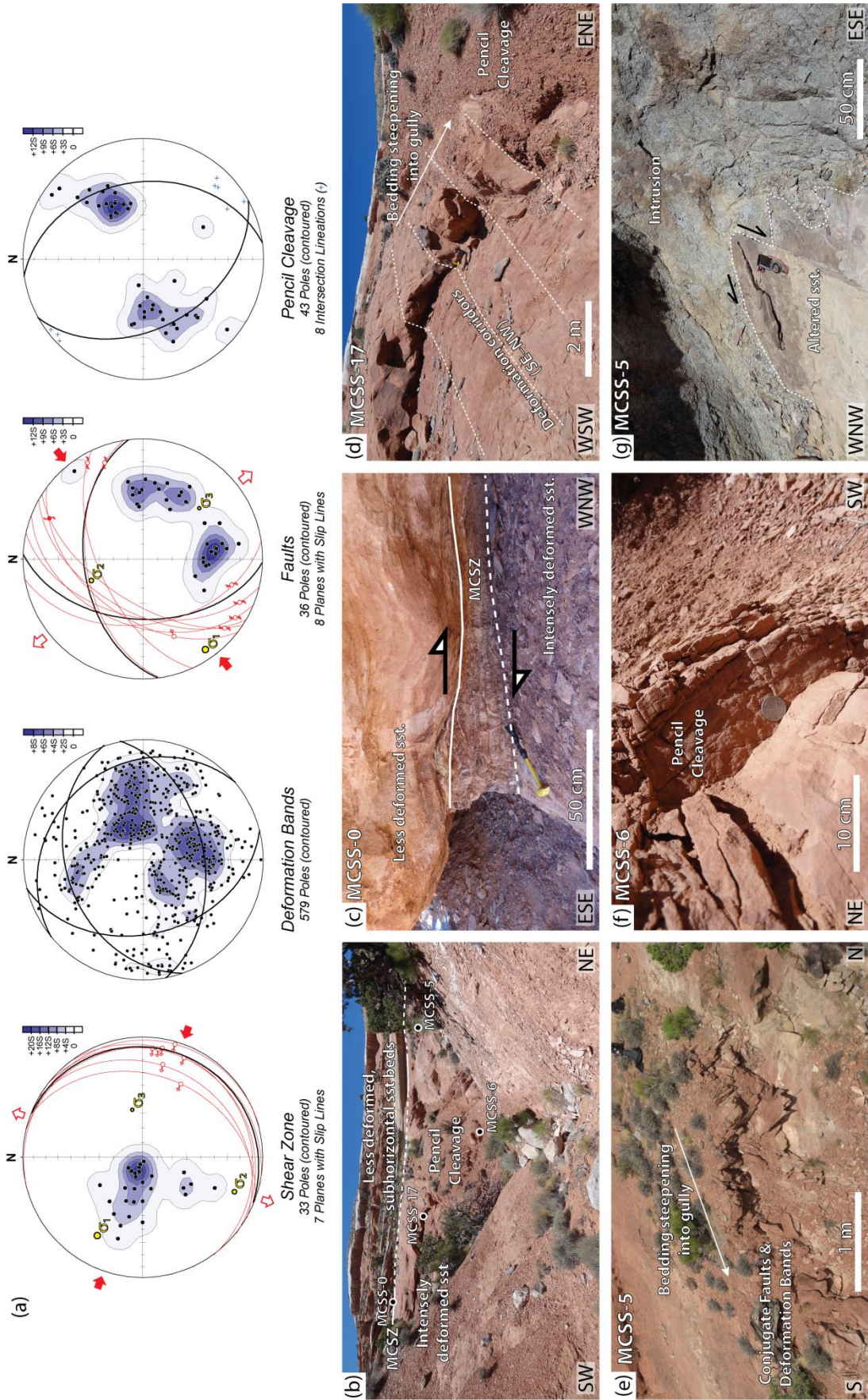


Fig. 5.14

Above this shear surface, beds are sub-horizontal to shallowly dipping ($<17^\circ$; Fig. 5.12b), concordant with the detachment surface, and deformation appears to be minor in comparison to that below. Below the shear surface, within Rattlesnake Gully (Fig. 12b), sandstone beds dip moderately to steeply ($16\text{--}81^\circ$) towards the gully axis (Fig. 5.12b), forming a synclinal fold structure (fold axis trending roughly SSE–NNW; Figs. 5.12c & 5.14b, d, e). Although the beds dip inward, away from the gully margins (and intrusion contacts), there is clear discordance between the moderately dipping beds and the steep intrusive margins (Fig. 5.13a, f).

Sandstone beds on the western side of the gully steepen towards the centre of the gully, with significant increases appearing to occur as they pass through ~SE–NW trending sub-vertical deformation corridors (Fig. 5.14d); these deformation corridors act as hinge zones, as seen in Whispering Wind Gully (see Fig. 5.10e for comparison). Similar steepening is also apparent on the eastern side of the gully, though steepening appears more rapid, and less controlled by deformation corridors (Fig. 5.14b, e). This contrast in steepening reflects a slight asymmetry to the synclinal geometry of the gully (i.e. the eastern side of the gully being slightly narrower and more steeply dipping; Fig. 5.12a, b, c).

With the exception of structures in the NE corner (structural stations MCSS-3, 4, 5 and 18), and far south (MCSS-28 and 30) of the gully, moderately dipping, conjugate sets of deformation bands strike sub-parallel to the trend of the gully and therefore, intrusion margins: rotating clockwise from NNW–SSE in the north (head of Rattlesnake Gully) to NNE–SSW in the south (Fig. 5.12c). In the NE-corner, these intrusion margin-parallel deformation structures still preside, alongside a second set of ENE–WSW trending deformation structures (Fig. 5.12c). While, in the far south of the gully, close to the southern tip of the eastern lobe, E–W trending structures predominate Fig. 5.12c).

Principal deformation structures within Rattlesnake Gully include deformation bands, faults, and pencil cleavage (Fig. 5.14). Two distinct trends can be seen within the deformation bands in the gully: NNW–SSE and ENE–WSW (Fig. 5.14a). Both of these trends appear to represent conjugate deformation band sets (Fig. 5.14a, d, e; note the quadrimodal distribution of poles to deformation bands on stereoplot). Intense deformation banding (dm- to cm- fracture spacing) is common throughout the gully, and

increases in intensity towards the gully axis (mm- to cm- fracture spacing). This increase in deformation intensity is characterised by a distinct zone of prolific pencil-cleavage (mm spacing) running along the gully centre (Fig. 5.14a,b,d, f). Similar trends can also be seen in the fault sets observed, although these slip-surfaces appear to favour only the north- and west- dipping structures (Fig. 5.14a); however this observation may simply be due to the lack of clearly identifiable slip-surfaces observed over the wider gully area (i.e. faults were mainly only identifiable in outcrops in the NE corner of the gully). Slickenlines on these fault sets show dominantly strike-slip shear, with conjugate dextral- and sinistral shear seen on N–S and ENE–WSW faults respectively (Fig. 14a). The faults can be seen offsetting the intrusion–host rock contact (Fig. 14g), similar to Zone 2a.

5.3.4. Zone 4: NW Margin

5.3.4.1. Intrusion and Host Rock Geometries

The NW margin of the Maiden Creek intrusion (Figs 5.3 & 5.15) is less well studied than the eastern margin. The mapped intrusive margin trends from roughly NNE–SSW in the west to roughly E–W in the north (Figs 5.3 & 5.15b). This change in trend is echoed by a domal intrusion morphology over much of this area (Fig. 5.15c). To the east of the area this simple domal morphology is less apparent, and the intrusion margin is characterised by steeper cliffs, locally draped by a bleached sandstone ridge (Fig. 5.15). According to varying morphologies and styles of deformation observed in the field, the NW margin can be divided into two subareas (Fig. 5.15): Zone 4a, which includes the western and north-western half-domal margin (Figs 5.15, & 5.16); and Zone 4b, the E–W trending northern margin and intrusion top surface (Figs 5.15, 5.16–5.19).

Figure 5.15 (*overleaf*)

NW Maiden Creek (Zone 4). (a) Aerial photograph of Zone 4. Bedding strike and dip in yellow. Black circles with white outlines show structural stations analysed in this study. Lower hemisphere equal area stereoplots show bedding measurements for Zones 4a and 4b. Poles to planes (contoured), mean bedding planes in black. Note the change in trend of the bedding, from NE–SW in Zone 4a to ESE–WSW in Zone 4b. (b) Zoom-in aerial photograph (from Google Earth™) for areas 4a and 4b, showing intrusion outcrop extent (grey coloured rock and red lines) and main structural stations discussed in text. (c) Panoramic field photograph showing the NW margin of the Maiden Creek intrusion as observed from the BLM dirt road looking SSE. Viewpoint location highlighted in (b).

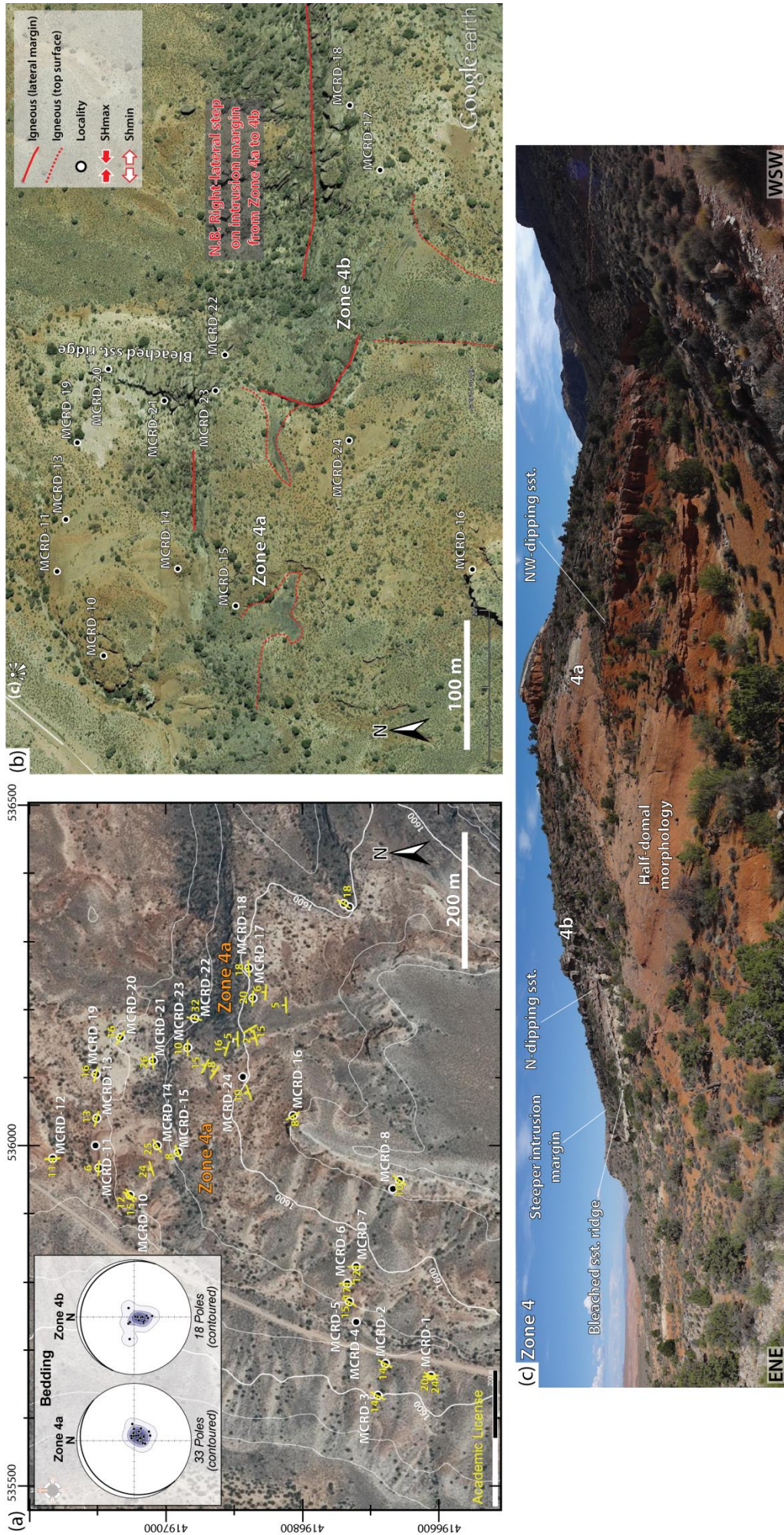


Fig. 5.15

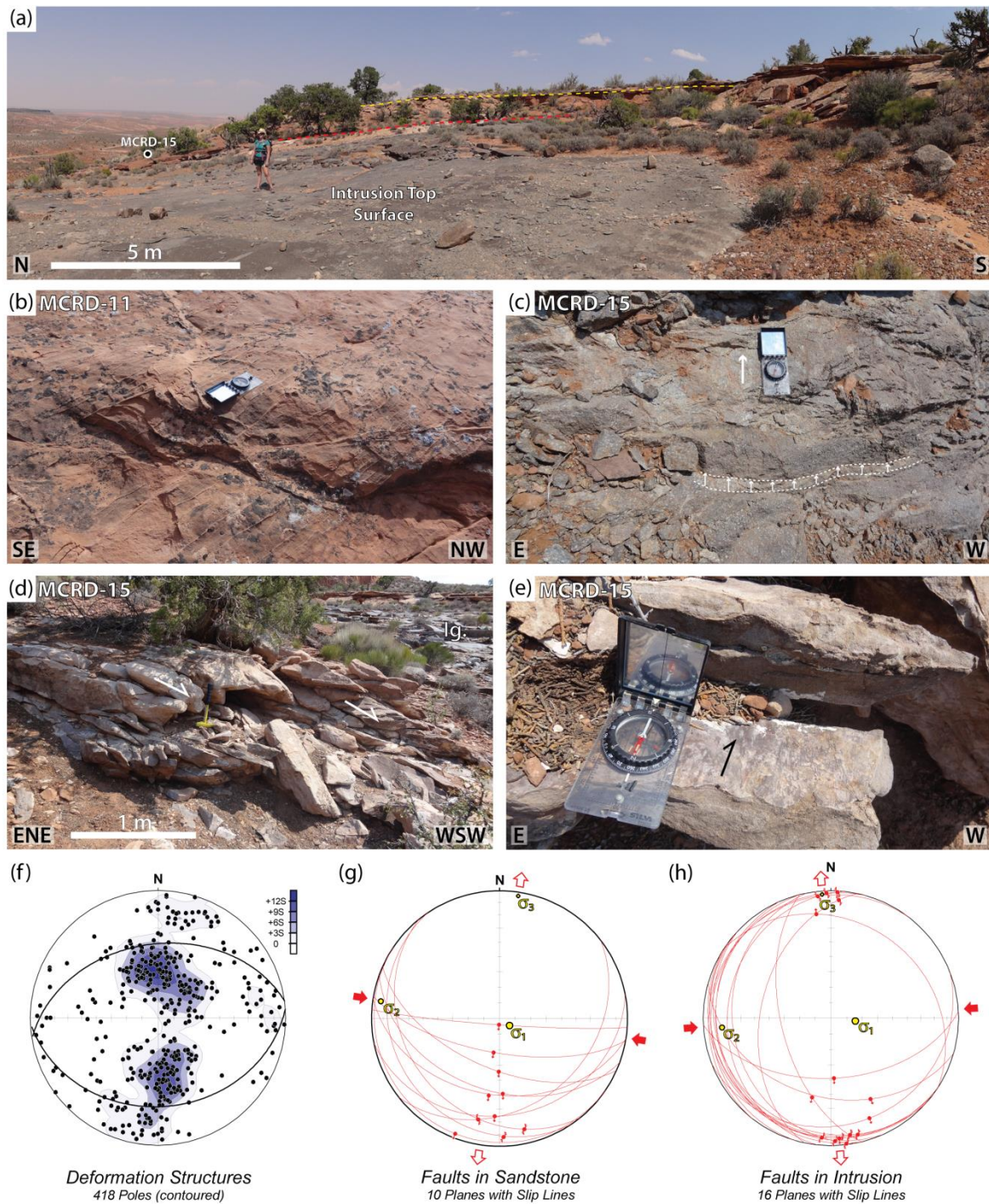


Figure 5.16. Zone 4a and the north-western margin of the Maiden Creek intrusion. (a) Field photograph of the intrusion top surface in Zone 4a. Here a broad, half-domal intrusion is visible, and overlying sandstone beds concordant with the intrusion show monoclinical folding. (b) Conjugate deformation bands in red sandstone beds, trending ~E–W. (c) Sub-horizontal faults on the top surface of the intrusion with slickenlines indicating top-to-the-north kinematics. (d) Faulted and baked sandstone immediately above the intrusion top surface. (e) Zoom-in of a principal slip surface in the sandstones in (d) showing excellent dip-slip slickenlines. (f)–(h) Series of lower hemisphere equal area stereoplots showing: (f) all planar deformation structures recorded at stations in Zone 4a (see Fig. 5.15a, b for locations); (g) faults within sandstone host rocks immediately above the intrusion top surface; and (h) faults within the uppermost metre of the intrusion. Poles to planes are contoured, mean planes in black, faults in red lines and kinematics shown by red slip lines.

Figure 5.17 (*overleaf*)

Bleached sandstone ridge (Zone 4b). (a) Photograph looking at the bleached sandstone ridge from the north-west. Location of key structural stations highlighted. (b) Outcrop and (c) zoom-in photographs at structural station MCRD-21. Note faulted contacts and geometries of bleached sandstone and overlying red sandstone. (d) Schematic sketch of structures shown in (c). Note steeply-dipping normal faults showing sub-metre offsets (see also (g) & (j)), and low angle (<30°) north-dipping reverse fault cross-cutting all other structures (see also (f) & (i)). (e) Conjugate deformation bands in bleached sandstone (structural station MCRD-19). (f) Well developed dip-slip slickenlines on reverse fault. Kinematics constrained using lunate (R-type) fractures of Petit (1987). (g) Steep faults showing normal offsets on bedding (MCDR-21). Outcrop is in footwall to the large reverse fault in (c). Lower hemisphere equal area stereoplots showing poles to planes (contoured) for: (h) conjugate deformation bands; (i) reverse faults and associated slickenlines (red slip lines shown on their corresponding fault planes); and (j) normal faults. Stress axes and S_{\min}/S_{\max} orientations calculated using kinematic inversion method of Reches (1987).

Figure 5.18 (*overleaf*)

Intrusion–host rock geometries and deformation structures in Zone 4b and on the top surface of the intrusion. (a) Panoramic field photograph looking WSW across the northern Maiden Creek intrusion margin (Zone 4b), as viewed from Rt. 276. Note bedding in host rocks (inc. bleached sandstone ridge) are truncated by the more steeply dipping intrusion margin surface. (b) Stepped intrusion top surface observed at structural station MCRD-24 (also shown as a solid red line in Fig. 5.15b, near MCRD-24). Note that the step on the intrusion top surface exhibits a smooth rounded geometry in outcrop, with highly deformed sandstones in the adjacent outcrop (zone of pencil cleavage). (c) Arcuate joint pattern on the top surface of the intrusion. Note here the intrusion is dipping gently to the north. (d) Concordant overlying beds on the top surface of the intrusion. (e) Conjugate set of deformation banding (cm-spacing) in red sandstone. (f) Zone of pencil cleavage immediately above the top surface of the intrusion, adjacent to and at the same height as the lateral margin of the step-up on the intrusion top surface. (g) and (h) are lower hemisphere equal area stereoplots of: (g) all planar deformation structures recorded on the intrusion top surface; and (h) pencil cleavage planes. Poles to planes are contoured and mean planes in black show roughly WNW–ESE trends for both all deformation structures and pencil cleavage. Pencil cleavage trends infer a ~ NNE–SSW oriented S_{\max} .

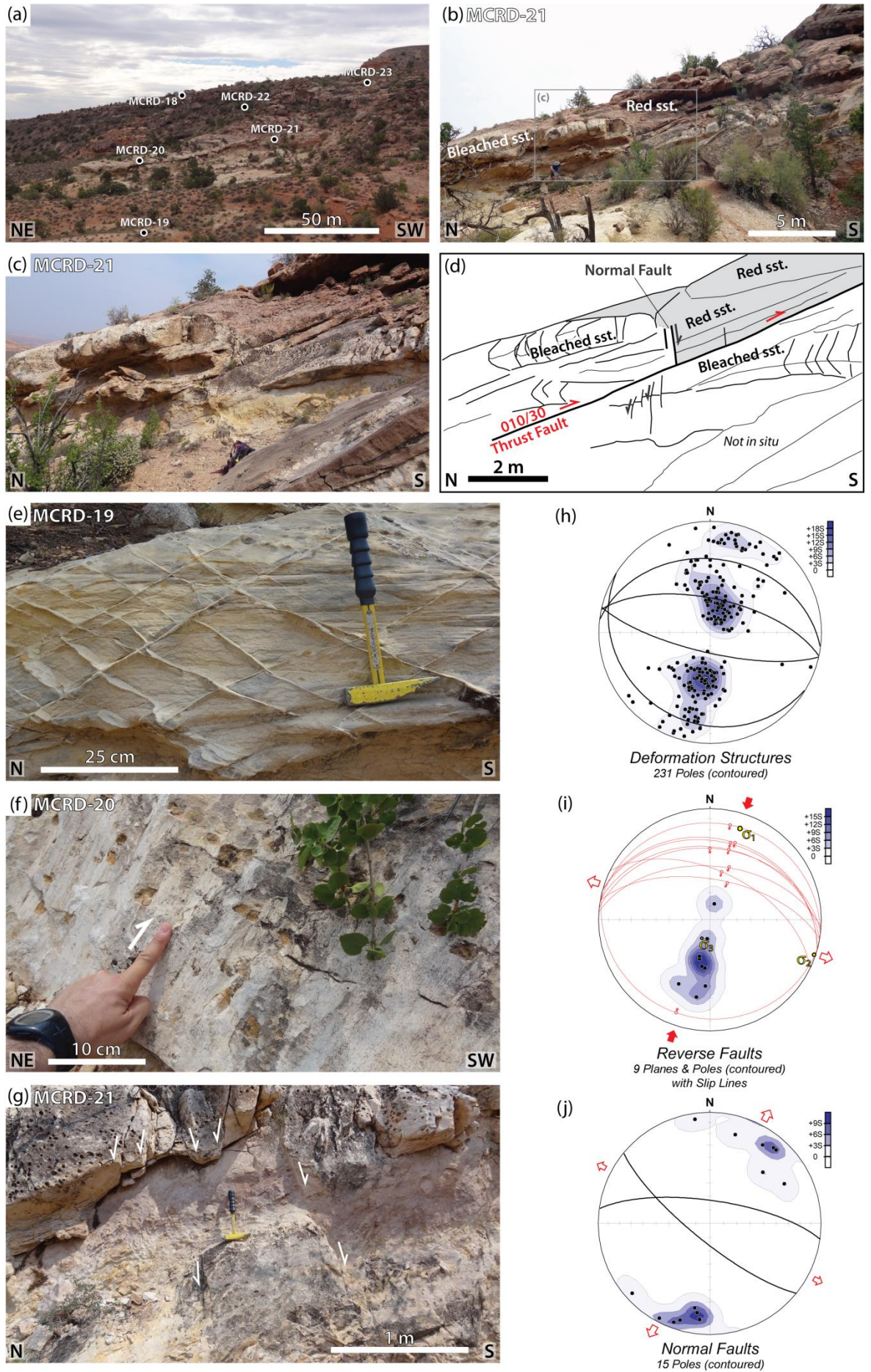


Fig. 5.17

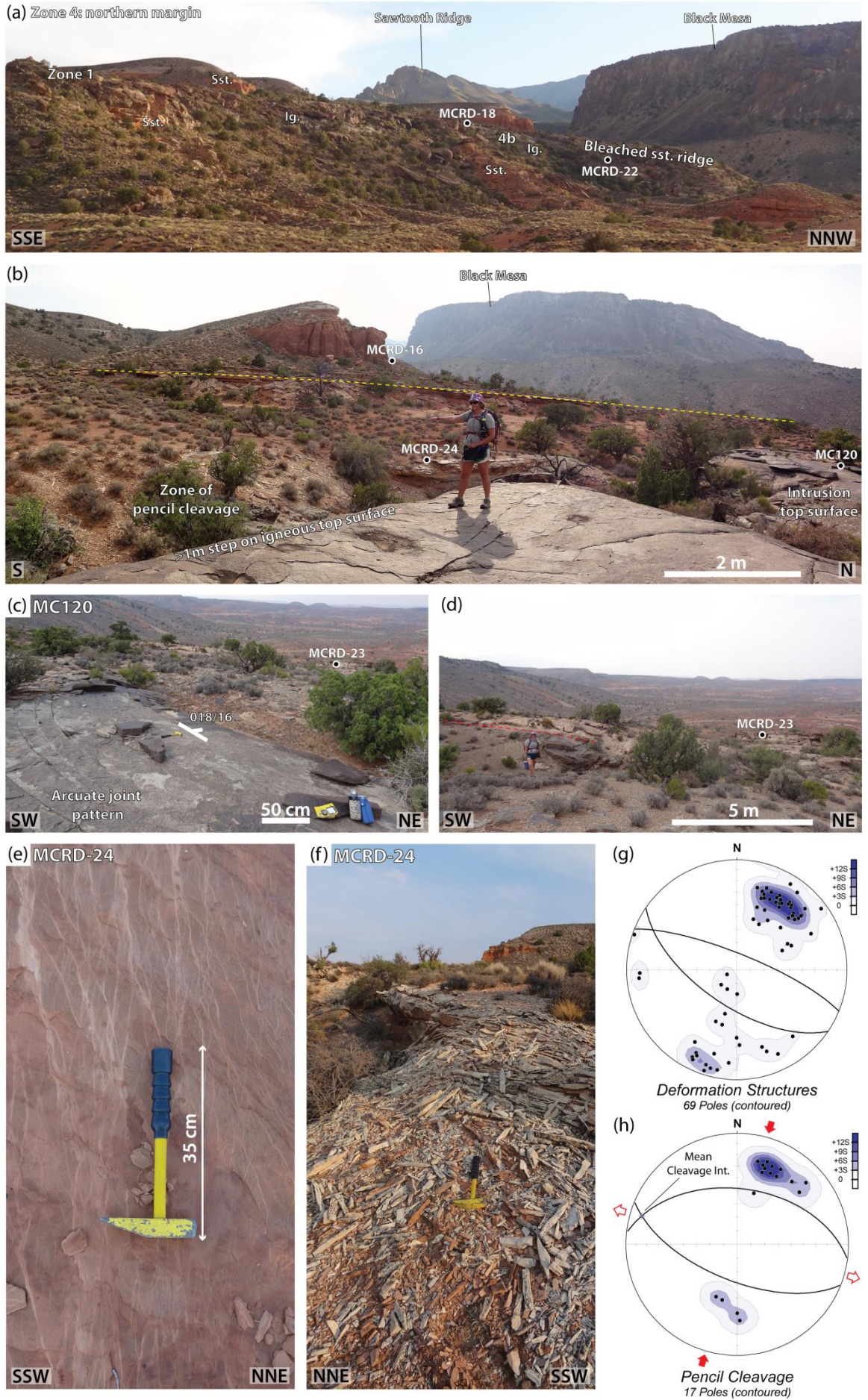


Fig. 5.18

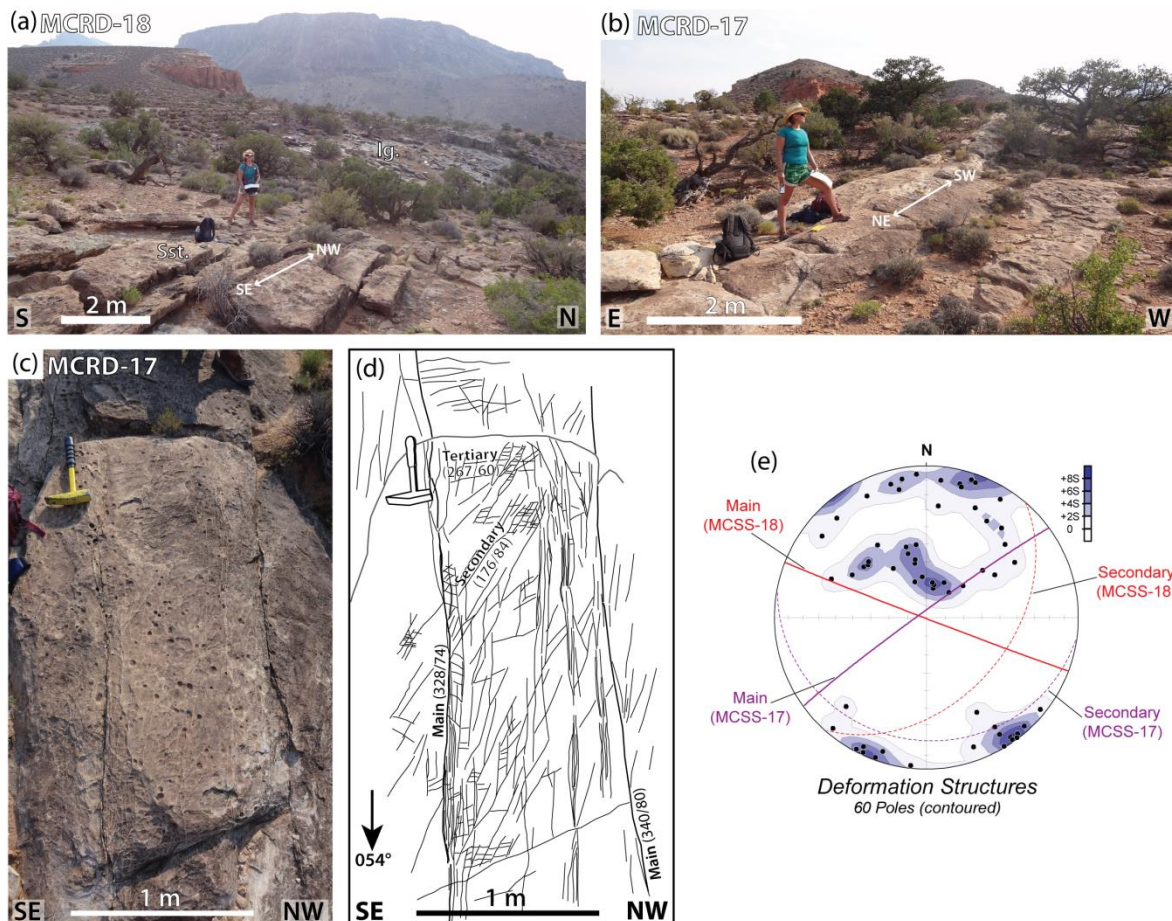


Figure 5.19. Further east on the northern margin, structural stations MCRD-17 and -18. (a) Photo of dispersed thin beds of sandstone host rock overlying the intrusion top surface in Zone 4b. The intrusion top surface appears relatively flat-lying. Note SE–NW trending deformation corridors at structural station MCRD-18. (b) Photo of structural station MCRD-17. Note NE–SW deformation corridors in the overlying sandstones. (c) And (d) show a zoom-in and schematic sketch of deformation bands and corridors in the sandstones overlying the intrusion at MCRD-17. (e) Lower hemisphere equal area stereoplot of deformation structures recorded at both stations. Deformation corridors (main trends) are sub-vertical, while secondary deformation bands are more shallowly-dipping. Note the main trend for MCSS-18 is the secondary trend for MCSS-17 and vice versa.

Along the NW and western margin of Maiden Creek (Zone 4a), igneous intrusion and overlying sandstones crop out in nearly equal measure (Fig. 5.15b). Excellent exposure of the intrusion–host rock contact, along with easily identifiable bedding planes between red and bleached sandstone horizons, help constrain the surface morphology of the intrusion in this area (Fig. 5.15b, c). The intrusion host–rock contact is concordant with shallowly- to moderately-dipping overlying sandstone beds, forming a wide-arching monoclinial (half-domal) morphology (Figs 5.16a & 5.20). This continuous arched (convex) intrusive contact can be traced over a wide area and defines Zone 4a.

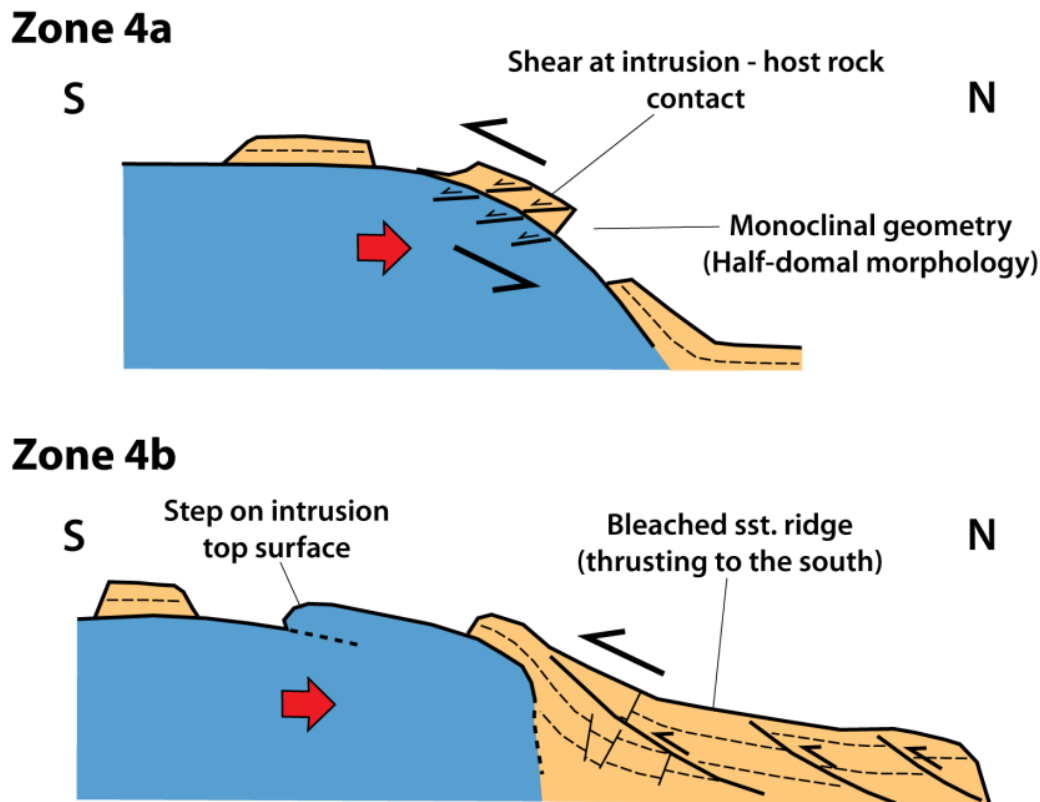


Figure 5.20. Schematic cross-sections across the intrusion margin in Zones 4a and 4b. See text for discussion.

The transition between Zones 4a and 4b is defined by a distinct N–S trending morphological structure. Within the intrusion outcrops this marks an abrupt step up (>1 m high) on the intrusion top surface (Figs 5.18b & 5.20), while in the host rock a distinctive ridge of bleached sandstone is apparent (Figs 5.15b, c & 5.17a, b). In map view, a clear lateral step in the margin is identifiable; the intrusion margin stepping to the south (right-lateral) by ~50 m (Fig. 5.15b). This step is spatially coincident with the N–S trending bleached sandstone ridge.

To the east of this ridge, the intrusion margin appears significantly steeper (Fig. 5.18a & 5.20). A shallowly N-dipping (<15°) intrusion top-surface (concordant overlying sandstone beds) appears to abruptly stop, transitioning laterally to intensely deformed, moderately N-dipping (~30°) sandstones. These moderately-dipping sandstones (also seen on the ridge) appear to drape the intrusion margin. Moving eastwards, the intrusion in Zone 4b appears to be continuous with the northern intrusive body of Zone 1.

5.3.4.2. *Syn-emplacement Deformation Structures*

5.3.4.2.1. *Zone 4a*

The overlying sandstones to the Maiden Creek intrusion in the NW are significantly deformed, with abundant deformation bands (on a cm- to dm- spacing), faults and tensile joints (Figs 5.15c & 5.16). From the SW to the NE of Zone 4a, a clockwise rotation of deformation structures is apparent, trending predominantly NE–SW along the western margin to E–W along the north-eastern margin, paralleling the intrusion margin.

On the steeper flanks of the intrusion host–rock monocline, conjugate deformation bands are the dominant deformation structure within the host rock (Fig. 5.16b). On the shallower-dipping upper flanks of the monocline, abundant (dm spacing) faults with distinct slip surfaces are apparent both on the top surface of the intrusion and within the overlying sandstones (Fig. 5.16c–e).

Red sandstone beds immediately (up to 5 m) above the top surface of the intrusion are highly deformed, cleaved, and baked (Fig. 5.16d). Prominent deformation bands (cm- to dm- spacing) trend roughly E–W, and dip moderately ($>40^\circ$) to the north and south (Fig. 5.16f). Faults within the sandstone also trend E–W, dipping to the south (Fig. 5.16g); dips ranging from shallow- (sub-horizontal) to steep- (sub-vertical). Well-defined slip surfaces with slickenlines (Fig. 5.16e) imply dip-slip movements along the fault planes, consistent with those observed in the intrusion. >5 m above the intrusion–host rock contact, the overlying sandstones are less faulted and deformation bands are fewer in number.

Within the intrusion, a dominant set of roughly E–W striking faults dip shallowly ($\sim 10^\circ$) to the south (Fig. 5.16c). Kinematic indicators include slickenlines, aligned stretched feldspar phenocrysts and lunate fractures (R criteria of Petit, 1987) and imply normal, dip-slip movement on fault planes (Fig. 5.16c, h). A less dominant, roughly N–S fault trend can also be seen (Fig. 5.16h), dipping shallowly to the west. Kinematics on these also show a N–S movement (i.e. strike-slip).

Kinematic inversion of faults both in the intrusion and the sandstone show \sim N–S oriented σ_{\min} and vertical σ_1 : consistent with top-to-the-south shear at the intrusion–host rock contact (Fig. 5.20).

5.3.4.2.2. Zone 4b

The morphology of the northern margin of the intrusion is dominated by a ~N–S trending, elongate ridge of bleached white sandstone beds (Figs 5.15b, c & 5.17a) that dip shallowly (<20°) to the north (Figs 5.15a & 5.16a–d) off the top surface of the intrusion. In contrast to the sandstone bedding in Zone 4a, the sandstone beds on the ridge and adjacent cliff-face to the west do not appear to be underlain by intrusive rocks (Fig. 5.20).

Structural data was collected at a series of structural stations along the ridge (MCRD-19–21; Figs 5.15a, b & 5.17a). At the most distal, northern structural station (MCRD-19), a well-defined system of conjugate deformation bands (cm- to dm- spacing) can be observed (Fig. 5.17e). These deformation bands trend roughly ESE–WNW and dip shallowly- to moderately- (~25°) to the north and south (Fig. 5.17e, h).

Moving inboard onto the ridge (MCRD-20; Fig. 5.17a), deformation bands are still apparent. However, a pronounced system of low-angle reverse faults can also be observed (Fig. 5.17f, i). Dip-slip slickenlines are well defined (Fig. 5.17f) and kinematics can be inferred using R shear criteria (lunate fractures) of Petit (1987).

Farther along the ridge (MCRD-21; Fig. 5.17a), a large (tens of metres in outcrop) low-angle reverse fault can be seen (Fig. 5.17b–d). Although no exact tie points were measured, offset on a bleached bedding horizon suggests a throw >5 m. A system of steeply-dipping normal faults can also be observed at this locality (Fig. 5.17c,d,g, j). These faults show decimetre to metre scale offsets on bedding. Low-angle, reverse faults cross-cut all other structures (Figs 5.17a–d & 5.20).

On the top surface of the intrusion (above the ridge; MCRD-23; Figs 5.15a, b & 5.18c, d), roughly ESE–WNW trending deformation bands dominate (Fig. 5.18g). However, at locality MCRD-24, an intense zone of pencil-cleavage can be seen, similarly trending ~ESE–WNW (Fig. 5.18f, h). This zone of pencil cleavage lies adjacent to, and topographically at the same height as, the stepped-intrusion geometry outlined above (Fig. 5.18b). Farther to the east (structural stations MCRD-17, 18; Figs 5.15a, b, 5.18a & 5.19), sandstones overlying the intrusion show deformation bands and ladder structures (deformation corridors) trending both ESE–WNW and NE–SW (Fig. 5.19).

5.3.5. Zone 5: SW Maiden Creek

5.3.5.1. Intrusion and Host Rock Geometries

The outcrops in Zone 5 (Fig. 5.3) are relatively flat-lying with excellent exposure (Fig. 5.21a–d). No intrusion outcrops in the SW Maiden Creek area (Fig. 5.21a, b), although Horsman et al. (2005) inferred the western/ south-western margin of the intrusion may pass through this area, following a NW–SE trend (Fig. 5.3).

5.3.5.2. Syn-emplacement Deformation Structures

The sandstone exposures exhibit abundant deformation bands (cm- to dm- spacing). Two dominant trends are apparent, striking NE–SW and E–W (Fig. 5.21). Both systems appear to consist of conjugate dipping planes (Fig. 5.21g, h). Deformation banding ranges from discrete planes (2–3 mm; Fig. 5.21g) to wider deformation corridors (~5 cm; Fig. 5.21f). NE–SW structures are more dominant in the north-west of the area, while E–W trending structures are more common to the south and east (Fig. 5.21b). E–W trending deformation corridors display dominantly sinistral offsets on bedding/ cross-bedding (Fig. 5.21f).

5.4. Discussion

This detailed study of the Maiden Creek intrusion has highlighted a highly complex intrusion geometry accompanied by equally complex and varied host rock and contact deformation structures.

Syn-emplacement deformation structures appear to be parallel to either intrusion margins (Fig. 5.22) and/ or, to a lesser extent, magma flow directions. Baer (1995) proposed that if magma intrudes under a brittle regime, the final intrusion geometries reflect the propagation history of the initial fractures. This paralleling of deformation bands with intrusion margins matches similar observations from Trachyte Mesa (Chapter 3).

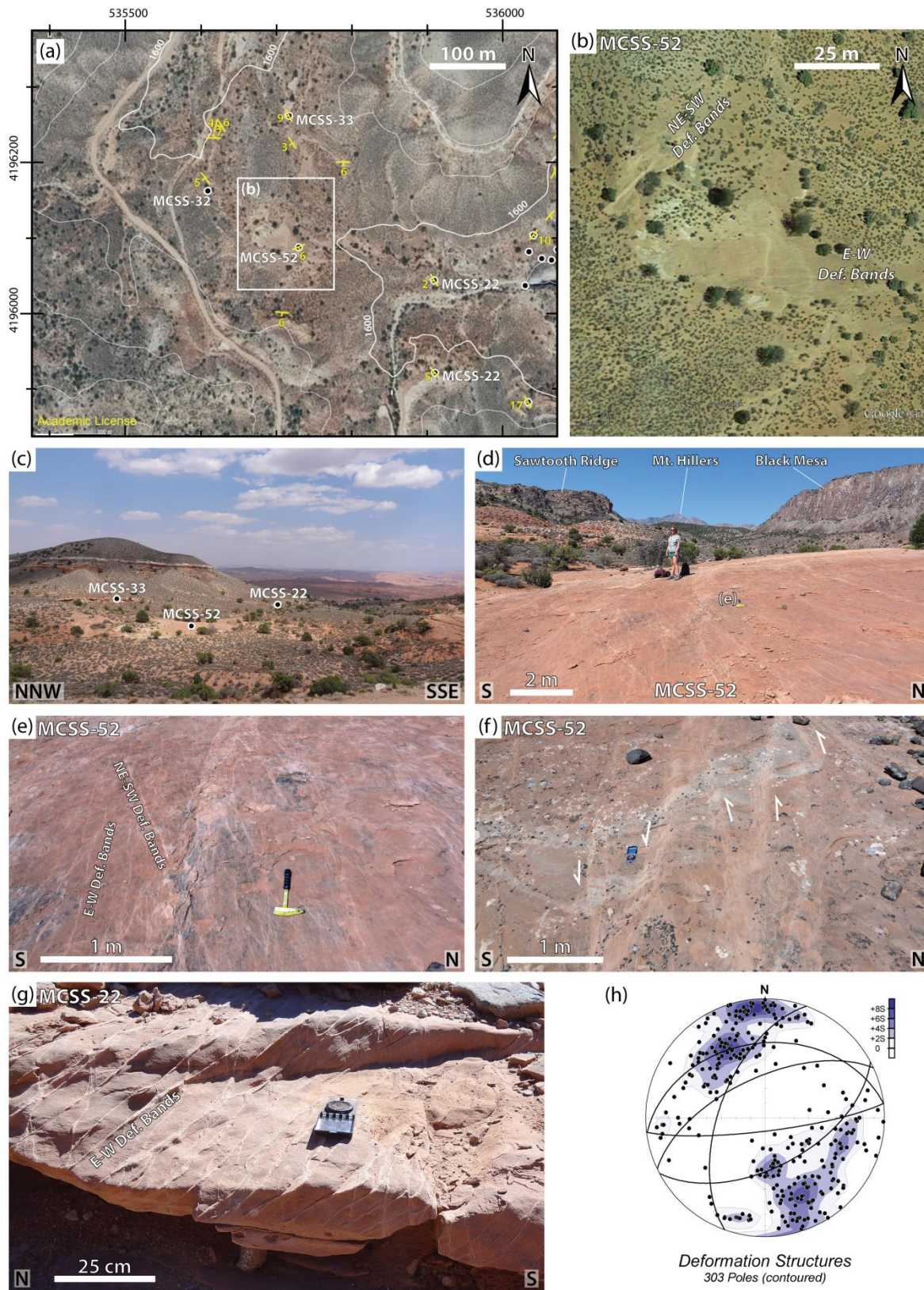


Figure 5.21. SW Maiden Creek. Aerial photograph of the SW Maiden Creek intrusion area. Bedding strike and dip in yellow. Black circles with white outlines show structural stations analysed in this study. (b) Google Earth™ image showing dominant, NE–SW and E–W trending, structures in a sub-horizontal, red sandstone outcrop covering an area of $\sim 50 \text{ m}^2$. (c) Zone 5 as viewed from the BLM dirt road, looking NNE. (d) Photo of the sub-horizontal sandstone outcrop shown in (b). Note deformation structures lining up with the elongate trend of the Sawtooth Ridge intrusion in the background. (e) Zoomed-in photo showing the two deformation trends. (f) Sinistral shear along roughly E–W deformation corridors, suggested by off-sets

on white sandstone horizons. (g) E–W trending conjugate deformation bands. (h) Lower hemisphere equal area stereoplot of all planar deformation structures recorded at structural stations in Zone 5. Poles to planes are contoured, and mean planes are shown by black lines.

Syn-emplacement deformation is largely confined to host rocks at the same structural level as the intrusion, with syn-emplacement deformation appearing to die out rapidly >5 m above the intrusion top surface (e.g. Figs 5.9 & 5.18b), and virtually no deformation apparent in outcrops beneath (Fig. 5.13e). However, a number of intense zones of deformation have been observed (Fig. 5.22b) at the emplacement level and, significantly, appear to be associated with the interaction of separate (adjacent) intrusive bodies (e.g. at the head of Rattlesnake Gully in Zone 3; Fig. 5.14).

A number of common deformation structural types can be observed at various localities around Maiden Creek. These include: faults and deformation bands; zones of intense pencil cleavage; sub-horizontal detachment surfaces and shear zones. Of interest, zones of compressional, extensional and strike-slip kinematics may all be observed across the various localities studied. Compressional deformation structures (including intense pencil cleavage) are consistently observed where host rock sandstones are found between two closely situated intrusive bodies (e.g. structural stations MCSS-41, Zone 1; MCSS-6, Zone 3; and MCRD-24, Zone4). Johnson and Pollard (1973) also observed this zone of intense compressional deformation along the intrusive margin, linking it to accommodation of magma emplacement. As these zones are only observed at outcrops between intrusive bodies, and not on outer margins, it is likely that the compression is the result of ‘squeezing’, associated with the lateral convergence of two bodies. In contrast, zones of extension are more commonly found on intrusion top surfaces and around the outer margins of the intrusion (e.g. Zones 2b and 4a).

Figure 5.22 (*overleaf*)

Spatial distribution of deformation structural trends over the Maiden Creek intrusion area. (a) Aerial photograph (from Google Earth™) of the Maiden Creek intrusion overlain with lower hemisphere equal area stereoplots for a selection of structural stations. Stereoplots show deformation structures plotted as poles to planes (contoured) with mean planes highlighted in black. Bedding planes in maroon. (b) Aerial photograph with structural trend defined. Structural trends are taken from mean planes from stereoplots in (a). Extent of igneous outcrop of the Maiden Creek intrusion is shown in blue. Pink lines show mapped shear zones/ detachment surfaces. White stars indicate zones of intense deformation (e.g. pencil cleavage).

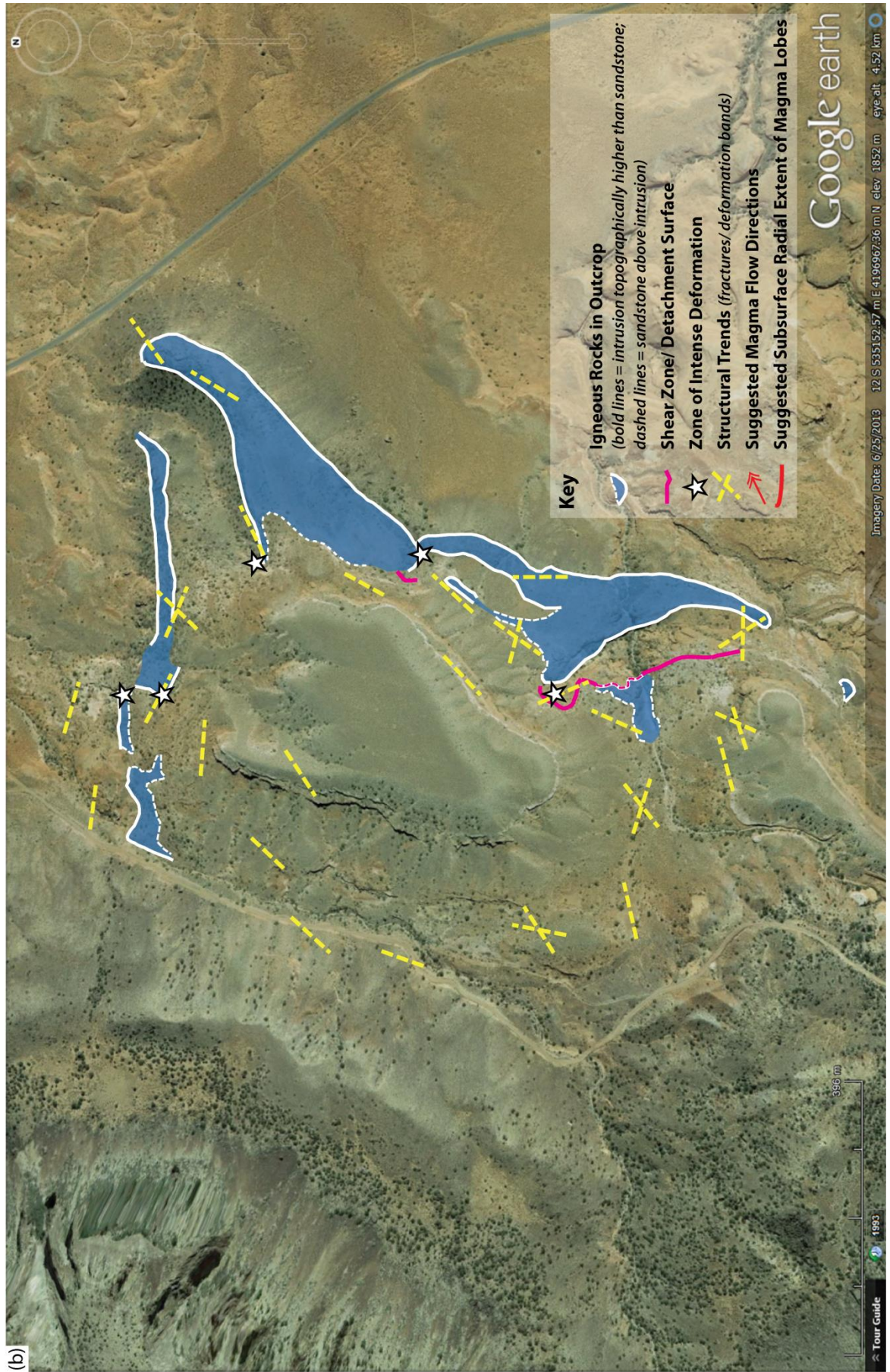


Fig. 5.22b

Based on the observed intrusion geometries and associated deformation styles established in this study, Maiden Creek may be described in terms of three distinct regions; (1) elongate lobate morphologies along the eastern intrusion margin (Zones 1–3); (2) a half-domal north-western margin (Zone 4); and (3) an unexposed south-eastern area (Zone 5).

5.4.1. Eastern Margin (Zones 1, 2 and 3)

Horsman et al. (2005, 2009) described the eastern margin of the Maiden Creek intrusion in terms of finger-like lobes (two in the north-east and two in south) emanating from the main intrusive body situated to the west (Fig. 5.23).

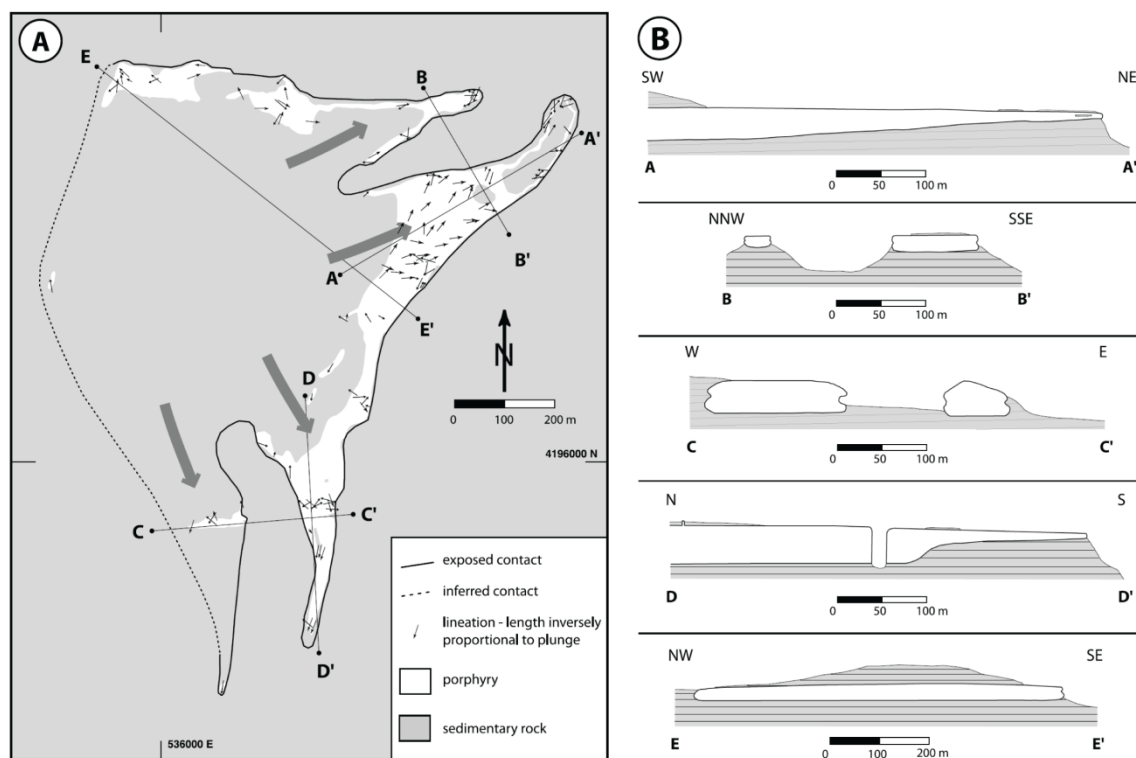


Figure 5.23. The model of Horsman et al. (2009) for the geometry and magma flow directions for the Maiden Creek intrusion. (a) Geological map showing the Maiden Creek as a sill intrusion with a main body located to the west with four-finger-like lobes (two in the north-east and two in the south) emanating from the main body. Black arrows indicate lineations from both field measurements and magnetic fabric data. Arrow length is inversely proportional to the steepness of plunge (i.e. short arrows indicate steeply-dipping fabrics). The large grey arrows show inferred magma flow directions, radially fanning from a feeder to the main sill in the west (below main sill body?). Locations of five cross-sections (A–A' to E–E') are shown on the map.

Igneous outcrop exposures in Zone 1 support the main NE–SW trending body having a lobate morphology. Interestingly, this trend of the main lobe echoes the dominant trend of Sawtooth Ridge (Fig. 5.2b). The NE–SW trending fabrics on the intrusion top surface (Fig. 5.4d), the north-easterly narrowing of the main lobe, and its tipping out in the NE all imply that the magma flow direction was from the SW towards the NE. This is supported by the strong AMS fabric signatures recorded by Horsman et al. (2005) (Fig. 5.23). In contrast, a lack of igneous outcrop exposures for the northern intrusive body in Zone 1 leaves unanswered questions about its true subsurface morphology. The highly elongate, steep-sided and narrow nature of the outcropping body, along with the lack of a flat top surface, does not resemble a typical lobe morphology.

Deformation structures observed at the head of the gully (structural stations MCSS-40 & -41) indicate a compressional system (NNW–SSE SHmax; ENE–WSW Shmin). The stepped geometry observed for the northern lateral margin of the main lobe (Fig. 5.5b, c) suggests that the significant faulting in the adjacent sandstone is synchronous with magma emplacement (i.e. syn-emplacement deformation); the intrusion exploiting active faults. Significant compression (as observed by abundant reverse faults, intense deformation banding and a zone of prolific pencil cleavage) is likely to be the result of lateral spreading of the main lobe resulting in ‘squeezing’ of the adjacent sandstones, in a narrow channel confined by the northern igneous body. Such structures suggest that the two intrusive bodies in Zone 1 are either contemporaneous, or that emplacement of the northern intrusive body occurred before the lateral spreading of the main lobe (i.e. forming a buttress).

Zone 3 displays many common features to those in Zone 1. The outcropping eastern intrusive body shows a similar lobate morphology to the main lobe in Zone 1 (Fig. 5.13). High intensity deformation can also be seen within sandstones at the level of the intrusion in the adjacent sandstone gully (i.e. Rattlesnake Gully, Fig. 5.14). Deformation within the gully is dominantly compressional (including a central zone of pencil cleavage with SHmax perpendicular to the intrusion margin; Fig. 5.12c). As with Zone 1 this is interpreted as ‘squeezing’ of the sandstones between two laterally expanding neighbouring intrusive bodies.

A well-established sub-horizontal shear zone has been identified in Zone 3, separating the highly deformed sandstones in the gully from less deformed sandstones above. This shear zone may be traced from the sandstone gully onto the top surface of both intrusive bodies. Kinematics of this shear zone indicate a top-to-the-W/ WNW movement, perpendicular to the main trend of the eastern intrusive lobe. A more detailed analysis of this shear zone is provided in Chapter 6; however, it is worth noting that these kinematics are in stark contrast to the N–S flow directions proposed by Horsman et al. (2005, 2009).

The complex nature of intrusion and host rock geometries in Zone 2 make the true 3D geometries hard to visualise. The area was described by Horsman et al. (2005) as a window through the intrusion (see fig. 2 of Horsman et al., 2005) to the underlying sandstone. However, in more recent work of Horsman et al. (2009) this window appears to be no longer highlighted (Fig. 5.23).

The geometry of the intrusion top surface along the eastern margin in Zone 2a (Fig. 5.6) appears to reflect a stepped structure. This is in contrast to the flat-lying intrusion top surface seen on the main lobe in Zone 1. Along this part of the eastern margin one can observe a series of elongate ridges trending NE–SW (Fig. 5.6d). In contrast to the en-echelon step-stair morphologies of Rickwood (1990), here, from west to east, a step-down followed by a step-up is observed (Fig. 5.6b, c; Fig. 5.24). Schofield et al. (2012a) attribute this non en-echelon morphology to the preferential exploitation of different horizons by magma, rather than step formation through the creation of a fracture ahead of the sill tip.

Assuming that the intrusion in Zone 2a has a stepped morphology, it is possible that the complex intrusion and host rock geometries observable within Whispering Wind Gully (Zone 2b) could be attributed to a window created by vertical separation of the sill sheet in Zone 2a into two or three parallel sheets as they propagate in a roughly NE direction along different structural horizons. This could explain the absence of igneous outcrops on the southern side of the gully, the reappearance of intrusion on the northern gully side the result of these segmented sheets once again coalescing (relay ramps and ‘broken bridges’ of Schofield et al., 2012a; Fig. 5.24; e.g. similar to the depiction in Fig. 5.1b).

The intensity of deformation of the sandstones within Whispering Wind Gully (Zone 2b) resembles that observed in Zones 1 and 3. Similar to Rattlesnake Gully in Zone 3, synclinal folding of the bedding can be seen in Whispering Wind Gully. However, in contrast to the dominantly compressional deformation observed in Zone 3, here, fault kinematics appear to favour extension (ESE–WNW; Figs 5.6d & 5.10). Differences in deformation style are interpreted to reflect contrasting emplacement mechanisms and associated deformation processes in stepped domains on intrusion top surfaces versus inter-lobe locations. A broken bridge scenario within Whispering Wind Gully could help to explain the extensional kinematics observed within the sandstone host rocks in the gully.

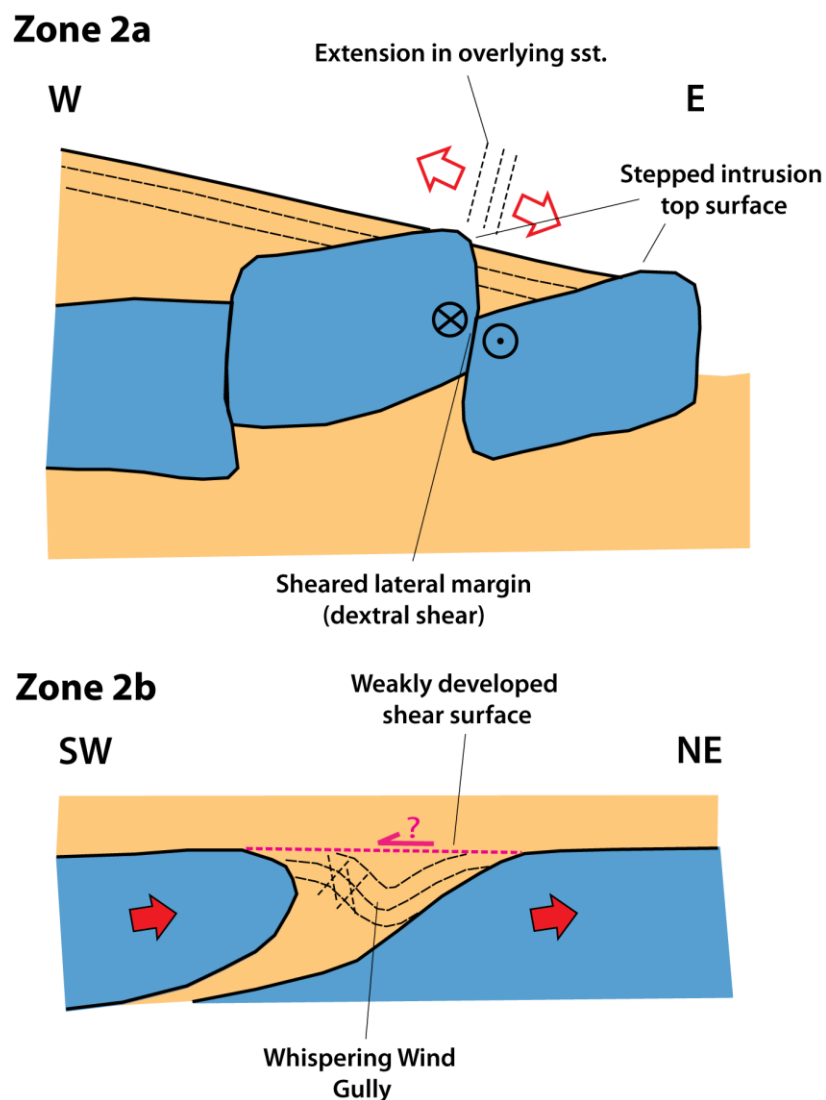


Figure 5.24. Schematic cross-sections across the intrusion in Zones 2a and 2b. (a) Schematic cross-section (E–W) across Zone 2a depicting proposed sub-surface geometry to explain off-set (stepped) intrusion top surface. (b) Schematic cross-section (NE–SW) across Zone 2b (Whispering Wind Gully) depicting proposed sill geometries to explain deformation of sandstone in gully. See also Fig. 5.1b for conceptual geometries.

5.4.1.1. Lobes, Steps and Bridges

It is likely that the main lobe in Zone 1 and the eastern margin (Zone 2) of the Maiden Creek intrusion have lobate morphologies. However, all deformation structures observed in this study are brittle, with faulting and associated zones of cataclasite (and to a much lesser extent, breccia), deformation banding, pencil-cleavage, joints all observed in the field. This dominantly brittle deformation is in stark contrast with literature supporting ductile deformation commonly associated with magma fingers and lobes (e.g. Tweto, 1951; Pollard et al., 1975; Schofield et al., 2012a).

Fundamentally, the studies of Tweto (1951), Pollard et al. (1975) and Schofield et al. (2012a) suggest a close relationship between magma finger and lobe formation with certain (weaker?) host rock lithologies (e.g. clays, shales, and coal) that deform in a ductile manner. Interestingly, the Maiden Creek intrusion is emplaced largely within more competent (indurated) red, sub-arkosic sandstones; with a thin, more muddy-/ shaley-sandstone horizon sitting directly above or close to the top surface of the intrusion. Schofield et al. (2012a) provided an alternative for the fingers and lobes model, suggesting that localised fluidisation may play a role in allowing the host rocks to behave in a ductile manner; hydrothermal activity and associated fluidisation processes mobilising grain boundaries within the host rocks. However, field evidence for such fluidisation is not apparent in the host rocks adjacent to the main magma lobe (Zone 1) or along the eastern margin (Zone 2) of Maiden Creek. The observations raise a number of key questions. Firstly, are lobe morphologies the main intrusion mechanism for the Maiden Creek intrusion, and if so, is magma lobe formation also facilitated by dominantly brittle deformation processes? Secondly, is there significant evidence for fluidisation at the microstructural scale (see Chapter 6 for more on microstructural analysis of samples from Zone 3)?

The stepped and broken bridge morphologies proposed to explain the complexities observed in Zone 2 are associated with more brittle deformation processes (e.g. Pollard et al., 1975; Rickwood, 1990; Schofield et al., 2012a). This is consistent with the dominantly brittle deformation observed over the whole of the Maiden Creek intrusion.

The palaeo-depth of emplacement for the Maiden Creek intrusion was likely ~3 km (Hintze & Kowallis, 2009; see Fig. 2.18a, Chapter 2). This puts the depth of emplacement

for Maiden Creek at the base of the proposed transition zone between fluidisation and brittle processes of Schofield et al. (2012a; Fig. 5.25). Similar to their example of the Whin Sill in the UK, this study supports the Maiden Creek intrusion displaying magma lobes as well as stepped and broken bridge morphologies.

5.4.1.2. *Kinematic Partitioning*

In both Zones 2 and 3 fault kinematics appear to vary spatially. Deformation structures adjacent to (<5 m) the intrusion appear to be dominated by strike-slip kinematics (Figs. 5.8, 5.10 & 5.14g), while in contrast farther away from the intrusion contact, faults tend to show more dip-slip characteristics (Fig. 5.6d). This may reflect a form of kinematic partitioning at the outcrop scale, and may be linked to the volumetric addition of magma. This kinematic partitioning fits with the model of Teyssier and Tikoff (1999) that suggests the range over which wrench-dominated faulting predominates at low-finite strains can increase as pure shear is accommodated by volumetric addition of magma (Fig. 5.26).

5.4.2. **NW Margin (Zone 4)**

As outlined above, the NW margin (Zone 4) comprises two distinct morphological and structural domains. In Zone 4a, the margin has a half-domal geometry trending from roughly NNE–SSW to E–W (Figs 5.3 & 5.15b). In contrast Zone 4b displays a much steeper, E–W trending, linear intrusion margin. Deformation structures and their orientations vary across these zones, echoing the change in both intrusion margin trend and margin geometry (Fig. 5.22).

The monoclinical geometries observed in Zone 4a show concordant sandstone beds draped (folded) over a single continuous intrusive sheet. Similar geometries have also been observed at Trachyte Mesa where ‘out-of-sequence’ stacking (‘under-accretion’ of Menand, 2008) has occurred (Morgan et al., 2008; Chapter 3, this study). There are two possible models for the sub-surface intrusion morphology in Zone 4a: (1) a classic domal laccolithic intrusion with a concave-upwards upper margin resulting from vertical inflation of a single sheet; or (2) a ‘Christmas tree’/ stacked laccolith geometry with under-accretion beneath an initial sheet; this first sheet arched upwards as a result of inflation of the sheets below.

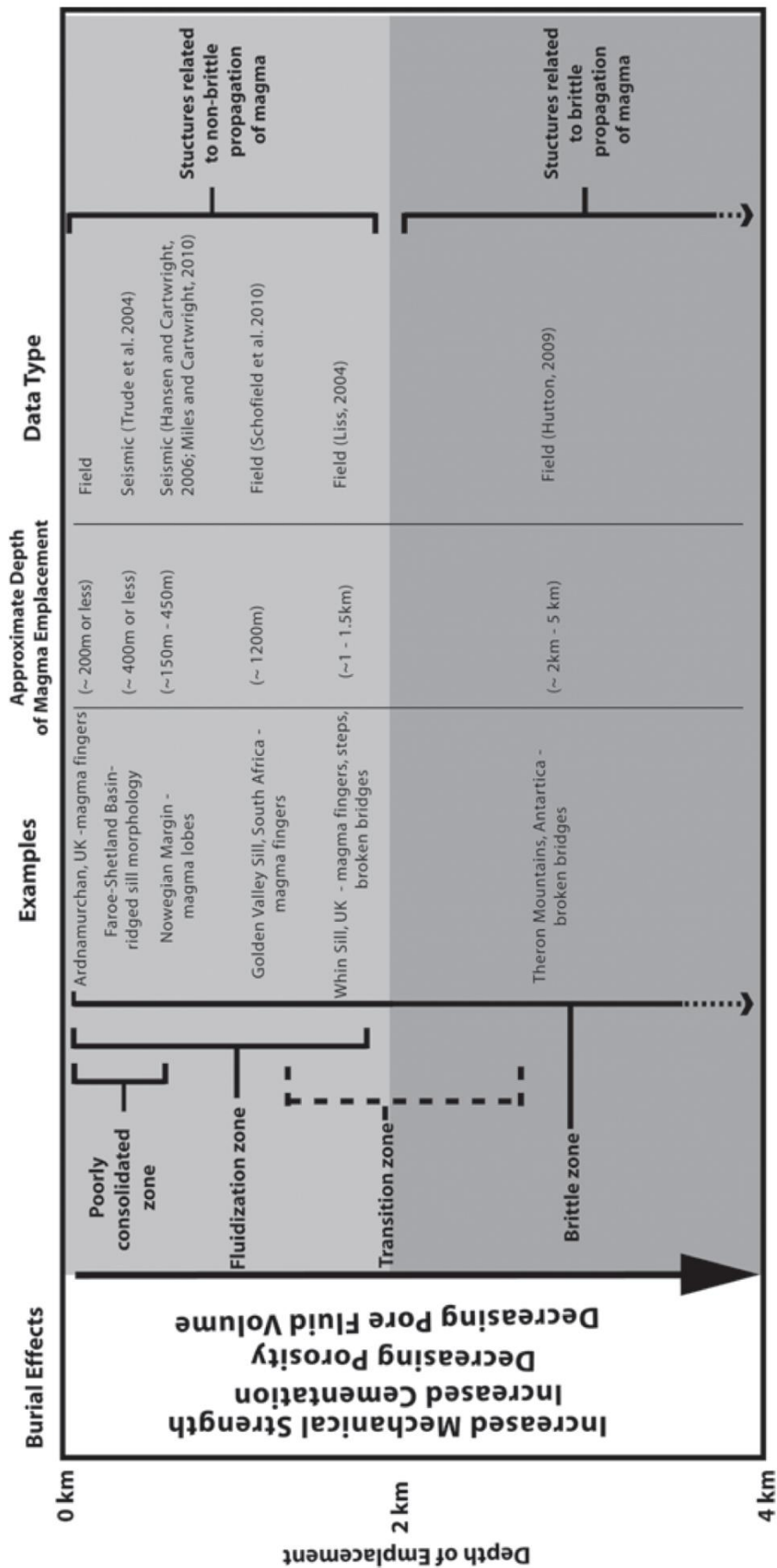


Figure 5.25. Table depicting observed relationships between depth of intrusion emplacement within a sedimentary basin, host rock properties, emplacement mechanisms and intrusion morphologies (from Schofield et al., 2012a).

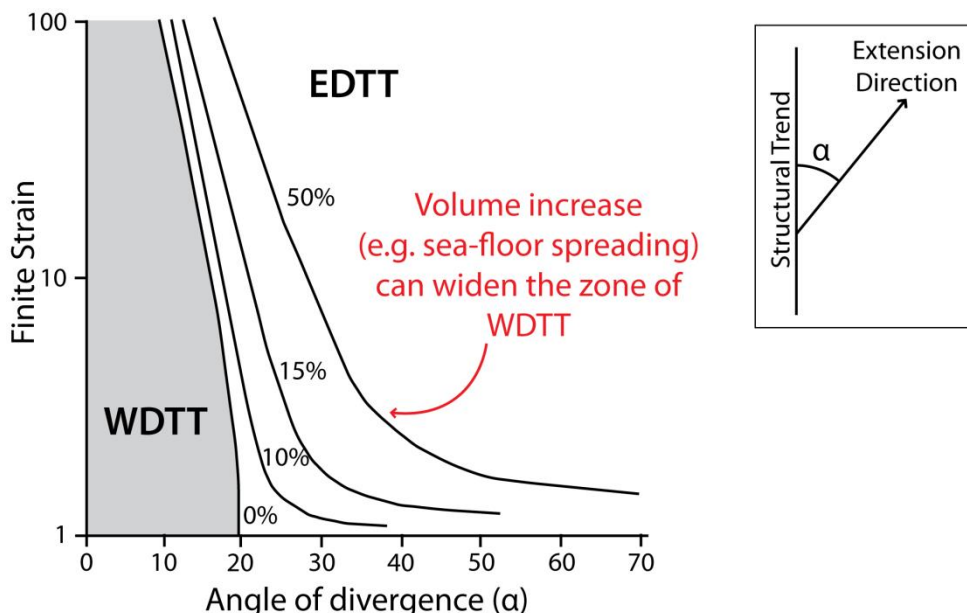


Figure 5.26. Plot showing range over which wrench dominated transtension (WDTT) may vary when magma addition is included (Teyssier & Tikoff, 1999). Angle α is the angle of divergence between the extension direction and a structural boundary. The normal range over which wrench dominated deformation predominates is normally at angles where the divergence angle is $<20^\circ$, however this range may increase when volumetric addition (i.e. magma addition) occurs. EDTT = extension dominated transtension).

In contrast, the intrusion geometry in Zone 4b appears more tabular, with a steep lateral margin (Fig. 5.18a). Sandstones are concordant over the intrusion top surface, whereas they abut the steep lateral margin.

The transition area from Zone 4a to 4b is another highly complex area. The step-up on the intrusion top surface (Fig. 5.18b) could, similar to Zone 2a on the eastern margin, be attributed to a stepped-sill (Fig. 5.1b) on a top surface. However, as this step up is visible along two different trends (N–S and ESE–WNW; Fig. 5.15b) a stepped geometry as depicted in Figure 5.1b is unlikely, as these steps are normally linear and parallel to the magma flow direction. This geometry is more easily explained by the localised stacking of adjacent intrusive sheets. Furthermore, the presence of a zone of pencil-cleavage adjacent to the step, implies compression and ‘squeezing’, consistent with sheet convergence (as observed in the sandstone gully in Zone 1 and Rattlesnake Gully in Zone 3); extension and strike-slip appearing to be more dominant in a stepped sill domain (e.g. Zone 2).

In Zone 4a, shallowly dipping faults on the intrusion top surface, and the immediate overlying sandstones (0–3 m), show top-to-the-south kinematics (Figs 5.16 & 5.20). These likely reflect magma flow and emplacement from south to north in this region. Similar top-to-the-south kinematics are also apparent in Zone 4b; however here the deformation is in the form of low-angle, reverse (i.e. thrust) faults seen along the bleached sandstone ridge (Figs 5.17 & 5.20). This change from low angle ‘extensional’ shear (Zone 4a), seen on the intrusion top surface, to compressional deformation, adjacent to the lateral margin, is coincident with steepening of the intrusion margin (Fig. 5.20). The steep extensional dip-slip faults observed in Zone 4b (bleached white sandstone ridge; Fig. 5.17) pre-date reverse thrust faulting. These may be related to an earlier phase of emplacement, or even pre-date emplacement (i.e. similar to regional Phase 1 structures observed at Trachyte Mesa, Chapter 3).

Horsman et al. (2005) demonstrated that AMS fabrics are variable across Zone 4, although two dominant trends are apparent: E–W (similar to host rock deformation trends observed in this study); and N–S (echoing kinematics in this study).

5.4.3. Unexposed SW Margin (Zone 5)

Although no intrusion outcrops may be observed in Zone 5, evidence from the other four zones may be applied to infer the sub-surface intrusion geometry. Deformation structures in Zones 1 to 4 commonly parallel intrusion margins and, to a lesser extent, flow directions (Fig. 5.22). In Zone 5, two distinct deformation trends are apparent: NE–SW; and E–W (Fig. 5.21). Both these trends are at a high angle (near perpendicular) to the inferred intrusion contact of Horsman et al. (2005, 2009; Fig. 5.23). Therefore, this simple inferred contact appears unlikely. NE–SW trending structures appear to line up well with the trend of the main lobe in Zone 1 (to the NE) and also with the trend of Sawtooth Ridge (to the SW). From this, it may be inferred that this system may parallel the main flow direction in the SW Maiden Creek intrusion. The E–W trending structures can be traced laterally towards the southern elongate intrusive bodies in Zone 3. These may reflect a southern lateral margin and/ or easterly flow direction to Maiden Creek. In either case this would imply a distinctly different sub-surface geometry to that of Horsman et al. (2005, 2009). An E–W trending magma flow direction (i.e. feeding the western lobe in Zone 3) would be consistent with kinematics observed for the shear zone

(Zone 3), as well as the roughly E–W mineral stretching lineations and AMS fabrics recorded by Horsman et al. (2005) (Fig. 5.23). Again this would have implications for the emplacement model proposed by Horsman et al. (2005, 2009) for the southern intrusive lobes being fed from the north.

5.4.4. A new model for development of the Maiden Creek intrusion

Figures 5.27 and 5.28 show a preliminary evolution of the Maiden Creek intrusion based on observations in this study. This new alternative model for the emplacement and final geometry of the Maiden Creek intrusion has been developed through the integration of: structural trends (consistent field relationships suggesting these parallel intrusion margins, and to a lesser extent, magma flow directions); kinematics (these reflecting magma flow); field observations of intrusion and host rock geometries; and locations of zones of intense deformation (field relationships suggesting that these are localised to transition zones between neighbouring intrusive bodies and their amalgamation). Accordingly, the Maiden Creek intrusion can be sub-divided into 5 principal intrusive bodies (Fig. 5.29): a main, central NE–SW trending lobe (Zones 2 and 1) displaying a complex intrusion top surface with steps and broken bridges; a half-domal ‘laccolithic’ body comprising the western and north-western margin (Zone 4a); an inclined magma sheet comprising the northern ridge (Zones 1 and 4b); and either two inclined magma sheets or a combination of a lobe (eastern lobe) and inclined sheet (western lobe) comprising the southern Maiden Creek intrusion (Zone 3).

All kinematics and structural trends appear to support a radial magma flow from a feeder system located in the south-west. A feeder system from the vicinity of Sawtooth Ridge is envisaged: note, the strong alignment between the main lobe seen in Zone 1, the dominant NE–SW trending deformation structures over much of the Maiden Creek intrusion (Fig. 5.22) and the trend of Sawtooth Ridge to the south-west (Figs 5.2b and 5.27). Growth of the intrusion from the south-west towards the north-east is then pictured with lateral spreading of magma outwards towards the north (Zone 4) and the east (Zone 3) as sub-horizontal stepped sheets and/ or inclined (saucer-shaped?) sheet morphologies. Whether pairs of finger-like lobes (model of Horsman et al., 2005, 2009) or a combination of lobe and inclined sill sheet morphologies (this model), in order to form the zones of intense compressional deformation (with zones of pencil cleavage) observed

in both the NE and southern Maiden Creek intrusion (i.e. Zones 1 and 3), two neighbouring intrusions must be emplaced either contemporaneously, or the outer body (with respect to the direction of magma flow and feeder) must be emplaced first in order to provide confined boundary conditions (i.e. the northern ridge before the main lobe in Zone 1, and the eastern lobe before the western body in Zone 3). Relative timings for the western/ north-western 'laccolithic' body are less constrained, and the growth of the western body could have been throughout the evolution of the entire intrusion. The final stages of emplacement are likely to be the emplacement of the intrusion in the north-east (i.e. the main lobe in Zone 1).

Horsman et al. (2005, 2009) suggested that the sub-surface geometry of the entirety of the Maiden Creek intrusion is flat lying and comprises of two vertically stacked sill sheets, perfectly matching each other in both thickness and extent (Fig. 5.25). Due to the complex lobate geometries proposed by Horsman et al. (2005, 2009), this perfectly matched stacked system does not seem viable. There is some evidence in the north (Zone 4) to support vertical stacking of sill sheets, however, over much of the rest of the intrusion, no strong evidence is apparent to support the dual stacking of sill sheets proposed by Horsman et al. (2005, 2009). Furthermore, additional complexities, both in terms of intrusion geometries and emplacement-related deformation structures, highlighted in this study further undermine the model for two stacked sill sheets. If the intrusion and host rock geometries in the Whispering Windy Gully area (Zone 2b) truly reflect a 'window' or gap in the intrusion created by the localised separation of coalesced stepped- magma lobes/ sill sheets and a broken bridge, it is unlikely that a second (over-accreted) sill sheet would mimic this complex geometry. Additionally, the observed intrusion geometry in the NW (Zone 4a), with an expansive and continuous half-domal intrusion top surface, suggests either one large laccolithic body, or under accretion of later magma sheets beneath an initial sheet; not over accretion as suggested by Horsman et al. (2005). Where an irregular lateral margin geometry (hour-glass shape; Fig. 5.13f) is observed, analysis of the adjacent host rock deformation structures imply that this geometry is more likely the result of the interaction of the magma with adjacent syn-emplacement faults, rather than two separate sheets. In Chapter 6 this aspect is discussed further using evidence from Zone 3.

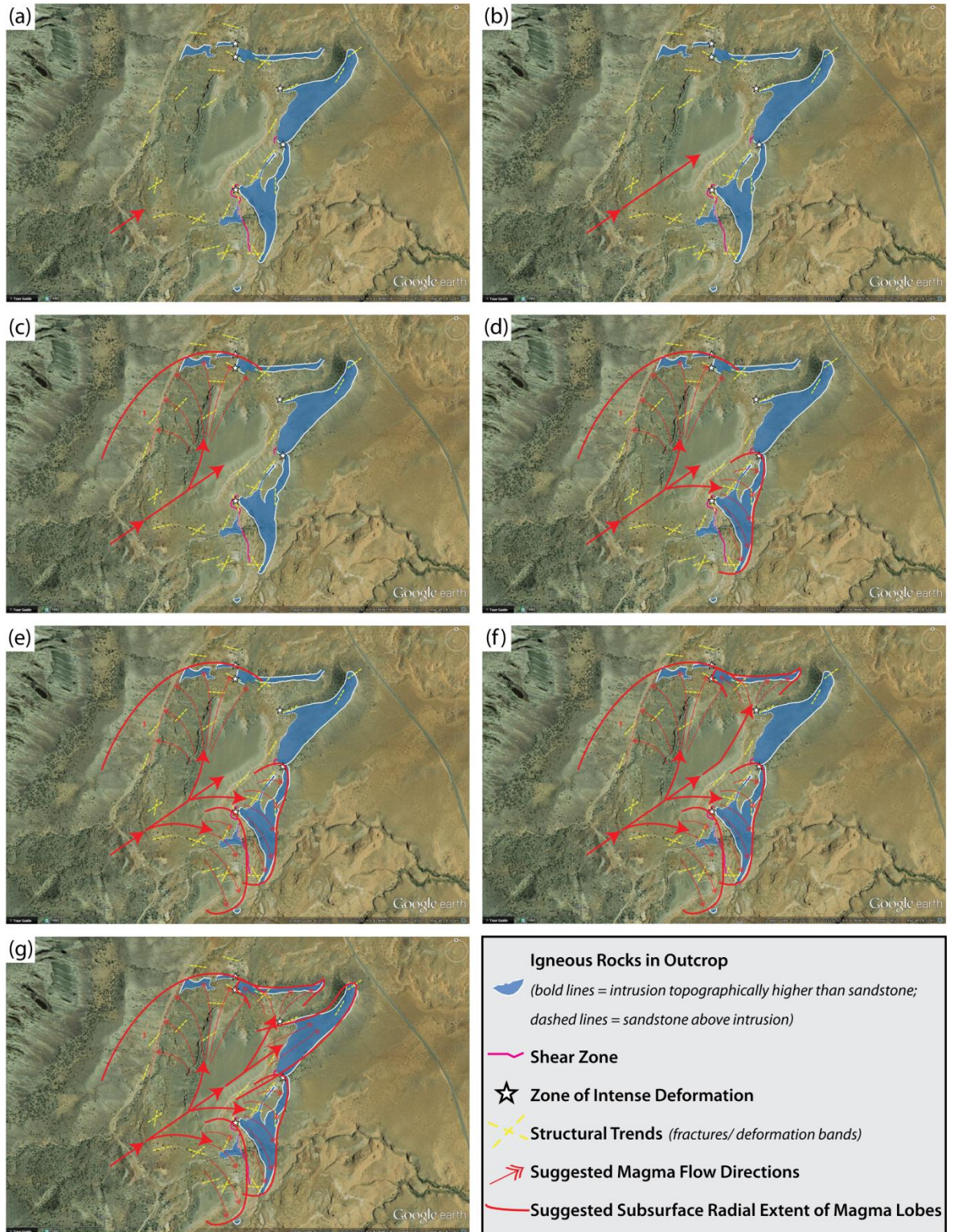


Figure 5.27. Possible emplacement evolution for the Maiden Creek intrusion based on observations, kinematics and structural trends identified in this study, and as discussed in text. Note this evolution is somewhat conceptual and needs further validation through additional fieldwork (inc. geophysical surveys).

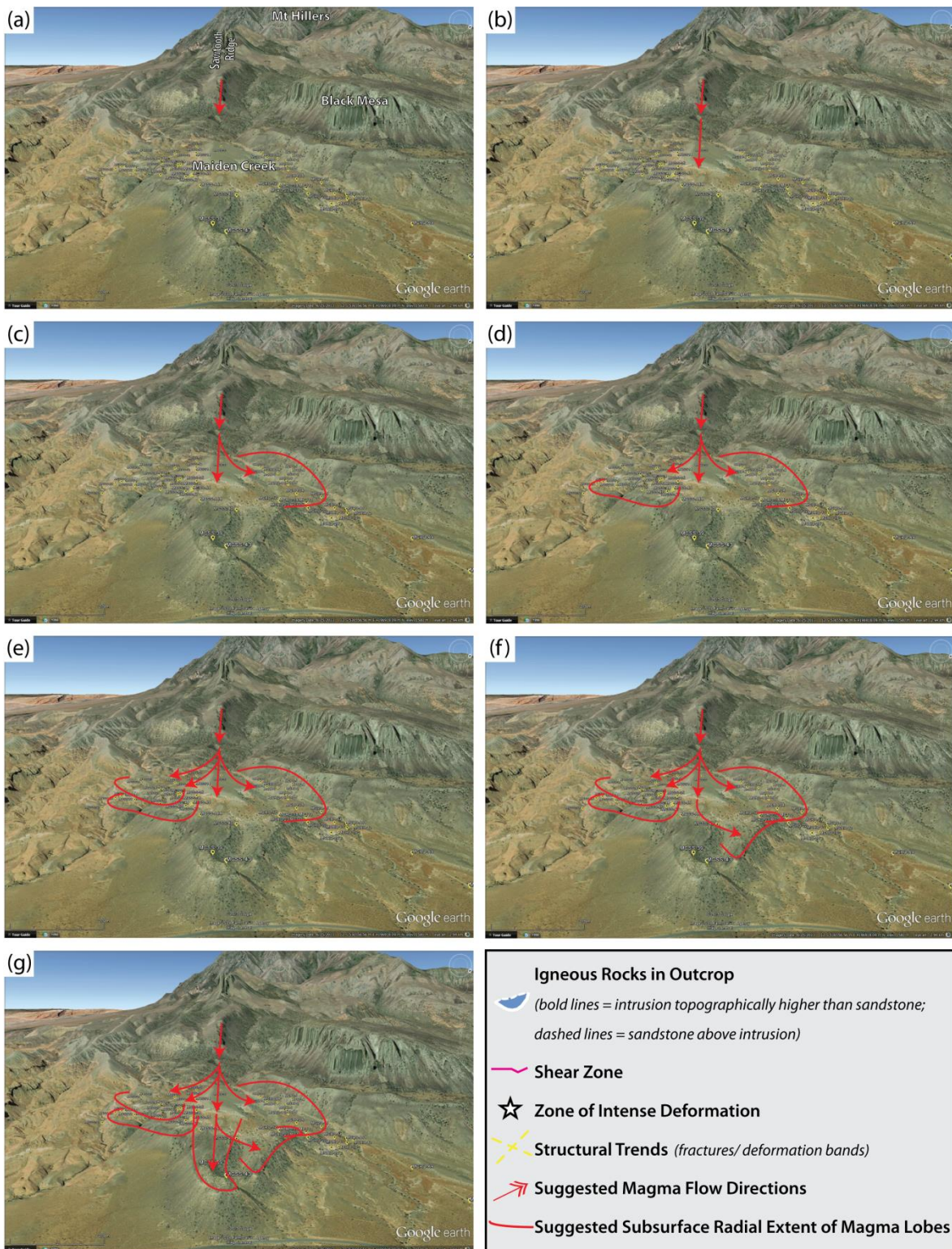


Figure 5.28. Same model as shown in Figure 5.27, annotated onto an oblique aerial view from Google Earth™. Note alignment of Sawtooth Ridge intrusion with the main igneous lobe in Zone 1.

Further constraints of the sub-surface morphology are required to fully understand the true emplacement evolution and final geometry of the Maiden Creek intrusion. This may come from integration of field studies (i.e. Horsman et al. (2005) and this study) with geophysical mapping techniques (e.g. gravity and magnetic surveys and ground-

penetrating radar). However, complex intrusion and host rock geometries and emplacement-related deformation structures suggest that the sub-surface extent and morphology of the Maiden Creek intrusion could be far more complex than previously proposed.

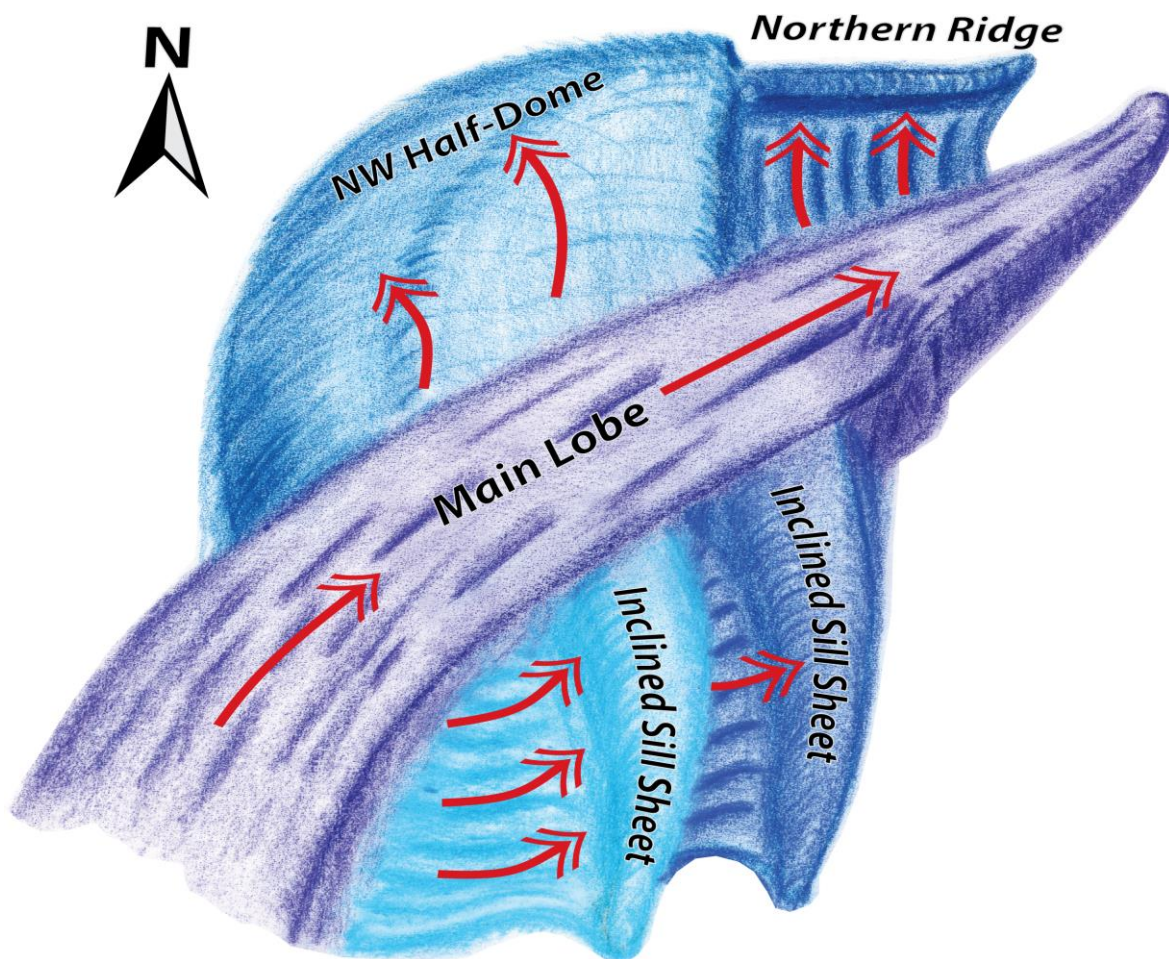


Figure 5.29. Conceptual 3D model for the proposed sub-surface geometry of the Maiden Creek intrusion. Maiden Creek intrusion is sub-divided into 5 principal intrusive bodies: a main, central NE–SW trending lobe (Zones 2 and 1) displaying a complex intrusion top surface with steps and broken bridges; a half-domal ‘laccolithic’ body comprising the western and north-western margin (Zone 4a); an inclined magma sheet comprising the northern ridge (Zones 1 and 4b); and two inclined magma sheets (eastern and western lobes) comprising the southern Maiden Creek intrusion (Zone 3). Magma flow directions are depicted by red arrows.

5.5. Conclusions

This study has provided a detailed analysis of intrusion contacts and syn-emplacement host rock deformation structures to the Maiden Creek intrusion. A new model is suggested for the emplacement, evolution and final geometry of the intrusion, with a main and central NE–SW trending lobate intrusive body the result of a principle north-easterly magma flow, originating from depth in the SW (and in line with the Sawtooth Ridge intrusion), with lateral expansion resulting from the radial spread of magma from the main NE flow direction towards the east and north-west. Intrusion and host rock geometries, along with host-rock syn-emplacement deformation structures, suggest a highly complex final geometry for the Maiden Creek intrusion, with 5 principle intrusive zones, and the amalgamation of smaller intrusive bodies within these. Deformation structures are dominantly brittle across the entire Maiden Creek intrusion, with magma emplaced largely within more competent sandstones. Interestingly, a thin interlayered shaley-siltstone unit sits immediately above much of the top surface of the intrusion, appearing to act as a detachment surface above which intrusion-related host rock deformation is seemingly lacking, and also perhaps playing some role in controlling the level of magma emplacement.

In addition to the new model for emplacement and final geometry, results suggest that much can be learnt about intrusion geometries and emplacement through the detailed analysis of these structures; these include:

- deformation structures commonly parallel intrusion margins, and in some cases flow directions;
- kinematic analysis can give a strong indication of likely magma flow directions;
- deformation styles (e.g. compressional, extensional, strike-slip) vary according to the local intrusion geometry (e.g. dominantly compressional between intrusive bodies; and more extensional around steps and corrugations on intrusion top surfaces); and
- local kinematic partitioning (between pure and simple shear) is also evident in syn-emplacement deformation structures in close proximity (< 5 m) to intrusion margins.

Therefore, even in areas where intrusion outcrop is not available, these learnings can be applied to infer underlying intrusion geometries (i.e. Zone 5).



6. Chapter 6: Syn-emplacement accommodation structures associated with the Maiden Creek intrusion, Henry Mountains, Utah.

| | | | |
|----------------|---------------|---|---------------|
| <i>Layout:</i> | 6.1. | Introduction | p. 249 |
| | 6.2. | Geological Setting | p. 250 |
| | 6.2.1. | <i>Henry Mountains</i> | p. 250 |
| | 6.2.2. | <i>Maiden Creek Intrusion</i> | p. 252 |
| | 6.2.3. | <i>Host rock - Entrada Sandstone</i> | p. 253 |
| | 6.3. | Digital mapping and 3D visualisation | p. 253 |
| | 6.4. | Intrusion – host rock geometries in study area | p. 256 |
| | 6.5. | Intrusion related deformation structures | p. 262 |
| | 6.5.1. | <i>Deformation structures above the MCSZ</i> | p. 263 |
| | 6.5.1.1. | <i>Deformation bands</i> | p. 263 |
| | 6.5.1.2. | <i>Faults</i> | p. 263 |
| | 6.5.1.3. | <i>Joints</i> | p. 263 |
| | 6.5.2. | <i>Deformation structures below the MCSZ</i> | p. 265 |
| | 6.5.2.1. | <i>Deformation bands</i> | p. 265 |
| | 6.5.2.2. | <i>Pencil cleavage</i> | p. 265 |
| | 6.5.2.3. | <i>Strike-slip faults</i> | p. 266 |
| | 6.5.3. | <i>Deformation structures at the intrusion–sandstone contact</i> | p. 266 |
| | 6.5.3.1. | <i>Lateral margin</i> | p. 266 |
| | 6.5.3.2. | <i>Deformation on intrusion top surface</i> | p. 268 |
| | 6.5.3.2.1. | <i>Stretched mineral lineations</i> | p. 268 |
| | 6.5.3.2.2. | <i>Low-angle faults</i> | p. 268 |
| | 6.5.3.2.3. | <i>Styolites</i> | p. 271 |
| | 6.6. | Spatial distribution of deformation structures | p. 271 |
| | 6.7. | Maiden Creek Shear Zone (MCSZ) | p. 273 |
| | 6.7.1. | <i>Outcrop observations and spatial extent</i> | p. 273 |
| | 6.7.2. | <i>Shear zone microstructures</i> | p. 274 |
| | 6.7.3. | <i>Variations in character</i> | p. 277 |
| | 6.8. | Discussion | p. 279 |
| | 6.8.1. | <i>MCSZ: a syn-emplacement accommodation structure</i> | p. 279 |
| | 6.8.2. | <i>Structural complexity and variations in strain within Rattlesnake Gully</i> | p. 281 |
| | 6.8.3. | <i>Models for emplacement and geometry of the southern Maiden Creek intrusion: a pair of finger-like lobes or deep rooted sills?</i> | P. 281 |
| | 6.7. | Conclusions | p. 286 |

Syn-emplacement accommodation structures associated with the Maiden Creek intrusion, Henry Mountains, Utah

This chapter is written for submission to Geosphere

Co-Authors*: **Penelope I.R. Wilson**, Ken J.W. McCaffrey, Robert E. Holdsworth

*(*note: all scientific work was undertaken by the student/ principal author P. Wilson, and input from co-authors on this work was at an advisory/ editorial level only)*

Abstract

The Maiden Creek intrusion is a small satellite intrusion to the Mount Hillers intrusive complex, Henry Mountains, Utah. Composed of an intermediate plagioclase-hornblende porphyritic magma, the intrusion is emplaced within the Entrada Sandstone Formation. These host rocks are an ideal lithology for the formation and preservation of deformation structures that record information about the emplacement of the intrusion, magma flow pathways and associated strains. Detailed observations of geometry and kinematics of accommodation-related deformation of two neighbouring, c. N–S trending, elongate intrusive bodies and host sandstones in a gully between have newly identified a sub-horizontal shear zone which separates less deformed sandstones above from highly deformed sandstones below in the gully, and acts as a structural detachment surface. Structural evidence in the southern area of the Maiden Creek intrusion is consistent with westerly-derived magma emplacement. Deformation structures in host rock sandstone outcrops within the gully between the southern intrusive bodies are dominantly compressional (c. E–W SHmax), while the spatial distribution and asymmetry of these structures imply a reverse (east-verging) shear component. From observations of both syn-emplacement deformation structures and exposed intrusion geometries, it is proposed that the southern Maiden Creek intrusion is comprised of two westerly-derived, deep-rooted sills. Overlying these deeper-rooted sills is the newly identified Maiden Creek Shear Zone (MCSZ). This structure, with its top-to-the-WNW shear sense, is an antithetic accommodation structure to the magma flow. Substantial amounts of strain observed through microstructural analysis of shear zone samples suggest that the MCSZ played a critical role in accommodating magma emplacement.

Keywords:

Sill emplacement; Shear zone; Microstructures, Accommodation structures; Intrusion; Henry Mountains

6.1. Introduction

Large volumes of igneous rock exist within the shallow upper crust (2–10 km) as intrusive bodies, ranging in size and geometry (Cruden & McCaffrey, 2001). An intrinsic part of our understanding of the emplacement of magma into the subsurface is reconciling the intrusion ‘space-problem’ (Hutton, 1996). First recognised by Charles Lyell in the nineteenth century (Pitcher, 1993), the ‘space-problem’ (or ‘room-problem’) refers to the physical processes that allow the substantial volumetric addition of magma at depth. Magma is commonly emplaced as a series of successive sub-horizontal tabular sheet-like intrusions (e.g. Hutton, 1996; Cruden & McCaffrey, 2001; Morgan et al., 2008) in the mid to upper crust. Such incremental growth means that only small volumes of additional rock need to be accommodated at any one time (e.g. Pitcher, 1970; Mahan et al., 2003; Glazner et al., 2004). Various studies have emphasised the role played by faults, shear zones and pre-existing host rock structures in controlling the emplacement and growth of magma bodies at depth (e.g. Hutton et al., 1990; McCaffrey et al., 1992; Neves et al., 1996; Holdsworth et al., 1999; Snoke et al., 1999; Passchier et al., 2005). Furthermore, most intrusions are syn-tectonic, and therefore emplaced into an active fault system which may accommodate the increase in rock volume.

There are three distinct and different types of accommodation structures when considering intrusion emplacement. There are those that are pre-existing structures which are then exploited by the magma as it is emplaced (e.g. Hutton & McErlean, 1991; Holdsworth et al., 1999; Magee et al., 2013). These we term **‘pre-emplacement’ accommodation structures**. The second type comprises large, tectonically-driven structures (such as transtensional faults) that are active at the time of magma emplacement, i.e. **‘syn-tectonic’ accommodation structures** (e.g. McCaffrey et al., 1992; Neves et al., 1996; Passchier et al., 2005). The third type consists of localised structures which develop directly in response to magma emplacement in order to accommodate the extra volume of rock within the subsurface (i.e. the intrusion ‘space-problem’). It is this final group of **‘syn-emplacement’ accommodation structures** and associated physical mechanisms that are the principal focus of this study.

Most field-based studies of intrusions have focused on the geometry and internal architecture of sills, laccoliths and plutons, using a variety of methods including: field mapping of internal contacts and external margins (e.g. Morgan et al., 2008; Magee et al.,

2012); geochronological studies (e.g. Coleman et al., 2004; Westerman et al., 2004); magnetic and macroscopic fabric studies (e.g. de Saint Blanquat & Tikoff, 1997; Horsman et al., 2005; Stevenson et al., 2007); and numerical and experimental modelling (e.g. Pollard & Johnson, 1973; Galland et al., 2009; Kavanagh et al., 2013). In comparison, only a small number of studies have paid particular attention to the structural processes that are occurring in the host rocks as these intrusions are emplaced (e.g. Johnson & Pollard, 1973; Jackson & Pollard, 1988; Morgan et al., 2008; Schofield et al., 2012). Furthermore, most papers that include observations on host-rock deformation structures do not consider the kinematics which can potentially preserve information concerning the emplacement mechanism, magma movement (i.e. flow direction) and associated strains.

The present study focuses on syn-emplacement accommodation structures related to the Maiden Creek intrusion in the Henry Mountains, Utah. This intrusion was likely emplaced at a palaeo-depth of ≥ 3 km (based on overburden thickness estimates; Hintze & Kowallis, 2009). The study combines results from traditional field mapping and structural studies, microstructural analysis and 3D visualisation (aided by laser scanning) in order to provide a detailed analysis of the geometries, kinematics and spatial distribution of syn-emplacement deformation structures in both the intrusion and importantly, the host rocks.

6.2. Geological Setting

6.2.1. Henry Mountains

The Henry Mountains, SE Utah form part of the Colorado Plateau (Fig. 6.1a), and are a classic region for the study of igneous intrusions and their emplacement. Following the ground-breaking research of Gilbert in the late 19th Century (Gilbert, 1877, 1896), a variety of studies have been carried out in the range (Hunt, 1953; Johnson & Pollard, 1973; Jackson & Pollard, 1988; Nelson & Davidson, 1993; Habert & de Saint Blanquat, 2004; Horsman et al., 2005; Morgan et al., 2008; de Saint-Blanquat et al., 2006; Wetmore et al., 2009; Wilson & McCaffrey, 2013).

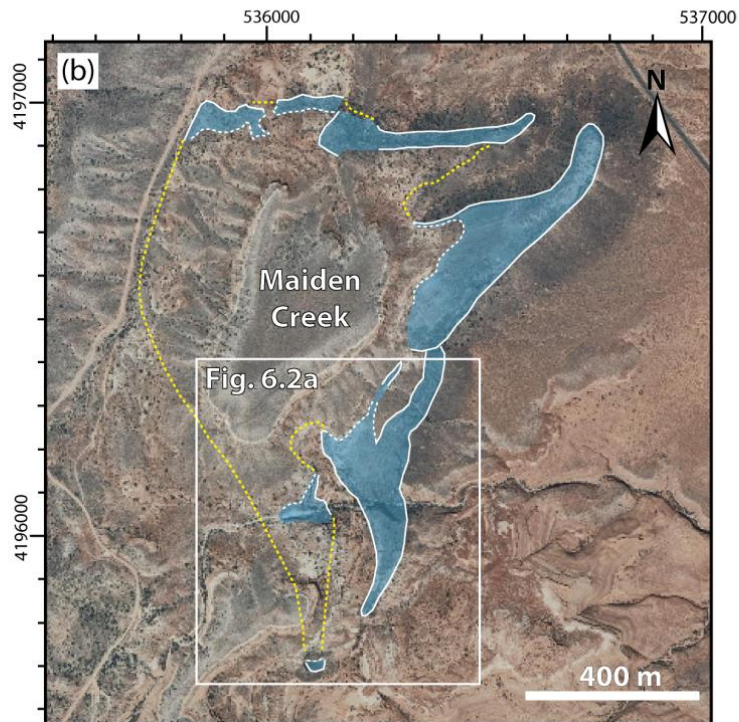
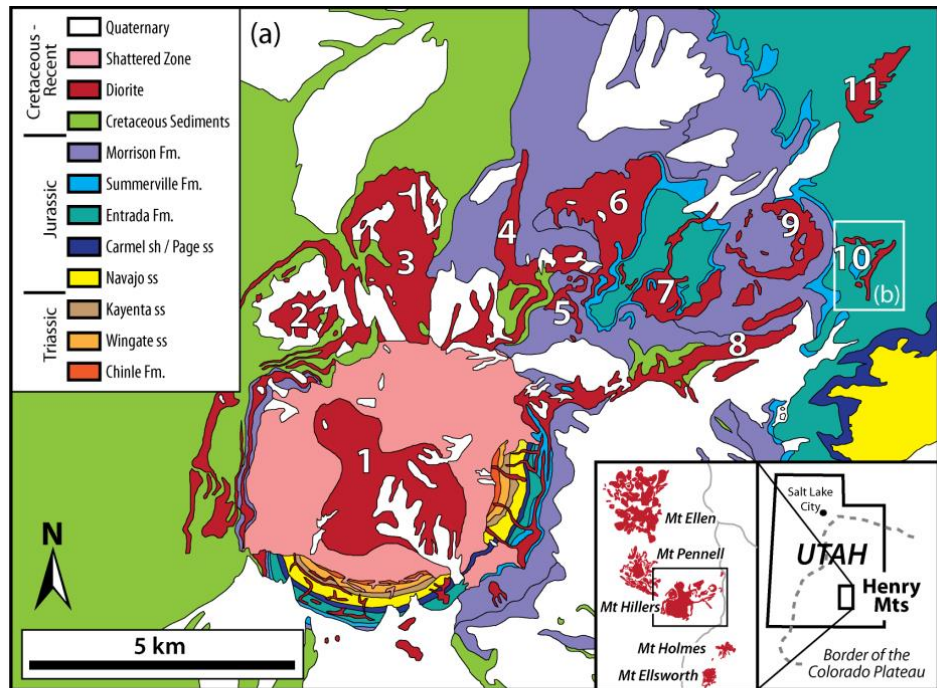


Figure 1. Maps of Henry Mountains and Mount Hillers intrusive complex. (a) Simplified geological map of Mount Hillers and its satellite intrusions (modified from Larson et al., 1985). Inset maps show the location of the Henry Mountains and its five principal peaks (Mts Ellen, Pennell, Hillers, Holmes and Ellsworth). (b) Aerial photograph of the Maiden Creek area. The extent of the igneous outcrop is shown in blue, while proposed sub-surface outline intrusion (Horsman et al., 2005) is depicted by the yellow-dashed lines. Numbers in (a) correspond to the intrusions that comprise the Mt Hillers intrusive complex. Using the names given in Hunt (1953), these are as follows: 1 – Mt Hillers central complex; 2 – Bulldog Peak intrusion; 3 – Stewart Ridge intrusion; 4 – Specks Ridge intrusion; 5 – Chaparral Hills Laccolith; 6 – Specks Canyon; 7 – speculated feeder system to the Trachyte Mesa intrusion (Hunt, 1953); 8 – Black Mesa intrusion; 9 – Sawtooth Ridge intrusion; 10 - Maiden Creek intrusion; and 11 – Trachyte Mesa intrusion.

Five principal peaks (from north to south: Mt Ellen; Mt Pennell; Mt Hillers; Mt Holmes; and Mt Ellsworth) make up the Henry Mountains, each peak corresponding to an intrusive centre (Fig. 6.1a). The igneous rocks are late-Palaeogene in age (Oligocene, 31.2 to 23.3 Ma K-Ar ages; Nelson et al., 1992), and most of the intrusions are of an intermediate, diorite composition (58–63% SiO₂; Hunt, 1953; Engel, 1959; Nelson et al., 1992). They have a porphyritic texture, with dominant feldspar (An₂₀ to An₆₀; 20–40%) and hornblende (5–15%) phenocrysts. Although broadly consistent in composition, the porphyritic textural characteristics vary significantly from one intrusion to another (Hunt, 1953; Nelson et al., 1992).

The intrusions were emplaced into a 3–6 km thick section of late Palaeozoic–Mesozoic sedimentary rocks overlying Precambrian crystalline basement (Jackson & Pollard, 1988; Hintze & Kowallis, 2009), and post-date minor Laramide orogenic activity (Late Cretaceous to Early Palaeogene in age; Davis, 1978; Davis, 1999) on the Colorado Plateau. Although Laramide structures are present locally (Davis, 1978; Jackson & Pollard, 1988; Bump & Davis, 2003), the strata into which the Henry Mountains intrusions are emplaced are nearly flat lying (Jackson & Pollard, 1988). Lack of significant pre- and post-emplacement tectonism aids the identification of both intrusion geometries and emplacement-related deformation structures. Furthermore, the original magmatic and solid-state fabrics within the intrusive bodies are unaffected by later deformation events.

6.2.2. Maiden Creek Intrusion

A number of small satellite intrusions flank the north and northeast margins of Mt Hillers (Fig. 6.1a). Due to their excellent exposures and 3D geometries, a number of these satellite intrusions have been studied, and are often referred to as classic examples of sill and laccolith intrusions (e.g. Gilbert, 1877; Hunt, 1953; Johnson & Pollard, 1973; Habert & de Saint Blanquat, 2004; Horsman et al., 2005; Morgan et al., 2005; de Saint-Blanquat et al., 2006; Morgan et al., 2008; Horsman et al., 2009; Wilson & McCaffrey, 2013). The Maiden Creek intrusion is one of the most distal satellite intrusions of the Mt Hillers complex, lying ~10 km NE from the main intrusive centre (Fig. 6.1a). Neighbouring satellite intrusions include Sawtooth Ridge, the Black Mesa bysmalith, and the Trachyte Mesa intrusions.

Maiden Creek is a small ($\sim 1 \text{ km}^2$ in map view; Fig. 6.1b), sub-horizontal intrusion and has been characterised as a sill in previous studies (Hunt, 1953; Johnson & Pollard, 1973; Horsman et al., 2005, 2009). It intrudes, and is concordant with, the Entrada Sandstone Formation of the Jurassic San Rafael Group (Gilbert, 1877; Hunt, 1953; Johnson & Pollard, 1973; Horsman et al., 2005). From the abundance of lateral contacts of the intrusion with surrounding host rocks, Horsman et al. (2005) inferred that the current map pattern corresponds closely to the original geometry of the intrusion. Horsman et al. (2005) suggested that the Maiden Creek intrusion is comprised of a main sill-like body (with a tabular geometry in 3D, elliptical in map view) with four finger-like lobes emanating from this central body: a pair of lobes trending roughly NE–SW in the north-east; and a second pair trending c. N–S to the south (Fig. 6.1b). Horsman et al. (2005, 2009) reported field observations of two vertically stacked bulbous terminations, along with a narrow band of solid-state fabrics within the intrusion, and further proposed that the intrusion consists of two vertically stacked sheets, the second sheet intruded above the first (i.e. over accretion; Menand, 2008) and with an almost identical thickness and extent to the first. It is the southern pair of intrusive lobes that forms the focus of the present paper (Fig. 6.2).

6.2.3. Host Rock - Entrada Sandstone Formation

The Entrada Sandstone is composed of white to red cross-bedded aeolian sandstone and red/ brown silty sandstone beds (Fig. 6.3a), interlayered with thin siltstone and shale beds (Fig. 6.3b; Aydin, 1978). Petrographical analysis of the Entrada Sandstone in the Maiden Creek area suggests that the sandstone is sub-arkosic (Fig. 6.3c–f) with dominant quartz grains (>90%) and minor feldspar (plagioclase and microcline) and lithic fragments ($\sim 5\text{--}10\%$). The average grain size of the quartz-dominated Entrada Sandstone is $\sim 0.15 \text{ mm}$ (Fig. 6.3c–f), although larger grain sizes are measured in some layers (Aydin, 1978). Undeformed Entrada Sandstone is highly porous, with porosities ranging between 15–35% (visually estimated using percentage estimation comparison charts of Tucker, 2001; Fig. 6.3c, d). Cementation is patchy ($\sim 3\text{--}5\%$ of the rock), with calcite spar being the most common cement (Fig. 6.3c, d), although Aydin (1978) also recorded siliceous and pelitic cements within some layers. The Entrada Sandstone, being highly porous, is the ideal lithology for the formation of compactional and cataclastic deformation bands (Fig. 6.3e, f; Aydin, 1978; Aydin & Johnson, 1978; Aydin & Johnson, 1983; Fossen et al., 2007), which may help to accommodate magma emplacement (Morgan et al., 2008).

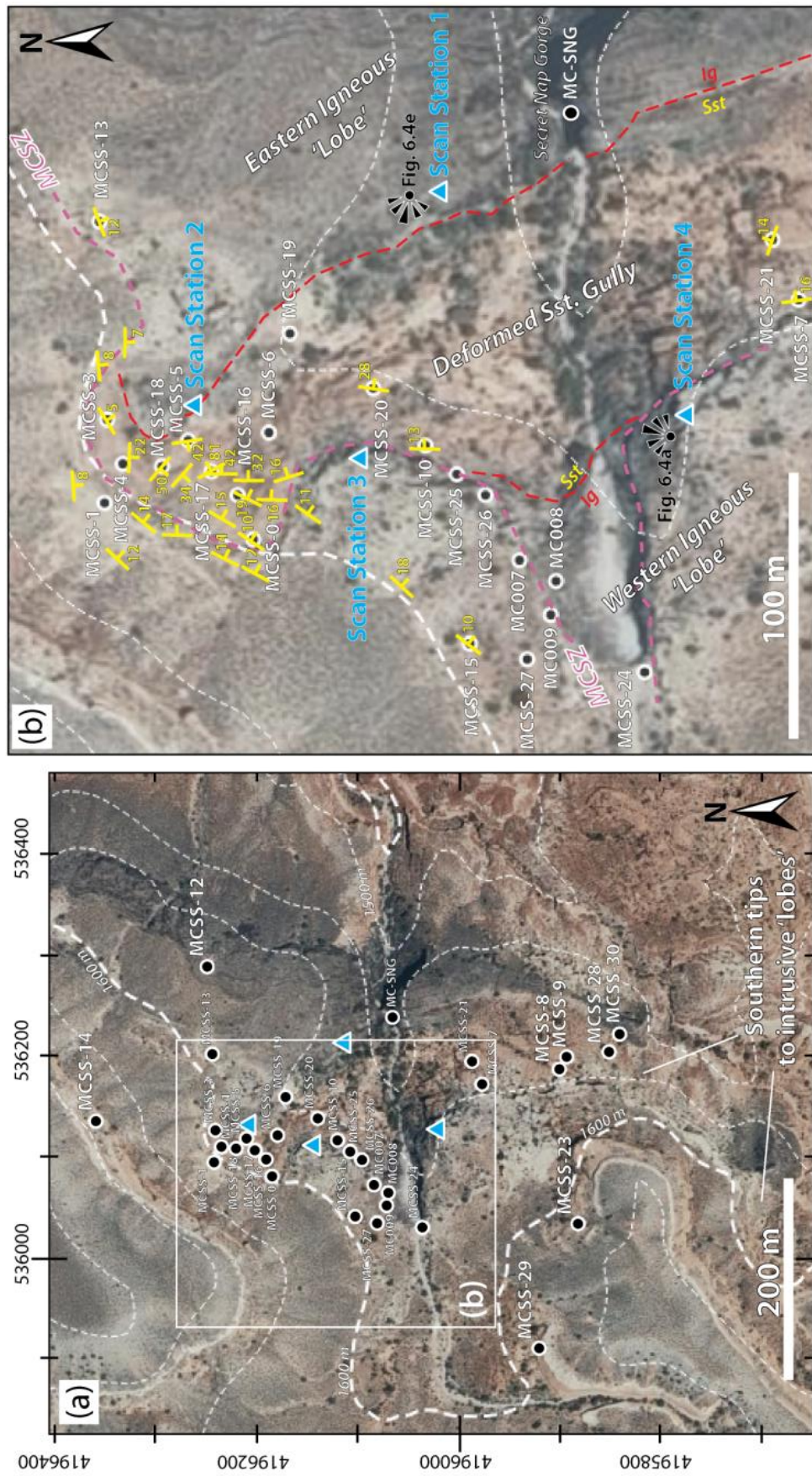


Figure 6.2. Maps of study area. (a) Aerial photograph of the study area around the two southern intrusive 'lobes' (area highlighted in Figure 1b). Topographic contours every 25 m, bold every 100 m. (b) Zoom-in on the northern section of the gully. Shear zone depicted by pink line; lateral intrusion contacts in red. Structural stations/ field localities referred to in text are shown by black circles with white outlines (see also Google Earth™ kmz file in Appendices); laser scan stations are shown by blue triangles; bedding measurements shown in yellow. Note viewpoint locations for panoramic photos in Fig 6.4.

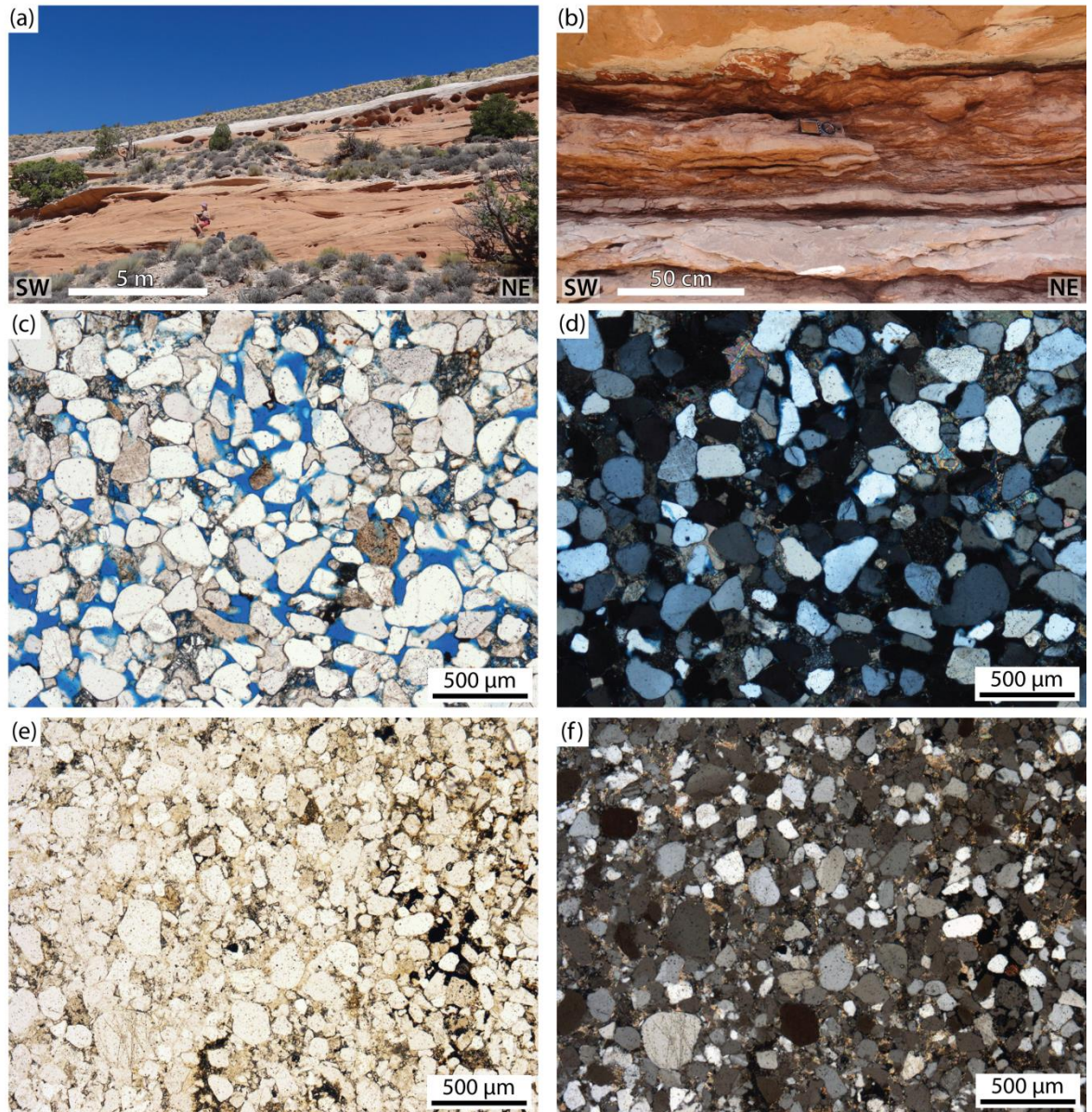


Figure 6.3 Entrada Sandstone Formation (host-rock). (a) Outcrop photograph showing white to red cross-bedded aeolian Entrada Sandstone around Maiden Creek. (b) Example of thin interlayered siltstone and shale beds (protolith to the MCSZ; see Section 6.7). (c)–(f) Photomicrographs of: (c) undeformed Entrada Sandstone showing significant porosity (blue dye) taken under plane polarised light (ppl); (d) same view as in (c) under cross-polarised light (xpl); (e) example of deformed Entrada Sandstone sampled ~1 m above the top surface of the Maiden Creek Intrusion (note grain size reduction due to cataclastic deformation and calcite cementation infilling pore space); and (f) same view as in (e) under cross-polarised light (xpl).

6.3. Digital Mapping and 3D Visualisation

Both the landscape (geomorphology) and intrusion–host rock geometries in the southern Maiden Creek study area are highly complex and difficult to visualise through description alone. In addition, it is also difficult to capture the 3D geometry, structural complexity and spatial distribution of the geological framework and deformation using conventional mapping methods. Digital mapping methods have the functionality to overcome this, and

aid the integration of spatially accurate, multiple datasets and data types. FieldMove™ has proven useful in this study when collecting relatively simple locality data (e.g. lithology, bedding; Fig. 6.2). Although Google Earth™ does not currently have in-built field mapping functionality, it has worked well as a quick reference tool for both visualisation and shared learning (see the kmz file in the Appendices for location of structural stations discussed in this study). Terrestrial Laser Scanning (TLS), although time-consuming at all stages (i.e. acquisition, processing and interpretation), has proved to be a valuable tool in order to build a 3D structural framework as well as providing an excellent virtual image of the outcrop (Figs 6.4c, d & 6.5).

TLS was carried at four Scan Stations (Fig. 6.2b) using a Leica ScanStation C10, in combination with an AshTech Pro 3 DGPS (Fig. 6.4a, e), in order to acquire regional (360° panorama) and high resolution laser scans of the southern Maiden Creek study area (Fig. 6.5). Structural interpretation of the laser scan data was then implemented using both RiSCAN PRO™ and GoCAD™ software to create a 3D geological framework model of emplacement-related deformation structures (Figs 6.4c, d & 6.5;). As well as capturing the overall geometry of exposed intrusion (Fig. 6.4) TLS has also helped to capture fracture and bedding geometries from inaccessible outcrops. Laser scan data provide unprecedented detail and allows spatial variation of fracture attributes to be quantified (e.g. fracture geometry, connectivity, and spatial correlation; see Section 6.5.3.1).

Figure 6.4c, d utilises the digital point cloud captured using TLS to map out the outcrop extent of igneous rock within the study area, while Figure 6.5e shows the detailed interpretations that may be achieved in areas of high resolution scans.

6.4. Intrusion–Host Rock Geometries in Study Area

Figure 6.1b shows the extent of the igneous outcrop in the southern Maiden Creek intrusion study area. The geomorphology of the area is dominated by a roughly N–S trending gully (Rattlesnake Gully; Figs 6.2 & 6.4), bound on either side by outcrops of igneous rock and steeply dipping sandstones (Fig. 6.4). Cropping out to the east is a continuous elongate, roughly N–S trending, 400 m long ridge of igneous rock (Figs 6.1b, 6.4 & 6.6a). From this elongate outcrop morphology, Horsman et al. (2005) described the igneous ridge as a finger-like lobe, which is referred to in this study as the eastern ‘lobe’.

This eastern lobe can be seen at the head of the gully (Figs 6.4 & 6.5) and appears to be thicker in the north (~35 m), thinning towards its southern tip (<10 m).

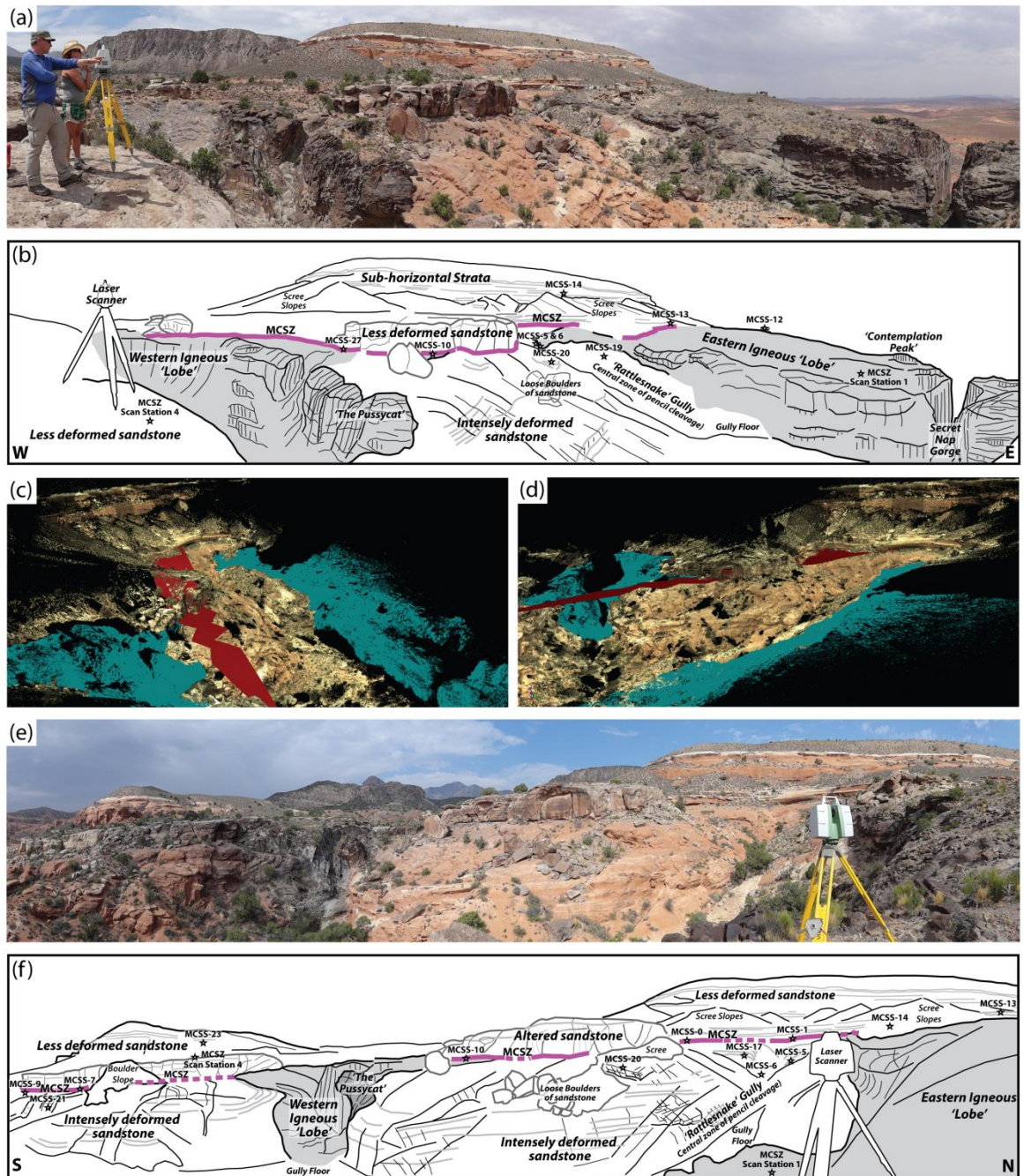


Figure 6.4 Panoramic photographs, annotated sketches and laser scan models showing outcrop geometries of the study area. (a)–(b) view from scan station 4, looking north; (c)–(d) screen captures from 3D laser scan models (in RiSCAN PRO) showing extent of igneous outcrop (teal colour) and extrapolated surface of MCSZ. Orientations roughly correspond to panoramic photo views in (a) and (e). (e)–(f) view from scan station 1, looking west (see Fig. 6.2b for photograph and scan station locations).

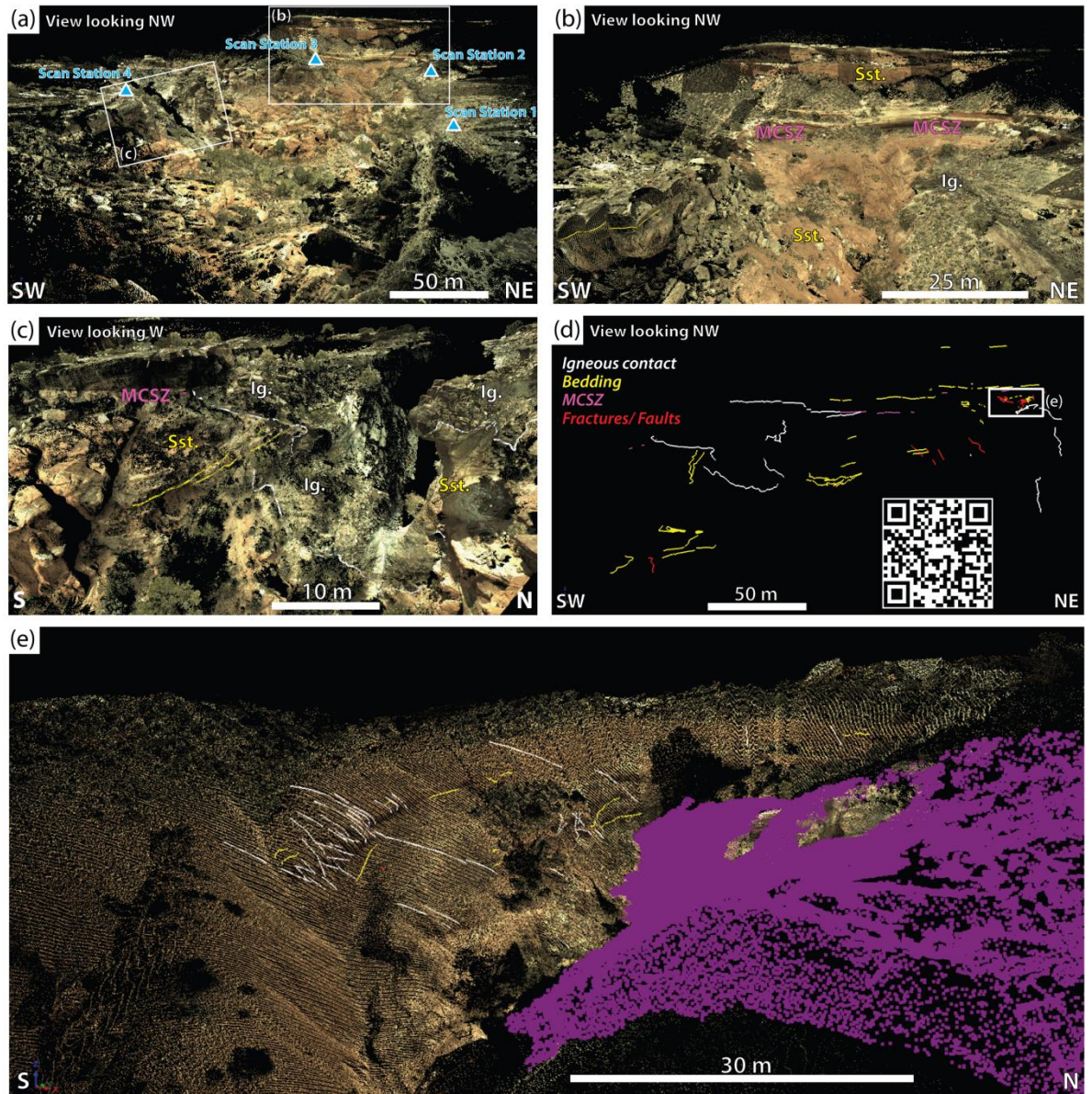


Figure 6.5 Examples of laser scan images and 3D modelling to map and visualise structural geometries in 3D. (a) Screen capture of RiSCAN PRO™ project of laser scan point cloud data across the study area. Compare image to panoramic photo in Fig. 6.4e. Scan stations highlighted in blue. (b) Zoom in of structurally complex zone in northern Rattlesnake Gully where MCSZ separates low-/moderately-deformed sandstones above from highly deformed sandstones below and between two igneous lobes, area highlighted in (a). See photo Fig. 6.8c for comparison. (c) Zoom in of folded sandstone units around irregular lateral margin of igneous lobe, and neighbouring Pussycat outcrop, area highlighted in (a). See photo Fig. 6.6b for comparison. (d) Line interpretation of laser scan point cloud data (same view as (a)). QR code is a link to an online fly through video (<https://www.youtube.com/watch?v=XnSJsytT-2Y>). (e) Example of interpreted laser scan point cloud of deformed sandstones adjacent to eastern igneous lobe at the head of Rattlesnake Gully, viewed in RiSCAN PRO™ (intrusion outcrop extent highlighted in purple).

Igneous outcrops are also observed along the western flank of Rattlesnake Gully (Fig. 6.1b & 6.4), although the continuous nature of these outcrops is less certain. Again, following

the terminology of Horsman et al. (2005), these outcrops are termed the western ‘lobe’ in this study. An E–W trending geomorphological incision formed by flash flooding provides excellent 3D exposure through both the eastern and western intrusive bodies. The incision cutting the eastern lobe is known locally as Secret Nap Gorge (Figs 6.2b & 6.4a, b; see Google Earth™ kmz file in Appendices for locations), while the incision cutting the western intrusive body has formed an amphitheatre dominated by a by a pillar-like outcrop known as ‘The Pussycat’ (Figs 6.4, 6.5c & 6.6b). Within this amphitheatre, the geometry of the eastern margin of the western lobe is well defined. Here the intrusion top surface is relatively flat-lying (Fig. 6.6b–d). The lateral contact in this area, shows a distinct angular hour-glass geometry (Fig. 6.6b), with upper and lower portions of the intrusion protruding further into the adjacent host rock than the middle portion of the intrusion. This also helps to form the geometry of The Pussycat. A distinct structural zonation is also apparent in the cliff face within the amphitheatre: sub-horizontal faults and fractures dominating the upper 5 m of the intrusion; and sub-vertical fractures predominating beneath (Fig. 6.6d).

The basal (lower) intrusion–host rock contact is not observed in Rattlesnake Gully (Fig. 6.4). However, a sub-horizontal, lower basal contact is exposed on the outer eastern margin of the eastern lobe.

Figure 6.6. *(overleaf)*

Intrusion outcrop geometries and fabrics. (a) view looking south along the eastern igneous lobe (Secret Nap Gorge in foreground). (b) view looking west, from same location as (a), showing irregular eastern margin of the Western intrusive body. Note similarity in shape of the Pussycat outcrop with the intrusion geometry in the rock face to the left (also compare to Fig, 5c for to see quality and resolution of laser scan data). (c) View looking north showing the MCSZ sitting on the top surface of the two intrusive ‘lobes’. (d) Structural zonation to the western lobe resulting from sub-horizontal/ low-faults and fractures related to the MCSZ in the uppermost few metres of the western lobe and sub-vertical fractures (cooling joints?) below these. (e) Photomicrograph (at 5x magnification) of an undeformed intrusion (intermediate plagioclase-hornblende porphyry) sample collected from the Maiden Creek study area. Note, large (0.5-5 mm) euhedral zoned plagioclase (Plg.) and smaller (0.1-0.5 mm) hornblende (Hbl.) phenocrysts in a fine crystalline matrix. (f) Photomicrograph (at 10x magnification) of zoned hornblende (Hbl.) phenocrysts. (g) Outcrop example of freshly exposed intrusion surface showing undeformed porphyritic texture ~10cm below intrusion top surface (note, compass-clinometer is resting on chilled intrusion top surface). Sample shown in (e) is from an equivalent outcrop to this. (h) zoom in photograph of area outlined in (g) showing localised shear deformation on planes sub-parallel to intrusion top surface.

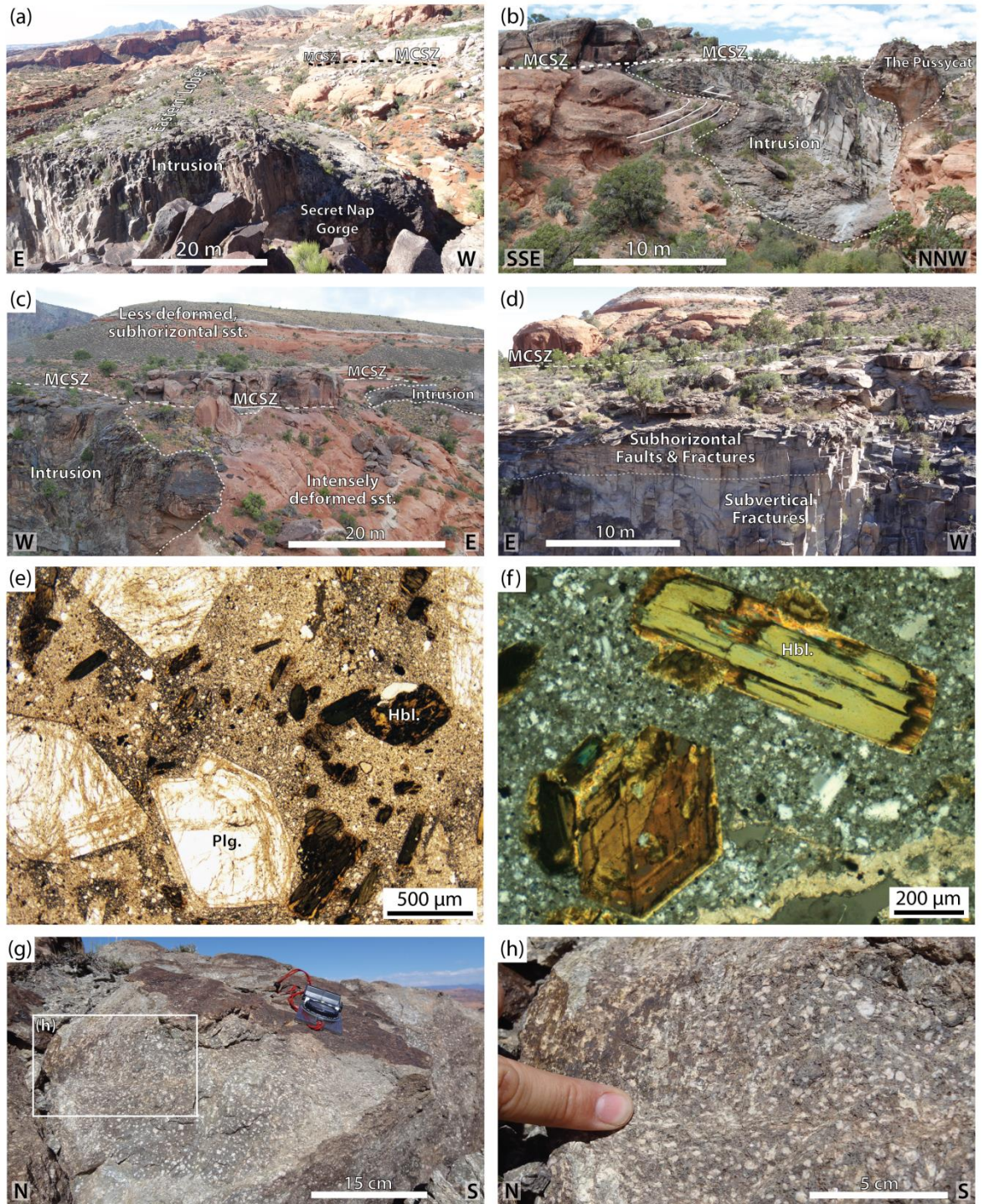


Fig. 6.6

Petrographic analyses of igneous samples collected at Maiden Creek show that the intrusion has a porphyritic texture dominated by zoned plagioclase feldspars and hornblendes within a fine-grained matrix (Fig. 6.6e, f, g). Although, the sample shown in Fig. 6.6e, f was collected from close to the intrusion top surface (<1 m; Fig 6.6g) of the western ‘lobe’ internal deformation appears to be minimal, with euhedral phenocrysts preserving crystallisation textures (e.g. twinning in the plagioclases, and cleavage in the

hornblendes; Fig. 6.6e, f). Deformation in this upper zone appears localised to discrete shear planes (Fig. 6.6h). In these shear planes, stretching of feldspars are apparent.

Aerial photographs of the field area show that the intrusion margins have a curved geometry bowing outwards to the east (Figs 6.1b & 6.2). The arcuate geometry of Rattlesnake Gully is defined by the curved geometries of the two intrusive lobes and their margins. Sandstones in the gully appear highly deformed (Figs 6.4 & 6.6c). This contrasts sharply with the exposures in the same sandstone units in the hillsides above (Figs 6.4 & 6.6c), and those at the same stratigraphic level outside the gully and adjacent to the outer margin of the intrusion, which show only minor deformation. Detailed geological and structural mapping shows that a sub-horizontal detachment surface, the Maiden Creek Shear Zone (MCSZ), separates these two zones (Figs 6.4 & 6.6b, c). The bedding in the low- to moderately-deformed overburden above MCSZ is shallowly dipping ($\sim 10^\circ$) to the SE (Fig 6.7a), striking parallel to the largest intrusive lobe of the Maiden Creek intrusion in the NE (Fig. 6.1b), as well as the dominant trend of the Sawtooth Ridge intrusion to the SW (Fig. 6.1a). In comparison, there is a greater spread of measurements for bedding in the sandstone gully below MCSZ and between the two intrusive lobes. Bedding appears to be flexed by the two intrusive lobes, dipping into the gully, creating a synclinal fold structure with convex limbs (fold axis trending c. SSE–NNW; Fig. 6.7c & 6.8).

Figure 6.7 (*overleaf*)

Summary stereoplots of field structural data. Equal area, lower hemisphere stereoplots of data showing poles to planes (contoured) sorted by spatial location with respect to the MCSZ. (a) bedding and deformation structures in sandstone above the MCSZ. (b) deformation structures within the MCSZ and on the top surface of the igneous lobes (mineral stretching lineations shown in rose diagram plot; radial marks depict 5% intervals of total percentage of measurements). (c) bedding and deformation structures in the sandstone gully below the MCSZ and between the southern igneous lobes. Mean planes for distinct cluster populations are shown for each plot. Fault and shear zone plots also show fault slip lines with movement direction indicated (red solid fill = normal fault slip; white fill = reverse slip).

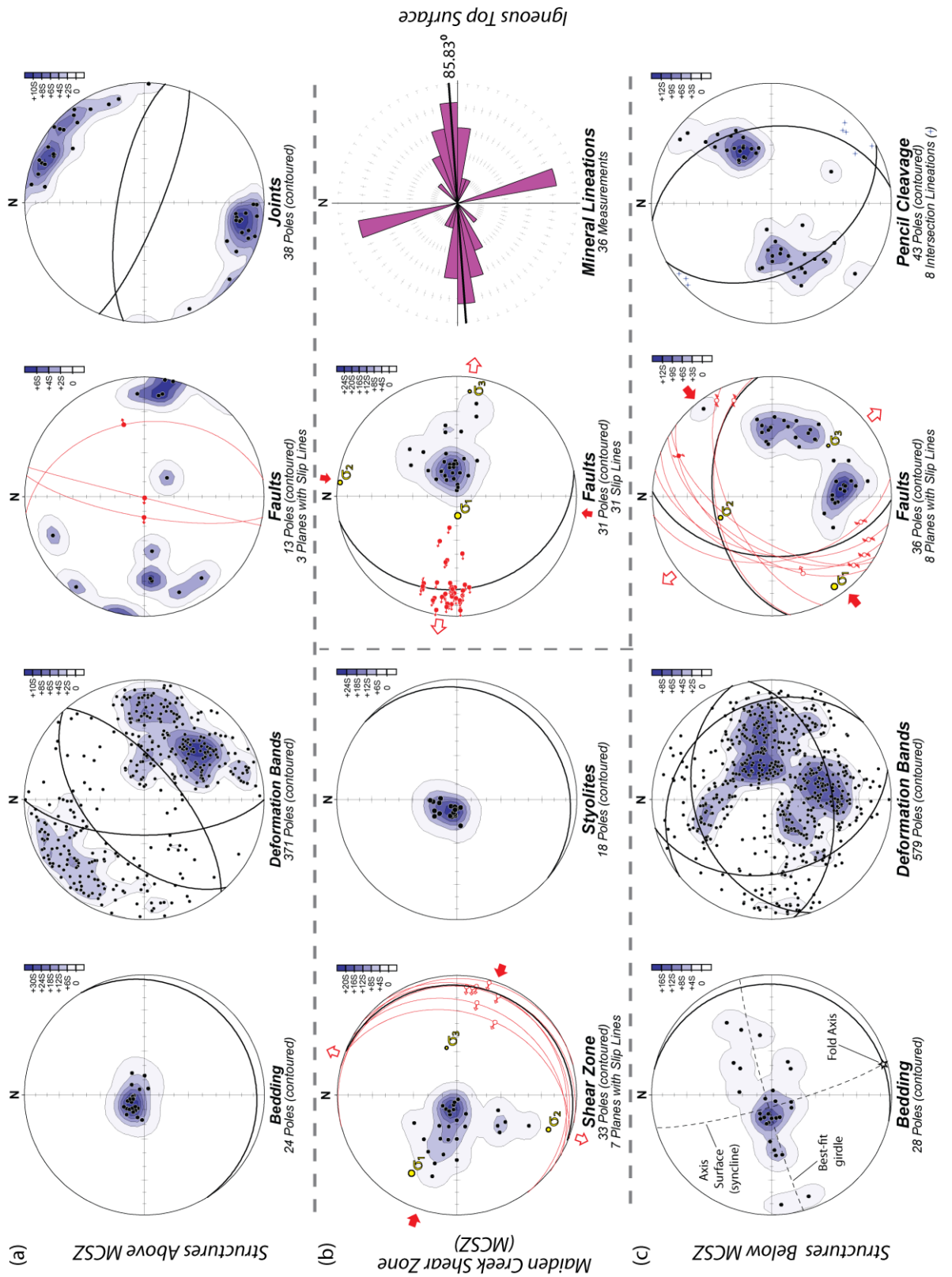


Fig. 6.7

6.5. Intrusion Related Deformation Structures

Deformation structures observed in the intrusion host rocks include deformation bands, faults, tensile joints, stylolites, and pencil cleavage (Fig. 6.7). Deformation structures and styles vary within host rocks above the MCSZ detachment surface, to those below MCSZ

within Rattlesnake Gully. For ease of description in the following section, deformation structures will be systematically described by zone and as depicted in Figure 6.7).

6.5.1. Deformation Structures Above the MCSZ

6.5.1.1. Deformation Bands

The sub-horizontal sandstone beds (Fig. 6.7a) above MCSZ show low- to moderate-deformation (Fig. 6.8a, b). Deformation bands (Figs 6.7a & 6.8b), characterised by narrow (mm-scale) zones of cataclasis, calcite cementation and resulting collapse of porosity (Fig. 6.3e, f), can be found throughout the Entrada Sandstone above the MCSZ. The spacing of these fractures is on a decimetre to metre-scale, i.e. low- to moderate-deformation (Figs 6.8b). These deformation bands show dominant normal (extensional), centimetre- to decimetre-scale offsets on bedding and cross-beds (Fig. 6.8b). These deformation bands appear to exhibit a polymodal fault pattern (e.g. Reches, 1987; Krantz, 1989) with a dominant NE–SW trend (Fig. 6.7a). Note, this NE–SW trend parallels the trend of the largest intrusive lobe of the Maiden Creek intrusion (Fig. 6.1b), as well as the dominant trend of the Sawtooth Ridge intrusion to the SW (Number 8 on Fig. 6.1a).

6.5.1.2. Faults

Some deformation bands exhibit clear slip surfaces (i.e. principal slip surfaces) from which slip sense can be determined. For the purposes of this study we have classified these as faults (Fig. 6.7a). In the sandstones above the MCSZ these faults dominantly trend N–S and show dip-slip normal slip (i.e. E–W extension; Figs 6.7a & 6.8b) with displacements of beds and cross-beds in the order of decimetres to metres.

6.5.1.3. Joints

A conjugate set of steeply-dipping tensile (Mode 1) joints trend WNW–ESE, and are oriented roughly perpendicular to the polymodal deformation bands (Fig. 6.7a). These joints are commonly found in sandstone outcrops located vertically above the intrusive lobes with a decimetre- to metre-scale spacing (e.g. Structural Station MCSS-13).

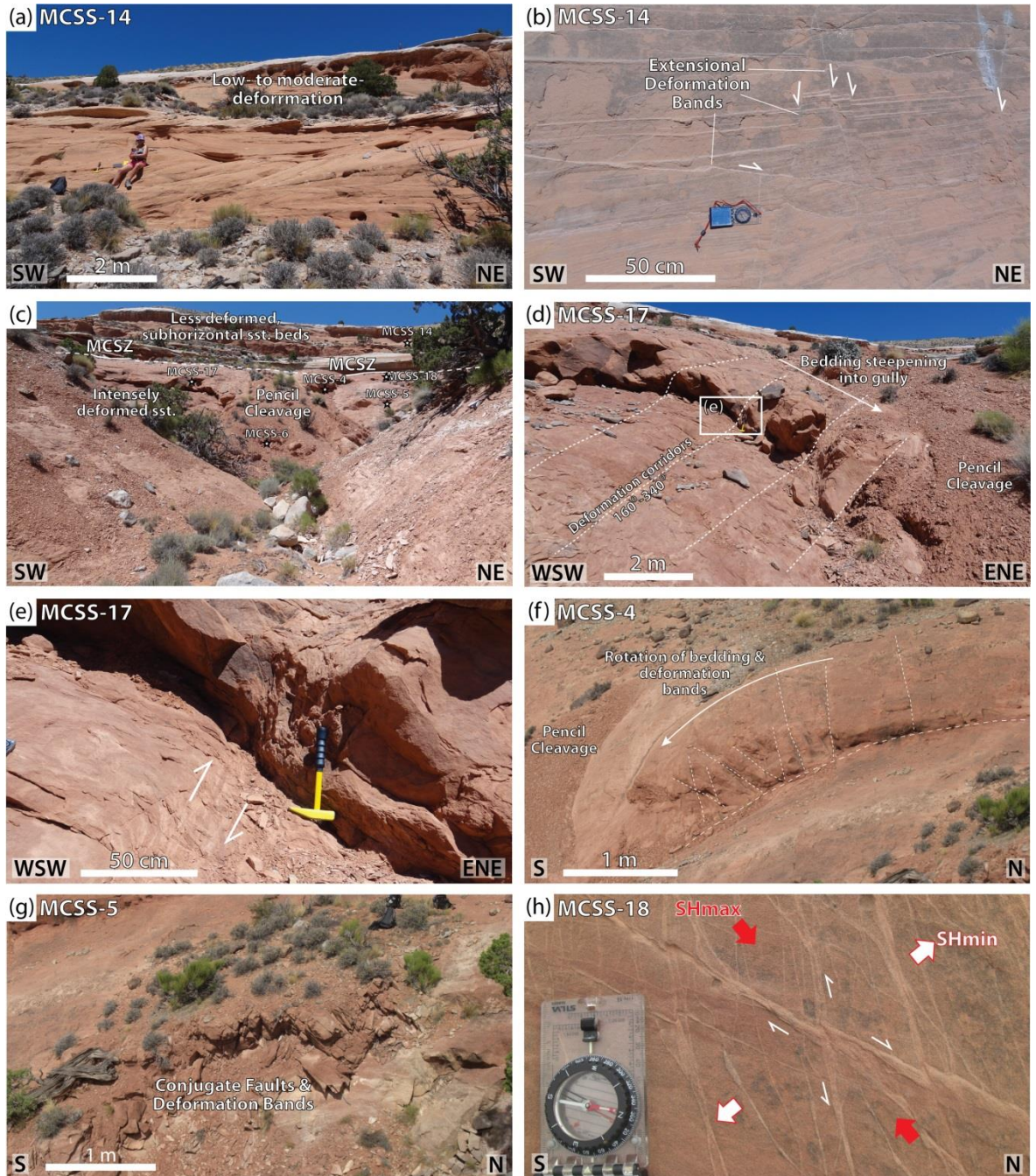


Figure 6.8. Field photographs showing deformation structures in the host-rock sandstones above and below the MCSZ. (a) low- to moderate-deformation in sandstone beds ~50 m above the MCSZ. (b) zoom in of sandstone in (a) showing extensional offsets on bedding along deformation bands. (c) head of the sandstone gully, view looking NW, showing low- to moderately-deformed sub-horizontal sandstone beds above the MCSZ, with intensely deformed and folded sandstone beds below. (d) 'kink-band' geometry to deformed sandstone beds flanking the western intrusive 'lobe' and increasing deformation banding with steepening of bedding into the gully and central zone of pencil cleavage. (e) zoom in of (d) showing 'kink-band' geometry as the folded beds pass through a vertical deformation corridor. (f) rotation of deformation banding about a horizontal axis corresponding to monoclinial folding (N.B. the lack of 'kink-banding' observed for the western 'limb') of beds flanking the eastern intrusive 'lobe'. (g) conjugate strike-slip faults and deformation bands. (h) deformation banding displaying strike-slip offsets on other deformation bands.

6.5.2. Deformation Structures Below the MCSZ

As described above, sandstone bedding within Rattlesnake Gully is folded to form a synclinal fold structure with convex limbs (i.e. steepening towards the axis) and a fold axis trending c. SSE–NNW along the centre of the gully axis (Figs 6.7c & 6.8c–g). Deformation structures within this zone include: intense (cm- to mm-spacing) deformation banding; conjugate strike-slip faulting; and pencil cleavage (Figs 6.7c & 6.8c–h).

6.5.2.1. Deformation Bands

Porosity-reducing deformation bands are prolific beneath the MCSZ in the sandstone gully. These deformation bands occur with centimetre-scale spacing immediately below the MCSZ, increasing in intensity (mm-spacing) towards the centre of the gully. In contrast to the deformation bands found above the MCSZ, those beneath show dominantly strike-slip and reverse (compressional) offsets (cm- to dm-spacing) on bedding (Fig. 6.8e, h). Although the orientation of deformation bands varies spatially (see section 6.6), two distinct trends are apparent: c. SSE–NNW; and c. ENE–WSW (Fig. 6.7c).

Sandstone beds flanking the western lobe show a stepped (kink band) geometry as they steepen into the centre of the gully (MCSS-17; Fig. 6.8c–e). This occurs due to the presence of several vertical deformation corridors (stepped ladder zones) trending c. NW–SE (Fig. 6.8d). This stepped geometry is less apparent on the beds flanking the eastern lobe. Instead, a clear rotation of deformation structures into the gully is associated with the steepening of the beds (MCSS-4; Fig. 6.8f).

6.5.2.2. Pencil Cleavage

As intensity of deformation increases towards the centre of Rattlesnake Gully, deformation bands start to take on a character more akin to a cleavage plane (i.e. discrete fractures planes rather than narrow zones of deformation). Two distinct conjugate cleavage planes are apparent, trending SSE–NNW, parallel to the gully axis (Fig. 6.7c). The centre of the gully is characterised by the development of a zone of pencil cleavage (MCSS-6; Fig. 6.8c); the result of mm-scale cleavage/ fracture spacing. Pencil cleavage intersections plunge shallowly to the SSE, and parallel the synclinal fold axis

within the gully (Fig. 6.7c). In this zone of pencil cleavage, bedding has been obliterated by the intense deformation.

6.5.2.3. *Strike-slip Faults*

Numerous fault planes (fractures and deformation bands with clear kinematic indicators) are observed in the sandstones flanking the eastern lobe (MCSS-5; Fig. 6.8g). These faults form a conjugate system with two dominant trends, NNE–SSW and ENE–WSW (Figs 6.7c & 6.7g, h). They show strike-slip kinematics (from slickenlines and cm-scale offsets on deformation bands and cross-beds) indicating a NE–SW shortening and SE–NW extension (Figs 6.7c & 6.8g, h). These faults can also be seen continuing from the sandstone into the intrusion (Fig.6.9).

6.5.3. *Deformation Structures at the Intrusion–Sandstone Contact*

Deformation structure types observed at the intrusion–sandstone contact include: strike-slip faults; stretched mineral lineations; low-angle faults; and stylolites. These structures have different spatial distributions relative to the nature (i.e. top surface versus lateral margin) of the intrusion–sandstone contact.

6.5.3.1. *Lateral Margin*

The western lateral margin of the eastern lobe (i.e. within Rattlesnake Gully) is relatively simple with sandstone flexed and truncated by a steep intrusion margin. Through detailed outcrop studies at Structural Station MCSS-5 (Fig. 6.2b; see Google Earth™ kmz file in Appendices for locations of structural stations) faults can be seen continuing from the sandstone into the neighbouring intrusion (Fig. 6.9c, d). Conjugate faults trending parallel to those in the neighbouring sandstone appear to control the geometry of the intrusion–host rock contact, forming an angular (or jagged) intrusion margin (Fig. 6.9c, d). These fault surfaces preserve excellent sub-horizontal, strike-slip, slickenlines (Fig. 6.9e, f) and also show possible evidence for pseudotachylite on fault surfaces at the intrusion–sandstone contact (Fig. 6.9f), while within the intrusion minerals appear to align parallel to the fault planes (Fig. 6.9d).

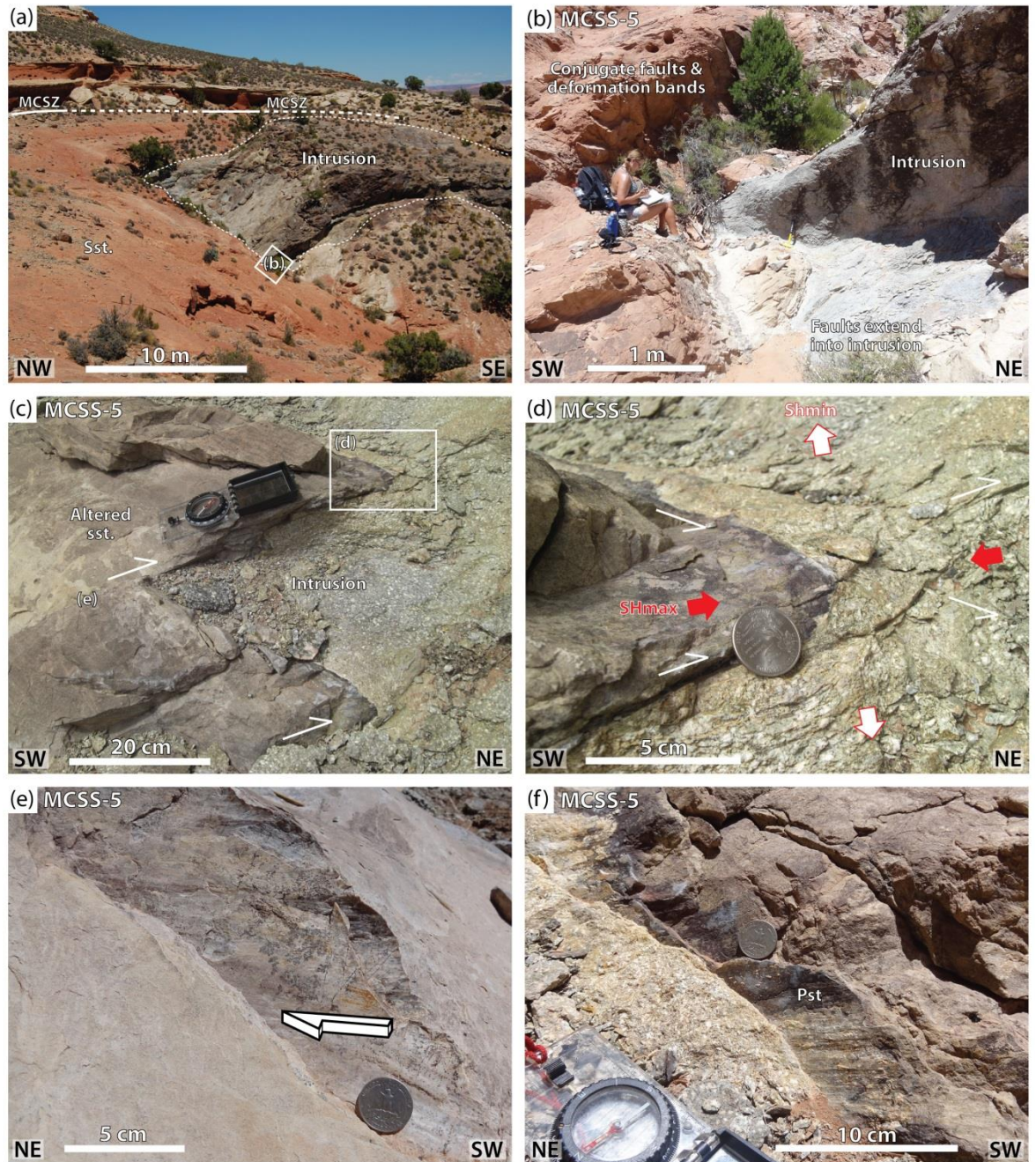


Figure 6.9. Field photographs showing deformation structures at the intrusion-sandstone contact. (a) intrusion-host rock contact along the western margin of the eastern lobe at the head of the gully; (b) conjugate strike-slip faults in the sandstones adjacent to the eastern lobe, extending into the intrusion; (c) stepped (jagged) intrusion-host rock contact controlled by syn-emplacement strike-slip faulting; (d) zoom in of (c) showing conjugate fractures in both intrusion and host rock. Note also the rounded tip to the sandstone protrusion with aligned elongate crystals in the neighbouring intrusive rock mimicking the contact geometry, highlighting that structures are syn-emplacement as they were active while magma was still able to behave in a ductile phase. (e) slickenlines indicating strike-slip movement along a fault plane within altered sandstone adjacent to the eastern lobe; and (f) Pseudotachylite(?) along a strike-slip fault surface within the intrusion.

Along the eastern margin of the western lobe (within Rattlesnake Gully) a similarly complex intrusion margin geometry is observed (Figs 6.6b & 6.10). Below ‘the Pussycat’ outcrop, faults within the sandstone can be observed dipping parallel to the intrusion contact (Fig. 6.10). These faults appear to show reverse shear from apparent offsets and sigmoidal shear fabrics (Fig. 6.10c). Due to accessibility issues at this outcrop, TLS was utilised to capture fault geometries (Fig. 6.10b). Fault planes were constructed in GoCAD™ (Fig. 6.10d) from interpreted polylines (RiSCAN™). A set of shallowly-dipping conjugate faults were identified (Fig. 6.10d, e), trending SSE–NNW, consistent with fault geometries at neighbouring outcrops measured in the field.

6.5.3.2. *Deformation on Intrusion Top Surface*

6.5.3.2.1. *Stretched Mineral Lineations*

At MCSS-10 (Fig. 6.2b; Google Earth™ kmz file in Appendices), below the shear zone, a dominant E–W trending linear fabric (086°–266°; Rose diagram in Fig. 4b & Fig. 10d) from aligned, stretched plagioclase phenocrysts can be observed on the top surface of both the eastern and western intrusive lobes (Fig. 6.7b & 6.11a, b). Two trends are observed (Fig. 6.7b): a dominant *c.* E–W trend, observed at multiple locations on both intrusive lobe top surfaces; and a weaker *c.* N–S trend. Stretched plagioclase phenocrysts can also be observed within shear bands in the uppermost metre of the intrusion (Fig. 6.6h)

6.5.3.2.2. *Low-angle Faults*

Low angle fault planes bisect the upper few metres of the western intrusive lobe (Figs 6.6d, 6.7b & 6.11c). These fault planes trend parallel to the *c.* N–S trend of the intrusion margin, and dip shallowly (~20°) to the west (Fig. 6.7). Slickenlines and lunate fractures on the slip surfaces indicate top-to-the-west kinematics (i.e. normal movement; structural stations MCSS-27, MC008 & MC009; Figs 6.2b, 6.7b & 6.11c). At structural stations MC009 and MCSS-27 (Fig. 6.2b), similar low-angle fault planes can be seen within altered sandstones directly on top of the intrusion (Fig. 6.11d). These low-angle faults within the sandstone exhibit a soft, white precipitate along fault surfaces, suggesting that they likely acted as a fluid conduit during alteration of the sandstone.

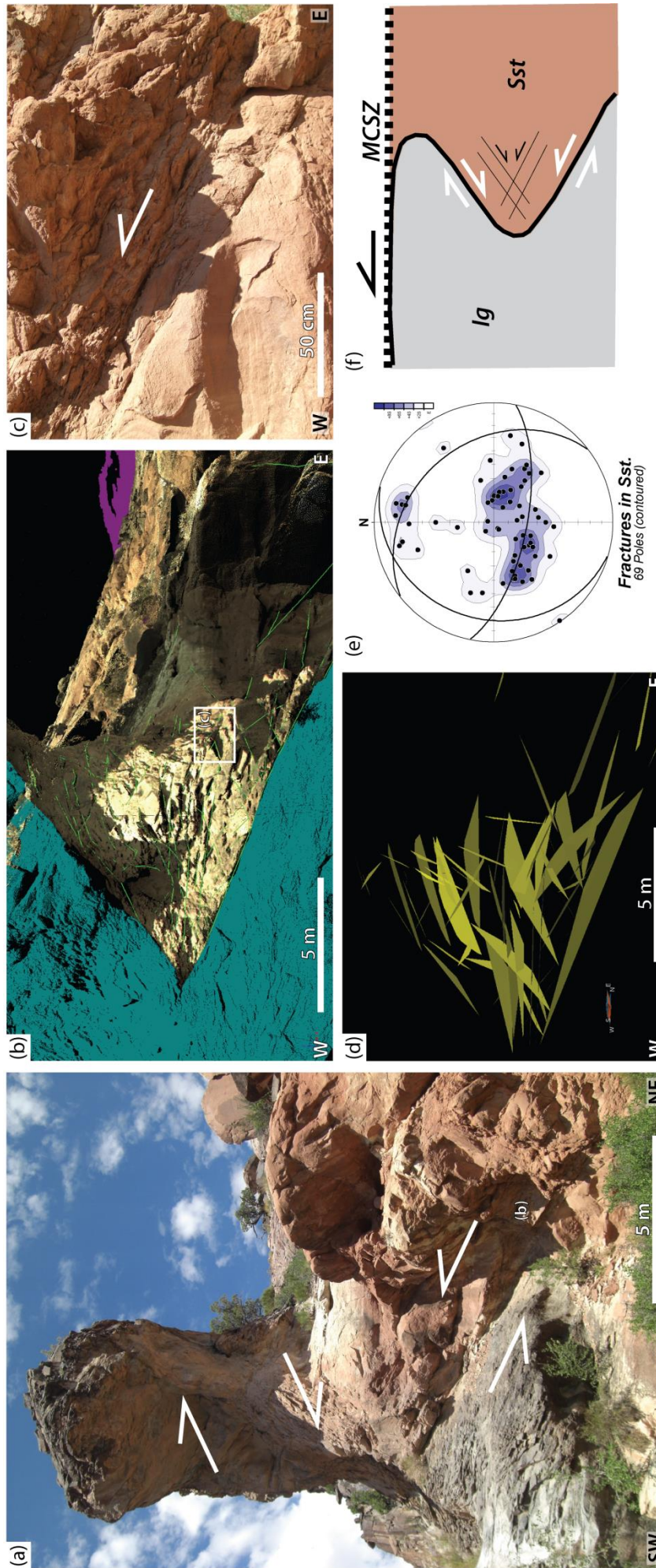


Figure 6.10. Pussycat outcrop geometry and deformation kinematics. (a) Outcrop photograph of the Pussycat, viewed from below (in Rattlesnake Gully). Note intrusion–sandstone contact geometry depicted by shear arrows. (b) High resolution laser scan image of the igneous sandstone contact area in the Pussycat (igneous outcrop extent highlighted by teal coloured point cloud, sandstone coloured by outcrop colouring, and picked faults and fractures depicted by green lines). (c) Outcrop photo showing faults and fractures cutting sandstones below the Pussycat, location highlighted in (b). East-dipping faults show reverse kinematics. (d) As access to the outcrop is difficult, fault planes were extrapolated from picked fault lines, shown in (b), to form 3D surfaces from which strike and dip values were extracted. (e) Equal area, lower hemisphere stereonet showing poles to planes (contoured) for fault planes derived from 3D laser scan analysis (d). Fault trends closely resemble those mapped nearby, although dips are significantly shallower. This is consistent with visual interpretations for this outcrop made in the field. (f) Schematic cartoon depicting the observed intrusion–host rock geometries observed at the Pussycat and the associated deformation structures in the neighbouring sandstone units.

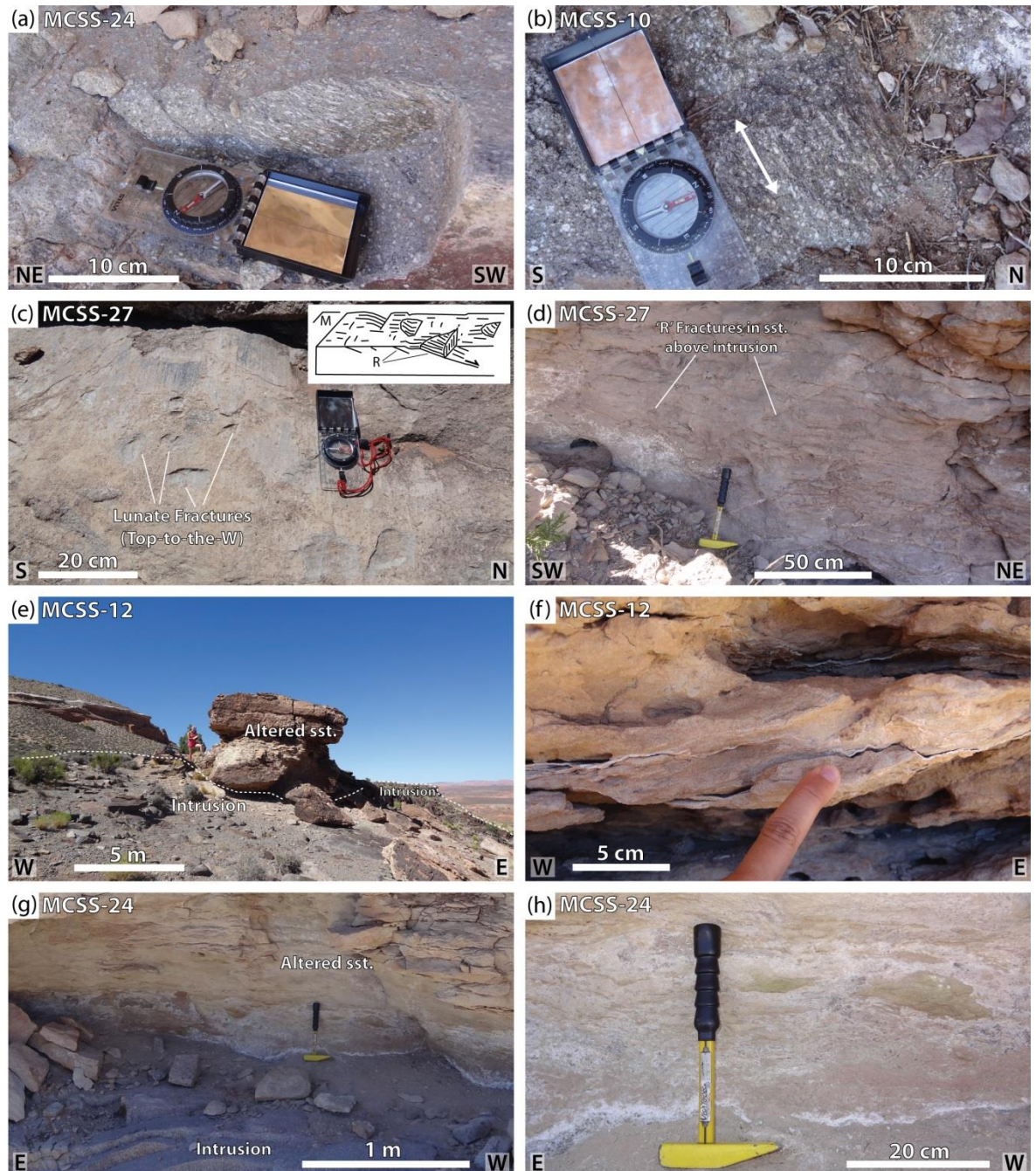


Figure 6.11. Field photographs showing deformation structures on the top surface of intrusion. (a) Stretched plagioclase phenocrysts in upper 5 cm of intrusion to surface. (b) Dominant E-W fabrics of stretched plagioclase lineations on the top surface of the western intrusion, immediately below the MCSZ. (c) Low-angle faults and lunate fractures (R1 faults; inset image from Petit, 1987) indicating top-to-the-WNW movement on the intrusion top surface (structural station MCSS-27). (d) Low-angle faults and fractures and sub-horizontal stylolites in altered sandstone above intrusion; geometry and kinematics of faults matching those cutting intrusive rocks on the intrusion top surface (c). (e) small outcrop of thermally and chemically altered sandstone above the eastern lobe. (f) zoom in of stylolites in the altered sandstone outcrop shown in (e). (g) Altered sandstones with stylolites and vein-filled fractures above western lobe (~30 m west of lateral margin), MCSZ not clearly identifiable. (h) zoom in photo of altered sandstones. Note nodular alteration zones and evidence for thermal fluid alteration.

6.5.3.2.3. *Styolites*

Styolites (serrated surfaces formed by the removal of material by dissolution) are observed within ~5 m thick horizons of altered sandstone located above the intrusive lobes (including structural stations MCSS-24, MCSS-27 and MCSS-12; Figs 6.2b, 6.7b & 6.11e–h). These Styolites occur on a decimetre- to metre-scale and are relatively simple in character, forming a wave-like surface (Fig. 6.11f). The styolites trend roughly NE–SW, dipping shallowly to the SE (Fig. 6.7b), and are oriented parallel to both the sandstone beds in which they are found, and the underlying intrusion top surface (Fig. 6.7a, b).

6.6. Spatial Distribution of Deformation Structures

The deformed sandstones in Rattlesnake Gully (i.e. between the two intrusive lobes) display considerable structural complexity and asymmetry. Deformation structures and geometries vary across and along the strike of the gully (Fig. 6.12). The strike of the deformation structures generally parallels the trend of the eastern and western intrusive lobes; trending *c.* SSE–NNW at the head of Rattlesnake Gully, rotating to *c.* N–S as you move south (Fig. 6.12a). In the south, where the gully opens out, and is only bound by intrusive rocks to the west, deformation bands switch orientation to trend ENE–WSW (structural stations MCSS-28 and -30; Fig. 6.12a). Deformation structures throughout most of Rattlesnake Gully are compressional. However, the E–W trending structures in the south display more extensional characteristics (i.e. opening ‘mode 1’ joints). These structures are perpendicular to the dominantly compressional deformation bands seen within the rest of the gully (Fig. 6.12).

As outlined above, bedding within Rattlesnake Gully shows a synclinal fold geometry (Fig. 6.7c–g), however, there is a distinct asymmetry to the eastern and western fold limbs (Fig 6.8. Beds on the western limb display a distinctive ‘kink band’ geometry as the, already steepening, beds pass through vertical deformation corridors (trending SSE–NNW; Figs 6.8d, e & 6.12b). These deformation corridors trend parallel to the synclinal fold axis (Fig. 6.7c). The deformation corridors show an apparent reverse movement: though, in detail, may potentially have a dextral oblique-slip component (consistent with strike-slip faults of a similar trend observed elsewhere in the gully). This ‘kink-band’ geometry is not observed for the beds forming the eastern ‘limb’; these instead forming a smoother monoclinical fold-limb dipping into the centre of the gully (Figs 6.8c, f & 6.12b).

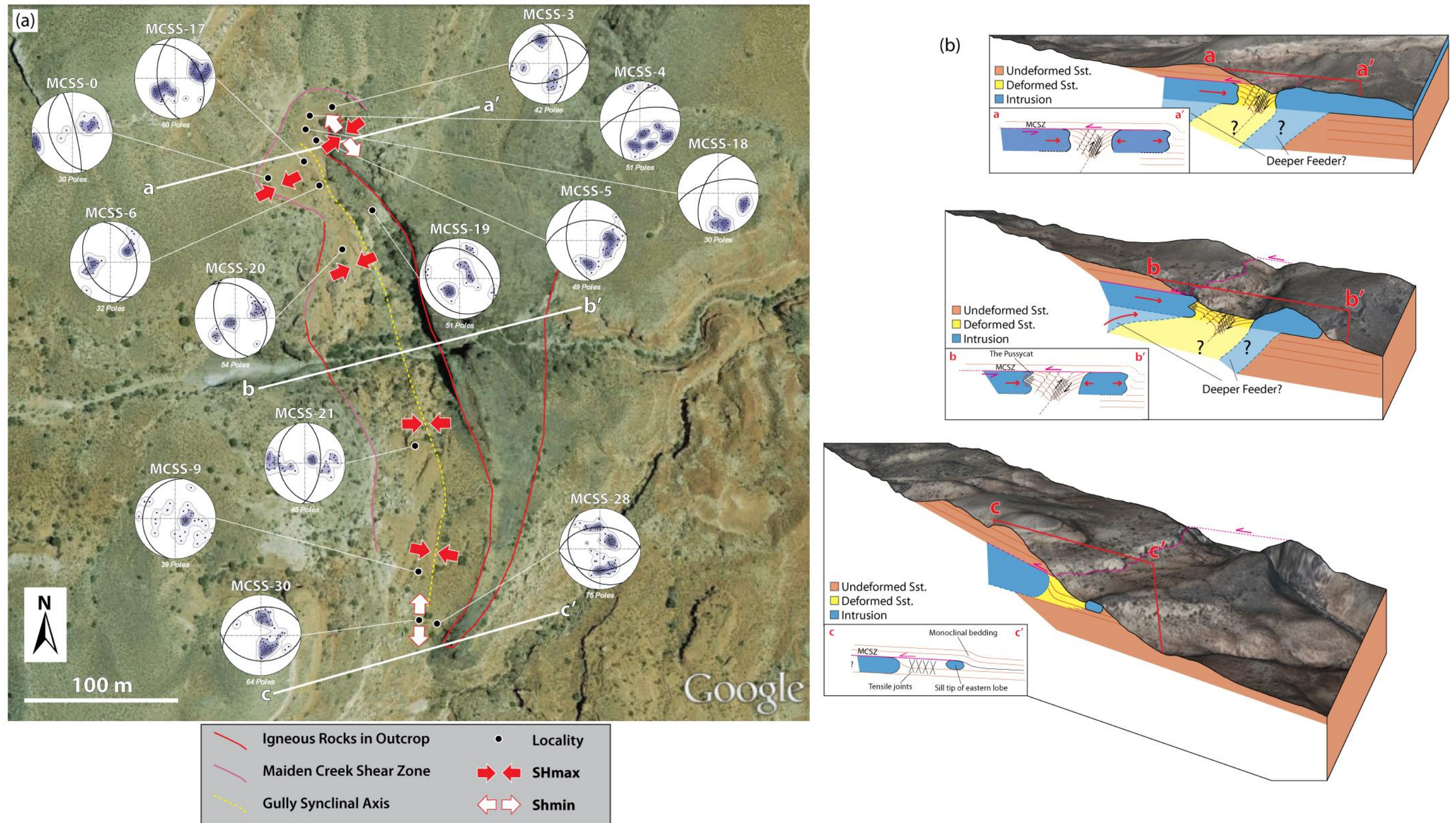


Figure 6.12. Spatial distribution of deformation structures across the Southern Maiden Creek sill study area. (a) Aerial photograph (from Google Earth™) over Southern Maiden Creek study area annotated to show spatial distribution of deformation structures. Fault/ deformation band geometries are depicted in lower hemisphere equal-area stereoplots (contoured poles to planes and mean planes shown). Red lines depict sandstone-igneous contacts, lilac lines show mapped MCSZ, and dashed-yellow line the synclinal axis (and associated zone of pencil cleavage). Red and white arrows depict inferred SHmax and Shmin orientations, interpreted from fault kinematics and structural trends. (b) Geological cross-sections across the study area (no vertical exaggeration). Surface topography comprises an aerial photograph draped over 5m DEM surface in Move™. Inset boxes depict observed geometries, while 3D sections show potential deeper subsurface extent (see section 6.8.3 for discussion). Cross-section locations are shown in (a).

Abundant deformation banding occurs within the sandstone beds on both sides of the gully, increasing in intensity towards the centre. On the eastern limb, conjugate deformation bands rotate about a horizontal axis towards the gully centre (Fig. 6.8f). A central zone of intense pencil cleavage runs along the fold hinge zone (Fig. 6.8c, d, f). The fold hinge zone, and zone of pencil cleavage, appear to be located closer to the lateral margin of the eastern lobe (i.e. off centre; Fig. 6.12), reflecting the asymmetry of the deformation in the gully.

Adjacent to the eastern lobe, or more specifically in the NE of Rattlesnake Gully (structural stations MCSS-4, -5, & -18; Figs 6.2 & 6.12a), a system of conjugate strike-slip faults are present within the sandstone beds flanking the intrusion (Figs 6.8f–h, 6.9 & 6.12) and at the sandstone–intrusion contact (Fig. 6.9). This strike-slip faulting is not apparent elsewhere in the gully.

6.7. Maiden Creek Shear Zone (MCSZ)

The Maiden Creek Shear Zone is a previously undocumented shallowly dipping to sub-horizontal structure, separating weakly deformed sandstone above the intrusion lobes from highly deformed sandstones below and within Rattlesnake Gully (Fig. 6.13). The shear zone can be traced along a sub-horizontal detachment surface in line with the top surface of the intrusive lobes (Figs 6.4, 6.12 & 6.13).

6.7.1. Outcrop Observations and Spatial Extent

The best and most accessible exposure of the MCSZ can be found at the head of Rattlesnake Gully, at the base of a small (~2 m high) sandstone cliff face created by the shear zone eroding faster than the surrounding host sandstones (structural station MCSS-0; Figs. 6.2b & 6.13a–c). Here, the shear zone separates the intensely deformed sandstones below (within Rattlesnake gully) from less deformed, sub-horizontal sandstone units above. The shear zone is sub-horizontal and characterised by a series of shallowly (<25°) ESE-dipping shear planes with consistent ESE–WNW trending slickenlines that are preserved on upper and lower shear plane surfaces (Fig. 6.7b). The shear zone appears to be at its thickest in this location, measuring ~0.7–1 m thick (Fig. 6.13b). On

sub-vertical surfaces that parallel the movement direction, C-type shear fabrics (cm-scale) indicate top-to-the-WNW kinematics along the shear zone (Figs 6.7b & 6.13c). The shear zone exhibits a strong foliated fabric with an interlayered sequence of thin (cm-scale) muddy brown layers, more competent hard red sandstone layers, as well as stretched quartz boudins (up to 10 cm long; Fig. 6.13c). Lithologies within the shear zone appear to resemble those of undeformed thin siltstone and shale beds observed locally within the Entrada Sandstone Formation (Fig. 6.3b). These layered siltstone and shale horizons were interpreted in the field as the likely protolith for the shear zone.

MCSZ can be traced onto the top surface of both intrusive lobes, though exposures are better on the western lobe (e.g. structural station MCSS-10; Fig. 6.13d, e). Here the shear zone is <15 cm thick, and shear fabrics are hard to identify due to lack of 3D exposures and inaccessibility (beneath a narrow overhang). However, slickenlines can still be recorded on lower and upper shear surfaces, these consistently trending ESE–WNW (Fig. 6.7b).

Moving further onto the top surface of the western lobe (<5 m), a discrete shear zone becomes harder to identify. However, deformation structures consistent with the kinematics of the MCSZ are still abundant. These include the c. E–W stretched plagioclase phenocrysts and the low-angle (top-to-the-west) faults in both the intrusion top surface and the overlying altered sandstones (Fig 6.7b & 6.11). Although not exhibiting simple shear, stylolites are also spatially coincident with these structures on the top surface (Fig. 6.11e–h). These structures can be identified for some distance (up to 50 m) onto the western lobe.

The MCSZ can also be traced further south along the eastern margin of the western lobe (structural stations MCSS-7 and MCSS-8; Figs 6.2 & 6.12).

6.7.2. Shear Zone Microstructures

Microstructural analysis was carried out on two samples collected from the MCSZ at structural station MCSS-0 (Figs 6.2b & 6.13). Two polished sections were cut in two different orientations: (1) a vertical section cut parallel to the movement direction (i.e. ESE–WNW); and (2) a section cut along a horizontal plane parallel to the shear surface.

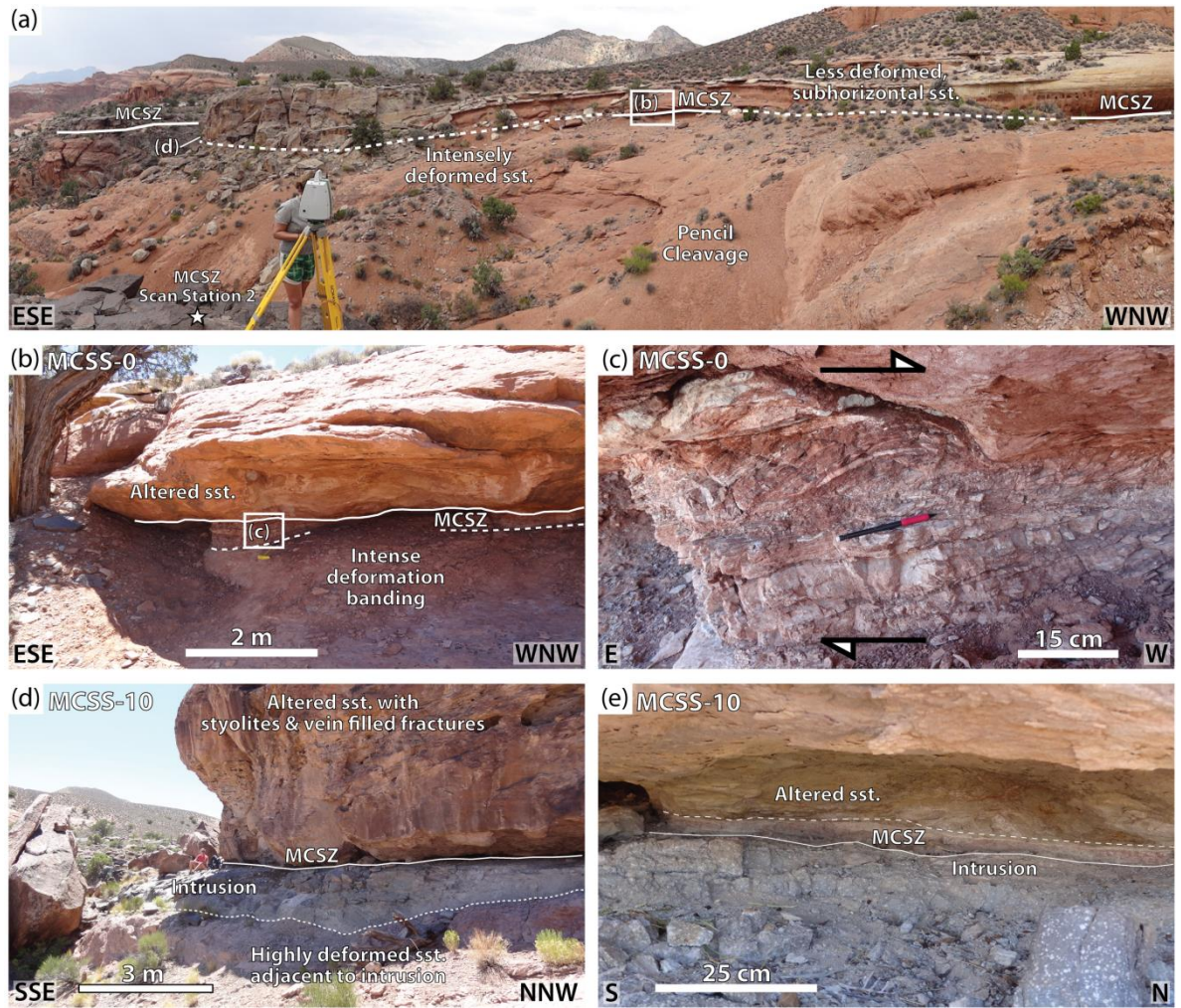


Figure 6.13. Outcrop photographs of the Maiden Creek Shear Zone (MCSZ). (a) Maiden Creek Shear Zone (MCSZ) separating low-moderately deformed sandstone above from highly deformed sandstone in the gully below (solid white lines depict zones where the MCSZ can be observed in outcrop, while dashed lines depict inferred continuation across areas of non-exposure). Extent of MCSZ defined in photo is ~200 m. (b) MCSZ outcrop area in the ‘sandstone-sandstone domain’, structural station MCSS-0, locality highlighted in (a). This locality represents the best exposed area for studying the MCSZ. (c) Shear zone fabrics (inc. C-type) observed in outcrop, showing top-to-the-west shear (area depicted in (b)). (d) MCSZ outcrop area in the ‘sandstone-igneous domain’, structural station MCSS-10, locality highlighted in (a). Note, MCSZ is a thin deformation zone on intrusion top surface with a c. 3-5 m thick unit of altered sandstone above. (e) Thin (<5cm) MCSZ zone separating intrusion from altered sandstone.

At the microstructural scale, a clear layered/ foliated fabric is apparent (Fig. 6.14a). Localised detachment surfaces (i.e. principal slip surfaces) separate broader, more distributed zones of deformation. These zones of deformation appear to reflect a distinct lithological layering, with quartz-dominated (sandstone) zones dispersed between layers of muddy, feldspar rich (shale and siltstone) zones (white and brown layers respectively in Fig. 6.14).

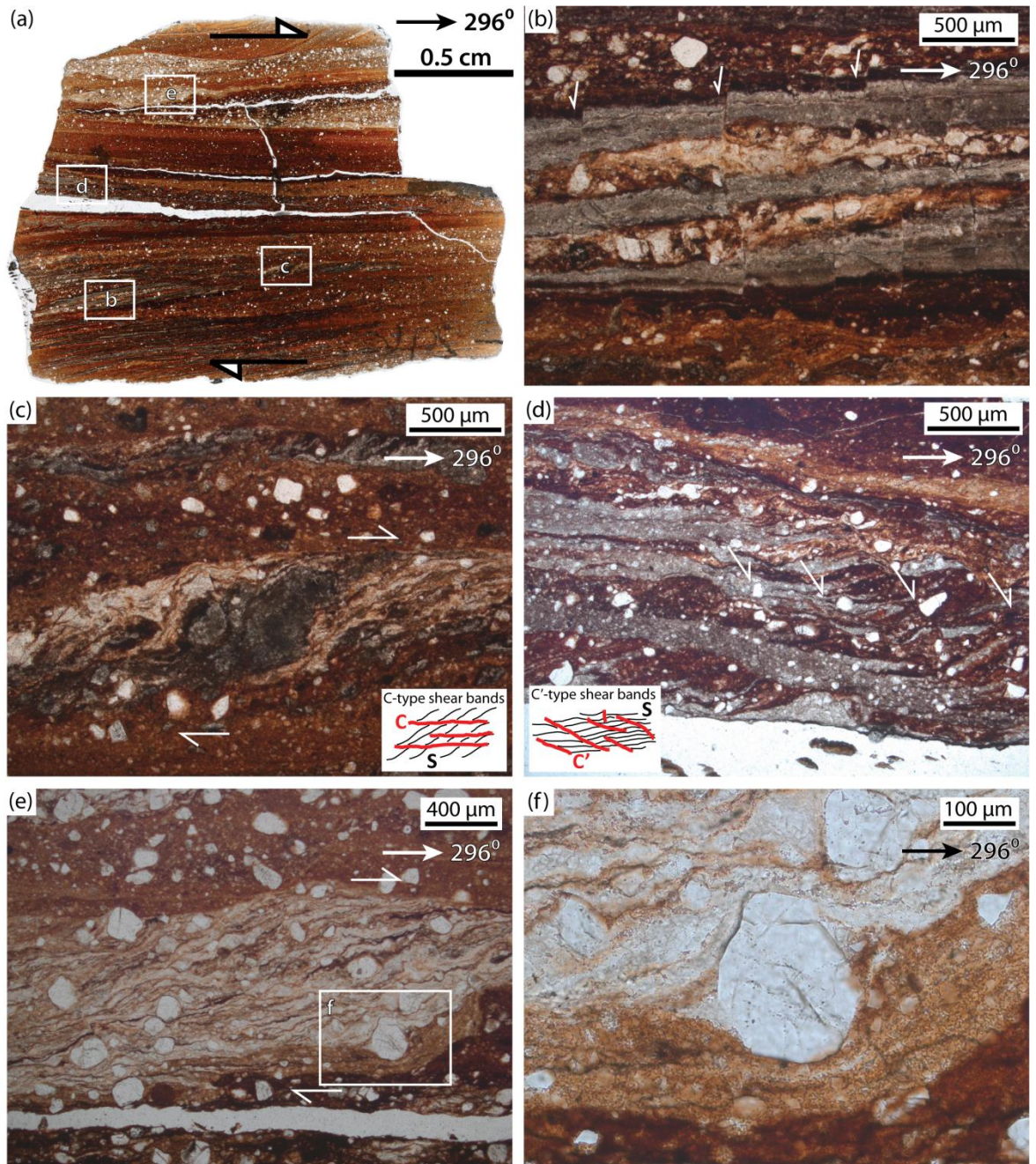


Figure 6.14. A series of photomicrographs of MCSZ microstructures and fabrics, all indicating top-to-the-WNW movement. (a) thin section photograph of sample MCSS 0 – S22. Note localised detachment surfaces and broader zones of foliation. Labelled boxes indicate locations of photomicrographs in (b) to (f). (b) varying shear layers offset by antithetic brittle micro-fractures and faults. (c) C-type shear band fabrics. (d) C'-type shear band fabrics. (e) cataclastic tails to quartz grains to form boudins. (f) zoom in of deformed quartz grain in (e).

Deformation microstructures within these different zones include inclined fault surfaces and tensile fractures (Fig. 6.14b), shear band cleavage (Fig. 6.14c–e), pressure solution seams (Fig. 6.14e), winged objects (σ -type porphyroclasts; Fig. 6.14c, e, f), and zones of ultra-cataclasite. A number of different shear fabrics and kinematic indicators are

apparent (Fig. 6.14). Both C-type (Fig. 6.14c, e) and C'-type (Fig. 6.14d) shear fabrics can be identified. Cataclastic tails are also observed for some larger clasts (Fig. 6.14e, f). These all show non-coaxial deformation with a top-to-the-WNW shear sense, consistent with field observations.

Deformation mechanisms appear to be dominated by cataclastic flow and the effects of pressure solution (the latter leading to the development of the distinct foliation). Cataclastic deformation appears to predominate in the quartz-rich (sandstone) layers, although brittle faults and tensile microfractures are apparent throughout. Microstructural analysis therefore suggests that deformation within the shear zone is dominantly brittle.

6.7.3. Variations in Character

As outlined above, the style of deformation associated with the MCSZ appears to vary spatially from above Rattlesnake Gully to that on the intrusion top surfaces (Fig. 6.15). Consequently, the MCSZ can be divided into two distinctly different domains: 1) the 'sandstone–sandstone' domain in Rattlesnake Gully; and 2) the 'intrusion–sandstone' domain on the top surface of the igneous 'lobes' (Fig. 6.15).

In the 'sandstone–sandstone' domain, the MCSZ is characterised by clear Principal Slip Surfaces (PSS) located at the top and base of a discrete horizon of shear fabrics, typically >10 cm to 1 m thick (Figs 6.13 & 6.15). Comparatively, in the 'intrusion–sandstone' domain, deformation associated with the MCSZ is partitioned across the intrusion–host rock contact (Fig. 6.15) into zones of pure shear/ flattening (i.e. stylolites; Fig. 6.11f) in the altered host rock (Fig. 6.11d–h), and simple shear (low-angle faults; Fig. 6.11c, d) within the uppermost few metres of the intrusion and the overlying sandstones. As a result, deformation associated with the MCSZ in the 'intrusion–sandstone' domain is more dispersed, characterised by a thicker deformation zone extending ~3 m vertically either side of the top surface of the intrusion and a less clearly defined principal shear zone (Fig. 6.15).

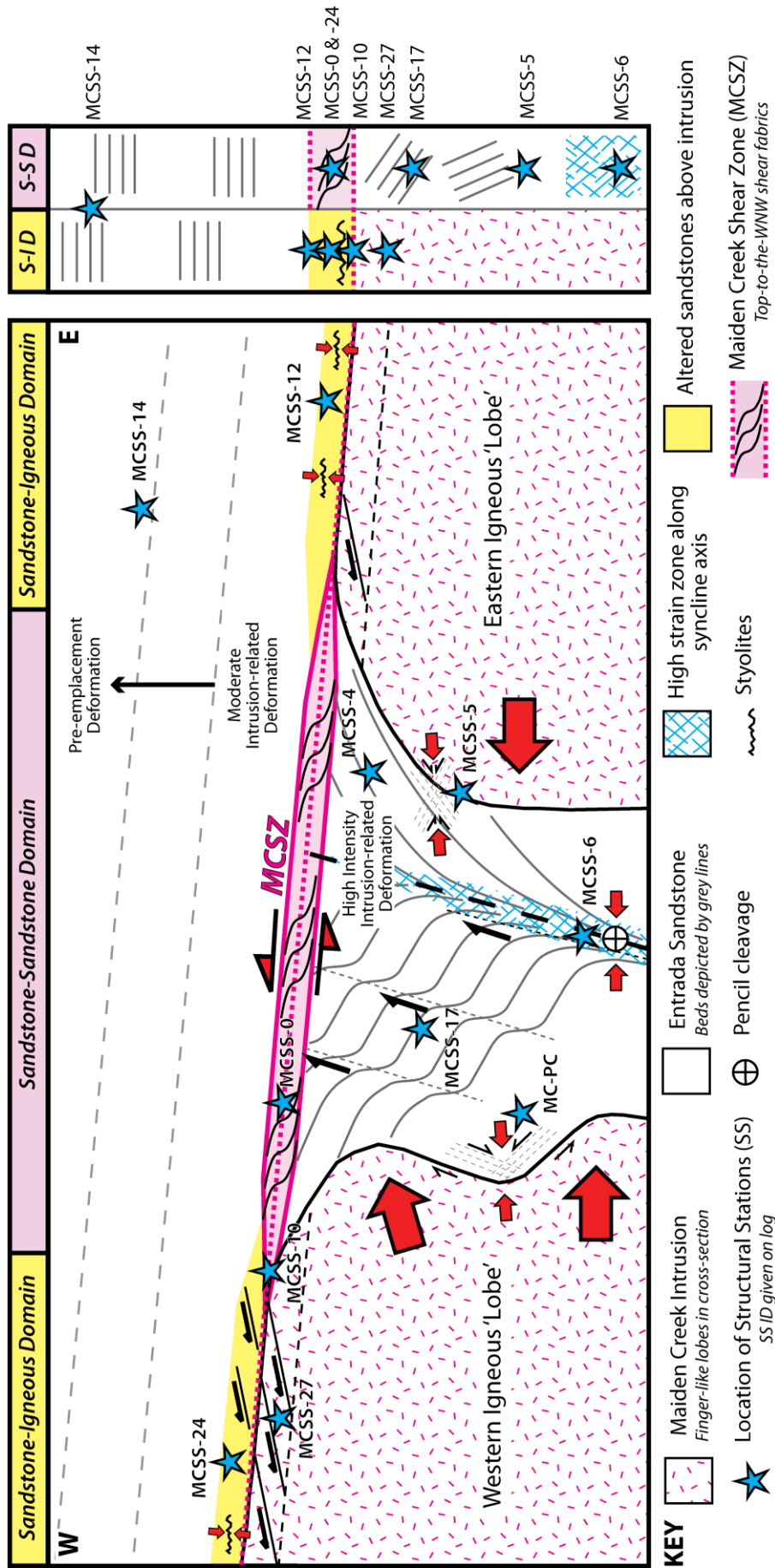


Figure 6.15. Schematic cross-section showing spatial distribution of deformation structures in the study area. Note zonation of the MCSZ: yellow zones depict sandstone-igneous domain, while pink zone shows sandstone-sandstone domain.

6.8. Discussion

6.8.1. MCSZ: a Syn-emplacement Accommodation Structure

The MCSZ appears to be a significant structure localised to the southern Maiden Creek intrusion area (Fig. 6.4); however, due to erosion, the true extent of the MCSZ cannot be mapped in detail. Spatially, the MCSZ is also coincident with the intrusion top surfaces of both the eastern and western intrusive lobes (Figs 6.4, 6.13d, e, & 6.15). Furthermore, it appears to define an upper limit to intrusion-related deformation of host rocks within Rattlesnake Gully (i.e. sandstones between the eastern and western lobes; Fig. 6.15). The kinematics of the MCSZ (i.e. top-to-the-WNW) are consistent with both shear fabrics and deformation structures observed on both intrusion top surfaces (e.g. low angle shear fabrics, E–W stretched plagioclase phenocrysts and low-angle faults; Figs 6.7b & 6.11).

Low-angle faults on the intrusion top surface show consistent top-to-the-WNW shear, matching that of the MCSZ (Fig. 6.7b & 6.11c). These low-angle faults can only be seen cutting the uppermost few metres of the intrusion. Below this, sub-vertical fractures predominate (Fig. 6.6d). As these brittle faults cross-cut the intrusion, a post-emplacement timing could be inferred. However, similar faults may also be identified in the altered sandstone immediately above the intrusion (Fig. 6.11d). Fluidisation along these low-angle faults in the altered sandstone indicates that they were present whilst the intrusion was still hot enough to be driving thermal fluids through the host rock. Assuming, therefore, that these low-angle faults in both the intrusion and the sandstones are contemporaneous in age, a syn-emplacement timing may be likely for these structures.

As the MCSZ in Rattlesnake Gully (i.e. the ‘sandstone–sandstone’ domain) appears both spatially and kinematically linked to the deformation on the top surface of the intrusive lobes (i.e. the ‘intrusion–sandstone’ domain), this strongly supports the MCSZ as being a syn-emplacement structure; shear occurring in response to the emplacement and flow of magma within the intrusive ‘lobes’.

Further evidence to support a syn-emplacement timing for the MCSZ (as opposed to post-emplacement localisation of deformation on the intrusion–host rock contact zone) is the lack of offset between the thermally and chemically altered overlying sandstones (Fig. 6.11d–h) with respect to the underlying intrusive bodies. If the MCSZ post-dated

emplacement of the intrusive bodies, we would expect to see an offset (top-to-the-west). However, this is not the case, as the spatial distribution of altered sandstone units corresponds perfectly to zones that overly intrusion outcrops (Fig.6.15).

Horsman et al. (2005) proposed a strong relationship between mineral stretching lineations and AMS (Anisotropy of Magnetic Susceptibility) fabrics for the Maiden Creek intrusion. They used these to infer magma flow directions (see Chapter 5, Fig. 5.23). Using this relationship and fabrics observed in this study, a *c.* W–E magma flow direction may be inferred for the western lobe. This would be consistent with the top-to-the-WNW kinematics observed in the MCSZ. This easterly magma flow direction would also be consistent with the regional model for a westerly-derived feeder system to the wider Maiden Creek intrusion (Horsman et al., 2005, 2009). Furthermore, a westerly-derived magma flow direction may explain the arcuate trend observed for the intrusive lobes and intervening Rattlesnake Gully (see Section 6.8.2; Fig. 6.16b, c).

An alternative model for the MCSZ is that it is simply a *décollement* or gravity-driven basal detachment surface, where the less-deformed rocks above are sliding down-dip due to the growth of the underlying intrusion. However, the movement on the shallowly ESE-dipping shear zone is up-dip (top-to-the-WNW), and therefore, this gravity driven movement appears unlikely in the absence of any evidence for a later regional tilting of the region. Furthermore, as the spatial distribution of the shear zone appears localized to the southern Maiden Creek intrusion, a regional *décollement*/ detachment surface model is less likely.

If the development and movement on the MCSZ, as proposed in this study, is contemporaneous with the emplacement of the southern Maiden Creek intrusion (i.e. a syn-emplacement structure), then its presence has significant implications in terms of magma flow directions, emplacement mechanisms and sub-surface intrusion geometries; the shear zone most likely resulting as a back thrust to underlying magma flow (see Section 8.3). Furthermore, if MCSZ is a syn-emplacement structure, forming directly in response to magma emplacement, then it also plays a significant role in accommodating the addition of magma within the shallow crust as the shear zone exhibits a substantial amount of strain.

6.8.2. Structural Complexity and Variations in Strain Within Rattlesnake Gully

The complex spatial distribution of deformation structures and geometries in the sandstone below the MCSZ and between the two intrusive ‘lobes’ likely reflects variations in strain within the gully. The strikes of deformation structures in the sandstones within Rattlesnake Gully parallel the intrusion margin of the eastern lobe. Deformation is dominantly compressive, with SHmax perpendicular to the synclinal fold hinge line (gully axis) and intrusion margins (Fig. 6.12a), resulting from ‘squeezing’ of the sandstone between the western and eastern lobes. Consequently, SHmax rotates from c. ENE–WSW at the head of the gully in the north, to E–W towards the centre of the gully, and ESE–WNW to the south (Fig. 6.12a). However, in the NE of Rattlesnake Gully strain is more complex; with a conjugate set of strike-slip faults observed in sandstones adjacent to the lateral margin of the eastern lobe (structural stations MCSS-4, -5 and -18; Figs 6.8f–h & 6.12a). The compressional (SHmax) axis associated with these conjugate sets is consistent with the strain axis observed along the rest of the gully. However, the dominantly strike-slip kinematics in this area suggests that strain was more non-coaxial in this area.

E–W trending extensional structures (i.e. tensile joints; structural stations MCSS-28 and 30; Fig 6.12a) observed in the south of Rattlesnake Gully are perpendicular to the dominantly compressional deformation bands seen within the rest of the gully (Fig. 6.12). This localised zone of extension-dominated deformation is coincident with the southern tip of the eastern lobe (Fig. 6.12a). Therefore, changes in strain and deformation trends (Fig. 6.12a) may reflect changes in the boundary conditions within Rattlesnake Gully: i.e. more compressive in the north where sandstones are bound by thick (>30m) intrusive lobes to both the west and east; and more extensional in the south where the sandstones are less constrained due to the thinning (<10 m) and termination of the eastern lobe (Fig. 6.12).

6.8.3. Models for Emplacement and Geometry of the Southern Maiden Creek Intrusion: a Pair of Finger-like Lobes or Deep-rooted Sills?

Figure 6.16 provides three possible models for the emplacement and geometry of the southern Maiden Creek intrusion. Model 1 (Fig. 6.16a) is after the proposed model of Horsman et al. (2005, 2009) for the emplacement of two N–S trending finger-like lobes. In

this model, magma propagates in a southerly direction from a main 'sill-like' intrusive body situated to the NW. In Model 2 (Fig. 6.16b) a western intrusive body (i.e. the western lobe) is derived from depth in the west, i.e. magma flow from west to east; while the eastern intrusive lobe propagates from the north to the south. Model 3 (Fig. 6.16c) involves both the eastern and western intrusive bodies propagating from depth in the WNW towards the ESE (magma flow laterally splaying from the main/ dominant SW–NE trend (and flow direction?) of the Maiden Creek intrusion.

Interpreting fabric data (mainly magnetic foliation and lineation results from AMS studies, coupled with field observations of linear fabrics (see figs 5, 9 & 10, pages 1433 & 1438-1439 of Horsman et al., 2005), Horsman et al. (2005) proposed that two radial (fanning) lineation patterns are seen at the Maiden Creek intrusion. The first lies within the main body, the second, within the fingers. From the lineation pattern observed from the main body, Horsman et al. (2005) speculated that, though not exposed, the feeder for the intrusion should be located towards the west or southwest. Horsman et al. (2005) suggested that a general alignment between lineation measurements and the N–S elongation of the two southern intrusive lobes indicates a southern flow of magma away from the main body out into the fingers (i.e. Model 1). Horsman et al. (2005) proposed that these finger-like lobes initially started as small protrusions along the margin of the main body, where swelling occurred as a result of local heterogeneity, such as fracture sets in the host rock. As the pressure built up in these small protrusions, magma propagation began outwards from the main body: this propagation continuing until magma at the margin of the finger ceased to have sufficient driving pressure to move the host rock sediments (Horsman et al., 2005). This emplacement mechanism for the finger-like lobes is similar to that proposed by Pollard et al. (1975) for fingers around the periphery of the Shonkin Sag Laccolith in Montana, USA.

In Model 1, compression in Rattlesnake Gully results from lateral expansion of both the western and eastern intrusive lobes as magma propagates in a southerly direction (Fig. 6.16a). Such compression of the host rock sandstones trapped between would most likely result in higher deformation in the sandstones immediately adjacent to the lateral margins of the lobes with deformation intensity decreasing towards the centre of the gully. Johnson and Pollard (1973) on studying deformation structures in host rock sandstones adjacent to and between two intrusive bodies in the NE of the Maiden Creek

intrusion (i.e. the north-easterly pair of finger-like lobes in the Horsman et al. (2005) model; Fig. 6.1b), reported intense fracturing within a ‘wedge-shaped area’, as depicted in Model 1 (Fig. 6.16a), with fracturing extending only ~10 m into the adjacent host rocks.

Model 1, although relatively simple, does not explain the spatial distribution, asymmetry, trend and kinematics of deformation structures observed within the host sandstones in Rattlesnake Gully. Although intense deformation banding (cm-spacing) is observed in sandstones proximal to the lateral intrusion margins, in contrast to the predicted wedge-shaped zone of fracturing close to the lateral margins, deformation intensity increases towards the centre of the gully (with mm-spacing for discrete pencil cleavage planes). Furthermore, in this model for lateral expansion and squeezing of sandstones trapped between two magma lobes, symmetrical folding and deformation would be expected throughout the gully (Fig. 6.16a); rather than the asymmetric synclinal fold (fold axis steeply dipping to the WSW; Fig. 6.7c) recorded in this study, and heterogeneous deformation, kinematics and strain (Figs 6.12 & 6.15). Model 1 could account for the strike-slip kinematics observed in sandstones adjacent to the lateral margin in the NE of Rattlesnake Gully (Figs 6.7c, 6.8f–h & 6.12) if the eastern intrusive lobe was emplaced subsequent to the emplacement of the western lobe; invoking a N–S oriented, dextral shear system within the gully. However, as the strike-slip faulting is not distributed along the entire gully (localised to the NE section), this emplacement model is unlikely. Most significantly, Model 1 cannot explain the kinematics of the MCSZ, as southerly propagating magma fingers would result in top-to-the-north shear in overlying host rocks, not top-to-the-WNW as implied from field and microstructural kinematics (Figs 6.7b, 6.13c and 6.14).

Both Models 2 and 3 (Fig. 6.16b, c) could account for the intense deformation observed in the gully, the asymmetrical folding of the sandstone beds, the variable kinematics, and importantly, the kinematics on the MCSZ. Model 2, similar to Model 1 after Horsman et al. (2005, 2009), infers a lobate morphology for the eastern intrusive body (i.e. the eastern lobe). However, in order to explain the top-to-the-WNW kinematics on the MCSZ, the western intrusive body propagates from the west to the east, with some amount of radial spreading (this accounting for the less dominant c. N–S stretched mineral lineations recorded in this study; Fig. 6.7c). In this model, magma propagates up through the shallow crust from a deeper feeder in the west towards the east, buttressing against the

host rock sandstones adjacent to the eastern lobe. This model would require the eastern intrusive lobe to have been emplaced first. Such easterly propagating magma flow from depth can account for not only the top-to-the-WNW kinematics of the MCSZ, but also the asymmetry of the folding in the host rocks, and the easterly-bowing (arcuate) trend of the intrusion margins, and associated trend of the Rattlesnake Gully.

Yet certain aspects of Model 2 are also problematic. Not only does this model necessitate a specific order in which the eastern and western intrusive bodies are emplaced, it still requires the eastern lobe to be fed from the north (i.e. a southerly magma flow direction). Detailed structural and kinematic mapping of the greater Maiden Creek intrusion (Chapter 5, this study) implies a dominant north-easterly magma flow direction (Figs. 5.26 & 5.27, Chapter 5) for the main NE–SW trending lobe (Fig. 6.1b). A north to south magma flow seems at odds with even lateral spreading from this main north-easterly magma flow direction.

Model 3 (Fig. 6.16c), however, with both the western and eastern intrusive bodies being fed from depth in the WNW (i.e. an E to ESE magma flow direction) overcomes many of the problems associated with both Models 1 and 2. Model 3 explains the high compressive strain within host rocks in Rattlesnake Gully, as well as the deformation and geometric asymmetry due to squeezing between two inclined magma sheets. The synclinal geometry and associated compressional structures within the gully imply a steeply-dipping reverse shear (i.e. the western lobe propagating in the hangingwall to the eastern lobe). The westerly-inclined central fold axis (and zone of pencil cleavage) may parallel a deeper, unexposed sill geometry. Model 3 also provides an explanation for the zone of strike-slip faulting in the sandstones adjacent to the lateral margin of the eastern intrusive body in the NE of Rattlesnake Gully (Fig. 6.12a). Assuming that the northern outcrop exposures at the head of the gully are close to the northern lateral ramp of a westerly-derived sill sheet, left-lateral shear would be expected along this margin.

Model 3, similar to model 2, can account for the development and kinematics of the MCSZ; the shear zone forming as a back-thrust to the westerly propagating magma sheets (the MCSZ acting as a sub-horizontal antithetic structure to the steeply-dipping sill sheets). This model works if both sheets are emplaced contemporaneously, as well as if the western body is emplaced post the emplacement of the eastern body.

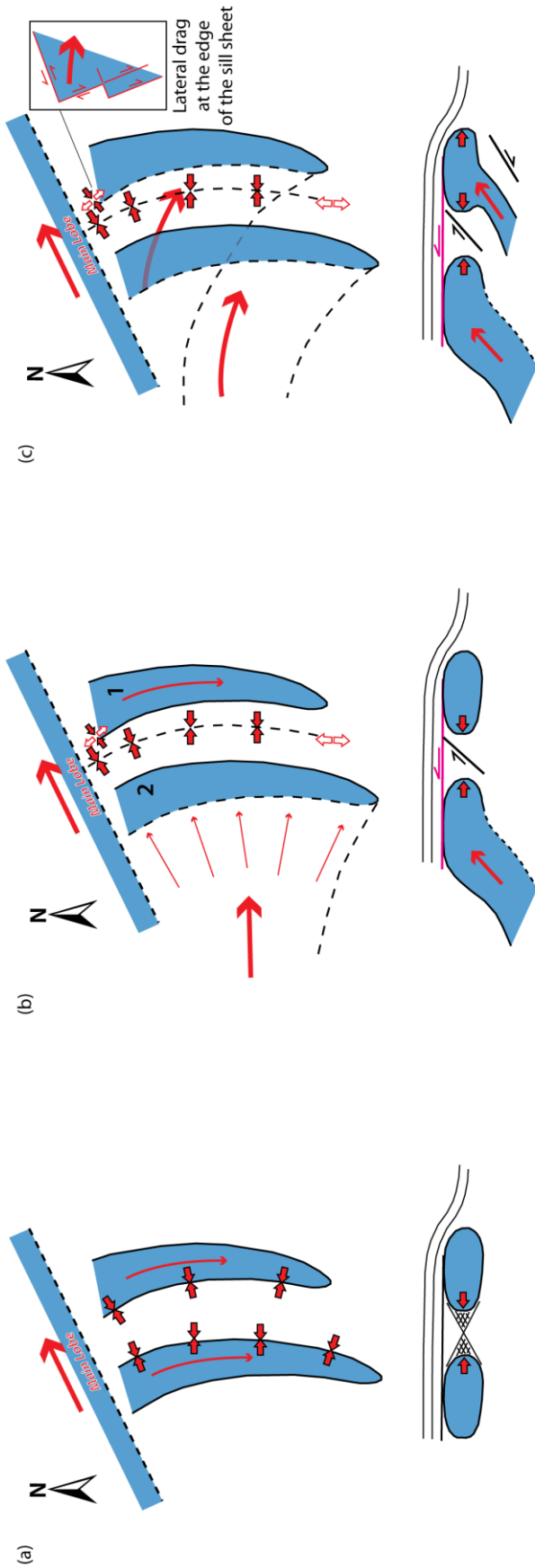


Figure 6.16. Three models for emplacement of the southern igneous bodies to the Maiden Creek intrusion (see discussion in section 6.8.3 for details).

Therefore, on the merits of each model in accounting for the observations in this study, Model 3, with two inclined sill sheets propagating from depth in the WNW towards the ENE, is favoured. In Model 3, observed igneous outcrop at the surface represents the steepest section at the tip of climbing sill sheets, i.e the frontal ramp. If the eastern intrusive body were comprised of two stacked finger-like lobes, as suggested by Horsman et al (2005), we would expect to see similar lateral bulbous geometries on both sides of the lobe. However, what we observe from the eastern intrusive body is a steeply-dipping flat surface on the western lateral margin (within Rattlesnake Gully; Fig. 6.4), and a more irregular, eastern margin. The simpler, western margin is consistent with the upper contact of a ramp section of a saucer-shaped sill. The irregular eastern lateral margins (observed for both the eastern and western intrusive bodies) are interpreted to represent the frontal tip of an upward propagating (saucer-shaped?) sill sheet. The irregular, hour-glass geometry of the eastern lateral margins (as seen in the Pussycat area; Fig. 6.5b, 6.6b, c, 6.10 & 6.15) likely reflects the interaction of magma with syn-emplacement faults. Furthermore, the curved (arcuate) margin trends of the southern intrusive bodies may be consistent with the likely map view geometry of saucer-shaped sills (Thompson and Hutton, 2004; Thompson & Schofield, 2008; Mathe-Sørensen et al., 2004).

Due to lack of exposure for the western intrusive body in particular, there are uncertainties with all 3 models for the emplacement and geometry of the southern Maiden Creek intrusion. Further data, such as geophysical data, are required in order to test the two alternate models for the intrusion geometry and emplacement mechanisms.

6.9. Conclusions

Structural evidence in the southern area of the Maiden Creek intrusion is consistent with westerly-derived magma emplacement. Deformation structures in the host rock sandstones outcropping within Rattlesnake Gully, between the southern intrusive bodies, are dominantly compressional (c. E–W SHmax), while the spatial distribution and asymmetry imply a reverse (east-verging) shear component. From our observations of both deformation structures and exposed intrusion geometries, we propose that the Maiden Creek intrusion in the south is comprised of two westerly-derived (saucer-shaped?) sills, in contrast to the previously suggested model for a pair of northerly-derived finger-like lobes (Horsman et al., 2005).

Overlying these deeper-rooted sills is the newly identified Maiden Creek Shear Zone (MCSZ). This structure, with its top-to-the-WNW shear sense, is an antithetic accommodation structure. The MCSZ acts as a detachment surface, separating highly deformed sandstones below (i.e. between the sills) from less deformed sandstones above. Although the style of deformation in the MCSZ varies from the intrusion top surfaces (i.e. sandstone–intrusion domain) to within the sandstone gully (sandstone–sandstone domain), kinematics are consistent and there is strong evidence to support a syn-emplacment timing for the structure. The substantial amount of strain seen through microstructural analysis suggests that the MCSZ is a significant structure in accommodating magma emplacement.

The spatial distribution of deformation structures in the sandstone gully is complex and reflects variations in strain relating to the arcuate trend of the sill-sheets. A zone dominated by strike-slip faulting in the north may be indicative of a lateral ramp geometry to the sill, and would be consistent with the left-lateral shear as the sill is emplaced. In the south, a change from compressional (c. E–W SHmax) to extensional (c. N–S Shmin) appears coincident with the southern termination of the eastern body and, therefore, a change in the boundary conditions.

Our observations and newly proposed emplacement model may have important implications for understanding how deformation structures accommodate the volumetric addition of magma in the sub-surface, and the modelling of sub-seismic deformation in and around intrusive bodies in the sub-surface.



7. Chapter 7: Discussion & Conclusions

| | | | |
|----------------|---------------|--|----------------------|
| <i>Layout:</i> | 7.1. | Summary of Project Aims | p. 289 |
| | 7.2. | Geometries and kinematics of deformation structures as a tool for understanding intrusion emplacement mechanisms and morphologies | p. 289 |
| | 7.3. | The importance of shear zones in accommodating the emplacement of intrusions in the shallow crust | p. 292 |
| | 7.4. | What controls intrusion emplacement: linking intrusion geometries, host rock deformation and accommodation structures, and space problems | p. 292 |
| | 7.5. | Further Work | p. 295 |
| | 7.5.1. | <i>Geophysical surveys</i> | <i>p. 295</i> |
| | 7.5.2. | <i>Microstructural analysis of intrusion-related deformation structures</i> | <i>p. 296</i> |
| | 7.5.3. | <i>Fracture spacing</i> | <i>p. 297</i> |
| | 7.5.4. | <i>Textural studies and crystal size distribution (CSD) of the intrusions</i> | <i>p. 297</i> |

7.1. Summary of Project Aims

This thesis aimed to develop a greater understanding of how igneous intrusive bodies are emplaced and accommodated within the shallow crust, and accordingly, set out five key questions to be addressed, these being:

- What is the effect of emplacement of shallow-crustal intrusions on the surrounding country rock?
- How is the additional volume of magma accommodated within the crust, i.e. the so called “space problem”?
- Can style of deformation be used to infer sub-surface intrusion geometries?
- What can the style of deformation tell us about emplacement mechanism?
- What controls the emplacement mechanism?

The following sections will draw on the data, observations, interpretations and discussions of the previous chapters in order to provide answers to these.

7.2. Geometries and Kinematics of Deformation Structures as a Tool for Understanding Intrusion Emplacement Mechanisms and Morphologies

Detailed geometric and kinematic studies of deformation structures in the host rocks to two satellite intrusions (Trachyte Mesa and Maiden Creek) to the Mount Hillers intrusive complex in the Henry Mountains, Utah, have highlighted the significant impact of the emplacement of shallow-crustal intrusions on surrounding host rock. Both intrusions in this study were emplaced within the Entrada Sandstone Formation, an ideal host rock for the formation of deformation bands and the preservation of structures. As a result, these provide an excellent record of emplacement-related deformation, magma movement (flow) directions and associated strains.

A number of deformation structural types can be observed in host rocks to both the Trachyte Mesa and Maiden Creek intrusions (Table 7.1). These include: faults and deformation bands; zones of intense pencil cleavage; sub-horizontal detachment surfaces and shear zones; and tensile (‘Mode 1’; Price, 1966) joints. Syn-emplacement deformation is greatest along the lateral margins (and tips?) of intrusive bodies. At both Trachyte Mesa and Maiden Creek, the intensity of deformation structures in overlying host rocks decreases quickly within the first 5–10 m, although distortion of the overlying beds may be apparent for a significant vertical distance beyond this (>30 m at Trachyte

Mesa). The rapid decrease in strain above Maiden Creek is potentially due to the presence of a significant sub-horizontal detachment surface, which locally shows high strain shear characteristics (i.e. the Maiden Creek Shear Zone)

Results from the various studies within this thesis suggest that much can be learnt about intrusion geometries and emplacement through the detailed analysis of syn-emplacement deformation structures. Significant findings include:

- deformation structures commonly parallel intrusion margins, and in some cases magma flow directions;
- kinematic analysis can give a strong indication of likely magma flow directions;
- deformation styles (e.g. compressional, extensional, strike-slip) vary according to the local intrusion geometry (e.g. dominantly compressional between intrusive bodies; and more extensional around steps and corrugations on intrusion top surfaces; Chapter 5);
- in stacked sill-sheet systems, insights into the order of stacking (i.e. over-, mid- and under-accretion; Menand, 2008) may be determined through the analysis of associated, emplacement-related, deformation structures (e.g. differences in structural style observed along the eastern and western structural transects, TMTE and TMTW, at Trachyte Mesa; Chapter 3);
- deformation structures can also be used in order to understand the growth mechanism of sill sheets, i.e. dip-slip faults linked to sill sheet terminations implying a two-stage growth model; 1) radial growth, and 2) vertical inflation (Chapter 3; after Hunt, 1953; and Corry, 1988); and
- an observation from the Maiden Creek intrusion (that may still need further investigation) is the local kinematic partitioning (between pure and simple shear) evident in syn-emplacement deformation structures in close proximity (<5 m) to intrusion margins (Chapter 5).

Consequently, even in areas where intrusion outcrop is not available, these findings can be applied to infer underlying intrusion geometries.

Table 7.1. *(overleaf)*

A comparison of geometries, deformation structures and emplacement models of the Trachyte Mesa and Maiden Creek intrusions.

| | Trachyte Mesa | Maiden Creek |
|---|---|---|
| Size | Satellite intrusion (~1.5 km ²) | Satellite intrusion (~1 km ²) |
| Proximity to Mt Hillers Intrusive Centre | ~12.5 km (most distal) | ~10.5 km (proximal–distal) |
| Trend/ Principle Magma Flow Direction | NE–SW/ ~ 045° | NE–SW to ENE–WSW/ ~060° |
| Geometry | Elongate body composed of multiple stacked sills/ sheets (over-accretion); Roof faulting and sill-climbing; Some ‘out-of-sequence’ stacking (under- or mid-accretion; Menand, 2008) | Complex geometry; <i>Model 1</i> : central ellipsoid body with 4 finger-like lobes (Horsman et al., 2005); or <i>Model 2</i> : multiple inclined (saucer-shaped?) sheets radiating outwards from an elongate central body (lobe/ feeder dyke; this study) |
| Deformation Structures | Conjugate deformation bands (<i>sub-horizontal extension</i>); Dip-slip faults (down to NW extension movement); Relaxation (cooling) ‘mode 1’ fractures with calcite infill | Conjugate deformation bands (<i>sub-horizontal compression</i>); Low-angle reverse faults at intrusion margins; Zones of intense deformation and pencil cleavage ; Sub-horizontal shear zones separating zones of intense deformation from less deformed rocks above; Styolites on top contact of intrusions; Relaxation (cooling), ‘mode 1’ fractures |
| Deformation Style | Extension dominated | Compression dominated at margins |
| Emplacement Mechanism | Sill stacking and ‘two-stage’ (1. radial; 2. vertical) growth | Variable and poorly understood |

7.3. The Importance of Shear Zones in Accommodating the Emplacement of Intrusions in the Shallow-Crust

At both Trachyte Mesa and Maiden Creek, shear surfaces and shear fabrics are identified on intrusion top surfaces at the intrusion–host rock contact/ interface. These shear structures and fabrics include: sub-horizontal shear zones; low-angle dip-slip faults; and stretched mineral lineations. Microstructural analysis suggests that the deformation processes associated with these shear fabrics are dominantly brittle (i.e. cataclastic flow). Kinematics of these shear structures are interpreted to reflect local magma flow directions. Morgan et al. (2008) also identified the importance of shear fabrics both at intrusion–host rock contacts, and also on surfaces internal to the intrusion (using these to infer the interface between stacked sill sheets).

At the Maiden Creek intrusion, shear zone/ detachment surfaces have also been identified at the level of emplacement (i.e. intrusion top surfaces) in sandstones between two neighbouring and separate intrusive bodies, and can be traced onto the top surfaces of the intrusions. These appear to be associated with a more shaley-siltstone horizon within more massive red and white sandstone units. The best example is the newly identified Maiden Creek Shear Zone (MCSZ), localised to the southern Maiden Creek intrusion (see Chapter 6). The MCSZ acts as a detachment surface, separating less-deformed sub-horizontal sandstone beds above from highly deformed and folded sandstones below and between the two intrusive bodies comprising the southern intrusion. Microstructural analysis of the MCSZ highlights a substantial amount of strain, suggesting that the MCSZ played a critical role in accommodating magma emplacement. Shear zone surfaces, like the MCSZ, may be important sub-seismic structures that need to be considered when interpreting intrusive bodies in the sub-surface.

7.4. What Controls Intrusion Emplacement: Linking Intrusion Geometries, Host Rock Deformation and Accommodation Structures, and Space Problems

Despite both the Trachyte Mesa and Maiden Creek intrusions having similar magmatic compositions (i.e. intermediate plagioclase-hornblende porphyry) and being emplaced within the same host rocks at a similar palaeo-depth (~1.5 km) in the shallow crust, the two intrusions display vastly different geometries and intrusion and host rock emplacement-related deformation (Table 7.1).

Horsman et al. (2009), in their synopsis of the various studies of satellite intrusions in the Henry Mountains, Utah (Horsman et al., 2005; de Saint Blanquat et al., 2006; Morgan et al., 2008), suggested that the various forms of sill and laccolith geometries lie on a hypothetical evolutionary timeline reflecting the addition of successive sill sheets (Fig. 7.1). In this scheme, sills (e.g. Maiden Creek) evolve to form laccoliths (e.g. Trachyte Mesa), laccoliths grow to become bysmaliths or punched laccoliths (e.g. Black Mesa), and these eventually grow to form plutonic scale intrusions. However, detailed mapping at Maiden Creek suggests that this intrusion has a far more complex geometry than that proposed by Horsman et al., (2005, 2009), and therefore is an unlikely precursor to Trachyte Mesa. Furthermore, observed deformation structures and interpreted emplacement mechanisms appear distinctly different (extension-dominated deformation along the margins of Trachyte Mesa, and dominantly compressional deformation at Maiden Creek; Table 7.1). Although the Black Mesa intrusion has not been studied as part of this research project, synergies can be found between the stacked sill sheets at Trachyte Mesa and the growth of a larger bysmalith (punched laccolith) such as Black Mesa.

An interesting observation to be made at both Trachyte Mesa and Maiden Creek is that the top surfaces of both intrusions appear to be at a stratigraphic level coincident with an interlayered shale-siltstone unit. This observation is in fitting with the early work of MacCarthy (1925) who noted the regularity with which laccoliths intrude along shale beds. Recent work of Kavanagh et al. (2006) using gelatine-based laboratory experiments showed that lithological discontinuities, such as interlayered shaley units within sandstones, are likely to form preferential pathways for horizontal magma propagation. As observed by Menand (2008) this modelling works well for the stacked sill-sheets of the Trachyte Mesa intrusion (with earlier emplaced sill sheets also forming preferential rigidity contrasts for further sheet emplacement).

However at Maiden Creek, there is less evidence for this stacked sill sheet model; with this study providing alternate models for the structural zonation and irregular/ hour-glass lateral margins, used by Horsman et al. (2005, 2009) to argue for stacked sill sheets (see Chapters 5 & 6). Furthermore, the bulk of the host rocks found adjacent to, and at the same structural level as, the Maiden Creek intrusion are massive sandstone units. Syn

emplacement deformation structures are clearly apparent and can be seen extending from the intrusion into the adjacent sandstones, suggesting that the magma was emplaced directly into the sandstone units. This could potentially provide an explanation for the dramatically different intrusion geometries observed at Maiden Creek in comparison to those at Trachyte Mesa. It therefore appears less likely that the Maiden Creek intrusion was emplaced solely by propagation along this upper shaley unit coincident with the intrusion top surface. However, the fact that the Maiden Creek Shear Zone (and other weakly deformed shear/ detachment surfaces observed elsewhere on the intrusion) is localised within this shaley-unit still supports it playing a role in constraining the upper level of emplacement.

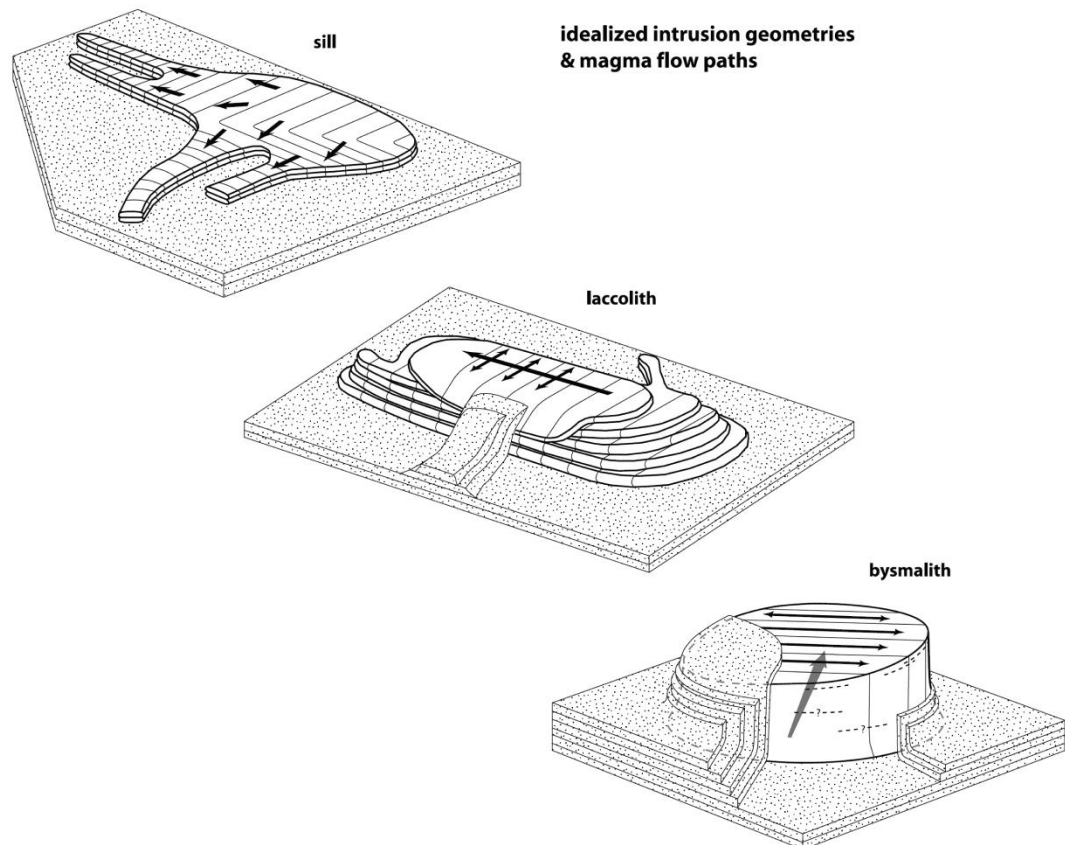


Figure 7.1 Schematic block diagrams of idealised intrusions, based on the Maiden Creek (sill), Trachyte Mesa (laccolith) and Black Mesa (bysmalith) intrusions, from Horsman et al. (2009). This cartoon depicts a hypothetical evolutionary timeline for the growth of intrusions, based on the addition of successive sill sheets.

At Trachyte Mesa, various sill tip terminations may be observed (bulbous terminations, steep-faulted terminations, and sill-climbing sheets; Chapter 3). Although not investigated in detail, sheets with bulbous terminations appear to lie deeper, within a more muddy red

sandstone unit, whereas faulted terminations and sill-climbing appear more common in sheets directly beneath more massive (competent) red and white sandstones. This may be due to the shaley units behaving in a more ductile manner, thus inhibiting brittle fault development at the sill-tips; while the more massive sandstone deforms in a brittle manner and is more prone to the development of faults as sill sheets inflate.

On the Colorado Plateau, three distinct basement trends are observed (Marshak & Paulsen, 1996; Fig. 2.6 in Chapter 2): NE–SW; NW–SE; and N–S. In the Four Corners area, and specifically the vicinity of the Henry Mountains, two distinct lineament trends are defined: the Four Corners lineament, trending c. NW–SE; and the Cataract and San Rafael lineaments, trending c. NE–SW (Huffman & Taylor, 1997; Fig. 2.6e, Chapter 2). Although the five intrusive centres that comprise the Henry Mountains trend c. N–S, a distinct step-to-the-east can be seen from Mount Pennell, through Mount Hillers, to Mount Holmes. These three peaks line up in a NW–SE orientation and are closely coincident with the basement lineament of the Four Corners outlined by Huffman and Taylor (1997). Furthermore, zooming into the scale of Mount Hillers and its satellite intrusions, a strong NE–SW orientation bias is apparent for many of the satellite intrusions (including Sawtooth Ridge, Maiden Creek and Trachyte Mesa). Basement trends may therefore have played a role in the location, magma ascent and emplacement of the Henry Mountains intrusions, both at the regional and the scale of individual satellite intrusions.

7.5. Further Work

7.5.1. Geophysical surveys

This study has highlighted several issues with the previously proposed model of Horsman et al. (2005, 2009) for the emplacement and final geometry of the Maiden Creek intrusion, whilst proposing an alternate model based on detailed geometric and kinematic studies of syn-emplacement deformation structures and exposed intrusion–host rock contact geometries. In order to test both the models of Horsman et al. (2005, 2009) and this study, additional field data is required. Geophysical methodologies could be used to resolve the sub-surface geometry and true extent of the intrusion.

Ground penetrating radar (GPR) using a geophone, if possible, could be used in key areas of interest across the Maiden Creek intrusion, i.e. in Rattlesnake Gully between the two

southern intrusive bodies of the intrusion (i.e. Zone 3), and also across the south-western area where no intrusion outcrops are present (i.e. Zone 5). GPR involves sending small pulses of energy into the ground and recording the strength and time it takes for any reflected signal to return to the surface and the transmitter. Using a low antenna frequency (e.g. 16–80 MHz), GPR can reach depths greater than 30 m. This could potentially be deep enough to explore for the presence of intrusion below the sandstone in both these areas and help determine the depth of the contact between intrusion and host rocks where not exposed; therefore imaging the top surface of the sub-surface intrusion. Gravity and magnetic studies (similar to those carried out around Trachyte Mesa by Wetmore et al., 2009) could also help to resolve the sub-surface extent of the Maiden Creek intrusion, whilst also providing information regarding the depth of the intrusive body. Geophysical data (i.e. sub-surface) could then be combined with the terrestrial laser scan (TLS) data (i.e. surface) already acquired for this study in order to produce an accurate 3D model of the Maiden Creek intrusion.

Furthermore, GPR is highly effective at detecting porosity changes and therefore, by proxy, could potentially provide information regarding changes in the intensity of deformation banding; deformation bands recorded in this study likely to impede fluid flow due to the significant reduction in porosity (typically <2.5% within deformation bands due to cataclasis, compaction and calcite cementation). Additionally, GRP also has the potential to pick out displacements along faults and shear zones.

N.B. a collaborative project with Profs. Steve Nelson and John McBride from Brigham Young University, Utah, to collect GPR and gravity/ magnetic is in the planning stages (currently delayed due to unforeseen circumstances).

7.5.2. Microstructural analysis of intrusion-related deformation structures

Microstructural analyses (petrographical and SEM studies) have been carried out for a number of samples of deformed rocks (both host rock and intrusion) collected during field season 1; however many more were also collected during field season 2 (from around the wider Maiden Creek intrusion study area; i.e. Zones 1, 2 and 4 in Chapter 5) which are yet to be cut and analysed. In order to progress aspects of Chapter 5 to publication, microstructural support may be beneficial.

7.5.3. Fracture spacing

Further analyses, such as quantitative porosity studies (similar to those of Morgan et al., 2008) could be carried out on the fracture spacing study samples. In addition, SEM studies, primarily Na-K mapping of polished thin sections, would help identify the amount of feldspar present in the samples and to see if the cataclasis along deformation bands preferentially occurs along certain lithological bands (e.g. those more rich in feldspars, or those more quartz-rich).

Stochastic modelling (e.g. using FracMan[®]) of fracture networks based on the results from Chapter 4 could be used to simulate fluid flow models in host rocks around shallow-level intrusions. The integration of laser scan imagery could also be considered (although further laser scans would need to be acquired).

7.5.4. Textural studies and crystal size distribution (CSD) of the intrusions

Originally the research project, in addition to studying syn-emplacement deformation of host rocks, also aimed to develop an understanding of the internal textural evolution of sill and laccolith intrusions, through carrying out micro-scale textural and geochemical studies of plagioclase-feldspar and hornblende phenocryst populations preserved within the intrusions of the Henry Mountains. Pilot studies were carried out on textural characteristics of igneous samples collected from the Mount Hillers intrusive complex. These included: petrographical analyses of thin sections; scanning electron microscopy (SEM) quantitative and qualitative studies of zoned plagioclase-feldspar phenocrysts, and trialling of automated methodologies for carrying out crystal size distribution (CSD) analyses of rock samples. However, it was decided to focus on the structural side of the project due to time constraints.

The pilot studies did, however, highlight several interesting lines of investigation. X-ray maps of zoned phenocrysts using an SEM to map qualitatively, for example, Na-rich versus Ca-rich zones in plagioclase could provide information regarding the various stages of magma ascent and emplacement, and time residency histories. Thermal barometry of amphibole phenocrysts (or xenoliths) could help to determine a number of parameters, including: temperature; pressure; depth of magma source; and rate of magma ascent.

Following extensive background research (literature review and conversations with experts in the field at Tata Steel laboratories in Holland), two possible effective work flows have been formulated for carrying out CSD analyses on samples analysed in this project. One is more automated and thus faster, but requires access to specific computer imagery software. The other, more traditional manual method is far more time consuming. However, the benefit of the manual methodology is that each step of the analytical work flow is transparent, whereas with the automated work flow the ability of the software to accurately pick out individual grains must be trusted, and the highly altered nature of many of the hornblende phenocrysts, along with the presence of several holes in the sections analysed, cause problems. Therefore the more laborious traditional and manual methodology for carrying out CSD studies is preferred. It was for this reason that CSD studies were not progressed further during the PhD project.

Of these various textural studies, crystal size distribution would be the most valuable addition to the structural data collected in this study, and could help to provide further insights into emplacement mechanisms of both intrusions. Magma viscosity plays a critical role in emplacement, and CSD studies could provide answers as to the crystal to melt ratio of the magmas as they were emplaced. Consistent CSD throughout an intrusive body would suggest that the textural characteristics of the magma had already been determined before being emplaced; whereas, varying CSD would imply that the magma was still in a state of flux during emplacement, continuing to crystallise and cool during and/ or post emplacement.

References

- Ablay, G.J., Clemens, J.D. and Petford, N., 2008. Large-scale mechanics of fracture-mediated felsic magma intrusion driven by hydraulic infiltration and buoyancy pumping. In: Thomson, K. and Petford, N. (Eds), *Structure and Emplacement of High-Level Magmatic Systems*. Geological Society of London, Special Publication, 302, 3-31.
- Adler, P.M. and Thovret, J.F., 1999. *Fractures and fractures networks (theory and applications of transport in porous media)*. Springer. 431 pp.
- Allmendinger, R.W., Hauge, T.A., Hauser, E.C., Potter, C.J., Klemperer, S.L., Nelson, K.D., Knuepfer, P. and Oliver, J., 1987. Overview of the COCORP 40 degree N Transect, western United States: The fabric of an orogenic belt. *Geological Society of America Bulletin*, 98, 308–319, doi:10.1130/0016-7606(1987)98<308:OOTCNT>2.0CO; 2
- Anderson, E.M., 1938. The dynamics of sheet intrusions. *Proceedings of the Royal Society of Edinburgh*, 58, 242-251.
- Anderson, E.M., 1951. *Dynamics of faulting and dyke formation with application to Britain (second edition)*. Edinburgh, Oliver and Boyd Limited, 206 pp.
- Annen, C., Blundy, J.D. and Sparks, R.S.J., 2006. The Genesis of Intermediate and Silicic Magmas in Deep Crustal Hot Zones. *Journal of Petrology*, 47, 505-539. doi: 10.1093/petrology/egi084
- Antonellini, M. and Aydin, A., 1995. Effect of faulting on fluid flow in porous sandstones: geometry and spatial distribution. *American Association of Petroleum Geologists Bulletin*, 79, 642-670.
- Armstrong, R.L., 1968. Sevier Orogenic Belt in Nevada and Utah. *Geological Society of America Bulletin*, 79, 429–458, doi:10.1130/0016-7606(1968)79[429:SOBINA]2.0.CO;2
- Armstrong R.L., Leeman W.P. and Malde H.E., 1975. K–Ar dating Quaternary and Neogene volcanic rocks of the Snake River Plain, Idaho. *American Journal of Science*, 275:3, 225–251.
- Atwater, T., 1970. Implications of plate tectonics for the Cenozoic tectonic evolution of western North America, *Geological Society of America Bulletin*, 81, 3513–3536, doi: 10.1130/0016-7606(1970)81[3513:IOPTFT]2.0.CO;2.
- Aydin, A., 1978. Small faults formed as deformation bands in sandstone. *Pure & Applied Geophysics*, 116, 913–930.

- Aydin, A. and Johnson, A.M., 1978. Development of faults as zones of deformation bands and as slip surfaces in sandstone. *Pure and Applied Geophysics*, 116, 931–942.
- Aydin, A. and Johnson, A.M., 1983. Analysis of faulting in porous sandstones. *Journal of Structural Geology*, 5, 19–31.
- Aydin, A., Borja, R.I. and Eichhubl, P. 2006. Geological and mathematical framework for failure modes in granular rock. *Journal of Structural Geology*, 28, 83–98.
- Bachmann, O. & Burgantz, G., 2008. The magma reservoirs that feed supereruptions. *Elements*, 4, 17–21.
- Baer, G., 1995. Fracture propagation and magma flow in segmented dykes: field evidence and fabric analysis, Makhtesh Ramon, Israel. In: Baer, G. and Heinmann, A.A. (eds.), *Physics and Chemistry of dykes*. Rotterdam, Balkema, 125-140.
- Bazard, D.R. and Butler, R.F., 1992. Paleomagnetism of the Middle Jurassic Summerville Formation, East Central Utah. *Journal of Geophysical Research*, 97, no. B4, 4377–4385.
- Bense, V.F., Van den Berg, E.H. and Van Balen, R.T. 2003. Deformation mechanisms and hydraulic properties of fault zones in unconsolidated sediments; the Roer Valley Rift System, The Netherlands. *Hydrogeology Journal*, 11, 319–332.
- Berkowitz, B., 1995. Analysis of fracture network connectivity using percolation theory. *Mathematical Geology*, 27, 467–483.
- Bird, P., 1988. Formation of the Rocky Mountains, western United States: A continuum computer model. *Science*, 239, 1501–1507, doi:10.1126/science.239.4847.1501.
- Blakey, R.C., 1989. Triassic and Jurassic geology of the Southern Colorado Plateau. In: Jenney, J. P. and Reynolds, S. J. (Eds), *Geologic evolution of Arizona: Tucson, Arizona Geological Society Digest 17*, 369–396.
- Blakey, R. C. and Ranney, W., 2008. *Ancient Landscapes of the Colorado Plateau*. Grand Canyon Association, 176 p.
- Bleeker, W. and Hall, B., 2007. The Slave Craton: Geology and metallogenic evolution. In: Goodfellow, W.D., ed., *Mineral Deposits of Canada: A Synthesis of Major Deposit-Types, District Metallogeny, the Evolution of Geological Provinces, and Exploration Methods*. Geological Association of Canada, Mineral Deposits Division, Special Publication No. 5, 849–879.
- Bradley, J., 1965. Intrusion of major dolerite sills. *Transactions of the Royal Society of New Zealand*, 3, 27–55.

- Breitkreuz, C. and Petford, N. (Eds) 2004. Physical Geology of High-Level Magmatic Systems. Geological Society, London, Special Publications, 234.
- Buckley, S.J., Howell, J.A., Enge, H.D. and Kurz, T.H., 2008a. Terrestrial laser scanning in geology: data acquisition, processing and accuracy considerations. *Journal of the Geological Society, London*, 165, 625-638. doi: 10.1144/0016-76492007-100
- Buckley, S.J., Enge, H.D., Carlsson, C. and Howell, J.A., 2008b. Terrestrial laser scanning for use in virtual outcrop geology. *The Photogrammetric Record*, 25, 225–239. doi: 10.1111/j.1477-9730.2010.00585.x
- Bump, A.P. and Davis, G.H., 2003. Late Cretaceous–early Tertiary Laramide deformation of the northern Colorado Plateau, Utah and Colorado. *Journal of Structural Geology*, 25, 421–440.
- Burchardt, S., 2009. Mechanisms of magma emplacement in the upper crust. PhD Thesis, University of Gothenburg, Sweden. 141 pp.
- Burchfiel, B.C., Cowan, D.S. and Davis, G.A., 1992. Tectonic overview of the Cordilleran orogen in the western United States. In: Burchfiel, B.C., Lipman, P.W., Zoback, M.L. (Eds.), *The Cordilleran Orogen: Conterminous US*. Geological Society of America, Boulder, CO, 407–479.
- Burke, D.B. and McKee, E.H., 1979. Mid-Cenozoic volcano-tectonic troughs in central Nevada. *Geological Society of America Bulletin*, 90, 181–184.
- Caputo, M.V. and Pryor, W.A., 1981. Middle Jurassic tide- and wave-influenced coastal facies and paleogeography, upper San Rafael Group, east-central Utah. In: Chidsey, Jr., T.C. (ed.), *Geology of east-central Utah*. Utah Geological Association, Publication 19, 9–25.
- Cartwright, J. and Hansen, D.M., 2006. Magma transport through the crust via interconnected sill complexes. *Geology*, 34, 929–932.
- Cashman, K.V. and Marsh, B.D., 1988. Crystal size distribution (CSD) in rocks and the kinetics and dynamics of crystallisation II. Makaopuhi lava cakes. *Contributions to Mineralogy and Petrology*, 99, 292–305.
- Cashman, K.V., 1990. Textural constraints on the kinetics of crystallization of igneous rocks. *Mineralogical Society of America Reviews in Mineralogy*, 24, 259–314.
- Chevallier, L. and Woodford, A., 1999. Morphotectonics and mechanism of emplacement of the dolerite rings and sills of the western Karoo, South Africa. *South African Journal of Geology*, 102, 43–54.

- Clelland, S.M., Simolox-Tohon, D. and Gibbs, A.D., 2011. Digital Geological Mapping – developing software to address the needs of students and professionals. GSA annual meeting 2011 (Abstract)
- Clemens, J. D., and C. K. Mawer. 1992. Granitic magma transport by fracture propagation. *Tectonophysics*, 204, 339-360.
- Coleman, D.S., Gray, W. and Glazner, A.F., 2004. Rethinking the emplacement and evolution of zoned plutons: geochronologic evidence for incremental assembly of the Tuolumne Intrusive Suite, California. *Geology*, 32, 433–436.
- Condon, S.M., 1997. Geology of the Pennsylvanian and Permian Cutler Group and Permian Kaibab Limestone in the Paradox Basin, Southeastern Utah and Southwestern Colorado. USGS Bulletin, 2000-P, 46pp.
- Coney, P.J. and Evenchick, C.A., 1994. Consolidation of the American Cordilleras. *Journal of South American Earth Sciences*, 7, 241–262, doi: 10.1016/0895-9811(94)90011–6.
- Corry, C.E., 1988. Laccoliths: Mechanics of Emplacement and Growth. Special Paper Geological Society of America, 220, 110 pp.
- Cross, T.A. and Pilger, R.H., 1978. Constraints on absolute motion and plate interaction inferred from Cenozoic igneous activity in the Western United States. *American Journal of Science*, 278, 865–902.
- Cosgrove, J.W. and Hiller, R.D., 1999. Forced-fold development within Tertiary sediments of the Alba Field, UKCS: evidence of differential compaction and post-depositional sandstone remobilization. In: Cosgrove, J.W. and Ameen, M.S. (eds), *Forced Folds and Fractures*. Geological Society of London Special Publication, 169, 61–71.
- Cruden, A.R. and McCaffrey, K.J.W., 2001. Growth of plutons by floor subsidence: Implications for rates of emplacement, intrusion spacing and melt-extraction mechanisms. *Physics and Chemistry of the Earth, part A: Solid Earth and Geodesy*, 26, 303–315.
- Cruden, A.R. and McCaffrey, K.J.W., 2002. Different scaling laws for sills, laccoliths and plutons: mechanical thresholds on roof lifting and floor depression. In: Breitzkreuz, C., Mock, A., Petford, N. (eds), *First International Workshop: Physical Geology of Subvolcanic Systems—Laccoliths, Sills, and Dykes (LASI)*, Volume 20 of *Wissenschaftliche Mitteilungen des Institutes für Geologie der TU Bergakademie Freiberg*, 15–17.

- Daines, M. J., 2000. Migration of melt. In: Sigurdsson, H., Houghton, B. F., McNutt, S. R., Rymer, H. and Stix, J. (eds.), *Encyclopedia of Volcanoes*. Academic Press, San Diego, pp. 69-88.
- Davidson, J.P., Morgan, D.J. and Charlier, B.L.A., 2007. Microsampling and isotopic analysis of igneous rocks: Implications for the study of magmatic systems. *Annual Reviews of Earth and Planetary Sciences*, 35, 273–311.
- Davis, G.H., 1978. Monocline fold pattern of the Colorado Plateau. In: Matthews, V.I. (Ed.), *Laramide Folding Associated with Basement Block Faulting in the Western United States*. Geological Society of America Memoir, 151, pp. 215–233.
- Davis, G.H., 1999. Structural geology of the Colorado Plateau region of southern Utah, with special emphasis on deformation bands. Geological Society of America, *Special Papers*, 342.
- Davis, G.H. and Bump, A.P., 2009. Structural geologic evolution of the Colorado Plateau. *Geological Society of America Memoirs*, 204, 99–124.
- DeCellas, P.G. and Coogan, J.C., 2006. Regional structure and kinematic history of the Sevier Fold and Thrust Belt, central Utah. *Geological Society of America Bulletin*, 118, 841–864.
- Delaney, P.T. and Pollard, D., 1981. Deformation of host rocks and flow of magma during growth of Minette dikes and breccia-bearing intrusions near Ship Rock, New Mexico. *United States Geological Survey Professional Paper* 1202.
- De Paola, N., Holdsworth, R.E., McCaffrey, K.J.W. and Barchi, M.R., 2005. Partitioned transtension: an alternative to basin inversion models. *Journal of Structural Geology*, 27, 607–625.
- de Saint Blanquat, M. and Tikoff, B., 1997. Development of magmatic to solid-state fabrics during syntectonic emplacement of the Mono Creek granite, Sierra Nevada Batholith, California. In: Bouchez, J.-L., Stephens, W. E. and Hutton, D. H. (eds), *Granite from melt segregation to emplacement fabrics*. Springer, 231–252.
- de Saint Blanquat, M., Habert, G., Horsman, E., Morgan, S., Tikoff, B., Launeau, P. and Gleizes, G., 2006. Mechanisms and duration of non-tectonically, assisted magma emplacement in the upper crust: Black Mesa pluton, Henry Mountains, Utah, *Tectonophysics*, 428, 1–31, doi:10.1016/j.tecto.2006.07.014.
- Dickinson, W.R., 1997. Tectonic implications of Cenozoic volcanism in central California. *Geological Society of America Bulletin*, 109, 936–954, doi:10.1130/0016-7606(1997)109<0936:OTIOCV>2.3.CO;2.

- Dickinson, W.R., 2002. The Basin and Range province as a composite extensional domain. *International Geology Review*, 44, 1–38, doi:10.2747/0020-6814.44.1.1.
- Dickinson, W.R. and Lawton, T.F., 2003. Sequential suturing as the ultimate control for Pennsylvanian Ancestral Rocky Mountains deformation. *Geology*, 31, 609–612, doi:10.1130/0091-7613(2003)031<0609:SISATU.>2.0.CO;2.
- Doelling, H.H., 1975. Geology and mineral resources of Garfield County, Utah. *Utah Geological and Mineral Society Bulletin* 107, 175 pp.
- Dolnick, E., 2001. *Down the Great Unknown: John Wesley Powell's 1869 journey of discovery and tragedy through the Grand Canyon*. Harper Collins Publishers, 384 pp.
- Dubiel, R.F., Huntoon, J.E., Condon, S.M. and Sanesco, J.D. 1996. Permian deposystems, paleogeography, and paleoclimate of the Paradox basin and vicinity. In: Longman, M.W. and Sonnenfield, M.D. (Eds.), *Paleozoic Systems of the Rocky Mountains Region*. Rocky Mountains Section, SEPM (Society of Sedimentary Geology), 2, 427-444.
- Du Toit, A. L., 1920. The Karoo dolerite of South Africa: a study of hypabyssal injection. *Transactions of the Geological Society of South Africa*, 23, 1–42.
- Ellam, R. M. and Hawkesworth, C. J., 1988. Is average continental crust generated at subduction zones? *Geology*, 16, 314-317.
- Engel, C.G., 1959. Igneous rocks and constituent hornblendes of the Henry Mountains, Utah. *Geological Society of America Bulletin*, 70, 951–980, doi: 10.1130/0016-7606(1959)70[951:IRACHO]2.0.CO;2.
- England, P.C. and Houseman, G.A., 1988. The mechanics of the Tibetan Plateau. *Royal Society of London Philosophical Transactions, ser. A*, 326, 301–320, doi: 10.1098/rsta.1988.0089.
- Farmin, R., 1941. Host-rock inflation by veins and dikes at Grass Valley, California. *Economic Geology*, 36, 143–174.
- Fillmore, R., 2011. *Geological evolution of the Colorado Plateau of Eastern Utah and Western Colorado*. The University of Utah Press, 496 pp.
- Fisher, Q.J. and Knipe, R.J. 2001. The permeability of faults within siliciclastic petroleum reservoirs of the North Sea and Norwegian Continental Shelf. *Marine and Petroleum Geology*, 18, 1063–1081.
- Flowers, R.M., Wernicke, B.P. and Farley, K.A., 2008. Unroofing, incision, and uplift history of the southwestern Colorado Plateau from apatite (U-Th)/He

- thermochronometry. *Geological Society of America Bulletin*, 120, 571–587, doi: 10.1130/B26231.1.
- Fossen, H. and Bale, A., 2007. Deformation bands and their influence on fluid flow. *American Association of Petroleum Geologists Bulletin*, 91, 1685-1700. doi:10.1306/07300706146
- Fossen, H., Schultz, R.A., Shipton, Z.K. and Mair, K., 2007. Deformation bands in sandstone: a review. *Journal of the Geological Society, London*, 164, 755–769, doi: 10.1144/0016-76492006-036.
- Fossen, H. 2010. *Structural Geology*. Cambridge University Press, 463 pp., ISBN: 978-0-521-51664-8.
- Fouch, M.J., 2012. The Yellowstone Hotspot: Plume or Not? *Geology*, 40, 479-480, doi: 10.1130/focus052012.1
- Francis, E. H., 1982. Magma and sediment – I. Emplacement mechanism of late Carboniferous tholeiite sills in northern Britain. *Journal of the Geological Society, London*, 139, 1–20.
- Frehner, M., 2011. Neutral lines in buckle folds. *Journal of Structural Geology*, 33, 1501-1508
- Frid, V., Bahat, D. and Rabinovich, A., 2005. Analysis of en echelon/hackle fringes and longitudinal splits in twist failed glass samples by means of fractography and electromagnetic radiation: *Journal of Structural Geology*, 27, 145-159.
- Gabrielse, H., Snyder, W.A. and Stewart, J.H., 1983. Sonoma orogeny and Permian to Triassic tectonism in western North America. *Geology*, 11, 484–486, doi: 10.1130/0091-7613(1983)11<484:SOAPTT>2.0.CO;2.
- Galland, O., Planke, S., Neumann, E.-R. and Malthe-Sørensen, A., 2009. Experimental modelling of shallow magma emplacement: application to saucer-shaped intrusions. *Earth and Planetary Sciences Letters*, 277, 373–383. DOI: 10.1016/j.epsl.2008.11.003
- Gibson, R.G. 1998. Physical character and fluid-flow properties of sandstone derived fault zones. In: Coward, M.P., Johnson, H. & Daltaban, T.S. (eds) *Structural Geology in Reservoir Characterization*. Geological Society, London, Special Publications, 127, 83–97.
- Gilbert, G.K., 1877. *Geology of the Henry Mountains, Utah*; U.S. Geographical and Geological Survey of the Rocky Mountain Region, 170 pp.
- Gilbert, G.K., 1896. Laccolites in southeastern Colorado. *Journal of Geology*, 4, 816–825.

- Gill, J. B., 1981. Orogenic andesites and plate tectonics. Springer, 390 pp.
- Glazner, A.F. and Bartley, J.M., 1984. Timing and tectonic setting of Tertiary low-angle normal faulting and associated magmatism in the Southwestern United States. *Tectonics*, 3, 385–396.
- Glazner, A.F., Bartley, J.M., Coleman, D.S., Gray, W. and Taylor, R.Z., 2004. Are plutons assembled over millions of years by amalgamation from small magma chambers? *GSA Today*, 4–11, doi: 10.1130/1052-5173(2004)013!0004:APAOMOO.
- Graham, D.J. and Midgley, N.G., 2000. Graphical representation of particle shape using triangular diagrams: an Excel spreadsheet method. *Earth Surface Processes and Landforms* 25, 1473-1477.
- Grove, T. L. and Kinzler, R. J., 1986. Petrogenesis of andesites. *Annual Review of Earth and Planetary Science*, 14, 417-454.
- Habert, G. and de Saint-Blanquat, M., 2004. Rate of construction of the Black Mesa bysmalith, Henry Mountains, Utah, USA. In: Breitskreutz, C. and Petford, N. (Eds) *Physical geology of high-level magmatic systems*. Geological Society, London, Special Publication, 234, 143–159.
- Hansen, D. M. and Cartwright, J., 2006. The three-dimensional geometry and growth of forced folds above saucer-shaped igneous sills. *Journal of Structural Geology*, 28, 1520–1535, doi: 10.1016/j.jsg.2006.04.004.
- Harry, D. L., Sawyer, D. S. and Leeman, W. P., 1993. The mechanics of continental extension in western North America: Implications for the magmatic and structural evolution of the Great Basin. *Earth and Planetary Sciences Letters*, 117, 59–71, doi:10.1016/0012-821X(93)90117-R.
- Hatcher, Jr., R.D., 2010. The Appalachian orogeny: A brief summary. *Geological Society of America Memoirs*, 206, 1–19, doi: 10.1130/2010.1206(01).
- Higgins, M.D., 2000. Measurement of crystal size distributions. *American Mineralogist*, 85, 1105–1116.
- Hincks, G. 2004. Earth Science Illustration Library [online]. Available from <http://www.garyhincks.com> and www.sciencephoto.com/media/167744/view
- Hintze, L.F., 1963. Geologic history of Utah. *Brigham Young University Geology Studies*, v. 20, pt. 3, 181 pp.
- Hintze, L.E. and Kowallis, B.J., 2009. A field guide to Utah's Rock: Geological History of Utah. *Brigham Young University Geology Studies Special Publication* 9, 225 pp.

- Hodgetts, D., Drinkwater, N.J., Hodgson, J., Kavanagh, J., Flint, S.S., Keogh, K.J. and Howell, J.A., 2005. Three-dimensional geological models from outcrop data using digital data collection techniques: an example from the Tanqua Karoo depocentre, South Africa. In: Curtis, A. and Wood, R. (eds), *Geological Prior Information: Informing Science and Engineering*. Geological Society of London, Special Publication 239, 57–75.
- Hoffman, P., 1988. United Plates of America, the birth of a craton: Early Proterozoic assembly and growth of Laurentia. *Annual Review of Earth and Planetary Science*, 16, 543–603.
- Holdsworth, R.E., McErlean, M.A. and R.A. Strachan, R.A., 1999. The influence of country rock structural architecture during pluton emplacement: the Loch Loyal syenites, Scotland. *Journal of the Geological Society of London*, 156, 163–175
- Holford, S.P., Schofield, N., Macdonald, J.D., Duddy, I.R. and Green, P.F., 2012. Seismic analysis of igneous systems in sedimentary basins and their impacts on hydrocarbon prospectivity: examples from the southern Australian margin. *The APPEA Journal*, 52.52.
- Horsman, E., Tikoff, B. and Morgan, S., 2005. Emplacement related fabric in a sill and multiple sheets in the Maiden Creek sill, Henry Mountains, Utah. *Journal of Structural Geology*, 27, 1426–1444. doi:10.1016/j.jsg.2005.03.003.
- Horsman, E., Morgan, S., de Saint-Blanquat, M., Habert, G., Nugent, A., Hunter, R.A. and Tikoff, B., 2009. Emplacement and assembly of shallow intrusions from multiple magma pulses, Henry Mountains, Utah. *Earth and Environmental Science Transactions of the Royal Society of Edinburgh*, 100, 117-132. doi: 10.1017/S1755691009016089.
- Horsman, E., Morgan, S., de Saint-Blanquat, M. and Tikoff, B., 2010 Emplacement and assembly of shallow intrusions, Henry Mountains. Field guide for the 2010 LASI IV conference, Utah, U.S.A.
http://www1.dst.unipi.it/dst/rocchi/LASI/Conferences_files/LASI4-Guidebook.pdf
- Huffman Jr., A.C. and Taylor, D.T., 1997. Relationship of Basement Faulting to Laccolithic Centers of Southeastern Utah and Vicinity. *U.S. Geological Survey Bulletin* 2158, 41–44.
- Humphreys, E., Hessler, E., Dueker, K., Farmer, G., Erslev, E. and Atwater, T., 2003. How Laramide-age hydration of North American lithosphere by the Farallon slab

- controlled subsequent activity in the western United States. *International Geology Review*, 45, 575–595, doi: 10.2747/0020-6814.45.7.575.
- Hunt, C.B., 1953. *Geology and Geography of the Henry Mountains Region, Utah*. U.S. Geological Survey Professional Paper, 228, 234 pp.
- Hunt, C.B., 1988. *Geology of the Henry Mountains, Utah, as recorded in the notebooks of G. K. Gilbert, 1875-1876*. Geological Society of America, Memoir 167, 229 pp.
- Hunt, G.L. 1988. Petrology of the Mt. Pennell central stock, Henry Mountains, Utah. *Brigham Young University Geology Studies*, 35, 81–100
- Hunt, C.B., 1997. Around the Henry Mountains with Charlie Hanks, Some Recollections. *U.S. Geological Survey Bulletin* 2158, 247–256.
- Huppert, H. and Sparks, R.S.J., 1988. The Generation of Granitic Magmas by Intrusion of Basalt into Continental Crust. *Journal of Petrology*, 29, 599-624. doi: 10.1093/petrology/29.3.599
- Hutton, D.H.W., 1996. The 'space problem' in the emplacement of granite. *Episodes, Journal of International Geoscience*, 19, no 4.
- Hutton, D.H.W., 2009. Insights into magmatism in volcanic margins: bridge structures and a new mechanism of basic sill emplacement – Theron Mountains, Antarctica. *Petroleum Geoscience*, 15, 269–278, doi:10.1144/1354-079309-841.
- Hutton, D. H. W., Dempster, T. J., Brown, P. E. and Decker, S. D., 1990. A new mechanism of granite emplacement: intrusion in active extensional shear zones. *Nature* 343, 452–455.
- Hutton, D.H.W. and McErlean, M., 1991. Silurian and Early Devonian sinistral deformation of the Ratagain granit, Scotland: constraints on the age of Caledonian movements on the Great Glen fault system. *Journal of the Geological Society, London*, 148, 1-4.
- Irwin, W.P., 1990. Geology and plate-tectonic development. In: Wallace, R.E. (ed.), *The San Andreas Fault system, California*: U.S. Geological Survey Professional Paper 1515, 61–80.
- Jackson, S.E. and Pollard, D.D., 1988. The laccolith-stock controversy: New results from the southern Henry Mountains, Utah. *Geological Society of America Bulletin*, 100, 117–139. doi: 10.1130/0016-7606.
- Jackson, S.E. and Pollard, D.D., 1990. Flexure and faulting of sedimentary host rocks during growth of igneous domes, Henry Mountains, Utah. *Journal of Structural Geology*, 12, 185–206, doi:10.1016/0191-8141(90)90004-I.

- Johnson, A.M. and Pollard, D.D., 1971. Mechanical Analysis of Rock Deformation Associated with High-level Intrusions: Final Report to the National Science Foundation. Rock Mechanics Laboratory, School of Earth Sciences, Stanford University, 500 pp.
- Johnson, A.M. and Pollard, D.D., 1973. Mechanics of growth of some laccolithic intrusion in the Henry Mountains, Utah, I: Field observations, Gilbert's model, physical properties and flow of the magma. *Tectonophysics*, 18, 261–309, doi: 10.1016/0040-1951(73)90050-4.
- Johnson, C.M., 1991. Large-scale crust formation and lithosphere modification beneath middle to late Cenozoic calderas and volcanic fields, western North America. *Journal of Geophysical Research*, B, 96, 13,485–13,507.
- Johnson, K.M., and Johnson, A.M., 2002. Mechanical analysis of the geometry of forced-folds. *Journal of Structural Geology*, 24, 401–410.
- Jones, R.R., McCaffrey, K.J.W., Wilson, R.W. and Holdsworth, R.E., 2005. Digital field data acquisition: towards increased quantification of uncertainty during geological mapping. In: Curtis, A. and Wood, R. (eds), *Geological Prior Information: Informing Science and Engineering*. Geological Society of London, Special Publication, 239, 43–56.
- Jones, R.R., McCaffrey, K.J.W., Clegg, P., Wilson, R.W., Holliman, N.S., Holdsworth, R.E., Imber, J. and Waggott, S., 2009. Integration of regional to outcrop digital data: 3D visualisation of multi-scale geological models. *Computers and Geosciences*, 35, 4–18.
- Jones, S.F., Wielens, H., Williamson, M.C. and Zentilli, M., 2007. Impact of magmatism on petroleum systems in the Sverdrup Basin, Canadian Arctic Islands, Nunavut: a numerical modelling study. *Journal of Petroleum Geology*, 30, 237–255.
- Kauffman, E.G., 1984. Paleobiogeography and evolutionary response dynamic in the Cretaceous Western Interior Seaway of North America. *Geological Association of Canada Special Paper* 27, 273–306.
- Kavanagh, J.L., Menand, T and Sparks, R.S.J., 2006. An experimental investigation of sill formation and propagation in layered elastic media. *Earth and Planetary Science Letters*, 245, 799–813.
- Kerr, A. D. and Pollard, D. D., 1998. Towards more realistic formulations for the analysis of laccoliths. *Journal of Structural Geology*, 20, 1783–1793.

- Knipe, R.J., Fisher, Q.J., Jones, G., Clennell, M.R., Farmer, A., Harrison, B., Kidd, B., Mcallister, E., Porter, J.R. and White, E.A., 1997. Fault seal analysis: successful methodologies, application and future directions. In: Møller-Pedersen, P. & Koestler, A.G. (eds) *Hydrocarbon Seals: Importance for Exploration and Production*. Norwegian Petroleum Society Special Publication, 7, 15–38.
- Koch, F.G., Johnson, A.M. and Pollard, D.D., 1981. Monoclinal bending of strata over laccolith intrusions. *Tectonophysics*, 74, T21–T31
- Kocurek, G. and Dott, R.H., 1983. Jurassic paleogeography and paleoclimate of the central and southern Rocky Mountains region. In: Reynolds, M.W. and Dolly, E.D. (eds), *Mesozoic paleogeography of the west-central United States*. Rocky Mountains Paleogeography Symposium 2, Society of Economic Palaeontologists and Mineralogists, 101–118.
- Krantz, R.W. (1989). Orthorhombic fault patterns: the odd axis model and slip vector orientations. *Tectonics*, 8, 483–495.
- Larson M.J, Bromfield C.S., Dubiel R.F., Patterson C.G. and Peterson F., 1985. Geologic map of the Little Rockies wilderness study area and the Mt. Hillers and Mt. Pennell study areas, and vicinity, Garfield County, Utah. U.S. Geological Survey Map MF-1776-B.
- Leaman, D. E., 1975. Form, mechanism, and control of dolerite intrusion near Hobart, Tasmania. *Journal of the Geological Society of Australia*, 22, 175–186.
- Li, Z.X, Bogdanova, S.V., Collins, A.S., Davidson, A., De Waele, B., Ernst, R.E., Fitzsimons, I.C.W., Fuck, R.A., Gladkochub, D.P., Jacobs, J., Karlstrom, K.E., Lu, S., Natapov, L.M., Pease, V., Pisarevsky, S.A., Thrane, K. and Vernikovsky, V., 2008. Assembly, configuration, and break-up history of Rodinia: a synthesis. *Precambrian Research*, 160, 179–210.
- Liu, L. and Gurnis, M., 2010. Dynamic subsidence and uplift of the Colorado Plateau. *Geology*, 38, 663–666.
- Lyell, C., 1830. *Principals of Geology, Being an Attempt to Explain the Former Changes of the Earth's Surface, by Reference to Causes Now in Operation* (Murray, London) 3 vols.
- MacCarthy, G.R., 1925. Some facts and theories concerning laccoliths. *Journal of Geology*, 33, 1–18.
- Magee, C., Stevenson, C. T., O'Driscoll, B. and Petronis, M., 2012. Local and regional controls on the lateral emplacement of the Ben Hiant dolerite intrusion,

- Ardnamurchan (NW Scotland). *Journal of Structural Geology*, 39, 66–82, doi.org/10.1016/j.jsg.2012.03.005
- Magee, C., Jackson C.A-L. and Schofield, N., 2013. The influence of normal fault geometry on igneous sill emplacement and morphology. *Geology*, 41, 407–410. ISSN:0091-7613
- Magee, C., Jackson, C.A-L. and Schofield, N., 2014. Diachronous sub-volcanic intrusion along deep-water margins: insights from the Irish Rockall Basin. *Basin Research*, 26, 85-105. doi: 10.1111/bre.12044
- Mahan, K.H., Bartley, J.M., Coleman, D.S., Glazner, A.F. and Carl, B., 2003. Sheeted intrusion of the synkinematic McDoogie pluton, Sierra Nevada, California. *Geological Society of America Bulletin*, 115, 1570–1582.
- Mahon, K. I., Harrison, T. M. and Drew, D. A., 1988. Ascent of a granitoid diapir in a temperature varying medium. *Journal of Geophysical Research* 93, 1174 - 1188.
- Mäkel, G.H., 2007. The modelling of fractured reservoirs: constraints and potential for fracture network geometry and hydraulics analysis. Geological Society, London, Special Publications, 292, 375-403.
- Malthe-Sørrensen, A., Planke, S., Svensen, H. and Jamtveit, B., 2004. Formation of saucer-shaped sills. In: Breiterkreuz, C. and Petford, N. (eds.), *Physical Geology of High-level Magmatic Systems*. Geological Society of London, Special Publications, 324, 215–227.
- Mandl, G., DeJong, L.N.J. and Maltha, A. 1977. Shear zones in granular material. *Rock Mechanics*, 9, 95–144.
- Manzocchi, T., 2002. The connectivity of two dimensional networks of spatially correlated fractures. *Water Resources Research* 38, doi:10.1029/2000WR000180.
- Marsh, B. D., 1984. Mechanics and energetics of magma formation and ascension. In: Boyd, F. R. (ed.), *Studies in Geophysics: Explosive Volcanism, Inception, Evolution and Hazards*. National Academic Press, Washington D.C., 67-83.
- Marsh, B.D., 1988a. Crystal size distribution (CSD) in rocks and the kinetics and dynamics of crystallization 1. Theory. *Contributions to Mineralogy and Petrology*, 99, 277–291.
- Marsh, B.D., 1988b. On the interpretation of crystal size distributions in magmatic systems. *Journal of Petrology*, 39, 553–599.
- Marsh, B.D., 1989. Magma chambers. *Annual Review of Earth and Planetary Sciences*, 17, 439–474.

- Marshak, S. and Paulsen, T., 1996. Midcontinent U.S. fault and fold zones: A legacy of Proterozoic intracratonic extensional tectonism? *Geology*, 24, 151–154.
- Marshak, S., Karlstrom, K. and Timmons, J.M., 2000. Inversion of Proterozoic extensional faults: An explanation for the pattern of Laramide and Ancestral Rockies intracratonic deformation. *Geology*, 28, 735–738, doi: 10.1130/0091-7613(2000)28<735:IOPEFA>2.0.CO;2.
- Mauldon, M., Dunne, W.M. and Rohrbaugh, M.B., 2001. Circular scanlines and circular windows: new tools for characterizing the geometry of fracture traces. *Journal of Structural Geology*, 23, 247-258.
- McClay, K.R. and Ellis, P.G. 1987. Geometries of extensional fault systems developed in model experiments. *Geology*, 15, 341–344.
- McCaffrey, K. J. W., 1992. Igneous emplacement in a transpressive shear zone: Ox Mountains igneous complex. *Journal of the Geological Society, London*, 149, 221-35.
- McCaffrey, K.J.W. and Cruden, A.R., 2002. Dimensional data and growth models for intrusions. In: Breitzkreuz, C., Mock, A., Petford, N. (eds.), *First International Workshop: Physical Geology of Subvolcanic Systems—Laccoliths, Sills, and Dykes (LASI)*, Volume 20 of *Wissenschaftliche Mitteilungen des Institutes für Geologie der TU Bergakademie Freiberg*, 37–39.
- McCaffrey, K. J. W. and Petford, N., 1997. Are granitic intrusions scale invariant? *Journal of the Geological Society, London*, 154, 1–4.
- McCaffrey, K. J. W., Jones, R. R., Holdsworth, R. E., Wilson, R. W., Clegg, P., Imber, J., Holliman, N. and Trinks, I., 2005. Unlocking the spatial dimension: Digital technologies and the future of geoscience fieldwork, *Journal of the Geological Society London*, 162, 927 – 938.
- McQuarrie, N. and Chase, C.G., 2000. Raising the Colorado Plateau. *Geology*, 28, 91–94, doi: 10.1130/0091-7613(2000)028<0091:RTCP>2.0.CO;2.
- McQuarrie, N. and Oskin, M., 2010. Palinspastic restoration of NAVDat and implications for the origin of magmatism in southwestern North America. *Journal of Geophysical Research*, 115, 16 pp., doi: 10.1029/2009JB006435.
- Menand, T., 2008. The mechanics and dynamics of sills in layered elastic rocks and their implications for growth of laccoliths and other igneous complexes, *Earth Planetary Sciences Letters*, 267, 93–99, doi: 10.1016/j.epsl.2007.11.043.

- Menand, T., de Saint-Blanquat, M. and Annen, C. J., 2011. Emplacement of Magma Pulses and Growth of Magma Bodies. *Tectonophysics*, 500, 1 – 2, doi: 10.1016/j.tecto.2010.05.014
- Menand, T., Annen, C. and de Saint Blanquat, M., 2015. Rates of magma transfer in the crust: Insights into magma reservoir recharge and pluton growth. *Geology*, 43, 199-202. doi: 10.1130/G36224.1
- Miall, A. D. and Blakey, R. C., 2008. The Phanerozoic tectonic and sedimentary evolution of North America. In: Miall, A. D. (Ed.), *Sedimentary Basins of United States and Canada*: Elsevier, Amsterdam p. 1-29.
- Morgan, D.J., Blake, S., Rogers, N.W., De Vivo, B., Rolandi, G. and Davidson, J.P., 2006. Magma chamber recharge at Versuvius in the century prior to the eruption of AD79. *Geology*, 34, 845–848.
- Morgan, S., Horsman, E., Tikoff, B., de Saint-Blanquat, M. and Habert, G., 2005. Sheet-like emplacement of satellite laccoliths, sills, and bysmaliths of the Henry Mountains, Southern Utah. *GSA Field Guides*, 6, 283-309. doi: 10.1130/2005.fld006(14)
- Morgan, S., Stanik, A., Horsman, E., Tikoff, B., de Saint Blanquat, M. and Habert., G., 2008. Emplacement of multiple magma sheets and wall rock deformation: Trachyte Mesa intrusion, Henry Mountains, Utah. *Journal of Structural Geology*, 30, 491–512, doi: 10.1016/j.jsg.2008.01.005.
- Moucha, R., Forte, A.M., Rowley, D.B., Mitrovica, J.X., Simmons, N.A. and Grand, S.P., 2009. Deep mantle forces and the uplift of the Colorado Plateau. *Geophysical Research Letters*, 36, L19310, doi: 10.1029/2009GL039778.
- Moulin, M., Aslanian, D. and Unternher, P., 2010. A new starting point for the South and Equatorial Atlantic Ocean. *Earth Science Reviews*, 97, 59–95, doi:10.1016/j.earscirev.2009.08.001.
- Mudge, M.R., 1968. Depth control of some concordant intrusions. *Geological Society of America Bulletin*, 79, 3, 315–332.
- Nelson, S.T., 1991. Mid-Tertiary magmatism of the Colorado Plateau – The Henry and La Sal Mountains, Utah. University of California, Los Angeles, PhD Thesis, 318 pp.
- Nelson, S.T., Davidson, J.P. and Sullivan, K.R., 1992. New age determinations of central Colorado Plateau laccoliths, Utah: Recognizing disturbed K–Ar systematics and re-evaluating tectonomagmatic relationships. *Geological Society of America Bulletin*, 104, 1547–1560.

- Nelson, S.T. and Davidson, J.P., 1993. Interactions between mantle-derived magmas and mafic crust, Henry Mountains, Utah. *Journal of Geophysical Research* B2, 98, 1837–1852.
- Nelson, S.T. and Davidson, J.P., 1997. The petrogenesis of the Colorado Plateau laccoliths and their relationship to regional magmatism. *U.S. Geological Survey Bulletin* 2158, 86–101.
- Neves, S. P., Vauchez, A. and Archanjo, C. J., 1996. Shear zone-controlled magma emplacement or magma-assisted nucleation of shear zones? Insights from northeast Brazil. *Tectonophysics*, 262, 349-364.
- Nicholson, R. and Pollard, D. D., 1985. Dilation and linkage of en-echelon cracks. *Journal of Structural Geology*, 7, 583-590.
- Ogilvie, S. R. and Glover, P. W. J., 2001. The petrophysical properties of deformation bands in relation to their microstructure: *Earth and Planetary Science Letters*, 193, 129–142.
- Paquette, J.L., Saint-Blanquat (de), M., Delpech, G., Horsman, E. and Morgan, S.S., 2010. LA-ICPMS U-Pb zircon dating of Mount Hillier laccolite and satellite intrusions: rapid emplacement and large Proterozoic inheritance. *Physical Geology of Subvolcanic Systems: Laccolith, Sills and Dykes, LASI IV conference, Utah, Abstracts*, p. 41.
- Parnell, J., Watt, G.R., Middleton, D., Kelly, J. and Barton, M., 2004. Deformation Band Control on Hydrocarbon Migration. *Journal of Sedimentary Research*, 74, 552–560. doi: 10.1306/121703740552
- Parsons, T. and Thompson, G. A., 1991. The role of magma overpressure in suppressing earthquakes and topography: Worldwide examples. *Science*, 253, 1399-1402.
- Parsons, T., Thompson, G.A. and Sleep, N.H., 1994. Mantle plume influence on Neogene uplift and extension of the U.S. western Cordillera? *Geology*, 22, 83–86, doi: 10.1130/0091-7613(1994)022<0083:MPIOTN>2.3.CO;2.
- Passchier, C. W. Zhang, J. S. and Konopasek, J., 2005. Geometric aspects of synkinematic granite intrusion into a ductile shear zone — an example from the Yunmengshan core complex, northern China. In: Bruhn, D. & Burlini, L. (eds), *High-Strain Zones: Structure and Physical Properties*. Geological Society London, Special Publication, 245, 65-80. doi: 10.1144/GSL.SP.2005.245.01.04
- Peterson, F., Ryder, R.T. and Law, B.E., 1980. Stratigraphy, sedimentology and regional relationships of the Cretaceous System in the Henry Mountain region, Utah. In:

- Picard, M.D., (ed.), Henry Mountains symposium: Utah Geological Association Publication 8, 15–170 .
- Petford, N., Lister, J.R. and Kerr, R.C., 1994. The ascent of felsic magmas in dykes. *Lithos*, 32, 161-164. doi:10.1016/0024-4937(94)90028-0
- Petit, J.-P., 1987. Criteria for the sense of movement on fault surfaces in brittle rocks. *Journal of Structural Geology*, 9, 597–608.
- Pierce K.L. and Morgan L.A., 2009. Is the track of the Yellowstone hotspot driven by a deep mantle plume? Review of volcanism, faulting, and uplift in light of new data. *Journal of Volcanology and Geothermal Research*, 188, 1–25, doi:10.1016/j.jvolgeores.2009.07.009.
- Pitcher, W.S., 1970. Ghost stratigraphy in intrusive granites: a review. In: Newall, G. and Rast, N. Eds.), *Mechanism of Igneous Intrusion*, Liverpool, Gallery Press, 123–140.
- Pollard, D.D. and Johnson, A.M., 1973. Mechanics of growth of some laccolithic intrusions in the Henry Mountains, Utah, II: bending and failure of overburden layers and sill formation. *Tectonophysics*, 18, 261–309.
- Pollard, D.D., Muller, O.H. and Dockstader, D.R., 1975. The form and growth of fingered sheet intrusions. *Geological Society of America Bulletin*, 3, 351–363.
- Poole, F., Perry, W.J., Jr., Madrid, P. and Amaya-Martinez, R., 2005. Tectonic synthesis of the Ouachita-Marathon-Sonora orogenic margin of southern Laurentia: Stratigraphic and structural implications for timing of deformational events and plate tectonic model. In: Anderson, T.H.; Nourse, J.A.; McKee, J.W.; Steiner, M.B. (Eds.), *The Mojave-Sonora megashear hypothesis: Development, assessment, and alternatives*. Geological Society of America Special Paper 393, Geological Society of America, Boulder, Colorado, 543-596.
- Powell, J. W. 1895. *Canyons of the Colorado*. 189 pp. ISBN: 0-7922-6636-1902.
- Powell, J. W., 1961. *The exploration of the Colorado River and its canyons*. Dover Publications Inc., 288 pp.
- Price, N.J. 1966. *Faults and joint development in brittle and semi-brittle rock*. New York Pergamon Press.
- Puskas, C. M., Smith, R. B., Meertens, C. M. and Chang W. L., 2007. Crustal deformation of the Yellowstone–Snake River Plain volcano-tectonic system: Campaign and continuous GPS observations, 1987–2004. *Journal of Geophysical Research*, 112, B03401, doi:10.1029/2006JB004325

- Ramirez, L.E., Palacios, C., Townley, B., Parada, M.A., Sial, A.N., Fernandez-Turiel, J.L., Gimeno, D., Garcia-Valles, M. and Lehmann, B., 2006. The Mantos Blancos copper deposit: an upper Jurassic breccia-style hydrothermal system in the coastal range of Northern Chile. *Mineral Deposits*, 41, 246–258.
- Rateau, R., Schofield, N. and Smith, M., 2013. The potential role of igneous intrusions on hydrocarbon migration, West of Shetland. *Petroleum Geoscience*, 19, 259–272.
- Rawling, G.C. and Goodwin, L.B. 2003. Cataclasis and particulate flow in faulted, poorly lithified sediments. *Journal of Structural Geology*, 25, 317–331.
- Reches, Z., 1987. Determination of the tectonic stress tensor from slip along faults that obey the Coulomb yield condition. *Tectonics*, 6, 849–861.
- Rickwood, P.C., 1990. The anatomy of a dyke and the determination of propagation and magma flow directions. In: Parker, A.J, Rickwood, P.C., and Tucker, D.H. (eds.), *Mafic Dykes and Emplacement Mechanisms*: Rotterdam, Balkema, 81-100.
- Riley, M.S., 2005. Fracture trace length and number distributions from fracture mapping. *Journal of Geophysical Research*, 110, B08414. doi: 10.1029/2004JB003164.
- Roberts, G. G., White, N. J., Martin-Brandis, G. L. and Crosby, A. G., 2012. An Uplift History of the Colorado Plateau and its surroundings from inverse modeling of longitudinal river profiles. *Tectonics*, 31, doi:10.1029/2012TC003107.
- Roberts, J.L., 1970. The intrusion of magma into brittle rocks. In: Newall, G and Rast, N. (Eds) *Mechanism of igneous intrusion*. *Geological Journal Special Issues*, 2, 287-338.
- Robinson, J.W. and McCabe, P.J., 1997. Sandstone-body and shale-body dimensions in a braided fluvial system: Salt Wash Sandstone Member (Morrison Formation), Garfield County, Utah. *American Association of Petroleum Geologists Bulletin*, 81, no. 8, 1267–1291.
- Rocchi, S., Westerman, D.S., Dini, A., Innocenti, F. and Tonarini, S., 2002. Two-stage laccolith growth at Elba Island (Italy). *Geology*, 30, 983–986.
- Rodriguez-Monreal, F., Villar, H.J., Baudino, R., Delpino, D. and Zencich, S., 2009. Modelling an atypical petroleum system: A case study of hydrocarbon generation, migration and accumulation related to igneous intrusions in the Neuquen Basin, Argentina. *Marine and Petroleum Geology*, 26, 590–605.
- Rohrbaugh, M.B., Dunne, W.M. and Mauldon, M., 2002. Estimating fracture trace intensity, density, and mean length using circular scan lines and windows. *Bulletin American Association of Petroleum Geologists*, 86, 2087-2102.

- Ross, M., 1997. Geology of the Tertiary Intrusive Centers of the La Sal Mountains, Utah – Influence of preexisting structural features on emplacement and morphology. U.S. Geological Survey Bulletin 2158, 62–85.
- Rotevatn, A., Sandve, T. H., Keilegavlen, E., Kolyukhin, D. and Fossen, H., 2013. Deformation bands and their impact on fluid flow in sandstone reservoirs: the role of natural thickness variations. *Geofluids*, 13, 359-371. doi: 10.1111/gfl.12030.
- Roy, M., Kelley, S., Pazzaglia, F., Cather, S. and House, M., 2004. Middle Tertiary buoyancy modification and its relationship to rock exhumation, cooling, and subsequent extension at the eastern margin of the Colorado Plateau. *Geology*, 32, 925–928, doi: 10.1130/G20561.1.
- Roy, M., Jordan, T.H. and Pederson, J., 2009. Colorado Plateau magmatism and uplift by warming of the heterogeneous lithosphere. *Nature*, 459, 978–984, doi:10.1038/nature08052
- Rutherford, M.J. and Gardiner, J.E., 1999. Chapter 12: Rates of Magma Ascent. In: Sigurdsson, H., Houghton, B., Rymer, H., Stix, J., and McNutt, S. (Eds). *Encyclopedia of Volcanoes*. Academic Press, 1417 pp.
- Sahagian, D., Proussevitch, A. and Carlson, W., 2002. Timing of Colorado Plateau uplift: Initial constraints from vesicular basalt-derived paleoelevations. *Geology*, 30, 807–810, doi:10.1130/0091-7613(2002)030<0807:TOCPUI>2.0.CO;2.
- Sanderson, D.J. and Nixon, C.W., 2015. The use of topology in fracture network characterization. *Journal of Structural Geology*, doi: 10.1016/j.jsg.2015.01.005.
- Schofield, N.J., 2009. Linking sill morphology to emplacement mechanisms. PhD thesis, University of Birmingham, 229 pp.
- Schofield, N., Stevenson, C. and Reston, T., 2010. Magma fingers and host rock fluidization in the emplacement of sills. *Geology*, 38, 63–66.
- Schofield, N.J., Brown, D.J., Magee, C. and Stevenson, C.T., 2012a. Sill morphology and comparison of brittle and non-brittle emplacement mechanisms. *Journal of the Geological Society, London*, 169, 127–141.
- Schofield, N.J., Heaton, L., Holford, S.P., Archer, S.G., Jackson, C.A.-L. and Jolley, D.W., 2012b. Seismic imaging of ‘broken bridges’: linking seismic to outcrop-scale investigations of intrusive magma lobes. *Journal of the Geological Society, London*, 169, 421–426, doi: 10.1144/0016-76492011-150

- Schutter, S.R., 2003a. Hydrocarbon occurrence and exploration in and around igneous rocks. In: Petford, N. and McCaffrey, K.J.W. (eds.), *Hydrocarbons in Crystalline Rocks*. Geological Society London Special Publication, 214, 7–33.
- Schutter, S.R., 2003b. Occurrences of hydrocarbons in and around igneous rocks. In: Petford, N. and McCaffrey, K.J.W. (eds.), *Hydrocarbons in Crystalline Rocks*. Geological Society London Special Publication, 214, 35–68.
- Seers, T.D. and Hodgetts, D., 2013. Comparison of digital outcrop and conventional data collection approaches for the characterization of naturally fractured reservoir analogues. In: Spence, G.H., Redfern, J., Aguilera, R., Bevan, T.G., Cosgrove, J.W., Couples, G.D., Daniel, J.M. (Eds), *Advances in the Study of Fractured Reservoirs*. Geological Society of London, Special Publication, 374, 51–77. doi: 10.1144/SP374.13
- Severinghaus, J. and Atwater, T., 1990. Cenozoic geometry and thermal state of the subducting slabs beneath western North America. In: Wernicke, B.P. (ed.), *Basin and Range extensional tectonics near the latitude of Las Vegas, Nevada*, Geological Society of America Memoir 176, 1–22.
- Shervais J.W. and Hanan B.B., 2008. Lithospheric topography, tilted plumes, and the track of the Snake River-Yellowstone hot spot. *Tectonics*, 27, TC5004, doi:10.1029/2007TC002181.
- Shipton, Z.K. and Cowie, P.A. 2001. Analysis of three-dimensional damage zone development over m to km scale range in the high-porosity Navajo sandstone, Utah. *Journal of Structural Geology*, 23, 1825–1844.
- Shipton, Z.K. and Cowie, P.A. 2003. A conceptual model for the origin of fault damage zone structures in high-porosity sandstone. *Journal of Structural Geology*, 25, 333–345.
- Skurtveit, E., Torabi, A., Alikarami, R. and Braathen, A. 2015. Fault baffle to conduit developments: reactivation and calcite cementation of deformation band fault in aeolian sandstone. *Petroleum Geoscience*, 21, 3–16. doi: 10.1144/petgeo2014-031
- Smart, K. J., Ferrill, D. A., Morris, A. P., Bichon, B. J., Riha, D. S. and Huyse, L., 2010. Geomechanical modeling of an extensional fault-propagation fold: Big Brushy Canyon monocline, Sierra Del Carmen, Texas. *AAPG bulletin*, 94, 221-240, doi: 10.1306/08050908169

- Snoke, A. W., Kalakay, T. J., Quick, J. E. and Sinigoi, S., 1999. Development of a deep-crustal shear zone in response to syntectonic intrusion of mafic magma into the lower crust, Ivrea–Verbano zone, Italy. *Earth and Planetary Science Letters*, 166, 31–45.
- Sonder, L.J. and Jones, C.H., 1999. Western United States extension: How the west was widened. *Annual Review of Earth and Planetary Sciences*, 27, 417–462, doi:10.1146/annurev.earth.27.1.417.
- Sparks, R.S.J., Baker, L., Brown, R.J., Field, M., Schumacher, J., Stripp, G. and Walters, A., 2006. Dynamical constraints on kimberlite volcanism. *Journal Volcanology Geothermal Research*, 155, 18–48.
- Spencer, J.E., 1996. Uplift of the Colorado Plateau due to lithosphere attenuation during Laramide low-angle subduction. *Journal of Geophysical Research*, 101, 13,595–13,609, doi:10.1029/96JB00818.
- Stanescio, J.D. and Campbell, J.A., 1989. Eolian and noneolian facies of the Lower Permian Cedar Mesa Sandstone Member of the Cutler Formation, southeastern Utah. *USGS Bulletin*, 1808-F, 13pp.
- Stanescio, J.D. and Dubiel, R.F., 1992. Fluvial and eolian facies of the Organ Rock Shale Member of the Cutler Formation, southeastern Utah [abs.]: *Geological Society of America, Abstracts with Programs*, v. 24, no. 6, p. 64.
- Stanescio, J.D., Huntoon, J.E. and Dubiel, R.F. 2000. Depositional environments and paleotectonics of the Organ Rock Formation of the Permian Cutler Group, southeastern Utah. In: Sprinkel, D.A., Chidsey Jr., T.C. and Anderson, P.B. (Eds.), *Geology of Utah's Parks and Monuments*. Utah Geological Association, 28, 581–605.
- Stearns, D. W., 1978. Faulting and forced folding in the Rocky Mountains foreland. *Geological Society of America Memoir*, 151, 1–37.
- Sternlof, K.R., Chapin, J.R., Pollard, D.D. and Durlofsky, L.J., 2004. Permeability effects of deformation band arrays in sandstone. *American Association of Petroleum Geologists Bulletin*, 88, 1315–1329.
- Stevenson, C.T.E., Owens, W.H., Hutton, D.H.W., Hood, D.N. and Meighan, I., 2007a. Laccolithic, as opposed to cauldron subsidence, emplacement of the Eastern Mourné pluton: Evidence from anisotropy of magnetic susceptibility. *Journal of Geological Society London*, 164, 99–110, doi: 10.1144/0016076492006-008.

- Stevenson, C.T.E., Owens, W.H. and Hutton, D.H.W., 2007b. Flow lobes in granite: The determination of magma flow direction in the Trawenagh Bay Granite, north-western Ireland, using anisotropy of magnetic susceptibility. *GSA Bulletin*, 119, 1368–1386, doi: 10.1130/B25970.1.
- Stewart, J.H., 1998. Regional characteristics, tilt domains, and extensional history of the late Cenozoic Basin and Range Province, western North America. In: *Faulds, J.E., and Stewart, J.H., eds., Accommodation Zones and Transfer Zones: The Regional Segmentation of the Basin and Range Province: Geological Society of America Special Paper 323*, 47–74, doi:10.1130/0-81372323-X.47.
- Stewart, J.H. and 19 others, 1998. Map showing Cenozoic tilt domains and associated structural features, western North America In: *Faulds, J.E., and Stewart, J.H., eds., Accommodation Zones and Transfer Zones: The Regional Segmentation of the Basin and Range Province: Geological Society of America Special Paper 323*, Plate 1, scale 1:5,000,000.
- Stokes, W.L., 1980. Stratigraphic interpretations of Triassic and Jurassic beds of the Henry Mountains area. In: *Picard, M.D., (ed.), Henry Mountains symposium: Utah Geological Association Publication 8*, 113–122.
- Sullivan, K.R., 1997. Isotopic ages of igneous intrusions in southeastern Utah. *U.S.G.S. Bulletin* 2158, pp. 33-35.
- Teyssier, C. and Tikoff, B., 1999. Fabric stability in oblique convergence and divergence. *Journal of Structural Geology*, 21, 969-974.
- Thomson, K., 2004. Sill complex geometry and internal architecture: a 3D seismic perspective. In: *Breitkreutz, C. and Petford, N. (eds.) Physical Geology of High-level Magmatic Systems. Geological Society London, Special Publication, 234*, 229–232.
- Thomson, K., 2007. Determining magma flow in sills, dikes and laccoliths and their implications for sill emplacement mechanisms. *Bulletin of Volcanology*, 67, 116-128.
- Thomson, K. and Hutton, D., 2004. Geometry and growth of sill complexes: insights using 3-d seismic from the North Rockall Trough. *Bulletin of Volcanology*, 66, 364–375.
- Thomson, K. and Petford, N., (eds) 2008. *Structure and Emplacement of High-Level Magmatic Systems. Geological Society of London, Special Publication, 302*.
- Thomson, K. and Schofield, N., 2008. Lithological and structural controls on the emplacement and morphology of sills in sedimentary basins. In: *Thomson, K. and*

- Petford, N. (Eds) Structure and Emplacement of High-Level Magmatic Systems. Geological Society of London, Special Publication, 302, 31–44.
- Tikoff, B. and Teyssier, C., 1992. Crustal-scale, en echelon "P-shear" tensional bridges: a possible solution to the batholithic room problem. *Geology*, 20, 927–930.
- Timmons, J.M., Karlstrom, K.E., Dehler, C.M., Geissman, J.W. and Heizler, M.T., 2001. Proterozoic multistage (ca. 1.1 and ca. 0.8 Ga) extension in the Grand Canyon Supergroup and establishment of northwest and north-south tectonic grains in the southwestern United States. *Geological Society of America Bulletin*, 113, 163–180, doi:10.1130/0016-7606(2001)113<0163:PMCAGE>2.0.CO;2.
- Timmons, J.M., Karlstrom, K.E. and Sears, J.W., 2003. Geologic structure of the Grand Canyon Supergroup. In: Beus, S.S. and Morales, M. (eds), *Grand Canyon Geology*, New York: Oxford University Press, 2nd Edition, 76–89.
- Tucker, M.E., 2001. *Sedimentary Petrology. An Introduction to the Origin of Sedimentary Rocks* (3rd Edition). Blackwell Science, Oxford, 262 pp.
- Turner, S.P., George, R.M.M, Evans, P.J., Hawkesworth, and Zellmer, P.J., 2000. Time-scales of magma formation, ascent and storage beneath subduction-zone volcanoes. *Philosophical Transactions of Royal Society of London, A*, 358, 1443-1464. DOI: 10.1098/rsta.2000.0598
- Tweto, O., 1951. Form and Structure of Sills Near Pando, Colorado: *Geological Society of America Bulletin*, 62, 507-532.
- Valentine, G. A. and Krogh, K. E. C., 2006. Emplacement of shallow dikes and sills beneath a small basaltic volcanic center – The role of pre-existing structure (Paiute Ridge, southern Nevada, USA). *Earth and Planetary Science Letters* 246, 217-230.
- von Buch, M., 1836. *Description physique des Iles Canaries*: Paris, 342 pp.
- Vignerresse, J.L. and Clemens, J.D. 2000. Granitic magma ascent and emplacement: neither diapirism nor neutral buoyancy. *Geological Society, London, Special Publications*, 174(1), 1-19, 10.1144/gsl.sp.1999.174.01.01.
- Walsh, J.J. and Watterson, J., 1993. Fractal analysis of fracture patterns using the standard box-counting technique: valid and invalid methodologies. *Journal of Structural Geology*, 15, 1509–1512.
- Webster, R.L., 2011. Chapter 19: Petroleum source rocks and stratigraphy of the Bakken Formation in North Dakota. In: Robinson, J.W., LeFever, J.A. and Gaswirth, S.B. (eds), *The Bakken-Three Forks Petroleum System in the Williston Basin*, Rocky Mountain Association of Geologists, 490–507

- Weimer, R.J., 1986. Relationship of unconformities, tectonics and sea-level changes in the Cretaceous of the western interior, US. *American Association of Petroleum Geologists Memoir* 41, 397–422.
- Westerman, D. S., Dini, A., Innocenti, F. and Rocchi S., 2004. Rise and fall of a nested Christmas-tree laccolith complex, Elba Island, Italy. In: Breitkreuz, C. & Petford, N. (eds). *Physical Geology of High-Level Magmatic Systems*. Geological Society of London, Special Publication, 234, 195-213.
- Wetmore, P. H., Connor, C. B., Kruse, S. E., Callihan, S., Pignotta, G., Stremtan, C. and Burke A., 2009. Geometry of the Trachyte Mesa intrusion, Henry Mountains, Utah: Implications for the emplacement of small melt volumes into the upper crust. *Geochem. Geophys. Geosyst.*, 10, Q08006, doi: 10.1029/2009GC002469.
- Whitmeyer, S.J. and Karlstrom, K.E., 2007. Tectonic model for the Proterozoic growth of North America. *Geosphere*, 3, 220–259.
- Wilson, P.I.R. and McCaffrey, K.J.W., 2013. Intrusion space problem: digital mapping and analysis of the Maiden Creek satellite intrusion, Henry Mountains Utah. *Geoscientist*, 23 (6), 16–19.
- Withjack, M.O., Olson, J. and Peterson, E., 1990. Experimental models of extensional forced folds. *AAPG Bulletin*, 74, 1038–1054.
- Wohletz, K. and Heiken, G., 1986. *Volcanology and Geothermal Energy*. University of California Press. 151 pp. <http://ark.cdlib.org/ark:/13030/ft6v19p151/>
- Wolfe, J.A., Forest, C.E. and Molnar, P., 1998. Paleobotanical evidence of Eocene and Oligocene paleoaltitudes in midlatitude western North America. *Geological Society of America Bulletin*, 110, 664–678, doi: 10.1130/0016-7606(1998)110<0664:PEOEAO>2.3.CO;2.
- Wright, J.C., Shawe, D.R. and Lohman, S.W., 1962. Definition of members of Jurassic Entrada Sandstone in east-central Utah and west-central Colorado. *Bulletin of the American Association of Petroleum Geologists*, 46, 205 –2070.

Appendices

Hardcopy:

- *Wilson, P.I.R. and McCaffrey, K.J.W., 2013. Intrusion space problem: digital mapping and analysis of the Maiden Creek satellite intrusion, Henry Mountains Utah. Geoscientist, 23 (6), 16–19.*

List of Digital Appendices:

Disk 1:

- *Glossary of Laccolith/ Sill terminology (after Corry, 1988)*
- *Regional Structural Data Table*
- *Trachyte Mesa Structural Data Table*
- *Maiden Creek Structural Data Table*
- *Sample Database*
- *Conference Presentations*

Disk 2:

- *Google Earth™ Project (kmz file)*
- *Terrestrial Laser Scan (TLS) Video Animations*
- *TLS methodology workflow*